UNIVERSIDAD NACIONAL AUTÓNOMA DE MEXICO

PROGRAMA DE MAESTRÍA Y DOCTORADO EN CIENCIAS QUÍMICAS

ÓXIDO DE GRAFENO Y NANOTUBOS DE CARBONO, EN FORMA DE POLVO Y PAPEL, DECORADOS CON NANOPARTÍCULAS DE PLATA Y PALADIO

TESIS

PARA OPTAR POR EL GRADO DE

DOCTORA EN CIENCIAS

PRESENTA

M. en C. DINORAH IVETTE RODRÍGUEZ OTAMENDI

ASESORAS

Prof. Dr. Elena Golovataya Dzhymbeeva (E.V. Basiuk)

INSTITUTO DE CIENCIAS APLICADAS Y TECNOLOGÍA (UNAM)

Prof. Dr. Petra Rudolf

ZERNIKE INSTITUTE FOR ADVANCED MATERIALS,
UNIVERSITY OF GRONINGEN

Ciudad de México, Enero 2025.

UNIVERSIDAD NACIONAL AUTÓNOMA DE MÉXICO

PROGRAMA DE MAESTRÍA Y DOCTORADO EN CIENCIAS QUÍMICAS

ÓXIDO DE GRAFENO Y NANOTUBOS DE CARBONO, EN FORMA DE POLVO Y PAPEL, DECORADOS CON NANOPARTÍCULAS DE PLATA Y PALADIO

TESIS

PARA OPTAR POR EL GRADO DE

DOCTORA EN CIENCIAS

PRESENTA

M. en C. DINORAH IVETTE RODRÍGUEZ OTAMENDI

ASESORAS

Prof. Dr. Elena Golovataya Dzhymbeeva

INSTITUTO DE CIENCIAS APLICADAS Y TECNOLOGÍA (UNAM)

Prof. Dr. Petra Rudolf

ZERNIKE INSTITUTE FOR ADVANCED MATERIALS
UNIVERISTY OF GRONINGEN

Ciudad de México, 2025.

Comité Tutor

Dr. Epifanio Cruz Zaragoza
Dr. Alfonso Ramón García Márquez

Comité Evaluador

Presidente	Dr. José Manuel Saniger Blesa
Vocal	Dra. Larissa Alexandrova
Vocal	Dr. Ernesto Rivera García
Vocal	Dra. Mildred Quintana Ruiz
Secretario	Dr. Epifanio Cruz Zaragoza

Graphene Oxide and Carbon Nanotubes in Powder and Paper Form, Decorated with Silver and Palladium Nanoparticles

PhD thesis

to obtain the degree of PhD at the
University of Groningen
On the authority of the
Rector Magnificus Prof. J.M.A. Scherpen
and in accordance with
the decision by the College of Deans

and

to obtain the degree of PhD of the
Universidad Nacional Autónoma de México
on the authority of the
Rector Dr. L. Lomelí Vanegas
and in accordance with
the decision of the Assessment Committee of the
Master and Doctoral Program of Chemical Sciences

Double PhD degree

This thesis will be defended in public on

Tuesday 18 February 2025 at 16;15 hours

by

Dinorah Ivette Rodríguez Otamendi

born on 07 August 1989
in Mexico City, Mexico

Supervisors

Prof. E. Golovataya Dzhymbeeva (E.V. Basiuk)
Prof. P. Rudolf

Assessment Committee

Prof. E. Rivera Garcia
Prof. D. Gournis
Dr G.F. Schneider
Prof. B.J. Kooi

UNIVERSIDAD NACIONAL AUTÓNOMA DE MÉXICO
UNAM POSGRADO Ciencias Químicas
ICAT Instituto de Ciencias Aplicadas y Tecnología
CONAHCYT CONSEJO NACIONAL DE HUMANIDADES CIENCIAS Y TECNOLOGÍAS

university of groningen / faculty of science and engineering / zernike institute for advanced materials

GRAPHENE OXIDE AND CARBON NANOTUBES IN POWDER AND PAPER FORM, DECORATED WITH SILVER AND PALLADIUM NANOPARTICLES

M.Sc. Dinorah Ivette Rodriguez Otamendi
PhD thesis
Universidad Nacional Autónoma de México
University of Groningen

This work was performed in the Laboratory of Bionanotechnology of the Institute of Applied Sciences and Technology (Instituto de Ciencias Aplicadas y Tecnología-ICAT), in the National Autonomous University of Mexico (México), and the Surfaces and Thin Films Group of the Zernike Institute of Advanced Materials, in the University of Groningen (the Netherlands), under the supervision of Prof. Dr. Elena Golovataya Dzhymbeeva, and Prof. Dr. Petra Rudolf, respectively. The Universidad Nacional Autónoma de México founded this project (UNAM, grant DGAPA-IN100821, CONAHCyT (Consejo Nacional de Humanidades, Ciencias y Tecnologías), and the University of Groningen (RUG).

Printed by: **Proefschrift Maken (NL)**
Cover design by: **Dinorah Ivette Rodriguez Otamendi** and **Eduardo Alain Rodríguez Otamendi**. The cover picture represents the feasible real-life applications of the newly formed advanced materials.
Zernike Institute for Advanced Materials. PhD thesis series number: 2025-02.
ISSN 1570-1530.

AGRADECIMIENTOS

Primeramente, a la Universidad Nacional Autónoma de México (UNAM, así como a Programa de Maestría y Doctorado en Ciencias Químicas. En segundo lugar, al Instituto de Ciencias Aplicadas y Tecnología (ICAT), por el acceso a la infraestructura requerida para llevar a cabo el presente trabajo de investigación. De igual manera, a la Universidad de Groningen en Países Bajos, por permitirme formar parte del Programa de Doble Grado con la UNAM, así como a la Facultad de Ciencia e Ingeniería (FSE) y al Instituto Zernike de Materiales Avanzados (ZIAM) para completar el desarrollo experimental del proyecto doctoral.

Al Consejo Nacional de Humanidades, Ciencias y Tecnologías (CONAHCYT) por la asignación de una beca nacional 2020 para formación a nivel posgrado, en modalidad doctorado (N° de CVU: 843540). A la Dirección General de Asuntos de Personal Académico por los recursos otorgados a través del proyecto UNAM-DGAPA-IN100821. Al Programa de Investigación de Materiales Avanzados del Zernike National Research Centre bajo el Plan de Incentivos de Bonificación (BIS, por sus siglas en inglés) del Ministerio holandés de Educación, Cultura y Ciencia por la beca otorgada durante mi estancia en Países Bajos, así como el apoyo financiero en la participación de conferencias nacionales e internacionales.

A nivel técnico, al Laboratorio Universitario de Caracterización Espectroscópica (LUCE) en el ICAT y a la Dra. Selene Rubí Islas Sánchez por su apoyo en las mediciones de espectroscopía Infrarroja. Al Dr. Edgar Álvarez Zauco por su asistencia en la obtención de curvas de Análisis termogravimétrico dentro de las instalaciones de la Facultad de Ciencias. Al Dr. Víctor Hugo Meza Laguna por su asistencia para la toma de micrografías por SEM y análisis EDS en las instalaciones del Instituto de Ciencias Nucleares (ICN). A la Dra. Moserrat Bizarro Sordo por el acceso a las instalaciones del Instituto de Investigaciones en Materiales (IIM), así como al Dr. Josué Esaú Romero-Ibarra por su apoyo en la toma de micrografías por TEM. En la Universidad de Groningen, al Dr. Dominic Gerlach por la capacitación en el uso y manejo de XPS, así como al Ing. Jacob Baas por el entrenamiento en el uso de XRD en polvo. De forma especial al Dr. Vladimir Bassiouk Endokimenko por sus valiosas aportaciones y sugerencias en el transcurso del proyecto de investigación.

A los miembros de mi Comité Tutor en la UNAM, Dr. Epifanio Cruz Zaragoza y Dr. Alfonso Ramon García Márquez por sus valiosas contribuciones y consejos a lo largo de cada evaluación semestral.

A los sinodales, miembros de jurado de mi examen doctoral, los Dres: José Manuel Saniger Blesa, Larissa Alexandrova, Ernesto Rivera García, Epifanio Cruz Zaragoza, y Mildred Quintana Ruiz por su dedicación y retroalimentación hacia mi trabajo doctoral.

Finalmente, a mis supervisoras, Prof. Dr. Elena Golovataya Dzhymbeeva y Prof. Dr. Petra Rudolf por permitirme formar parte de los grupos de investigación de Sustratos Nanoestructurados y Superficies y Películas Delgadas, en las respectivas entidades académicas, así como por su continua mentoría, dedicación y conocimientos compartidos para la planeación y desarrollo del presente trabajo de investigación.

To my family and beloved people...

To Mexico and The Netherlands...

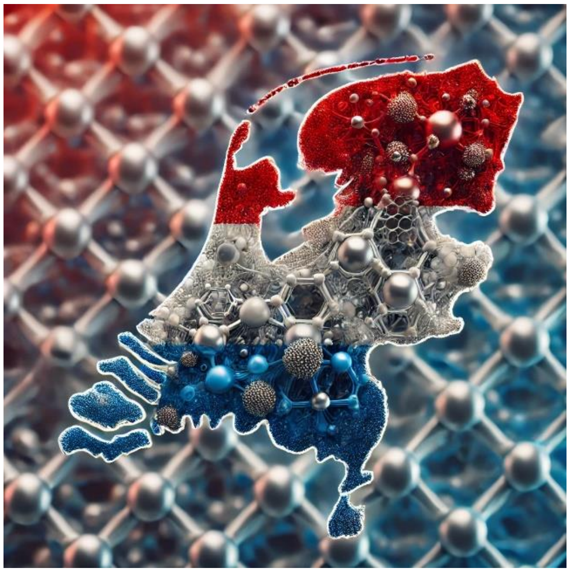

TABLE OF CONTENTS

LIST OF ACRONYMS

Ag_{13}	Cluster composed of thirteen Ag atoms
AgNC	Silver nanocluster
AgNPs	Silver nanoparticles
ATR	Attenuated total reflectance
BE	Binding energy
BEC	Backscattered electron composition micrographs
BF	Bright-field imaging
BP	Buckypaper
BP+Ag	Buckypaper containing silver nanoparticles
BP+DAO	Buckypaper functionalised with 1,8-diaminooctane
BP+DAO+Ag	Buckypaper functionalised with 1,8-diaminooctane and containing silver nanoparticles
BP+DAO+Pd	Buckypaper functionalised with 1,8-diaminooctane and containing palladium nanoparticles
BP+ODA	Buckypaper functionalised with 1-octadecylamine
BP+ODA+Ag	Buckypaper functionalised with 1-octadecylamine and containing silver nanoparticles
BP+ODA+Pd	Buckypaper functionalised with 1-octadecylamine and containing palladium nanoparticles
BP+Pd	Buckypaper containing palladium nanoparticles
CNSMs	Carbon nano-structured materials
CNTs	Carbon nanotubes
CVD	Chemical vapour deposition
DAO	1,8-diaminooctane
DF	Dark-field imaging
DFT	Density functional theory

DNP	Double numerical basis set
DTA	Differential thermal analysis
EDS	Energy-dispersive X-ray spectroscopy
EELS	Electron energy-loss spectroscopy
fcc	Face-centred cubic structure
FTIR	Fourier transform infrared spectroscopy
FWHM	Full width at half maximum
GO	Graphene oxide
GO+Ag	Graphene oxide containing silver nanoparticles
GO+Ag_{13}	Graphene oxide complex holding a Ag_{13} cluster
GO+DAO	Graphene oxide functionalised with 1,8-diaminooctane
GO+DAO+Ag	Graphene oxide functionalised with 1,8-diaminooctane and containing silver nanoparticles
GO+DAO+Pd	Graphene oxide functionalised with 1,8-diaminooctane and containing palladium nanoparticles
GO+DAO-$4H^+$	Protonated graphene oxide functionalised with 1.8-diaminooctane
GO+DAO-$4H^+$+Ag_{13}	Protonated graphene oxide complex functionalised with 1.8-diaminooctane holding a Ag_{13} cluster
GO+DAO-$4H^+$+Pd_{16}	Protonated graphene oxide complex functionalised with 1.8-diaminooctane holding a Pd_{16} cluster
GO+ODA	Graphene oxide functionalised with 1-octadecylamine
GO+ODA+Ag	Graphene oxide functionalised with 1-octadecylamine and containing silver nanoparticles
GO+ODA+Ag_{13}	Graphene oxide complex functionalised with 1-octadecylamine holding a Ag_{13} cluster
GO+ODA+Pd	Graphene oxide functionalised with 1-octadecylamine and containing palladium nanoparticles
GO+ODA+Pd_{16}	Graphene oxide complex functionalised with 1-octadecylamine holding a Pd_{16} cluster
GO+Pd	Graphene oxide containing palladium nanoparticles

GO+Pd_{16}	Graphene oxide complex holding a Pd_{16} cluster
GOP	Graphene oxide paper
GOP+Ag	Graphene oxide paper containing silver nanoparticles
GOP+DAO	Graphene oxide paper functionalised with 1,8-diaminooctane
GOP+DAO+Ag	Graphene oxide paper functionalised with 1,8-diaminooctane containing silver nanoparticles
GOP+DAO+Pd	Graphene oxide paper functionalised with 1,8-diaminooctane containing palladium nanoparticles
GOP+ODA	Graphene oxide paper functionalised with 1-octadecylamine
GOP+ODA+Ag	Graphene oxide paper functionalised with 1-octadecylamine containing silver nanoparticles
GOP+ODA+Pd	Graphene oxide paper functionalised with 1-octadecylamine containing palladium nanoparticles
GOP+Pd	Graphene oxide paper containing palladium nanoparticles
HAADF	High-Angle Annular Dark-Field
HOMO	Highest Occupied Molecular Orbital
HRTEM	High-Resolution Transmission Electron Microscopy
I.R.	Intensity ratio
IR	Infrared
LUMO	Lowest Unoccupied Molecular Orbital
M.R.	Mixing ratio
MNPs	Metallic nanoparticles
MWCNTs	Multiwalled carbon nanotubes
MWCNTs$_{(ox)}$	Oxidized multiwalled carbon nanotubes
MWCNTs+Ag	Oxidized multiwalled carbon nanotubes containing silver nanoparticles
MWCNTs+DAO	Oxidized multiwalled carbon nanotubes functionalised with 1,8-diaminooctane

MWCNTs+DAO+Ag	Oxidized multiwalled carbon nanotubes functionalised with 1,8-diaminooctane containing silver nanoparticles
MWCNTs+DAO+Pd	Oxidized multiwalled carbon nanotubes functionalised with 1,8-diaminooctane containing palladium nanoparticles
MWCNTs+ODA	Oxidized multiwalled carbon nanotubes functionalised with 1-octadecylamine
MWCNTs+ODA+Ag	Oxidized multiwalled carbon nanotubes functionalised with 1-octadecylamine containing silver nanoparticles
MWCNTs+ODA+Pd	Oxidized multiwalled carbon nanotubes functionalised with 1-octadecylamine containing palladium nanoparticles
MWCNTs+Pd	Oxidized multiwalled carbon nanotubes containing palladium nanoparticles
NPs	Nanoparticles
ODA	1-octadecylamine
PBE	Perdew-Burke-Ernzerhof functional
PBE-D2	Perdew-Burke-Ernzerhof functional with Long-Range Dispersion Correction
Pd_{16}	Cluster composed of sixteen Pd atoms
PdNPs	Palladium nanoparticles
SEI	Secondary electron images
SEM	Scanning electron microscope
STEM	Scanning transmission electron microscopy
SWCNTs	Single-walled carbon nanotubes
TEM	Transmission electron microscopy
TGA	Thermogravimetric analysis
XPS	X-ray photoelectron spectroscopy
XRD	X-ray diffraction

CHAPTER 1

Introduction

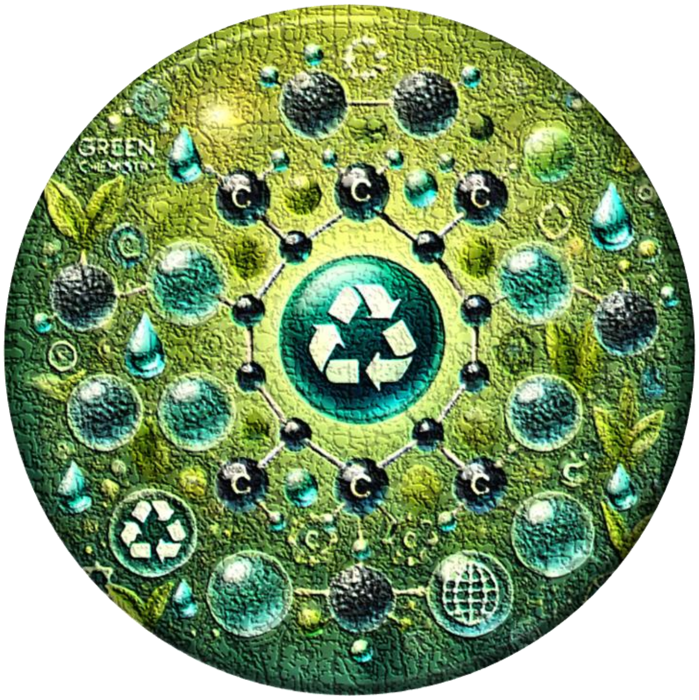

ABSTRACT

This chapter provides a general introduction to Green Chemistry and the materials used in this project: graphene oxide, carbon nanotubes, and silver and palladium nanoparticles. Then, details of the motivation for this research are presented. Finally, the chapter concludes with a short summary of the main results and highlights of each chapter.

1.1. Green chemistry

Nanotechnology has emerged as one of the most transformative advancements in the past 50 years, driving innovation across a wide range of fields by enabling the development of nanomaterials with precise size, shape, and functionality. However, conventional synthesis methods for these nanomaterials often face significant environmental challenges, including generating hazardous by-products and consuming non-renewable resources. In response to these concerns, green synthesis approaches have gained substantial attention as a more sustainable alternative.[1]

The integration of green chemistry principles into nanotechnology is not just a trend but a necessity for the future development of nanomaterials. By employing green synthesis techniques, it is possible to minimize the formation of harmful by-products. including the use of plant extracts, microorganisms, microwave heating, and ultrasound, are being explored to create ***Green Chemistry***, which focuses on designing chemical products and processes that reduce or eliminate the use or generation of hazardous substances, plays a crucial role in this transition. It encompasses the entire life cycle of a chemical product, from its inception and manufacturing to its use and eventual disposal. The integration of green chemistry principles into nanotechnology is not just a trend but a necessity for the future development of nanomaterials. By employing green synthesis techniques, it is possible to reduce the environmental impact of nanomaterial production and minimize the formation of harmful by-products. Various green synthetic methods, including the use of plant extracts, microorganisms, microwave heating, and ultrasound, are being exploited to create nanomaterials in a more eco-friendly manner.[2]

The 12 Principles of Green Chemistry, established by Paul Anastas and John Warner,**[3]** and schematically presented in Fig. 1.1, serve as a guiding framework for the development of safer and more sustainable chemical processes. These principles emphasize waste prevention, atom economy, the use of less hazardous substances, energy efficiency, renewable feedstocks, and the design of chemicals that degrade harmlessly after use. They also advocate for real-time monitoring to prevent pollution and the minimization of accident risks during chemical processes. These principles are increasingly being applied to the field of nanotechnology to ensure that the environmental and safety concerns associated with nanomaterial synthesis are addressed from the outset.

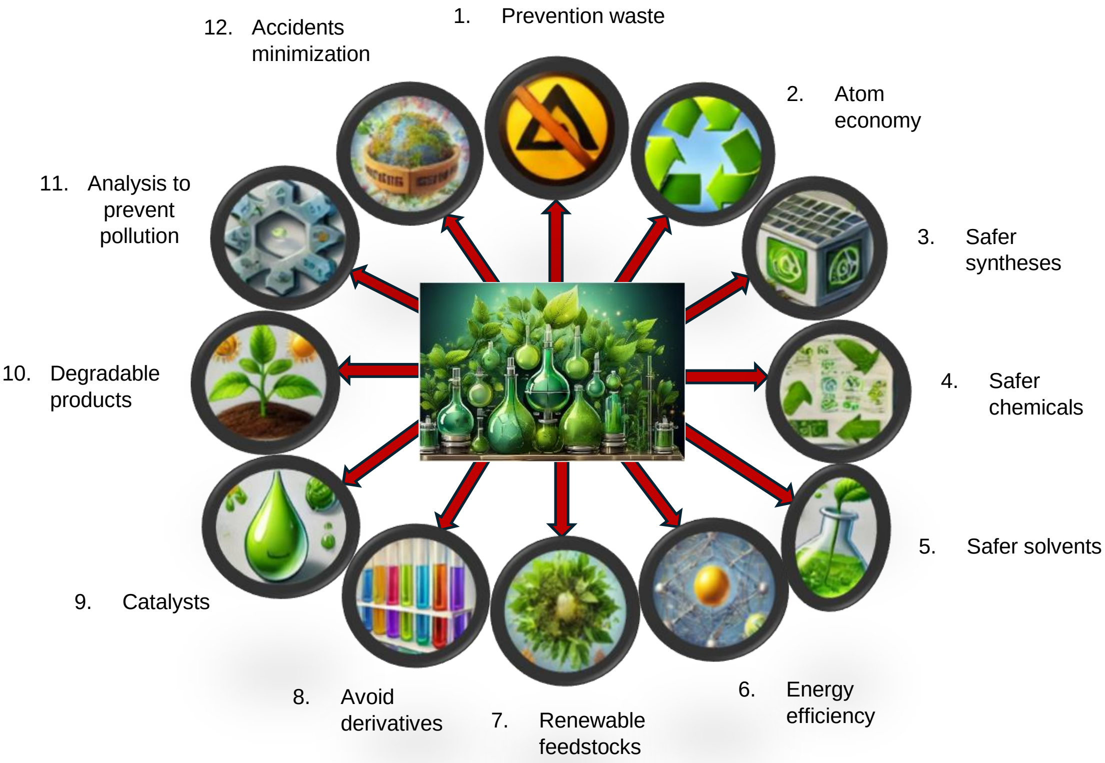

Fig. 1. 1. Principles of Green Chemistry proposed by Anastas and Warner.

1.2. Carbon materials

Carbon (C), the sixth element on the periodic table, is a Group XIV nonmetal with a unique ability to form a wide variety of chemical bonds. This is due to its four valence electrons, which allow it to bond with other small atoms, including other carbon atoms, to form stable covalent bonds.[4] Particularly, it can form long chains of strong and stable interconnected C-C bonds (concatenation). Carbon is the fourth most common element in the Universe and ranks fifteenth in the Earth's crust. The name "carbon" comes from the Latin word "carbo" which means *coal* or *charcoal*; it also derives from the French word "charbon" meaning *coal*.[5]

Carbon is present in nature in different allotropic forms (see Fig. 1.2), diamond, graphite, graphene, lonsdaleite, fullerenes, amorphous carbon and carbon nanotubes.[6,7] Each of these allotropes exhibits distinct physical and chemical properties, making carbon one of the most versatile elements. Of particular interest in the field of nanotechnology are graphene oxide (GO) and multiwalled carbon nanotubes (MWCNTs) which have gained prominence due to their exceptional mechanical, optical, thermal, electronic and magnetic properties.[8,9] These materials offer tremendous potential for a wide range of applications, from electronics and energy storage to biomedical devices and environmental remediation.

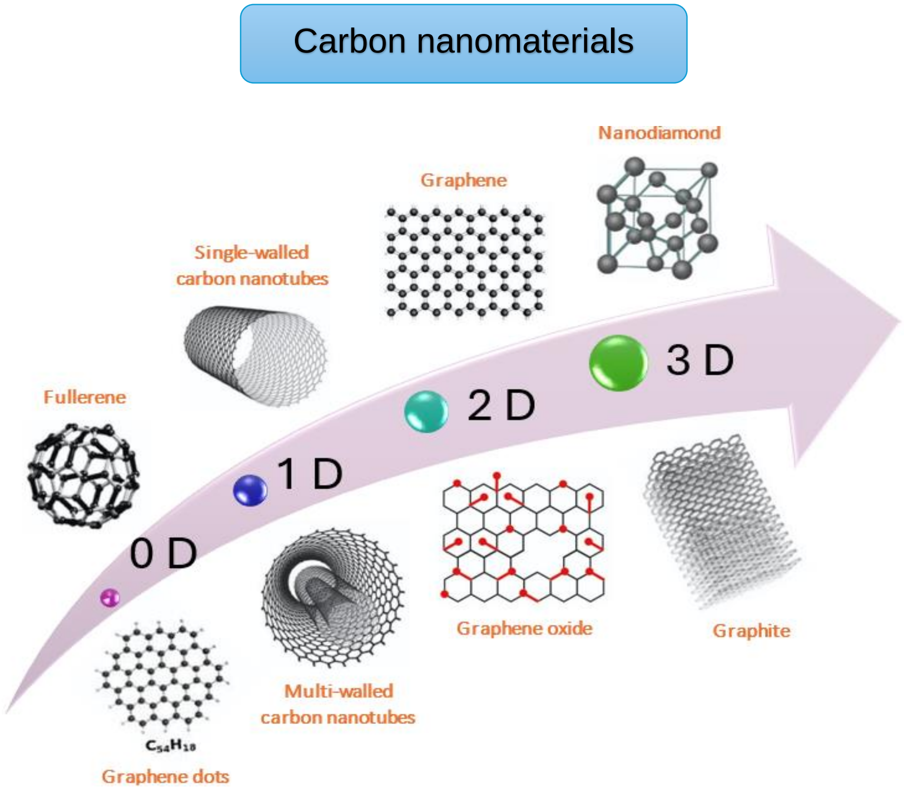

Fig. 1.2. Carbon allotropes in different dimensions

1.2.1. Graphene oxide

Graphene oxide (GO) is derived from graphite by introducing several oxygen-containing functional groups into its structure and like graphite, it can be exfoliated into a two-dimensional material. The oxygenated groups, often considered structural defects, are typically located on the edges (primarily carboxyl groups, –COOH) and on the basal planes (epoxide and hydroxyl groups, –OH), as sketched in Fig. 1.3. The degree of oxidation can vary, but in highly oxidized GO, the carbon-to-oxygen atomic ratio is approximately 2:1.[10]

The incorporation of oxygen atoms into the carbon framework transforms the hybridization of carbon atoms from sp^2 in the graphene matrix to sp^3 in the GO structure. This modification changes GO's electrical properties, converting it from a conductor to an insulator. Despite this, GO offers significant advantages over graphene, particularly in terms of its dispersibility and processability in various solvents, including water. These characteristics make GO a valuable component in numerous composites and hybrid materials.[8]

The "graphene era" began in 2004 with the work of Novoselov and Geim, which sparked renewed interest in GO. Initially, GO was viewed as a potential precursor to graphene, but it has since been recognized as a unique and interesting material in its own right. GO is produced from graphite by oxidation with strong oxidizing agents in a concentrated acid medium. Three main methods of GO preparation can be differentiated: the Brodie method[11], the Staudenmaier method[12], and the Hummers method.[13] The Brodie method involves using potassium chlorate ($KClO_3$) as an oxidizing agent in fuming nitric acid (HNO_3). The partially oxidized product of the first reaction is isolated, purified and subjected to further oxidation steps to achieve the desired level of oxidation. The Staudenmaier method uses $KClO_3$ in a mixture of concentrated nitric and sulfuric acids (HNO_3 and H_2SO_4). Hummers' method uses potassium permanganate ($KMnO_4$) as the oxidizing agent in $H_2SO_{4(conc)}$. This method is faster and more effective than the other methods, provided the graphite particles are sufficiently small. When large graphite flakes are used, a partially oxidized graphite-GO hybrid is obtained.[14]

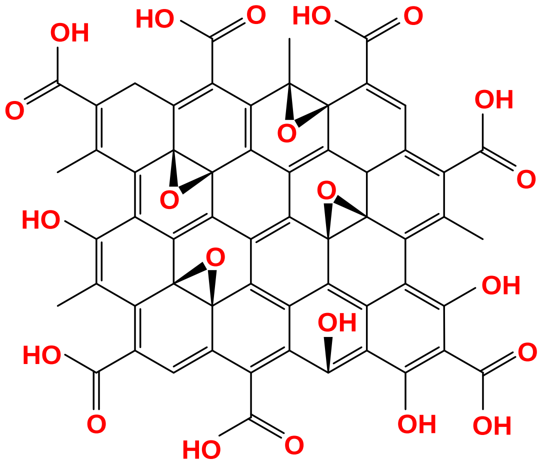

Fig. 1.3. Structure of the graphene oxide sheet.

1.2.2. Carbon nanotubes

Carbon nanotubes (CNTs) consist of rolled graphene sheets that form tubular structures. The topology is described by their chiral vector, the vector along the rolling direction that connects the centres of the two hexagons, which will overlap when the CNTs closes.[15] In the cylindrical structure this vector therefore becomes the circumference of the nanotube. Possessing different diameters and lengths, one way to classify them is based on their chiral vector; three types are distinguished, as shown in Fig. 1.4:

1. Zigzag. The graphene sheet is rolled so that the ideal edges of the open tube are zigzag-shaped.

2. Armchair. The graphene sheet is rolled and rotated 30° relative to the zigzag configuration, resulting in an armchair-shaped edge.

3. Chiral. The graphene sheet is rotated at an angle between 0° and 30°, producing a structure that is intermediate between zigzag and armchair.

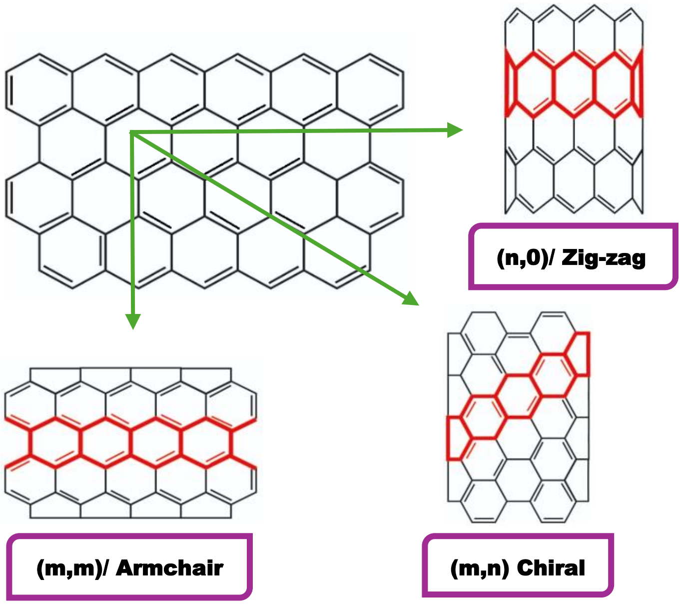

Fig. 1.4. Classification of nanotubes according to their chiral vector: armchair, chiral, and zigzag.

The CNTs can be opened or closed at their ends. Open-ended CNTs often have functional groups attached to the terminal carbon atoms or may feature free bonds, while closed CNTs have fullerene-like caps at their ends (Fig. 1.5). Structural defects in CNTs as reactive sites and can be classified into several categories: [15]

- Topological defects: pentalenes (5-carbon cycles with adjacent double bonds causing curvature).
- Unsaturated bonds resulting from vacancies, displacements, and other disruptions in the carbon lattice.
- Chemical defects caused by covalent bonding of atoms or molecules to the carbon network.

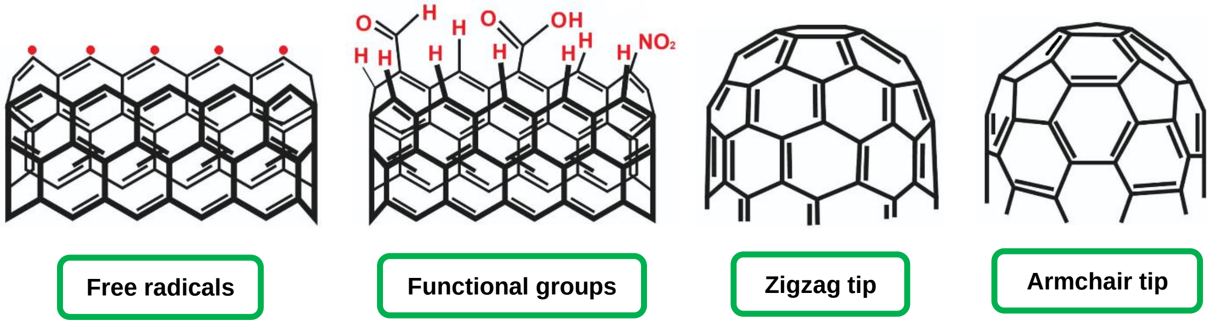

Fig. 1.5. Different types of CNT terminations: free bonds, functional groups at the ends, zigzag CNT tips, and armchair CNT tips.

CNTs exist as *Single-Walled Carbon Nanotubes* (SWCNTs), which have the simplest geometry, with diameters from 0.4 to 3 nm, and *Multi-Walled Carbon Nanotubes* (MWCNTs).[16] The latter consists of several concentric SWCNTs with diameters ranging from 2 to 100 nm.[17] MWCNTs have two advantages over SWCNT, a greater rigidity due to their multi-layer structure, plus offering more possibilities for large-scale production.[9] MWCNTs usually exhibit metallic behaviour and possess unique ballistic conduction properties.[18,19] There are two main synthesis methods for carbon nanotubes: sublimation of graphite with subsequent condensation, and decomposition of carbon-containing compounds. The first group of methods requires very high temperatures (up to 4000 °C), achievable through techniques like electric arcs, laser ablation process, solar radiation or resistive heating of graphite.[20-23] The arc discharge method was the first technique utilised for the synthesis of carbon filaments and fibres. The second group includes methods such as chemical vapour deposition (CVD), polymer pyrolysis, and hydrothermal synthesis from aqueous or organic solutions (supercritical toluene).[22] Among these, CVD is the most widely used technique to manufacture CNTs on an industrial scale due to its relative simplicity and efficiency, typically operating at temperatures between 500 to 1300 °C.[24] More recent methods such as electron/ion beam irradiation, flame synthesis, pyrolysis, electrolysis, template methods, and solar approaches have been employed as well. All these methods allow for the synthesis of moderately high quantities of CNTs with a relatively precise number of layers.[24]

Despite their remarkable properties, CNTs pose challenges in terms of manipulation due to their low reactivity. To enhance their processability, oxygenated groups can be introduced into their structure through chemical oxidation. This process involves treating CNTs with a mixture of acids (HNO_3 and $H_2SO_{4(conc)}$ generally), which opens the ends of the tubes, creates holes in the walls and shortens their length. The oxidized CNTs (referred as $CNTs_{(ox)}$) contain primarily –COOH and –OH groups at their ends and walls, providing reactive sites for further functionalization.[25]

1.3. Functionalization of nano-structured carbon

Incorporating new functional groups into carbon nano-structured materials (CNSMs) allows us to modulate their properties to suit multiple applications. For carbon nanotubes, this functionalization can be applied to the tips and/or walls, while for graphene oxide it can be targeted at the planes or edges.[26] As illustrated in Fig. 1.6, both covalent grafting of molecules and ligand-capped nanoparticles and non-covalent attachment, also of very long polymers, is possible.

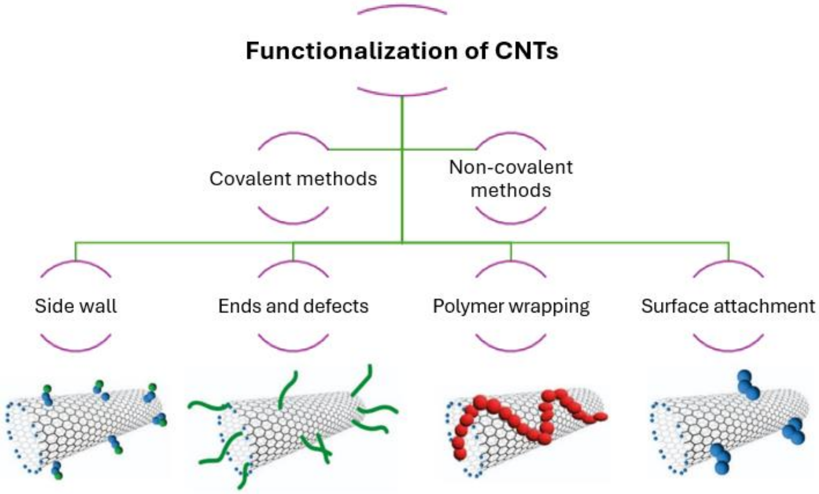

Fig. 1.6. Functionalization methods of carbon nanotubes.

The *solventless gas-phase functionalization* method proposed by Basiuk *et al.* (2002)[28,29] and illustrated in Fig. 1.7, has enabled the chemical modification of CNSMs such as CNTs, GO, highly ordered pyrolytic graphene, fullerenes and nanodiamonds with organic macrocycles, thiols and amines. This procedure requires controlled thermal activation at reduced pressure to generate precursor vapours to which the carbonaceous material is exposed. Under these conditions, the functionalizing molecules must have a high thermal stability and low vapour pressure to easily volatilise at temperatures between 150 – 200 °C.[30,31] One advantage of this method is that it does not require additional purification processes, as excess and unreacted reagents are removed *in situ* under dynamic vacuum and heating, apart from relatively short reaction times, in comparison to other functionalization techniques.[26,28-32] Therefore, this approach represents a rapid, efficient, eco-friendly and non-invasive alternative for the modification of CNSM properties.

1.3.1. Covalent functionalization of GO and CNTs. Advantages of amine-functionalization

Since carboxylic acids are the predominant oxygenated groups present in the structure of GO and oxidized CNTs, covalent functionalization typically occurs *via* amide-formation. This involves condensation reactions between amino groups of the amines and carboxylic groups on the edges of GO and ends and walls of carbon nanotubes.[10,25] To a lesser extent, covalent functionalization can also occur *via* the epoxide ring-opening addition of amine moieties onto the edges and basal planes of GO.[33] Non-covalent attachment of $-NH_2$ groups to defect sites on CNTs is also possible.[34] Amine functionalization increases the organic affinity and enhances biocompatibility, solubility and selectivity.[35] In the case of GO, functionalization can modulate its electronic structure, thereby, varying its conductivity. In MWCNTs functionalization preserves their electronic structure while introducing new superficial features, thus expanding their range of applications.[36-38]

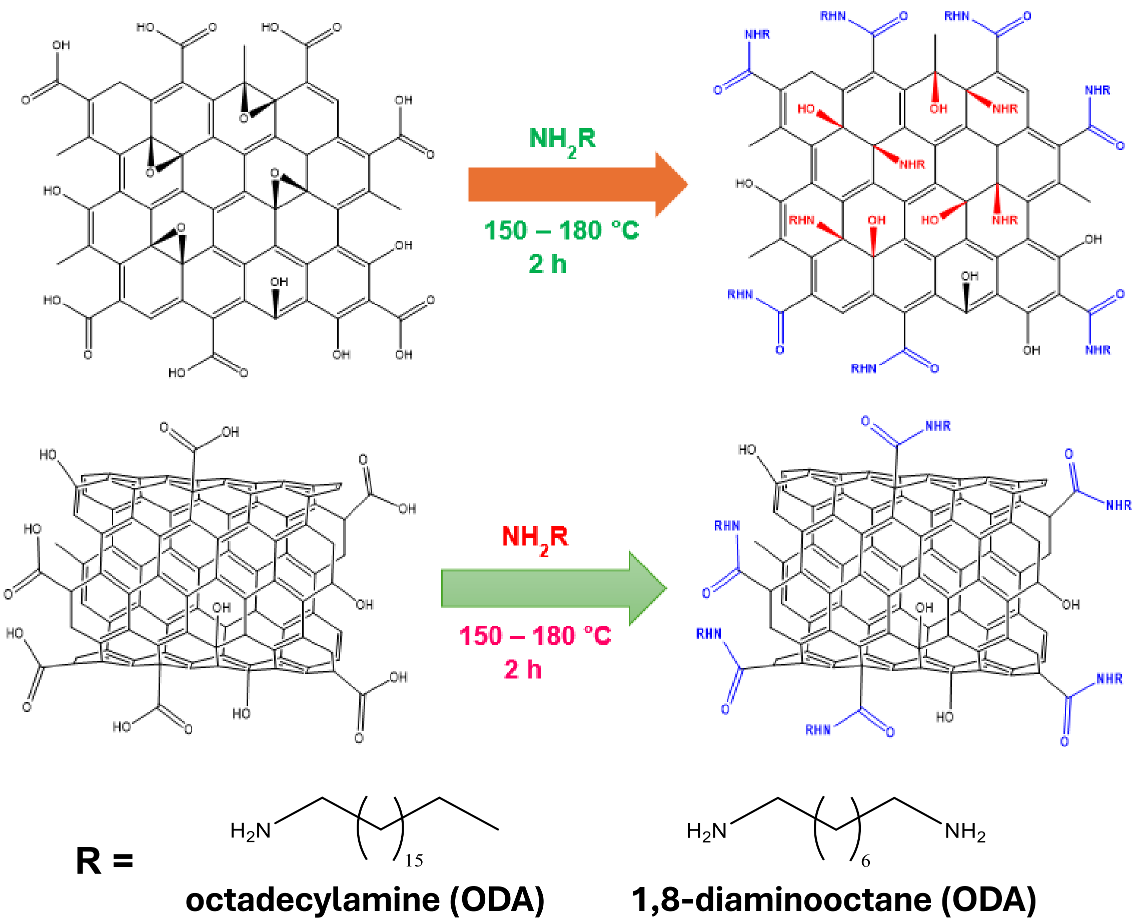

Fig. 1.7. Reaction scheme of the one-step solvent-free functionalization method proposed by Basiuk *et al*. (2002) for GO and MWNCTs.

1.3.2. Paper-like structures

The research and development of macroscopic lamellar structures known as “paper”, relatively simple to manipulate, facilitates a thorough exploration of their properties and applications in various fields, like energy conversion, advanced engineering materials, purification, and antimicrobial agents, among others.[39-43] Two main structures are being widely studied within the scientific community: *graphene oxide paper* - known as GOP- and *buckypaper* (better known as BP) made from carbon nanotubes. The assembly of either GO sheets or carbon nanotubes is possible due to Van der Waals forces[44] and hydrogen bonds between adjacent functional groups, exhibiting outstanding tensile strength, flexibility, and stiffness.[41,45,46] aimed to develop new thermal and electrical materials, catalyst, filtration, membranes, sensors, transmitters, flame retardants, etc.[47-51]

GOP can be formed from aqueous GO dispersions through methods like vacuum-directed filtration, where the GO sheets stack on the membrane and are smoothed by the directed water flow or through evaporation, where the loss of water drives the assembly of the final macroscopic structure.[41,45] On the other hand, the properties of BP are determined by the nature of CNTs (purity, number of walls, length, diameter, morphology, etc.), which can be modulated by applying different experimental approaches, including covalent functionalization.[31,52,53] BP can be also prepared by vacuum filtration like GOP but here the starting product is an aqueous CNT dispersion, prepared by using surfactants and ultrasonication.[54] Undispersed waste is removed by centrifugation. The final dispersion is filtered through a membrane using a vacuum pump to have a directed flow. The resulting foil is cleaned with distilled water to remove surplus surfactant. Alternative methods for BP fabrication include frit compression[54] and domino compression[55], which are not described in detail because they were not applied in the projects described in this dissertation. Variants of BPs prepared with SWCNTs and MWCNTs were found to be permeable to common gases such as oxygen, nitrogen, CO_2, and methane.[56-58]

1.4. Nanoparticles

Nanoparticles (NPs) are intrinsically meta-stable, tending to disintegrate under conventional chemical processes or to aggregate to decrease their surface tension, which can diminish their catalytic activity, limiting their practical applications.[59] One way to favour their stabilization implies using adequate supports.[60-62]Although various materials, such as aluminium, silica, metal oxides and double-layer hydroxides, have been investigated as supports, carbon nanostructures are increasingly favoured because of their superior mechanical, chemical and thermal properties. In addition to conferring stability to the NPs, CNSMs also provide a greater contact area between the reagents in a chemical process and heterogeneous catalysis. Precise selection of suitable supports and stabilising agents allows for modulation of the resulting nanomaterials' characteristics.[63,64]

1.4.1. Synthesis and deposition of metallic nanoparticles

Specifically, metallic nanoparticles (MNPs) are greatly interesting due to their unique properties such as high surface area, high stability, easy processing, and narrow size distribution (1 – 100 nm), which, together with their ability to give rise to plasmonic resonances, are particularly significant for applications in medicine, catalysis, waste treatment, etc. Their most important characteristic is the surface-to-volume ratio.[65-67]

In the liquid-phase chemical synthesis of metallic nanoparticles (MNPs), various precursors are used, including complexes like $HAuCl_4$ and H_2PtCl_6 and inorganic salts, such as $RhCl_3$ and $PdCl_2$. Common reducing agents are citric acid and its salts, sodium and potassium tartrate, formaldehyde, methanol, hydroxylamine hydrochloride, sodium borohydride ($NaBH_4$), hydrogen peroxide (H_2O_2), glucose, carbon monoxide (CO), and hydrogen (H_2). Stabilizing agents such as polyvinyl alcohol (PVA), and polyvinylpyrrolidone (PVP) are also employed.[68-70]

Covalent functionalization is important in this context, as it ensures a stronger bonding of MNPs to the external surface of CNSMs. Oxygenated groups (–OH, –COOH and –C=O mainly) and newly formed functionalities can act as stable anchorage sites, promoting uniform nucleation of MNPs through coordination binding or electrostatic interactions with ions.[25,71]

1.4.2. Advantages of metallic nanoparticles

Oxides of metals like Mn, Ni, Cu, Co and Ag have been studied extensively as electrode materials, showing promising results. However, their poor electrical conductivity can have a negative effect on the specific capacity and recycling stability. Combining these materials with metallic species is expected to yield synergistic properties, resulting in improved capacitive performance and functionality.[72-75]

Noble metals, due to their relative inertness, are particularly interesting for technological applications. They possess excellent catalytic, electronic, magnetic, optical and mechanical properties.[76-78] Studies have shown that noble metal-based materials can enhance the specific capacitance, improve conductivity and impart thermal and chemical stability to electrode and supercapacitor materials. Therefore, including noble-metal nanomaterials in electrodes is expected to lead to better conductivity and greater specific capacitance by forming channels that facilitate electron transfer during charging/discharge cycles.[79-81] In nanotechnology, metals such as gold, silver and palladium are emerging as the most promising bioengineering materials, particularly in the design of diagnostic tools, and devices for the treatment of diseases and drug delivery.[82-86]

1.4.2.1. Silver

Silver is of particular interest due to its unique combination of biocompatibility, high electrical conductivity, and outstanding electrocatalytic activity. Its physical, chemical and electronic properties have become increasingly important in areas such as chemistry, physics, biology, medicine and material science,[87-89] and is an essential material for applications in energy storage, surface-enhanced Raman spectroscopy and catalysis. Among the precious metals, silver is preferred for its lower cost compared to other metals. Recently, silver nanoparticles (AgNPs) have been used as conductive dopants in electrode materials for lithium-ion batteries and supercapacitors.[90-92] Furthermore, silver's historical use as a microbial and antiviral agent continues to evolve; in ancient times, AgNPs-based compounds were applied to treat wound infections,[93] and today, silver-based creams like "Ag-sulfadiazine" are used for treating deep wounds.[94] The magnetic, transparent and electronic properties of AgNPs are also harnessed to control microbial activity.[95-97] The properties of silver are summarised in Table 1. Its electronic and crystal structure are shown in Fig. 1.8.

Table 1. Properties of silver[98]

General properties	Crystal structure
Atomic number: 47	**Space group:** Fm-3m
Atomic weight: 107.9	**Space group number:** 225
Atomic radius: 172 pm (Van der Waals)	**Structure:** ccp (cubic close-packed)
Electron configuration: $[\mathrm{Kr}]5s^1 4d^{10}$	
Oxidation states: -2,-1, 1,2,3 (an amphoteric oxide)	

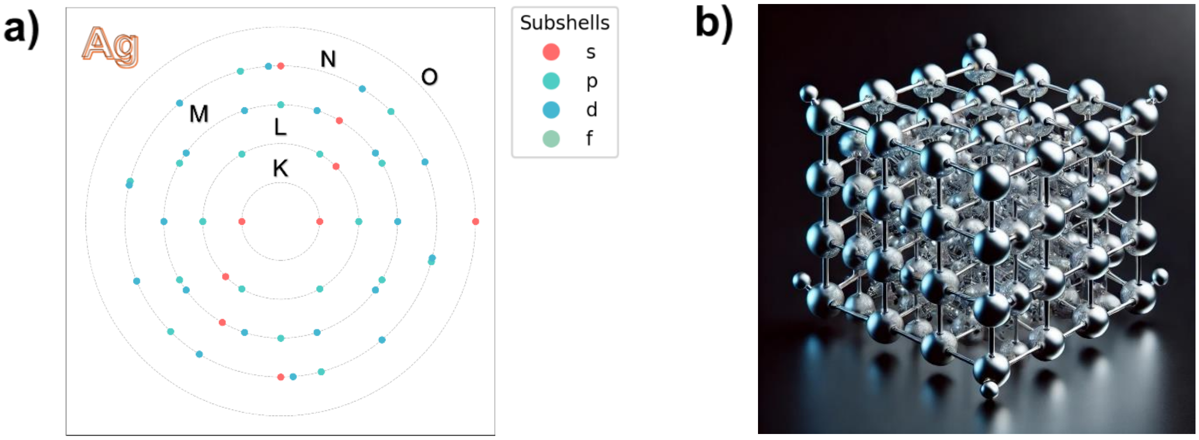

Fig. 1.8. a) The Kossel shell structure of silver. b) Silver crystal structure image.

1.4.2.2. Palladium

Palladium is a lustrous, steel-white metal that remains unaffected by tarnishing in atmospheric conditions. At ambient temperature, it can absorb hydrogen up to 900 times its own volume. When heated, hydrogen can easily permeate through it, facilitating gas purification processes. While bulk Pd is utilized in the production of precision instruments such as watch components and surgical implements[99], Pd nanoparticles are recognized for their remarkable electronic, mechanical, and catalytic properties[100,101]. These nanoparticles exhibit high reactivity in various chemical reactions, including hydrogenation, oxidation, and carbon-carbon coupling[102-104]. Furthermore, Pd is noted for its excellent selectivity, minimal toxicity, and robust thermal stability.[103,105,106] In the field of medicine, palladium-based materials are employed for therapeutic applications, showcasing notable antibacterial and cytotoxic effects.

In addition, Pd nanoparticles have shown great promise in fuel cell applications, offering enhanced activity and durability compared to traditional Pt-based catalysts.[107-109] Recently, they have also been explored for sensors, antibacterial coatings, and cytotoxic activity.[110-112] The properties of palladium are summarised in Table 2. Its electronic and crystal structure are shown in Fig. 1.9.

Table 2. Properties of palladium[98]

General properties	Crystal structure
Atomic number: 46	**Space group:** Fm-3m
Atomic weight: 106.4	**Space group number:** 225
Atomic radius: 202 pm (Van der Waals)	**Structure:** ccp (cubic close-packed)
Electron configuration: $[\mathrm{Kr}]4d^{10}$	
Oxidation states: 0,+1,+2,+3,+4 (a mildly basic oxide)	

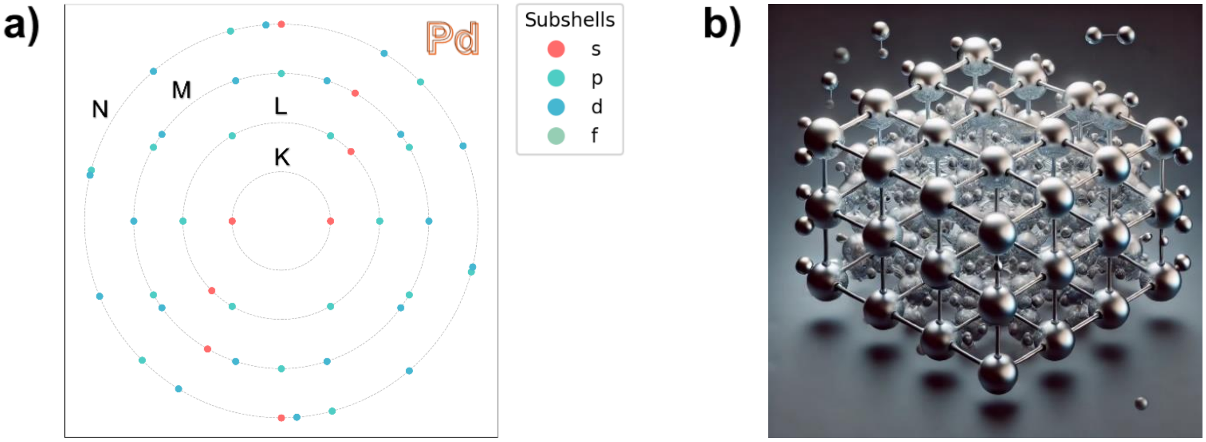

Fig. 1.9. a) The Kossel shell structure of palladium. b) Palladium crystal structure image.

1.5. Synthesis of hybrid materials

Hybrid materials can be synthesised *via ex-situ* and *in-situ* methods. The *ex-situ* approach involves the separate preparation of inorganic components followed by their bonding to the carbonaceous surface. In contrast, the *in-situ* method synthesises inorganic components in the presence of carbon material, leading to the growth of particles or thin films directly on the carbon surface.[113-115] Both approaches can be realised *via* diverse routes, among which solar-gel and hydrothermal reactions are particularly attractive due to their simplicity and because they require only low temperatures.

Combining the properties of metallic nanoparticles and CNSMs, hybrid structures find suitable applications in electronics, catalysis, electrochemical biosensing, drug delivery, antimicrobial agents, and purification systems,[116-122] (Fig. 1.10) attacking some water and air pollution problems, as well as recycling. Concurrently, they are considered the most promising emerging trend in biomedical applications,[123] involving biocompatibility, cellular specificity, and high availability for disease diagnostics, drug delivery, cancer treatments, and bioimaging.[99] Particularly in biomedicine, studies on nanocomposites containing silver have demonstrated a direct relationship between silver nanoparticle size and antimicrobial and/or catalytic activity, such that particles smaller than 10 nm displayed higher bactericidal activity by increasing surface area and enhancing cellular penetration.[124,125]

1.5.1. Wet impregnation

Wet impregnation is a widely used method for synthesizing hybrids of carbonaceous materials and metal nanoparticles. It involves the chemical reduction of metal salts in the liquid phase, with stabilizing and dispersing agents employed to prevent MNP agglomeration, thereby controlling their size and morphology.[126–135] In this process a carrier material is impregnated in a metal precursor solution, then dried and calcined and/or reduced to obtain dispersed MNPs onto the surface of CNSMs. Through this method, tiny particles ranging from 2 – 15 nm in size have been produced.[136-140] We chose this method for the projects described in this dissertation based on literature reports that particles as small as 6 to 1.7 nm have been synthesized using citric acid as a reducing and stabilizing agent in combination with metal salts and GO and CNTs as substrates.[141-146] The stabilizing forces in these hybrid systems include the electrostatic attraction of amino groups and metal species to the electron-rich graphene surface,[147,148] as well as coordination bonds.[149,150] Amino groups, along with hydroxyl and carboxylate groups in carbon materials, thus act as nucleation centres for MNPs. We, therefore, decided to include the chemical modification of graphene oxide and carbon nanotubes by grafting amines among the topics studied in the PhD project object of this thesis. Amines are also particularly valuable due to their chemical affinity with biological molecules, adding an ecological benefit.[1]

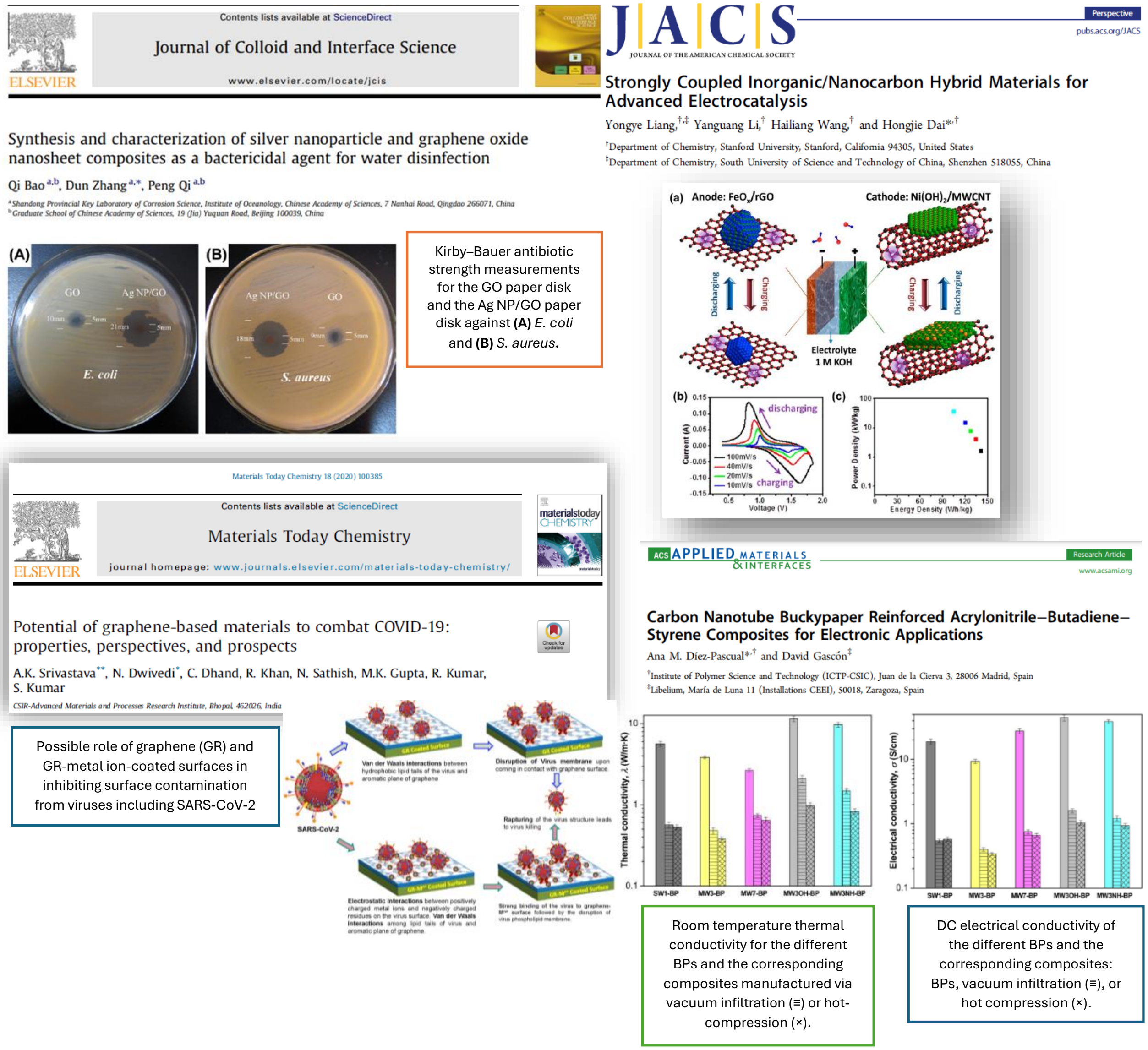

Contents lists available at ScienceDirect

Journal of Colloid and Interface Science

www.elsevier.com/locate/jcis

Synthesis and characterization of silver nanoparticle and graphene oxide nanosheet composites as a bactericidal agent for water disinfection

Qi Bao [a,b], Dun Zhang [a,*], Peng Qi [a,b]

[a] Shandong Provincial Key Laboratory of Corrosion Science, Institute of Oceanology, Chinese Academy of Sciences, 7 Nanhai Road, Qingdao 266071, China
[b] Graduate School of Chinese Academy of Sciences, 19 (Jia) Yuquan Road, Beijing 100039, China

Kirby–Bauer antibiotic strength measurements for the GO paper disk and the Ag NP/GO paper disk against **(A)** *E. coli* and **(B)** *S. aureus*.

JACS
JOURNAL OF THE AMERICAN CHEMICAL SOCIETY

Perspective
pubs.acs.org/JACS

Strongly Coupled Inorganic/Nanocarbon Hybrid Materials for Advanced Electrocatalysis

Yongye Liang,[†,‡] Yanguang Li,[†] Hailiang Wang,[†] and Hongjie Dai*[,†]

[†] Department of Chemistry, Stanford University, Stanford, California 94305, United States
[‡] Department of Chemistry, South University of Science and Technology of China, Shenzhen 518055, China

Materials Today Chemistry 18 (2020) 100385

Contents lists available at ScienceDirect

Materials Today Chemistry

journal homepage: www.journals.elsevier.com/materials-today-chemistry/

Potential of graphene-based materials to combat COVID-19: properties, perspectives, and prospects

A.K. Srivastava[**], N. Dwivedi[*], C. Dhand, R. Khan, N. Sathish, M.K. Gupta, R. Kumar, S. Kumar

CSIR-Advanced Materials and Processes Research Institute, Bhopal, 462026, India

Possible role of graphene (GR) and GR-metal ion-coated surfaces in inhibiting surface contamination from viruses including SARS-CoV-2

ACS APPLIED MATERIALS & INTERFACES

Research Article
www.acsami.org

Carbon Nanotube Buckypaper Reinforced Acrylonitrile–Butadiene–Styrene Composites for Electronic Applications

Ana M. Díez-Pascual*[,†] and David Gascón[‡]

[†] Institute of Polymer Science and Technology (ICTP-CSIC), Juan de la Cierva 3, 28006 Madrid, Spain
[‡] Libelium, María de Luna 11 (Installations CEEI), 50018, Zaragoza, Spain

Room temperature thermal conductivity for the different BPs and the corresponding composites manufactured via vacuum infiltration (≡) or hot-compression (×).

DC electrical conductivity of the different BPs and the corresponding composites: BPs, vacuum infiltration (≡), or hot compression (×).

Fig. 1.10. Applications in various fields for hybrid materials based on GO, and MWCNTs decorated with AgNPs and PdNPs (included with permission).

1.6. Research aims and hypothesis

Our particular interest in working with graphene oxide and multiwalled carbon nanotubes as substrates stems from their chemical similarities and structural differences, which makes them particularly suitable for grafting silver and palladium nanoparticles of varying sizes and shapes using ecologically acceptable synthesis methods. To assemble hybrid materials, 1-octadecylamine (ODA) and 1.8-diamiooctane (DAO) were employed as functionalizing molecules to modulate their physical and chemical properties. We focussed on paper-like materials due to their superior handling characteristics, while simultaneously conducting comparative studies with analogous powder systems.

The primary goal of the research project described in this thesis was to synthesize nanostructured hybrid materials based on graphene oxide and multiwalled carbon nanotubes in two macroscopic forms: powder and paper-like, chemically functionalized with aliphatic amines to support either silver or palladium nanoparticles primarily through covalent interactions. Given the inherent chemical affinity between noble metals and heteroatoms, we hypothesize that stable coordination centres for silver and palladium species will form with available oxygen and/or nitrogen atoms on the structure of both non-functionalized and functionalized GO and MWCNTs$_{(ox).}$ This interaction is expected to guide the formation of new materials with enhanced properties, influenced by the characteristics of the substrate and the functionalizing molecules in terms of size and morphology.

This research has achieved the following key objectives:

1. *Employing greener methods to fabricate hybrid materials*. The synthesis was guided by the principle of sustainability, with a focus on utilizing environmentally friendly techniques, namely solventless gas-phase functionalization for grafting the amine molecules and wet impregnation for the decoration of the substrates with AgNPs and PdNPs.

2. *Studying the chemical and physical properties of the new hybrids*. FTIR, X-ray photoelectron and energy-dispersive X-ray spectroscopies, scanning and transmission electron microscopy, thermal analysis, X-ray diffraction, dispersibility and conductivity measurements were performed to characterize the materials' composition, structure/morphology, and functionality.

3. *Investigating the influence of the substrate and functionalization on nanoparticle morphology*: The research focused on understanding how the substrate (GO or MWCNTs), as well as the derivatization effects, functionality, and chain length of the modifiers (ODA and DAO), affect the morphology, size, and distribution of the metallic nanoparticles. This study aimed to establish correlations between the synthesis conditions and the resulting material properties, thereby optimizing the fabrication process.

4. *Complementing experimental results through Density Functional Theory calculations:* In Chapters 3 and 4 we attempted to further understand the interactions between metallic nanoparticles with the GO-based matrix *via* the theoretical geometry and formation energies of the respective hybrid materials.

1.7. Thesis outline

The dissertation has been structured as follows:

- ***Chapter 2*** details the synthesis of the nanomaterials and the fabrication of the paper samples as well as presenting a brief description of the principles of the characterization techniques employed for the synthetized nanomaterials, and providing the experimental conditions relative to the measurements performed.

- ***Chapter 3*** explains the one-step, solvent-free chemical functionalization and nanoparticle formation/deposition method used to create graphene oxide/silver hybrids. The target materials were fabricated with short reaction times, and under mild conditions, with amine functionalization leading to more controlled silver nanoparticle size and distribution. The results suggest the applied protocol as a greener synthesis method with potential applications in catalysis and biomedicine.

- ***Chapter 4*** discusses the synthesis and characterization of graphene oxide/palladium hybrids employing an analogous protocol to the one for the AgNPs decoration detailed in Chapter 3. It illustrates how reaction time and substrate macrostructure influence the particle shape and distribution, underscoring the potential for developing novel hybrid materials with synergetic properties by combining traditional and sustainable methods.

- ***Chapter 5*** focusses on the synthesis and characterization of nanohybrids based on multiwalled carbon nanotubes chemically modified with 1-octadecylamine (ODA) and 1,8-diaminooctane (DAO), followed by silver nanoparticle formation/decoration. The synthetic route, previously employed in the study described in Chapter 3, offers an efficient and environmentally friendly pathway for producing MWCNT-based nanohybrids in paper and powder forms, aligning with *green chemistry principles*. The need for scalable synthetic techniques to harness these materials for practical applications is emphasised.

- ***Chapter 6*** details the synthesis of nanohybrid s based on *buckypaper* and multiwalled carbon nanotubes modified with ODA and DAO, and decorated with palladium nanoparticles, employing the *in-situ* pathway adapted from that described in Chapter 4 for AgNPs. Characterization results indicate that DAO-modified substrates favoured Pd nucleation, although optimization is needed to obtain metallic species instead of palladium oxides and Pd carboxylates. The potential applications of these hybrids in electronics, catalysis, electrochemical biosensing, drug delivery, and antimicrobial agents are discussed, together with the need for further research on scalability and toxicity.

The thesis concludes with a short summary of the results obtained and an outlook on future research.

1.8. References

(1) Singh, N. B. (2022). Chapter 12 - Green synthesis of nanomaterials. In C. M. Hussain (Ed.), *Handbook of Microbial Nanotechnology* (pp. 225–254). Academic Press, Cambridge, Massachusetts, U.S.A. https://doi.org/10.1016/B978-0-12-823426-6.00007-3.
(2) de Marco, B. A., Rechelo, B. S., Tótoli, E. G., Kogawa, A. C., & Salgado, H. R. N. (2019). Evolution of green chemistry and its multidimensional impacts: A review. *Saudi Pharmaceutical Journal*, *27*(1), 1–8. https://doi.org/10.1016/j.jsps.2018.07.011.
(3) U.S. Environmental Protection Agency. (2013, February 12). *Basics of Green Chemistry*. US EPA. https://www.epa.gov/greenchemistry/basics-green-chemistry.
(4) Lumen. (2019). *Properties of Carbon. Introduction to Chemistry*. Lumenlearning.com. https://courses.lumenlearning.com/introchem/chapter/properties-of-carbon.
(5) Karthik, P. S., Himaja, A. L., & Singh, S. P. (2014). Carbon-allotropes: synthesis methods, applications and future perspectives. *Carbon Letters*, *15*(4), 219–237. https://doi.org/10.5714/cl.2014.15.4.219.
(6) Hirsch, A. (2010). The era of carbon allotropes. Nature Materials, 9(11), 868–871. https://doi.org/10.1038/nmat2885.
(7) Cheng, K., Wallaert, S., Ardebili, H., & Karim, A. (2022). Advanced triboelectric nanogenerators based on low-dimension carbon materials: A review. *Carbon*, *194*, 81–103. https://doi.org/10.1016/j.carbon.2022.03.037.
(8) Dimiev, A. M., & Siegfried Eigler. (2017). Graphene oxide: fundamentals and applications. Chichester, West Sussex John Wiley & Sons, Inc., New York, U.S.A.
(9) Fischer, J. E. (2006). Chapter 4. Carbon Nanotubes: Structure and Properties. In Y. Gogotsi (Ed.), *Nanomaterials Handbook* (pp. 80–115). CRC Press, Taylor and Francis Group. Boca Raton, Florida, U.S.A..
(10) Dreyer, D. R., Park, S., Bielawski, C. W., & Ruoff, R. S. (2010). The chemistry of graphene oxide. *Chem. Soc. Rev.*, *39*(1), 228–240. https://doi.org/10.1039/b917103g.
(11) Brodie, B. C. (1859). XIII. On the atomic weight of graphite. *Philosophical Transactions of the Royal Society of London*, *149*, 249–259. https://doi.org/10.1098/rstl.1859.0013.
(12) Staudenmaier, L. (1898). Verfahren zur Darstellung der Graphitsäure. *Berichte Der Deutschen Chemischen Gesellschaft*, *31*(2), 1481–1487. https://doi.org/10.1002/cber.18980310237.
(13) Hummers, W. S., & Offeman, R. E. (1958). Preparation of Graphitic Oxide. *Journal of the American Chemical Society*, *80*(6), 1339–1339. https://doi.org/10.1021/ja01539a017.
(14) Chen, X., Qu, Z., Liu, Z., & Ren, G. (2022). Mechanism of Oxidization of Graphite to Graphene Oxide by the Hummers Method. *ACS Omega*, *7*(27), 23503–23510. https://doi.org/10.1021/acsomega.2c01963.
(15) Krueger, A. (2010). Carbon Materials and Nanotechnology. Wiley-VCH, Weinheim, Germany.
(16) Balasubramanian, K. y Burghard, M. (2005). Chemically Functionalized Carbon Nanotubes. *Small*, *1*. 180–192.
(17) Sattler, K. D. (2011). Handbook of Nanophysics Nanotubes and Nanowires, 1st ed.; Taylor and Francis Group, Boca Raton, Florida, U.S.A.
(18) Pierson, Hug O. 1993. Handbook of Carbon, Graphıte, Dıamond and Fullerenes: Properties, Processing and Applications. William Andrews Publishing, Norwich, New Yourk, U.S.A..
(19) Basiuk, Vladimir A, and Elena V Basiuk. 2008. *Chemistry of Carbon Nanotubes*. Stevenson Ranch: Calif.
(20) Sengupta, J. (2018, January 1). Carbon Nanotube Fabrication at Industrial Scale. (pp.172-194) Elsevier BV, Amsterdam, The Netherlands. https://doi.org/10.1016/b978-0-12-813351-4.00010-9.
(21) Maser, W. K., Benito, A. M., & Martínez M. Teresa. (2002). Production of carbon nanotubes: the light approach. *Carbon*, *40*(10), 1685–1695. https://doi.org/10.1016/s0008-6223(02)00009-x.
(22) Szabó, A., Perri, C., Csató, A., Giordano, G., Vuono, D., & Nagy, J. B. (2010). Synthesis Methods of Carbon Nanotubes and Related Materials. *Materials*, *3*(5), 3092–3140. https://doi.org/10.3390/ma3053092.
(23) Paradise, M., & Goswami, T. (2007). Carbon nanotubes – Production and industrial applications. (pp. 28(5), 1477-1489) Elsevier BV, Amsterdam, The Netherlans.
(24) Fathy, N A., Basta, A H., & Lotfy, V F. (2020). Novel trends for synthesis of carbon nanostructures from agricultural wastes. (pp.59-74) Elsevier BV, Amsterdam, The Netherlands. https://doi.org/10.1016/b978-0-12-819786-8.00004-9.

(25) Zanella, R., Basiuk, E. V., & Saniger, J. M. (2008). Metal Nanoparticles on Carbon Nanotubes: Synthesis, Characterization, and Applications. In V. A. Basiuk & E. V. Basiuk (Eds.), *Chemistry of Carbon Nanotubes* (pp. 1–40). American Scientific Publishers, Stevenson Ranch, California, U.S.A.

(26) Basiuk , E. V., & Basiuk , V. A. (2015). Solvent-Free Functionalization of Carbon Nanomaterials. In V. A. Basiuk & E. V. Basiuk (Eds.), *Green Processes for Nanotechnology. From Inorganic to Bioinspired Nanomaterials* (pp. 163–205). Springer International Publishing, Cham, Switzerland.

(27) Jun, L. Y., Mubarak, N. M., Yee, M. J., Yon, L. S., Bing, C. H., Khalid, M., & Abdullah, E. C. (2018). An overview of functionalised carbon nanomaterial for organic pollutant removal. *Journal of Industrial and Engineering Chemistry*, *67*, 175–186. https://doi.org/10.1016/j.jiec.2018.06.028.

(28) Basiuk, E. V., Basiuk, V. A., Bañuelos, J.-G., Saniger-Blesa, J.-M., Pokrovskiy, V. A., Gromovoy, Taras. Yu., Mischanchuk, A. V., & Mischanchuk, B. G. (2002). Interaction of Oxidized Single-Walled Carbon Nanotubes with Vaporous Aliphatic Amines. *The Journal of Physical Chemistry B*, *106*(7), 1588–1597. https://doi.org/10.1021/jp0120110.

(29) Basiuk, E. V., & Basiuk, V. A. (2014). Green Chemistry of Carbon Nanomaterials. *Journal of Nanoscience and Nanotechnology*, *14*(1), 644–672. https://doi.org/10.1166/jnn.2014.9011.

(30) Basiuk, E. V., Monroy-Peláez, M., Puente-Lee, I., & Basiuk, V. A. (2004). Direct Solvent-Free Amination of Closed-Cap Carbon Nanotubes: A Link to Fullerene Chemistry. *Nano Letters*, *4*(5), 863–866. https://doi.org/10.1021/nl049746b.

(31) Basiuk (Golovataya-Dzhymbeeva), Elena V., Ochoa-Olmos, O., Contreras-Torres, Flavio F., Meza-Laguna, V., Alvarez-Zauco, E., Puente-Lee, I., & Basiuk, Vladimir A. (2011). “Green” Functionalization of Pristine Multi-Walled Carbon Nanotubes with Long-Chain Aliphatic Amines. *Journal of Nanoscience and Nanotechnology*, *11*(6), 5546–5554. https://doi.org/10.1166/jnn.2011.3431.

(32) Ramírez-Calera, I. J., Meza-Laguna, V., Gromovoy, T. Yu., Chávez-Uribe, Ma. I., Basiuk, V. A., & Basiuk, E. V. (2015). Solvent-free functionalization of fullerene C_{60} and pristine multi-walled carbon nanotubes with aromatic amines. *Applied Surface Science*, *328*, 45–62. https://doi.org/10.1016/j.apsusc.2014.11.188.

(33) Georgakilas, V. (2014). Addition of Organic Groups through Reactions with Oxygen Species of Graphene Oxide. In V. Georgakilas (Ed.), *Functionalization of Graphene* (pp. 59–92). Wiley-VCH, Weinheim, Germany.

(34) Carrillo, A., Swartz, J. A., Gamba, J. M., Kane, R. S., Nirupama Chakrapani, Wei, B., & Ajayan, P. M. (2003). Noncovalent Functionalization of Graphite and Carbon Nanotubes with Polymer Multilayers and Gold Nanoparticles. *Nano Letters*, *3*(10), 1437–1440. https://doi.org/10.1021/nl034376x.

(35) Liu, Y., Yu, D., Zeng, C., Miao, Z., & Dai, L. (2010). Biocompatible Graphene Oxide-Based Glucose Biosensors. *Langmuir*, *26*(9), 6158–6160. https://doi.org/10.1021/la100886x.

(36) Koskin, A. P., Larichev, Y. V., Mishakov, I. V., Mel’gunov, M. S., & Vedyagin, A. A. (2020). Synthesis and characterization of carbon nanomaterials functionalized by direct treatment with sulfonating agents. *Microporous and Mesoporous Materials*, *299*, 110130–110130. https://doi.org/10.1016/j.micromeso.2020.110130.

(37) Luong, N. D., Sinh, L. H., Johansson, L.-S., Campell, J., & Seppälä, J. (2015). Functional Graphene by Thiol-ene Click Chemistry. *Chemistry - a European Journal*, *21*(8), 3183–3186. https://doi.org/10.1002/chem.201405734.

(38) McGlynn, R. J., Brunet, P., Chakrabarti, S., Boies, A., Maguire, P., & Mariotti, D. (2022). High degree of N-functionalization in macroscopically assembled carbon nanotubes. *Journal of Materials Science*, *57*(28), 13314–13325. https://doi.org/10.1007/s10853-022-07463-7.

(39) Vallés, C., David Núñez, J., Benito, A. M., & Maser, W. K. (2012). Flexible conductive graphene paper obtained by direct and gentle annealing of graphene oxide paper. *Carbon*, *50*(3), 835–844. https://doi.org/10.1016/j.carbon.2011.09.042.

(40) Zhang, Y., & Chung, T.-S. (2017). Graphene oxide membranes for nanofiltration. *Current Opinion in Chemical Engineering*, *16*, 9–15. https://doi.org/10.1016/j.coche.2017.03.002.

(41) Dikin, D. A., Stankovich, S., Zimney, E. J., Piner, R. D., Dommett, G. H. B., Evmenenko, G., Nguyen, S. T., & Ruoff, R. S. (2007). Preparation and characterization of graphene oxide paper. *Nature*, *448*(7152), 457–460. https://doi.org/10.1038/nature06016.

(42) Chen, H., Müller, M. B., Gilmore, K. J., Wallace, G. G., & Li, D. (2008). Mechanically Strong, Electrically Conductive, and Biocompatible Graphene Paper. *Advanced Materials*, *20*(18), 3557–3561. https://doi.org/10.1002/adma.200800757.

(43) Huang, W. (2017). Graphene Oxide Papers. In W. Huang (Ed.), *Nanopapers: From Nanochemistry and Nanomanufacturing to Advanced Applications* (pp. 1–26). Elsevier B.V., Amsterdam, The Netherlands.

(44) Sears, K., Dumée, L., Schütz, J., She, M., Huynh, C., Hawkins, S., Duke, M., & Gray, S. (2010). Recent Developments in Carbon Nanotube Membranes for Water Purification and Gas Separation. *Materials*, *3*(1), 127–149. https://doi.org/10.3390/ma3010127.

(45) Compton, O. C., & Nguyen, S. T. (2010). Graphene Oxide, Highly Reduced Graphene Oxide, and Graphene: Versatile Building Blocks for Carbon-Based Materials. *Small*, *6*(6), 711–723. https://doi.org/10.1002/smll.200901934.

(46) Vijayabhaskar, A., Shanmugasundaram, M., (2017). Usage of Carbon nanotubes and nanofibers in cement and concrete: A review. *International Journal of Engineering and Technology*, *9*(2), 564–569. https://doi.org/10.21817/ijet/2017/v9i2/170902045.

(47) Trakakis, G., Tasis, D., Parthenios, J., Galiotis, C., & Papagelis, K. (2013). Structural Properties of Chemically Functionalized Carbon Nanotube Thin Films. *Materials*, *6*(6), 2360–2371. https://doi.org/10.3390/ma6062360.

(48) Wu, Q., Zhang, C., Liang, R., & Wang, B. (2008). Fire retardancy of a buckypaper membrane. *Carbon*, *46*(8), 1164–1165. https://doi.org/10.1016/j.carbon.2008.03.021.

(49) Zhu, W., Ku, D., Zheng, J. P., Liang, Z., Wang, B., Zhang, C., Walsh, S., Au, G., & Plichta, E. J. (2010). Buckypaper-based catalytic electrodes for improving platinum utilization and PEMFC's performance. *Electrochimica Acta*, *55*(7), 2555–2560. https://doi.org/10.1016/j.electacta.2009.12.026.

(50) Gross, A J., Holzinger, M., & Cosnier, S. (2019). 1. Buckypapers for bioelectrochemical applications. (pp. 1-22) De Gruyter eBooks, Berlin, Germany.

(51) Zheng, T., Wang, G., Xu, N., Lu, C., Qiao, Y., Zhang, D., & Wang, X. (2018). Preparation and Properties of Highly Electroconductive and Heat-Resistant CMC/Buckypaper/Epoxy Nanocomposites. *Nanomaterials*, *8*(12), 969–969. https://doi.org/10.3390/nano8120969.

(52) Sun, Y.-P., Fu, K., Lin, Y., & Huang, W. (2002). Functionalized Carbon Nanotubes: Properties and Applications. *Accounts of Chemical Research*, *35*(12), 1096–1104. https://doi.org/10.1021/ar010160v.

(53) Park, E. (2013). Preparation, Characterization and Applicability of Covalently Functionalized MWNT. In S. Suzuki (Ed.), *Physical and Chemical Properties of Carbon Nanotubes*, InTech, Rijeka, Croatia. https://doi.org/10.5772/50883.

(54) Whitby, R. L. D., Fukuda, T., Maekawa, T., James, S. L., & Mikhalovsky, S. V. (2008). Geometric control and tuneable pore size distribution of buckypaper and buckydiscs. *Carbon*, *46*(6), 949–956. https://doi.org/10.1016/j.carbon.2008.02.028.

(55) Wang, D., Song, P., Liu, C., Wu, W. y Fan, S. (2008). Highly oriented carbon nanotube papers made of aligned carbon nanotubes, *Nanotechnology*, 19(7):075609. https://doi.org/ 10.1088/0957-4484/19/7/075609

(56) Chang, Y. X., Zhou, L. L., Li, G. X., Li, L., & Yuan, L. M. (2007). Single-Wall Carbon Nanotubes Used as Stationary Phase in HPLC. *Journal of Liquid Chromatography & Related Technologies*, *30*(19), 2953–2958. https://doi.org/10.1080/10826070701589057.

(57) Rashid, Md. H.-O., & Ralph, S. F. (2017). Carbon Nanotube Membranes: Synthesis, Properties, and Future Filtration Applications. *Nanomaterials*, *7*(5), 99. https://doi.org/10.3390/nano7050099.

(58) Cong, H., Zhang, J., Radosz, M., & Shen, Y. (2007). Carbon nanotube composite membranes of brominated poly(2,6-diphenyl-1,4-phenylene oxide) for gas separation. *Journal of Membrane Science*, *294*(1-2), 178–185. https://doi.org/10.1016/j.memsci.2007.02.035.

(59) Cornelio, B., Rance, G. A., Laronze-Cochard, M., Fontana, A., Sapi, J., & Khlobystov, A. N. (2013). Palladium nanoparticles on carbon nanotubes as catalysts of cross-coupling reactions. *Journal of Materials Chemistry A*, *1*(31), 8737–8744. https://doi.org/10.1039/C3TA11530E.

(60) Fihri, A., Bouhrara, M., Nekoueishahraki, B., Basset, J.-M., & Polshettiwar, V. (2011). Nanocatalysts for Suzuki cross-coupling reactions. *Chemical Society Reviews*, *40*(10), 5181. https://doi.org/10.1039/c1cs15079k.

(61) Georgakilas, V., Gournis, D., Tzitzios, V., Pasquato, L., Guldi, D. M., & Prato, M. (2007). Decorating carbon nanotubes with metal or semiconductor nanoparticles. *Journal of Materials Chemistry*, *17*(26), 2679. https://doi.org/10.1039/b700857k.

(62) Dresselhaus, M. S., Dresselhaus, G., & Avouris, P. (Eds.). (2001). *Carbon Nanotubes: Synthesis, Structure, Properties, and Applications*. Springer Science & Business Media, Heidelberg, Germany.

(63) Yin, S.-F., Xu, B.-Q., Ng, C.-F., & Au, C.-T. (2004). Nano Ru/CNTs: a highly active and stable catalyst for the generation of CO -free hydrogen in ammonia decomposition. *Applied Catalysis B: Environmental*, *48*(4), 237–241. https://doi.org/10.1016/j.apcatb.2003.10.013.

(64) Akbayrak, S., & Özkar, S. (2012). Ruthenium (0) Nanoparticles Supported on Multiwalled Carbon Nanotube As Highly Active Catalyst for Hydrogen Generation from Ammonia–Borane. *ACS Applied Materials & Interfaces*, *4*(11), 6302–6310. https://doi.org/10.1021/am3019146.

(65) Kumar, A., Mazinder Boruah, B., & Liang, X.-J. (2011). Gold Nanoparticles: Promising Nanomaterials for the Diagnosis of Cancer and HIV/AIDS. *Journal of Nanomaterials*, *2011*, 1–17. https://doi.org/10.1155/2011/202187.

(66) Sharma, V. K., Sayes, C. M., Guo, B., Pillai, S., Parsons, J. G., Wang, C., Yan, B., & Ma, X. (2019). Interactions between silver nanoparticles and other metal nanoparticles under environmentally relevant conditions: A review. *Science of the Total Environment*, 653, 1042–1051. https://doi.org/10.1016/j.scitotenv.2018.10.411.

(67) Singh, P. K., Kumar, P., & Das, A. K. (2018). Unconventional Physical Methods for Synthesis of Metal and Non-metal Nanoparticles: A Review. *Proceedings of the National Academy of Sciences, India Section A: Physical Sciences*, *89*(2), 199–221. https://doi.org/10.1007/s40010-017-0474-2.

(68) Corzo Lucioni, A. (2012, March 27). Síntesis de nanopartículas de oro obtenidas por reducción de H[$AuCl_4$]. *Revista de La Sociedad Química Del Perú*, *78*(2), 79–90. http://www.scielo.org.pe/pdf/rsqp/v78n2/a03v78n2.pdf.

(69) Kharissova, O. V., Dias, H. V. R., Kharisov, B. I., Pérez, B. O., & Pérez, V. M. J. (2013). The greener synthesis of nanoparticles. *Trends in Biotechnology*, *31*(4), 240–248. https://doi.org/10.1016/j.tibtech.2013.01.003.

(70) Bulychev, B. M., Storozhenko, P. A., & Fokin, V. N. (2009). "One-step" synthesis of nonsolvated aluminum hydride. *Russian Chemical Bulletin*, *58*(9), 1817–1823. https://doi.org/10.1007/s11172-009-0247-4.

(71) Li, J., Kuang, D., Feng, Y., Zhang, F., Xu, Z., Liu, M., & Wang, D. (2013). Green synthesis of silver nanoparticles–graphene oxide nanocomposite and its application in electrochemical sensing of tryptophan. *Biosensors and Bioelectronics*, *42*, 198–206. https://doi.org/10.1016/j.bios.2012.10.029.

(72) Simon, P., & Gogotsi, Y. (2008). Materials for electrochemical capacitors. *Nature Materials*, *7*(11), 845–854. https://doi.org/10.1038/nmat2297.

(73) Konstantinov, K., Wang, G., Lao, Z. J., Liu, H. K., & Devers, T. (2009). Nanostructured Metal Oxides as Electrode Materials for Electrochemical Capacitors. *Journal of Nanoscience and Nanotechnology*, *9*(2), 1263–1267. https://doi.org/10.1166/jnn.2009.c134.

(74) Fu, M., Zhuang, Q., Zhu, Z., Zhang, Z., Chen, W., Liu, Q., & Yu, H. (2020). Facile synthesis of V2O5/graphene composites as advanced electrode materials in supercapacitors. *Journal of Alloys and Compounds*, *862*, 158006–158006. https://doi.org/10.1016/j.jallcom.2020.158006.

(75) Zhang, H., Zhang, X., Lin, H., Wang, K., Sun, X., Xu, N., Li, C., & Ma, Y. (2015). Graphene and maghemite composites based supercapacitors delivering high volumetric capacitance and extraordinary cycling stability. *Electrochimica Acta*, *156*, 70–76. https://doi.org/10.1016/j.electacta.2015.01.041.

(76) Geonmonond, R. S., Silva, A. G. M. D., Camargo, P. H. C., Geonmonond, R. S., Silva, A. G. M. D., & Camargo, P. H. C. (2018). Controlled synthesis of noble metal nanomaterials: motivation, principles, and opportunities in nanocatalysis. *Anais Da Academia Brasileira de Ciências*, *90*(1), 719–744. https://doi.org/10.1590/0001-3765201820170561.

(77) Pareek, V., Bhargava, A., Gupta, R., Jain, N., & Panwar, J. (2017). Synthesis and Applications of Noble Metal Nanoparticles: A Review. *Advanced Science, Engineering and Medicine*, *9*(7), 527–544. https://doi.org/10.1166/asem.2017.2027.

(78) Habibullah, G., Viktorova, J., & Ruml, T. (2021). Current Strategies for Noble Metal Nanoparticle Synthesis. *Nanoscale Research Letters*, *16*(1). https://doi.org/10.1186/s11671-021-03480-8.

(79) Li Li Zhang, Lei, Z., Zhang, J., Tian, X., & Xiu Song Zhao. (2011). Supercapacitors: Electrode Materials Aspects. In *Encyclopedia of Inorganic and Bioinorganic Chemistry* (pp. 1-23). Singapore, Singapore. https://doi.org/10.1002/9781119951438.eibc0464.

(80) Wang, R., Han, M., Zhao, Q., Ren, Z., Guo, X., Xu, C., Hu, N., & Lu, L. (2017). Hydrothermal synthesis of nanostructured graphene/polyaniline composites as high-capacitance electrode materials for supercapacitors. *Scientific Reports*, *7*(1). https://doi.org/10.1038/srep44562.

(81) Elemike, E. E., Onwudiwe, D. C., Wei, L., Chaogang, L., & Zhiwei, Z. (2019). Noble metal –semiconductor nanocomposites for optical, energy and electronics applications. *Solar Energy Materials and Solar Cells*, *201*, 110106. https://doi.org/10.1016/j.solmat.2019.110106.

(82) Giljohann, David A., Seferos, Dwight S., Daniel, Weston L., Massich, Matthew D., Patel, Pinal C., & Mirkin, Chad A. (2010). Gold Nanoparticles for Biology and Medicine. *Angewandte Chemie International Edition*, *49*(19), 3280–3294. https://doi.org/10.1002/anie.200904359.

(83) Zhang. (2013). DETECTION OF CANCER BIOMARKERS WITH NANOTECHNOLOGY. *American Journal of Biochemistry and Biotechnology*, *9*(1), 71–89. https://doi.org/10.3844/ajbbsp.2013.71.89.

(84) Chen, P. (2012). Interfacing Biology with Nanoelectronics. *Journal of Biosensors & Bioelectronics*, *03*(02). https://doi.org/10.4172/2155-6210.1000e105.

(85) Segura, R. (2012). Non-covalent assembly of hybrid nanostructures of gold and palladium nanoparticles with carbon nanotubes. *International Journal of Materials Research*, *103*(7), 901–905. https://doi.org/10.3139/146.110693.

(86) Singh, P., Pandey, S. K., Singh, J., Srivastava, S., Sachan, S., & Singh, S. K. (2015). Biomedical Perspective of Electrochemical Nanobiosensor. *Nano-Micro Letters*, *8*(3), 193–203. https://doi.org/10.1007/s40820-015-0077-x.

(87) Xu, L., Wang, Y.-Y., Huang, J., Chen, C.-Y., Wang, Z.-X., & Xie, H. (2020). Silver nanoparticles: Synthesis, medical applications and biosafety. *Theranostics*, *10*(20), 8996–9031. https://doi.org/10.7150/thno.45413.

(88) Jardón-Romero, E. A., Lara-Carrillo, E., González-Pedroza, M. G., Sánchez-Mendieta, V., Salmerón-Valdés, E. N., Toral-Rizo, V. H., Olea-Mejía, O. F., López-González, S., & Morales-Luckie, R. A. (2022). Antimicrobial Activity of Biogenic Silver Nanoparticles from Syzygium aromaticum against the Five Most Common Microorganisms in the Oral Cavity. *Antibiotics*, *11*(7), 834. https://doi.org/10.3390/antibiotics11070834.

(89) Vs, R., Sp, D., Mh, S., & T, P. (2018). In vitro studies on oxidative stress-independent, Ag nanoparticles-induced cell toxicity of Candida albicans, an opportunistic pathogen. *International Journal of Nanomedicine*, *Volume 13*, 91–96. https://doaj.org/article/0162e83f574b4bd6b67c971943c7bdb2.

(90) Jang, J., Kim, J., Churl Kyoung Lee, & Kwon, K. (2023). Synthesis of Silver Nanoparticles using Pulse Electrolysis in 1-n-butyl-3-methylimidazolium Chloride Ionic Liquid. *Journal of Electrochemical Science and Technology*, *14*(1), 15–20. https://doi.org/10.33961/jecst.2022.00570.

(91) Wang, Z., Zhang, X., Zhou, S., Edström, K., Strømme, M., & Nyholm, L. (2018). Lightweight, Thin, and Flexible Silver Nanopaper Electrodes for High-Capacity Dendrite-Free Sodium Metal Anodes. *Advanced Functional Materials*, *28*(48), 1804038. https://doi.org/10.1002/adfm.201804038.

(92) Venkatesan, J., Gupta, P. K., Seong Eun Son, Hur, W., & Gi Hun Seong. (2022). Silver-Based Hybrid Nanomaterials: Preparations, Biological, Biomedical, and Environmental Applications. *Journal of Cluster Science*, *34*(1), 23–43. https://doi.org/10.1007/s10876-021-02212-3.

(93) Nam, G., Rangasamy, S., Purushothaman, B., & Song, J. M. (2015). The Application of Bactericidal Silver Nanoparticles in Wound Treatment. *Nanomaterials and Nanotechnology*, *5*, 23. https://doi.org/10.5772/60918.

(94) Aziz, Z. A. A., Mohd-Nasir, H., Ahmad, A., Mohd. Setapar, S. H., Peng, W. L., Chuo, S. C., Khatoon, A., Umar, K., Yaqoob, A. A., & Mohamad Ibrahim, M. N. (2019). Role of Nanotechnology for Design and Development of Cosmeceutical: Application in Makeup and Skin Care. *Frontiers in Chemistry*, *7*. https://doi.org/10.3389/fchem.2019.00739.

(95) Ullah Khan, S., Saleh, T. A., Wahab, A., Ullah Khan, M. H., Khan, D., Ullah Khan, W., Rahim, A., Kamal, S., Ullah Khan, F., & Fahad, S. (2018). Nanosilver: new ageless and versatile biomedical therapeutic scaffold. *International Journal of Nanomedicine*, *13*, 733–762. https://doi.org/10.2147/ijn.s153167.

(96) Song, J. M. (2010). Silver as antibacterial agent: metal nanoparticles to nanometallopharmaceuticals (Silver based antibacterial nanometallopharmaceuticals). *2010 IEEE International Conference on Nano/Molecular Medicine and Engineering*, 98–101. https://doi.org/10.1109/nanomed.2010.5749812.

(97) Zhang, X.-F., Liu, Z.-G., Shen, W., & Gurunathan, S. (2016). Silver Nanoparticles: Synthesis, Characterization, Properties, Applications, and Therapeutic Approaches. *International Journal of Molecular Sciences*, *17*(9), 1534. https://doi.org/10.3390/ijms17091534.

(98) Los Alamos National Laboratory. (2021). *Periodic Table of Elements: Los Alamos National Laboratory*. Periodic.lanl.gov. https://periodic.lanl.gov/47.shtml.

(99) Yaqoob, S. B., Adnan, R., Rameez Khan, R. M., & Rashid, M. (2020). Gold, Silver, and Palladium Nanoparticles: A Chemical Tool for Biomedical Applications. *Frontiers in Chemistry*, *8*. https://doi.org/10.3389/fchem.2020.00376.

(100) Bakuru, V. R., Velaga, B., Peela, N. R., & Kalidindi, S. B. (2018). Hybridization of Pd Nanoparticles with UiO-66(Hf) Metal-Organic Framework and the Effect of Nanostructure on the Catalytic Properties. *Chemistry - a European Journal*, *24*(60), 15978–15982. https://doi.org/10.1002/chem.201803200.

(101) Pattadar, D. K., Sharma, J. N., Mainali, B. P., & Zamborini, F. P. (2019). Anodic stripping electrochemical analysis of metal nanoparticles. *Current Opinion in Electrochemistry*, *13*, 147–156. https://doi.org/10.1016/j.coelec.2018.12.006.

(102) Feng, X., Hempenius, M. A., & Vancso, G. J. (2018). Metal Nanoparticle Foundry with Redox Responsive Hydrogels. *Macromolecular Chemistry and Physics*, *219*(22). https://doi.org/10.1002/macp.201800223.

(103) Feng, Y., Shao, Q., Huang, B., Zhang, J., & Huang, X. (2018). Surface engineering at the interface of core/shell nanoparticles promotes hydrogen peroxide generation. *National Science Review*, *5*(6), 895–906. https://doi.org/10.1093/nsr/nwy065.

(104) Sawoo, S., Srimani, D., Dutta, P., Lahiri, R., & Sarkar, A. (2009). Size controlled synthesis of Pd nanoparticles in water and their catalytic application in C–C coupling reactions. *Tetrahedron*, *65*(22), 4367–4374. https://doi.org/10.1016/j.tet.2009.03.062.

(105) Shen, Y., Bi, L., Liu, B., & Dong, S. (2003). Simple preparation method of Pd nanoparticles on an Au electrode and its catalysis for dioxygen reduction. *New Journal of Chemistry*, *27*(6), 938–938. https://doi.org/10.1039/b300566f.

(106) Liu, T., Xie, L., Li, Y., Li, X., Pang, S., & Zhang, T. (2013). Hydrogen/deuterium storage properties of Pd nanoparticles. *Journal of Power Sources*, *237*, 74–79. https://doi.org/10.1016/j.jpowsour.2013.03.015.

(107) Chen, A., & Ostrom, C. (2015). Palladium-Based Nanomaterials: Synthesis and Electrochemical Applications. *Chemical Reviews*, *115*(21), 11999–12044. https://doi.org/10.1021/acs.chemrev.5b00324.

(108) Zhang, L., Chang, Q., Chen, H., & Shao, M. (2016). Recent advances in palladium-based electrocatalysts for fuel cell reactions and hydrogen evolution reaction. *Nano Energy*, *29*, 198–219. https://doi.org/10.1016/j.nanoen.2016.02.044.

(109) Burdușel, A.-C., Gherasim, O., Grumezescu, A. M., Mogoantă, L., Ficai, A., & Andronescu, E. (2018). Biomedical Applications of Silver Nanoparticles: An Up-to-Date Overview. *Nanomaterials*, *8*(9), 681. https://doi.org/10.3390/nano8090681.

(110) Adams, C. P., Walker, K. A., Obare, S. O., & Docherty, K. M. (2014). Size-Dependent Antimicrobial Effects of Novel Palladium Nanoparticles. *PLoS ONE*, *9*(1), e85981. https://doi.org/10.1371/journal.pone.0085981.

(111) Chaloupka, K., Malam, Y., & Seifalian, A. M. (2010). Nanosilver as a new generation of nanoproduct in biomedical applications. *Trends in Biotechnology*, *28*(11), 580–588. https://doi.org/10.1016/j.tibtech.2010.07.006.

(112) Leso, V., & Iavicoli, I. (2018). Palladium Nanoparticles: Toxicological Effects and Potential Implications for Occupational Risk Assessment. *International Journal of Molecular Sciences*, *19*(2), 503. https://doi.org/10.3390/ijms19020503.

(113) Jian Nong Wang, Zhang, L., Jun Jie Niu, Yu, F., Zhao Ming Sheng, Yu Zeng Zhao, Chang, H., & Pak, C. (2007). Synthesis of High Surface Area, Water-Dispersible Graphitic Carbon Nanocages by an in-Situ Template Approach. *Chemistry of Materials*, *19*(3), 453–459. https://doi.org/10.1021/cm062491d.

(114) Saikia, M., Das, T., Dihingia, N., Fan, X., Silva, L. F. O., & Saikia, B. K. (2020). Formation of carbon quantum dots and graphene nanosheets from different abundant carbonaceous materials. *Diamond and Related Materials*, *106*, 107813. https://doi.org/10.1016/j.diamond.2020.107813.

(115) Grashchenko, A. S., Kukushkin, S. A., Osipov, A. V., & Redkov, A. V. (2021). Method for the modification of graphite subsurface layer to a solid mixture of SiC and graphite. *Journal of Physics. Conference Series*, *2086*(1), 012012–012012. https://doi.org/10.1088/1742-6596/2086/1/012012.

(116) Arora, S., Kumar, V., Yadav, S., Singh, S., Bhatnagar, D., & Kaur, I. (2014). Carbon Nanotubes as Drug Delivery Vehicles. Solid State Phenomena, 222, 145–158. https://doi.org/10.4028/www.scientific.net/ssp.222.145.

(117) Chu, H., Wei, L., Cui, R., Wang, J., & Li, Y. (2010). Carbon nanotubes combined with inorganic nanomaterials: Preparations and applications. *Coordination Chemistry Reviews*, *254*(9-10), 1117–1134. https://doi.org/10.1016/j.ccr.2010.02.009.

(118) Eudes Lorençon, Ferlauto, A. S., Sergio de Oliveira, Miquita, D. R., Resende, R. R., Lacerda, R. G., & Ladeira, L. O. (2009). Direct Production of Carbon Nanotubes/Metal Nanoparticles Hybrids from a Redox Reaction between Metal Ions and Reduced Carbon Nanotubes. *ACS Applied Materials & Interfaces*, *1*(10), 2104–2106. https://doi.org/10.1021/am900424m.

(119) Hu, Y., & Guo, C. (2011). Carbon Nanotubes and Carbon Nanotubes/Metal Oxide Heterostructures: Synthesis, Characterization and Electrochemical Property. In M. Naraghi (Ed.), Carbon Nanotubes - Growth and Applications. IntechOpen. 978-953-51-4462-5.

(120) Li, K., & Li, H. (2011). Fabrication and Applications of Carbon Nanotube-Based Hybrid Nanomaterials by Means of Non-Covalently Functionalized Carbon Nanotubes. In S. Bianco (Ed.), Carbon Nanotubes - From Research to Applications. IntechOpen. 978-953-51-5567-6.

(121) Navrotskaya, A. G., Darya Aleksandrova, Krivoshapkina, E. F., Sillanpää, M., & Krivoshapkin, P. V. (2020). Hybrid Materials Based on Carbon Nanotubes and Nanofibers for Environmental Applications. *Frontiers in Chemistry, 8*. https://doi.org/10.3389/fchem.2020.00546.

(122) Rodríguez-Manzo, J. A., Banhart, F., Terrones, M., Terrones, H., Grobert, N., Ajayan, P. M., Sumpter, B. G., Meunier, V., Wang, M., Bando, Y., & Golberg, D. (2009). Heterojunctions between metals and carbon nanotubes as ultimate nanocontacts. *Proceedings of the National Academy of Sciences of the United States of America*, 106(12), 4591–4595. https://doi.org/10.1073/pnas.0900960106.

(123) Zhang, D., Liu, T., Cheng, J., Liang, S., Chai, J., Yang, X., Wang, H., Zheng, G., & Cao, M. (2019). Controllable synthesis and characterization of tungsten disulfide nanosheets as promising nanomaterials for electronic devices. *Ceramics International*, *45*(9), 12443–12448. https://doi.org/10.1016/j.ceramint.

(124) Morones, J. R., Elechiguerra, J. L., Camacho, A., Holt, K., Kouri, J. B., Ramírez, J. T., & Yacaman, M. J. (2005). The bactericidal effect of silver nanoparticles. *Nanotechnology*, *16*(10), 2346–2353. https://doi.org/10.1088/0957-4484/16/10/059.

(125) Marambio-Jones, C., & Hoek, E. M. V. (2010). A review of the antibacterial effects of silver nanomaterials and potential implications for human health and the environment. *Journal of Nanoparticle Research*, *12*(5), 1531–1551. https://doi.org/10.1007/s11051-010-9900-y.

(126) Ayán-Varela, M., Fernández-Merino, M. J., Paredes, J. I., Villar-Rodil, S., Fernández-Sánchez, C., Guardia, L., Martínez-Alonso, A., & Tascón, J. M. D. (2014). Highly efficient silver-assisted reduction of graphene oxide dispersions at room temperature: mechanism, and catalytic and electrochemical performance of the resulting hybrids. *Journal of Materials Chemistry A*, *2*(20), 7295–7305. https://doi.org/10.1039/c3ta15307j.

(127) Mohammadnejad, J., Yazdian, F., Omidi, M., Rostami, A. D., Rasekh, B., & Fathinia, A. (2018). Graphene oxide/silver nanohybrid: Optimization, antibacterial activity and its impregnation on bacterial cellulose as a potential wound dressing based on GO-Ag nanocomposite-coated BC. *Engineering in Life Sciences*, *18*(5), 298–307. https://doi.org/10.1002/elsc.201700138.

(128) Navalon, S., Dhakshinamoorthy, A., Alvaro, M., & Garcia, H. (2016). Metal nanoparticles supported on two-dimensional graphenes as heterogeneous catalysts. *Coordination Chemistry Reviews*, *312*, 99–148. https://doi.org/10.1016/j.ccr.2015.12.005.

(129) Golzar, H., Yazdian, F., Hashemi, M., Omidi, M., Mohammadrezaei, D., Rashedi, H., Farahani, M., Ghasemi, N., Shabani shayeh, J., & Tayebi, L. (2018). Optimizing the hybrid nanostructure of functionalized reduced graphene oxide/silver for highly efficient cancer nanotherapy. *New Journal of Chemistry*, *42*(15), 13157–13168. https://doi.org/10.1039/c8nj01764f.

(130) Cai, N., Fu, J., Zeng, H., Luo, X., Han, C., & Yu, F. (2018). Reduced graphene oxide-silver nanoparticles/nitrogen-doped carbon nanofiber composites with meso-microporous structure for high-performance symmetric supercapacitor application. *Journal of Alloys and Compounds*, *742*, 769–779. https://doi.org/10.1016/j.jallcom.2018.01.011.

(131) Shuai, C., Guo, W., Wu, P., Yang, W., Hu, S., Xia, Y., & Feng, P. (2018). A graphene oxide-Ag co-dispersing nanosystem: Dual synergistic effects on antibacterial activities and mechanical properties of polymer scaffolds. *Chemical Engineering Journal*, *347*, 322–333. https://doi.org/10.1016/j.cej.2018.04.092.

(132) Li, J., Sun, Y., Wang, J., Tian, J., Zhang, X., Yang, H., & Lin, B. (2018). Synthesis, structure and electrochemical properties of novel ternary composite reduced-graphene oxide/Ag nanoparticles/poly(p-phenylenediamine). *Journal of Alloys and Compounds*, *749*, 783–793. https://doi.org/10.1016/j.jallcom.2018.03.326.

(133) Vi, T. T. T., & Lue, S. J. (2016). Preparation of silver nanoparticles loaded graphene oxide nanosheets for antibacterial activity. *IOP Conference Series: Materials Science and Engineering*, *162*(1), 012033. https://doi.org/10.1088/1757-899x/162/1/012033.

(134) Bao, Q., Zhang, D., & Qi, P. (2011). Synthesis and characterization of silver nanoparticle and graphene oxide nanosheet composites as a bactericidal agent for water disinfection. *Journal of Colloid and Interface Science*, *360*(2), 463–470. https://doi.org/10.1016/j.jcis.2011.05.009.

(135) Abdelhalim, A. O. E., Galal, A., Hussein, M. Z., & El Sayed, I. E.-T. . (2016). Graphene Functionalization by 1,6-Diaminohexane and Silver Nanoparticles for Water Disinfection. *Journal of Nanomaterials, 2016*, 1–7. https://doi.org/10.1155/2016/1485280.

(136) Gomes, H. T., Samant, P. V., Serp, Ph., Kalck, Ph., Figueiredo, J. L., & Faria, J. L. (2004). Carbon nanotubes and xerogels as supports of well-dispersed Pt catalysts for environmental applications. *Applied Catalysis B: Environmental*, *54*(3), 175–182. https://doi.org/10.1016/j.apcatb.2004.06.009.

(137) Zhang, A. M., Dong, J. L., Xu, Q. H., Rhee, H. K., & Li, X. L. (2004). Palladium cluster filled in inner of carbon nanotubes and their catalytic properties in liquid phase benzene hydrogenation. *Catalysis Today*, *93-95*, 347–352. https://doi.org/10.1016/j.cattod.2004.06.122.

(138) Yin, S.-F., Xu, B.-Q., Ng, C.-F., & Au, C.-T. (2004). Nano Ru/CNTs: a highly active and stable catalyst for the generation of CO -free hydrogen in ammonia decomposition. *Applied Catalysis B: Environmental*, *48*(4), 237–241. https://doi.org/10.1016/j.apcatb.2003.10.013.

(139) Zhong, Z., Liu, B., Sun, L., Ding, J., Lin, J., & Tan, K. L. (2002). Dispersing and coating of transition metals Co, Fe and Ni on carbon materials. *Chemical Physics Letters*, *362*(1-2), 135–143. https://doi.org/10.1016/s0009-2614(02)01044-8.

(140) ROS, T., KELLER, D., VANDILLEN, A., GEUS, J., & KONINGSBERGER, D. (2002). Preparation and Activity of Small Rhodium Metal Particles on Fishbone Carbon Nanofibres. *Journal of Catalysis*, *211*(1), 85–102. https://doi.org/10.1006/jcat.2002.3695.

(141) Hrapovic, S., Liu, Y., Male, K. B., & Luong, J. H. T. (2004). Electrochemical Biosensing Platforms Using Platinum Nanoparticles and Carbon Nanotubes. *Analytical Chemistry*, *76*(4), 1083–1088. https://doi.org/10.1021/ac035143t.

(142) Male, K. B., Hrapovic, S., Liu, Y., Wang, D., & Luong, J. H. T. (2004). Electrochemical detection of carbohydrates using copper nanoparticles and carbon nanotubes. *Analytica Chimica Acta*, *516* (1-2), 35–41. https://doi.org/10.1016/j.aca.2004.03.075.

(143) Zanella, R., Basiuk, E. V., Santiago, P., Basiuk, V. A., Mireles, E., Puente-Lee, I., & Saniger, J. M. (2005). Deposition of Gold Nanoparticles onto Thiol-Functionalized Multiwalled Carbon Nanotubes. *The Journal of Physical Chemistry B*, *109*(34), 16290–16295. https://doi.org/10.1021/jp0521454.

(144) Lee, K. Y., Kim, M., Hahn, J., Suh, J. S., Lee, I., Kim, K., & Han, S. W. (2006). Assembly of Metal Nanoparticle−Carbon Nanotube Composite Materials at the Liquid/Liquid Interface. *Langmuir*, *22*(4), 1817–1821. https://doi.org/10.1021/la052435b.

(145) Jiang, L., & Gao, L. (2003). Modified carbon nanotubes: an effective way to selective attachment of gold nanoparticles. *Carbon*, *41*(15), 2923–2929. https://doi.org/10.1016/s0008-6223(03)00339-7.

(146) Ellis, A. V., K. Vijayamohanan, Goswami, R., N. Chakrapani, Ramanathan, L. S., Ajayan, P. M., & G. Ramanath. (2003). Hydrophobic Anchoring of Monolayer-Protected Gold Nanoclusters to Carbon Nanotubes. *Nano Letters*, *3*(3), 279–282. https://doi.org/10.1021/nl025824o.

(147) Gurunathan, S., Hyun Park, J., Choi, Y.-J., Woong Han, J., & Kim, J.-H. (2016). Synthesis of Graphene Oxide-Silver Nanoparticle Nanocomposites: An Efficient Novel Antibacterial Agent. *Current Nanoscience*, *12*(6), 762–773. https://doi.org/10.2174/1573413712666160721143424.

(148) Bao, Q., Zhang, D., & Qi, P. (2011). Synthesis and characterization of silver nanoparticle and graphene oxide nanosheet composites as a bactericidal agent for water disinfection. *Journal of Colloid and Interface Science*, *360*(2), 463–470. https://doi.org/10.1016/j.jcis.2011.05.009.

(149) Zhang, H., & Cui, H. (2009). Synthesis and Characterization of Functionalized Ionic Liquid-Stabilized Metal (Gold and Platinum) Nanoparticles and Metal Nanoparticle/Carbon Nanotube Hybrids. *Langmuir*, *25*(5), 2604–2612. https://doi.org/10.1021/la803347h.

(150) Divya, K. P., Miroshnikov, M., Dutta, D., Vemula, P. K., Ajayan, P. M., & John, G. (2016). *In Situ* Synthesis of Metal Nanoparticle Embedded Hybrid Soft Nanomaterials. *Accounts of Chemical Research*, *49*(9), 1671–1680. https://doi.org/10.1021/acs.accounts.6b00201.

CHAPTER 2

Procedures and Techniques

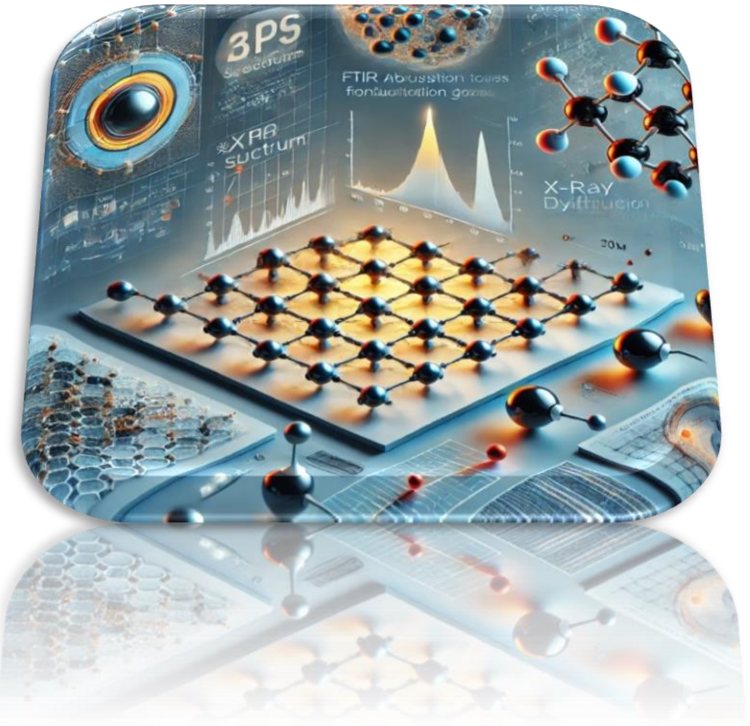

ABSTRACT

In this chapter, we describe the methods used for fabricating graphene oxide and carbon nanotube paper, for modulating the physical and chemical properties of graphene oxide and carbon nanotubes in powder and paper form *via* amine functionalisation, and for *in situ* formation and deposition of silver and palladium nanoparticles onto these nanomaterials. The details of the characterization tools utilized in the projects described in this dissertation are also given.

2.1. Synthesis and sample preparation procedures

2.1.1 Fabrication of free-standing graphene oxide paper

For the fabrication of graphene oxide paper (GOP), aqueous dispersions of single-layer graphene oxide powder (GO, ≥ 99 wt% purity, platelet diameter of 300–800 nm and thickness of 0.7–1.2 nm) purchased from Cheap Tube Inc., were used in a concentration of 6.66 mg/mL, homogenised by ultrasonic treatment and subsequently filtered using a vacuum filtration system from Sigma-Aldrich, employing cellulose acetate membranes (0.45 µm pore size, 47 mm diameter, Healthcare Life Sciences, Whatman). The circular GOP sheets thus obtained were detached from the cellulose filters, dried and stored under vacuum[1](Fig. 2.1).

2.1.2 Fabrication of free-standing carbon nanotube paper

For the fabrication of the multiwalled carbon nanotube-based paper, hereinafter called *buckypaper* and abbreviated as BP, we employed the starting material in powder form, purchased from Nanostructured & Amorphous Materials Inc. (MWCNTs, 95 wt% purity, inner diameter < 8 nm and length of 10 – 50 µm). A general two-step protocol was employed for the BP formation, which includes the pre-oxidation of the raw carbon material, followed by the construction of the buckypaper itself.[2] (Fig. 2.2):

1. Oxidation of carbon nanotubes

To improve the processability of the as-received carbon nanotubes while avoiding damaging their physical structure as much as possible, they were treated with nitric acid (65.7%, from J.T. Baker) at a temperature range between 80 – 100°C for 1 h.[2] Subsequently, several thorough washes with distilled water were performed to achieve a neutral pH. The oxidized nanotubes (hereinafter named $\text{MWCNTs}_{(ox)}$) were dried and stored under vacuum.

2. Formation of mouldable structures

Firstly, an aqueous dispersion of 0.2 % w/v of Triton™ X-100 surfactant was prepared. Then, 60 mg of $\text{MWCNTs}_{(ox)}$ were added. The as-formed suspension was magnetically stirred for 15 min, followed by 3 h sonication. After that, the suspension was centrifuged for 10 min at 3000 rpm to remove surplus material. The dispersion obtained was vacuum-filtered ($P = 10^{-2}$ Torr, Sigma-Aldrich setup) for 2 h through nylon membranes (0.45 µm pore size, 45 mm diameter, Healthcare Life Sciences, Whatman). Thereafter the material was washed with methanol and distilled water to eliminate any remaining surfactant. The detachment of the circular buckypaper sheet was favoured by heating to 60 °C for approximately 10 min. [1] Finally, the buckypaper is cooled and stored under environmental conditions.

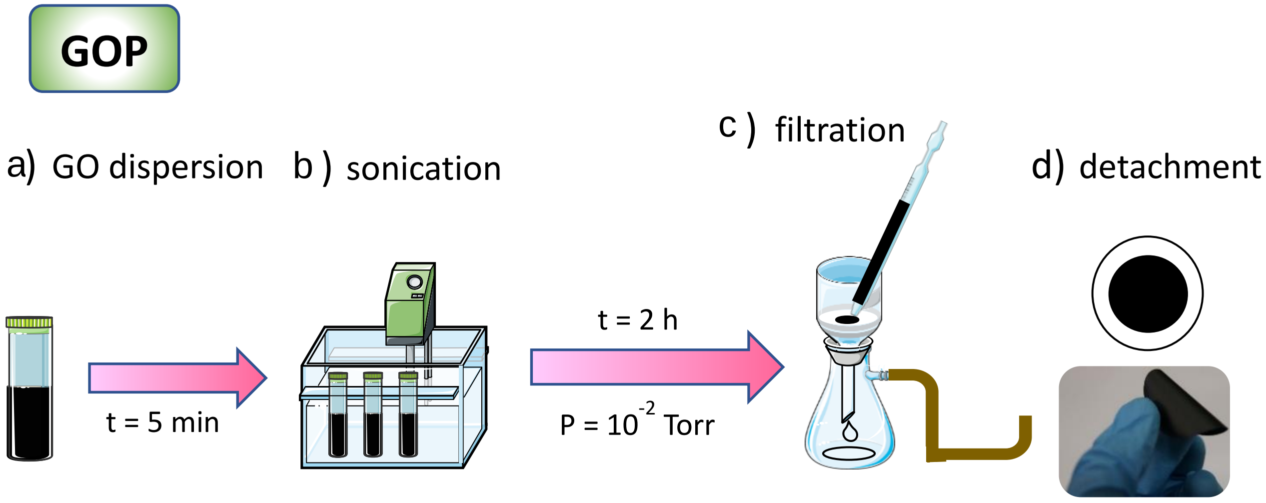

Fig. 2.1. Scheme of the graphene oxide paper preparation

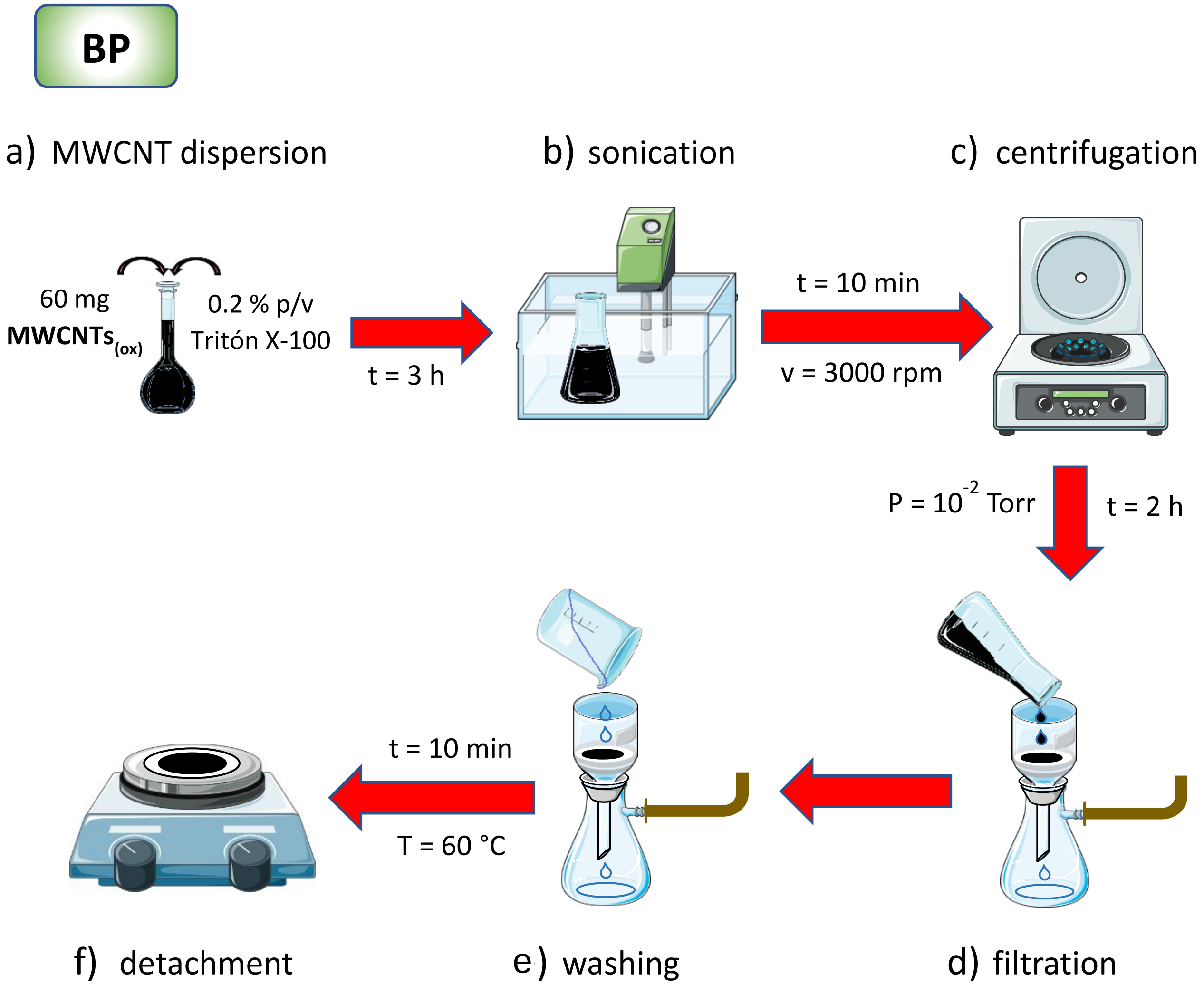

Fig. 2.2. Scheme of the carbon nanotube paper preparation

2.1.3 Amine gas-phase functionalisation of graphene oxide, graphene oxide paper, carbon nanotubes and carbon-nanotube paper

The amine functionalisation of the materials described in Chapters 3 to 6 was carried out following a protocol outlined in our earlier publications[1-4] and optimized for the present purposes. In all the cases two aliphatic amines with different functionalities were employed: 1) 1-octadecylamine (≥ 99 %; named ODA in the following), and 2) 1,8-diaminooctane (≥ 98 %; labelled as DAO), both purchased from Sigma-Aldrich. The amine-functionalized samples are identified as GO+ODA, GO+DAO, GOP+ODA, GOP+DAO, MWCNTs+ODA, MWCNTs+DAO, BP+ODA, and BP+DAO in the following.

The yield was improved by employing a carbonaceous material/amine weight-to-weight w/w ratio of 1:1. For the powder series a direct pre-contact with the amines was required placing them together in a glass tube (Fig. 2.3a). For the functionalization of paper samples, it is important to prevent direct contact with amines (Fig. 2.3b). For this purpose, the amine was positioned at the lowermost section of the reaction vessel, and a hollow glass support was placed atop it. Either GOP or BP was put on top of the support to ensure uniform functionalization throughout. The functionalization process comprised three steps: (1) degassing for 1 h at approximately 100 °C under constant evacuation pressure of 10^{-2} Torr; (2) functionalization reaction under static vacuum of 10^{-2} Torr for 2 h in a temperature range of 160–180 °C; (3) degassing at 100 °C under continuous evacuation for an additional hour, with the purpose of removing excess amine (Fig. 2.4).

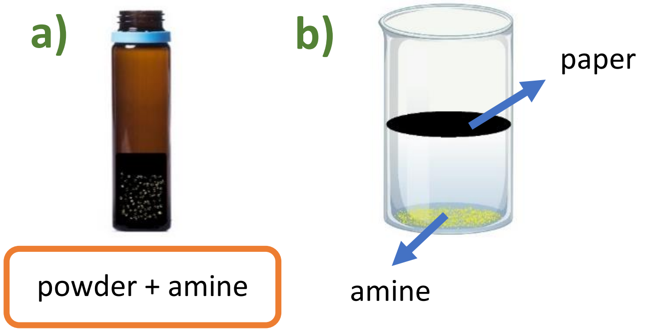

Fig. 2.3. Schematic representation of the functionalization process. a) Scheme of the reaction for the powdered materials. b) Scheme of the reaction for the paper-like materials.

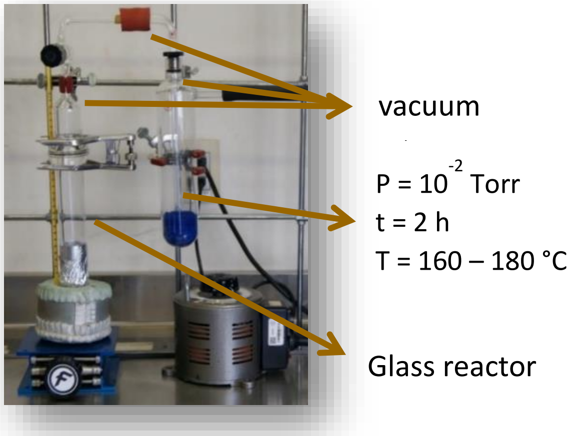

Fig. 2.4. Photograph of the gas-phase reaction system for the chemical functionalization of carbonaceous materials.

2.1.4 In situ formation and deposition of silver and palladium nanoparticles

2.1.4.1 Silver nanoparticles

The procedure to prepare and deposit silver nanoparticles (AgNPs) was based on the previously employed protocol for the decoration of C_{60} films and graphene oxide powder and paper,[4,5] consisting of the chemical reduction of Ag^+ ions with citric acid as a reducing/stabilizing agent (Fig. 2.5).

For preparing the hybrids, either powder or paper GO or $MWCNTs_{(ox)}$ were mixed with 2-propanol (≥ 99.8 %, Sigma-Aldrich) using a ratio of 0.5 mg/mL. Immediately afterwards, solutions of citric acid (≥ 99.5 %, Sigma-Aldrich) 0.01 M and silver nitrate [$AgNO_3$] (≥ 99 %, Sigma Aldrich), 0.005 M using 2-propanol (≥ 99.8 %, Sigma-Aldrich) as a solvent, were prepared and simultaneously added dropwise to the reaction vessel while continuously stirring at room temperature for 30 min. The samples were decanted and washed twice using 2-propanol (≥ 99.8 %, Sigma-Aldrich). Finally, all samples were dried and stored under vacuum at room temperature. The samples decorated with AgNPs are labelled as GO+Ag, GO+ODA+Ag, GO+DAO+Ag, GOP+Ag, GOP+ODA+Ag, GOP+DAO+Ag, MWCNTs+Ag, MWCNTs+ODA+Ag, MWCNTs+DAO+Ag, BP+Ag, BP+ODA+Ag, and BP+DAO+Ag.

2.1.4.2 Palladium nanoparticles

For the preparation and deposition of palladium nanoparticles (PdNPs), we developed a protocol based on the methods reported by Roy *et al.*,[6] Dar *et al.*,[7] and Li *et al.*,[8] which consisted of the reduction of Pd^{2+} ions using palladium chloride [$PdCl_2$] (≥ 99 %, Sigma-Aldrich), as a precursor and citric acid (≥ 99.5 %, Sigma-Aldrich) as a reducing/stabilising agent. For achieving homogeneous dispersions, it was necessary to dissolve the metallic precursor in a 0.2 N solution of hydrochloric acid [HCl] (≥ 37 %, Sigma-Aldrich), heated at about 70 °C, which was then diluted with distilled water to obtain $PdCl_2$ 0.005 M (Fig. 2.5).

To prepare the hybrids, amine-functionalized and pristine powder, paper GO, or $MWCNTs_{(ox)}$ were immersed in 0.005 M $PdCl_2$ in a proportion of 0.5 mg/mL. Then, 20 mL of a 0.05 M solution of citric acid (≥ 99.5 %, Sigma-Aldrich) was added to the reaction vessel upon continuous stirring at room temperature (see further details in Chapters 4 and 6). Afterwards, the samples underwent two cycles of washing using distilled water, followed by a drying step and stored under vacuum at room temperature. The samples decorated with PdNPs are labelled as GO+Pd, GO+ODA+Pd, GO+DAO+Pd, GOP+Pd, GOP+ODA+Pd, GOP+DAO+Pd, MWCNTs+Pd, MWCNTs+ODA+Pd, MWCNTs+DAO+Pd, BP+Pd, BP+ODA+Pd, and BP+DAO+Pd.

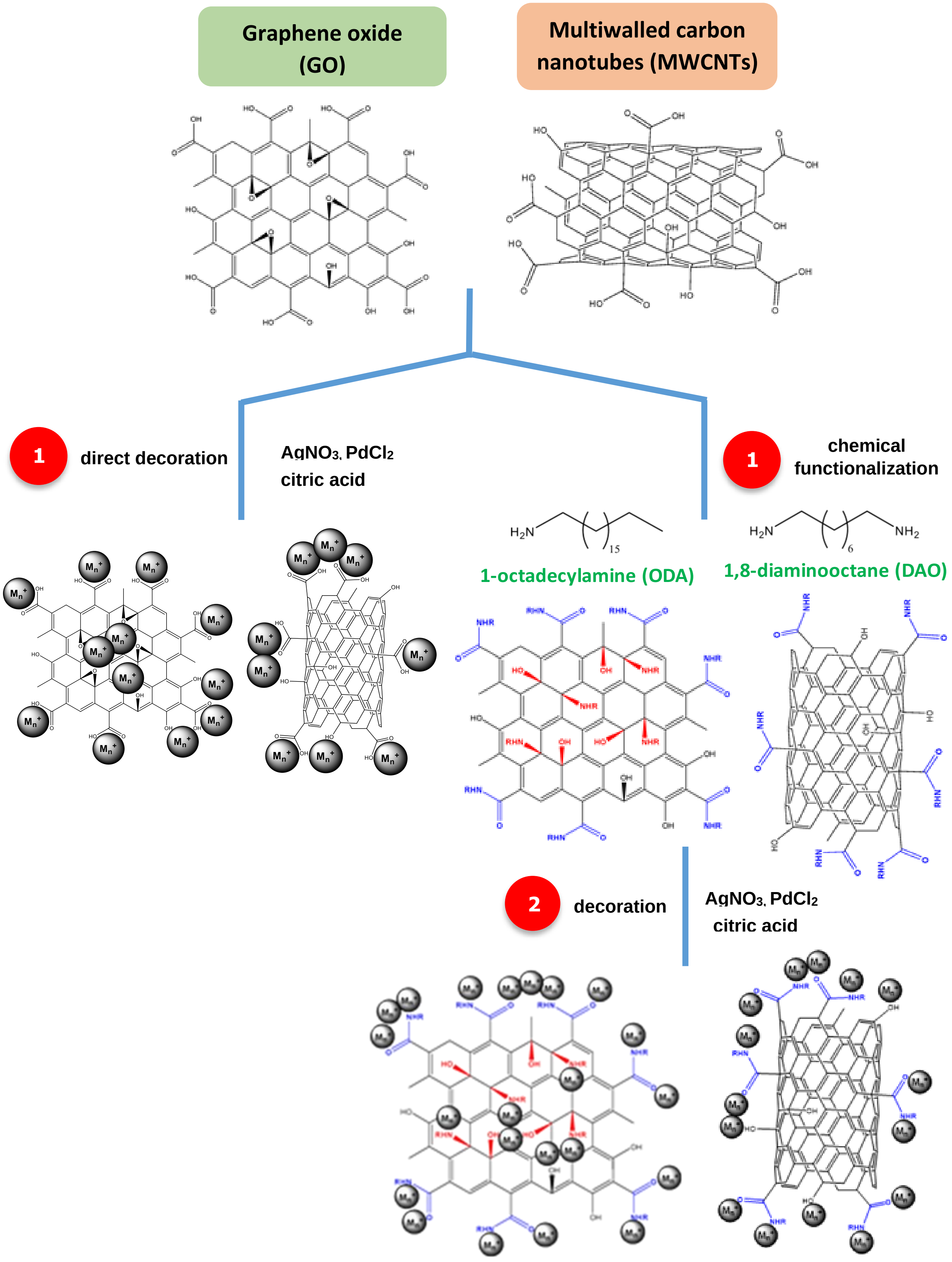

Fig. 2.5. General scheme for the metal coordination of either silver or palladium atoms with oxygen and/or nitrogen atoms within the carbonaceous matrix of GO and MWCNTs.

2.2. Characterization techniques

2.2.1 Dispersion tests

To assess changes in the chemical nature when passing from the pristine materials to the hybrids, dispersibility tests in different solvents, namely distilled water, 2-propanol (≥ 99.8 %), and toluene (99.8 %) acquired from Sigma-Aldrich, were performed as described in Chapters 3 to 6. For this purpose, dispersions of all the samples were prepared in a concentration of 0.5 mg/mL of solvent. These dispersions were then subjected to an ultrasonic bath for 10 minutes at room temperature. Changes in stability were monitored through a sequence of photographs taken at several time intervals in the period starting after just finishing the sonication (0 h) and ending 24 h later. The studies were carried out both at the Institute of Applied Sciences and Technology at UNAM and the Zernike Institute for Advanced Materials at UG.

2.2.2 Fourier Transform Infrared Spectroscopy

Mid-infrared (IR) spectroscopy is a well-established technique for the identification of chemical compounds. The bands in the IR spectrum of a sample are associated with the excitation of vibrational modes of the molecules in the sample and are thus directly linked with the various chemical bonds and functional groups present. Therefore, the IR spectrum of a compound is one of its most characteristic physical properties and can be regarded as its "fingerprint". [9] IR absorption only occurs if the vibrating bond has a net dipole moment.[9,10] In traditional IR spectroscopy, specific IR frequencies are selected for the analysis, which is a long and cumbersome procedure. This problem was solved with the advent of Fourier transform infrared spectroscopy (FTIR), where a blackbody source combined with a Michelson interferometer provides the IR light; for each mirror position of the interferometer a combination of IR frequencies hits the sample and the detector registers how much of the light is absorbed. These data are displayed in a time domain spectrum called interferogram that is converted to a frequency domain spectrum by the application of a mathematical procedure known as Fourier transform.[10] Fourier Transform Infrared (FTIR) spectroscopy is a powerful technique used to analyse the composition of materials by identifying the bonds present from their interaction with infrared radiation. There are two common methods employed in FTIR spectroscopy for sample preparation and analysis: the KBr pellet method and the Attenuated Total Reflectance (ATR) method[11-13] (Fig. 2.6).

KBr Pellet Method

Differences

- *Sample preparation:* In this method, the sample is typically ground into a fine powder and then mixed with potassium bromide (KBr) powder, which is transparent to infrared radiation. The mixture is then compressed into a pellet.
- *Transmission measurement:* By measuring the transmission of infrared light through the pellet, the IR spectrum is obtained.

Advantages

1. *Broad Applicability*: Suitable for solid samples in powder form.
2. *High transmittance*: The KBr pellets typically have high transmittance in the mid-infrared region, allowing for sensitive detection of sample components.

Disadvantages

1. *Sample destruction*: Since the sample needs to be ground, its physical and chemical properties can be altered.
2. *Limited sensitivity*: For samples with weak absorption bands, the sensitivity may be relatively low.
3. *Susceptible to water absorption:* KBr pellets are hygroscopic and can absorb moisture from the environment, which may interfere with the spectra.

Attenuated Total Reflectance Method

Principle

Attenuated Total Reflectance (ATR) FTIR spectroscopy involves bringing the sample into contact with an internal reflection element (IRE), such as a diamond or a zinc selenide crystal. Infrared light is directed through the crystal at an angle such that it undergoes total internal reflection. The evanescent wave generated at the crystal/sample interface interacts with the sample, and the resulting spectrum is measured.

Differences

- *Sample preparation:* With this method, the sample is typically placed in direct contact with an ATR crystal.
- *Reflection measurement:* Here the infrared radiation undergoes multiple internal reflections within the ATR crystal, leading to attenuated total reflection. The resulting spectrum is measured from the reflected radiation.

Advantages

1. *Minimal sample preparation:* Requires minimal to no sample preparation, making it faster and simpler compared to the KBr pellet method.
2. *Versatility:* Suitable for analysing a wide range of sample types, including solids, liquids, and thin films.
3. *High sensitivity:* Capable of detecting small quantities of samples, making it useful for trace analysis.
4. *Real-time analysis:* Provides rapid results, making it suitable for process monitoring and *in situ* measurements.

Disadvantages

1. *Surface sensitivity:* Primarily probes the outermost layer of the sample, which may not be representative of the bulk material.
2. *Spectral artefacts:* ATR spectra may exhibit some spectral artefacts, such as baseline distortions, due to the interaction between the sample and ATR crystal.
3. *Limited penetration depth:* The depth of penetration varies with the wavelength of light and the refractive index of the sample, limiting its applicability for thick samples.

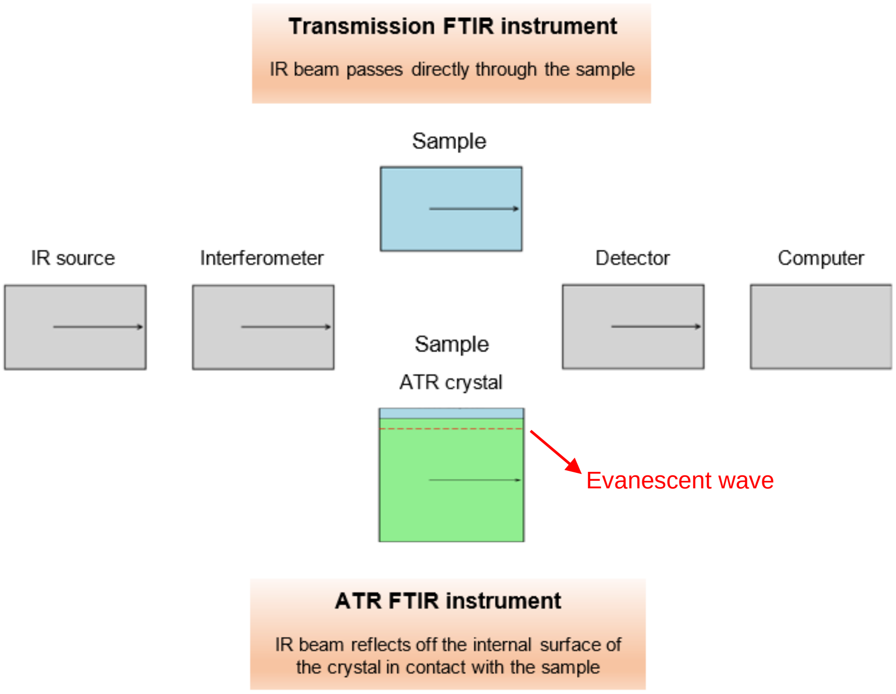

Fig. 2.6. Schematic representation of transmission FTIR and of ATR FTIR.

All FTIR spectra were acquired at standard conditions (room temperature and atmospheric pressure). For the projects reported in Chapters 3 and 4, they were measured employing a Nicolet iS50R ThermoScientific spectrometer in attenuated total reflectance (ATR). Each spectrum was the sum of 32 scans, collected in the range of 500–4000 cm^{-1} with a resolution of 4 cm^{-1}. The data were collected in the Institute of Applied Sciences and Technology at UNAM. The FTIR spectra in Chapters 5 and 6 were collected in diffuse reflectance mode on a Shimadzu IRTracer-100 spectrometer, using a Happ-Genzel apodization ranging from 500 to 4000 cm^{-1}. Each spectrum was the average of 100 scans, collected at 2 cm^{-1} resolution. KBr pellets at 0.1 % w/w were fabricated for these purposes. These studies were carried out at the Zernike Institute of Advanced Materials at UG.

2.2.3 X-Ray Photoelectron Spectroscopy

X-ray photoelectron Spectroscopy (XPS) is a surface-sensitive quantitative technique that allows us to determine the elemental composition and obtain information on the chemical environment and oxidation state of the elements composing a material[14].

Theory and Fundamentals

1. *Photoelectric effect:* The XPS technique is based on the photoelectric effect, first explained by Albert Einstein. When a material is bombarded with X-rays, it emits electrons. The energy of these electrons (photoelectrons) is characteristic of the elements present in the material.

2. *Binding energy:* The key parameter in XPS is the binding energy of the electrons. It is the energy required to remove an electron from a specific core level of an atom. In XPS one measures the kinetic energy of these electrons and, knowing the energy of the X-ray source and the work function of the analyser, the binding energy can be calculated.

3. *Instrumentation:* The primary components of an XPS system include an X-ray source, a sample holder, an ultra-high vacuum chamber, and an electron detector.

4. *Peaks in XPS spectra*: In an XPS spectrum, peaks correspond to the photoelectron signals of different core levels of the elements present. The position of a peak gives the binding energy, and since the binding energy is characteristic of the specific core level from which the photoelectron was emitted, the corresponding atom can be identified. Hydrogen cannot be detected because the cross-section for photoionization with X-rays is too low. The intensity of the peak is directly proportional to the number of atoms of that element in the probed volume and can therefore be used to determine the concentration of the element.

5. *Information on chemical environment and oxidation state*: The energy necessary for the emission of a core electron strongly depends on the valence electron distribution, and therefore shifts in peak binding energies can provide information about the chemical state of the elements.

6. *Depth profiling:* XPS can be used for depth profiling by varying the angle of electron collection or by sputtering the surface with ions to remove layers of material.

Applications and examples[15]

- *Material characterization:* XPS is widely used in the characterization of surface chemistry of materials in fields like metallurgy, ceramics, and polymers.
- *Corrosion analysis*: XPS is vital for studying the surface chemistry of corroded metals, helping to understand corrosion and consequently prevent it.
- *Semiconductor research:* XPS provides essential information on the surface chemistry of semiconductors, crucial for the development of electronic devices.
- *Catalysis:* In catalysis research, XPS helps in understanding the surface composition and state of catalysts.
- *Environmental science:* XPS is used for the analysis of environmental contaminants and the effects of pollution on different materials.

X-ray photoelectron spectroscopy (XPS) measurements of the samples described in Chapters 4 to 6 were performed by using a Surface Science Instruments SSX-100 ESCA spectrometer, equipped with a monochromatic Al Kα X-ray source (hν = 1486.4 eV) (Fig. 2.7). The pressure in the analysis chamber was maintained at 1×10^{-9} mbar during data acquisition and the electron take-off angle with respect to the surface normal was 37°. The samples were mounted on double-sided carbon tape. To compensate for the sample charging, a molybdenum grid was mounted above the samples. The XPS data were acquired by using a spot size of 1000 μm in diameter and selecting an energy resolution of 1.7 eV for the survey spectra and of 1.3 eV for the detailed spectra of core-level regions. The XPS spectra were analysed by means of the least-squares curve-fitting program Winspec (developed at the LISE laboratory of the University of Namur, Belgium). The spectral analysis included a Shirley background subtraction; peak profiles were taken as a convolution of Gaussian and Lorentzian functions. The fitting was carried out with the number of peaks according to the structure of the molecules on the surface. Binding energies were referenced to the C 1*s* photoemission peak centred at 284.5 eV.[16] The associated uncertainty for the binding energy of peak positions deduced from the deconvolution was ± 0.1 eV. The photoemission peak areas of each element, used to estimate the amount of each species on the surface, were normalized by the sensitivity factors of each element tabulated for the SSX-100 photoelectron spectrometer. All measurements were carried out on freshly prepared samples. Three different spots per sample were measured for reproducibility. The measurements were performed in the Surfaces and Thin Films Group of the Zernike Institute of Advanced Materials at UG.

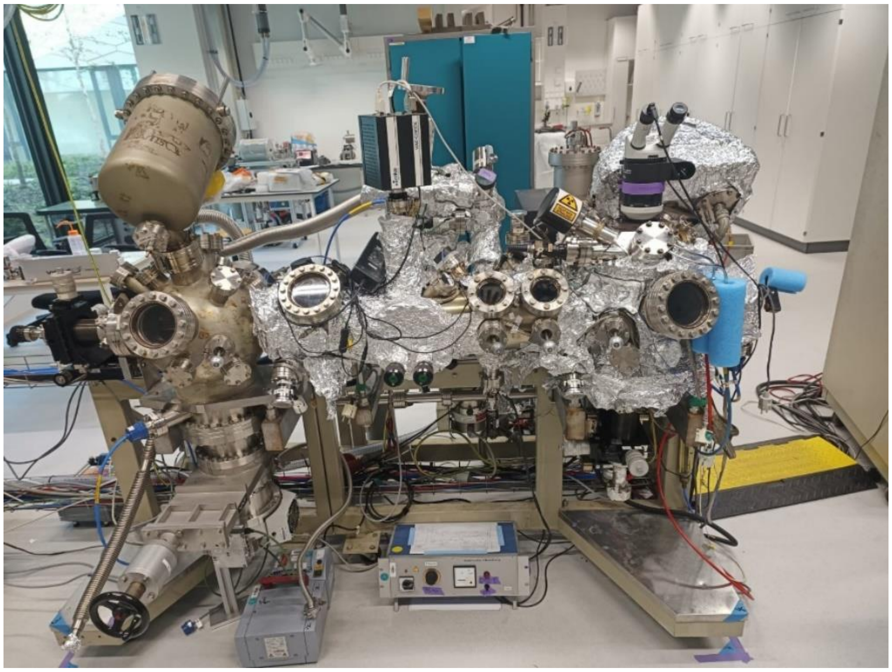

Fig. 2.7. Photograph of the XPS spectrometer setup.

2.2.4 Thermal analysis

Thermal analysis comprises a series of techniques where changes of mass in a sample as a function of temperature or time are monitored within a controlled atmosphere saturated mostly with nitrogen, helium, or air, or under vacuum. Among the most common techniques are thermogravimetric analysis (TGA) and differential thermal analysis (DTA).[17,18]

TGA measures the mass of a sample as it is heated, cooled, or held at a constant temperature (Fig. 2.8). The data is typically presented as a plot of mass against temperature or time, which is called a thermogram. This plot provides information regarding the thermal stability and composition of the initial sample, the intermediate products that may form and the composition of the solid residue (if any). To get useful information, the sample should evolve into a volatile product because of various physical and chemical processes taking place in the sample upon heating. This measurement provides information about physical phenomena, such as phase transitions, absorption and desorption; as well as chemical phenomena including chemisorption, thermal decomposition, and solid-gas reactions (*e.g*. oxidation or reduction).

DTA measures the temperature difference between a sample and a thermally inert reference material subjected to a controlled temperature program. The data is presented as a plot of the temperature difference against the sample temperature or time (DTA curve, or thermogram). Changes in the sample, either exothermic or endothermic, can be detected, such as glass transitions, crystallization, melting and sublimation. A DTA curve can be used only as a fingerprint for identification purposes but usually, it helps to determine phase diagrams, heat change measurements and decomposition in various atmospheres.

Thermogravimetric and differential thermal analysis (TGA–DTA) reported in Chapters 3 to 6 were carried out using a STA 449 C Jupiter instrument from Netzsch Gerätebau GmbH. For the tests, samples of approximately 10 mg were exposed to an airflow of 100 mL/min, and a heating ramp of 10 °C /min up to 1000 °C. The thermograms were collected by Dr Edgar Álvarez-Zauco of the Faculty of Science at UNAM.

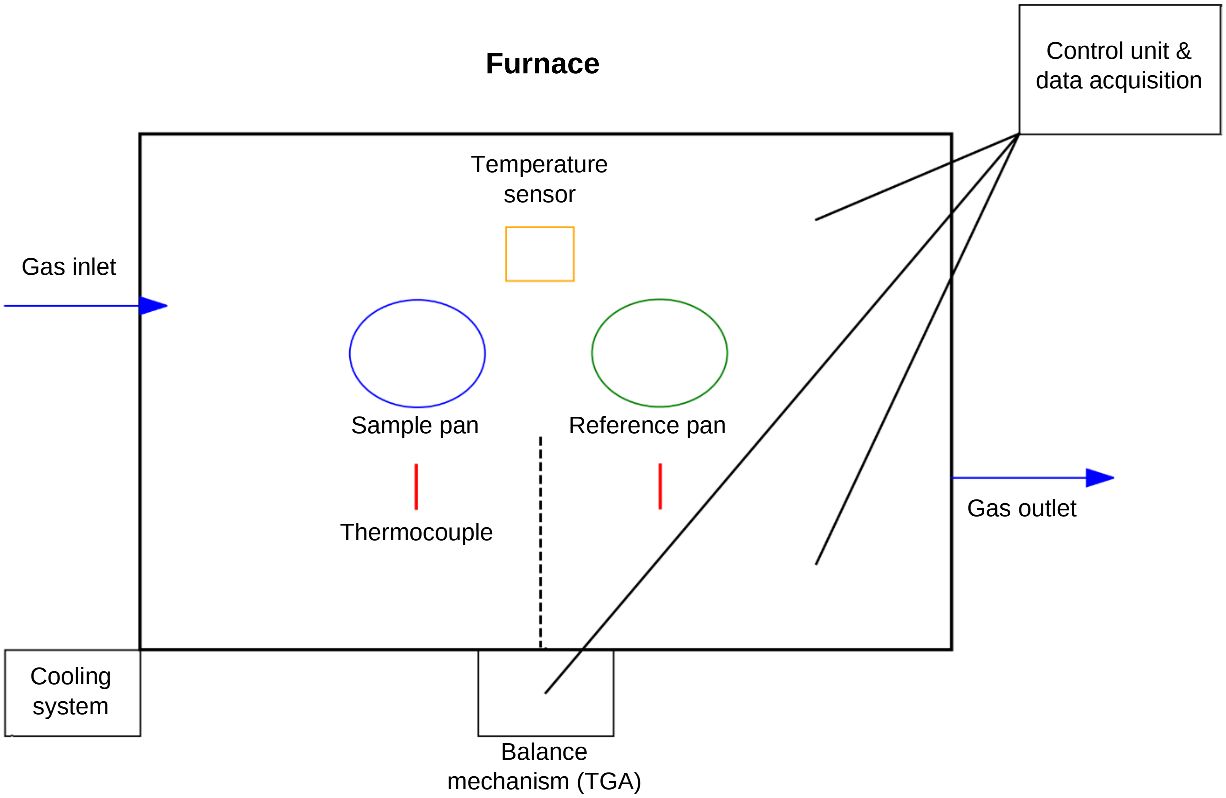

Fig. 2.8. Scheme of a typical thermal and differential analysis setup.

2.2.5 X-Ray Diffraction

X-ray diffraction (XRD) is a very useful characterization tool to study, non-destructively, the crystallographic structure of materials and thin films. In crystalline phases, XRD enables the determination of various structural properties such as strain, grain size, phase composition, and defect structure. In amorphous materials such as polymers, it is used to determine the atomic arrangements.[19] XRD offers unparalleled accuracy in measuring atomic spacing. The main use of powder diffraction is to identify components in a sample by a search/match procedure. Each crystalline phase gives rise to a specific diffraction pattern that serves as its fingerprint. In a mixture each compound contributes its pattern independently of the others, facilitating the characterization and identification of the different phases. Furthermore, the areas under each diffraction peak correlate with the amount of each phase present in the sample.

Experimental arrangements

In X-ray diffraction, measurements are performed differently on single crystals and polycrystalline samples than on powder samples. For lab setups crystalline samples typically have sizes of 0.3 mm in diameter. In powder or polycrystalline diffraction, it is important to have a sample with a smooth plane surface. Normally, the sample is ground down to particles of diameters of about 0.002 mm to 0.005 mm. The ideal sample is homogeneous, and the crystallites are randomly distributed. The sample is pressed into a sample holder so that a smooth flat surface is obtained.

A typical powder XRD instrumentation consists of four main components: 1) the X-ray source, 2) the sample stage, 3) the receiving optics and 4) the X-ray detector. The source and the detector with their associated optics lie on the circumference of the focusing circle and the sample stage is at the centre of the circle (Fig. 2.9).

Bragg's law is the basis of XRD analysis. It relates the wavelength (λ) of the reflected X-ray, the spacing between the atomic planes (d) and the angle of diffraction (θ) as follows:

$$2d \sin \theta = n \lambda \qquad 1)$$

With this law, it is possible to accurately determine the crystal structure. The angle between the plane in the crystal structure of the sample and the X-ray source is θ, known as Bragg’s angle and the angle between the transmitted and diffracted beams will always be 2θ. For the XRD analysis, fine powdered samples are mounted on the sample holder and this powder is assumed to have randomly oriented crystallites. When a beam of X-ray incident on the sample, X-rays are scattered by each atomic plane in the sample. If the scattered beams are in phase, they interfere constructively and the intensity maximum at that particular angle is obtained. The atomic planes from where the X-rays are scattered are referred to as ‘reflecting planes’[19]. The intensity of the diffraction signal is usually plotted against the diffraction angle 2θ, but d [nm] or 1/d [nm^{-1}] may also be used. The most common wavelength used in XRD is 1.5406 Å (Cu K_α).[20]

The X-ray powder diffraction data reported in Chapter 3 was obtained using a D8 Advance Bruker diffractometer with a Bragg-Brentano geometry and Cu K_α radiation (λ = 1.5406 Å). To properly prepare the sample for XRD studies, it was finely pulverized and afterwards sieved using different meshes. Finally, the resulting powder was deposited in a tube for XRD analysis. The XRD spectra were recorded in a 2θ range from 4° to 110° by Ing. Antonio Morales-Espino in the

Physics Institute at UNAM. The Cambridge Crystallographic Data Centre database was employed to identify the crystallographic phases.

The spectra of the powder samples discussed in Chapters 4 to 6 were obtained on a D8 Advance Bruker diffractometer with a monochromatic Cu K_α X-ray source (λ = 1.5418 Å) and a secondary beam graphite monochromator, using a LYNXEYE detector (1D mode). The samples were finely ground with an agate mortar, and the patterns were recorded in a 2θ range from 3° to 60°, in steps of 0.02° and with a counting time of 1.0 s per step. The diffractograms were collected at the Zernike Institute of Advanced Materials at UG.

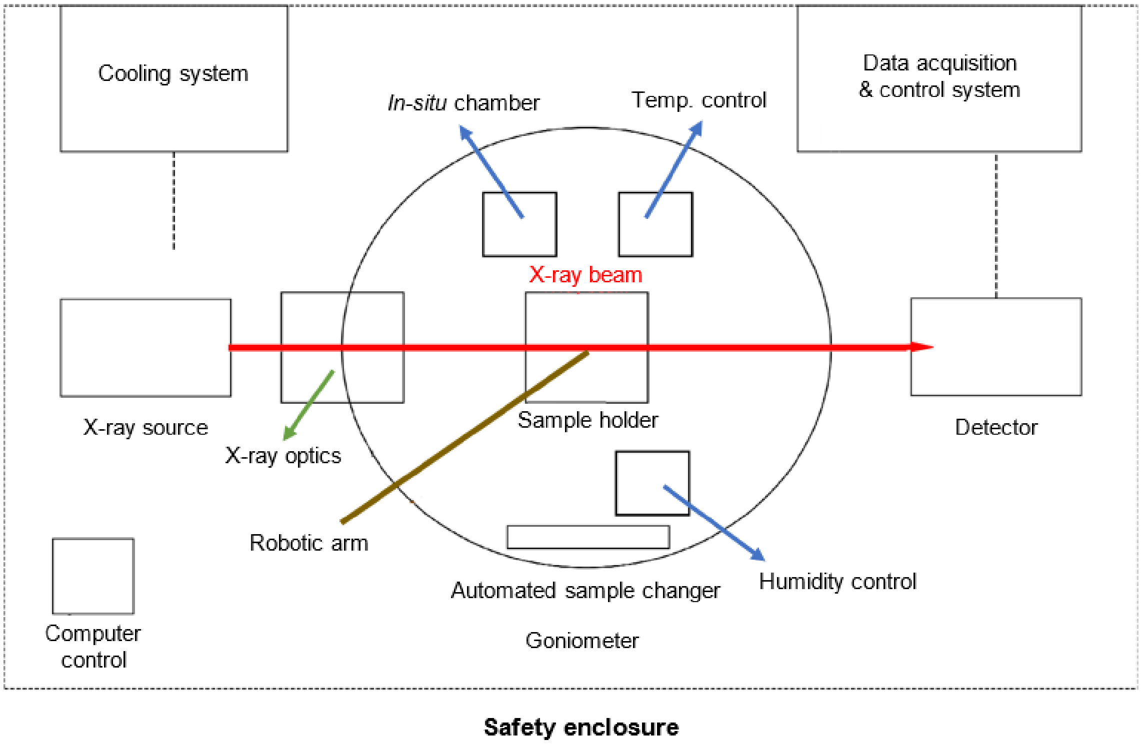

Fig. 2.9. Schematic diagram of a modern automated XRD diffractometer.

2.2.6 Scanning Electron Microscopy/ Energy-Dispersive X-ray Spectroscopy

The Scanning Electron Microscope (SEM) operates by bombarding a sample with high-energy electrons and then analysing the electrons backscattered or emitted from the sample and the X-rays generated in the interaction of the primary electrons with the sample. Information about the sample’s topography, morphology, composition, grain orientation, and crystallography is obtained. Morphology relates to the sample's shape and size, while topography refers to surface features, including texture, smoothness, or roughness.[21,22]

In the Scanning Electron Microscope (SEM), electrons are generated in an electron gun, then accelerated and focused into a fine beam that scans across the sample's surface. When these high-energy electrons interact with the target material, they can either be backscattered or lose energy to excite the sample's atoms, leading to the emission of X-rays and secondary electrons as the excited states decay. These emissions are detected point-by-point as the beam moves across the surface, producing detailed images that can resolve features as small as 10 nm. SEM can only image conducting surfaces, as insulating surfaces accumulate charge when struck by electrons, distorting the image. To overcome this, a very thin metal coating can be applied to insulating surfaces, allowing them to be imaged effectively.

The topography of the sample influences electron reflection and the emission probability of secondary electrons, differing between protrusions and flat regions. Also, heavier atoms are more effective in backscattering than lighter ones. By plotting the backscattered electrons against the beam position on the sample, a detailed SEM image depicting the sample's surface features is formed (Fig. 2.10).

In addition to imaging morphology, SEM also detects X-rays and Auger electrons generated by the interaction of the electron beam with the sample's surface atoms. The electrons with typical energies chosen between 5 keV and 30 keV or higher, can create core holes in atoms by ejecting core electrons. These excited atoms decay as shallower electrons fill the core holes, releasing energy (ΔE) either as a photon (X-ray emission) or transferring it to another electron, causing an Auger emission. The likelihood of each process depends on the atomic number, with Auger decay being more common in lighter atoms and X-ray emission prevalent in heavier atoms. The energy difference (ΔE) between the initial and final electron levels during decay is characteristic of the specific atom, allowing for the identification of the sample's surface elements. As the electron beam scans the surface, the SEM not only detects backscattered and secondary electrons but also collects X-rays (Fig. 2.11). This capability, known as Energy-Dispersive X-ray Spectroscopy (EDS), enables simultaneous mapping of the sample's morphology and elemental composition. The detector's geometry, such as the solid angle, is optimized to increase the collection efficiency of X-rays, allowing for more accurate and sensitive EDS measurements. This is particularly beneficial for analysing beam-sensitive samples, like biological specimens or certain semiconductors, where lower energy electron beams are required.[23] EDS is particularly useful for analysing microstructural features, surface contamination, and the characterization of thin films and coatings.[23,24]

SEM imaging from samples described in Chapters 3 to 6 was performed with a JEOL JSM-6510LV instrument, operated at an acceleration voltage of 20 kV, and coupled to an INCA Energy 250 Energy Dispersive X-ray (EDS) Microanalysis System from Oxford Instruments.

In all the cases two imaging modes were used: to achieve a good spatial resolution, secondary electron images (SEI) were obtained, and to reveal compositional differences based on the atomic number, backscattered electron composition (BEC) micrographs were acquired. For powder samples micrographs at 10, 5 and 0.5 µm were collected, whereas 10, 1 and 0.5 µm were obtained for the paper-like materials. EDS spectra were acquired for every sample in 5 different spots with a diameter of 30 µm. Imaging was performed by Dr Víctor Meza-Laguna in the Nuclear Science Institute at UNAM.

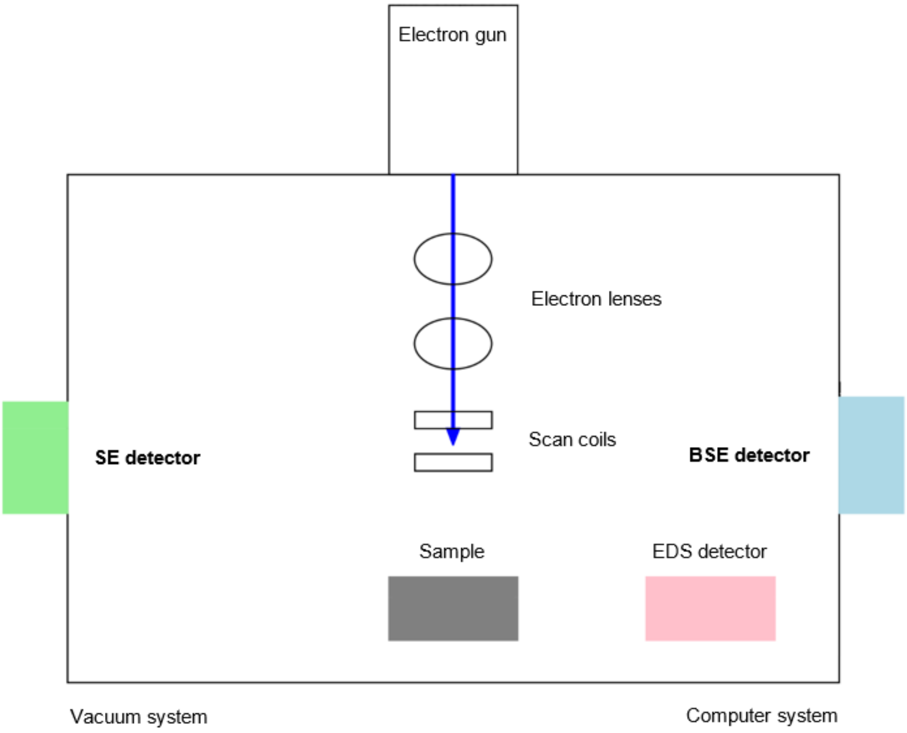

Fig. 2.10. Schematic representation of a scanning electron microscope coupled with EDS.

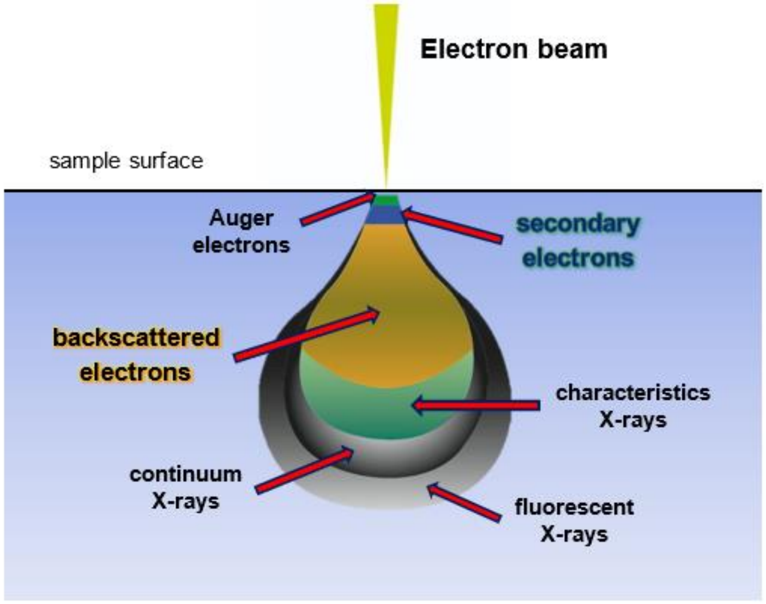

Fig. 2.11. Schematic of the electron beam interaction with a specimen.

2.2.7 Transmission Electron Microscopy

Transmission electron microscopy (TEM) is one of the most advanced and versatile characterization techniques,[25] which is used to observe the internal structure of samples at the atomic or molecular level.

Fundamentals and physical principles[26]

1. *Electron source:* TEM uses electrons as the source of illumination. These electrons are produced by heating a filament (W or LaB_6) and accelerated in a vacuum to high energies. Alternatively, field emission is used to produce the electrons when coherence and high brightness are required.

2. *Electron lenses:* Electromagnetic lenses focus the electrons into a thin, coherent beam that passes through the sample. The electron beam interacts with the specimen, with some electrons being scattered while others pass through.

3. *Sample preparation:* Samples must be very thin (typically less than 100 nm) to allow electrons to pass through. This is necessary because electrons are scattered or absorbed by the material.

4. *Image formation:* The interaction of the electrons with the sample produces an image or a diffraction pattern of the internal structure of the specimen. This interaction depends on the atomic number, crystal structure, and thickness of the sample, affecting the electron's path and creating contrast in the resulting image.

5. *Detection:* The transmitted or scattered electrons are then magnified and focused onto a detector, such as a photographic plate or a CCD camera, to form an image.

Imaging

There are three major imaging modes in TEM: 1) conventional TEM, 2) High-Resolution Transmission Electron Microscopy (HRTEM), and 3) Scanning Transmission Electron Microscopy (STEM)[27] (Fig. 2.12).

1) Conventional transmission electron microscopy

In conventional TEM, a thin specimen is irradiated with an electron beam and a direct image is recorded on the image plane with an objective lens by calculating the scattered amplitudes in a specified direction. Conventional TEM usually works at an acceleration voltage of 100–200 kV and operates in three modes: low magnification, high magnification, and diffraction mode. It can be used for bright-field and dark-field imaging (see below), selected area electron diffraction, micro- and nano-diffraction, and high-resolution imaging. It provides a two-dimensional projection of three-dimensional objects with clear information on size, shape, and structure.[28,29] Zero-dimensional point defects (impurities and vacancies) are invisible in conventional TEM.[30,31]

2) High-resolution transmission electron microscopy

High-resolution transmission electron microscopy (HRTEM) is used to provide micrographs of crystal surfaces at 1 nm spatial resolution. HRTEM with a resolving power of approximately 0.05 nm can be obtained with aberration correctors.[32,33] Suitable micrograph processing with quantitative recording leads to the accurate and reliable determination of defects and inhomogeneities.[34,35]

The image formation process in HRTEM is perceived to occur in two stages. Interaction between incident electrons and atoms of a specimen results in elastic and inelastic scattering. Electrons scattered elastically play a major role in the formation of high-resolution bright-field micrographs. Therefore, HR imaging is always performed in the bright-field imaging mode. On the other hand, electrons scattered inelastically give compositional information using electron energy-loss spectroscopy (EELS) techniques and imaging information through STEM.

3) Scanning transmission electron microscopy

In this mode, a highly focused beam is scanned over the sample and images are collected in dark-field imaging mode. In scanning transmission electron microscope (STEM), the contrast depends solely on the atomic number, Z^{α}, in which α is greater than 1 and all types of electrons (elastically and inelastically scattered, as well as non-scattered) are detected by using an annular detector positioned below the sample.[36-38] That's why this mode is also named high-angle annular dark-field scanning transmission electron microscopy (HAADF-STEM). The STEM mode is also suitable for energy-dispersive spectroscopy (EDS) analysis at the nanoscale and can provide concentration profiles by using EELS in imaging spectral mode.

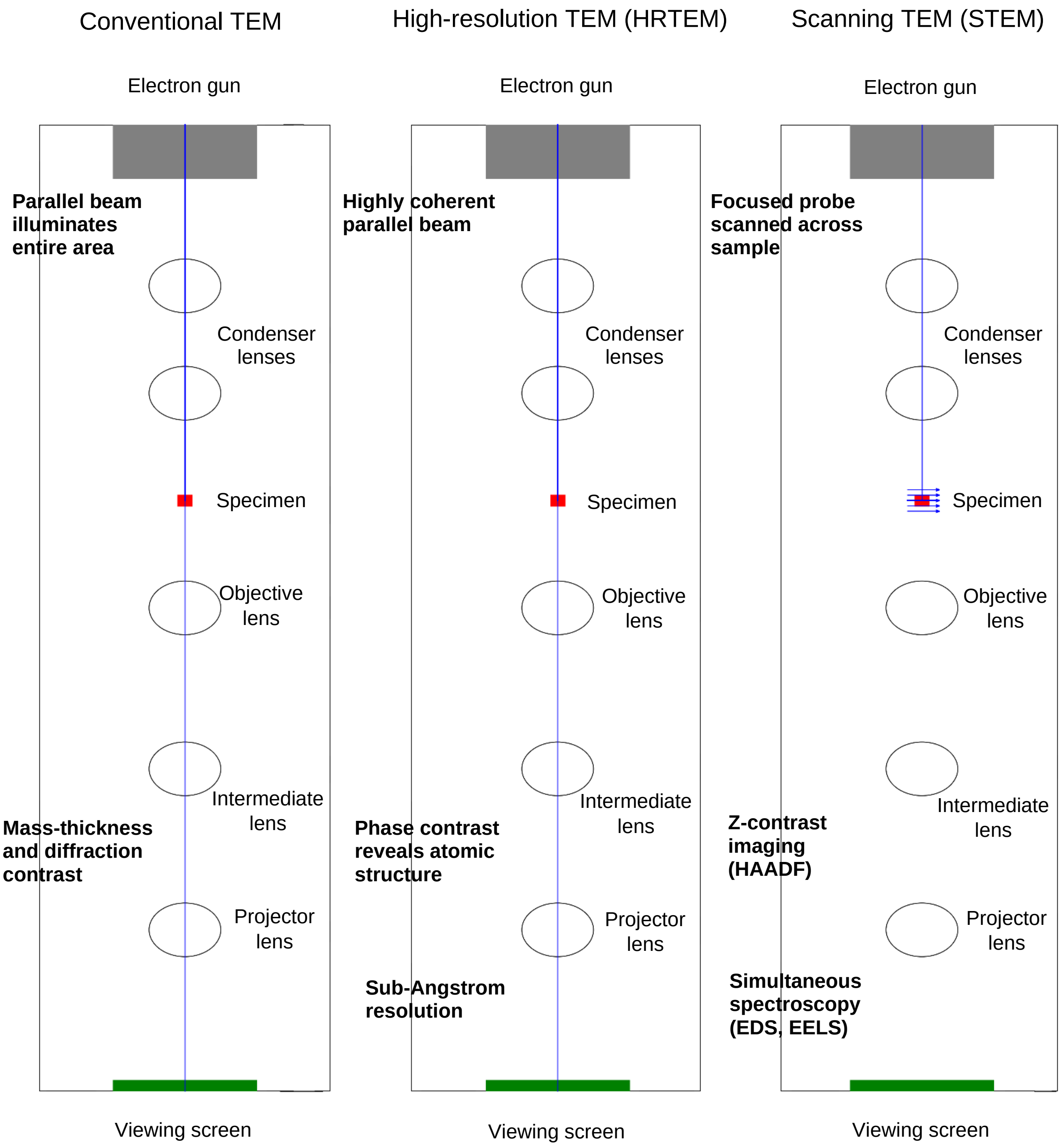

Fig. 2.12. Schematic of a transmission electron microscope (TEM) showing the three important imaging modes: conventional TEM, High-resolution TEM (HRTEM), and Scanning TEM (STEM).

Bright Field vs. Dark Field Techniques[27]

- *Bright Field TEM:* This is the most common imaging mode. The image is formed by electrons that pass directly through the specimen without being scattered, or only scattered elastically. Areas of the specimen that scatter electrons appear darker on a bright background (Fig. 2.13).

- *Dark Field TEM:* In dark-field imaging, the TEM is adjusted so that only electrons scattered by the specimen contribute to the image, while directly transmitted electrons are excluded. This results in bright features on a dark background. Dark-field imaging is useful for highlighting specific features within the specimen, such as defects in crystalline materials (Fig. 2.13).

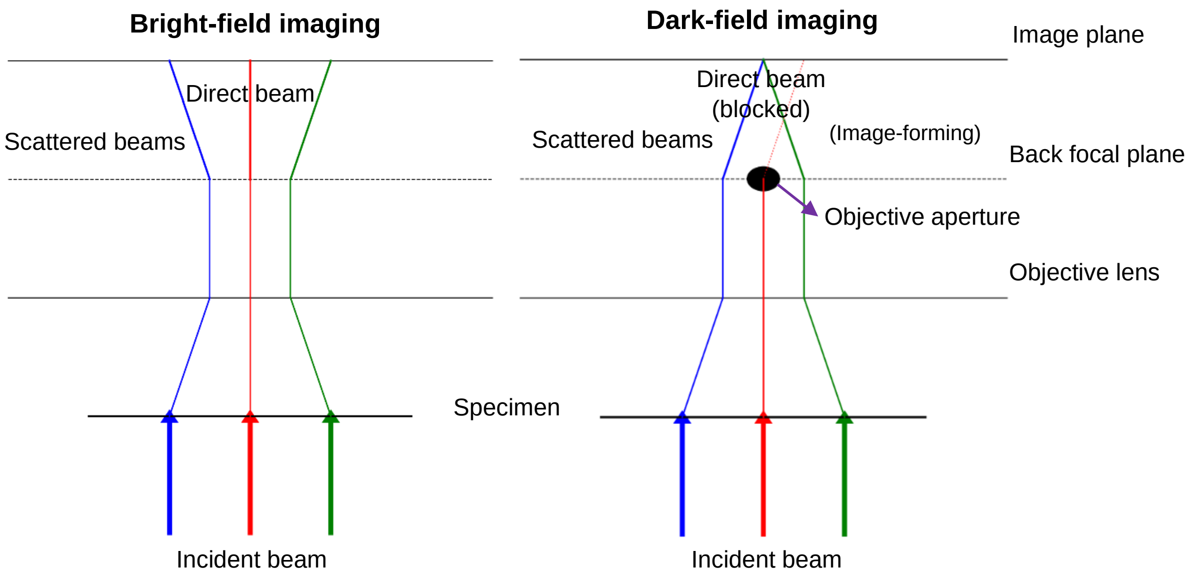

Fig. 2.13 Ray diagrams of bright-field and dark-field imaging.

TEM imaging was carried out in three different setups:

1) a JEOL JEM-2010F Field Emission Electron Microscope operated at 1.9 Å resolution and 200 kV voltage was employed for the bright-field studies of the samples discussed in Chapter 3. For high-resolution TEM studies, the Ag-decorated graphene oxide and graphene oxide paper samples were deposited onto 200-mesh copper grids previously covered by collodion (nitrocellulose) and carbon films, followed by cleaning *via* plasma treatment. Imaging was performed by Dr Samuel Tehuacanero-Núnez, and Dr Samuel Tehuacanero-Cuapa at the Physics Institute of UNAM.

2) a JEOL JEM-ARM200F Atomic Resolution Analytical STEM with a Schottky field emission gun and advanced aberration correction, operated at 1.0 Å resolution and a 200 kV acceleration voltage for dark-field TEM imaging of the samples discussed in Chapter 3 and for both bright-field (BF) and dark-field (DF) imaging of the samples discussed in Chapter 4. Lacey carbon films on 200 mesh copper TEM grids (Agar Scientific) were used to support drop-casted samples dispersed in 2-propanol (≥ 99.8 % purity). Dispersion was promoted by a 10-minute ultrasonic bath. The grids were dried at room temperature and cleaned by plasma treatment before measurements. Micrographs reported in Chapter 3 were collected at 20 nm, whereas the micrographs in Chapter 4 were acquired in BF mode at 200, 100 and 20 nm and in DF mode at 0.5 µm, 100 and 20 nm in different spots on each sample. All the imaging was performed by Dr Josué Esaú Romero-Ibarra at the Materials Research Institute at UNAM.

3) a FEI Tecnai T20 microscope, operating at an acceleration voltage of 200 kV was used to acquire TEM/STEM images of the samples discussed in Chapters 5 and 6. The samples were drop-casted from water, ethanol or toluene dispersions on plain carbon-coated grids, after homogenizing the dispersion *via* a 5-minute ultrasonic bath. Grids were dried at room temperature. Imaging was performed in BF mode at 200, 100, 50, 20 and 10 nm. STEM EDS mapping was done by combining the HAADF (High-angle annular dark field) imaging with the specific elemental counts measured with a Xmax T80 SDD detector operated by INCA software. All these studies were performed by Dr Marc A. Stuart at the Groningen Biomolecular Sciences and Biotechnology Institute of the Faculty of Science and Engineering at UG.

2.3. Theoretical calculations

Density functional theory (DFT) calculations were performed for the GO-silver and palladium-containing hybrid materials to gain theoretical insight into the mechanisms of interaction of AgNPs and PdNPs with pristine and amine-functionalized GO as well as into the geometry and formation energies of the resulting hybrids. Calculations were performed using the software package DFT module DMol[39-42] of Materials Studio. We used the Perdew-Burke-Ernzerhof (PBE) functional[43] within the generalized gradient approximation, along with a long-range dispersion correction by Grimme[44] (commonly referred to as PBE-D2), extensively used for DFT of noncovalent, covalent and coordination bonding of a broad variety of chemical species to graphene and GO models.[45-52]

The double numerical basis set DNP, which has a polarization *d*-function added on all non-hydrogen atoms, as well as a polarization *p*-function added on all H atoms, was combined with the DSPP pseudopotentials. All the models under the study were treated as open-shell systems. The settings for full geometry optimisation and calculation of electronic parameters included 'fine' computation quality and convergence criteria (namely, 10^5 Ha energy change, 0.002 Ha/Å maximum force, 0.005 Å maximum displacement, and 10^{-6} SCF tolerance). All the calculations were spin-unrestricted. The global orbital cutoff[53] was set to 4.5 Å, as defined by the presence of either silver or palladium atoms. Since setting orbital occupancy to Fermi-type does not always allow for the reasonably fast and successful SCF convergence, for the most complex systems the latter was aided by using thermal smearing[53-55], the value of which was reduced stepwise from 0.005 to 10− 4 Ha, and the final calculation was refined with Fermi orbital occupancy[54] (with a few exceptions). For the sake of consistency, all other isolated nanoclusters and complexes were calculated with the same settings.

The formation energies $\Delta E_{\mathrm{GOmodel+MNC}}$ for the complexes (or ΔE for simplicity) of different GO models (GOmodel) with either a silver or a palladium nanocluster (MNC, where M=Ag or Pd) were calculated using the following general equation:

$$\Delta E_{GOmodel+MNC} = E_{GOmodel+MNC} - (E_{GOmodel} + E_{MNC})$$

where E_{i} is the corresponding absolute energy.

Theoretical studies were performed in the Department of Radiation Chemistry and Radiochemistry within the Institute of Nuclear Sciences (ICN), in collaboration with the research group led by Prof. Dr Vladimir Bassiouk Evdokimenko, at the National Autonomous University of Mexico, Mexico.

2.3. References

(1) Alzate-Carvajal, N., Acevedo-Guzmán, D. A., Meza-Laguna, V., Farías, M. H., Pérez-Rey, L. A., Abarca-Morales, E., García-Ramírez, V. A., Basiuk, V. A., & Basiuk, E. V. (2018). One-step nondestructive functionalization of graphene oxide paper with amines. RSC Advances, 8(28), 15253–15265. https://doi.org/10.1039/c8ra00986d.

(2) Basiuk, E. V., Ramírez-Calera, I. J., Meza-Laguna, V., Abarca-Morales, E., Pérez-Rey, L. A., Re, M., Prete, P., Lovergine, N., Álvarez-Zauco, E., & Basiuk, V. A. (2015). Solvent-free functionalization of carbon nanotube buckypaper with amines. *Applied Surface Science*, *357*, 1355–1368. https://doi.org/10.1016/j.apsusc.2015.09.252.

(3) Rodríguez-Otamendi, D. I., Bizarro, M., Meza-Laguna, V., Álvarez-Zauco, E., Rudolf, P., Basiuk, V. A., & Basiuk, E. V. (2023). Eco-friendly synthesis of graphene oxide–palladium nanohybrids. *Materials Today Communications*, *35*, 1–13. https://doi.org/10.1016/j.mtcomm.2023.106007.

(4) Rodríguez-Otamendi, D. I., Meza-Laguna, V., Acosta, D., Álvarez-Zauco, E., Huerta, L., Basiuk, V. A., & Basiuk, E. V. (2021). Eco-friendly synthesis of graphene oxide–silver nanoparticles hybrids: The effect of amine derivatization. *Diamond and Related Materials*, *111*(108208), 1–21. https://doi.org/10.1016/j.diamond.2020.108208.

(5) Meza-Laguna, V., Basiuk, E. V., Alvarez-Zauco, E., Acosta-Najarro, D., & Basiuk, V. A. (2007). Cross-Linking of C_{60} Films with 1,8-Diaminooctane and Further Decoration with Silver Nanoparticles. *Journal of Nanoscience and Nanotechnology*, *7*(10), 3563–3571. https://doi.org/10.1166/jnn.2007.681.

(6) Roy, P. S., Bagchi, J., & Bhattacharya, S. K. (2009). Size-controlled synthesis and characterization of polyvinyl alcohol coated palladium nanoparticles. *Transition Metal Chemistry*, *34*(4), 447–453. https://doi.org/10.1007/s11243-009-9215-y.

(7) Dar, R. A., Giri, L., Karna, S. P., & Srivastava, A. K. (2016). Performance of palladium nanoparticle–graphene composite as an efficient electrode material for electrochemical double layer capacitors. *Electrochimica Acta*, *196*, 547–557. https://doi.org/10.1016/j.electacta.2016.02.197.

(8) Li, J., Chen, W., Zhao, H., Zheng, X., Wu, L., Pan, H., Zhu, J., Chen, Y., & Lu, J. (2017). Size-dependent catalytic activity over carbon-supported palladium nanoparticles in dehydrogenation of formic acid. *Journal of Catalysis*, *352*, 371–381. https://doi.org/10.1016/j.jcat.2017.06.007.

(9) Ismail, A. A., van de Voort, F. R., & Sedman, J. (1997). Chapter 4 Fourier transform infrared spectroscopy: Principles and applications. *Techniques and Instrumentation in Analytical Chemistry*, *18*, 93–139. https://doi.org/10.1016/s0167-9244(97)80013-3.

(10) Sharma, S. K., Verma, D. S., Khan, L. U., Kumar, S., & Khan, S. B. (Eds.). (2018). *Handbook of Materials Characterization*. Springer International Publishing AG, Sao Luis, Brazil.

(11) Stuart, B. H. (2004). *Infrared Spectroscopy: Fundamentals and Applications*. John Wiley & Sons, Ltd, The Atrium, Southern Gate, Chichester, West Sussex, England.

(12) El-Azazy, M. (Ed.). (2019). Infrared Spectroscopy - Principles, Advances, and Applications. IntechOpen, London, United Kingdom.

(13) Petit, T., & Puskar, L. (2018). FTIR spectroscopy of nanodiamonds: Methods and interpretation. *Diamond and Related Materials*, *89*, 52–66. https://doi.org/10.1016/j.diamond.2018.08.005.

(14) Moulder, J. F., Stickle, W. F., Sobol, P. E., & Bomben, K. D. (1992). *Handbook of X-ray Photoelectron Spectroscopy* (J. Chastain & R. C. King Jr, Eds.). Physical Electronics, Inc., Eden Prairie, Minnesota, U.S.A.

(15) Nunney, T., & White, R. (2011). Characterizing Materials for Energy Generation Using X-ray Photoelectron Spectroscopy (XPS). *Microscopy Today*, *19*(2), 22–28. https://doi.org/10.1017/s1551929511000022.

(16) Biesinger, M. C. (2022). Accessing the robustness of adventitious carbon for charge referencing (correction) purposes in XPS analysis: Insights from a multi-user facility data review. *Applied Surface Science*, *597*, 153681. https://doi.org/10.1016/j.apsusc.2022.153681.

(17) Abraham, J., Mohammed, A. P., Ajith Kumar, M. P., George, S. C., & Thomas, S. (2018). Chapter 8 - Thermoanalytical Techniques of Nanomaterials. In O. S. Oluwafemi, N. Kalarikkal, & S. Thomas (Eds.), *Characterization of Nanomaterials Advances and Key Technologies* (pp. 213–236). Woodhead Publishing.

(18) Cheremisinoff, N. P. (1996). 2 - THERMAL ANALYSIS. In N. P. Cheremisinoff (Ed.), *Polymer Characterization Laboratory Techniques and Analysis* (pp. 17–24). William Andrew Publishing.

(19) Sharma, R., Bisen, D., Shukla, U., & Sharma, B. (2012). X-ray diffraction: a powerful method of characterising nanomaterials. *Science and Technology*, *4*(8), 77–79. https://core.ac.uk/download/pdf/236010365.pdf

(20) Noor Fakher Khdr, Rasheed, B. G., & Ahmed, B. M. (2021). Review on Nanomaterials Properties Produced by Laser Technique. IOP Conference Series: Materials Science and Engineering, 1094(1), 012154–012154. https://doi.org/10.1088/1757-899x/1094/1/012154.

(21) Alyamani, A., & Lemine, O. M. (2011). FE-SEM Characterization of Some Nanomaterial. In V. Kazmiruk (Ed.), *Scanning Electron Microscopy* (pp. 463-472). IntechOpen, London, United Kingdom.

(22) Nanoscience Instruments. (2018). *Scanning electron microscopy - nanoscience instruments*. Nanoscience Instruments. https://www.nanoscience.com/techniques/scanning-electron-microscopy/.

(23) Goldstein, J. I., Newbury, D. E., Joy, D. C., Lyman, C. E., Echlin, P., Lifshin, E., Sawyer, L., & Michael, J. R. (2003). *Scanning Electron Microscopy and X-Ray Microanalysis* (3rd edition). Springer Science & Business Media, LLC, New York, U.S.A.

(24) Jenkins, R.; J L De Vries (1970). *Practical X-Ray Spectrometry*; Springer-Verlag: New York, U.S.A.

(25) Zocco, T. G., & Schwartz, A. J. (2003). A brief history of TEM observations of plutonium and its alloys. JOM, 55(9), 24–27. https://doi.org/10.1007/s11837-003-0024-z.

(26) Williams, D. B., & Carter, C. B. (2009). *Transmission Electron Microscopy. A Textbook for Materials Science*. Part 1: Basics (2nd. Edition). Springer Science & Business Media, LLC, New York, U.S.A.

(27) Javed, Y., Ali, K., Akhtar, K., Irfan Hussain, J., Ahmad, G., & Arif, T. (2018). TEM for Atomic-Scale Study: Fundamental, Instrumentation, and Applications in Nanotechnology. In *Handbook of Materials Characterization*. Springer Verlag, New York, U.S.A.

(28) Bals, S., Tirry, W., Geurts, R., Yang, Z., & Schryvers, D. (2007). High-Quality Sample Preparation by Low kV FIB Thinning for Analytical TEM Measurements. Microscopy and Microanalysis, 13(2), 80–86. https://doi.org/10.1017/s1431927607070018.

(29) Sun, B. B., Wang, Y. B., Wen, J., Yang, H., Sui, M. L., Wang, J. Q., & Ma, E. (2005). Artifacts induced in metallic glasses during TEM sample preparation. Scripta Materialia, 53(7), 805–809. https://doi.org/10.1016/j.scriptamat.2005.06.007.

(30) Rosenauer, A., Krause, F. F., Müller, K., Schowalter, M., & Mehrtens, T. (2014). Conventional Transmission Electron Microscopy Imaging beyond the Diffraction and Information Limits. *Physical Review Letters*, *113*(9), 096101 https://doi.org/10.1103/physrevlett.113.096101.

(31) C Barry Carter, & Williams, D. B. (2016). *Transmission Electron Microscopy Diffraction, Imaging, and Spectrometry*. Springer International Publishing, New York, U.S.A.

(32) Garcia-Martinez, J., & Li, K. (2015). *Mesoporous zeolites: preparation, characterization and applications*. Wiley-VCH Verlag Gmbh & Co. KGaA,Weinheim, Germany.

(33) Kirkland, A., & Young, N. (2012). Advances in high-resolution transmission electron microscopy for materials science. *Microscopy and Analysis, 26*(6), 19–24. John Wiley & Sons, Ltd. https://analyticalscience.wiley.com/do/10.1002/micro.262/full/i632c4d2f0f62c011db9adf3632d985ad-1700055154437.pdf.

(34) Yao, N., & Zhong Lin Wang. (2006). *Handbook of Microscopy for Nanotechnology*. Springer Verlag, New York, U.S.A.

(35) Evgeni Gusev, Copel, M., Cartier, E. A., Jacob, I., Krug, C., & Gribelyuk, M. A. (2000). High-resolution depth profiling in ultrathin Al2O3 films on Si. *Applied Physics Letters*, *76*(2), 176–178. https://doi.org/10.1063/1.125694.

(36) Dellby, N., Krivanek, O. L., Nellist, P. D., Batson, P. E., & Lupini, A. R. (2001). Progress in aberration-corrected scanning transmission electron microscopy. Microscopy, 50(3), 177–185. https://academic.oup.com/jmicro/article/50/3/177/831850

(37) LeBeau, J. M., Findlay, S. D., Allen, L. J., & Stemmer, S. (2008). Quantitative Atomic Resolution Scanning Transmission Electron Microscopy. *Physical Review Letters*, *100*(20), 260101. https://doi.org/10.1103/physrevlett.100.206101.

(38) Muller, D. A. (2009). structure and bonding at the atomic scale by scanning transmission electron microscopy. *Nature Materials*, *8*(4), 263–270. https://doi.org/10.1038/nmat2380.

(39) Delley, B. (1990). An all-electron numerical method for solving the local density functional for polyatomic molecules. *The Journal of Chemical Physics*, *92*(1), 508–517. https://doi.org/10.1063/1.458452.

(40) Delley, B. (1996). Fast Calculation of Electrostatics in Crystals and Large Molecules. *The Journal of Physical Chemistry*, *100*(15), 6107–6110. https://doi.org/10.1021/jp952713n.

(41) Delley, B. (2000). From molecules to solids with the DMol3 approach. *The Journal of Chemical Physics*, *113*(18), 7756–7764. https://doi.org/10.1063/1.1316015.

(42) Delley, B., Ellis, D. E., Freeman, A. J., Evert Jan Baerends, & Post, D. E. (1983). Binding energy and electronic structure of small copper particles. *Physical Review B*, *27*(4), 2132–2144. https://doi.org/10.1103/physrevb.27.2132.

(43) Perdew, J. P., Burke, K., & Ernzerhof, M. (1996). Generalized Gradient Approximation Made Simple. *Phys. Rev. Lett.*, *77*(18), 3865–3868. https://doi.org/10.1103/physrevlett.77.3865.

(44) Grimme, S. (2006). Semiempirical GGA-type density functional constructed with a long-range dispersion correction. *Journal of Computational Chemistry*, *27*(15), 1787–1799. https://doi.org/10.1002/jcc.20495.

(45) Wang, Y., Xu, Z., & Moe, Y. N. (2012). On the performance of local density approximation in describing the adsorption of electron donating/accepting molecules on graphene. *Chemical Physics*, *406*, 78–85. https://doi.org/10.1016/j.chemphys.2012.08.008.

(46) Pier Luigi Silvestrelli, & Ambrosetti, A. (2014). Including screening in van der Waals corrected density functional theory calculations: The case of atoms and small molecules physisorbed on graphene. *The Journal of Chemical Physics*, *140*(12), 1–8. https://doi.org/10.1063/1.4869330.

(47) Zhou, Q., Ju, W., Su, X., Yong, Y., & Li, X. (2017). Adsorption behavior of SO_2 on vacancy-defected graphene: A DFT study. *Journal of Physics and Chemistry of Solids*, *109*, 40–45. https://doi.org/10.1016/j.jpcs.2017.05.007.

(48) Basiuk, E. V., Martínez-Herrera, M., Álvarez-Zauco, E., Henao-Holguín, L. V., Puente-Lee, I., & Basiuk, V. A. (2014). Noncovalent functionalization of graphene with a Ni(ii) tetraaza[14]annulene complex. *Dalton Trans.*, *43*(20), 7413–7428. https://doi.org/10.1039/c3dt52645c.

(49) Basiuk, V. A., Alzate-Carvajal, N., Laura Verónica Henao-Holguín, Rybak-Akimova, E. V., & Basiuk, E. V. (2016). Coordination functionalization of graphene oxide with tetraazamacrocyclic complexes of nickel(II): Generation of paramagnetic centers. *Applied Surface Science*, *371*, 16–27. https://doi.org/10.1016/j.apsusc.2016.02.166.

(50) Basiuk, V. A., Rybak-Akimova, E. V., & Basiuk, E. V. (2017). Graphene oxide and nanodiamond: same carboxylic groups, different complexation properties. *RSC Advances*, *7*(28), 17442–17450. https://doi.org/10.1039/c7ra01685a.

(51) Basiuk, V. A., Bolivar-Pineda, L. M., Meza-Laguna, V., Rybak-Akimova, E. V., & Basiuk, E. V. (2018). Carbon Nanotubes and Graphene Promote Pyrolysis of Free-Base Phthalocyanine. *The Journal of Physical Chemistry Letters*, *9*(15), 4420–4427. https://doi.org/10.1021/acs.jpclett.8b02141.

(52) Basiuk, V. A., Mykola Kakazey, Vlasova, M., & Basiuk, E. V. (2019). Effect of structural defects on the strength of adsorption of La and Lu species on graphene. *Diamond and Related Materials*, *100*, 107597–107597. https://doi.org/10.1016/j.diamond.2019.107597.

(53) Basiuk, E. V., Huerta, L., & Basiuk, V. A. (2019). Noncovalent bonding of 3d metal(II) phthalocyanines with single-walled carbon nanotubes: A combined DFT and XPS study. *Applied Surface Science*, *470*, 622–630. https://doi.org/10.1016/j.apsusc.2018.11.159.

(54) Basiuk, V. A. (2011). Electron smearing in DFT calculations: A case study of doxorubicin interaction with single-walled carbon nanotubes. *International Journal of Quantum Chemistry*, *111*(15), 4197–4205. https://doi.org/10.1002/qua.23003.

(55) Basiuk, V. A., Prezhdo, O. V., & Basiuk, E. V. (2020). Thermal smearing in DFT calculations: How small is really small? A case of La and Lu atoms adsorbed on graphene. *Materials Today Communications*, *25*(115665), 101595–101595. https://doi.org/10.1016/j.mtcomm.2020.101595.

CHAPTER 3

Eco-friendly synthesis of graphene oxide–silver nanoparticle hybrids: The effect of amine derivatization

This chapter has been published as:

Rodríguez-Otamendi, D. I., Meza-Laguna, V., Acosta, D., Álvarez-Zauco, E., Huerta, L., Basiuk, V. A., & Basiuk, E. V. (2021). Eco-friendly synthesis of graphene oxide–silver nanoparticles hybrids: The effect of amine derivatization. *Diamond and Related Materials*, *111*(108208), 1–21. https://doi.org/10.1016/j.diamond.2020.108208.

ABSTRACT

This chapter reports on the deposition of silver nanoparticles (AgNPs) onto graphene oxide (GO) in the form of powder and paper (GOP), covalently functionalised with amines and non-functionalized, for comparison. The functionalised supports were fabricated through eco-friendly solvent-free treatment with two aliphatic amines: 1-octadecylamine (ODA) and 1,8-diaminooctane (DAO). AgNPs were generated *in situ* by using silver nitrate as a precursor and citric acid as a non-toxic and eco-friendly reducing agent. Detailed characterization of the chemical composition of GO-Ag hybrids obtained was done by using Fourier-transform infrared, X-ray photoelectron and energy dispersive X-ray spectroscopy, thermogravimetric and differential thermal analysis, as well as X-ray diffraction. The morphology was studied by scanning and transmission electron microscopy. In addition, we compared the electrical conductivity of GOP samples before and after functionalization with amines and decoration with Ag particles. While considerable particle agglomeration was observed on GOP and GO powder, the prior amine functionalization gave rise to a more controlled formation of Ag NPs in terms of size and surface distribution, with the best results obtained on 1,8-diaminooctane-functionalized supports. According to the results of density functional theory calculations, the binding of Ag NPs is the strongest on GO, followed by ODA and finally DAO-functionalized material, which correlates with the size and distribution of Ag nanoparticles observed experimentally.

3.1 Introduction

Graphene oxide (GO) sheets incorporate a variety of oxygen-containing functionalities, including epoxy, hydroxyl, carbonyl and carboxyl groups, distributed either throughout the basal plane or at the edges, according to the widely accepted structural model proposed by Lerf–Klinowski (LK)[1]. As a result, GO contains a combination of sp^2 and sp^3-hybridized carbon atoms. Subjecting the above groups to versatile chemical reactions provides opportunities for tailoring the physical-chemical properties of GO (see[2-6] and references therein). In addition, it is due to the polar nature of oxidized functionalities that GO can produce stable dispersions in water, contrary to non-functionalized graphene.

The development of paper-like material based on GO, commonly referred to as graphene oxide paper (GOP), attracted close attention due to the possibility of designing promising materials with tunable properties for such diverse applications as supercapacitors, chemical and biochemical sensors, photosensors, magnetic and thermal conductive materials, nanofiltration membranes, and bactericidal agents for water disinfection, among others (see[7-11] and references therein). One should add that, due to the great interest towards the synthesis and uses of metal nanoparticles (NPs), it turned out to be especially attractive to combine properties of the two types of materials, for practical applications in electronics, catalysis, electrochemical biosensing, drug delivery, and antimicrobial agents. Within this area GO is considered as an excellent support for dispersing and stabilizing, for example, silver nanoparticles (AgNPs), since it combines a large specific surface area and abundant oxygenated functionalities, acting as the anchoring sites for strong attachment of nanoparticles.

The synthetic approaches to GO-supported AgNPs (hereafter referred to as GO-Ag) rely upon the solution-phase chemical reduction of silver salts, involving some steps with the use of stabilizing and dispersing agents to prevent AgNP agglomeration and to control their size and morphology.[6,12-32] It is important to emphasize that both the latter parameters and AgNP surface distribution strongly depend on the entire synthetic sequence employed. For example, the average size of AgNPs was found to be about 18 nm when GO-Ag nanocomposite was synthesized from non-functionalized GO by the sonochemical method coupled with subsequent shock freezing.[6] A very different route suggested by Vi and co-authors[27,28] contemplated the attachment of AgNPs onto GO layers through grafted thiol groups. These works[27,28] can serve as a good example of multi-step and labour-intensive approaches to GO-Ag nanohybrids, mainly due to the prior functionalization of the support material. In particular, it includes prolonged stirring and the sonication-assisted reaction of GO with NaSH to produce covalently bonded thiol groups on GO, followed by its filtering, washing and drying in a vacuum. The main idea was to use NaSH as an effective cross-linker via GO–SH formation. The authors expected that the coordination of thiol groups could prevent AgNP agglomeration and enable precise control of particle size. Indeed, Ag content of 31-65% was afforded in this way, with 1–2 nm nanoparticle size.[28] This is an important achievement, especially given the well-known fact that AgNPs, due to their high surface energy, are highly reactive and easily susceptible to agglomeration (one of the important practical consequences of this phenomenon is a loss of their antibacterial activity[29]).

The approaches using biological molecules instead of toxic chemicals, such as hydrazine and sodium borohydride, merit special mention due to their ecological value. They can be exemplified by a study,[30] where pepsin was employed as the reducing and stabilising agent, resulting in AgNPs with an average size of 20 nm deposited evenly onto GO sheets. The method proposed is relatively quick, and the stabilizing action of pepsin is due to its amino groups, with hydroxyl and carboxylate groups acting as the centres of AgNP nucleation through the formation of coordination bonds or simple electrostatic interactions with silver ions. The results obtained[30] are in good agreement with other reports (for example,[31]) on the preparation of GO-Ag hybrids, suggesting that the abundant oxygenated functionalities of GO sheets allow for the anchoring of metal ions and facilitate their further in situ reduction into corresponding metal NPs.

The study mentioned above[30] is not the only one which illustrates the role of amino groups in Ag NP stabilization. In the work on the graphene functionalization with 1,6-diaminohexane and further deposition of Ag NPs for water disinfection,[32] the authors mentioned that among the forces stabilizing the hybrid obtained might be the electrostatic attraction of amino groups and silver species to the electron-rich graphene surface. The functionalization with triethylene tetramine followed by reduction under hydrothermal conditions was reported in[13] to obtain AgNPs with sizes in the range of 10-20 nm, uniformly distributed over the surface of reduced GO due to strong adsorption interactions between the two components.

Some thermal and chemical treatments employed for GO functionalization turn out to be rather harsh, giving rise to undesirable alterations in the structure of GO-based materials. In particular, this can happen in a liquid reaction medium, especially when the object of chemical modification is GOP. A promising approach, which can help to avoid negative effects associated with the use of a liquid reaction medium proved to be the solvent-free functionalization, which was successfully applied by our research group for both covalent and noncovalent attachment of variable chemical species, including amines, to different carbon nanomaterials, including GO powder and GOP.[3,4,33] Provided that the amine reagent (which can be aliphatic or aromatic, monofunctional or bifunctional) has sufficient thermal stability and volatility, the solvent-free approach is a fast, efficient, eco-friendly and nondestructive way to systematically tune GO properties. The general functionalization protocol contemplates moderate heating at 150-180 °C under reduced pressure, and the covalent amine attachment proceeds through both amidation of COOH groups and epoxy ring opening reactions.

It is well known that the size of metal nanoparticles is a crucial factor influencing their antibacterial and/or catalytic activity. In particular, AgNPs with sizes of <10 nm proved to have higher bactericidal activity because of the increase in surface area and ease of cell penetration.[34,35] The fact that the smallest AgNPs deposited onto GO were afforded due to its prior covalent functionalization and that simple amines are suitable reagents for the latter purpose, motivated us to undertake the present study. We sought to obtain GO and GOP-based hybrid materials decorated with small-sized silver NPs without considerable agglomeration. Stable centres for the coordination of Ag species were created by means of the gas phase functionalization of GO and GOP with 1-octadecylamine (ODA) and 1,8-diaminooctane (DAO) as representative monofunctional and bifunctional amine, respectively. AgNPs were generated *in situ* by using silver nitrate as a precursor and citric acid as a non-toxic and eco-friendly reducing agent. In control experiments, the same silver deposition procedure was carried out with non-functionalized GO and GOP. Since chemical modification of GOP without compromising its integrity is an especially challenging task (see[4] and references therein), the main emphasis in our report is on this material, with the results obtained on GO powder serving in some cases merely for comparison.

3.2 Experimental section

3.2.1 Materials

GO powder (≥ 99 wt% purity, platelet diameter of 0.5–3 µm and thickness of 0.55–1.2 nm) from Nanostructured & Amorphous Materials, Inc., was used. 1-Octadecylamine (ODA; ≥ 99%), 1,8-diaminooctane (DAO; ≥ 98%), citric acid (≥ 99.5%), silver nitrate (≥99 %), and 2-propanol (≥99.8 %) from Sigma-Aldrich were utilized as received.

3.2.2 Fabrication of free-standing graphene oxide paper

The fabrication of graphene oxide paper (GOP) was performed employing the procedure described in Chapter 2 *(see section 2.1.1)*

3.2.3 Amine gas-phase functionalization of graphene oxide

We followed the general functionalization protocol described previously.[3,4] GO or GOP samples were placed together with amines in a Pyrex glass reactor, at GOP/amine w/w and GO/amine w/w ratio of 1:1. The functionalization reaction was carried out as explained in Chapter 2 *(refer to section 2.1.3 for further details).* The functionalized samples obtained are denoted hereafter as GO+ODA, GO+DAO, GOP+ODA and GOP+DAO.

3.2.4. Deposition of silver nanoparticles

We employed the procedure of AgNP deposition reported previously for C_{60} films functionalized with DAO[36] *(for further details, see section 2.1.4.1).* The amine-functionalized samples decorated with AgNPs are denoted as GO+ODA+Ag, GO+DAO+Ag, GOP+ODA+Ag and GOP+DAO+Ag in the following. The same process with non-functionalized GO and GOP was repeated as a control experiment, and the samples obtained were labelled as GO+Ag and GOP+Ag, respectively.

3.2.5. Characterization

Fourier-transform infrared (FTIR), thermal analysis (TGA–DTA), X-ray diffraction (XRD), and electron microscopy (SEM and TEM) studies were carried out as described in Chapter 2 Section 2.2.

For conductivity measurements on GOP samples, a Keithley 2601B Source Meter Unit (SMU) was employed, operated under ambient conditions in DC mode and controlled by a PC. For the measurements, the 4-point technique was used. The samples were cut into strips of 10-20 mm length and 3-5 mm width, and immediately rubbed on foil to eliminate static charge.

The specimens were placed perpendicularly to parallel copper electrodes. The dimensions of the electrodes, printed on a circuit board, were 0.25 mm in width, separated by 2.8 mm. Electric contact was established by lightly pressing a piece of glass slide above the sample by using a clip. Before each measurement, specimens were stored in a vacuum desiccator for 24 h. The conditions optimized for the present studies were as follows: an initial and final current of 1000 nA, a stabilization time of 0.5 s, and 20 measurement steps. Further technical details of the conductivity measurements can be found in reference 4.

3.3 Theoretical calculations

To gain theoretical insight into the mechanisms of interaction of AgNPs with non-functionalized and amine-functionalized GO as well as into the geometry and formation energies of the resulting Pd-GO hybrids, density functional theory (DFT) calculations were performed according to the described set-up in Chapter 2 *(see section 2.3).*

The formation energies $\Delta E_{\mathrm{GOmodel+AgNC}}$ for the complexes (or ΔE for simplicity) of different GO models (GOmodel) with a silver nanocluster (AgNC) were calculated using the following general equation:

$$\Delta E_{GOmodel+AgNC} = E_{GOmodel+AgNC} - (E_{GOmodel} + E_{AgNC})$$

where E_{i} is the corresponding absolute energy.

3.4 Results and discussion

3.4.1 Characterization of GO+Ag and GOP+Ag hybrids

To visualize the changes in the chemical nature of GO powder and GOP samples upon functionalization with amines and further decoration with AgNPs, we performed dispersibility tests as explained previously in Chapter 2, section 2.2.1. The results are shown in Figs 3.1 and 3.2 for GO powder and GOP, respectively. The results obtained for GO powder samples in many regards match those presented for GOP mats. On the other hand, very clear differences can be found for DAO-functionalized materials: in the case of aqueous medium, GO+DAO and GO+DAO+Ag are less dispersible than GOP+DAO and GOP+DAO+Ag, whereas an opposite effect is seen in 2-propanol. The increase in hydrophobicity upon decoration with AgNPs can be observed more clearly, producing not only the decrease in dispersibility of GO+DAO+Ag in water but also an increase in dispersibility of the same powder sample in 2-propanol, compared to GO+DAO. Of all dispersions tested, the most stable ones are those formed by GO+DAO+Ag and GO+Ag in 2-propanol, remaining almost unchanged after 24 h.

For the water test (top images in Fig. 3.2), one can see that GOP was dispersed completely after ultrasonic treatment, forming a brown dispersion, which is consistent with a generally hydrophilic nature due to the presence of a large number of oxidized functionalities.

The introduction of ODA moieties incorporating long hydrocarbon chains changed the character of the GOP+ODA sample to hydrophobic, thus resulting in its immediate precipitation. At the same time, GOP+DAO formed stable (even after 24 h) brown dispersion, due to the presence of two terminal amino groups (one covalently bonded to the GO surface and one dangling) in DAO moieties, enhancing the hydrophilic character of this sample. The series of tests carried out in 2-propanol (bottom images in Fig. 3.2) gave similar results (to those obtained in water) for GOP and GOP+ODA, whereas GOP+DAO only partially disintegrated after ultrasonication, and then remained essentially unchanged after 24 h. Such a distinctive behaviour can be attributed to cross-linking adjacent GO sheets with bifunctional DAO molecules, as observed in our previous study on GOP amino functionalization.[4] The effect of AgNP deposition on dispersibility in 2-propanol is generally opposite to the one in water. That is, GOP+Ag, GOP+ODA+Ag and GOP+DAO+Ag are better dispersed than GOP, GOP+ODA, and GOP+DAO in 2-propanol, and *vice versa*, in water. In addition, one should point to faster precipitation (after 24 h) of GOP+DAO+Ag than GOP+DAO in water, and higher stability of GOP+Ag and GOP+ODA+Ag dispersions in 2-propanol as compared to the corresponding paper samples before silver deposition.

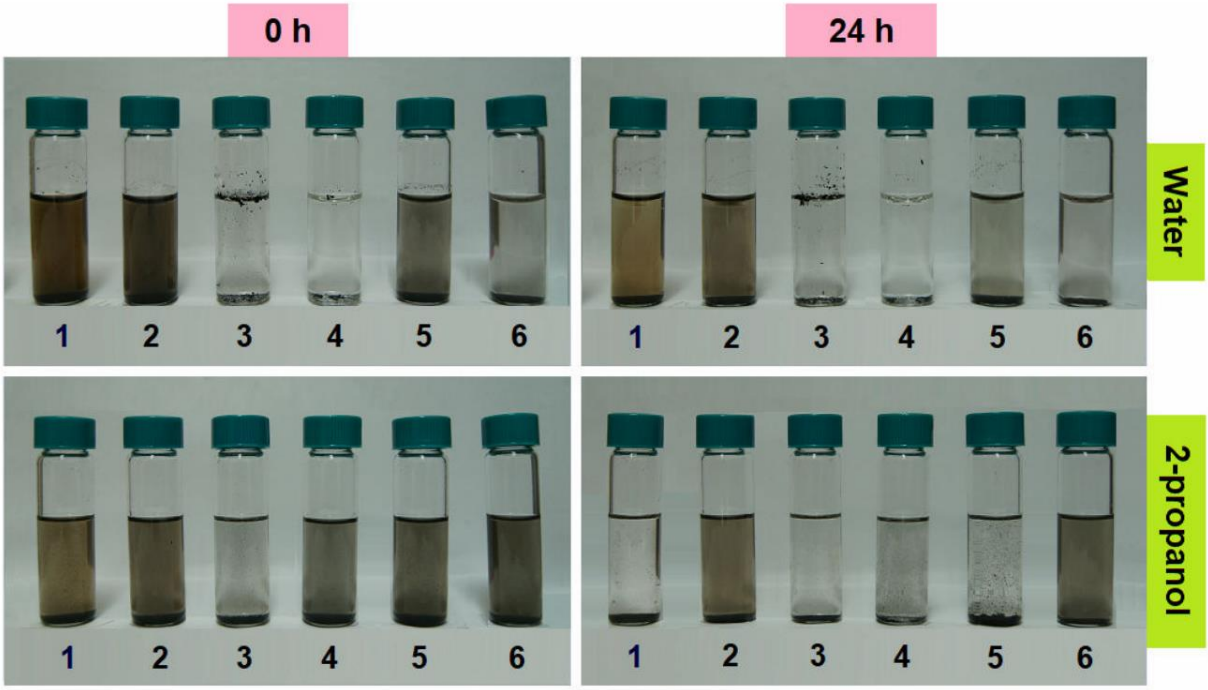

Fig. 3.1. Dispersibility tests for GO powder samples in water and in 2-propanol: (1) GO, (2) GO+Ag, (3) GO+ODA, (4) GO+ODA+Ag, (5) GO+DAO, and (6) GO+DAO+Ag. Images were taken immediately after 10-min ultrasonication (0 h, in left) and after 24 h (right).

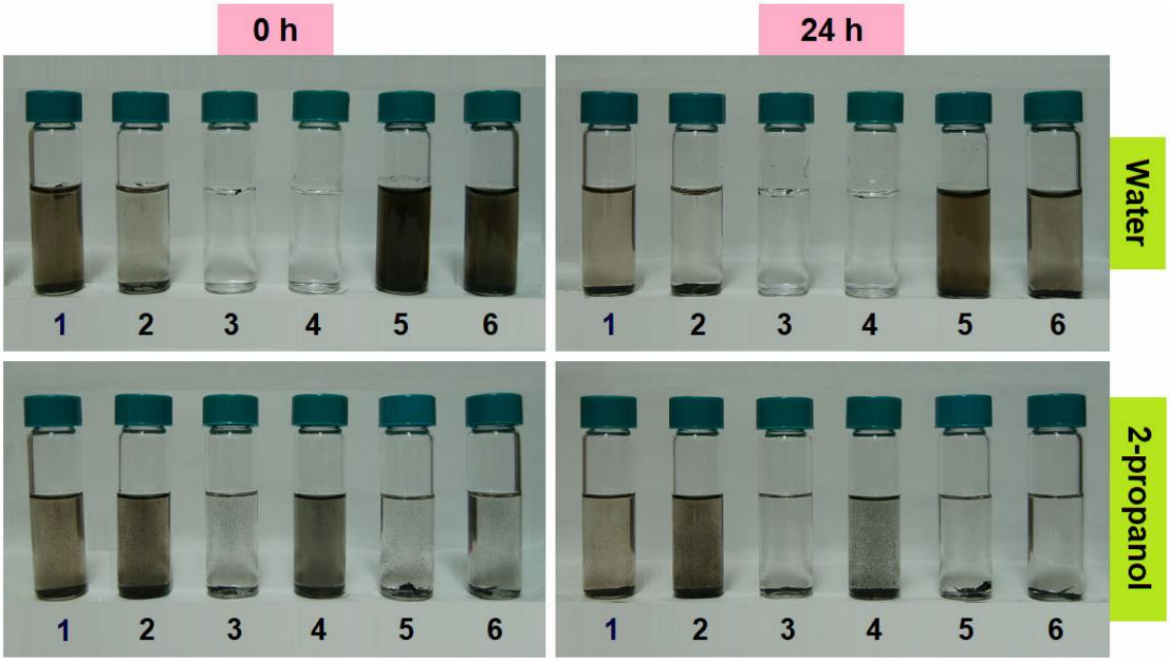

Fig. 3.2. Dispersibility tests for GOP samples in water and in 2-propanol: (1) GOP, (2) GOP+Ag, (3) GOP+ODA, (4) GOP+ODA+Ag, (5) GOP+DAO, and (6) GOP+DAO+Ag. Images were taken immediately after 10-min ultrasonication (0 h, in left) and after 24 h (right).

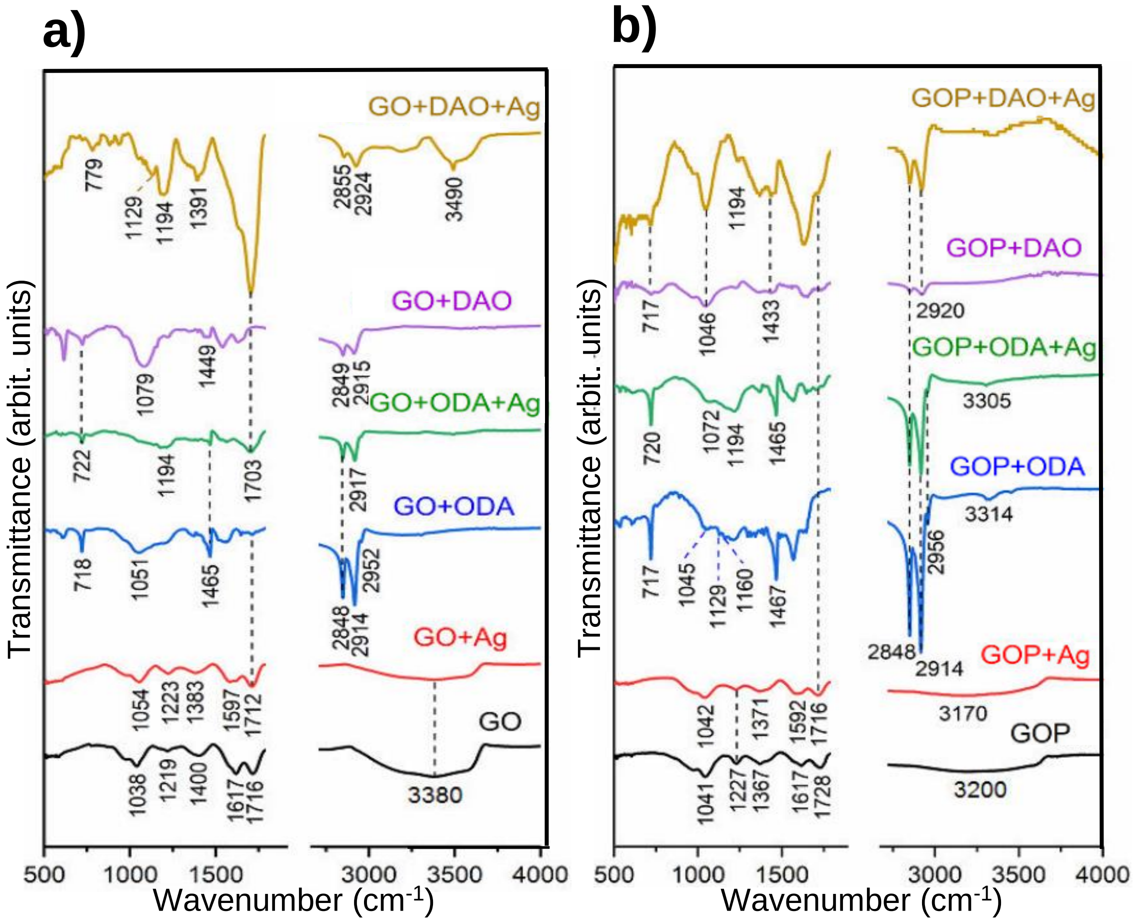

Fig. 3.3. FTIR spectra of non-functionalized and amine-functionalized: a) GO powder, and b) GOP samples before and after decoration with AgNPs.

FTIR measurements were carried out to monitor changes in the chemical groups present in the GO and GOP samples due to amino functionalization and decoration with AgNPs (Figs 3.3 a & b); for experimental details see Chapter 2. The FTIR spectra of the GO powder samples, both before and after amino functionalization (Fig. 3.3a) include a decrease down to the total disappearance of carboxylic $\nu_{C=O}$ band at 1712-1716 cm^{-1} and of the C–O signal at 1038 cm^{-1}, as well as the appearance of new bands in the range of 1200-1700 cm^{-1}, which are commonly associated with vibrations of amide groups.[37,38] Some specific features for amine-functionalized GO powder include sharp bands at 2848-2855 and 2914-2952 cm^{-1}, corresponding to symmetric and asymmetric ν_{C-H} vibrations in long aliphatic hydrocarbon chains of ODA and DAO.

In principle, one could expect that Ag atoms/ions at the NP surface might convert neutral COOH functionalities into COO^{-} ions, which would manifest themselves with a stretching COO^{-} mode at around 1600 cm.$^{-1}$ Nevertheless, one should remember that the citric acid solution used for AgNP generation has a pH≈3, so that carboxylic groups remain protonated in GOP+Ag and GO+Ag; the same applies to unreacted COOH groups (if any) in all ODA and DAO-functionalized samples. On the other hand, in the case of GO+ODA+Ag and GO+DAO+Ag some signs of Ag deposition appear as an increase in absorption at 1194 and 1703 cm^{-1}. In addition, the appearance of a diffuse band at 3490 cm^{-1} in the spectrum of GO+DAO+Ag (Fig. 3.3a), can be explained by the coordination of AgNPs to the nitrogen atoms in dangling NH_2 groups of 1,8-diaminooctane.

The spectrum of GOP (Fig. 3.3b) contains characteristic peaks due to abundant oxygenated functional groups. Among them are the hydroxyl ν_{O-H} band at 3200 cm^{-1} with the corresponding δ_{O-H} band at 1617 cm^{-1}, $\nu_{C=O}$ vibrations in COOH groups centred at 1728 cm^{-1}, asymmetric ν_{C-O} vibrations at 1367 cm^{-1} due to epoxy C–O–C groups, a peak at 1227 cm^{-1} due to the δ_{O-H} mode of C–O–H groups, and C–O single-bond stretching vibrations at 1041 cm.$^{-1}$

The most obvious changes caused by amine functionalization are a decrease in the intensity of the $\nu_{C=O}$ band (down to its total disappearance in GOP+ODA) and the C–O signal at 1041 cm^{-1}, along with the appearance of characteristic normal modes due to amide groups in the range of 1200-1700 cm^{-1}, serving as evidence of COOH group derivatization. These features include an 'amide I' $\nu_{C=O}$ absorption between 1600 and 1700 cm^{-1}, with a less pronounced (mostly as a shoulder) 'amide II' δ_{N-H} absorption at 1500-1575 cm^{-1}. The fact that they are not well resolved can be explained by the presence of large amounts of non-amide NH groups, whose δ_{N-H} mode masks the one of 'amide I'. The plausible explanation suggested previously is that amines react not only with carboxylic groups but also add onto epoxy functionalities, abundant in GO, *via* ring-opening reaction.[3,4] An 'amide III' feature might contribute to a set of bands at 1200-1400 cm^{-1}. The modes manifesting themselves at lower wavenumbers can also be due to C(=O)–NH bond formation, in particular, at 625-800 cm^{-1}, due to 'amide IV' and 'amide V' vibrations, as well as at 530-620 cm^{-1}, due to 'amide VI' absorption[37,38]. At the same time, the band at 717-720 cm^{-1} is typical for aliphatic chains longer than $(CH_2)_4$,[39] being especially sharp in GOP+ODA, which can be associated with a bigger size of hydrocarbon chains, and possibly with a higher content of ODA moieties. Correspondingly, asymmetric and symmetric ν_{C-H} bands of alkyl groups in ODA and DAO at 2914-2956 and 2848 cm^{-1}, respectively, are among the most intense ones observed. Additionally, the spectrum of GOP+ODA presents amine bands ν_{N-H} around 3310 cm^{-1} and ν_{C-N} at 1129-1160 cm^{-1}. Finally, the absorption features at 1433 and 1465-1467 cm^{-1} for GOP+DAO and GOP+ODA, respectively, are due to δ_{C-H} vibrations.

Thermogravimetric analysis (TGA) and differential thermal analysis (DTA) measurements, performed as detailed in Chapter 2, were used to characterize the changes in the thermal behaviour of GOP and GO powder due to the modification with amines and subsequent decoration with AgNPs. The TGA–DTA characteristics of GO powder (Fig. 3.4a) include three weight losses due to physisorbed water (13.9 %, until 109 °C), pyrolysis of oxygenated functionalities (34.7 %, until 300 °C), and graphene lattice combustion (51.3 %, until 660 °C). The DTA curve contains two major exothermic peaks at 214 and 602 °C, matching the main weight loss steps in the TGA curve. For GO+Ag (Fig. 3.4b), the first and second steps remain essentially the same (with some variations in temperature and percentage), being related to the evaporation of physisorbed water (12.8 %, until 98 °C) and pyrolysis of oxygen-containing groups (36.1 %, until 323 °C). However, instead of the single final weight loss due to the graphene network decomposition, two distinct losses are clearly seen in the present case, 19.4 % until 545 °C and 30.5 % until 682 °C. This might be associated with a considerably low Ag content in GO+Ag (1.50 – 0.17 wt % = 1.33 wt %), and thus with the occurrence of Ag-catalyzed and non-catalyzed combustion of the graphene backbone. The three major peaks in the DTA curve for GO+Ag powder are found at 212, 532 and 663 °C.

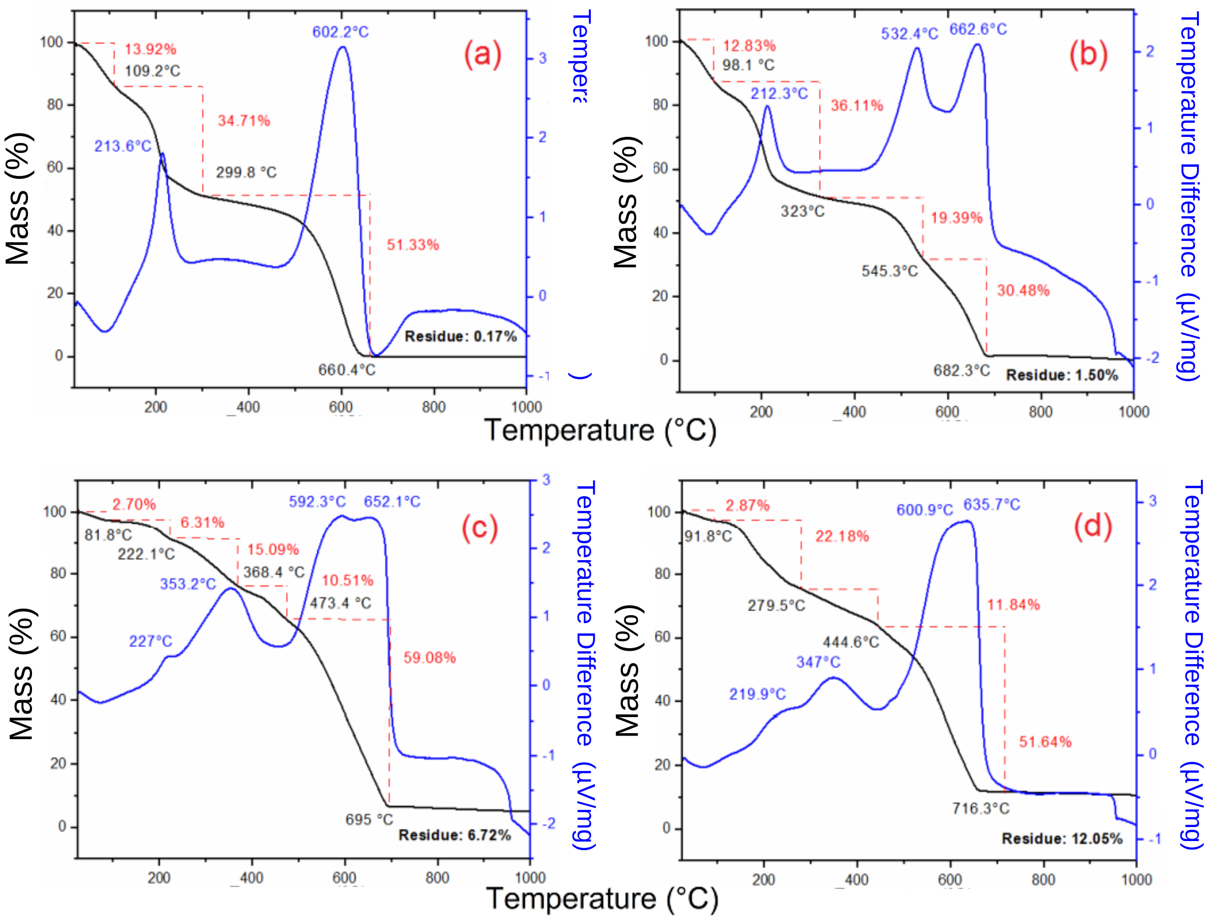

Fig. 3.4. TGA (black) and DTA (blue) curves for GO powder samples: a) GO, b) GO+Ag, c) GO+ODA+Ag, and d) GO+DAO+Ag.

A less pronounced splitting of the final weight loss step can be seen in the case of GO+ODA+Ag (Fig. 3.4c), with two DTA maxima at 592 and 652 °C. At the same time, the silver content is estimated to be much higher in the present case (6.72 % – 0.17 wt % = 6.55 wt %). A similar observation can be done for the GO+DAO+Ag powder sample (Fig. 3.4d), where the Ag fraction is evaluated to be 12.05 wt % – 0.17 wt % = 11.88 wt %.

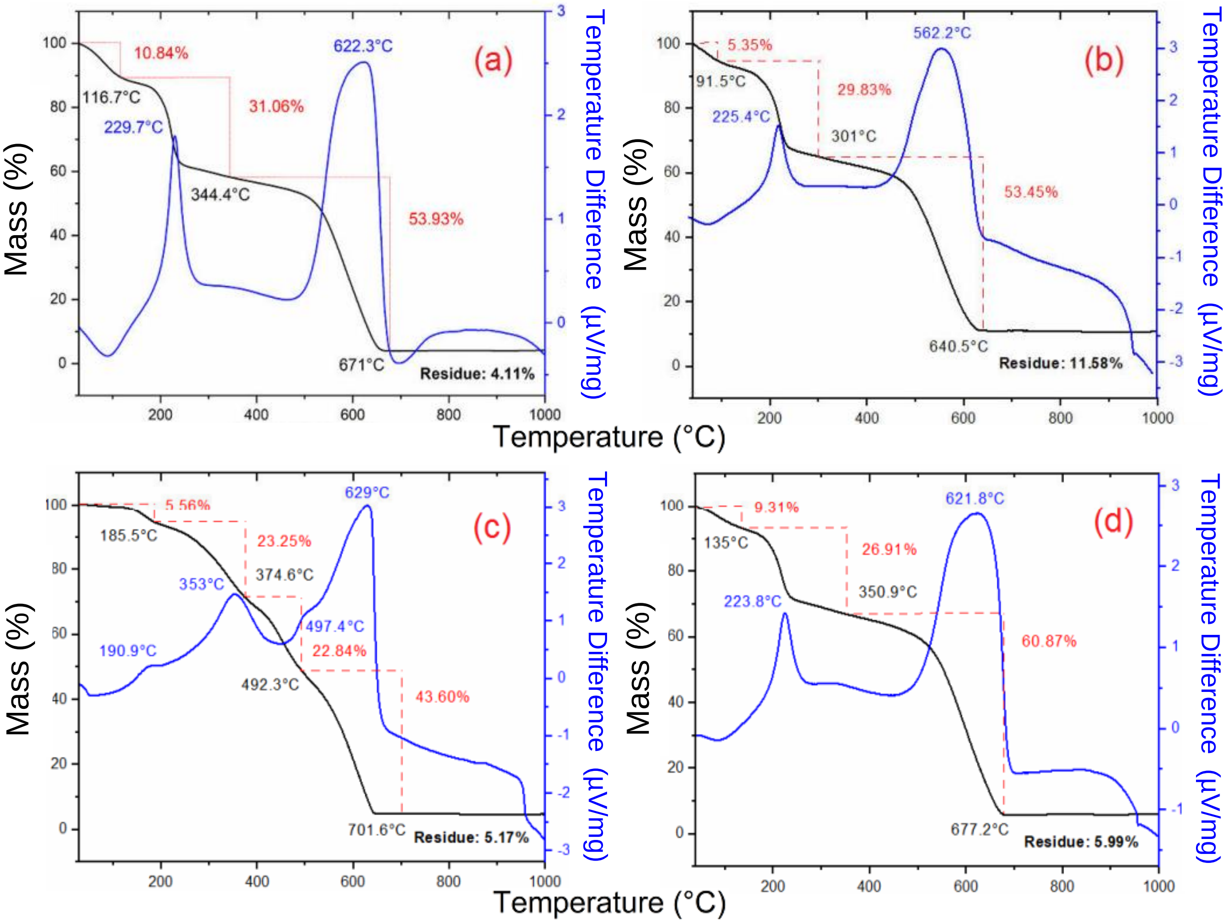

Fig. 3.5. TGA (black) and DTA (blue) curves for GOP samples: a) GOP, b) GOP+Ag, c) GOP+ODA+Ag, and d) GOP+DAO+Ag.

The TGA curve for GOP (Fig. 3.5a), exhibits three weight loss steps, typical for graphene oxide.[4] The first weight loss (of 10.8 %, until 117 °C) is attributed to the evaporation of physisorbed water. The second one (of 31.1 %, until 344 °C) is caused by the pyrolysis of intrinsic oxygenated groups of GO, primarily COOH moieties. The third step (of 53.9 %, until 671°C) corresponds to the graphene backbone decomposition. The DTA curve has two exothermic peaks at 230 and 622 °C, matching the second and third weight loss steps in TGA. For the Ag-decorated sample, GOP+Ag (Fig.3.5b), qualitatively the same weight loss pattern is observed, namely: physisorbed water evaporation (5.4 %, until 92 °C), pyrolysis of oxygenated groups (29.8 %, until 301 °C), and graphene network decomposition (53.5 %, until 641 °C). The Ag content of 7.47 wt % is obtained by subtraction of 4.11 wt % (GOP; Fig. 3.5a) from the residual weight of 11.58 wt %. The two exothermic peaks at 225 and 562 °C in the DTA curve are likewise similar to those found for non-functionalized GOP, except that the second one is strongly shifted (by 60 °C) to lower temperatures. This can be explained by the catalytic effect of silver on the combustion of the graphene backbone.

The thermograms obtained for graphene oxide paper after amine-functionalization and decoration with AgNPs (Figs.3.5c,d) exhibit significant differences in comparison to GOP+Ag, due to the presence of new chemical moieties. In particular, for the ODA-functionalized sample, the most important weight losses in the TGA curve are the ones of 5.6 % until 186 °C, 23.3 % until 375 °C, 22.8 % until 492 °C, and 43.6 % until 702 °C. The corresponding exothermic peaks in the DTA curve for GOP+ODA+Ag are found at 191, 353, 497 and 629 °C, which can be associated with the pyrolysis of initial oxygenated groups (present in GOP), of amide derivatives, of amines added onto epoxy groups, and of graphene lattice, respectively. The estimated AgNP content is 1.06 wt % (a difference between 5.17 wt % and 4.11 wt % residue in TGA of GOP). The three main weight losses recorded by TGA for the GOP+DAO+Ag sample are 9.3 % until 135 °C due to physisorbed water (DAO is hydrophilic, contrary to ODA), of 26.9 % until 351 °C due to pyrolysis of residual (from GOP) oxygenated groups along with their amino/amide derivatives, and of 60.9% until 677 °C, corresponding to the combustion of the graphene lattice. The estimated (in the same way as for GOP+Ag and GOP+ODA+Ag) silver content is 1.88 wt %. The peaks found in DTA are those at 224 ~ 351 (low and broad) and 622 °C. One should note that the final major peak due to the decomposition of graphene backbone in GOP+ODA+Ag and GOP+DAO+Ag shifted back to higher temperatures: apparently, the low Ag content of about 1-2 % is insufficient to produce as pronounced catalytic effect as the one observed in the case of GOP+Ag (silver content of 7.47 wt %).

When comparing the present TGA–DTA results for ODA and DAO-functionalized samples (both powders and GOP mats) decorated with AgNPs with those reported previously for aliphatic amine-functionalized GOP[4], one can see that silver deposition lowers the final combustion temperature of graphene backbone very significantly. For example, while for GOP+ODA it was 745 °C[4], for GOP+ODA+Ag and GO+ODA+Ag it dropped to 702 and 695 °C, respectively. For GOP functionalized with 1,12-diaminododecane (a homologue of DAO), it was 750 °C[4], whereas for GOP+DAO+Ag and GO+DAO+Ag it was 677 and 716 °C, respectively. The second important trend has to do with whether AgNPs were deposited onto a powder sample or a compact mat: the estimated silver content for GO+ODA+Ag and GO+DAO+Ag is 6.55 wt % and 11.88 wt %, whereas for GOP+ODA+Ag and GOP+DAO+Ag it dramatically decreases to 1.06 wt % and 1.88 wt %, respectively. Apparently, compacting GO powder into paper hinders the accessibility of AgNPs to functionalizing groups within the mat. The third observation to mention is that the silver content of DAO-functionalized samples is almost twice as high as that of ODA-functionalized materials. The most logical explanation is that the use of bifunctional reagents such as DAO provides additional amino groups serving as coordination centres for anchoring and stabilization of AgNPs as previously observed for 1,12- diaminododecane.[4,13,30,32]

General morphological changes due to the decoration of GO powder and GOP-derived materials with AgNPs were studied by using scanning electron microscopy (SEM). For the experimental details see Chapter 2. Figs 3.6 and 3.7 present the micrographs obtained for the powder and paper samples respectively.

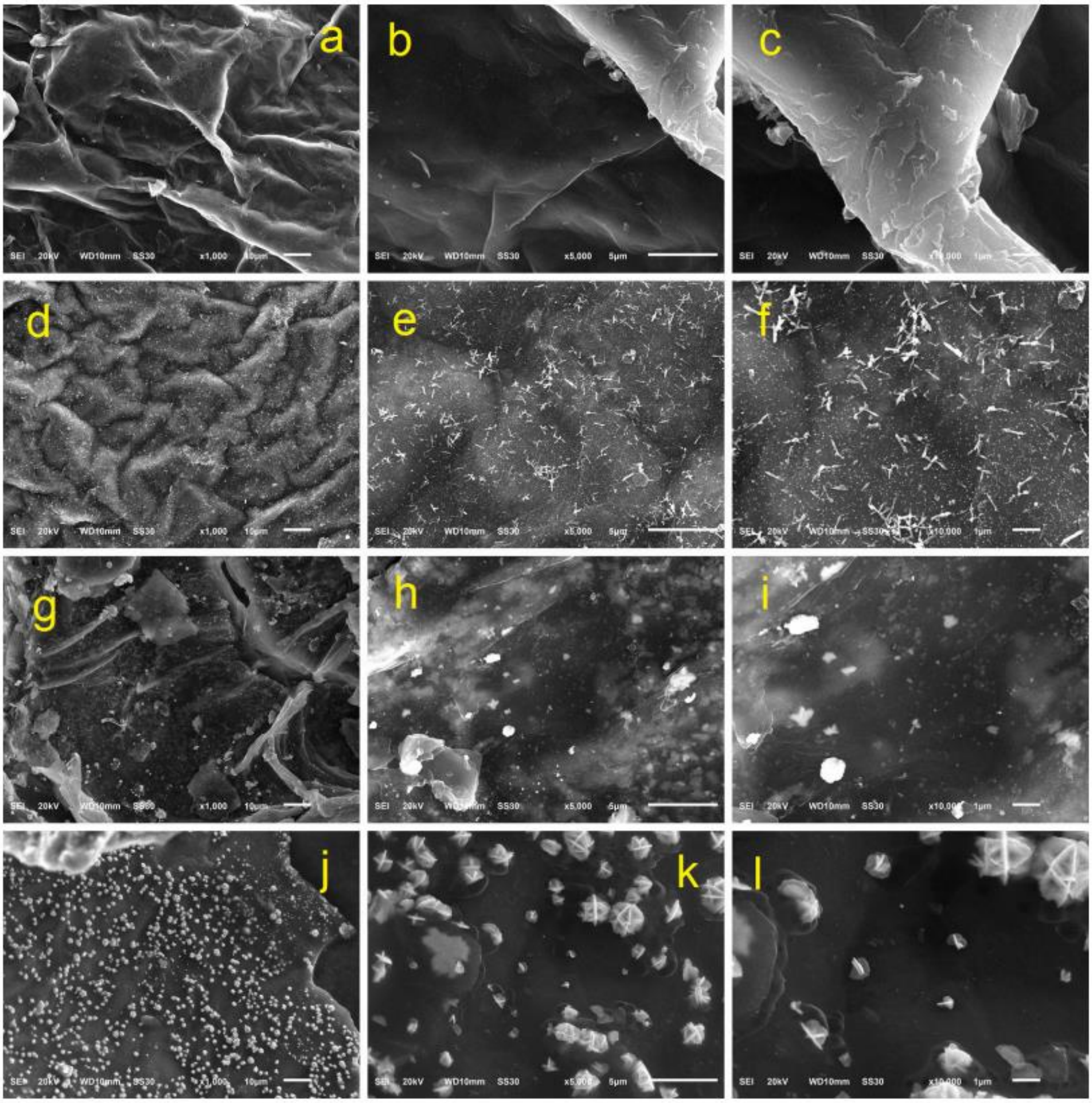

Fig. 3.6. Representative SEM images of GO (a-c), GO+Ag (d-f), GO+ODA+Ag (g-i), and GO+DAO+Ag (j-l). Scale bar: left column, 10 µm; middle column, 5 µm; right column, 1 µm.

Larger-sized silver particles with interesting morphology were detected in GO+Ag-containing hybrids. (Fig. 3.6). All three Ag-decorated GO varieties look very different from GO powder (Fig. 3.6a-c), but in their own way. On the GO+ODA+Ag surface (Fig. 3.6g-i), silver particles are irregularly shaped, notably agglomerated and broadly variable in size. For the GO+DAO+Ag powder sample (Fig. 3.6 j-l), remarkably flower-like particles are found, reminding of what is commonly known as 'desert rose' selenite in morphology. Many of these particles are 1-3 µm in size and cover rather uniformly some surface sites. Similar microstructures consisting of single-crystalline plates of metallic silver were synthesized in other studies[40,41] targeting the design of non-enzymatic H_2O_2 sensors and other bioanalytical applications, where Ag particles with high active surface area would be of special importance. The synthetic approach proposed by these authors[41] aims at an enzyme-induced particle growth on solid substrates, and the complex morphology obtained contrasts with the auto-catalytically grown spherical particles, which maintain their overall geometrical appearance while increasing their diameter.

The formations covering the GO+Ag surface (Fig. 3.6d-f) do not look like metal particles, be they either regularly or irregularly shaped. Instead, they remind of rolled individual graphene sheets, roughly 1 µm in length and up to 100 nm in diameter. A similar phenomenon has been observed by Quintana *et al.* (2012)[42] when sonicating graphite in dimethylformamide upon the addition of ferrocene aldehyde. The tubular structures appeared exclusively at the edges of graphene layers and contained Fe clusters. We therefore speculate that silver clusters cause a similar strong distortion of smaller GO sheets causing them to roll up. EDS measurements of Ag content at these sites yielded elevated (as for all samples) values of around 10 wt %. Taking into account that EDS analysis is very superficial and does not reflect the elemental composition inside multilayer platelets of GO, the above estimates do not contradict the averaging value of 1.33 % from TGA.

For GOP samples, differences in mat thickness were determined from cross-section SEM images (Fig. 3.7 a,d,g,j). The values found for GOP (22 µm) and for GOP+Ag (23 µm) were identical within the error bar, implying that the amount of silver which penetrated inside the mats (between individual GO sheets) is insignificant. For their amine-functionalized counterparts, the mat thickness estimates gave 119 µm for GOP+ODA+Ag and 34 µm for GOP+DAO+Ag. In other words, while GOP+Ag and GOP+DAO+Ag samples exhibit no and a minor increase in the thickness, respectively, is the thickness increase is about five-fold for GOP+ODA+Ag compared to GOP. An important contribution to this effect is due to amine functionalization: we already observed in our earlier work[4] that the pristine mat thickness of 16 µm increases to 28 µm for GOP+ODA, and to 20 µm for GOP functionalized with 1,12-diaminododecane (a GOP+DAO analogue). Still, this ‘swelling’ is much weaker than the one observed for GOP+DAO+Ag (Fig. 3.7j) and especially for GOP+ODA+Ag (Fig. 3.7g), which can thus be attributed mainly to more efficient intercalation of silver into amine-functionalized GOP, even though the Ag content within the mats turned to be below EDS detection limit.

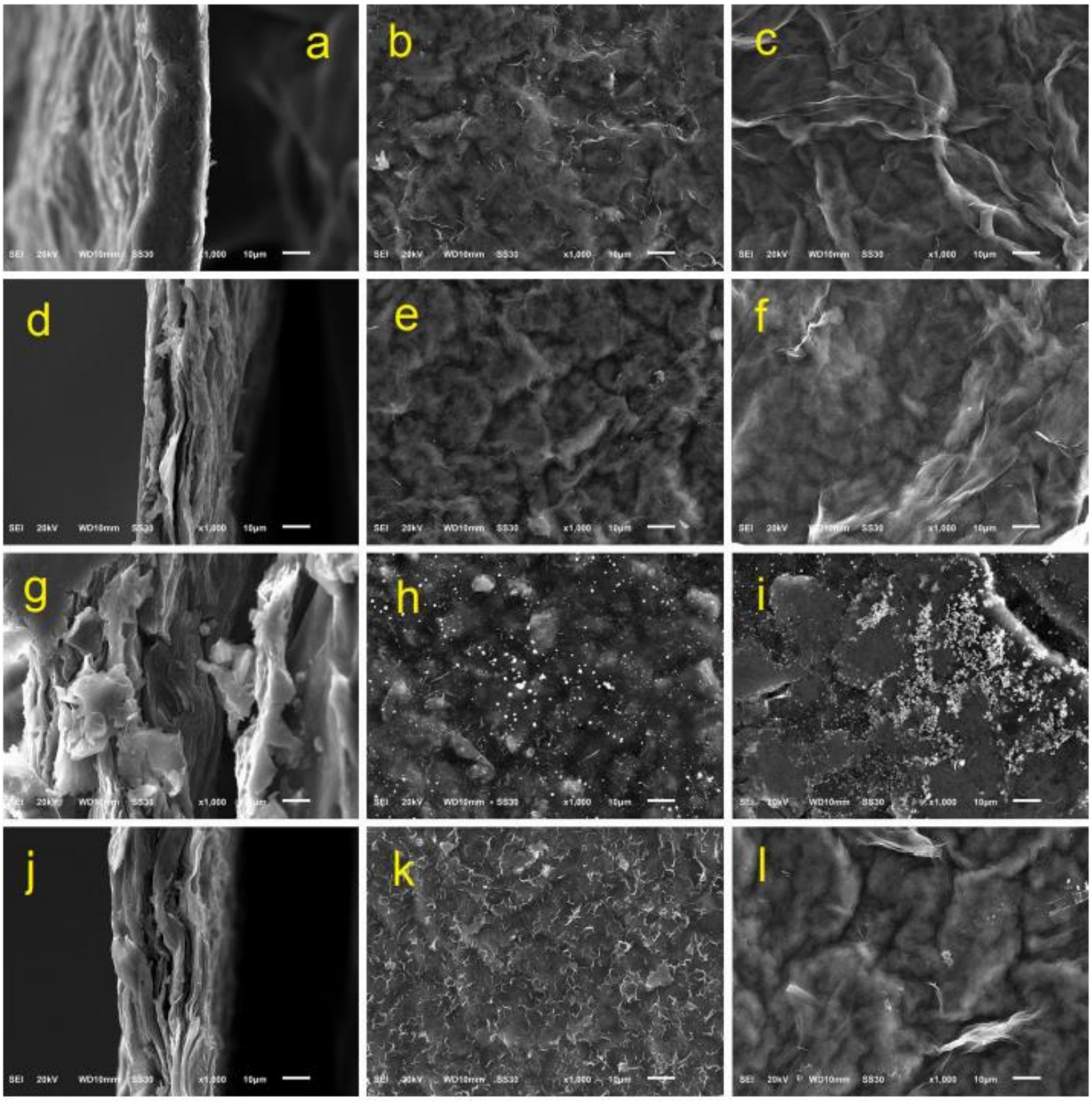

Fig. 3.7. Representative SEM images of GOP (a-c), GOP+Ag (d-f), GOP+ODA+Ag (g-i), and GOP+DAO+Ag (j-l). The left column (a,d,g,j) shows cross-section images; the middle column (b,e,h,k) corresponds to the lower mat side, which was in contact with the filter membrane during GOP fabrication; the right column (c,f,i,l) corresponds to the upper mat side. The scale bar corresponds to 10 µm in all images.

The SEM images grouped in the middle and right columns of Fig. 3.7 show the differences in surface morphologies observed at the lower and the upper (with respect to the membrane filter employed in GOP fabrication) mat sides, respectively. The lower side seems to have a more compact and uniform morphology; a likely reason is that during the filtration process, well-shaped platelets are sedimented first at the filter surface. Additionally, for GOP+ODA+Ag one can observe micrometre-sized (roughly 1-3 µm) white agglomerates of silver particles, which cover some surface sites rather densely (especially at the upper surface; Fig. 3.7i). This contrasts with GOP+DAO+Ag, where only a few such particles can be seen. Taking into account that the Ag content of the two amine-functionalized samples was comparable (of the order of 1 %) according to TGA, as well as the limited resolution of SEM at the nanoscale, one can suggest that the size of Ag particles is typically much smaller in GOP+DAO+Ag.

The crystallinity of the silver particles in GO+DAO+Ag can be illustrated by the results of XRD shown in Fig. 3.8. The pattern recorded contains several peaks, which can be indexed to the (111), (200), (220), (311) and (222) crystal planes, well-known for Ag particles.[40,43,44] Possible building blocks to form desert rose-like morphologies are single-crystalline silver plates, which are intertwined to form nanoflowers up to a size of several micrometres, with this process strongly dependent on the synthesis conditions.[43,44] An enhanced number of amine/imine centres for Ag coordination, existing in GO+DAO+Ag due to the bifunctional nature of 1,8-diaminooctane, might be one of the factors favouring the peculiar nucleation process leading to the flower-like particles.

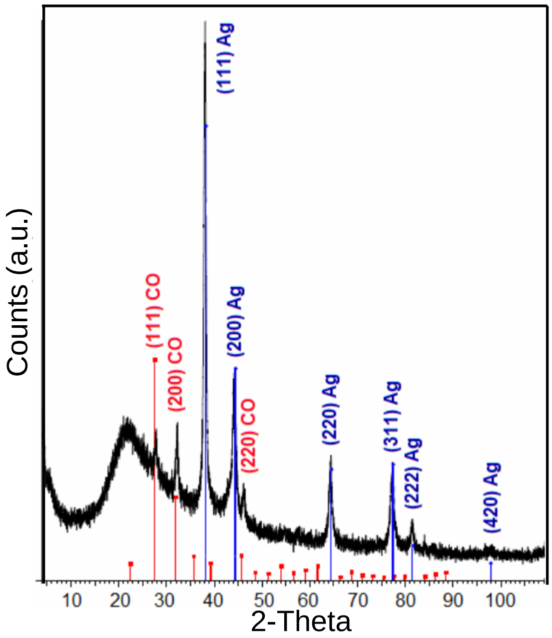

Fig. 3.8. XRD diffractogram for the GO+DAO+Ag sample.

Detailed information on the size and morphology of AgNPs deposited onto GO powder and GOP was obtained by employing bright-field (Figs. 3.9 and 3.10) and dark-field (Fig. 3.11) TEM. Both GO+Ag and GOP+Ag samples contain multiple twinned round/rectangular particles; this type of morphology is associated with a lack of control during the particle nucleation and growth.[45,46] Their sizes fluctuate in a range of 10-30 nm for GO+Ag (Fig. 3.9 c,d), and 15-35 nm for GOP+Ag (Fig. 3.10 c,d), that is, essentially in the same range. The formation of AgNPs at non-functionalized GO surfaces is governed by the coordination of silver species to the O donor atoms of oxygenated groups, which serve as numerous and efficient sites for nanoparticle nucleation and growth, however with a clear tendency to agglomeration and/or coalescence.

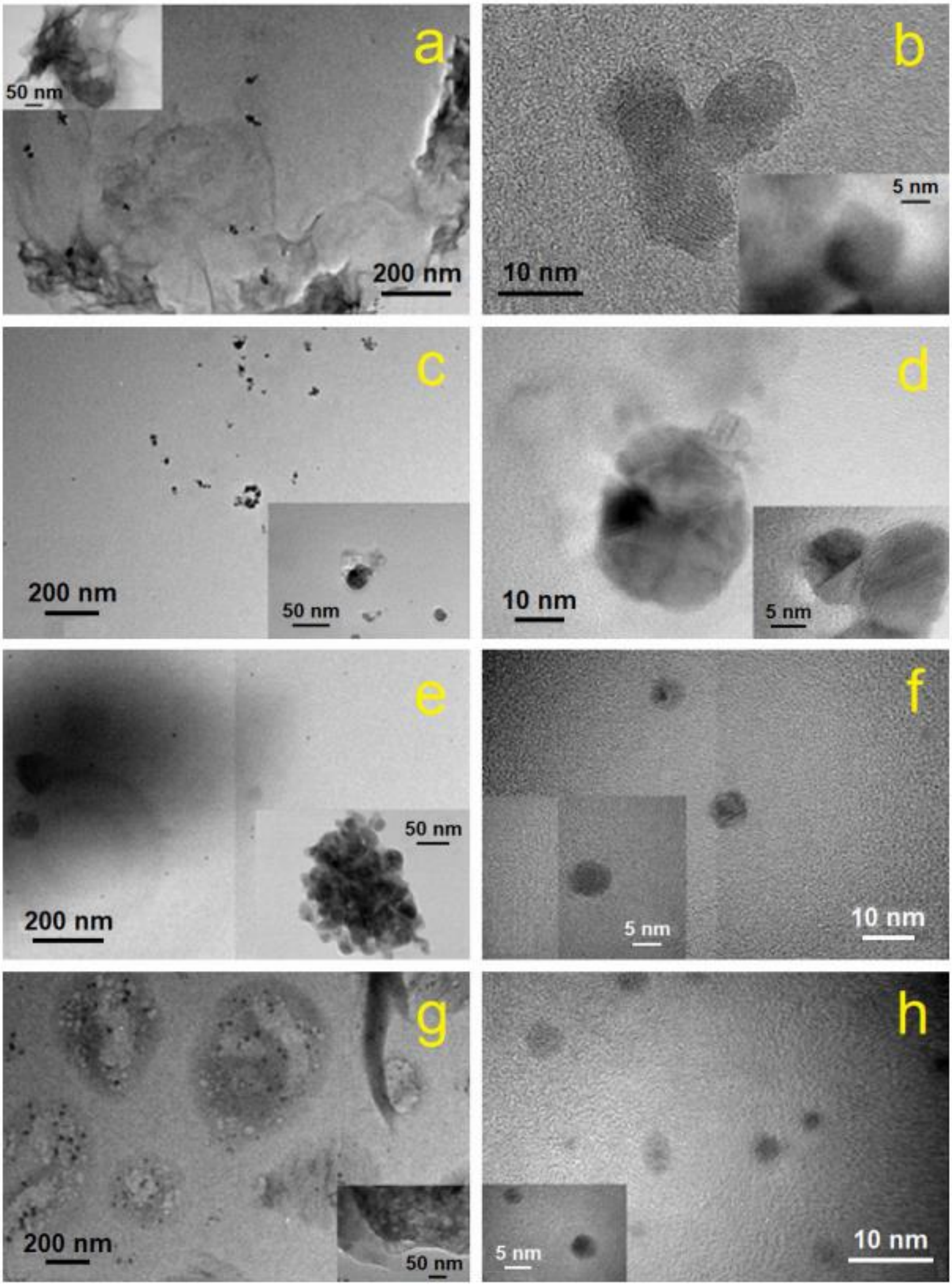

Fig. 3.9. TEM and HRTEM images of GO (a,b), GO+Ag (c,d), GO+ODA+Ag (e,f) and GO+DAO+Ag (g,h). The insets represent high-magnification imaging when smaller nanoparticles can be differentiated.

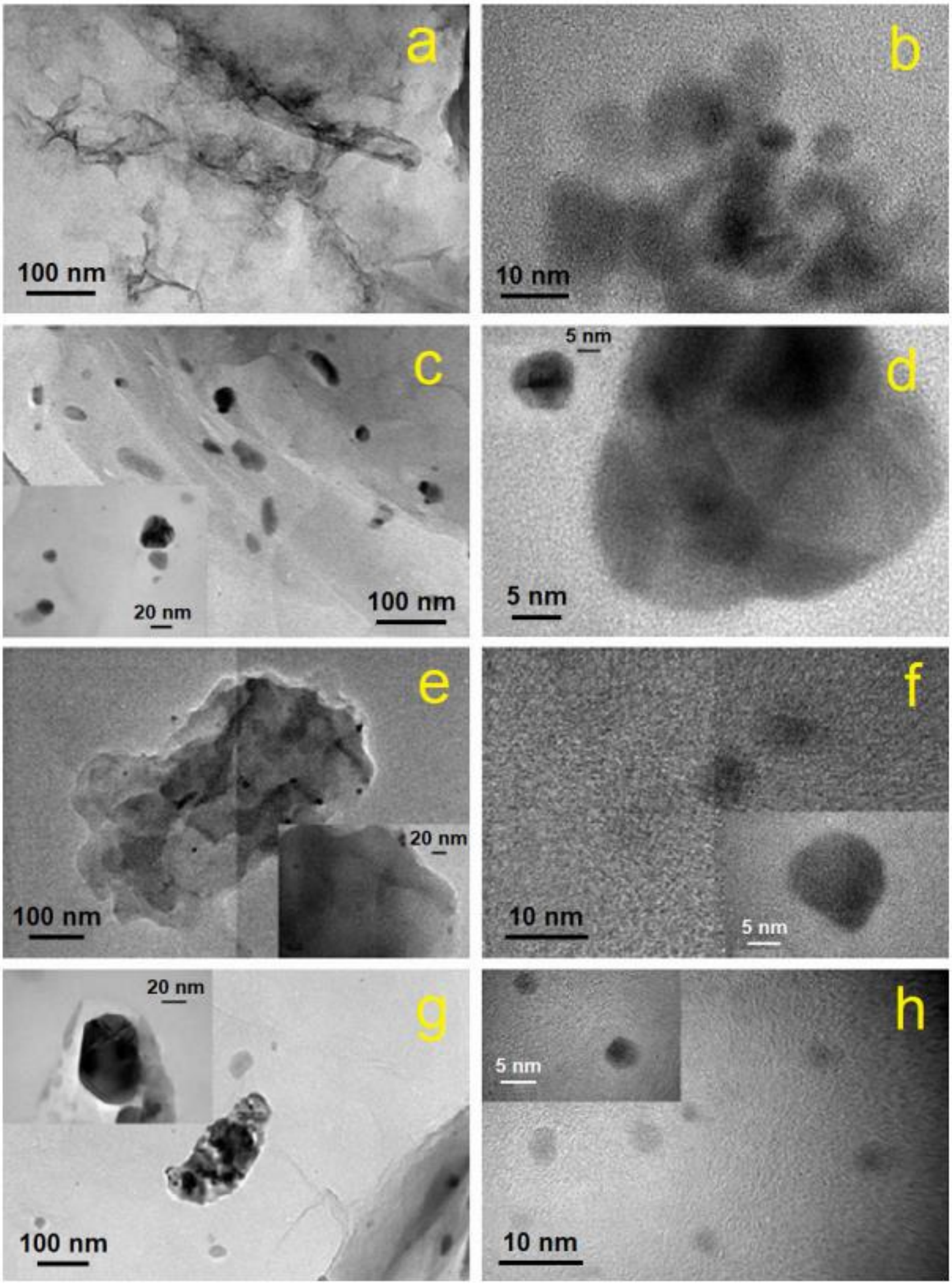

Fig. 3.10. TEM and HRTEM images of GOP (a,b), GOP+Ag (c,d), GOP+ODA+Ag (e,f) and GOP+DAO+Ag (g,h). The insets represent high-magnification imaging when smaller nanoparticles can be differentiated.

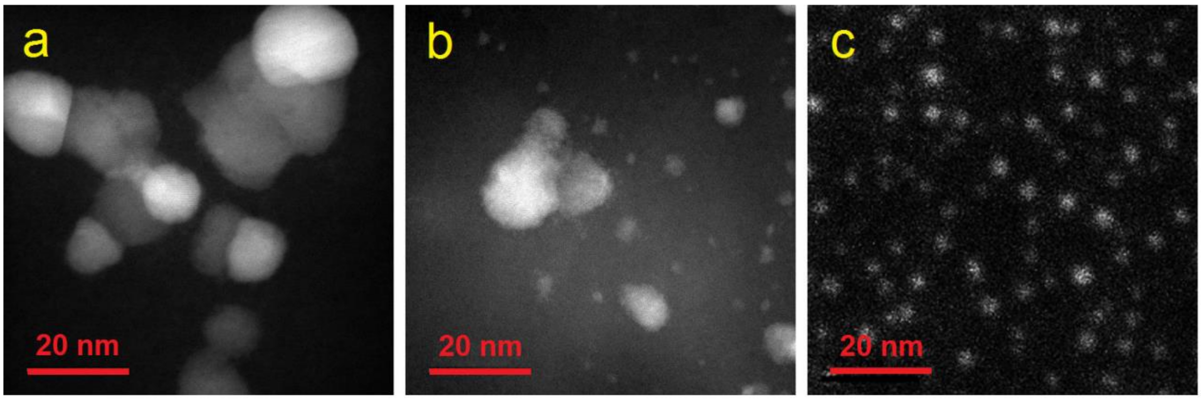

Fig. 3.11. Z-Contrast dark-field TEM images for (a) GO+Ag, (b) GO+ODA+Ag and (c) GO+DAO+Ag.

In line with the results of SEM imaging (Figs. 3.6g-i and 3.7h,i), AgNPs in GO+ODA+Ag (Fig. 3.9e,f), and GOP+ODA+Ag (Fig. 3.10e,f) were found to be generally irregularly shaped and randomly distributed. Most of them have a size of 3-15 nm, but the formation of larger agglomerates of up to ca. 200 nm can be observed as well (Fig. 3.9e). While similar relatively large agglomerates were found also in GOP+DAO+Ag (Fig. 3.10g), much more typical for the 1,8- diaminooctane-functionalized materials is the presence of small AgNPs of around 5 nm (Figs. 3.9h and 3.10h). Here it is appropriate to mention the study by Mohan *et al.* (2019)[47] on morphological transformation of silver nanoparticles influenced by different factors. These authors showed that AgNP agglomeration can be provoked by an oxidative environment, whereas exposure to nitrogen-rich solutions did not lead to aggregation. In the present context, one can suggest that for amine functionalized samples, the formation of AgNPs occurs *via the* reduction of metal ions coordinated to N donor atoms of the covalently attached amine molecules. This results in a more homogeneous size distribution and prevents the agglomeration observed in GO powder and GOP, where the interaction of Ag with oxidized functionalities provokes the formation of particles with different sizes and their coalescence.

The latter conclusions are strongly supported by the results of Z-contrast dark-field TEM imaging presented in Fig. 3.11, which allows for a more explicit comparison of the sizes and morphology of AgNPs found in GO+Ag, GO+ODA+Ag and GO+DAO+Ag, nearly at the nucleation level. The image in Fig. 3.11c clearly shows that the GO+DAO+Ag sample surface has a very homogeneous coverage with small-size Ag NPs of about 3-5 nm, contrary to GO+ODA+Ag and especially GO+Ag.

The fact that direct functionalization of prefabricated GOP is the only approach allowing for systematic tuning of its physical (including electronic) characteristics[4], motivated us to monitor the changes in conductivity/resistivity due to amine functionalization followed by Ag deposition. The results are summarized in Table 1. When analyzing the effect of amine functionalization, one can see that, compared to GOP, the conductivity increases by one order of magnitude for GOP+ODA, and by two orders of magnitude for GOP+DAO: thus, the general increase in conductivity (and, correspondingly, decrease in resistivity) is consistent with our earlier results.[4] The effect of silver decoration turned out to be insignificant, compared to the above. In particular, for GOP+Ag *vs.* GOP and GOP+DAO+Ag *vs.* GOP+DAO, the conductivity/resistivity remains of the same order of magnitude. Only for GOP+ODA+Ag compared to GOP+ODA the conductivity increases by one order of magnitude. These results can be explained in terms of the content and distribution of Ag particles in the following way. Despite the highest silver content in GOP+Ag (7.5% according to TGA), AgNPs deposited onto GO surfaces (see TEM micrographs in Figs 3.9c,d and 3.10c,d) are relatively large without appreciable electric contact between them. An additional factor might be that groups of silver particles are found confined within the rolls observed by SEM (Fig. 3.6d-f), which contributes to their mutual isolation and consequent loss of electric contact. The differences in elemental Ag content for GOP+ODA+Ag and GOP+DAO+Ag are relatively insignificant, at 1.06 wt % and 1.88 wt %, respectively. However, the former contains extended surface sites densely covered with Ag particles and their agglomerates (see SEM image in Fig. 3.7i), which enhance electric contact, whereas in the latter AgNPs are small and more uniformly dispersed throughout GOP+DAO+Ag surface (as also in GO+DAO+Ag; see Figs. 3.9g,h and 3.11c).

Table 1. Conductivity and resistivity results for non-functionalized and amine-functionalized GOP samples with and without AgNPs.

Sample	Conductivity (S/cm)	Resistivity(Ω•cm)
GOP	$(1.05 \pm 0.06) \times 10^{-5}$	$(0.96 \pm 0.05) \times 10^{5}$
GOP+Ag	$(0.73 \pm 0.07) \times 10^{-5}$	$(1.38 \pm 0.13) \times 10^{5}$
GOP+ODA	$(2.04 \pm 0.12) \times 10^{-4}$	$(4.93 \pm 0.28) \times 10^{3}$
GOP+ODA+Ag	$(0.79 \pm 0.04) \times 10^{-3}$	$(1.27 \pm 0.07) \times 10^{3}$
GOP+DAO	$(2.21 \pm 0.09) \times 10^{-3}$	$(4.54 \pm 0.18) \times 10^{2}$
GOP+DAO+Ag	$(1.54 \pm 0.19) \times 10^{-3}$	$(6.58 \pm 0.89) \times 10^{2}$

3.4.2 Theoretical modelling

Some explanation of the experimental results obtained was attempted by employing theoretical DFT calculations. Extended dimensions of both realistic individual GO sheets and AgNPs are computationally prohibitive, so the models to be handled had to be considerably smaller. One of the most appropriate choices to simulate an AgNP proposed by Ma's group[48-50] (and also used by Lim *et al*.[51]) is a cluster composed of thirteen Ag atoms shown in Fig. 3.12. In all the above works[48-51] the computational methodology of choice was the same PBE general gradient approximation functional as the one widely employed for DFT studies of noncovalent, covalent and coordination bonding of a broad variety of chemical species to graphene and GO models[52-59]. According to Mulliken analysis for the optimized Ag_{13} geometry, the cluster contains different external atoms in terms of the sign and magnitude of charge: from negative of − 0.075 to positive of 0.031 *e*. This implies the possibility of electrostatic attraction of Ag_{13} to both positively and negatively charged atoms or functional groups of non-functionalized and functionalized GO.

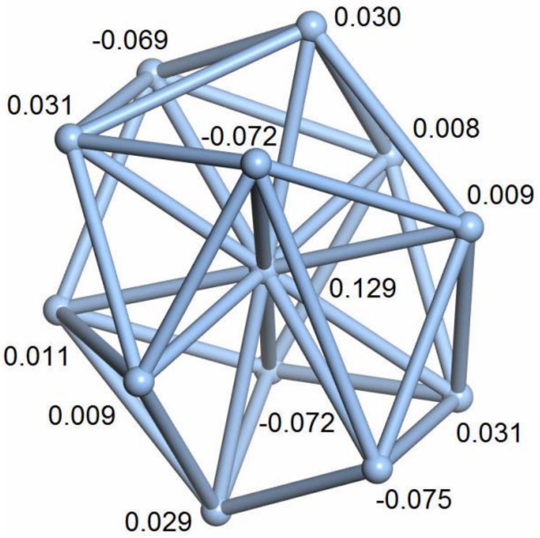

Fig. 3.12. Optimised geometry of the Ag_{13} cluster used to simulate AgNPs, showing atomic charges obtained by Mulliken analysis.

On the other hand, the models to be selected for non-functionalized and amine-functionalized GO had to match the size of Ag_{13} cluster: the ones based on ten fused aromatic-ring systems described previously[56,57] satisfy this criterion. Since due to the size limitation it is unfeasible to contemplate the whole variety of possible oxygenated functionalities existing in realistic GO, we limited them to six carboxylic and eight aromatic ketone groups, as previously described in Basiuk *et al.* (2016)[56] and illustrated in Fig. 3.13 for GO model. To simulate GO+ODA and GO+DAO species covalently functionalized with amines, all four COOH groups of the GO model were converted into the corresponding amide derivatives (Fig. 3.13). Furthermore, in the case of GO+DAO we had to take into account that the Ag deposition takes place under acidic conditions: accordingly, all four terminal NH_2 groups, which are not involved in covalent bonding through the formation of amide derivatives, were protonated (GO+DAO-$4H^+$ model).

The numerical results of DFT calculations are summarized in Table 2. Fig. 3.13 schematically represents the complexation of GO, GO+ODA and GO+DAO-$4H^+$ models with Ag_{13} nanocluster. One can make several important observations in terms of the formation energies and geometries of the complexes. First, the strongest bonding of silver was found on the GO model, with the formation energy of -176.2 kcal/mol. Here, Ag_{13} is strongly attracted not only to one carboxylic group (whose proton becomes substituted) but also to two carbonyl O atoms and one C atom of the graphene backbone; the short bonds formed can be qualified as covalent ones. The above interactions result in strong bending distortion of GO model, along with some flattening of Ag_{13} nanocluster. It is appropriate to recall the SEM images (Fig. 3.6d-f) revealing the effect of rolling GO sheets and/or stacks in GO+Ag sample: the above simulation results could serve as a plausible explanation of its origin.

Table 2. Total energies (*E*, in Ha), HOMO, LUMO and HOMO-LUMO gap energies (in eV) for separated Ag_{13} cluster, non-functionalized and amine-functionalized GO models and their corresponding complexes with Ag_{13}, as well as formation energies (ΔE, in kcal/mol) for the complexes with Ag_{13}, as calculated by using PBE GGA functional with Grimme's dispersion correction in conjunction with DNP basis set.

Structure	*E* (Ha)	ΔE (kcal/mol)	E_{HOMO} (eV)	E_{LUMO} (eV)	HOMO-LUMO gap (eV)
Ag_{13}	-67595.2584005		-3.415	-3.352	0.063
GO	-2954.3392083		-6.925	-5.818	1.107
GO+Ag_{13}	-70549.8783335	-176.2	-4.868	-4.765	0.103
GO+ODA	-5702.6813267		-6.482	-5.622	0.860
GO+ODA+Ag_{13}	-73298.1170641	-111.3	-4.220	-4.163	0.057
GO+DAO-4H^+	-4354.7740818		-6.599	-5.733	0.866
GO+DAO-4H^++Ag_{13}[a]	-71950.1465917	-71.6	-4.939	-4.844	0.095

[a] This is the only set of calculations that were impossible to complete with Fermi occupancy, but it was done at thermal smearing of 0.0001 Ha. Nevertheless, we showed for very different model systems that cluster DFT calculations using the latter value yield the same results (geometries, total energies, spin and frontier orbital distribution, etc.) as those performed with Fermi occupancy.[60,61]

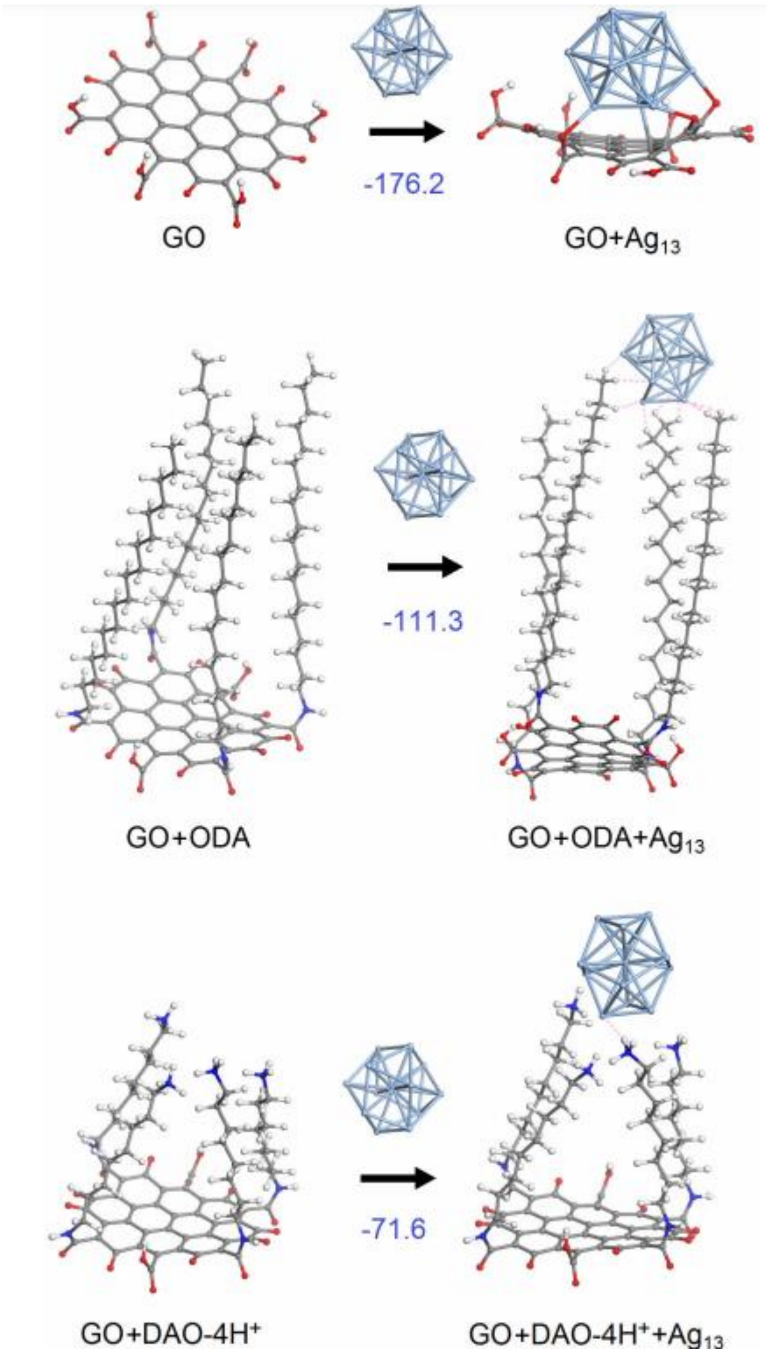

Fig. 3.13. Optimized geometries of GO, GO+ODA and GO+DAO-4H$^+$ models (left) and of the corresponding complexes with Ag$_{13}$ nanocluster (right). The values shown in blue are the formation energies (in kcal/mol) for GO+Ag$_{13}$, GO+ODA+Ag$_{13}$ and GO+DAO-4H$^+$+Ag$_{13}$ complexes. The pink dashed lines show close contacts shorter than 2.8 Å.

In terms of bonding strength, GO+Ag is followed by GO+ODA+Ag$_{13}$ (-111.3 kcal/mol) and GO+DAO-4H$^+$+Ag$_{13}$ (-71.6 kcal/mol) complexes. Correspondingly, the pattern of interaction appears to be different for ODA and DAO moieties. In Fig. 3.13 one can see that Ag$_{13}$ cluster forms as many as eight contacts (pink dashed lines) shorter than 2.8 Å with terminal alkyl groups of three octadecyl radicals of GO+ODA+Ag$_{13}$, whereas only one such close approach forms and with only one protonated 8-amino group of GO+DAO-4H$^+$+Ag$_{13}$, which explains the weaker bonding (that is, less negative formation energy).

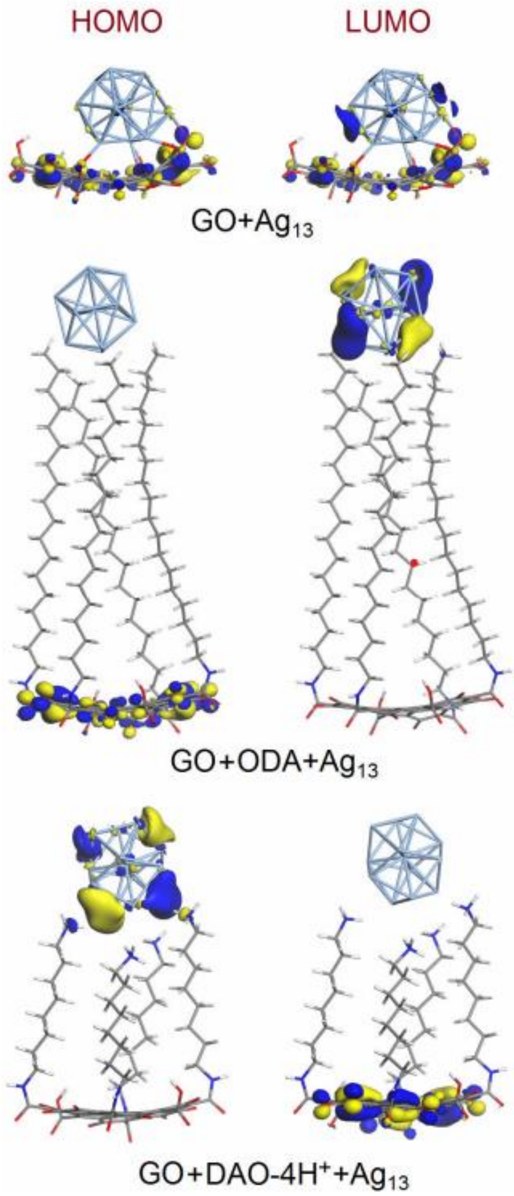

Fig. 3.14. HOMO and LUMO plots (isosurfaces at 0.03 a.u.) for GO+Ag$_{13}$, GO+ODA+Ag$_{13}$ and GO+DAO-4H^{+}+Ag$_{13}$ complexes.

The differences in the electronic structure of the three complexes with the Ag_{13} cluster were analyzed in terms of energy (Table 2) and distribution (Fig. 3.14) of frontier orbitals HOMO and LUMO. The HOMO-LUMO gap energies calculated for individual components Ag_{13}, GO, GO+ODA and GO+DAO-4H$^+$ are 0.063, 1.107, 0.860 and 0.866 eV, respectively (Table 2). Since silver nanocluster has the lowest gap energy of all, it is logical to expect that the gap values of GO, GO+ODA and GO+DAO-4H$^+$ will decrease upon complexation with Ag_{13}. Indeed, they drop by roughly one order of magnitude in all cases: to 0.103, 0.057 and 0.095 eV for GO+Ag_{13}, GO+ODA+Ag_{13} and GO+DAO-4H$^+$+ Ag_{13}, respectively. While these changes are relatively uniform for all the complexes, the same cannot be said about frontier orbital localization (Fig. 3.14). The very strong (in terms of binding energy and formation of new bonds) interaction in the case of GO+Ag_{13} results in the localization of both HOMO and LUMO on carbon nanocluster, with only an insignificant fraction of LUMO found on Ag_{13}. Here one should remind that the most common HOMO-LUMO distribution for the complexes of carbon nanoclusters with organic and metal-containing coordination compounds is when LUMO is localized on carbon nanocluster and HOMO, on the second interacting component (see, for example[36,55,62,63] and references therein). In the present study, this type of HOMO-LUMO distribution can be observed only for GO+DAO-4H$^+$+Ag_{13}, whereas for GO+ODA+Ag_{13} the orbital localization is inverted. The fact that the two of them in GO+Ag_{13} are found on carbon nanocluster can be interpreted as the loss of reactivity of silver component in both electrophilic and nucleophilic processes, which in practice might have important undesirable consequences for catalytic, electrocatalytic and biomedical applications of AgNPs deposited onto GO-based materials.

3.5 Conclusions

Both GO powder and GOP can be successfully functionalized with aliphatic amines and serve as supports for the decoration with Ag particles. At the same time, differences were found between the paper and powder-based materials. An important trend can be seen in the silver content estimated from TGA curves, which is 6.55 wt % and 11.88 wt % for GO+ODA+Ag and GO+DAO+Ag, whereas for GOP+ODA+Ag and GOP+DAO+Ag it dramatically decreases to 1.06 wt % and 1.88 wt %, respectively. Apparently, compacting GO powder into paper hinders the Ag species from reaching the functionalizing groups within the mat. From the above values, it follows also that the silver content of DAO-functionalized samples is almost twice as high compared to that of ODA-derived materials. A logical explanation is that the use of bifunctional reagents such as DAO provides additional amino groups serving as coordination centres for anchoring and stabilization of AgNPs.

The most relevant information on the size and morphology of AgNPs was obtained from bright-field and dark-field TEM imaging. Both GO+Ag and GOP+Ag samples contain twinned particles of round/rectangular form with different grain boundaries; this type of morphology is associated with a lack of control during the particle nucleation and growth. Their sizes vary in a range of 10-30 nm for GO+Ag, and 15-35 nm for GOP+Ag. AgNPs in GO+ODA+Ag and GOP+ODA+Ag are generally irregularly shaped and randomly distributed. Most of them have a size of 3-15 nm, but the formation of larger agglomerates of up to ca. 200 nm was observed as well. While similar relatively large agglomerates were found also in GOP+DAO+Ag, much more typical for the 1,8-diaminooctane-functionalized materials is the presence of small Ag NPs of around 5 nm. One can suggest that for amine-functionalized samples, the formation of AgNPs occurs *via* the reduction of metal ions coordinated to N donor atoms of the covalently attached amine molecules. This results in a more homogeneous size distribution and prevents the agglomeration observed in GO powder and GOP, where the interaction of Ag with oxidized functionalities provokes the formation of particles with different sizes and their coalescence.

According to the results of DFT calculations, the binding of AgNPs (represented by Ag_{13} cluster model) is the strongest on GO, followed by ODA and finally DAO-functionalized material. This correlates with the size and distribution of Ag nanoparticles observed experimentally by TEM. In addition, the strong interaction of Ag_{13} cluster with the GO model distorting the graphene backbone might serve as an explanation of the rolling effect detected by SEM for GO+Ag hybrid.

The results obtained expand the spectrum of possible uses of eco-friendly solvent-free functionalization techniques to the fabrication of silver-decorated carbon nanomaterials, where the size and uniform distribution of Ag NPs is an important prerequisite for successful electrochemical, catalytic and biomedical applications.

3.6 References

(1) Lerf, A., He, H., Forster, M., & Klinowski, J. (1998). Structure of Graphite Oxide Revisited‖. *The Journal of Physical Chemistry B*, *102*(23), 4477–4482. https://doi.org/10.1021/jp9731821.

(2) Dimiev, A. M., & Siegfried Eigler. (2017). *Graphene oxide: fundamentals and applications*. Chichester, West Sussex John Wiley Et Sons, Inc.

(3) Alzate-Carvajal, N., Basiuk, E. V., Meza-Laguna, V., Puente-Lee, I., Farías, M. H., Bogdanchikova, N., & Basiuk, V. A. (2016). Solvent-free one-step covalent functionalization of graphene oxide and nanodiamond with amines. *RSC Advances*, *6*(114), 113596–113610. https://doi.org/10.1039/c6ra22658b.

(4) Alzate-Carvajal, N., Acevedo-Guzmán, D. A., Meza-Laguna, V., Farías, M. H., Pérez-Rey, L. A., Abarca-Morales, E., García-Ramírez, V. A., Basiuk, V. A., & Basiuk, E. V. (2018). One-step nondestructive functionalization of graphene oxide paper with amines. *RSC Advances*, *8*(28), 15253–15265. https://doi.org/10.1039/c8ra00986d.

(5) Loh, K. P., Bao, Q., Eda, G., & Chhowalla, M. (2010). Graphene oxide as a chemically tunable platform for optical applications. *Nature Chemistry*, *2*(12), 1015–1024. https://doi.org/10.1038/nchem.907.

(6) Kumari, S., Sharma, P., Yadav, S., Kumar, J., Vij, A., Rawat, P., Kumar, S., Sinha, C., Bhattacharya, J., Srivastava, C. M., & Majumder, S. (2020). A Novel Synthesis of the Graphene Oxide-Silver (GO-Ag) Nanocomposite for Unique Physiochemical Applications. *ACS Omega*, *5*(10), 5041–5047. https://doi.org/10.1021/acsomega.9b03976.

(7) Vallés, C., David Núñez, J., Benito, A. M., & Maser, W. K. (2012). Flexible conductive graphene paper obtained by direct and gentle annealing of graphene oxide paper. *Carbon*, *50*(3), 835–844. https://doi.org/10.1016/j.carbon.2011.09.042.

(8) Zhang, Y., & Chung, T.-S. (2017). Graphene oxide membranes for nanofiltration. *Current Opinion in Chemical Engineering*, *16*, 9–15. https://doi.org/10.1016/j.coche.2017.03.002.

(9) Dikin, D. A., Stankovich, S., Zimney, E. J., Piner, R. D., Dommett, G. H. B., Evmenenko, G., Nguyen, S. T., & Ruoff, R. S. (2007). Preparation and characterization of graphene oxide paper. *Nature*, *448*(7152), 457–460. https://doi.org/10.1038/nature06016.

(10) Chen, H., Müller, M. B., Gilmore, K. J., Wallace, G. G., & Li, D. (2008). Mechanically Strong, Electrically Conductive, and Biocompatible Graphene Paper. *Advanced Materials*, *20*(18), 3557–3561. https://doi.org/10.1002/adma.200800757.

(11) Huang, W. (2018). Graphene Oxide Nanopapers. In W. Huang (Ed.), *Nanopapers: From Nanochemistry and Nanomanufacturing to Advanced Applications* (pp. 1–26). Elsevier.

(12) Cobos, M., De-La-Pinta, I., Quindós, G., Fernández, M. J., & Fernández, M. D. (2020). Graphene Oxide–Silver Nanoparticle Nanohybrids: Synthesis, Characterization, and Antimicrobial Properties. *Nanomaterials*, *10*(2), 376. https://doi.org/10.3390/nano10020376.

(13) Cheng, Y., Li, H., Fang, C., Ai, L., Chen, J., Su, J., Zhang, Q., & Fu, Q. (2019). Facile synthesis of reduced graphene oxide/silver nanoparticles composites and their application for detecting heavy metal ions. *Journal of Alloys and Compounds*, *787*, 683–693. https://doi.org/10.1016/j.jallcom.2019.01.320.

(14) Ayán-Varela, M., Fernández-Merino, M. J., Paredes, J. I., Villar-Rodil, S., Fernández-Sánchez, C., Guardia, L., Martínez-Alonso, A., & Tascón, J. M. D. (2014). Highly efficient silver-assisted reduction of graphene oxide dispersions at room temperature: mechanism, and catalytic and electrochemical performance of the resulting hybrids. *J. Mater. Chem. A*, *2*(20), 7295–7305. https://doi.org/10.1039/c3ta15307j.

(15) Mohammadnejad, J., Yazdian, F., Omidi, M., Rostami, A. D., Rasekh, B., & Fathinia, A. (2018). Graphene oxide/silver nanohybrid: Optimization, antibacterial activity and its impregnation on bacterial cellulose as a potential wound dressing based on GO-Ag nanocomposite-coated BC. *Engineering in Life Sciences*, *18*(5), 298–307. https://doi.org/10.1002/elsc.201700138.

(16) Navalon, S., Dhakshinamoorthy, A., Alvaro, M., & Garcia, H. (2016). Metal nanoparticles supported on two-dimensional graphenes as heterogeneous catalysts. *Coordination Chemistry Reviews*, *312*, 99–148. https://doi.org/10.1016/j.ccr.2015.12.005.

(17) Golzar, H., Yazdian, F., Hashemi, M., Omidi, M., Mohammadrezaei, D., Rashedi, H., Farahani, M., Ghasemi, N., Shabani shayeh, J., & Tayebi, L. (2018). Optimizing the hybrid nanostructure of functionalized reduced graphene oxide/silver for highly efficient cancer nanotherapy. *New Journal of Chemistry*, *42*(15), 13157–13168. https://doi.org/10.1039/c8nj01764f.

(18) Cai, N., Fu, J., Zeng, H., Luo, X., Han, C., & Yu, F. (2018). Reduced graphene oxide-silver nanoparticles/nitrogen-doped carbon nanofiber composites with meso-microporous structure for high-performance symmetric supercapacitor application. *Journal of Alloys and Compounds*, *742*, 769–779. https://doi.org/10.1016/j.jallcom.2018.01.011.

(19) Li, J., Kuang, D., Feng, Y., Zhang, F., Xu, Z., Liu, M., & Wang, D. (2013). Green synthesis of silver nanoparticles–graphene oxide nanocomposite and its application in electrochemical sensing oftryptophan. *Biosensors and Bioelectronics*, *42*, 198–206. https://doi.org/10.1016/j.bios.2012.10.029.

(20) Zeng, F., Xu, D., Zhan, C., Liang, C., Zhao, W., Zhang, J., Feng, H., & Ma, X. (2018). Surfactant-Free Synthesis of Graphene Oxide Coated Silver Nanoparticles for SERS Biosensing and Intracellular Drug Delivery. *ACS Applied Nano Materials*, *1*(6), 2748–2753. https://doi.org/10.1021/acsanm.8b00444.

(21) Chen, J., Xiao, P., Gu, J., Huang, Y., Zhang, J., Wang, W., & Chen, T. (2014). Au nanoparticle-loaded PDMAEMA brush grafted graphene oxide hybrid systems for thermally smart catalysis. *RSC Adv.*, *4*(84), 44480–44485. https://doi.org/10.1039/c4ra05592f.

(22) Shuai, C., Guo, W., Wu, P., Yang, W., Hu, S., Xia, Y., & Feng, P. (2018). A graphene oxide-Ag co-dispersing nanosystem: Dual synergistic effects on antibacterial activities and mechanical properties of polymer scaffolds. *Chemical Engineering Journal*, *347*, 322–333. https://doi.org/10.1016/j.cej.2018.04.092.

(23) Liu, C., Shen, J., Liao, C. Z., Yeung, K. W. K., & Tjong, S. C. (2018). Novel electrospun polyvinylidene fluoride-graphene oxide-silver nanocomposite membranes with protein and bacterial antifouling characteristics. *Express Polymer Letters*, *12*(4), 365–382. https://doi.org/10.3144/expresspolymlett.2018.31.

(24) Zhu, Z., Su, M., Ma, L., Ma, L., Liu, D., & Wang, Z. (2013). Preparation of graphene oxide–silver nanoparticle nanohybrids with highly antibacterial capability. *Talanta*, *117*, 449–455. https://doi.org/10.1016/j.talanta.2013.09.017.

(25) Jiang, Y., Carboni, D., Malfatti, L., & Innocenzi, P. (2018). Graphene Oxide-Silver Nanoparticles in Molecularly-Imprinted Hybrid Films Enabling SERS Selective Sensing. *Materials*, *11*(9), 1674. https://doi.org/10.3390/ma11091674.

(26) Li, J., Sun, Y., Wang, J., Tian, J., Zhang, X., Yang, H., & Lin, B. (2018). Synthesis, structure and electrochemical properties of novel ternary composite reduced-graphene oxide/Ag nanoparticles/poly(p-phenylenediamine). *Journal of Alloys and Compounds*, *749*, 783–793. https://doi.org/10.1016/j.jallcom.2018.03.326.

(27) Vi, T. T. T., & Lue, S. J. (2016). Preparation of silver nanoparticles loaded graphene oxide nanosheets for antibacterial activity. *IOP Conference Series: Materials Science and Engineering*, *162*(1), 012033. https://doi.org/10.1088/1757-899x/162/1/012033.

(28) Vi, T., Rajesh Kumar, S., Rout, B., Liu, C.-H., Wong, C.-B., Chang, C.-W., Chen, C.-H., Chen, D., & Lue, S. (2018). The Preparation of Graphene Oxide-Silver Nanocomposites: The Effect of Silver Loads on Gram-Positive and Gram-Negative Antibacterial Activities. *Nanomaterials*, *8*(3), 163. https://doi.org/10.3390/nano8030163.

(29) Yun, H., Kim, J. D., Choi, H. C., & Lee, C. W. (2013). Antibacterial Activity of CNT-Ag and GO-Ag Nanocomposites Against Gram-negative and Gram-positive Bacteria. *Bulletin of the Korean Chemical Society*, *34*(11), 3261–3264. https://doi.org/10.5012/bkcs.2013.34.11.3261.

(30) Gurunathan, S., Hyun Park, J., Choi, Y.-J., Woong Han, J., & Kim, J.-H. (2016). Synthesis of Graphene Oxide-Silver Nanoparticle Nanocomposites: An Efficient Novel Antibacterial Agent. *Current Nanoscience*, *12*(6), 762–773. https://doi.org/10.2174/1573413712666160721143424.

(31) Bao, Q., Zhang, D., & Qi, P. (2011). Synthesis and characterization of silver nanoparticle and graphene oxide nanosheet composites as a bactericidal agent for water disinfection. *Journal of Colloid and Interface Science*, *360*(2), 463–470. https://doi.org/10.1016/j.jcis.2011.05.009.

(32) Abdelhalim, A. O. E., Galal, A., Hussein, M. Z., & El Sayed, I. E.-T. . (2016). Graphene Functionalization by 1,6-Diaminohexane and Silver Nanoparticles for Water Disinfection. *Journal of Nanomaterials*, *2016*, 1–7. https://doi.org/10.1155/2016/1485280.

(33) Basiuk, E. V., Monroy-Torres, B., Carrero, J. C., & Basiuk, V. A. (2020). Effects of solvent-free amine functionalization of graphene oxide and nanodiamond on bacterial growth. *Fullerenes, Nanotubes and Carbon Nanostructures*, 1–9. https://doi.org/10.1080/1536383x.2020.1811235.

(34) Morones, J. R., Elechiguerra, J. L., Camacho, A., Holt, K., Kouri, J. B., Ramírez, J. T., & Yacaman, M. J. (2005). The bactericidal effect of silver nanoparticles. *Nanotechnology*, *16*(10), 2346–2353. https://doi.org/10.1088/0957-4484/16/10/059.

(35) Marambio-Jones, C., & Hoek, E. M. V. (2010). A review of the antibacterial effects of silver nanomaterials and potential implications for human health and the environment. *Journal of Nanoparticle Research*, *12*(5), 1531–1551. https://doi.org/10.1007/s11051-010-9900-y.

(36) Meza-Laguna, V., Basiuk, E. V., Alvarez-Zauco, E., Acosta-Najarro, D., & Basiuk, V. A. (2007). Cross-Linking of C_{60} Films with 1,8-Diaminooctane and Further Decoration with Silver Nanoparticles. *Journal of Nanoscience and Nanotechnology*, *7*(10), 3563–3571. https://doi.org/10.1166/jnn.2007.681.

(37) Barth, A. (2007). Infrared spectroscopy of proteins. *Biochimica et Biophysica Acta (BBA) - Bioenergetics*, *1767*(9), 1073–1101. https://doi.org/10.1016/j.bbabio.2007.06.004.

(38) Kong, J., & Yu, S. (2007). Fourier Transform Infrared Spectroscopic Analysis of Protein Secondary Structures. *Acta Biochimica et Biophysica Sinica*, *39*(8), 549–559. https://doi.org/10.1111/j.1745-7270.2007.00320.x.

(39) Coates, J. (2000). Interpretation of infrared spectra, a practical approach. In R. A. Meyers (Ed.), *Encyclopedia of Analytical Chemistry* (pp. 10815–10837). John Wiley & Sons Ltd.

(40) El-Nagar, G. A., Sarhan, R. M., Abouserie, A., Maticiuc, N., Bargheer, M., Lauermann, I., & Roth, C. (2017). Efficient 3D-Silver Flower-like Microstructures for Non-Enzymatic Hydrogen Peroxide (H_2O_2) Amperometric Detection. *Scientific Reports*, *7*(1). https://doi.org/10.1038/s41598-017-11965-9.

(41) Schneidewind, H., Schüler, T., Strelau, K. K., Weber, K., Cialla, D., Diegel, M., Mattheis, R., Berger, A., Möller, R., & Popp, J. (2012). The morphology of silver nanoparticles prepared by enzyme-induced reduction. *Beilstein Journal of Nanotechnology*, *3*, 404–414. https://doi.org/10.3762/bjnano.3.47.

(42) Quintana, M., Marek Grzelczak, Konstantinos Spyrou, Calvaresi, M., Bals, S., Kooi, B., Gustaaf Van Tendeloo, Rudolf, P., Zerbetto, F., & Prato, M. (2012). A Simple Road for the Transformation of Few-Layer Graphene into MWNTs. *Journal of the American Chemical Society*, *134*(32), 13310–13315. https://doi.org/10.1021/ja303131j

(43) Heidarpour, F., Ghani, W. A. W. A. K., Ahmadun, F. R. B., Sobri, S., Zargar, M., & Mozafari, M. R. (2010). Nano silver-coated polypropylene water filter: I. Manufacture by electron beam gun using a modified Balzers 760 machine. *Digest Journal of Nanomaterials and Biostructures* , *5*(3), 787–796.

(44) Anandalakshmi, K., Venugobal, J., & Ramasamy, V. (2015). Characterization of silver nanoparticles by green synthesis method using Pedalium murex leaf extract and their antibacterial activity. *Applied Nanoscience*, *6*(3), 399–408. https://doi.org/10.1007/s13204-015-0449-z.

(45) Mo, J., Stefanov, B. I., Lau, T. H. M., Chen, T., Wu, S., Wang, Z., Gong, X.-Q., Wilkinson, I., Schmid, G., & Tsang, S. C. E. (2019). Superior Performance of Ag over Pt for Hydrogen Evolution Reaction in Water Electrolysis under High Overpotentials. *ACS Applied Energy Materials*, *2*(2), 1221–1228. https://doi.org/10.1021/acsaem.8b01777.

(46) Barwal, I., Ranjan, P., Kateriya, S., & Yadav, S. (2011). Cellular oxido-reductive proteins of Chlamydomonas reinhardtii control the biosynthesis of silver nanoparticles. *Journal of Nanobiotechnology*, *9*(1), 56. https://doi.org/10.1186/1477-3155-9-56.

(47) Mohan, S., Princz, J., Ormeci, B., & DeRosa, M. C. (2019). Morphological Transformation of Silver Nanoparticles from Commercial Products: Modeling from Product Incorporation, Weathering through Use Scenarios, and Leaching into Wastewater. *Nanomaterials*, *9*(9), 1258. https://doi.org/10.3390/nano9091258.

(48) Ma, W., & Chen, F. (2012). Optical and electronic properties of Cu doped Ag clusters. *Journal of Alloys and Compounds*, *541*, 79–83. https://doi.org/10.1016/j.jallcom.2012.06.105

(49) Ma, W., & Chen, F. (2014). Experimental and Theoretical Studies on the Interaction between Isonicotinic Acid Molecules and Silver Nanoclusters. *Spectroscopy Letters*, *47*(10), 754–760. https://doi.org/10.1080/00387010.2013.843567

(50) Zhang, S., Ma, W., Zhang, F., Jing, C., & Wu, R. (2018). Theoretical and experimental study on adsorption of benzoic acid molecules on silver clusters. *Ferroelectrics*, *528*(1), 99–107. https://doi.org/10.1080/00150193.2018.1448624

(51) Lim, J., Kang, S., Kim, J., Kim, W. Y., & Ryu, S. (2017). Non-empirical atomistic dipole-interaction-model for quantum plasmon simulation of nanoparticles. *Scientific Reports*, *7*(1). https://doi.org/10.1038/s41598-017-16053-6.

(52) Wang, Y., Xu, Z., & Moe, Y. N. (2012). On the performance of local density approximation in describing the adsorption of electron donating/accepting molecules on graphene. *Chemical Physics*, *406*, 78–85. https://doi.org/10.1016/j.chemphys.2012.08.008

(53) Pier Luigi Silvestrelli, & Ambrosetti, A. (2014). Including screening in van der Waals corrected density functional theory calculations: The case of atoms and small molecules physisorbed on graphene. *The Journal of Chemical Physics*, *140*(12), 1–8. https://doi.org/10.1063/1.4869330

(54) Zhou, Q., Ju, W., Su, X., Yong, Y., & Li, X. (2017). Adsorption behavior of SO2 on vacancy-defected graphene: A DFT study. *Journal of Physics and Chemistry of Solids*, *109*, 40–45. https://doi.org/10.1016/j.jpcs.2017.05.007

(55) Basiuk, E. V., Martínez-Herrera, M., Álvarez-Zauco, E., Henao-Holguín, L. V., Puente-Lee, I., & Basiuk, V. A. (2014). Noncovalent functionalization of graphene with a Ni(ii) tetraaza[14]annulene complex. *Dalton Trans.*, *43*(20), 7413–7428. https://doi.org/10.1039/c3dt52645c

(56) Basiuk, V. A., Alzate-Carvajal, N., Laura Verónica Henao-Holguín, Rybak-Akimova, E. V., & Basiuk, E. V. (2016). Coordination functionalization of graphene oxide with tetraazamacrocyclic complexes of nickel(II): Generation of paramagnetic centers. *Applied Surface Science*, *371*, 16–27. https://doi.org/10.1016/j.apsusc.2016.02.166

(57) Basiuk, V. A., Rybak-Akimova, E. V., & Basiuk, E. V. (2017). Graphene oxide and nanodiamond: same carboxylic groups, different complexation properties. *RSC Advances*, *7*(28), 17442–17450. https://doi.org/10.1039/c7ra01685a

(58) Basiuk, V. A., Bolivar-Pineda, L. M., Meza-Laguna, V., Rybak-Akimova, E. V., & Basiuk, E. V. (2018). Carbon Nanotubes and Graphene Promote Pyrolysis of Free-Base Phthalocyanine. *The Journal of Physical Chemistry Letters*, *9*(15), 4420–4427. https://doi.org/10.1021/acs.jpclett.8b02141

(59) Basiuk, V. A., Mykola Kakazey, Vlasova, M., & Basiuk, E. V. (2019). Effect of structural defects on the strength of adsorption of La and Lu species on graphene. *Diamond and Related Materials*, *100*, 107597–107597. https://doi.org/10.1016/j.diamond.2019.107597

(60) Basiuk, V. A. (2011). Electron smearing in DFT calculations: A case study of doxorubicin interaction with single-walled carbon nanotubes. *International Journal of Quantum Chemistry*, *111*(15), 4197–4205. https://doi.org/10.1002/qua.23003

(61) Basiuk, V. A., Prezhdo, O. V., & Basiuk, E. V. (2020). Thermal smearing in DFT calculations: How small is really small? A case of La and Lu atoms adsorbed on graphene. *Materials Today Communications*, *25*(115665), 101595–101595. https://doi.org/10.1016/j.mtcomm.2020.101595

(62) 79. Chávez-Colorado, E., & Basiuk, V. A. (2017). Noncovalent interactions of free-base phthalocyanine with elongated fullerenes as carbon nanotube models. *Structural Chemistry*, *28*(6), 1765–1773. https://doi.org/10.1007/s11224-017-0955-6

(63) Basiuk, E. V., Huerta, L., & Basiuk, V. A. (2019). Noncovalent bonding of 3d metal(II) phthalocyanines with single-walled carbon nanotubes: A combined DFT and XPS study. *Applied Surface Science*, *470*, 622–630. https://doi.org/10.1016/j.apsusc.2018.11.159.

CHAPTER 4

Advancing eco-friendliness of nanotechnology: a novel synthesis approach for powder and paper-like nanohybrids based on graphene oxide and palladium nanoparticles

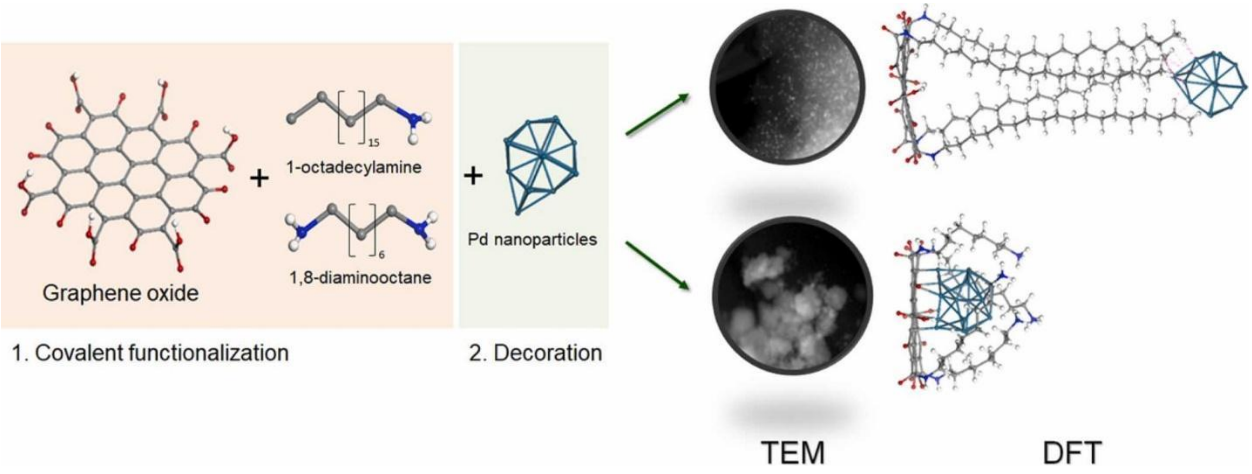

The results concerning the nanohybrids in powder form have been published as:

Rodríguez-Otamendi, D. I.; Bizarro, M.; Meza-Laguna, V.; Álvarez-Zauco, E.; Rudolf, P.; Basiuk, V. A.; Basiuk, E. V. Eco-Friendly Synthesis of Graphene Oxide–Palladium Nanohybrids. *Materials Today Communications* **2023**, *35*, 106007–106007. https://doi.org/10.1016/j.mtcomm.2023.106007.

ABSTRACT

In this chapter we report on nanostructured hybrids of graphene oxide and palladium in powder and paper forms that were fabricated by means of one-step solvent-free gas phase treatment of graphene oxide with the aliphatic amines 1-octadecylamine and 1,8-diaminooctane, followed by *in situ* decoration with palladium in the liquid medium using palladium chloride as the precursor and citric acid as a mild and environmentally friendly stabilizing and reducing agent. The proposed synthesis method represents an eco-friendly alternative for obtaining nanohybrids of graphene oxide and palladium nanoparticles under mild conditions. Spectroscopic studies evidenced -COOH group derivatization of graphene due to the amidation reaction for the powder sample, while for the paper sample, the functionalization occurred through both amidation and epoxy ring opening reactions. Transmission electron microscopy demonstrated the formation of nanometer-sized crystalline palladium particles and evidenced that the diamine-functionalization results in larger particle sizes than observed for monoamine- or non-functionalized graphene oxide powder. For the paper samples also the formation of large agglomerates of up to ca. 100 nm was observed.

4.1 Introduction

In recent years graphene oxide (GO) has emerged as a highly promising material for applications ranging from energy storage (batteries and supercapacitors), catalysis,[1–4] and sensors, to building blocks of conducting and thermal materials, filtration membranes and bactericidal agents.[5-9] Combining the properties of metal nanoparticles with those of GO through covalent assembly, results hybrid architectures offering additional technological possibilities[10–18] due to their large surface area, plasmon resonance, highly stable nature, and in general, easy processing.[19–21] It has been demonstrated that amino groups, along with the oxygen-containing groups already present in GO,[22] act as nucleation points for metal nanoparticles formed through coordination bonds or electrostatic interactions with metal ions.[23–26] One of the simplest methods for metal nanoparticle deposition is liquid phase chemical reduction of the respective salts with the help of stabilizing and dispersing agents, which help to avoid agglomeration and therefore control size and morphology,[11–19] favouring the uniform distribution of nanoparticles on the GO surface.[27]

In our previous work,[28] we demonstrated that the formation of nanostructured hybrid materials employing amine-functionalized GO to support silver nanoparticles (AgNPs) can be achieved via a simple and eco-friendly gas-phase treatment. We have shown that this method of synthesis does not require additional purification processes because the surplus reagents can be eliminated *in situ* through moderate dynamic vacuum and heating conditions. With respect to conventional techniques where toxic solvents are employed and several reaction steps are involved,[29,30] the one-step gas-phase amine functionalization method has the advantage of yielding AgNPs with a controlled size distribution and a higher surface density, which are important requirements for applications of GO hybrid materials in several fields.[31–34] This motivates a further study on other noble metals like palladium in view of exploiting not only the peculiar electronic, mechanical, and catalytic properties of the derived nanoparticles,[35–37] but also their application for therapeutic purposes based on their antibacterial and cytotoxic activity.[38–40]

On the other hand, paper-like materials play an important role in various applications, spanning from protective layers[41] to chemical filters[42] to energy-related applications such as Li-ion batteries,[43] supercapacitors,[44-47] fuel cells[48] and hydrogen storage.[49] These flexible, self-supporting foils become integral components in novel membrane-based processes,[50] offering substantial advantages over traditional separation and recovery methods for food ingredients.[51] Carbon-based foils, recognized for their chemical resistance, temperature stability, and fluid impermeability, have found their way into packing and gasketing,[52-54] as well as into sensorics.[55-58]

The particular amphiphilic behaviour of GO[59] results crucial for the assembly into macrostructures including Langmuir-Blodgett films[60] and GO paper.[61] Through vacuum-assisted flow-directed filtration of colloidal dispersions, GO sheets can be joined to form a free-standing stacked, layered arrangement, yielding paper-like films with thicknesses ranging from 1 to 30 mm.[62,63] Among the various methods, vacuum filtration has emerged as a rapid, cost-effective route for fabricating GO paper (GOP), displaying superior mechanical strength compared to other paper-like materials.[64]

In the pursuit of enhanced functionalities, several studies explored the incorporation of metals,[65] polymers,[66-68] and ceramics[69] into paper-like materials, leveraging their exceptional mechanical properties and tuneable chemical properties.[52-54,70] One such endeavour involves the integration of palladium nanoparticles (PdNPs) into GOP to facilitate glucose sensing.[71]

The main purpose of the work detailed in this chapter was to demonstrate that it is possible under eco-friendly and mild conditions to obtain nanohybrids based on GO in powder and paper form and palladium nanoparticles (PdNPs) by applying a gas-phase pretreatment of GO with amine molecules, which thanks to their chemical affinity toward biological molecules,[72] confer an additional ecological value to this study. In detail, a comparative analysis was undertaken, assessing the properties of GO-PdNP hybrids derived from GO and its amine- functionalized counterparts.

4.2 Experimental section

4.2.1 Materials

Single-layer graphene oxide powder (≥ 99 wt% purity, platelet diameter of 300–800 nm and thickness of 0.7–1.2 nm) acquired from Cheap Tube, Inc., was used. 1-Octadecylamine (ODA; ≥ 99%), 1,8-diaminooctane (DAO; ≥ 98%), citric acid (≥ 99.5%), palladium chloride (≥ 99%), 2-propanol (≥ 99.8%) and hydrochloric acid (≥ 37%) purchased from Sigma-Aldrich were utilized as received. Graphene oxide paper (GOP) was prepared as described in Chapter 2 *(see section 2.1.1)*.

4.2.2 Amine gas-phase functionalization of graphene oxide

The amine functionalization of GO and GOP was carried out as explained in Chapter 2 *(see section 2.1.3)* applying the specific pre-treatment necessary for each microstructure (powder/paper-like). In the following the 1-octadecylamine-functionalized samples are labelled GO+ODA and GOP+ODA, while the 1,8-diaminooctane-functionalized samples are denoted as GO+DAO and GOP+DAO.

4.2.3. Deposition of palladium nanoparticles

We optimized the protocol for PdNP formation/deposition based on the methods reported by Roy *et al.*,[73] Dar *et al.*,[74] and Li *et al.*[75] *(see Chapter 2, section 2.1.4.2)*. Compared to Dar *et al.*,[74] we reduced the reaction time of 7 h by adopting the acidic solution of $PdCl_2$ employed by Li *et al.*[75] and, to assure the complete reduction reaction of the precursor, the citric acid concentration was 10 times higher. When optimizing the reaction conditions, it was found that a reaction time of 10 min was suitable for fabricating GO-based powder samples, whereas, for the paper-like hybrids, a reaction time of one hour was needed.

For preparing the hybrids, the GO samples were immersed in 0.005 M $PdCl_2$ and 0.05 M citric acid upon continuous stirring at room temperature for either 10 min or 1 h, depending on the case *(for further details, see Chapter 2, section 2.1.4.2).*

The amine-functionalized samples decorated with PdNPs are labelled hereafter as GO+ODA+Pd, GOP+ODA+Pd, GO+DAO+Pd, and GOP+DAO+Pd. Control samples obtained by applying the identical treatment to GO and GOP (lacking amine functionalization) are denoted as GO+Pd and GOP+Pd in the following.

4.3 Results and discussion

4.3.1 Characterization of GO+Pd and GOP+Pd hybrids

As a first evaluation of the chemical nature of GO and GOP before and after functionalization with amines and further decoration with PdNPs, a series of dispersibility tests were conducted in water and 2-propanol. Figs 4.1 and 4.2 illustrate the outcomes of these dispersibility tests. For GO, brownish dispersions were formed in both water and 2-propanol, which precipitated after 24 h. Amine-functionalized GO formed unstable dispersions in water, whereas in 2-propanol the stability of the dispersions decreased with time and almost total precipitation was observed after 24 h. These results confirm that the surfaces modified with long chains of ODA and DAO acquire a more hydrophobic character. Once decorated with PdNPs, the amine-functionalized GO solids precipitated to the bottom of the beakers in both solvents practically immediately after sonication.

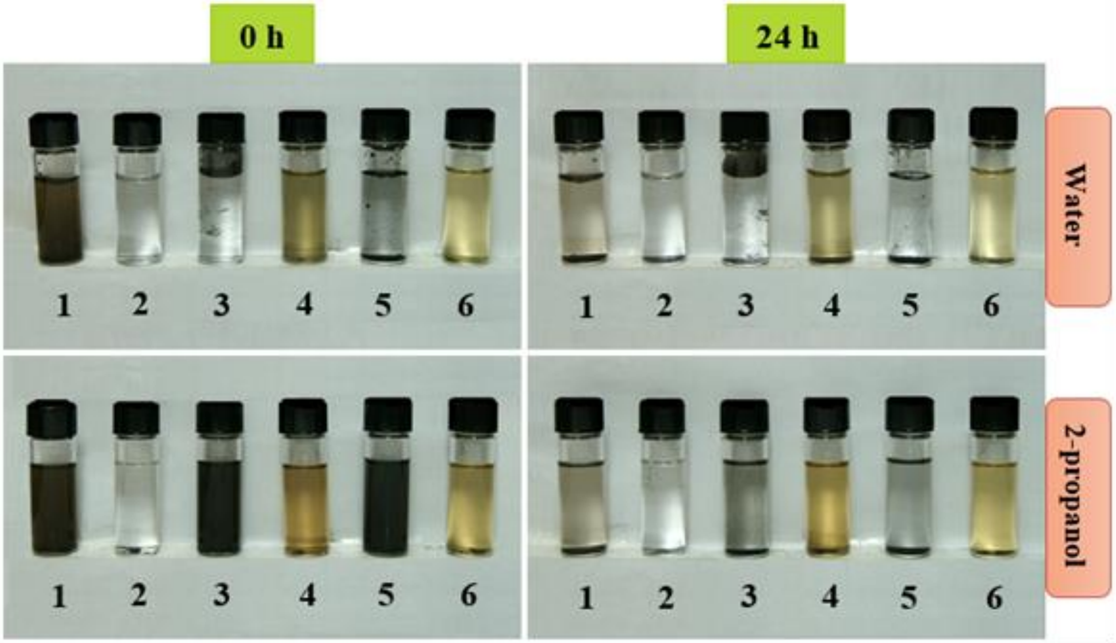

Fig. 4.1. Dispersibility tests for GO samples in water and 2-propanol: (1) GO, (2) GO+Pd, (3) GO+ODA, (4) GO+ODA+Pd, (5) GO+DAO, and (6) GO+DAO+Pd. The images were taken immediately after 10-min ultrasonication (0 h) and after 24 h.

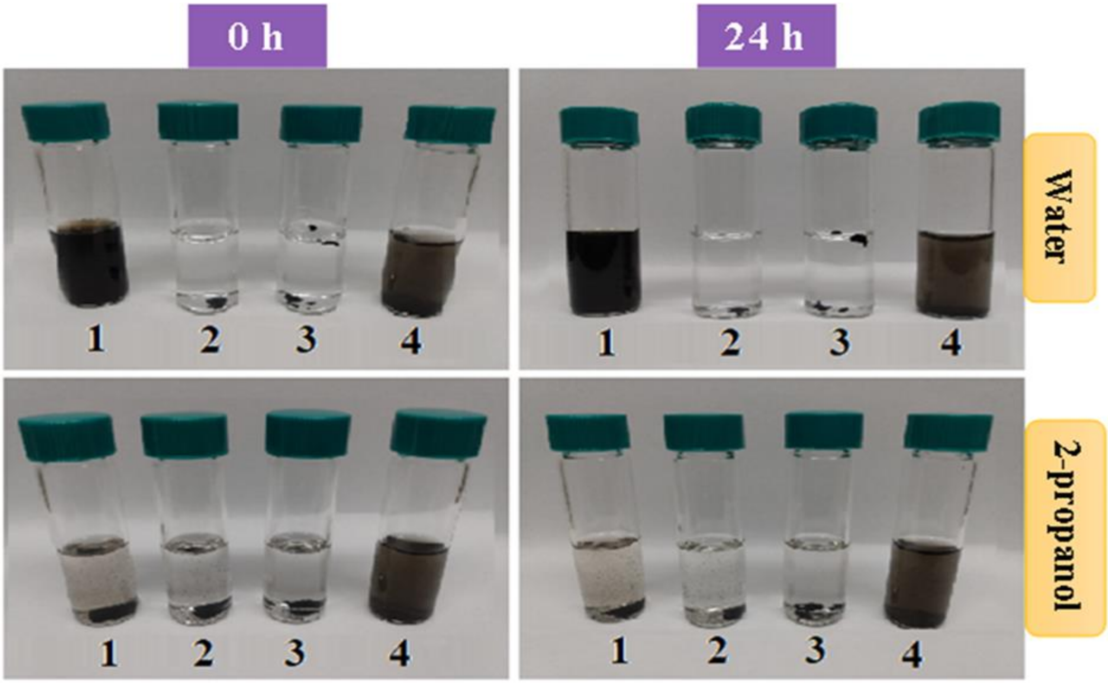

Fig. 4.2. Dispersibility tests for graphene oxide paper samples in water and 2-propanol: (1) GOP, (2) GOP+Pd, (3) GOP+ODA+Pd, and (4) GOP+DAO+Pd. The images were taken immediately after 10-min ultrasonication and 1 day after (0 h and 24 h, respectively).

Due to the inherent hydrophilic nature of GO, the graphene oxide paper experienced complete disintegration upon ultrasonic treatment, yielding brownish dispersions in both water and 2-propanol, which precipitated over a 24 h period. However, this propensity is notably reversed by the presence of PdNPs in GOP+Pd mats, which exhibited robust stability in both solvents. Conversely, PdNPs deposition onto GOP+DAO and GOP+ODA samples caused contrasting effects. The presence of two terminal amino groups in DAO enhanced the hydrophilic character of GOP+DAO+Pd sample, resulting in complete paper disintegration upon ultrasonic treatment in both solvents. In contrast, the introduction of ODA long hydrocarbon chains changed the character of GOP to hydrophobic, which was further augmented by the decoration with palladium particles.[76] Consequently, GOP+ODA+Pd demonstrated remarkable resistance to disintegration even after ultrasonic treatment. This observation can also be attributed to substantial structural modifications and enhanced mechanical stability of GOP imparted by the amine molecules with the longest alkyl chain, in agreement with our earlier work, which reported a remarkable Young's modulus of 256.19 GPa for GOP+ODA samples.[77]

The effectiveness of amine derivatization *via* GO surface chemistry was verified with the help of FTIR spectroscopy (Fig. 4.3). The spectrum of GO and GOP shows the fingerprint bands of the oxygen-containing moieties: the hydroxyl band (ν_{OH}) at 3592 cm^{-1} for GO and 3491 cm^{-1} for GOP; the δ_{OH} signal at 1607 cm^{-1} (GO), and 1590 cm^{-1} (GOP); $\nu_{C=O}$ vibrations in COOH groups at 1718-1719 cm^{-1}; and the characteristic $\nu_{C\text{-}O(asym)}$ band of epoxy bonds[78] evident at 1373-1380 cm^{-1}. Furthermore, bands at 1241-1247 cm^{-1} and 1051-1038 cm^{-1} are attributed to the O-H bending and symmetric stretching vibrations of C-O in C–O–H groups[79], respectively. Unsaturated ketone groups could be responsible for the band appearing at 964-965 cm^{-1}.[77]

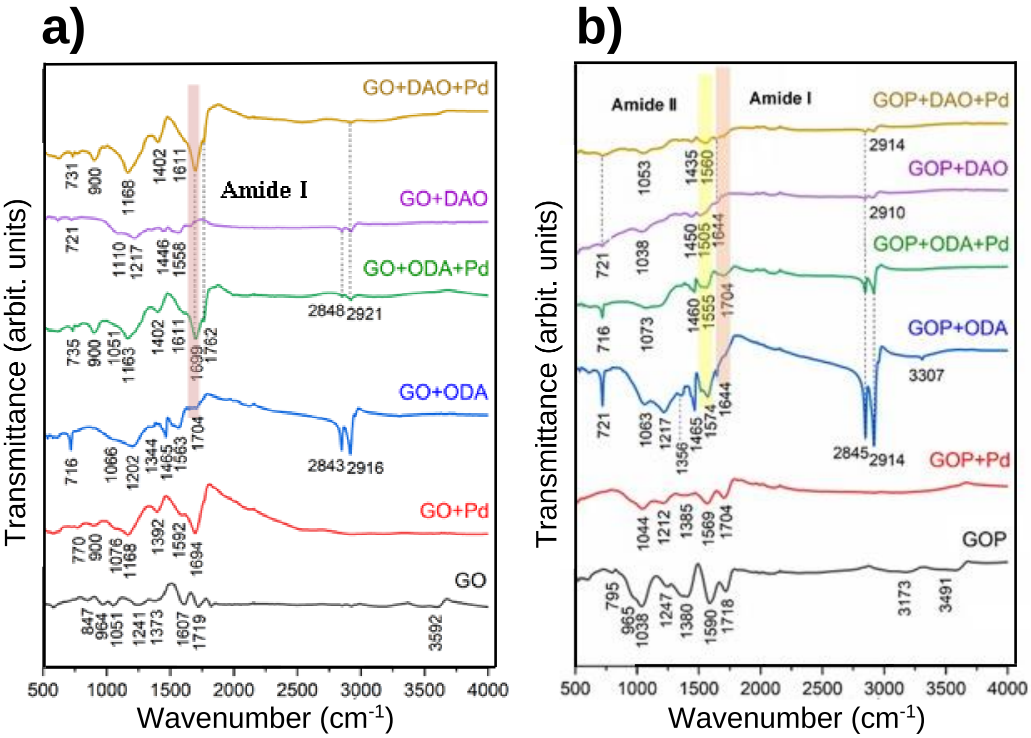

Fig. 4.3. FTIR spectra of non-functionalized and amine-functionalized: a) GO, and b) GOP samples before and after decoration with PdNPs.

Upon functionalization with amines, there is a pronounced intensity decrease and shifting for the $\nu_{C=O}$ signal in GO, from 1704-1719 cm^{-1} to 1694-1699 cm^{-1}, due to the characteristic 'amide I' band between 1600 and 1700 cm^{-1}, accompanied by the 'amide II' band at 1558-1563 cm^{-1}.[22, 80,81] For GOP this decrease leads to the near-total disappearance of the carboxylic $\nu_{C=O}$ band and the C–O signal at 1038 cm^{-1}. For the GOP series, the new 'amide I' and 'amide II' modes appear at 1644-1704 cm^{-1}, and 1505-1574 cm^{-1}, respectively. The set of bands located at 1200-1400 cm^{-1} can be assigned to the 'amide III' mode. [80,81] It is important to mention that the 'amide I' absorption can be masked by δ_{NH} modes of non-amide NH groups, which are prevalent in the structure.

Prominent bands of alkyl groups, namely those corresponding to $\nu_{CH(asym)}$ and $\nu_{CH(sym)}$ of the aliphatic chains in ODA and DAO, at 2916-2921 cm^{-1} and 2843-2848 cm^{-1} for GO+ODA series and GO+DAO series, respectively, and at 2910-2914 cm^{-1} and 2845 cm^{-1} for the GOP+ODA and GOP+DAO series, respectively, clearly corroborate the effective amine derivatization.

For GO-Pd samples, significant changes can be observed in the signals corresponding to the vibrations of the oxygenated groups. Particularly, the increased intensity, signal broadening and shifting of the $\nu_{C=O}$ absorption from COOH functionalities might indicate the coordination of palladium species to oxygen in these groups. GO+ODA+Pd and GO+DAO+Pd samples show the same trend. Other important changes for these samples include an almost total disappearance of 'amide II' δ_{NH} absorption at 1558-1563 cm^{-1}, a decrease of the ν_{C-O} band at 1051-1076 cm^{-1} and an increase in intensity of ν_{C-N} signals at 1163-1168 cm^{-1}. All these changes point to the coordination of palladium to nitrogen and oxygen atoms present on GO+ODA and GO+DAO surfaces.

Additional absorption features at 1435-1450 and 1460-1465 cm^{-1} observed for GOP+DAO and GOP+ODA, respectively, arise from δ_{CH} vibrations, and are particularly prominent in ODA-functionalized samples, due to the long hydrocarbon chain. Vibrations of aliphatic chains longer than $(CH_2)_4$ are associated with the bands positioned at 716 -795 cm^{-1},[82] notably intense for the ODA–functionalized sample.

To elucidate the effects on the thermal behaviour of GO and GOP ensuing from the amine functionalization and subsequent palladium decoration, thermogravimetric and differential thermal analysis (TGA–DTA) were employed. The TGA curves for GO and GOP (Figs. 4.4a and 4.5a, respectively), exhibit the characteristic weight loss steps of graphene oxide.[28,76,77] The initial stage, corresponding to the evaporation of physiosorbed water, encompasses a loss of 10.3 %, until 136 °C for GO, and 11.8 % up to 137 °C for GOP. Secondly, the pyrolysis of intrinsic oxygenated groups (hydroxyl, carboxyl, epoxy) occurs through a weight loss of 28.4 % heating up to 245 °C for GO, and 40.7 %, until 206 °C for GOP. Finally, the main weight loss, which reflects the graphene lattice combustion, comprises 60.6 %, until 690 °C[83] in the powdered GO, whereas for graphene oxide paper, this step corresponds to 46.8 % up to 607 °C. The DTA curve in GO (Fig. 4.4a) features two exothermic peaks at 211 and 668 °C, and at 206 and 596 °C in GO paper (Fig. 4.5a), coinciding with the principal weight loss steps of the TGA curves.

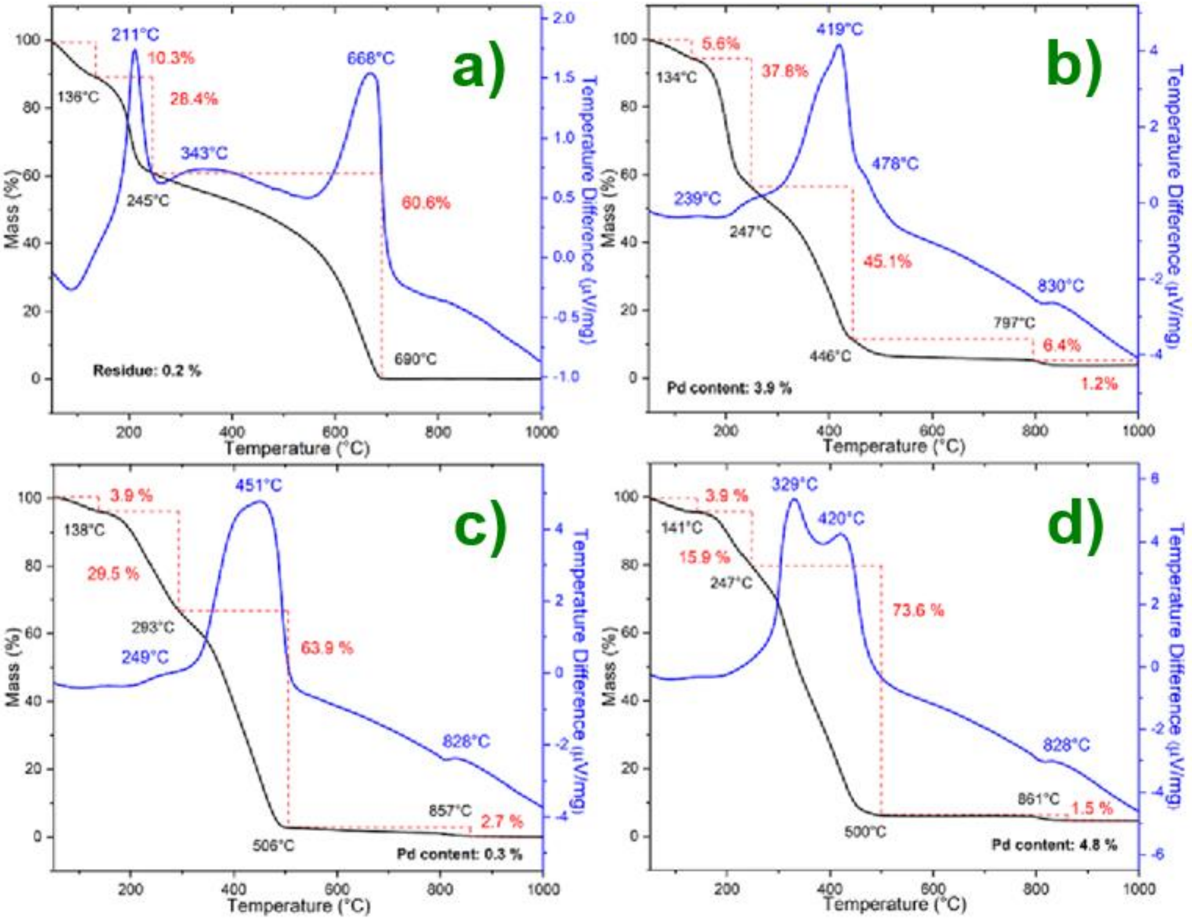

Fig. 4.4. TGA (black) and DTA (blue) curves for graphene oxide samples: a) GO, b) GO+Pd, c) GO+ODA+Pd, and d) GO+DAO+Pd.

For GO+Pd (Fig. 4.4b), the pattern of weight loss includes four steps. The first is related to the evaporation of physisorbed water (5.6 %, until 134 °C), the second refers to the pyrolysis of oxygenated groups (37.8 %, until 247 °C), the third one to the combustion of the main graphene backbone (45.1 %, until 446 °C), and the fourth weight loss (6.4 %, until 797 °C) can be attributed to a portion of the palladium present in the sample. In fact, at temperatures above 420 °C, Pd slowly oxidizes to PdO_2[84] and PdO_2 decomposes to Pd at temperatures beyond 780°C. The last ramp (1.2 %, until 1000°C) mirrors the metallic Pd content. So the total palladium content in the sample is around 11.5 %. The DTA peaks refer to the combustion of the main components in the system, namely the oxygen-containing groups (239 °C), the graphene lattice (419 °C and 478 °C), and the palladium oxide (shoulder at 830 °C). The second and the third peaks are strongly shifted to lower temperatures in comparison to the GO sample; this can be explained by the catalytic effect of palladium on the combustion of the graphene backbone, similar to what we saw previously for GO hybrids with silver nanoparticles (see Chapter 3 or reference 28).

Fig. 4.5b illustrates the thermal behaviour of the GOP+Pd sample mirroring characteristics akin to GOP but with notable disparities: a reduced content of physisorbed water (weight loss of 7.1 %) removed at 117 °C, 20 °C lower compared to GOP. Additionally, oxygen-containing functionalities decomposed up to 240 °C giving rise to a weight loss of 17.8 % in comparison with 40.7 % for GOP. The final step of the TGA curve, accounting for 73.8 % weight loss until 586 °C (by 21°C higher than for GOP), pertains to the combustion of the graphene backbone, with a contribution of Pd present in the sample. Notably, Pd progressively oxidizes to PdO_2 beyond 420 °C.[76,84] Comparison of the DTA curve post-Pd decoration (Fig. 4.5b) to the one recorded prior to it (Fig. 4.5a) reveals that the first peak, pertaining to the oxygen-containing groups, is broader, reduced in area, and shifted 8 °C to a higher temperature of 215 °C. The second peak is considerably broader, and its maximum is centred at 497 °C, with a less pronounced shoulder at 455 °C. This shift by 92 °C to a lower temperature than for GOP is attributed to the catalytic effect of palladium on the graphene backbone combustion, similar to previous observations (see also Chapter 3) for GO hybrids with Pd and Ag nanoparticles.[28,76] A Pd content of 0.6 % is estimated for this sample.

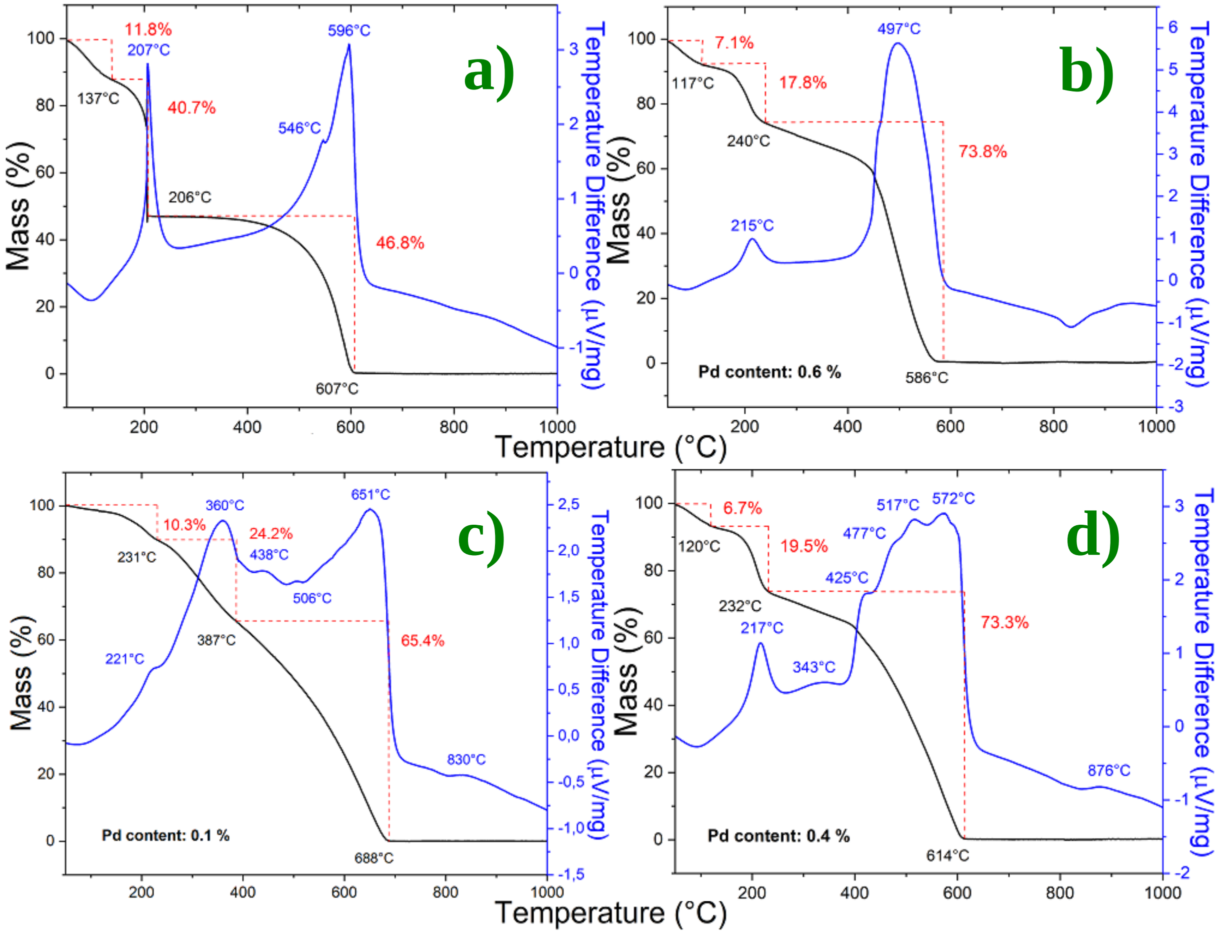

Fig. 4.5. TGA (black) and DTA (blue) curves for GOP samples: a) GOP, b) GOP+Pd, c) GOP+ODA+Pd, and d) GOP+DAO+Pd.

For both amine-functionalized samples (Fig. 4.4c,d), the same percentage of 3.9 % for the loss of physisorbed water was observed when heating up to 141 °C for GO+ODA+Pd, and up to 138 °C for GO+DAO+Pd. However, the loss steps for the oxygenated groups present noticeable differences; while for GO+ODA+Pd the corresponding percentage is 15.9 % and the weight loss extends until 247 °C, for GO+DAO+Pd the percentage is almost double, 29.5 %, and the weight loss extends until 293 °C. In the case of GO+ODA+Pd the main weight loss corresponds to the combustion of graphene lattice, 73.6 % of the sample are lost when heating up to 500°C, while for GO+DAO+Pd the weight loss is slightly smaller, 63.9 %, and the temperature range slightly wider (heating up to 506 °C). Similarly to GO+Pd, these weight losses occur at lower temperatures compared to GO, due to an apparent catalytic effect of the metal. Both thermograms show a shoulder at 828 °C, related to the decomposition of palladium oxide, with an estimated content of 2.7 % for GO+ODA+Pd, and 1.5 % for GO+DAO+Pd. The metallic Pd content is 0.3 % for GO+ODA+Pd, and 4.8 % for GO+DAO+Pd, bringing the total palladium content to 3.0 and 6.3 %, respectively.

When comparing the TGA-DTA results for the GO+Pd series with those previously reported for the GO+Ag homologues (see Chapter 3 and reference 28), one notices that palladium importantly impacts the combustion temperature of the graphitic backbone; whereas for GO+Ag the pyrolysis starts at 682 °C, for GO+Pd it commences already at 446 °C. In the case of aminated samples, for GO+ODA+Ag pyrolysis starts at 695 °C, but for GO+ODA+Pd it begins already at 506 °C, likewise for GO+DAO+Ag the combustion temperature is 716 °C, while for GO+DAO+Pd it is 500 °C. This testifies to a better catalytic performance of palladium nanoparticles in comparison to silver. Another important difference concerns the final weight loss from 797 to 861 °C in all the palladium-containing samples and corresponding to the thermal decomposition of palladium oxide; this trend is not observed in the silver-functionalized samples because silver does not oxidize. A third dissimilarity is related to the final residue. While in the non-aminated samples, the percentage of metal-containing residue is higher for palladium (GO+Pd: 11.5 %; GO+Ag: 1.5 %), in the aminated samples one sees an opposite trend, namely a metal content of 3.0 % for GO+ODA+Pd and 6.3 % for GO+DAO+Pd, while for GO+ODA+Ag the silver content is 6.7 % and for GO+DAO+Ag it is 12.1 %.

The thermograms of amine-functionalized and Pd-decorated GOP (Fig. 4.5c,d), reveal distinctive discrepancies compared to GOP+Pd, attributed to amine moieties. GOP+ODA+Pd exhibits three primary weight losses in the TGA curve: 10.3 % up to 231 °C, 24.2 % up to 387 °C, and 65.4 % up to 688 °C. The initial weight loss corresponds to the pyrolysis of residual oxygen-containing groups, amide derivatives and amines grafted to epoxy groups.[78] The second loss stems from graphene lattice combustion, while the final one relates to the decomposition of Pd oxide. As observed for GO+Pd powder samples,[76] graphene lattice combustion occurs at a lower temperature compared to GOP, due to an apparent catalytic effect of the metal. The metallic Pd content is 0.1 % for GOP+ODA+Pd. Its DTA curve shows a complex exothermic behaviour, marked by peaks located at 221, 360, 438, 506 and 651°C, attributed to the pyrolysis of oxygen-containing groups and amino/amide derivatives, and to graphitic backbone combustion, combined with Pd oxidation to PdO_2 at temperatures over 420 °C. The distinct rise at 830°C reflects the metallic Pd content (0.1 %).

Similarly, GOP+DAO+Pd shows a three-step weight loss pattern in the TGA curve: 6.7 % up to 120 °C (attributed to the evaporation of more abundant physisorbed water, due to DAO's larger hydrophilicity), 19.5 % up to 232 °C (associated with the pyrolysis of oxygen-containing groups and amine/amide functionalities), and 73.3 % up to 614 °C (indicative of graphene backbone combustion). A metallic Pd content of approximately 0.4 % was deduced for GOP+DAO+Pd. Its DTA curve exhibits a similarly complex pattern to that of GOP+ODA+Pd. The initial well-defined peak (217 °C) correlates with the pyrolysis of oxygen-containing groups. The maxima at 343, 425, 477, 517 and 572 °C correspond to pyrolysis of organic functionalities, graphitic backbone combustion, and Pd oxidation. The additional peak at 876 °C is related to the decomposition of Pd oxide. The estimated metallic Pd content is 0.4 %.

To characterize the differences in morphology of the samples due to the functionalization with amines and further decoration with palladium particles, backscattered electron composition scanning electron microscopy images were acquired as detailed in Chapter 2 for the GO series (Fig. 4.6). The respective particle size distributions are presented in the histograms of Fig. 4.7, where an asymmetrical distribution of sizes is observed for all GO+Pd, GO+ODA+Pd and GO+DAO+Pd samples and small particle sizes are more abundant.

The brightest spots highlight the presence of palladium particle agglomerates. For GO+Pd samples (Fig. 4.6a-c) triangular and apparently octahedral shapes[85,86] with a narrow size distribution ranging from 0.04 to 0.34 µm and an average size of 0.13 µm (Fig. 4.7a) are observed. The micrographs for GO+ODA+Pd (Fig. 4.6d–f), show mostly spherical palladium clusters in a broader range (0.03-1.2 µm) with an average particle size of about 0.26 µm (Fig. 4.7b). Equally to the case of GO+Pd, also for GO+DAO+Pd (Fig. 4.6g–i) different geometric shapes are seen, with sizes ranging from 0.02 to 0.85 µm, and an average particle size of 0.14 µm (Fig. 4.7c). Comparing the particle size distributions, one notices that those for GO+Pd and GO+DAO+Pd are narrower than that of the ODA-functionalized sample. These observations agree with E. Ramirez *et al.*[87] who have demonstrated the predominant role of chemical equilibria between all potential coordinating agents in stabilizing the nanoparticles; here this concerns the ligands resulting from the precursor, the amine and the reducing agent. Since the chemical activity expressed in milliequivalent (mEq) of ODA is lower than for DAO, for lower amine content we found aggregated particles but with a more regular shape. The size and shape of particles are governed by the nature of the stabilizing ligands and, in the case of weak ligands such as amines, by the quantity of ligands added.

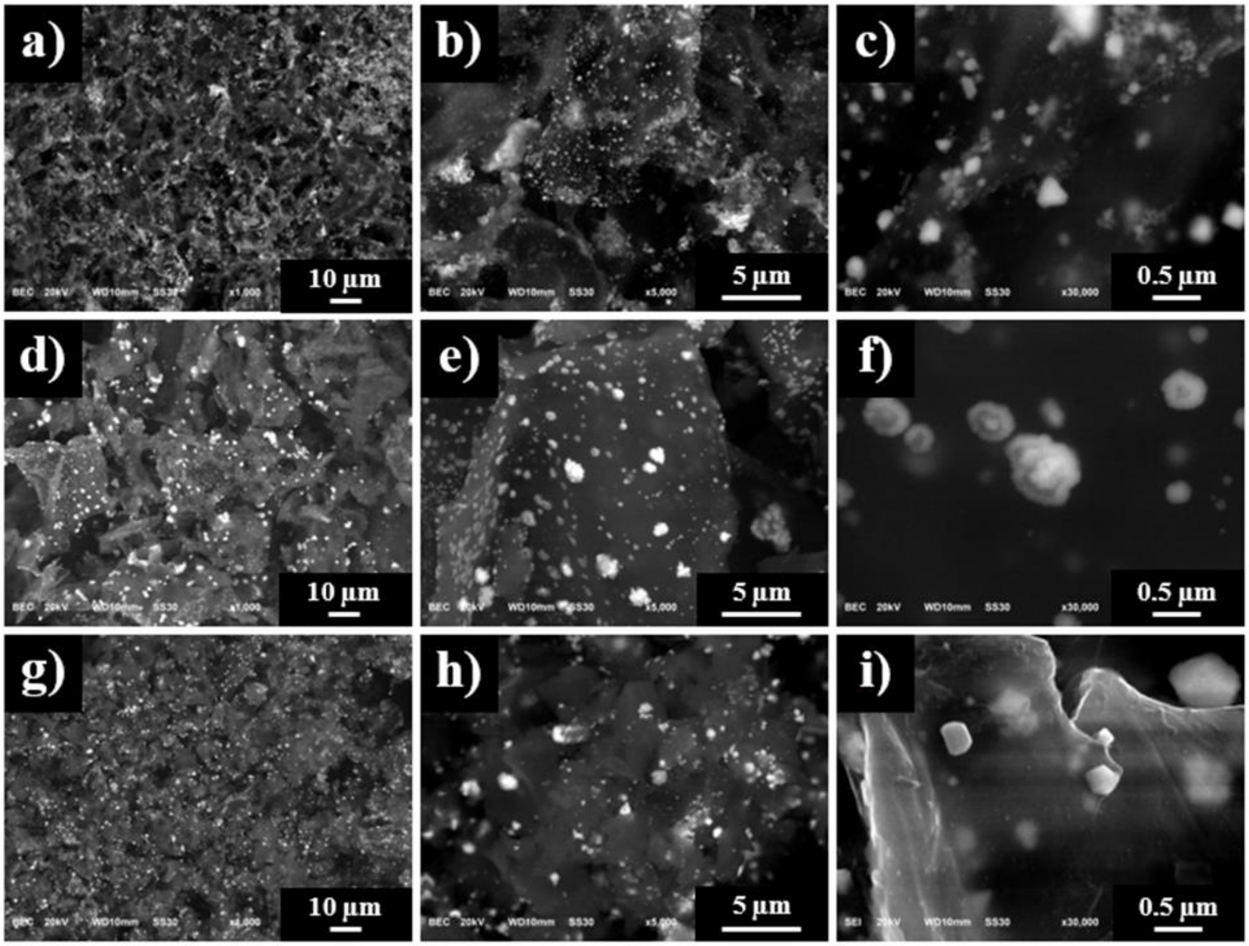

Fig. 4.6. Representative SEM images for GO+Pd (a-c), GO+ODA+Pd (d–f), and GO+DAO+Pd (g–i) at different magnification. Scale bars: 10 µm (left column); 5 µm (middle column), and 0.5 µm (right column).

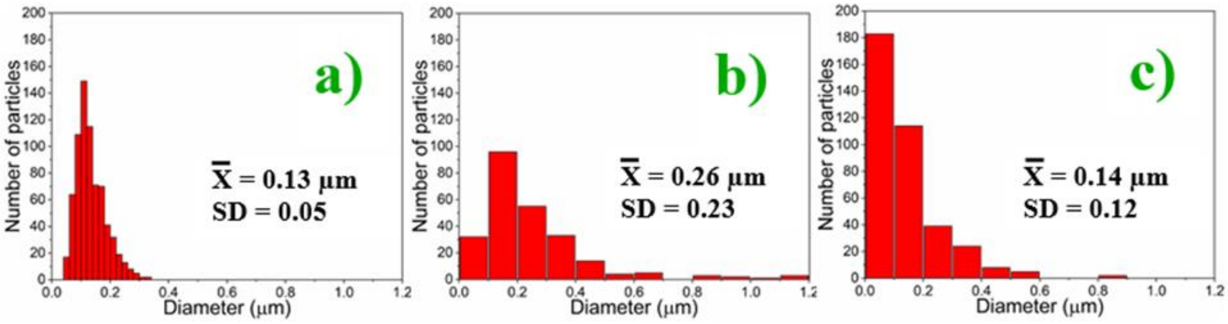

Fig. 4.7. Particle size distribution histograms obtained by analysing the SEM images for (a) GO+Pd, (b) GO+ODA+Pd and (c) GO+DAO+Pd.

On the other hand, morphological changes in the newly formed GOP and palladium-based hybrids were collecting secondary electron images with the scanning electron microscope, as explained in Chapter 2. Firstly the differences in paper thickness were estimated from cross-section images (Fig. 4.8a,d,g). GOP+Pd was about 20 µm thick; amine functionalization of GOP caused a small increase to 29 µm for GOP+DAO+Pd but had a much more dramatic effect for GOP+ODA+Pd where the thickness increased to 71 µm. This phenomenon can be interpreted as a 'swelling' effect, stemming from the integration of long DAO and ODA functionalizing chains into interlayer space between GO nanosheets, followed by the intercalation of Pd species into the same interlayer space. As we previously observed for amine-functionalized GOP decorated with silver nanoparticles (see Chapter 3 or reference 28), this effect is notably more pronounced in the case of ODA since, given its molecular structure, ODA could act as a coating on nanoparticles in solution, avoiding particle aggregation by reducing the van der Waals forces between them and/or by keeping them apart by steric interactions.[88,89] Therefore, these as-formed coatings are physiosorbed onto the nanoparticle surfaces during the solution-based synthesis controlling the growth and precipitation of the nanoparticles. These physical changes in the new materials promote the tunning of characteristics like dispersibility as discussed above (Fig 4.2). Whereas the ODA moieties have a hydrophobic character, the DAO ones tend to have a hydrophilic behaviour, which has a clear impact on the final spacing between the nanoparticles in assemblies.[90] The micrographs presented in the middle and right columns of Fig. 4.8 reveal topographical differences between the two sides of the papers, which have their origin in the filtering process employed for GOP fabrication. The side that was closest to the membrane filter, has a more compact and uniform appearance, meanwhile, the other side exhibits a more inhomogeneous surface. This characteristic is attributed to the preferential sedimentation of smaller and lighter GO sheets during vacuum filtration, resulting in denser packing. This tendency has been prevalent in other graphene oxide paper-like studies.[28,77]

To distinguish clearly between GO and PdNPs, we analysed backscattered electron composition (BEC SEM) images (Figs. 4.9 and 4.10). In these micrographs, the brightest spots indicate the presence of micrometre-sized palladium particles. Notably, round-shaped particles are visible, attached to both sides of the graphene oxide papers. The cross-sectional images in Fig. 4.10a,d,g reveal that Pd particles are also embedded within the bulk of the GO paper.

The images also highlight differences between the various types of GO papers. Specifically, the GOP+Pd samples exhibit less Pd nanoparticle agglomeration, likely due to the dispersant effect of the reducing agent, citric acid, during PdNP formation. The carboxylate groups, initially strongly adsorbed on the GO surface,[91,92] serve as nucleation sites for Pd grafting by ion exchange or coordination reaction. Once Pd(II) is reduced to Pd(0), the carboxyl anions exert hydrophobic or Coulombic forces between Pd clusters,[93,94] regulating the size and distribution of PdNPs on the carbonaceous surface.

In contrast, the amine-functionalized samples display irregularly shaped, significantly agglomerated and large-sized palladium particles (Figs. 4.9 and 4.10d-i). The cross-sectional images (Figs. 4.9 and 4.10g) of GOP+DAO+Pd exhibit prominent bright spots, suggesting that bifunctional amine moieties not only favour the intercalation of PdNPs by providing extra coordinating groups[95] but also promote nanoparticle aggregation.

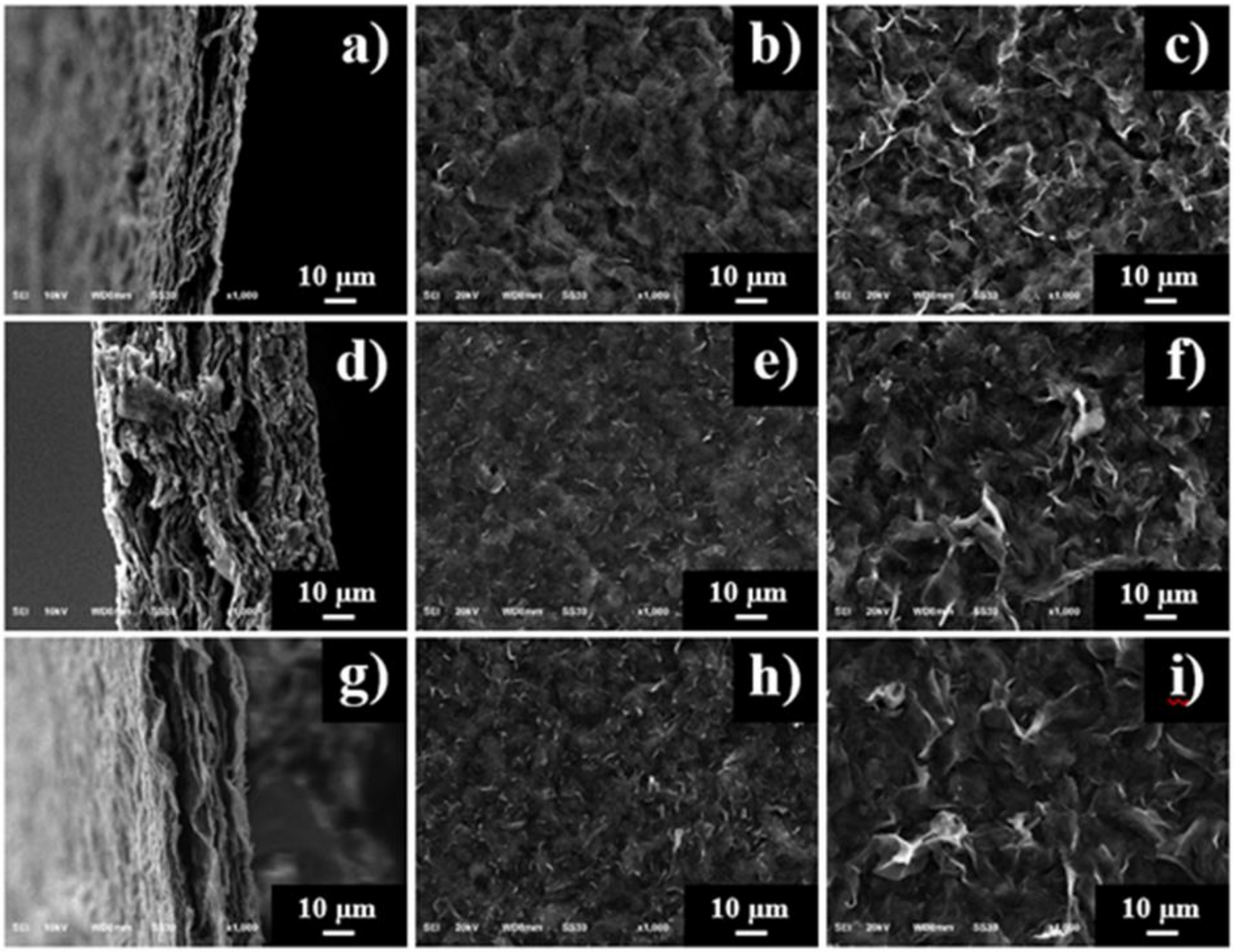

Fig. 4.8. Secondary electron SEM images of GOP+Pd (a–c), GOP+ODA+Pd (d–f), and GOP+DAO+Pd (g–i). The left column (a, d, g) shows the cross-section images of the different specimens; the middle column (b,e,h) corresponds to the lower mat side that was in contact with the filter membrane during GOP fabrication, and the right column (c,f,i) shows the upper mat side. Scale bar: 10 µm.

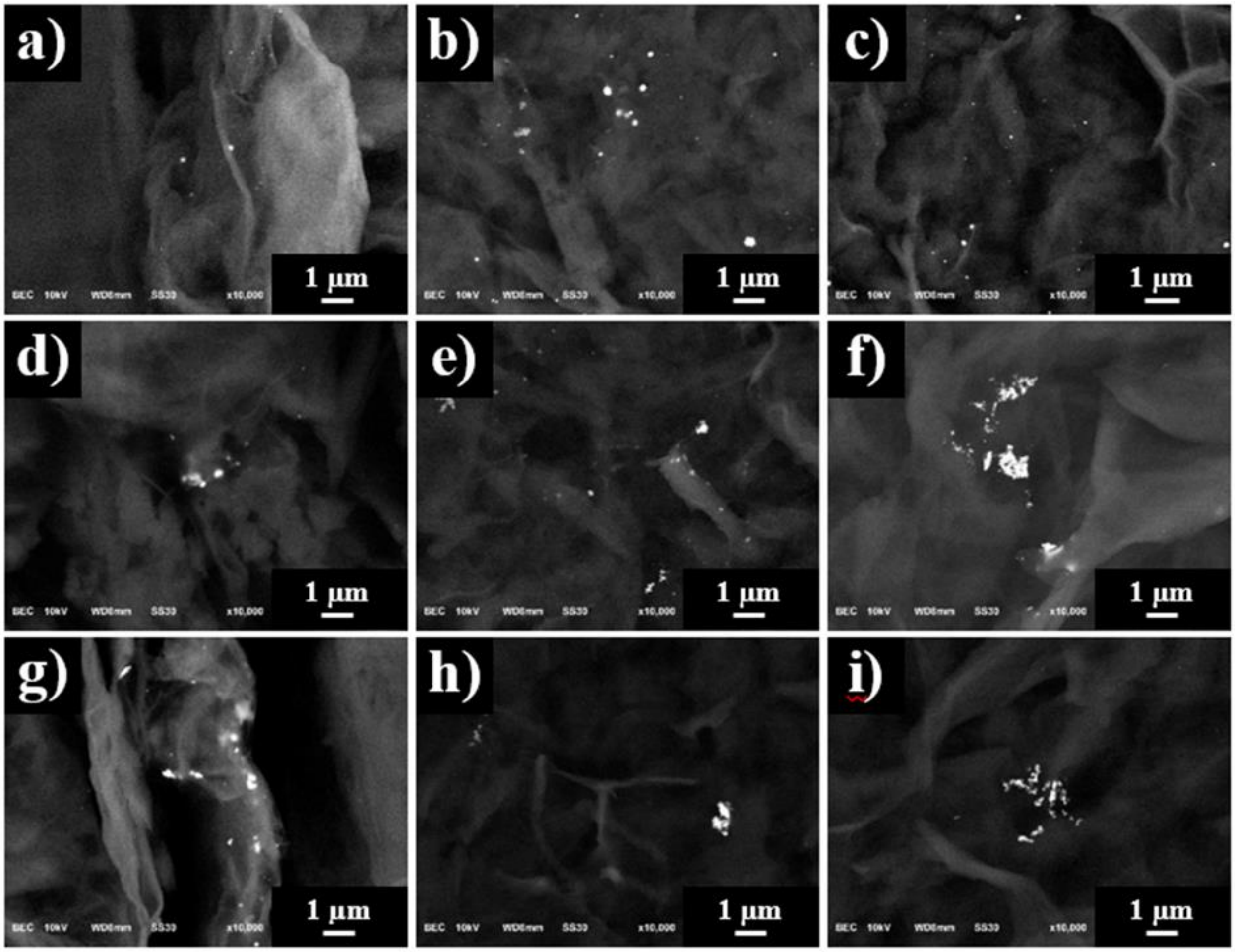

Fig. 4.9. Backscattered electron SEM images of GOP+Pd (a–c), GOP+ODA+Pd (d–f), and GOP+DAO+Pd (g–i). The left column (a,d,g) shows the cross-section images of the different specimens; the middle column (b,e,h) corresponds to the lower mat side that was in contact with the filter membrane during GOP fabrication, and the right column (c,f,i) shows the upper mat side. Scale bar: 1 µm.

Comparing the average Pd particle sizes of the paper samples with those of the powder samples,[76] it is that the macrostructure of the substrate influences the size and distribution of the *in situ* formed palladium nanoparticles. The PdNPs are smaller in the layered samples compared to the powders (0.05, 0.2, and 0.06 µm smaller in GOP+Pd, GOP+ODA+Pd, and GOP+DAO+Pd in comparison to GO+Pd, GO+ODA+Pd, and GO+DAO+Pd, respectively), likely due to the surface area of GO which ranges from 400 m^2/g up to 1500 m^2/g, is importantly reduced when forming GO paper.[96,97]

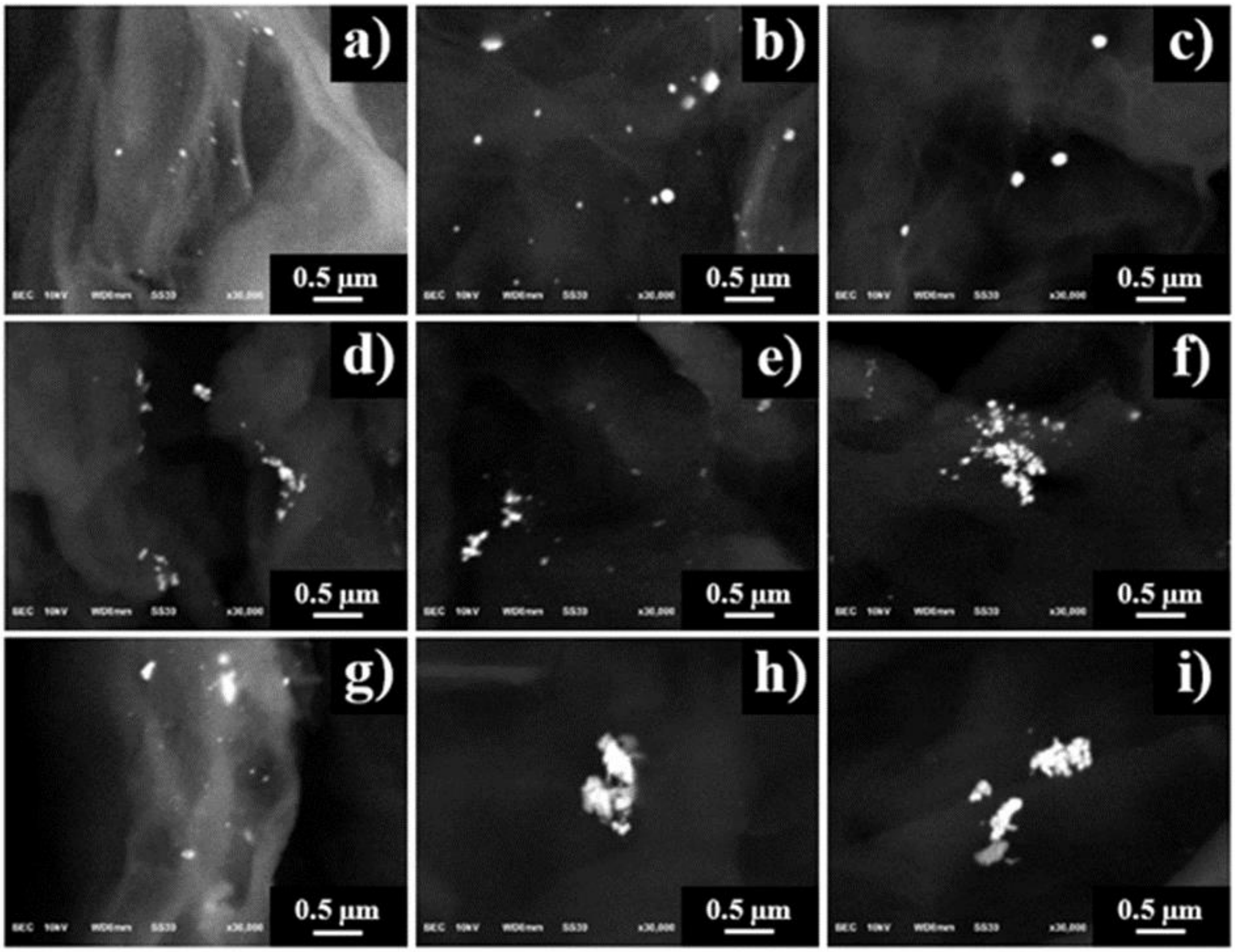

Fig. 4.10. Backscattered electron SEM images of GOP+Pd (a–c), GOP+ODA+Pd (d–f), and GOP+DAO+Pd (g–i). The left column (a,d,g) shows the cross-section images of the different specimens; the middle column (b,e,h) corresponds to the lower mat-side that was in contact with the filter membrane during GOP fabrication, and the right column (c,f,i) shows the upper mat side. Scale bar: 0.5 µm.

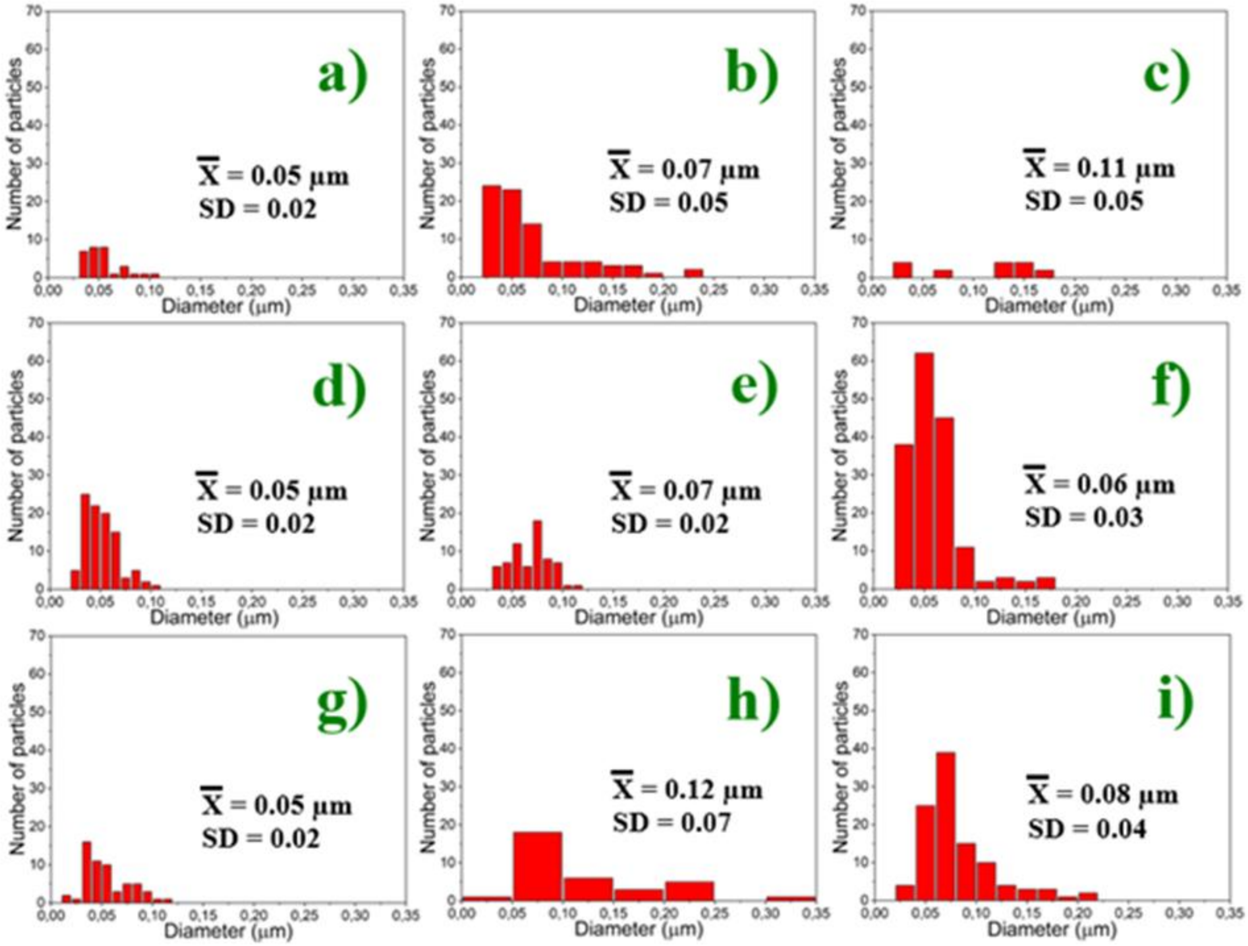

Fig. 4.11. Particle size distribution histograms obtained by SEM imaging for GOP+Pd (a–c), GOP+ODA+Pd (d–f), and GOP+DAO+Pd (g–i). The left column (a,d,g) shows the particles size distribution on the cross-section; the middle column (b,e,h) shows the distribution of particles on the lower mat side that was in contact with the filter membrane during GOP fabrication; and the right column (c,f,i) shows the particles size distribution on the upper mat side.

Additionally, the elemental composition of the materials was determined through energy-dispersive X-ray spectroscopy (EDS) analysis, as detailed in Chapter 2 and reported in Tables 1 and 2. For the powder-based series (Table 1), the metal content decreased as follows: GO+Pd (10.0 ± 5.2 wt%; 1.4 ± 0.8 at%); GO+DAO+Pd (6.9 ± 4.1 wt%; 0.9 ± 0.6 at%), and GO+ODA+Pd (2.5 ± 0.4 wt%; 0.3 ± 0.04 at%). Despite the differences in particle size, the trends observed in the histograms in Fig. 4.7 align with those of the thermal studies. Similarly, the EDS results for the paper-form materials (Table 2) showed that when comparing both sides, there is a tendency to concentrate more Pd particles in the GOP's near-surface regions. However, the local stoichiometry varied significantly from point to point because of the small volume probed by EDS and the (partial) aggregation of Pd therein. Comparing the metal content in these GOP near-surface regions, revealed higher values for GOP+ODA+Pd (6.6 ± 8.2 wt%; 0.9 ± 1.1 at%), followed by GOP+DAO+Pd (5.6 ± 6.6 wt%; 0.7 ± 0.8 at%), and GOP+Pd (1.8 ± 0.7 wt%; 0.2 ± 0.1 at%). The higher standard deviation compared to the average values for palladium content indicates that the metal is embedded in a heterogeneous manner within the carbonaceous matrix. Regarding the Pd content in the surface layer that was in contact with the filtration membrane during GOP fabrication, the order is as follows: GOP+Pd (1.9 ± 0.5 wt%; 0.2 ± 0.1 at%); GOP+DAO+Pd (1.3 ± 0.3 wt%; 0.15 ± 0.03 at%); GOP+ODA+Pd (0.2 ± 0.3 wt%; 0.02 ± 0.04 at%). The decoration with palladium is more controlled on this side of the mat and more substantial in the non-aminated specimen.

Table 1. Palladium content as deduced from the EDS results for the GO/PdNP series

Sample	Weight %	Atomic %
GO+Pd	C (K): 56.4 ± 8.8 O (K): 33.6 ± 4.3 Pd (L): 10.0 ± 5.2	C (K): 67.8 ± 6.3 O (K): 30.8 ± 5.6 Pd (L): 1.4 ± 0.8
GO+ODA+Pd	C (K): 62.9 ± 0.4 O (K): 34.0 ± 0.7 Pd (L): 2.5 ± 0.4	C (K): 70.7 ± 0.5 O (K): 28.7 ± 0.5 Pd (L): 0.3 ± 0.04
GO+DAO+Pd	C (K): 58.7 ± 6.3 O (K): 33.6 ± 3.4 Pd (L): 6.9 ± 4.1	C (K): 68.9 ± 4.4 O (K): 29.8 ± 4.0 Pd (L): 0.9 ± 0.6

Table 2. Palladium content as deduced from the EDS results for the GOP/PdNP series

	Region			
	Lower face		Upper face	
Sample	Weight %	Atomic %	Weight %	Atomic %
GOP+Pd	C (K): 67.7 ± 1.1 O (K): 30.1 ± 1.2 Pd (L): 1.9 ± 0.5	C (K): 74.7 ± 1.0 O (K): 24.9 ± 1.0 Pd (L): 0.2 ± 0.1	C (K): 66.6 ± 2.2 O (K): 31.2 ± 3.0 Pd (L): 1.8 ± 0.7	C (K): 73.7 ± 2.4 O (K): 25.9 ± 2.5 Pd (L): 0.2 ± 0.1
GOP+ODA+Pd	C (K): 91.0 ± 2.0 O (K): 8.6 ± 1.7 Pd (L): 0.2 ± 0.3	C (K): 93.3 ± 1.4 O (K): 6.7 ± 1.4 Pd (L): 0.02 ± 0.04	C (K): 84.1 ± 8.8 O (K): 9.1 ± 0.6 Pd (L): 6.6 ± 8.2	C (K): 91.6 ± 2.2 O (K): 7.5 ± 1.1 Pd (L): 0.9 ± 1.1
GOP+DAO+Pd	C (K): 89.8 ± 2.3 O (K): 8.7 ± 2.3 Pd (L): 1.3 ± 0.3	C (K): 93.0 ± 1.8 O (K): 6.8 ± 1.8 Pd (L): 0.15 ± 0.03	C (K): 87.0 ± 8.0 O (K): 7.3 ± 1.5 Pd (L): 5.6 ± 6.6	C (K): 93.3 ± 2.4 O (K): 6.0 ± 1.6 Pd (L): 0.7 ± 0.8

When comparing Pd loading as determined by different techniques, some differences emerge. While EDS revealed significant values (1.9 wt% for GOP+Pd, 3.4 wt% for GOP+ODA+Pd and 3.5 wt% for GOP+DAO+Pd), TGA studies displayed a general Pd loading of less than 1.0 wt% (0.6, 0.1 and 0.4 wt %, respectively). The two techniques probe the material differently, as TGA/DTA is mass-dependent, while EDS is area-dependent. In TGA/DTA the sample amount varies from 5 to 10 mg covering a holder area of several mm^2, whereas EDS measures a surface area of a diameter ~6 µm, with a mass scarcely reaching 1 mg. So we can conclude that while the total Pd content is below 1 wt%, the graphene oxide paper decorated with the diamine shows the highest local variations in Pd decoration.

Further insights into the morphology, size, and distribution of smaller GO-supported palladium particles were gained through bright field (Fig. 4.12) and dark field (Fig. 4.13) TEM imaging. The corresponding particle size distribution histograms are presented in Fig. 4.14. In GO+Pd (Figs. 4.12 and 4.13a-c) a pronounced agglomeration of differently shaped metallic particles is evident. The size distribution of these particles is broad, ranging from 2 to 15 nm, with an average particle size of 5.7 ± 2.3 nm (Fig. 4.14a). In ODA-functionalized GO, spherical particles with diameters ranging from 1 to 13 nm are observed, with an average size of 4.2 ± 1.4 nm (Fig. 4.14b). Conversely, DAO-functionalized GO exhibited much larger particles with diameters ranging from 6 to 450 nm, and an average size of 52.5 ± 83.5 nm (Fig. 4.14c). The agglomeration observed in the non-aminated sample can be associated with the strong interaction of sterically unprotected Pd species with the GO surface. The smallest particle size achieved in GO+ODA+Pd can be explained by the presence of the ODA moieties, which mitigate strong attraction to the graphitic backbone. In GO+DAO+Pd, the two coordinating sites of DAO favour a higher content of metallic nanoparticles, as mirrored by the histograms in Figs. 4.7 and 4.14, and the Pd content determined in the EDS studies (Table 1).

Similarly to the Ag-containing samples discussed in Chapter 3, larger particles with a broader size distribution were observed in the GO+Pd series, despite a slightly lower palladium content. This emphasizes the inherent tendency of either silver or palladium nanoparticles to agglomerate on non-functionalized graphene oxide, underlining the importance of nitrogen-containing ligands in nucleation and growth regulation [87].

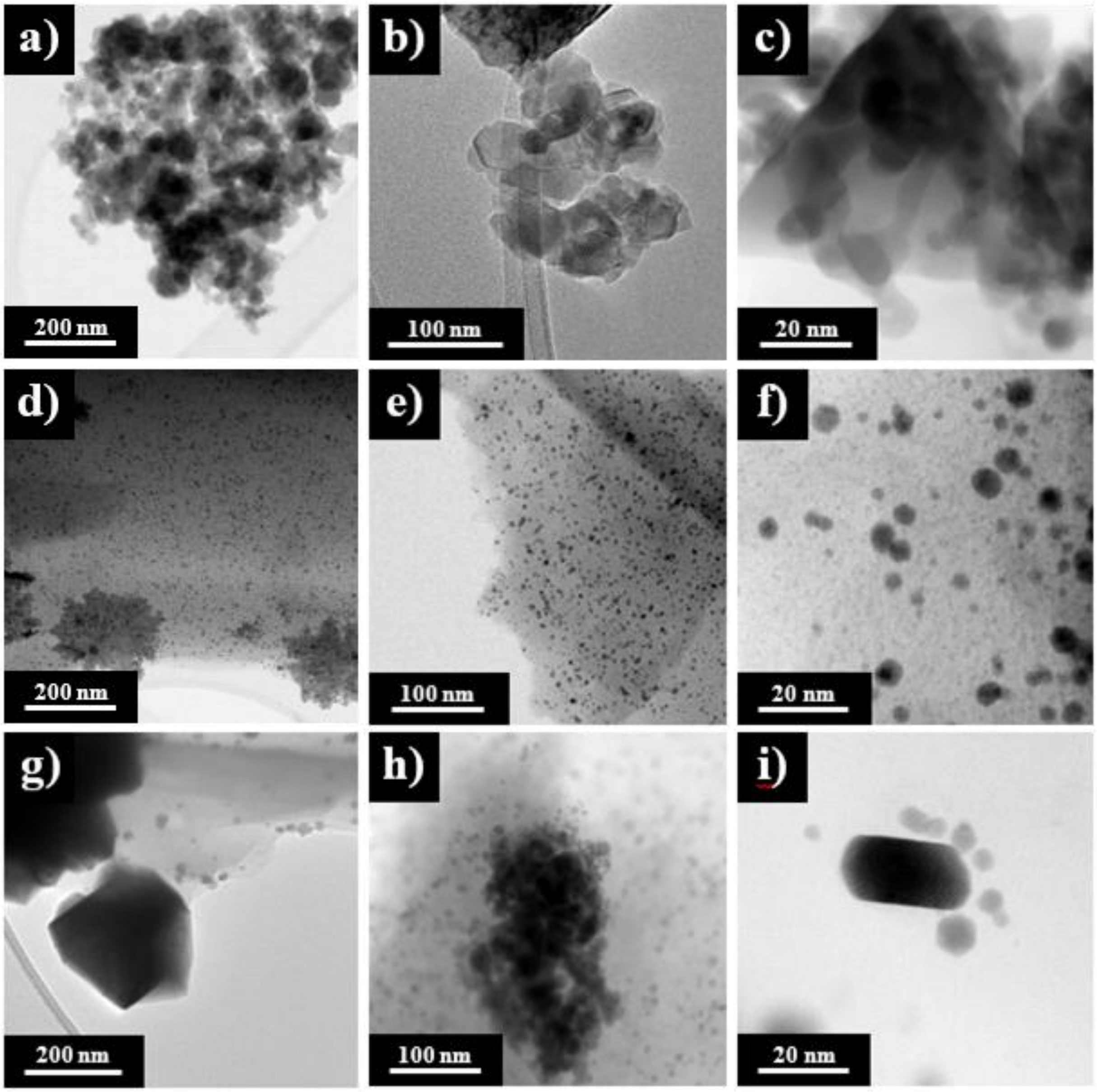

Fig. 4.12. Bright-field TEM imaging for GO+Pd (a-c), GO+ODA+Pd (d-f) and GO+DAO+Pd (g-i) at different magnification. Scale bars: 200 nm (left column); 100 nm (middle column), and 20 nm (right column).

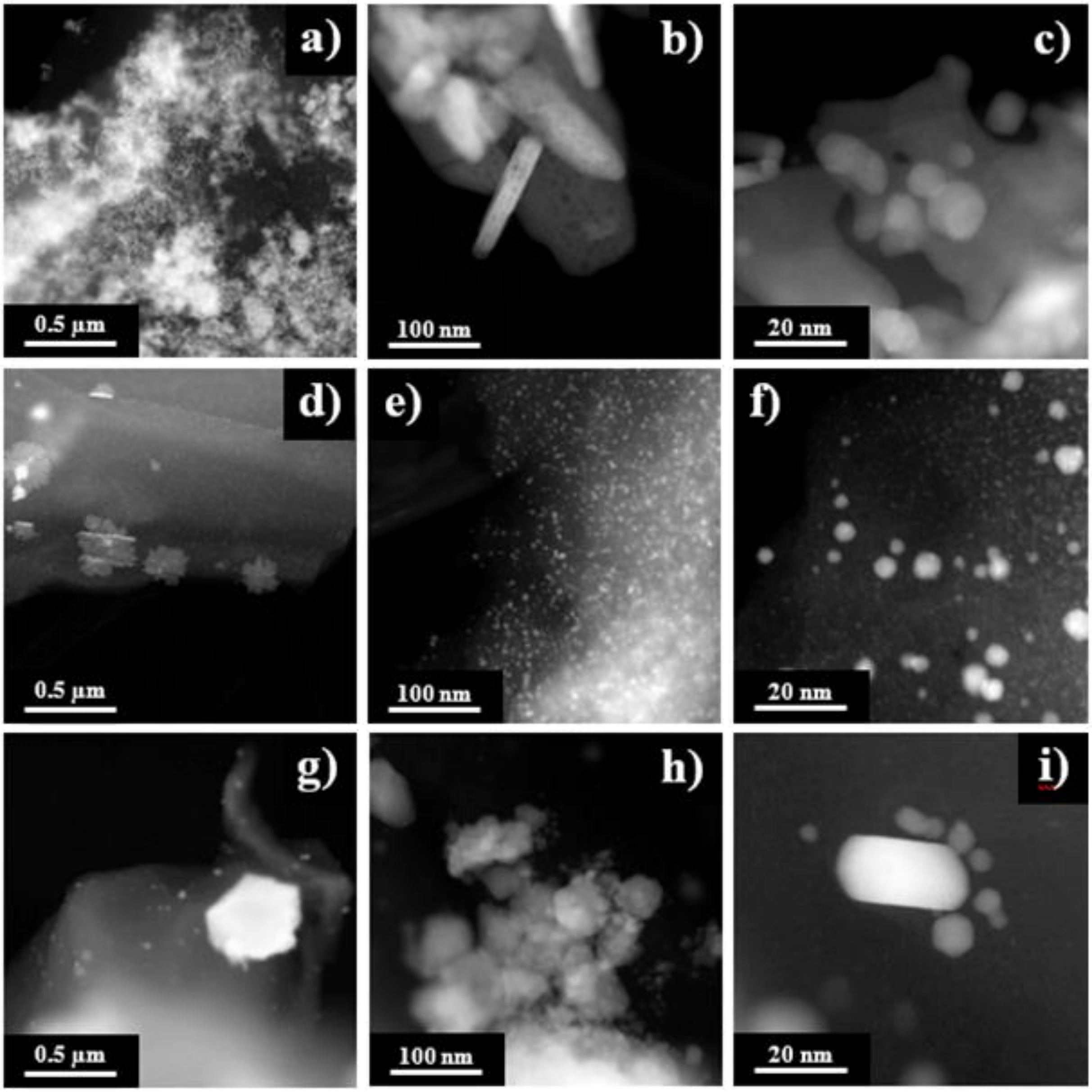

Fig. 4.13. Z-Contrast dark-field TEM images for GO+Pd (a-c), GO+ODA+Pd (d-f) and GO+DAO+Pd (g-i) at different magnification. Scale bars: 0.5 µm (left column); 100 nm (middle column), and 20 nm (right column).

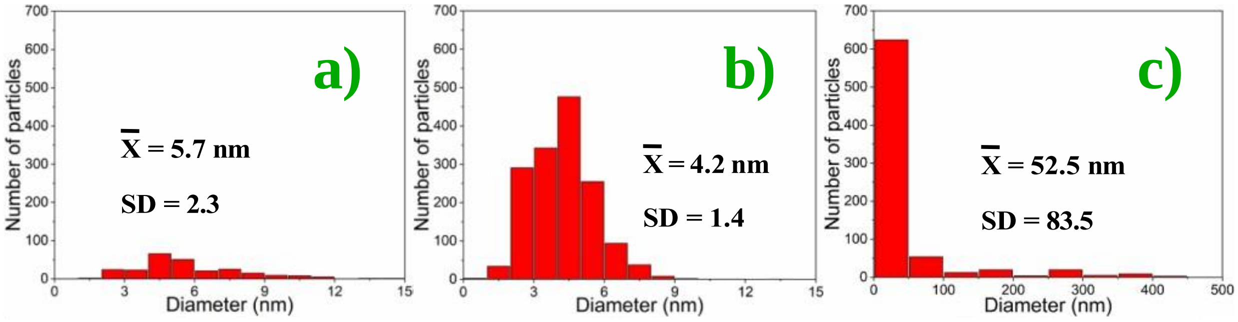

Fig. 4.14. Particle size distribution histograms obtained from the TEM images of: a) GO+Pd, b) GO+ODA+Pd and c) GO+DAO+Pd.

As for hybrids in powder form, bright-field (Fig. 4.15) and dark-field (Fig. 4.16) TEM micrographs were also collected for the hybrids in paper form. These images revealed PdNPs with variable sizes and morphologies. While a spherical shape predominated in GOP+Pd, other shapes were observed for GOP+ODA+Pd and GOP+DAO+Pd. The particle size histograms derived from the TEM images are shown in Fig. 4.17. In GOP+Pd, particles measuring between 1 to 5 nm were observed, with an average size of 2.8 ± 0.9 nm. In ODA-functionalized GOP, most particles were smaller than 5 nm (average size of 2.9 ± 2.5 nm), but a few outliers with diameters up to 15 nm are also seen, suggesting some degree of PdNPs agglomeration. In DAO-functionalized GOP, significant PdNP coalescence was apparent, with large agglomerates of up to 100 nm, making particle shape identification challenging. The average particle size in this sample was estimated at 7.1 ± 5.1 nm.

Interestingly, the combined data from electron microscopy highlight the formation of aggregates with diameters ranging from 60 to 80 nm, composed of smaller particles with sizes from 3 to 7 nm. This finding is particularly noteworthy since it indicates that in layered graphene oxide-based materials, there is a tendency for more controlled creation and deposition of metallic nanoparticles, in contrast to the hybrids in powder form, which exhibited a broader size distribution ranging from 260 to 130 nm,[76] containing smaller particles with diameters from 50 to 2 nm.

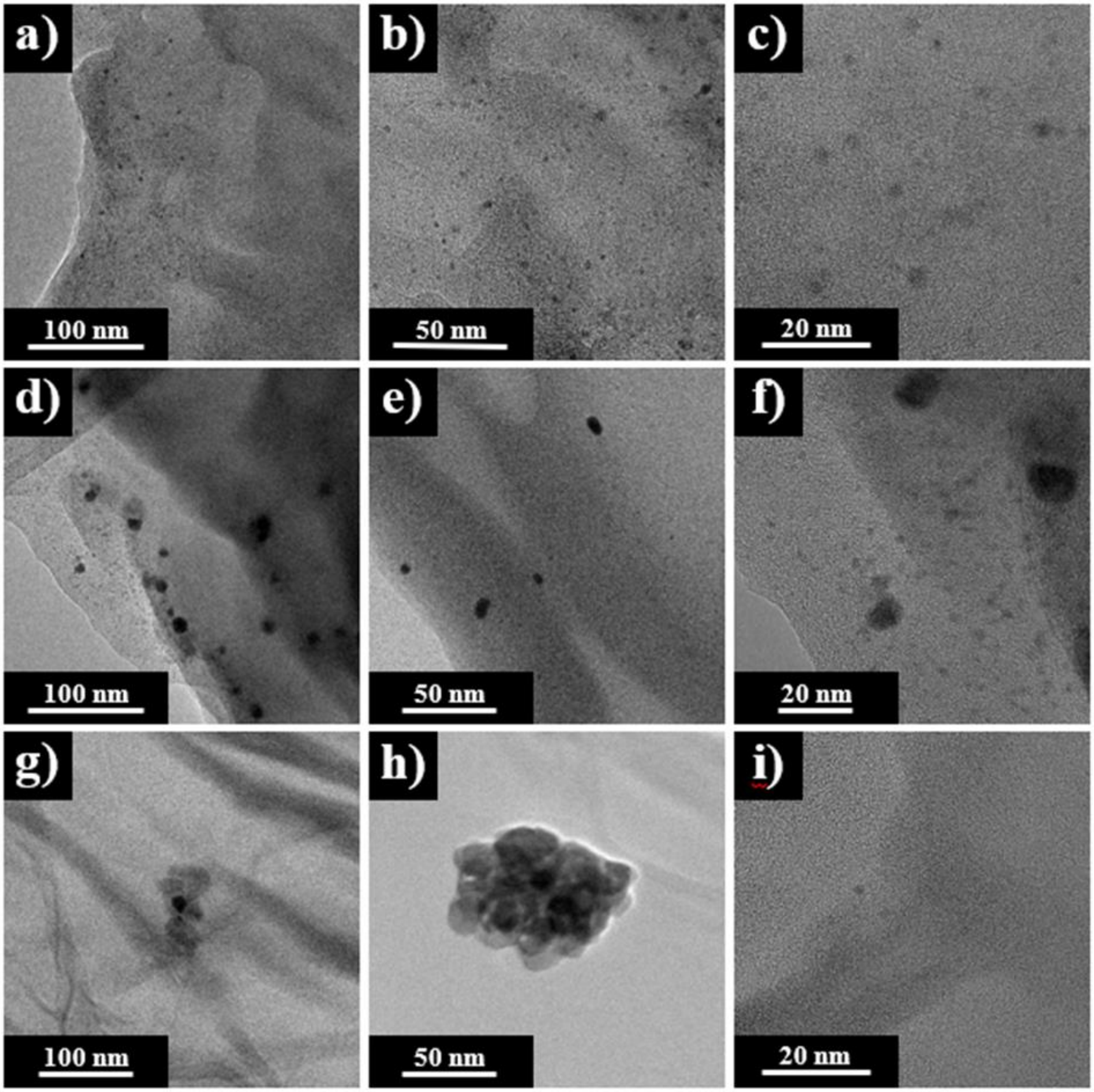

Fig. 4.15. Bright-field TEM imaging for GOP+Pd (a-c), GOP+ODA+Pd (d-f) and GOP+DAO+Pd (g-i). Scale bars: 100 nm (left column); 50 nm (middle column), and 20 nm (right column).

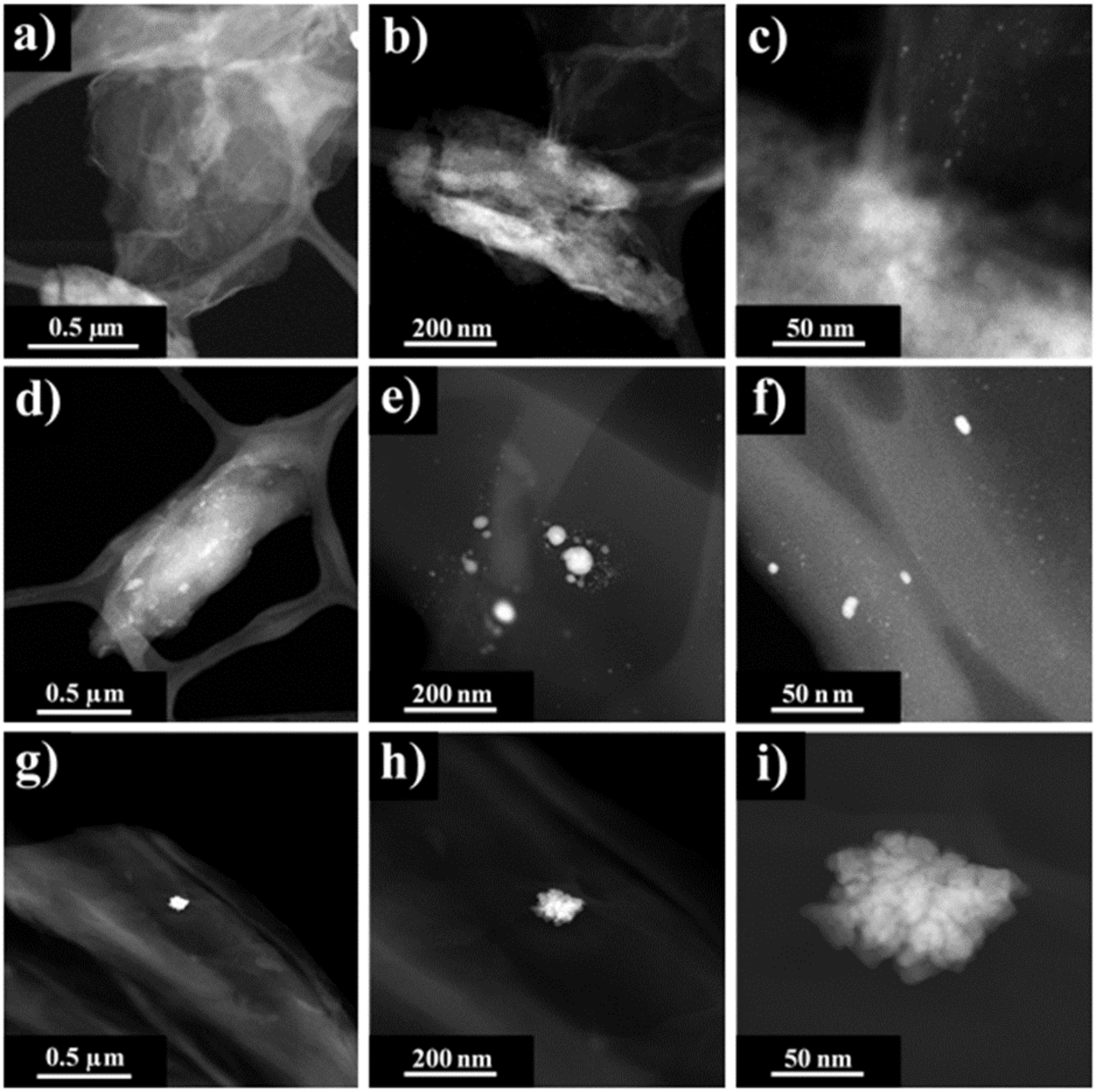

Fig. 4.16. Z-Contrast dark-field TEM images for GOP+Pd (a-c), GOP+ODA+Pd (d-f) and GOP+DAO+Pd (g-i) at different magnification. Scale bars: 0.5 µm (left column); 200 nm (middle column), and 50 nm (right column).

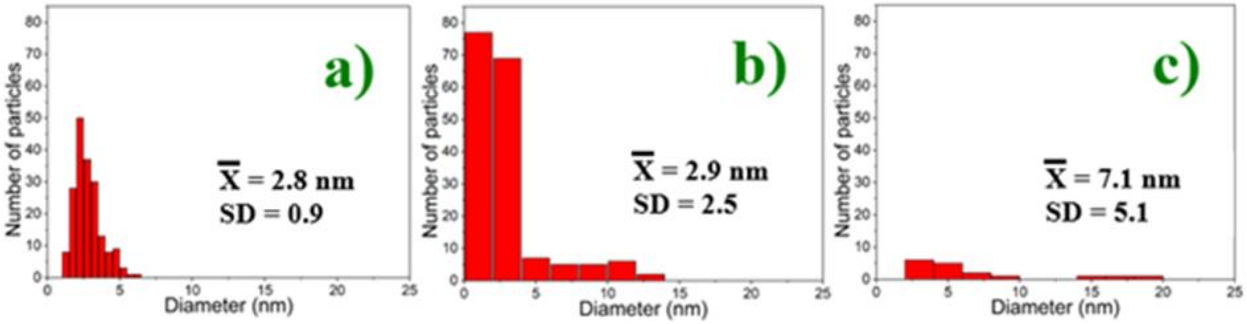

Fig. 4.17. Particle size distribution histograms obtained by TEM imaging for: a) GOP+Pd, b) GOP+ODA+Pd and c) GOP+DAO+Pd.

The crystallinity of the GO-PdNPs hybrids was investigated by XRD and the diffractograms acquired on the powder samples are shown in Fig. 4.18. The GO sample presents the characteristic (001) diffraction peak at $2\theta = 11.2°$ (*d*-spacing of 0.79 ± 0.007 nm).[98-101] According to Dékány, Krüger-Grasser, and Weiss[102], GO presents *d*-spacing between 0.61 up to 1.1 nm depending on the amount of water adsorbed. The modification with amines resulted in a broadening of the main GO peak and a shift from 11.2° to 11.7° (d_{001} = 0.76 ± 0.007 nm) for GO+ODA, and to 12.5° (d_{001} = 0.71 ± 0.009 nm) for GO+DAO. This slight shrinking of the interlamellar space could be associated with the hydrophobic characteristics of the aliphatic chain of the amine moieties. Referring to the GO+Pd, GO+ODA+Pd and GO+DAO+Pd hybrids, a noticeable broadening of the graphitic peak is clearly seen at $2\theta = 13.4°$ (*d*-spacing of 0.66 nm) and points to smaller coherently diffracting domains and hence to (partial) exfoliation.[103] According to Kaniyoor *et al*.,[103] this phenomenon might be provoked by the acidic treatment to induce the decoration with PdNPs; in fact a partial removal of oxygenated functionalities (a certain degree of reduction) and water molecules, decreases the interlayer spacing in comparison to GO.[104-107] The FT-IR and TGA/DTA results discussed above support this interpretation. It is reasonable to assume that the acidic treatment of aminated-GO also has an impact on the flake thickness *via* exfoliation-reduction,[103] which causes the broad (001) Bragg reflection peak. The exfoliation seems to continue during Pd decoration since for both GO+ODA+Pd and GO+DAO+Pd hybrids the 001 peak has almost totally disappeared, indicating that the coherently diffracting domains are very small. The slightly narrower *d*-spacing for GO+DAO is probably due to cross-linking by bifunctional molecules like 1,8 diamino octane onto the GO network, resulting in a more compact hybrid.[108,109]

The appearance of new peaks assigned to (111) and (200) Bragg reflections at $2\theta = 40.2°$ and 46.7° respectively, confirmed that the palladium nanoparticles that are large enough to be detected in XRD, have a face-centred cubic (fcc) crystalline structure.[110] The fact that the intensity of the peaks in aminated samples is higher than in the non-aminated GO+Pd indicates more periodicity in crystalline arrangements due to the complexation effect by the nitrogen in amines. The lack of these stabilizing agents in the chemical environment of GO+Pd promotes chaotic/random arrangements; consequently, the height of the peak is reduced. These phenomena match the discussion of the SEM and TEM images (*vide supra*), where we saw that ligand moieties have an impact on the nucleation patterns of metallic particles.

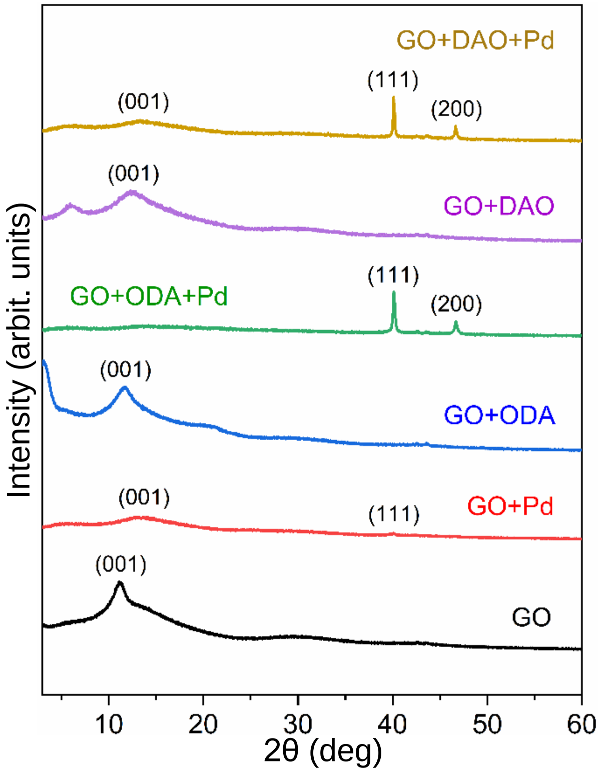

Fig. 4.18. XRD diffractogram of non-functionalized and amine-functionalized GO samples before and after decoration with Pd nanoparticles.

To provide more comprehensive insights into the chemical state of elements within the GOP before and after decoration with PdNPs, XPS characterization was carried out on the upper side of the GOP mats, as these exhibited the highest metallic content according to the EDS results (Table 2).

The overall composition of the set of samples is from the survey spectra (Fig. 4.19), which show that carbon and oxygen are the dominant elements in all samples. A small Pd 3*d* peak is discernible for GOP+Pd, while for GOP+ODA+Pd and GOP+DAO+Pd, the spectroscopic signatures of both nitrogen and palladium are present. Figs 4.20 and 4.21 show the detailed spectra of the various core-level regions. The deconvolution of the C 1*s* core line shows essentially five peaks. The main peak, corresponding to the sp^2/sp^3 matrix, is centred at 284.5 eV[111] in all the cases. In GOP (left bottom side in Fig. 4.20), the C 1*s* core line fitting displays four oxygenated components: 1) C-O bonds of the GO lattice, 2) alcohol and/or ether moieties (C–OH, C–O–C), 3) carbonyl groups (C=O), and 4) carboxyl groups (COO) at 285.3, 286.4, 287.3, and 288.9 eV, respectively. The binding energies and the relative spectral intensities for each component are reported in Table 3.

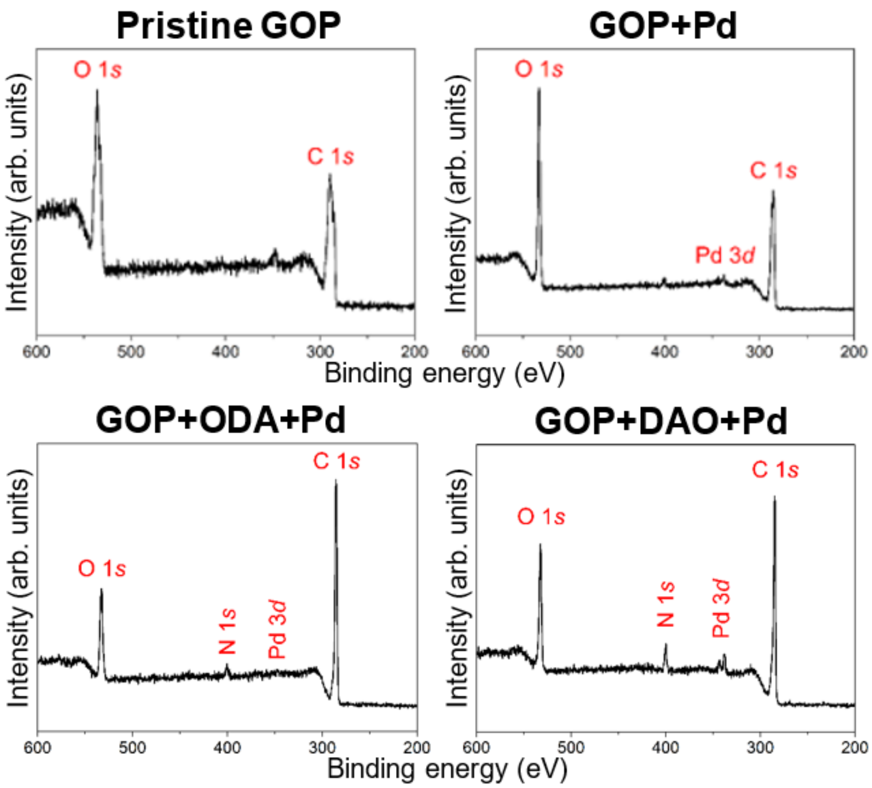

Fig. 4.19. Survey XPS spectra for GOP, GOP+Pd, GOP+ODA+Pd and GOP+DAO+Pd samples.

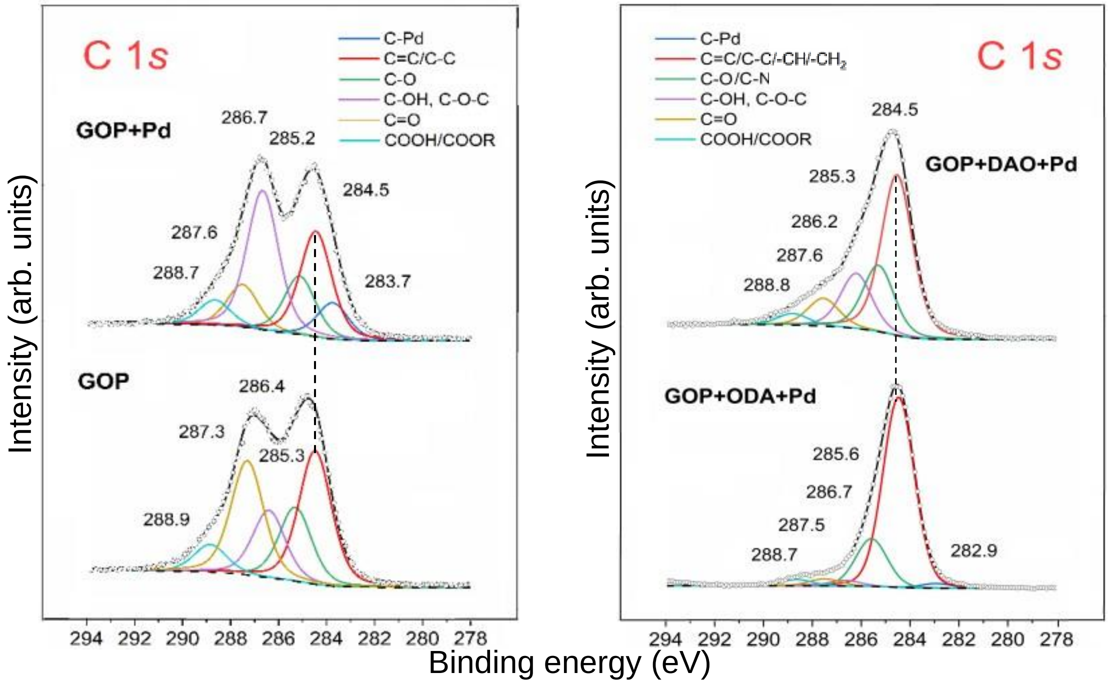

Fig. 4.20. XPS spectra of the C 1*s* core level region of GOP, GOP+Pd, GOP+ODA+Pd and GOP+DAO+Pd samples. Raw data are presented as dots, and the various components deduced from the fit are colour-coded, while their sum is shown in black.

Table 3. XPS binding energies and relative spectral intensities of components of the C 1*s* core level spectra corresponding to the various chemical species present in non-functionalized and Pd-decorated graphene oxide paper samples

	Components (eV)					
Sample	**C-Pd (%)**	**C=C/C-C (%)**	**C-O (%)**	**C-OH, C-O-C (%)**	**C=O (%)**	**O=C-O (%)**
GOP	---	**284.5** (32.0)	285.3 (17.8)	286.4 (16.2)	287.3 (27.4)	288.8 (6.6)
GOP+Pd	283.8 (8.9)	(25.9)	285.1 (14.4)	286.7 (34.2)	287.5 (10.4)	288.7 (6.1)
	C-Pd (%)	**C=C/C-C/-CH/ -CH_2**	**C-O/C-N (%)**	**C-OH, C-O-C (%)**	**C=O (%)**	**O=C-O (%)**
GOP+ODA+Pd	282.9 (1.8)	(72.6)	285.6 (18.2)	286.7 (2.2)	**287.5** (2.7)	288.7 (2.5)
GOP+DAO+Pd	---	(50.0)	285.3 (20.6)	286.2 (17.1)	(8.7)	288.8 (3.6)

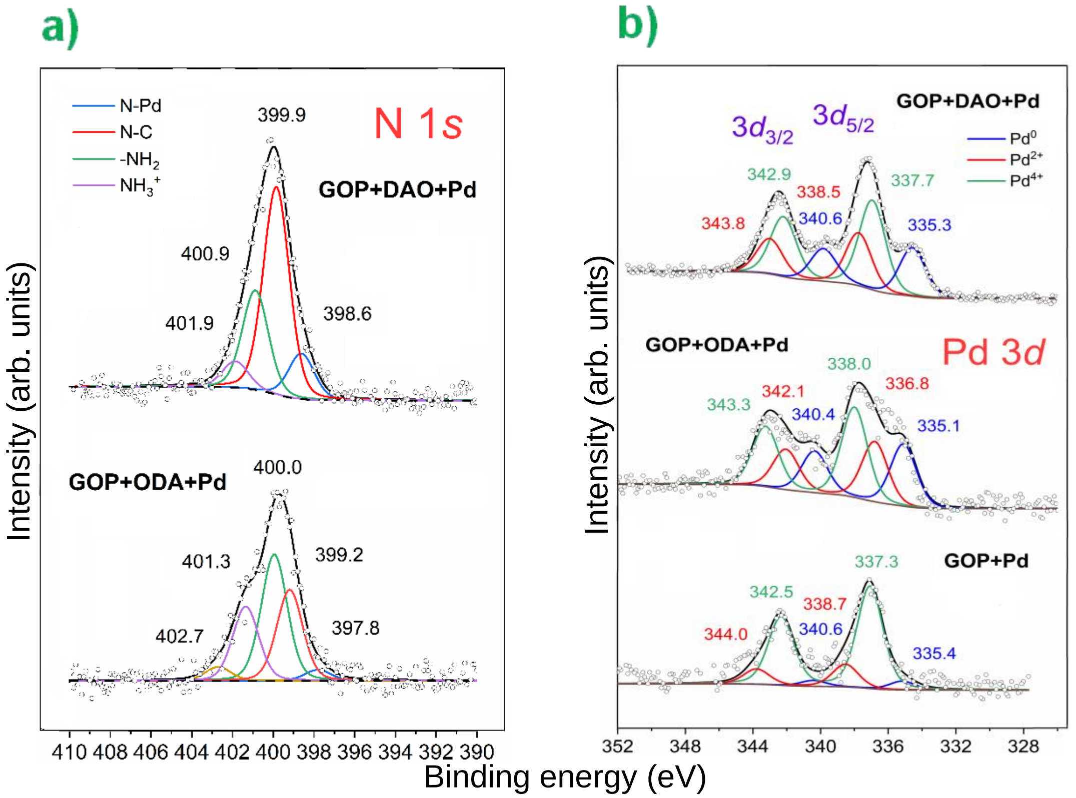

Fig. 4.21. XPS spectra of the: a) N 1*s* and b) Pd 3*d* core level regions for GOP+Pd, GOP+ODA+Pd and GOP+DAO+Pd samples. Raw data are presented as dots, and the various components deduced from the fit are colour coded, while the sum is shown, in black.

Similar features are observed in palladium-containing GOP's at 284.5-288.9 eV binding energy range. The primary distinction is the new component with the lowest binding energy referring to covalent bonding between carbon and palladium[112,113] in GOP+Pd and GOP+ODA+Pd (283.8 and 282.9 eV, respectively). These peaks contribute 8.9 % to the C 1*s* intensity for GOP+Pd, and 1.8 % for GOP+ODA+Pd. The other components, attributed to oxygenated functionalities, appear in increasing BE: C-O < C–OH, C–O–C < C=O < COO^-. Further information about binding energies and relative spectral intensities for each component are reported in Table 3.

It is important to note that the relative intensity of the spectral components corresponding to carbonyl/carboxyl groups in aminated samples are noticeably reduced to (2.7 % and 2.5 % for GOP+ODA+Pd and to 8.7 % and 3.6 % GOP+DAO+Pd) for an increase in intensity of the component at 285.3 – 285.6 eV due to C-N bonds from the amine groups attached to the graphene-matrix[114-116] (18.2 % for GOP+ODA+Pd, versus 20.6 % for GOP+DAO+Pd). All the results are summarized in Table 3.

The detailed spectra of the N 1*s* core level region (Fig. 4.21a) allow us to identify several nitrogenated species (Table 4). At a BE of 399.2-399.9 eV one finds the component due to C-N bonds of the aliphatic amines, as well as of the amino groups resulting from the addition onto epoxy rings[5,62], representing 28.8 % of the total N 1*s* spectral intensity for the ODA-containing sample, and 54.7 % for the DAO-containing sample. The peak at a BE of 400.0 – 400.9 eV refers to the amino groups in both amines (relative intensity 39.9 % in ODA- and 26.3 % in DAO-containing paper), whereas the component at 401.4 – 401.9 eV is due to the fraction of protonated -NH species formed in the acidic environment during PdNP formation and deposition,[5,60], contributing 23.5 % and 7.0 % to the N 1*s* spectral intensity in ODA- and DAO-functionalized samples, respectively. Crucially, the evidence of coordination binding between nitrogen and palladium atoms is clearly observed in the peak appearing at 397.8 – 398.6 eV[117,118], which accounts for 3.4% of the N 1*s* spectral intensity in GOP+ODA+Pd and 12.0 % in GOP+DAO+Pd. This peak indicates the formation of a Pd-N bond, confirming the interaction between the amine groups and palladium nanoparticles. Another small peak at 402.7 eV in the GOP+ODA+Pd sample arises. Unfortunately, the assignment of this peak remains to be very problematic so far.[119]

Table 4. XPS binding energies and relative spectral intensities of components of the N 1*s* core level spectra corresponding to the various chemical species present in the aminated GOP+Pd samples

	Components (eV)			
Sample	**N-Pd (%)**	**N-C (%)**	**$-NH_2$ (%)**	**NH_3^+ (%)**
GOP+ODA+Pd	397.8 (3.4)	399.2 (28.8)	400.0 (39.9)	401.4 (23.5)
GOP+DAO+Pd	398.6 (12.0)	399.9 (54.7)	400.9 (26.3)	401.9 (7.0)

The spectra in the Pd 3*d* core level region region (Fig. 4.21b), show two well-resolved asymmetrical peaks corresponding to the spin-orbit split Pd $3d_{5/2}$ and Pd $3d_{3/2}$ peaks. The $3d_{5/2}$ peak can be deconvoluted in three main components corresponding to different oxidation states: Pd(0), Pd(II) and Pd(IV). The metallic form[120] gives rise to the component in the BE range 335.1 – 335.4 eV, which contributes with a relative spectral intensity of 6.5 % for GOP+Pd, of 29.2 % for GOP+ODA+Pd, and 25.5 % for GOP+DAO+Pd. Bivalent palladium appears in different positions according to the following hypothesis: in the case of GOP+Pd and GOP+DAO+Pd, it is positioned in a BE range of 338.5-338.7 eV due to the possible complexation with carboxylate ions derived from the deprotonation of the carboxylic acids of citric acid used for the PdNPs formation[121] where the reported BE for the complexes formed varies between 338.6 – 338.8 eV.[122,123] The corresponding relative spectral intensity runs of 17.1 % for GOP+Pd, and 26.7 % for GOP+DAO+Pd. In GOP+ODA+Pd this chemical species is positioned in 336.8 eV, reflecting PdO formation[124,125] with a spectral intensity of 28.4 %. Tetravalent palladium appears in a BE between 337.3 – 338.0 eV attributed to PdO_2 formation[126,127] with relative spectral intensities: 76.4 % (GOP+Pd), 42.4 % (GOP+ODA+Pd), and 47.9 (GOP+DAO+Pd). The results are summarized in Table 5.

Table 5. XPS binding energies and relative spectral intensities of components of the Pd3*d* core level spectra corresponding to palladium in various oxidation states present in the palladium-decorated GOP samples

			Components (eV)			
Species	**Pd (0)**		**Pd (II)**		**Pd (IV)**	
line **sample**	**3$d_{5/2}$ (%)**	**3$d_{3/2}$ (%)**	**3$d_{5/2}$ (%)**	**3$d_{3/2}$ (%)**	**3$d_{5/2}$ (%)**	**3$d_{3/2}$ (%)**
GOP+Pd	335.4 (6.5)	340.6	338.7 (17.1)	344.0	337.3 (76.4)	342.5
GOP+ODA+Pd	335.1 (29.2)	340.4	336.8 (28.4)	342.1	338.0 (42.4)	343.3
GOP+DAO+Pd	335.3 (25.5)	340.6	338.5 (26.7)	343.8	337.7 (47.9)	342.9

Derived from the data above, the atomic elemental composition for the GOP/PdNPs set was calculated (Table 6). As expected, the estimated nitrogen percentage was dimly raised in GOP+DAO+Pd (2.1 %) in comparison to the ODA-containing homologous (1.0 %) because of DAO bifunctionality. Consequently, palladium was deposited in the highest amount (1.6 %), followed by GOP+Pd (0.2 %), and lately, GOP+ODA+Pd (0.1%).

Table 6. Elemental composition of the different graphene oxide paper samples as derived from the XPS spectra collected on the opposite side to the filtration membrane.

Sample	**Atomic %**
GOP+Pd	C: 77.3
	O: 22.6
	Pd: 0.2
GOP+ODA+Pd	C: 91.9
	O: 7.0
	N: 1.0
	Pd: 0.1
GOP+DAO+Pd	C: 84.5
	O: 11.8
	N: 2.1
	Pd: 1.6

4.3.2 Theoretical modelling

We attempted to provide an explanation for the experimental results by modelling the properties of the hybrids with DFT calculations. The use of realistic-size GO and PdNP models are obviously computationally prohibitive, but relatively small models can already highlight some trends. An appropriate and computationally accessible choice to simulate a Pd nanoparticle is the Pd_{16} cluster (Fig. 4.22), which was proposed by Nava *et al*.[128] This cluster has a maximal lateral extension of 7.1 Å and can also be synthesized experimentally in a ligand-stabilized form.[129] In the case of GO, we employed the models of GO, GO+ODA and GO-DAO successfully tested in our previous study on AgNP decoration of the same substrates.[28]

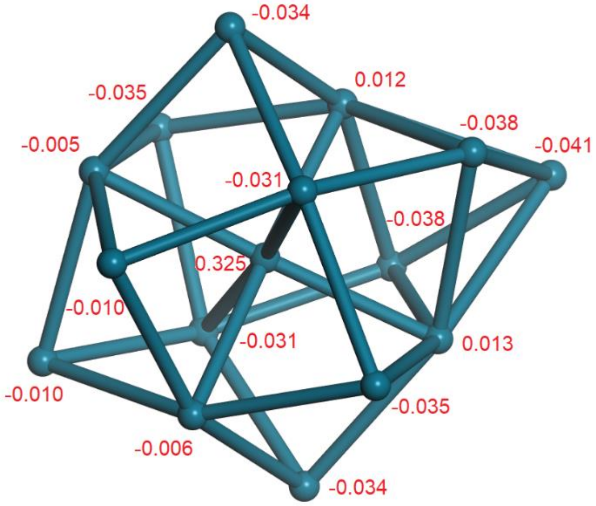

Fig. 4.22. Optimized geometry of the Pd_{16} cluster used to simulate PdNPs, showing atomic charges obtained by Mulliken analysis.

The optimized Pd_{16} geometry (Fig. 4.22) is rather symmetric. As shown by the Mulliken analysis, the atoms of the cluster differ in terms of the sign and magnitude of charge: from − 0.041 *e* to 0.013 *e*. In other words, both positively and negatively charged chemical species (either atoms or functional groups) can interact electrostatically with Pd_{16} and this will be important for how the metal nanoparticles can bind to non-functionalized and functionalized GO. As described previously[28], a computationally feasible choice of GO models is based on a ten-fused aromatic-ring system.[130,131] To represent the oxygen-containing functionalities of GO, we introduced six carboxylic and eight aromatic ketone groups. The models for GO+ODA and GO+DAO were derived from the GO model by converting four of its six COOH groups into the corresponding amides.[28] In the case of GO+DAO we additionally accounted for the fact that the Pd deposition is carried out under acidic experimental conditions, by protonating the four NH_2 termini, which did not form amide derivatives; the resulting model is referred to as GO+DAO-4H$^+$. Fig. 4.23 schematically describes the mechanism and energy of the complexation of a Pd_{16} cluster with the models for GO, GO+ODA and GO+DAO-4H$^+$. One can see that the weakest bonding (− 62.2

kcal/mol) was found on GO+ODA. In this case, Pd_{16} remains on the top of the model, forming close contacts mainly with the terminal CH_3 groups of octadecyl moieties. The other two cases are very different, with very low negative values of formation energies (*i.e.* very strong bonding) for both GO (− 135.2 kcal/mol) and especially GO+DAO-4H$^+$ (− 179.5 kcal/mol). The most interesting distinctive feature is that the Pd cluster directly chemisorbs on the graphene backbone by forming short Pd-C bonds, which can be qualified as covalent. This happens even on GO+DAO-4H$^+$, despite the presence of rather long DAO moieties. This direct contact between the Pd_{16} cluster and the graphene backbone 'smears' palladium atoms over the GO surface, contrary to the case of GO+ODA+Pd_{16}, where Pd_{16} generally conserves its symmetric shape. A possible explanation is that ODA substituents are sufficiently long, and thus 'shield' and protect palladium from the strong attraction to the GO surface. The 'smearing' of Pd atoms observed theoretically can explain PdNP coalescence and agglomeration observed experimentally on GO and GO+DAO, whereas PdNPs deposited onto GO+ODA do not tend to coalesce and remain small, though the Pd elemental content is relatively small as well.

As it could be expected, the differences in geometries and mechanisms of nanohybrid formation give rise to notable differences in the electronic structure; we analyzed specifically the energy and distribution of frontier orbitals HOMO and LUMO (Table 7 and Fig. 4.24). The HOMO-LUMO gap energies calculated for individual components are 0.313 eV for Pd_{16}, 1.105 eV GO, 0.854 eV for GO+ODA and 0.863 eV for GO+DAO-4H$^+$ are (Table 7). It is logical to expect that, since Pd_{16} has the lowest gap energy of all these components, its complexation with GO, GO+ODA and GO+DAO-4H$^+$ will result in lower HOMO-LUMO gap energies for the corresponding hybrids. As one can see, the HOMO-LUMO gap dramatically decreases to 0.163 eV for GO+Pd_{16}, 0.008 eV for GO+ODA+Pd_{16} and 0.144 eV for GO+DAO-4H$^+$+Pd_{16}. An especially interesting observation is that Pd functionalization decreases the gap energy by two orders of magnitude, namely from 0.854 eV for GO+ODA to 0.008 eV for GO+ODA+Pd_{16}. The frontier orbital localization (Fig. 4.24) matches the differences in HOMO-LUMO gap energies. The very strong interaction in the cases of GO+Pd_{16} and GO+DAO-4H$^+$+Pd_{16} results in the localization of both the HOMO and the LUMO on the same Pd atoms and an insignificant charge density on GO. On the contrary, in GO+ODA+Pd_{16} the HOMO and the LUMO are very well separated, with the HOMO localized exclusively on GO, and the LUMO exclusively on Pd_{16}.

The fact that the LUMO in all three cases is centred on Pd might imply that the latter remains active in electrophilic processes; in addition, the presence of the HOMO on the same atoms in GO+Pd_{16} and GO+DAO-4H$^+$+Pd_{16} can be linked to Pd cluster activity in nucleophilic processes. In turn, this might have important positive consequences for catalytic, electrocatalytic and biomedical applications of PdNPs deposited onto GO and GO-based materials.

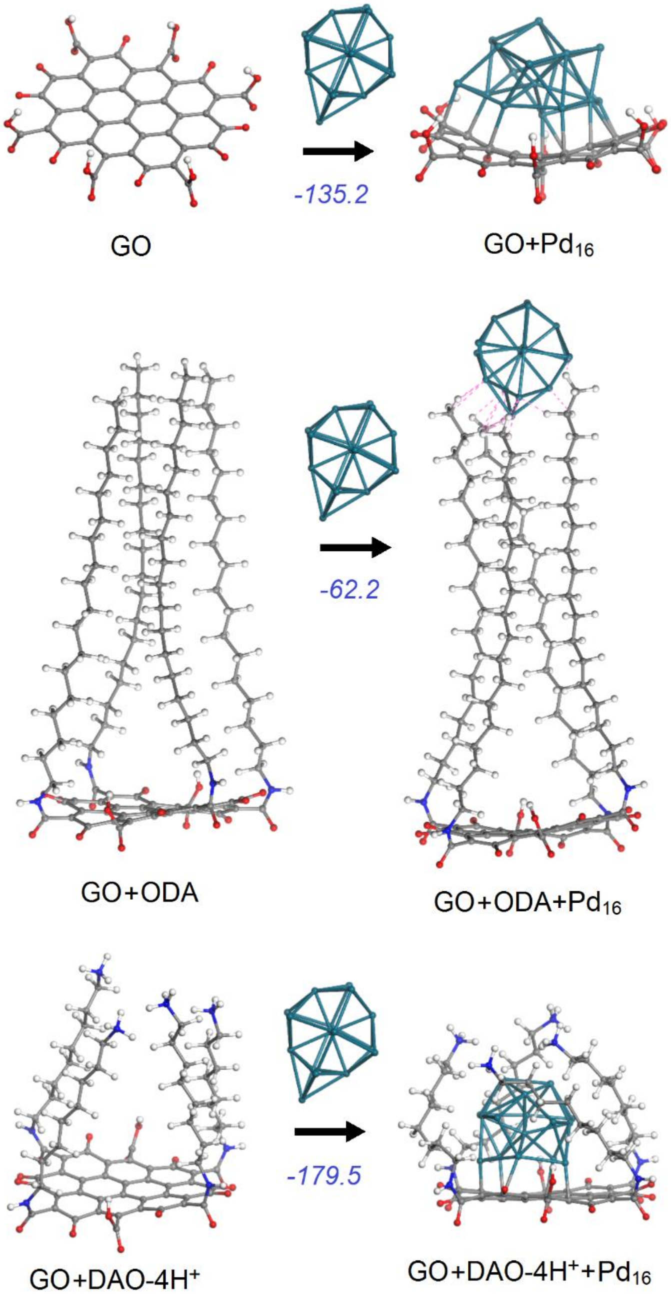

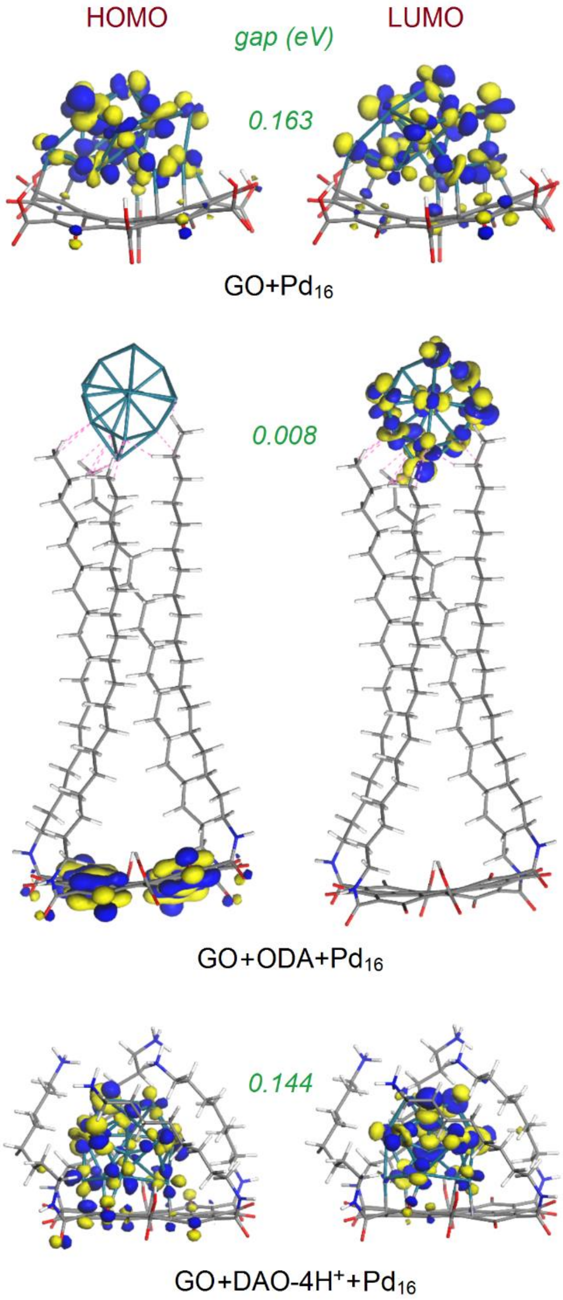

Fig. 4.23. Optimized geometries of the GO, GO+ODA and GO+DAO-4H$^+$ models (left) and of their hybrids formed with a Pd$_{16}$ nanocluster (right) in aqueous medium. The values shown in blue are the formation energies (in kcal/mol) for GO+Pd$_{16}$, GO+ODA+Pd$_{16}$ and GO+DAO-4H$^+$+Pd$_{16}$ hybrids. The pink dashed lines indicate closest approaches shorter than 2.8 Å.

Fig. 4.24. HOMO and LUMO plots (isosurfaces at 0.03 a.u.) of the GO+Pd$_{16}$, GO+ODA+Pd$_{16}$ and GO+DAO-4H$^+$+Pd$_{16}$ hybrids, with the HOMO-LUMO gap values shown in green.

Table 7. Total energies (*E*, in Ha), HOMO, LUMO and HOMO-LUMO gap energies (in eV) for an isolated Pd_{16} cluster, non-functionalized and amine-functionalized GO models and their corresponding complexes with Pd_{16}, as well as formation energies (ΔE, in kcal/mol) for the complexes with Pd_{16}, as calculated by using PBE GGA functional with Grimme's dispersion correction in conjunction with DNP basis set and DSPP pseudopotentials.

Structure	*E* (Ha)	ΔE (kcal/mol)	E_{HOMO} (eV)	E_{LUMO} (eV)	HOMO-LUMO gap (eV)
Pd_{16}	-2613.7569726		-4.533	-4.220	0.313
GO	-2954.3392137		-6.923	-5.818	1.105
GO+Pd_{16}	-5568.3115699	**-135.2**	-5.635	-5.472	0.163
GO+ODA	-5702.6968554		-6.476	-5.622	0.854
GO+ODA+Pd_{16}	-8316.5529615	**-62.2**	-5.037	-5.029	0.008
GO+DAO-4H^+	-4354.7741375		-6.596	-5.733	0.863
GO+DAO-4H^++Pd_{16}	-6968.8172249	**-179.5**	-5.763	-5.619	0.144

4.4 Conclusions

This study described in this chapter demonstrated the successful fabrication of palladium-containing graphene oxide hybrids in both powder and paper form through a multi-step approach encompassing vacuum filtration, eco-friendly gas-phase functionalization with amines, and decoration with palladium nanoparticles using citric acid as a green reducing agent. X-ray photoelectron spectroscopy confirmed that the amine molecules were grafted to graphene oxide sheets through both amidation reaction and amine addition onto epoxy rings.

The combination of dispersibility tests, FTIR, XRD, TGA/DTA, as well as SEM/EDS and TEM imaging demonstrated the advantages of applying gas-phase functionalization with amine molecules under an eco-friendly approach to create supports withstanding Pd nanoparticle decoration in liquid media.

Thermal and Energy Dispersive X-ray studies exhibited a superior palladium content in the non-aminated GO+Pd sample in comparison to amine-functionalized GO. XRD results showed Pd (111) and (200) peaks indicating that the larger palladium nanoparticles, which are visible to this technique, crystallize with face-centered cubic (fcc) structure.

Dispersibility tests demonstrated the incompatibility of the powdered-based GO/PdNPs hybrids towards polar solvents. Therefore, further investigation applying non-polar reagents is required to explore plausible practical applications. In paper-like species, those tests proved the enhanced mechanical stability of paper mats achieved through palladium decoration. 1-octadecylamine emerged as the more effective molecule for strengthening graphene oxide paper because it minimises Pd nanoparticle aggregation. EDS studies confirmed that the less dense face of the paper exhibits the most uniform palladium coverage indicating that also the structural characteristics of the substrate play an important role in Pd distribution.

Electron microscopy evidenced the differences in PdNP nucleation, distribution, size and shape, which are strongly influenced by the structure of the amine molecule and the amount of stabilizing agents involved (citric acid, and amine moieties). and in the case of paper, on the local density in the zone of study. In particular, the different interactions between the solvent, amines grafted to GO, the GO itself and the nanoparticles significantly impact the processing of the nanoparticles in solution on the paper or powder surface as well as on the NPs' final properties.

Bright-field and dark-field TEM imaging revealed that GO+Pd samples contained irregularly shaped and randomly distributed particles, whereas ODA-functionalized GO showed a more homogeneous size distribution and very little agglomeration. DAO-functionalized samples exhibited a broader range of particles with different sizes, shapes, and coalescence. The average Pd particle sizes on GO functionalized with diamines were ten times larger than on GO, and on GO with monoamines.

Referring to theoretical supporting data, the fact that the LUMO in all three cases is centered on Pd, might imply that the latter remains active in electrophilic processes; in addition the presence of the HOMO on the same atoms in GO+Pd_{16} and GO+DAO-4H^++Pd_{16} can be linked to Pd cluster activity in nucleophilic processes. In turn, this might have important positive consequences for catalytic, electrocatalytic and biomedical applications of PdNPs deposited onto GO-based materials.

The described research underscores that by combining traditional and sustainable methodologies and taking advantage of the *d* orbitals of noble metals for forming coordination bonds with the functionalized carbon matrix, promising avenues for creating advanced materials emerge.

4.5 References

(1) Kumar, K. S.; Choudhary, N.; Jung, Y.; Thomas, J. Recent Advances in Two-Dimensional Nanomaterials for Supercapacitor Electrode Applications. *ACS Energy Letters* **2018**, *3* (2), 482–495. https://doi.org/10.1021/acsenergylett.7b01169.

(2) Zhuang, G.; Gao, Y.; Zhou, X.; Tao, X.; Luo, J.; Gao, Y.; Yan, Y.; Gao, P.; Zhong, X.; Wang, J. ZIF-67/COF-Derived Highly Dispersed Co3O4/N-Doped Porous Carbon with Excellent Performance for Oxygen Evolution Reaction and Li-Ion Batteries. *Chemical Engineering Journal* **2017**, *330*, 1255–1264. https://doi.org/10.1016/j.cej.2017.08.076.

(3) Diez-Pascual, A.; Luceño Sánchez, J.; Peña Capilla, R.; García Díaz, P. Recent Developments in Graphene/Polymer Nanocomposites for Application in Polymer Solar Cells. *Polymers* **2018**, *10* (2), 217. https://doi.org/10.3390/polym10020217.

(4) Hu, M.; Yao, Z.; Wang, X. Graphene-Based Nanomaterials for Catalysis. *Industrial & Engineering Chemistry Research* **2017**, *56*, 3477–3502. https://doi.org/10.1021/acs.iecr.6b05048.

(5) Dikin, D. A.; Stankovich, S.; Zimney, E. J.; Piner, R. D.; Dommett, G. H. B.; Evmenenko, G.; Nguyen, S. T.; Ruoff, R. S. Preparation and Characterization of Graphene Oxide Paper. *Nature* **2007**, *448* (7152), 457–460. https://doi.org/10.1038/nature06016.

(6) Vallés, C.; David Núñez, J.; Benito, A. M.; Maser, W. K. Flexible Conductive Graphene Paper Obtained by Direct and Gentle Annealing of Graphene Oxide Paper. *Carbon* **2012**, *50* (3), 835–844. https://doi.org/10.1016/j.carbon.2011.09.042.

(7) Zhang, Y.; Chung, T.-S. Graphene Oxide Membranes for Nanofiltration. *Current Opinion in Chemical Engineering* **2017**, *16*, 9–15. https://doi.org/10.1016/j.coche.2017.03.002.

(8) Chen, H.; Müller, M. B.; Gilmore, K. J.; Wallace, G. G.; Li, D. Mechanically Strong, Electrically Conductive, and Biocompatible Graphene Paper. *Advanced Materials* **2008**, *20* (18), 3557–3561. https://doi.org/10.1002/adma.200800757.

(9) Huang, W. Graphene Oxide Nanopapers. In *Nanopapers: From Nanochemistry and Nanomanufacturing to Advanced Applications*; Elsevier Science, 2017.

(10) Cobos, M.; De-La-Pinta, I.; Quindós, G.; Fernández, M. J.; Fernández, M. D. Graphene Oxide–Silver Nanoparticle Nanohybrids: Synthesis, Characterization, and Antimicrobial Properties. *Nanomaterials* **2020**, *10* (2), 376. https://doi.org/10.3390/nano10020376.

(11) Cheng, Y.; Li, H.; Fang, C.; Ai, L.; Chen, J.; Su, J.; Zhang, Q.; Fu, Q. Facile Synthesis of Reduced Graphene Oxide/Silver Nanoparticles Composites and Their Application for Detecting Heavy Metal Ions. *Journal of Alloys and Compounds* **2019**, *787*, 683–693. https://doi.org/10.1016/j.jallcom.2019.01.320.

(12) Ayán-Varela, M.; Fernández-Merino, M. J.; Paredes, J. I.; Villar-Rodil, S.; Fernández-Sánchez, C.; Guardia, L.; Martínez-Alonso, A.; Tascón, J. M. D. Highly Efficient Silver-Assisted Reduction of Graphene Oxide Dispersions at Room Temperature: Mechanism, and Catalytic and Electrochemical Performance of the Resulting Hybrids. *J. Mater. Chem. A* **2014**, *2* (20), 7295–7305. https://doi.org/10.1039/c3ta15307j.

(13) Navalon, S.; Dhakshinamoorthy, A.; Alvaro, M.; Garcia, H. Metal Nanoparticles Supported on Two-Dimensional Graphenes as Heterogeneous Catalysts. *Coordination Chemistry Reviews* **2016**, *312*, 99–148. https://doi.org/10.1016/j.ccr.2015.12.005.

(14) Golzar, H.; Yazdian, F.; Hashemi, M.; Omidi, M.; Mohammadrezaei, D.; Rashedi, H.; Farahani, M.; Ghasemi, N.; Shabani shayeh, J.; Tayebi, L. Optimizing the Hybrid Nanostructure of Functionalized Reduced Graphene Oxide/Silver for Highly Efficient Cancer Nanotherapy. *New Journal of Chemistry* **2018**, *42* (15), 13157–13168. https://doi.org/10.1039/c8nj01764f.

(15) Cai, N.; Fu, J.; Zeng, H.; Luo, X.; Han, C.; Yu, F. Reduced Graphene Oxide-Silver Nanoparticles/Nitrogen-Doped Carbon Nanofiber Composites with Meso-Microporous Structure for High-Performance Symmetric Supercapacitor Application. *Journal of Alloys and Compounds* **2018**, *742*, 769–779. https://doi.org/10.1016/j.jallcom.2018.01.011.

(16) Zeng, F.; Xu, D.; Zhan, C.; Liang, C.; Zhao, W.; Zhang, J.; Feng, H.; Ma, X. Surfactant-Free Synthesis of Graphene Oxide Coated Silver Nanoparticles for SERS Biosensing and Intracellular Drug Delivery. *ACS Applied Nano Materials* **2018**, *1* (6), 2748–2753. https://doi.org/10.1021/acsanm.8b00444.

(17) Shuai, C.; Guo, W.; Wu, P.; Yang, W.; Hu, S.; Xia, Y.; Feng, P. A Graphene Oxide-Ag Co-Dispersing Nanosystem: Dual Synergistic Effects on Antibacterial Activities and Mechanical Properties of Polymer Scaffolds. *Chemical Engineering Journal* **2018**, *347*, 322–333. https://doi.org/10.1016/j.cej.2018.04.092.

(18) Jiang, Y.; Carboni, D.; Malfatti, L.; Innocenzi, P. Graphene Oxide-Silver Nanoparticles in Molecularly-Imprinted Hybrid Films Enabling SERS Selective Sensing. *Materials* **2018**, *11* (9), 1674. https://doi.org/10.3390/ma11091674.

(19) Kumar, A.; Mazinder Boruah, B.; Liang, X.-J. Gold Nanoparticles: Promising Nanomaterials for the Diagnosis of Cancer and HIV/AIDS. *Journal of Nanomaterials* **2011**, *2011*, 1–17. https://doi.org/10.1155/2011/202187.

(20) Sharma, V. K.; Sayes, C. M.; Guo, B.; Pillai, S.; Parsons, J. G.; Wang, C.; Yan, B.; Ma, X. Interactions between Silver Nanoparticles and Other Metal Nanoparticles under Environmentally Relevant Conditions: A Review. *Science of The Total Environment* **2019**, *653*, 1042–1051. https://doi.org/10.1016/j.scitotenv.2018.10.411.

(21) Singh, P. K.; Kumar, P.; Das, A. K. Unconventional Physical Methods for Synthesis of Metal and Non-Metal Nanoparticles: A Review. *Proceedings of the National Academy of Sciences, India Section A: Physical Sciences* **2018**, *89* (2), 199–221. https://doi.org/10.1007/s40010-017-0474-2.

(22) Dreyer, D. R.; Park, S.; Bielawski, C. W.; Ruoff, R. S. The Chemistry of Graphene Oxide. *Chem. Soc. Rev.* **2010**, *39* (1), 228–240. https://doi.org/10.1039/b917103g.

(23) Gurunathan, S.; Hyun Park, J.; Choi, Y.-J.; Woong Han, J.; Kim, J.-H. Synthesis of Graphene Oxide-Silver Nanoparticle Nanocomposites: An Efficient Novel Antibacterial Agent. *Current Nanoscience* **2016**, *12* (6), 762–773. https://doi.org/10.2174/1573413712666160721143424.

(24) Bao, Q.; Zhang, D.; Qi, P. Synthesis and Characterization of Silver Nanoparticle and Graphene Oxide Nanosheet Composites as a Bactericidal Agent for Water Disinfection. *Journal of Colloid and Interface Science* **2011**, *360* (2), 463–470. https://doi.org/10.1016/j.jcis.2011.05.009.

(25) Li, Z.; Gao, J.; Xing, X.; Wu, S.; Shuang, S.; Dong, C.; Paau, M. C.; Choi, M. M. F. Synthesis and Characterization of N-Alkylamine-Stabilized Palladium Nanoparticles for Electrochemical Oxidation of Methane. *The Journal of Physical Chemistry C* **2009**, *114* (2), 723–733. https://doi.org/10.1021/jp907745v.

(26) Dimiev, A. M.; Siegfried Eigler. *Graphene Oxide : Fundamentals and Applications*; Chichester, West Sussex John Wiley Et Sons, Inc, 2017.

(27) Li, J.; Kuang, D.; Feng, Y.; Zhang, F.; Xu, Z.; Liu, M.; Wang, D. Green Synthesis of Silver Nanoparticles–Graphene Oxide Nanocomposite and Its Application in Electrochemical Sensing Oftryptophan. *Biosensors and Bioelectronics* **2013**, *42*, 198–206. https://doi.org/10.1016/j.bios.2012.10.029.

(28) Rodríguez-Otamendi, D. I.; Meza-Laguna, V.; Acosta, D.; Álvarez-Zauco, E.; Huerta, L.; Basiuk, V. A.; Basiuk, E. V. Eco-Friendly Synthesis of Graphene Oxide–Silver Nanoparticles Hybrids: The Effect of Amine Derivatization. *Diamond and Related Materials* **2021**, *111*, 108208. https://doi.org/10.1016/j.diamond.2020.108208.

(29) Kumari, S.; Sharma, P.; Yadav, S.; Kumar, J.; Vij, A.; Rawat, P.; Kumar, S.; Sinha, C.; Bhattacharya, J.; Srivastava, C. M.; Majumder, S. A Novel Synthesis of the Graphene Oxide-Silver (GO-Ag) Nanocomposite for Unique Physiochemical Applications. *ACS Omega* **2020**, *5* (10), 5041–5047. https://doi.org/10.1021/acsomega.9b03976.

(30) Vi, T. T. T.; Lue, S. J. Preparation of Silver Nanoparticles Loaded Graphene Oxide Nanosheets for Antibacterial Activity. *IOP Conference Series: Materials Science and Engineering* **2016**, *162* (1), 012033. https://doi.org/10.1088/1757-899x/162/1/012033.

(31) Kim, H.-S.; Lee, H.; Han, K.-S.; Kim, J.-H.; Song, M.-S.; Park, M.-S.; Lee, J.-Y.; Kang, J.-K. Hydrogen Storage in Ni Nanoparticle-Dispersed Multiwalled Carbon Nanotubes. *The Journal of Physical Chemistry B* **2005**, *109* (18), 8983–8986. https://doi.org/10.1021/jp044727b.

(32) Ang, L.-M.; Hor, T. S. A.; Xu, G.-Q.; Tung, C.; Zhao, S.; Wang, J. L. S. Electroless Plating of Metals onto Carbon Nanotubes Activated by a Single-Step Activation Method. *Chemistry of Materials* **1999**, *11* (8), 2115–2118. https://doi.org/10.1021/cm990078i.

(33) Karthik, P. S.; Himaja, A. L.; Singh, S. P. Carbon-Allotropes: Synthesis Methods, Applications and Future Perspectives. *Carbon letters* **2014**, *15* (4), 219–237. https://doi.org/10.5714/cl.2014.15.4.219.

(34) Zhang, D.; Liu, T.; Cheng, J.; Liang, S.; Chai, J.; Yang, X.; Wang, H.; Zheng, G.; Cao, M. Controllable Synthesis and Characterization of Tungsten Disulfide Nanosheets as Promising Nanomaterials for Electronic Devices. *Ceramics International* **2019**, *45* (9), 12443–12448. https://doi.org/10.1016/j.ceramint.2019.03.177.

(35) Bukuru, V. R.; Velaga, B.; Peela, N. R.; Kalidindi, S. B. Hybridization of Pd Nanoparticles with UiO-66(Hf) Metal-Organic Framework and the Effect of Nanostructure on the Catalytic Properties. *Chemistry - A European Journal* **2018**, *24* (60), 15978–15982. https://doi.org/10.1002/chem.201803200.

(36) Pattadar, D. K.; Sharma, J. N.; Mainali, B. P.; Zamborini, F. P. Anodic Stripping Electrochemical Analysis of Metal Nanoparticles. *Current Opinion in Electrochemistry* **2019**, *13*, 147–156. https://doi.org/10.1016/j.coelec.2018.12.006.

(37) Yaqoob, S. B.; Adnan, R.; Rameez Khan, R. M.; Rashid, M. Gold, Silver, and Palladium Nanoparticles: A Chemical Tool for Biomedical Applications. *Frontiers in Chemistry* **2020**, *8* (376), 1–15. https://doi.org/10.3389/fchem.2020.00376.

(38) Adams, C. P.; Walker, K. A.; Obare, S. O.; Docherty, K. M. Size-Dependent Antimicrobial Effects of Novel Palladium Nanoparticles. *PLoS ONE* **2014**, *9* (1), 85–98. https://doi.org/10.1371/journal.pone.0085981.

(39) Chaloupka, K.; Malam, Y.; Seifalian, A. M. Nanosilver as a New Generation of Nanoproduct in Biomedical Applications. *Trends in Biotechnology* **2010**, *28* (11), 580–588. https://doi.org/10.1016/j.tibtech.2010.07.006.

(40) Leso, V.; Iavicoli, I. Palladium Nanoparticles: Toxicological Effects and Potential Implications for Occupational Risk Assessment. *International Journal of Molecular Sciences* **2018**, *19* (2), 503. https://doi.org/10.3390/ijms19020503.

(41) Ruben, B.; Zhang, G.; Xin, T.; Giorgio, S.; Victor, M.; Gloria, G.; Michele, F.; Filippo, P.; Shuhui, S.; Nadhira, L.; Ana C, T. Graphene Oxide/Reduced Graphene Oxide Films as Protective Barriers on Lead against Differential Aeration Corrosion Induced by Water Drops. *Nanoscale Advances* **2020**, *2* (11), 5412–5420. https://doi.org/10.1039/d0na00212g.

(42) Kalita, H., Tyagi, H., Aslam, M. Surface tailored graphene oxide paper: An efficient filter for dye pollutants. *Environmental Science: Water Research & Technology* **2020,** 1-39. https://doi:10.1039/c9ew01129c.

(43) Cetinkaya, T.; Ozcan, S.; Uysal, M.; Guler, M. O.; Akbulut, H. Free-Standing Flexible Graphene Oxide Paper Electrode for Rechargeable Li–O2 Batteries. *Journal of Power Sources* **2014**, *267*, 140–147. https://doi.org/10.1016/j.jpowsour.2014.05.081.

(44) Sun, D.; Yan, X.; Lang, J.; Xue, Q. High Performance Supercapacitor Electrode Based on Graphene Paper via Flame-Induced Reduction of Graphene Oxide Paper. *Journal of Power Sources* **2013**, *222*, 52–58. https://doi.org/10.1016/j.jpowsour.2012.08.059.

(45) Li, Y.-F.; Liu, Y.-Z.; Zhang, W.-K.; Guo, C.-Y.; Chen, C.-M. Green Synthesis of Reduced Graphene Oxide Paper Using Zn Powder for Supercapacitors. *Materials Letters* **2015**, *157*, 273–276. https://doi.org/10.1016/j.matlet.2015.05.114.

(46) Zhang, L. L.; Zhao, X.; Stoller, M. D.; Zhu, Y.; Ji, H.; Murali, S.; Wu, Y.; Perales, S.; Clevenger, B.; Ruoff, R. S. Highly Conductive and Porous Activated Reduced Graphene Oxide Films for High-Power Supercapacitors. *Nano Letters* **2012**, *12* (4), 1806–1812. https://doi.org/10.1021/nl203903z.

(47) Zhang, H.; Li, A.; Yuan, Y.; Wei, Y.; Zheng, D.; Geng, Z.; Zhang, H.; Li, G.; Zhang, F. Preparation and Characterization of Colorful Graphene Oxide Papers and Flexible N-Doping Graphene Papers for Supercapacitor and Capacitive Deionization. *Carbon Energy* **2020**, *2* (4), 656–674. https://doi.org/10.1002/cey2.59.

(48) Ravikumar; Scott, K. Freestanding Sulfonated Graphene Oxide Paper: A New Polymer Electrolyte for Polymer Electrolyte Fuel Cells. *Chemical Communications* **2012**, *48* (45), 5584. https://doi.org/10.1039/c2cc31771k.

(49)Aboutalebi, S. H.; Aminorroaya-Yamini, S.; Nevirkovets, I.; Konstantinov, K.; Liu, H. K. Enhanced Hydrogen Storage in Graphene Oxide-MWCNTs Composite at Room Temperature. *Advanced Energy Materials* **2012**, *2* (12), 1439–1446. https://doi.org/10.1002/aenm.201200154.

(50) Zhao, S.; Li, M.; Wu, X.; Yu, S. H.; Zhang, W.; Luo, J.; Wang, J.; Geng, Y.; Gou, Q.; Sun, K. Graphene-Based Free-Standing Bendable Films: Designs, Fabrications, and Applications. *Materials Today Advances* **2020**, *6*, 100060. https://doi.org/10.1016/j.mtadv.2020.100060.

(51) Medhekar, N. V.; Ramasubramaniam, A.; Ruoff, R. S.; Shenoy, V. B. Hydrogen Bond Networks in Graphene Oxide Composite Paper: Structure and Mechanical Properties. *ACS Nano* **2010**, *4* (4), 2300–2306. https://doi.org/10.1021/nn901934u.

(52) Dowell, M. B.; Howard, R. A. Tensile and Compressive Properties of Flexible Graphite Foils. *Carbon* **1986**, *24* (3), 311–323. https://doi.org/10.1016/0008-6223(86)90232-0.

(53) Leng, Y.; Gu, J.; Cao, W.; Zhang, T.-Y. Influences of Density and Flake Size on the Mechanical Properties of Flexible Graphite. *Carbon* **1998**, *36* (7-8), 875–881. https://doi.org/10.1016/s0008-6223(97)00196-6.

(54) Iii, R.; Greinke, R. Influence of Expansion Volume of Intercalated Graphite on Tensile Properties of Flexible Graphite. *Phys Rev B* **1993**, *47*, 10823–10854.

(55) Zhu, N.; Han, S.; Gan, S.; Ulstrup, J.; Chi, Q. Graphene Paper Doped with Chemically Compatible Prussian Blue Nanoparticles as Nanohybrid Electrocatalyst. *Advanced Functional Materials* **2013**, *23* (42), 5297–5306. https://doi.org/10.1002/adfm.201300605.

(56) Chen, X.; Yu, S.; Yang, L.; Wang, J.; Jiang, C. Fluorescence and Visual Detection of Fluoride Ions Using a Photoluminescent Graphene Oxide Paper Sensor. *Nanoscale* **2016**, *8* (28), 13669–13677. https://doi.org/10.1039/c6nr02878k.

(57) Huang, N.-J.; Cao, C.-F.; Li, Y.; Zhao, L.; Zhang, G.-D.; Gao, J.-F.; Guan, L.-Z.; Jiang, J.-X.; Tang, L.-C. Silane Grafted Graphene Oxide Papers for Improved Flame Resistance and Fast Fire Alarm Response. *Composites Part B: Engineering* **2019**, *168*, 413–420. https://doi.org/10.1016/j.compositesb.2019.03.053.

(58) Selvakumar, D.; Sivaram, H.; Alsalme, A.; Alghamdi, A.; Jayavel, R. Freestanding Flexible, Pure and Composite Form of Reduced Graphene Oxide Paper for Ammonia Vapor Sensing. *Scientific Reports* **2019**, *9* (1). https://doi.org/10.1038/s41598-019-45408-4.

(59) Neto, A.; Eudes Eterno Fileti. Elucidating the Amphiphilic Character of Graphene Oxide. *Physical Chemistry Chemical Physics* **2018**, *20* (14), 9507–9515. https://doi.org/10.1039/c8cp00797g.

(60) Cote, L. J.; Kim, F.; Huang, J. Langmuir−Blodgett Assembly of Graphite Oxide Single Layers. *Journal of the American Chemical Society* **2008**, *131* (3), 1043–1049. https://doi.org/10.1021/ja806262m.

(61) Dikin, D. A.; Stankovich, S.; Zimney, E. J.; Piner, R. D.; Dommett, G. H. B.; Evmenenko, G.; Nguyen, S. T.; Ruoff, R. S. Preparation and Characterization of Graphene Oxide Paper. *Nature* **2007**, *448* (7152), 457–460. https://doi.org/10.1038/nature06016.

(62) Wenyi Huang. *Nanopapers : From Nanochemistry and Nanomanufacturing to Advanced Applications*; Elsevier Inc. C: Amsterdam (Radarwag 29, Po Box 211, 1000 Ae Amsterdam, Netherlands) ; Oxford (The Boulevard, Mlangford Lane, Kidlington, Oxford Ox5 1Gb, United Kingdom) ; Cambridge (50 Hamsphire Street, 5Th Floor, Cambridge, Ma 02139, United States), 2018.

(63) Bai, H.; Li, C.; Wang, X.; Shi, G. On the Gelation of Graphene Oxide. *The Journal of Physical Chemistry C* **2011**, *115* (13), 5545–5551. https://doi.org/10.1021/jp1120299.

(64) Li, P.; Yang, M.; Liu, Y.; Qin, H.; Liu, J.; Xu, Z.; Liu, Y.; Meng, F.; Lin, J.; Wang, F.; Gao, C. Continuous Crystalline Graphene Papers with Gigapascal Strength by Intercalation Modulated Plasticization. *Nature Communications* **2020**, *11* (1). https://doi.org/10.1038/s41467-020-16494-0.

(65) Chen, J.; Zhang, G.; Luo, B.; Sun, D.; Yan, X.; Xue, Q. Surface Amorphization and Deoxygenation of Graphene Oxide Paper by Ti Ion Implantation. *Carbon* **2011**, *49* (9), 3141–3147. https://doi.org/10.1016/j.carbon.2011.03.045.

(66) Tian, Y.; Cao, Y.; Wang, Y.; Yang, W.; Feng, J. Realizing Ultrahigh Modulus and High Strength of Macroscopic Graphene Oxide Papers through Crosslinking of Mussel-Inspired Polymers. *Advanced Materials* **2013**, *25* (21), 2980–2983. https://doi.org/10.1002/adma.201300118.

(67) Ravikumar; Scott, K. Freestanding Sulfonated Graphene Oxide Paper: A New Polymer Electrolyte for Polymer Electrolyte Fuel Cells. *Chemical Communications* **2012**, *48* (45), 5584. https://doi.org/10.1039/c2cc31771k.

(68) Park, S.; Mohanty, N.; Suk, J. W.; Nagaraja, A.; An, J.; Piner, R. D.; Cai, W.; Dreyer, D. R.; Berry, V.; Ruoff, R. S. Biocompatible, Robust Free-Standing Paper Composed of a TWEEN/Graphene Composite. *Advanced Materials* **2010**, *22* (15), 1736–1740. https://doi.org/10.1002/adma.200903611.

(69) Zhang, X.; An, Y.; Han, J.; Han, W.; Zhao, G.; Jin, X. Graphene Nanosheet Reinforced ZrB_2–SiC Ceramic Composite by Thermal Reduction of Graphene Oxide. *RSC Advances* **2015**, *5* (58), 47060–47065. https://doi.org/10.1039/c5ra05922d.

(70) Gao, Y.; Liu, L.-Q.; Zu, S.-Z.; Peng, K.; Zhou, D.; Han, B.-H.; Zhang, Z. The Effect of Interlayer Adhesion on the Mechanical Behaviors of Macroscopic Graphene Oxide Papers. *ACS Nano* **2011**, *5* (3), 2134–2141. https://doi.org/10.1021/nn103331x.

(71) Li, Z.-H.; Zhao, X.-L.; Song, R.-M.; Chen, C.; Wei, P.-J.; Zhu, Z.-G. Free-Standing Palladium Modified Reduced Graphene Oxide Paper Based on One-Pot Co-Reduction and Its Sensing Application. *Chemical Physics Letters* **2018**, *712*, 71–77. https://doi.org/10.1016/j.cplett.2018.09.047.

(72) Bandekar, J. Amide Modes and Protein Conformation. *Biochimica et Biophysica Acta (BBA) - Protein Structure and Molecular Enzymology* **1992**, *1120* (2), 123–143. https://doi.org/10.1016/0167-4838(92)90261-b.

(73) Roy, P. S.; Bagchi, J.; Bhattacharya, S. K. Size-Controlled Synthesis and Characterization of Polyvinyl Alcohol Coated Palladium Nanoparticles. *Transition Metal Chemistry* **2009**, *34* (4), 447–453. https://doi.org/10.1007/s11243-009-9215-y.

(74) Dar, R. A.; Giri, L.; Karna, S. P.; Srivastava, A. K. Performance of Palladium Nanoparticle–Graphene Composite as an Efficient Electrode Material for Electrochemical Double Layer Capacitors. *Electrochimica Acta* **2016**, *196*, 547–557. https://doi.org/10.1016/j.electacta.2016.02.197.

(75) Li, J.; Chen, W.; Zhao, H.; Zheng, X.; Wu, L.; Pan, H.; Zhu, J.; Chen, Y.; Lu, J. Size-Dependent Catalytic Activity over Carbon-Supported Palladium Nanoparticles in Dehydrogenation of Formic Acid. *Journal of Catalysis* **2017**, *352*, 371–381. https://doi.org/10.1016/j.jcat.2017.06.007.

(76) Rodríguez-Otamendi, D. I.; Bizarro, M.; Meza-Laguna, V.; Álvarez-Zauco, E.; Rudolf, P.; Basiuk, V. A.; Basiuk, E. V. Eco-Friendly Synthesis of Graphene Oxide–Palladium Nanohybrids. *Materials Tootamray Communications* **2023**, *35* (106007), 1–13. https://doi.org/10.1016/j.mtcomm.2023.106007.

(77) Alzate-Carvajal, N.; Acevedo-Guzmán, D. A.; Meza-Laguna, V.; Farías, M. H.; Pérez-Rey, L. A.; Abarca-Morales, E.; García-Ramírez, V. A.; Basiuk, V. A.; Basiuk, E. V. One-Step Nondestructive Functionalization of Graphene Oxide Paper with Amines. *RSC Advances* **2018**, *8* (28), 15253–15265. https://doi.org/10.1039/c8ra00986d.

(78) McGrail, B. T.; Rodier, B. J.; Pentzer, E. Rapid Functionalization of Graphene Oxide in Water. *Chemistry of Materials* **2014**, *26* (19), 5806–5811. https://doi.org/10.1021/cm5031409.

(79) Yuan, R.; Yuan, J.; Wu, Y.; Chen, L.; Zhou, H.; Chen, J. Efficient Synthesis of Graphene Oxide and the Mechanisms of Oxidation and Exfoliation. *Applied Surface Science* **2017**, *416*, 868–877. https://doi.org/10.1016/j.apsusc.2017.04.181.

(80) Barth, A. Infrared Spectroscopy of Proteins. *Biochimica et Biophysica Acta (BBA) - Bioenergetics* **2007**, *1767* (9), 1073–1101. https://doi.org/10.1016/j.bbabio.2007.06.004.

(81) Kong, J.; Yu, S. Fourier Transform Infrared Spectroscopic Analysis of Protein Secondary Structures. *Acta Biochimica et Biophysica Sinica* **2007**, *39* (8), 549–559. https://doi.org/10.1111/j.1745-7270.2007.00320.x.

(82) Coates, J. P. The Interpretation of Infrared Spectra: Published Reference Sources. *Applied Spectroscopy Reviews* **1996**, *31* (1-2), 179–192. https://doi.org/10.1080/05704929608000568.

(83) Spyrou, K.; Rudolf, P. An Introduction to Graphene. In *Functionalization of Graphene*; Georgakilas , V., Ed.; Wiley-VCH: Weinheim, 2014; pp. 1–20.

(84) Yen, P.-W.; Chou, T. Temperature Programmed Oxidation of Palladium Catalyst: Effect of Support on the Oxygen Adsorption Behavior. *Applied Catalysis A-General* **2000**, *198* (1-2), 23–31. https://doi.org/10.1016/s0926-860x(99)00507-4.

(85) Liu, X.; Zhao, X.; Zhou, M.; Cao, Y.; Wu, H.; Zhu, J. Highly Stable and Active Palladium Nanoparticles Supported on a Mesoporous UiO66@Reduced Graphene Oxide Complex for Practical Catalytic Applications. *European Journal of Inorganic Chemistry* **2016**, *2016* (20), 3338–3343. https://doi.org/10.1002/ejic.201600367.

(86) Premkumar, T.; Lee, K.; Geckeler, K. E. Shape-Tailoring and Catalytic Function of Anisotropic Gold Nanostructures. *Nanoscale Research Letters* **2011**, *6* (1), 1–12. https://doi.org/10.1186/1556-276x-6-547.

(87) Ramirez, E.; Jansat, S.; Philippot, K.; Lecante, P.; Gomez, M.; Masdeu-Bultó, A. M.; Chaudret, B. Influence of Organic Ligands on the Stabilization of Palladium Nanoparticles. *Journal of Organometallic Chemistry* **2004**, *689* (24), 4601–4610. https://doi.org/10.1016/j.jorganchem.2004.09.006.

(88) Collier, C. P.; Vossmeyer, T.; Heath, J. R. NANOCRYSTAL SUPERLATTICES. *Annual Review of Physical Chemistry* **1998**, *49* (1), 371–404. https://doi.org/10.1146/annurev.physchem.49.1.371.

(89) Israelachvilli, J. N. *Intermolecular and Surface Forces*; Academic Press: London, 2010.

(90) Godfrey Alig, A. R.; Akbulut, M.; Golan, Y.; Israelachvili, J. Forces between Surfactant-Coated ZnS Nanoparticles in Dodecane: Effect of Water. *Advanced Functional Materials* **2006**, *16* (16), 2127–2134. https://doi.org/10.1002/adfm.200500705.

(91) Yu, R.; Chen, L.; Liu, Q.; Lin, J.; Tan, K.-L.; Ng, S. C.; Chan, H. S. O.; Xu, G.-Q.; Hor, T. S. A. Platinum Deposition on Carbon Nanotubes via Chemical Modification. *Chemistry of Materials* **1998**, *10* (3), 718–722. https://doi.org/10.1021/cm970364z.

(92) Chen, J. Paul.; Wu, S.; Chong, K.-H. Surface Modification of a Granular Activated Carbon by Citric Acid for Enhancement of Copper Adsorption. *Carbon* **2003**, *41* (10), 1979–1986. https://doi.org/10.1016/s0008-6223(03)00197-0.

(93) Henglein, A.; Giersig, M. Formation of Colloidal Silver Nanoparticles: Capping Action of Citrate. *The Journal of Physical Chemistry B* **1999**, *103* (44), 9533–9539. https://doi.org/10.1021/jp9925334.

(94) Guo, J. W.; Zhao, T. S.; Prabhuram, J.; Wong, C. W. Preparation and the Physical/Electrochemical Properties of a Pt/c Nanocatalyst Stabilized by Citric Acid for Polymer Electrolyte Fuel Cells. *Electrochimica Acta* **2005**, *50* (10), 1973–1983. https://doi.org/10.1016/j.electacta.2004.09.006.

(95) Song, F.-Z.; Zhu, Q.-L.; Tsumori, N.; Xu, Q. Diamine-Alkalized Reduced Graphene Oxide: Immobilization of Sub-2 Nm Palladium Nanoparticles and Optimization of Catalytic Activity for Dehydrogenation of Formic Acid. *ACS Catalysis* **2015**, *5* (9), 5141–5144. https://doi.org/10.1021/acscatal.5b01411.

(96) Scheuermann, G. M.; Rumi, L.; Steurer, P.; Bannwarth, W.; Mülhaupt, R. Palladium Nanoparticles on Graphite Oxide and Its Functionalized Graphene Derivatives as Highly Active Catalysts for the Suzuki−Miyaura Coupling Reaction. *Journal of the American Chemical Society* **2009**, *131* (23), 8262–8270. https://doi.org/10.1021/ja901105a.

(97) McAllister, M. J.; Li, J.-L.; Adamson, D. H.; Schniepp, H. C.; Abdala, A. A.; Liu, J.; Herrera-Alonso, M.; Milius, D. L.; Car, R.; Prud'homme, R. K.; Aksay, I. A. Single Sheet Functionalized Graphene by Oxidation and Thermal Expansion of Graphite. *Chemistry of Materials* **2007**, *19* (18), 4396–4404. https://doi.org/10.1021/cm0630800.

(98) Chen, J.; Yao, B.; Li, C.; Shi, G. An Improved Hummers Method for Eco-Friendly Synthesis of Graphene Oxide. *Carbon* **2013**, *64*, 225–229. https://doi.org/10.1016/j.carbon.2013.07.055.

(99) Chen, J.; Li, Y.; Huang, L.; Li, C.; Shi, G. High-Yield Preparation of Graphene Oxide from Small Graphite Flakes via an Improved Hummers Method with a Simple Purification Process. *Carbon* **2015**, *81*, 826–834. https://doi.org/10.1016/j.carbon.2014.10.033.

(100) Wang, C.; Liu, Z.; Wang, S.; Zhang, Y. Preparation and Properties of Octadecylamine Modified Graphene Oxide/Styrene-Butadiene Rubber Composites through an Improved Melt Compounding Method. *Journal of Applied Polymer Science* **2015**, *133* (4), n/a-n/a. https://doi.org/10.1002/app.42907.

(101) Gao, W. The Chemistry of Graphene Oxide. In *Graphene Oxide: Reduction Recipes, Spectroscopy, and Applications*; Springer, Cham: Switzerland, 2015; pp. 61–95.

(102) Imre Dékány; R. Krüger-Grasser; André Weiß. Selective Liquid Sorption Properties of Hydrophobized Graphite Oxide Nanostructures. *Colloid and Polymer Science* **1998**, *276* (7), 570–576. https://doi.org/10.1007/s003960050283.

(103) Adarsh Kaniyoor; Tessy Theres Baby; T. Arockiadoss; N. Rajalakshmi; Sundara Ramaprabhu. Wrinkled Graphenes: A Study on the Effects of Synthesis Parameters on Exfoliation-Reduction of Graphite Oxide. *Journal of Physical Chemistry C* **2011**, *115* (36), 17660–17669. https://doi.org/10.1021/jp204039k.

(104) Díez, N.; Śliwak, A.; Gryglewicz, S.; Grzyb, B.; Gryglewicz, G. Enhanced Reduction of Graphene Oxide by High-Pressure Hydrothermal Treatment. *RSC Advances* **2015**, *5* (100), 81831–81837. https://doi.org/10.1039/c5ra14461b.

(105) Choudhary, S.; Mungse, H. P.; Khatri, O. P. Dispersion of Alkylated Graphene in Organic Solvents and Its Potential for Lubrication Applications. *Journal of Materials Chemistry* **2012**, *22* (39), 21032–21039. https://doi.org/10.1039/c2jm34741e.

(106) Mungse, H. P.; Khatri, O. P. Chemically Functionalized Reduced Graphene Oxide as a Novel Material for Reduction of Friction and Wear. *The Journal of Physical Chemistry C* **2014**, *118* (26), 14394–14402. https://doi.org/10.1021/jp5033614.

(107) Wang, G.; Yang, J.; Park, J.; Gou, X.; Wang, B.; Liu, H.; Yao, J. Facile Synthesis and Characterization of Graphene Nanosheets. *The Journal of Physical Chemistry C* **2008**, *112* (22), 8192–8195. https://doi.org/10.1021/jp710931h.

(108) Basiuk, E. V.; Basiuk, V. A.; Meza-Laguna, V.; Contreras-Torres, F. F.; Martínez, M.; Rojas-Aguilar, A.; Salerno, M.; Zavala, G.; Falqui, A.; Brescia, R. Solvent-Free Covalent Functionalization of Multi-Walled Carbon Nanotubes and Nanodiamond with Diamines: Looking for Cross-Linking Effects. *Applied Surface Science* **2012**, *259*, 465–476. https://doi.org/10.1016/j.apsusc.2012.07.068.

(109) Hung, W.-S.; Tsou, C.-H.; De Guzman, M.; An, Q.-F.; Liu, Y.-L.; Zhang, Y.-M.; Hu, C.-C.; Lee, K.-R.; Lai, J.-Y. Cross-Linking with Diamine Monomers to Prepare Composite Graphene Oxide-Framework Membranes with Varying *d-Spacing*. *Chemistry of Materials* **2014**, *26* (9), 2983–2990. https://doi.org/10.1021/cm5007873.

(110) Rahim Molaei; Farhadi, K.; Mehrdad Forough; Salahaddin Hajizadeh. Green Biological Fabrication and Characterization of Highly Monodisperse Palladium Nanoparticles Using Pistacia Atlantica Fruit Broth. *Journal of Nanostructures* **2018**, *8* (1), 47–54. https://doi.org/10.22052/jns.2018.01.006.

(111) Biesinger, M. C. Accessing the Robustness of Adventitious Carbon for Charge Referencing (Correction) Purposes in XPS Analysis: Insights from a Multi-User Facility Data Review. *Applied Surface Science* **2022**, *597*, 153681. https://doi.org/10.1016/j.apsusc.2022.153681.

(112) Deniau, G.; Azoulay, L.; Jégou, P.; Le Chevallier, G.; Palacin, S. Carbon-To-Metal Bonds: Electrochemical Reduction of 2-Butenenitrile. *Surface Science* **2006**, *600* (3), 675–684. https://doi.org/10.1016/j.susc.2005.11.021.

(113) Nie, R.; Jiang, H.; Lu, X.; Zhou, D.; Xia, Q. Highly Active Electron-Deficient Pd Clusters on N-Doped Active Carbon for Aromatic Ring Hydrogenation. *Catalysis Science & Technology* **2016**, *6* (6), 1913–1920. https://doi.org/10.1039/c5cy01418b.

(114) Zhao, Q.; Zhu, Y.; Sun, Z.; Li, Y.; Zhang, G.; Zhang, F.; Fan, X. Combining Palladium Complex and Organic Amine on Graphene Oxide for Promoted Tsuji–Trost Allylation. *Journal of materials chemistry. A, Materials for energy and sustainability* **2015**, *3* (6), 2609–2616. https://doi.org/10.1039/c4ta05205f.

(115) Soğukömeroğulları, H. G.; Karataş, Y.; Celebi, M.; Gülcan, M.; Sönmez, M.; Zahmakiran, M. Palladium Nanoparticles Decorated on Amine Functionalized Graphene Nanosheets as Excellent Nanocatalyst for the Hydrogenation of Nitrophenols to Aminophenol Counterparts. *Journal of Hazardous Materials* **2019**, *369*, 96–107. https://doi.org/10.1016/j.jhazmat.2019.02.027.

(116) Richardson, M. J.; Johnston, J. H. Sorption and Binding of Nanocrystalline Gold by Merino Wool Fibres—an XPS Study. *Journal of Colloid and Interface Science* **2007**, *310* (2), 425–430. https://doi.org/10.1016/j.jcis.2007.01.075.

(117) Wu, G.; Johnston, C. M.; Mack, N. H.; Artyushkova, K.; Ferrandon, M.; Nelson, M.; Lezama-Pacheco, J. S.; Conradson, S. D.; More, K. L.; Myers, D. J.; Zelenay, P. Synthesis–Structure–Performance Correlation for Polyaniline–Me–c Non-Precious Metal Cathode Catalysts for Oxygen Reduction in Fuel Cells. *Journal of Materials Chemistry* **2011**, *21* (30), 11392. https://doi.org/10.1039/c0jm03613g.

(118) Ghosh, A.; Chandran, P.; Ramaprabhu, S. Palladium-Nitrogen Coordinated Cobalt Alloy towards Hydrogen Oxidation and Oxygen Reduction Reactions with High Catalytic Activity in Renewable Energy Generations of Proton Exchange Membrane Fuel Cell. *Applied Energy* **2017**, *208*, 37–48. https://doi.org/10.1016/j.apenergy.2017.10.022.

(119) Auciello, O.; Jean-François Veyan; Arellano-Jimenez, M. J. Comparative X-Ray Photoelectron Spectroscopy Analysis of Nitrogen Atoms Implanted in Graphite and Diamond. *Frontiers in Carbon* **2023**, *2*. https://doi.org/10.3389/frcrb.2023.1279356.

(120) Venezia, A. M., Rossi, A., Duca, D., Martorana, A., & Deganello, G. (1995). Particle size and metal-support interaction effects in pumice supported palladium catalysts. *Applied Catalysis A: General, 125*(1), 113–128. https://doi.org/10.1016/0926-860x(94)00286-x.

(121) Farmer, S., Kennepohl, D., & Morsch, L. (2024). Reactions of Carboxylic Acids - An Overview. In Organic Chemistry. LibreTexts . https://chem.libretexts.org/Bookshelves/Organic_Chemistry/Organic_Chemistry_(Morsch_et_al.).

(122) Nefedov, V. I., Zakharova, I. A., Moiseev, I. I., Porai-Koshitz, M. A., Vargaftik, M. N., & Belov, A. P. (1973). Study of palladium complex compounds by X-ray photoelectron spectroscopy. *Russian Journal of Inorganic Chemistry*, *18*(12), 3264-3268.

(123) Nefedov, V. I., Salyn, Y. V., Moiseev, I. I., Sadovskii, A. P., Berenbljum, A. S., Knizhnik, A. G., & Mund, S. L. (1979). *ESCA and X-ray spectral study of Pd(0), Pd(I) and Pd(II) compounds with triphenylphosphine ligands. Inorganica Chimica Acta, 35, L343–L344*. doi:10.1016/s0020-1693(00)93391-7.

(124) A. Tressaud; S. Khairoun; H. Touhara; Watanabe, N. X-Ray Photoelectron Spectroscopy of Palladium Fluorides. *Zeitschrift für anorganische und allgemeine Chemie* **1986**, *540* (9-10), 291–299. https://doi.org/10.1002/zaac.19865400932.

(125) Shyu, J. Z.; Otto, K.; Watkins, W. L. H.; Graham, G. W.; Belitz, R. K.; Gandhi, H. S. Characterization of Pd/γ-Alumina Catalysts Containing Ceria. *Journal of Catalysis* **1988**, *114* (1), 23–33. https://doi.org/10.1016/0021-9517(88)90005-x.

(126) Shafeev, G. A.; J.-M. Themlin; Bellard, L.; Marine, W.; A. Cros. Enhanced Adherence of Area-Selective Electroless Metal Plating on Insulators. *Journal of vacuum science & technology. A. Vacuum, surfaces, and films* **1996**, *14* (2), 319–326. https://doi.org/10.1116/1.579895.

(127) Ki Wook Kim; Alexej Gossmann; Winograd, N. X-Ray Photoelectron Spectroscopic Studies of Palladium Oxides and the Palladium-Oxygen Electrode. *Analytical Chemistry* **1974**, *46* (2), 197–200. https://doi.org/10.1021/ac60338a037.

(128) Nava, P.; Sierka, M.; Ahlrichs, R. Density Functional Study of Palladium Clusters. *Physical Chemistry Chemical Physics* **2003**, *5* (16), 3372–3381. https://doi.org/10.1039/b303347c.

(129) Tran, N. T.; Kawano, M.; Dahl, L. F. High-Nuclearity Palladium Carbonyl Trimethylphosphine Clusters Containing Unprecedented Face-Condensed Icosahedral-Based Transition-Metal Core Geometries: Proposed Growth Patterns from a Centered Pd13 Icosahedron. *Journal of the Chemical Society, Dalton Transactions* **2001**, No. 19, 2731–2748. https://doi.org/10.1039/b103547a.

(130) Basiuk, V. A.; Alzate-Carvajal, N.; Laura Verónica Henao-Holguín; Rybak-Akimova, E. V.; Basiuk, E. V. Coordination Functionalization of Graphene Oxide with Tetraazamacrocyclic Complexes of Nickel (II): Generation of Paramagnetic Centers. *Applied Surface Science* **2016**, *371*, 16–27. https://doi.org/10.1016/j.apsusc.2016.02.166.

(131) Basiuk, V. A.; Rybak-Akimova, E. V.; Basiuk, E. V. Graphene Oxide and Nanodiamond: Same Carboxylic Groups, Different Complexation Properties. *RSC Advances* **2017**, *7* (28), 17442–17450. https://doi.org/10.1039/c7ra016.

CHAPTER 5

Innovative nanohybrids: crafting silver nanoparticles onto multiwalled carbon nanotube powder and paper

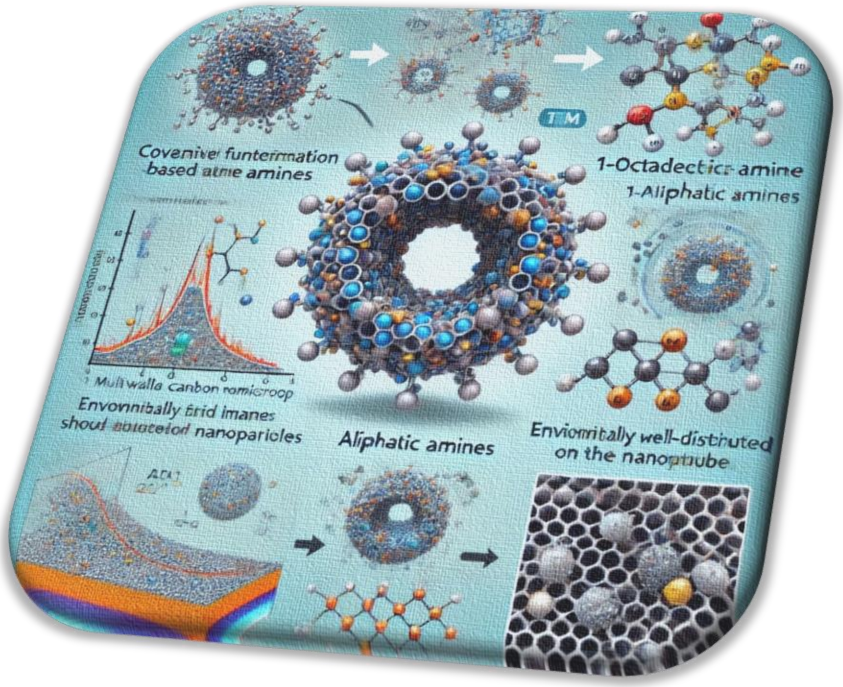

ABSTRACT

This chapter reports on the synthesis and characterization of nanohybrids based on multiwalled carbon nanotubes chemically modified with aliphatic amines 1-octadecylamine and 1,8-diaminooctane)— and further decoration with silver nanoparticles. Two macroscopic types were studied: powder and paper-like hybrids. Pre-oxidation of the carbon nanotubes was necessary to assure processability, and buckypaper was fabricated using an established protocol. Ag nanoparticles were generated using silver nitrate and citric acid as a mild/eco-friendly reducing agent.

Dispersibility tests showed good solvent dispersibility, particularly in the paper series when a non-ionic surfactant was included. FTIR confirmed surface chemistry changes from amine functionalization. Thermal analysis revealed that higher silver content reduced thermal stability, especially in the powder series. Scanning electron microscopy demonstrated better Ag nanoparticle size distribution and coverage on amine-functionalized nanotubes. Energy dispersive X-ray and X-ray photoelectron spectroscopy showed consistent chemical composition, with the latter indicating higher oxygen, metallic silver, and nitrogen in aminated samples. X-ray diffraction revealed changes in crystallinity and interlamellar spacing, influenced by nitrogenated ligands.

5.1 Introduction

Nanomaterials have garnered significant attention across various sectors due to their unique properties and versatility. Among these, carbon nanotubes (CNTs) and buckypaper (BP) stand out as promising candidates for both structural and functional applications.[1-9] While extensive research exists on CNTs in powder form, the fabrication of buckypaper offers several compelling advantages,[10-14] for example superior mechanical properties. In fact, buckypaper, a self-supporting film composed of entangled carbon nanotubes, exhibits exceptional tensile strength, flexibility, and stiffness.[7] These unique properties make buckypaper an ideal candidate for high-performance applications, such as in the aerospace and automotive industries.[15] Particularly, multiwalled carbon nanotubes (MWCNTs) have shown immense potential across various applications, due to their unique structural, electrical, and thermal properties.[16] Notably, their high electrical and thermal conductivity, large surface area, remarkable mechanical strength, and enhanced electron transport capabilities surpass those of single-walled carbon nanotubes (SWCNTs), making MWCNTs an attractive candidate for the development of advanced nanomaterials.[16,17]

Functionalization of carbon materials, such as through the introduction of amine, thiol, or other functional groups, enhances the dispersion and integration of nanotubes within another matrix, leading to improved mechanical, electrical, and thermal properties of the resulting nanocomposites.[18] Compared to traditional approaches, gas-phase functionalization offers the advantage of precisely controlling the degree of functionalization while preserving the inherent properties of the carbon nanotubes.[19-22] The synergistic combination of metal nanoparticles and the carbonaceous framework can lead to advanced materials with diverse applications in biomedical engineering, energy storage, and environmental remediation.[23-27] MWCNTs serve as an ideal platform for the synthesis and stabilization of silver nanoparticles (AgNPs), owing to their high surface area and effective anchoring sites.[26,28-31]Advantages of focusing on silver include high electrical and thermal conductivity, catalytic properties, and antimicrobial activity.[32] Integrating silver nanoparticles in carbon nanotube foil results in the formation of highly stable and homogeneous structures with unique optical, electronic, and catalytic characteristics,[33] applicable in fields such as sensing and biomedical devices.[17] Understanding the formation, structural characteristics, and interfacial interactions in these systems is essential for optimizing their performance and enabling practical utilization.

The primary objective of this study was to demonstrate the feasibility of creating nanomaterials based on MWCNTs and AgNPs under mild and environmentally friendly conditions by pre-treating MWCNTs with amine molecule vapour. A thorough comparison of the characteristics of MWCNT-AgNP hybrids made from pure nanotubes and their gas-phase functionalized equivalents using aliphatic amines was conducted. Focusing on the shape and dispersion of AgNPs, this study advances the environmentally sustainable synthesis of materials that may serve for diverse applications. For instance, combining the intrinsic properties of metals with bioactive ligands such as amines offers numerous opportunities for designing compounds targeting specific biological processes.[34-36]

5.2 Experimental section

5.2.1 Materials

Multiwalled carbon nanotubes (≥ 95 wt% purity, diameter: < 8 nm and length of 10-50 µm) acquired from Nanostructured & Amorphous Materials Inc., were used. Reagents 1-Octadecylamine (ODA; ≥ 99 %), 1,8-diaminooctane (DAO; ≥ 98 %), citric acid (≥ 99.5 %), silver nitrate (≥ 99 %), 2-propanol (≥ 99.8 %) nitric acid and Triton™ X-100 (laboratory grade) from Sigma-Aldrich were used as received.

5.2.2 Oxidation of multiwalled carbon nanotubes

To modify the reactivity of the pristine carbon nanotubes, while taking care to preserve their intrinsic properties, they were subjected to acid treatment at controlled temperatures as explained in detail in Chapter 2 *(see section 2.1.2 point 1).* The sample obtained at this point is hereafter called $MWCNTs_{(ox)}$.

5.2.3 Fabrication of free-standing multiwalled carbon nanotubes paper

For the fabrication of the multiwalled carbon nanotubes-based paper, hereinafter called *buckypaper* and abbreviated as BP, the protocol explained in Chapter 2 *(see section 2.1.2 point 2),* was employed.

5.2.4 Amine gas-phase functionalization of oxidized multiwalled carbon nanotubes

The chemical functionalization of $MWCNTs_{(ox)}$ in powder or paper form was carried out as explained in Chapter 2 *(see section 2.1.3)*. In the following, the 1-octadecylamine-funtionalized samples are labelled as MWCNTs+ODA and BP+ODA, while the 1,8-diaminooctane-functionalized samples are denoted as MWCNTs+DAO and BP+DAO.

5.2.5. Deposition of silver nanoparticles

We employed the protocol explained in Chapter 2 *(see section 2.1.4.1)* for the AgNPs formation and deposition applied in our previous works.[37,38] The functionalized and silver-decorated samples are denoted hereafter as MWCNTs+ODA+Ag, BP+ODA+Ag, MWCNTs+DAO+Ag, and BP+DAO+Ag. Control samples obtained by applying only thermal treatment to $MWCNTs_{(ox)}$ and BP (without amine functionalization) are labelled MWCNTs+Ag and BP+Ag in the following.

5.3 Results and discussion

5.3.1 Characterization of MWCNTs+Ag and BP+Ag hybrids

As a first approach to detect changes in the surface chemistry following amine functionalization and decoration with silver nanoparticles, we performed dispersibility tests using solvents with different polarities. Two series of tests were performed: the powder samples were dispersed in toluene and 2-propanol (Fig. 5.1) and the paper-like samples were tested in water and 2-propanol (Fig. 5.2). These solvents were chosen after preliminary testing with several candidates to identify those that produced the most significant differences in dispersibility.

Fig. 5.1 shows the photographs of MWCNTs dispersed in toluene and 2-propanol immediately after sonicating for 10 min (0 h) and after 24 h.

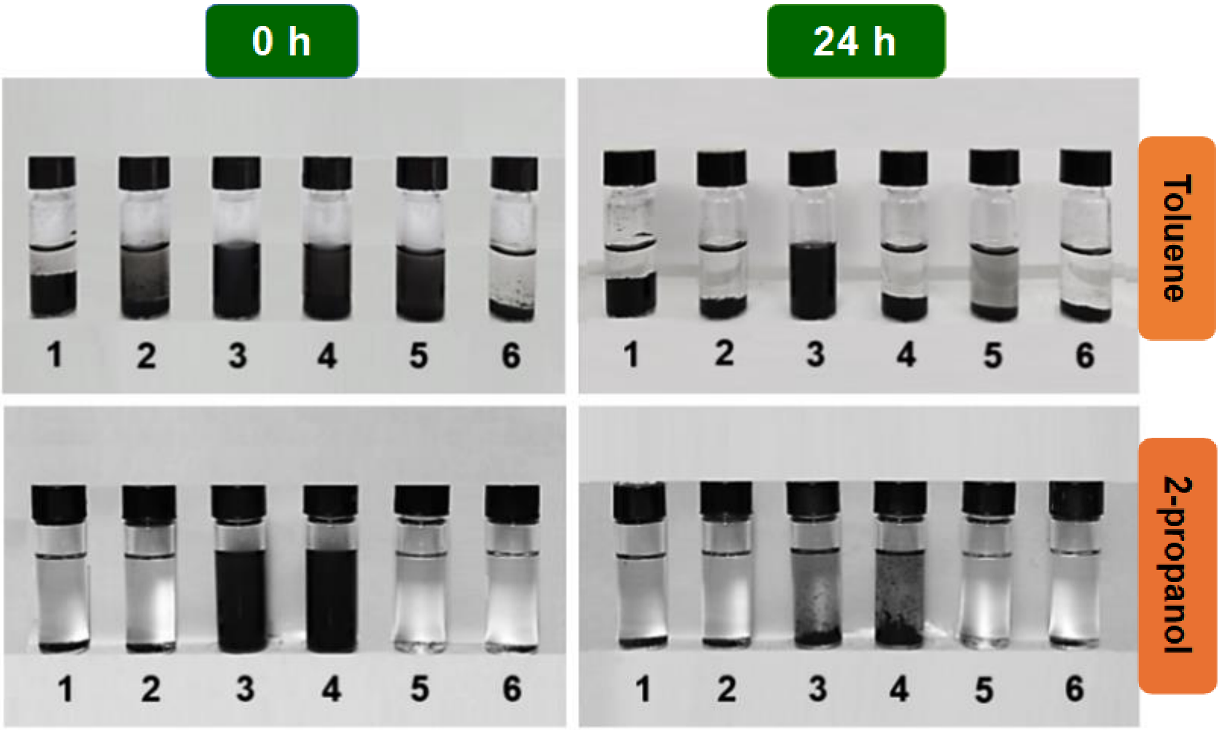

Fig. 5.1. Dispersibility tests for MWCNTs samples in toluene and 2-propanol: (1) MWCNTs$_{(ox)}$, (2) MWCNTs+Ag, (3) MWCNTs+ODA, (4) MWCNTs+ODA+Ag, (5) MWCNTs+DAO, and (6) MWCNTs+DAO+Ag. The images were taken immediately after 10-min ultrasonication (0 h) and 24 h later.

Despite the oxidation of nanotubes, they preserve some hydrophobic characteristics, leading to partial solubility in toluene. However, the decoration with silver and the functionalization with amines play a crucial role in the dispersibility of the systems, generally restoring hydrophobic behaviour. Notably, MWCNTs+DAO+Ag remained partially soluble in toluene. After 24 hours, most dispersions had become unstable, except for the sample containing only ODA, whose long hydrocarbon chain promoted its hydrophobic characteristics over time. In 2-propanol, which has an intermediate polarity,[39] significant differences were observed. The ODA-containing samples remained well dispersed, likely due to the solvent's ability to dissolve many non-polar compounds.[40] and this trend remained in time. The non-functionalized and DAO-functionalized samples, however, exhibited instability in both solvents, suggesting that these samples share some common surface characteristics.

Fig. 5.2 illustrates the dispersibility of the carbon nanotube-based paper in two polar solvents (water and 2-propanol). Notably, most samples remained dispersible, a behaviour differing from the powder samples. This discrepancy can be attributed to the use of Triton X-100 as a surfactant in buckypaper fabrication. During sonication, the surfactant molecules detach and dissolve in both solvents, enhancing dispersibility.[41] When the nanotubes are functionalized with ODA, its hydrophobic properties hinder solubility in water, but dispersibility in 2-propanol is favourable for both powder and paper forms. The DAO-containing samples exhibited a lower chemical affinity for 2-propanol, especially in the powder form, likely due to the absence of the surfactant.

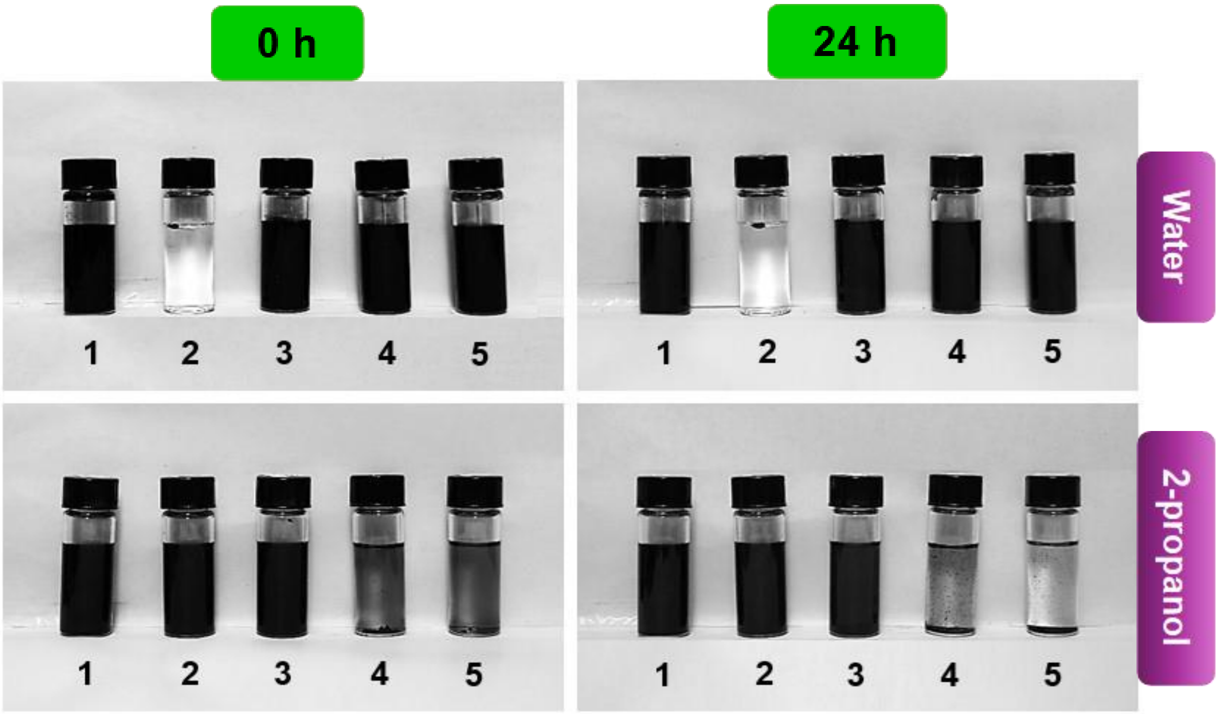

Fig. 5.2. Dispersibility tests for BP samples in water and 2-propanol: (1) BP+Ag, (2) BP+ODA, (3) BP+ODA+Ag, (4) BP+DAO, and (5) BP+DAO+Ag. The images were taken immediately after 10-min ultrasonication (0 h) and 24 h later.

To further understand the impact of amine derivatization and AgNP decoration on the materials' surface chemistry, Fourier transform infrared (FTIR) spectroscopy measurements were conducted as explained in Chapter 2 (Fig. 5.3). The broad bands from 3455 to 3389 cm^{-1} are associated with -OH stretching in carboxyl and hydroxyl groups ($\nu_{\text{O-H}}$),[42] while the aminated samples displayed additional broad bands from 3431 to 3344 cm^{-1}, stemming from $\nu_{\text{N-H}}$ vibrations of secondary amines. This testifies to the covalent attachment of both ODA and DAO through amidation, giving rise to C-N bonds between graphitic sidewalls of adjacent MWCNTs.[43] (Fig. 5.3b).

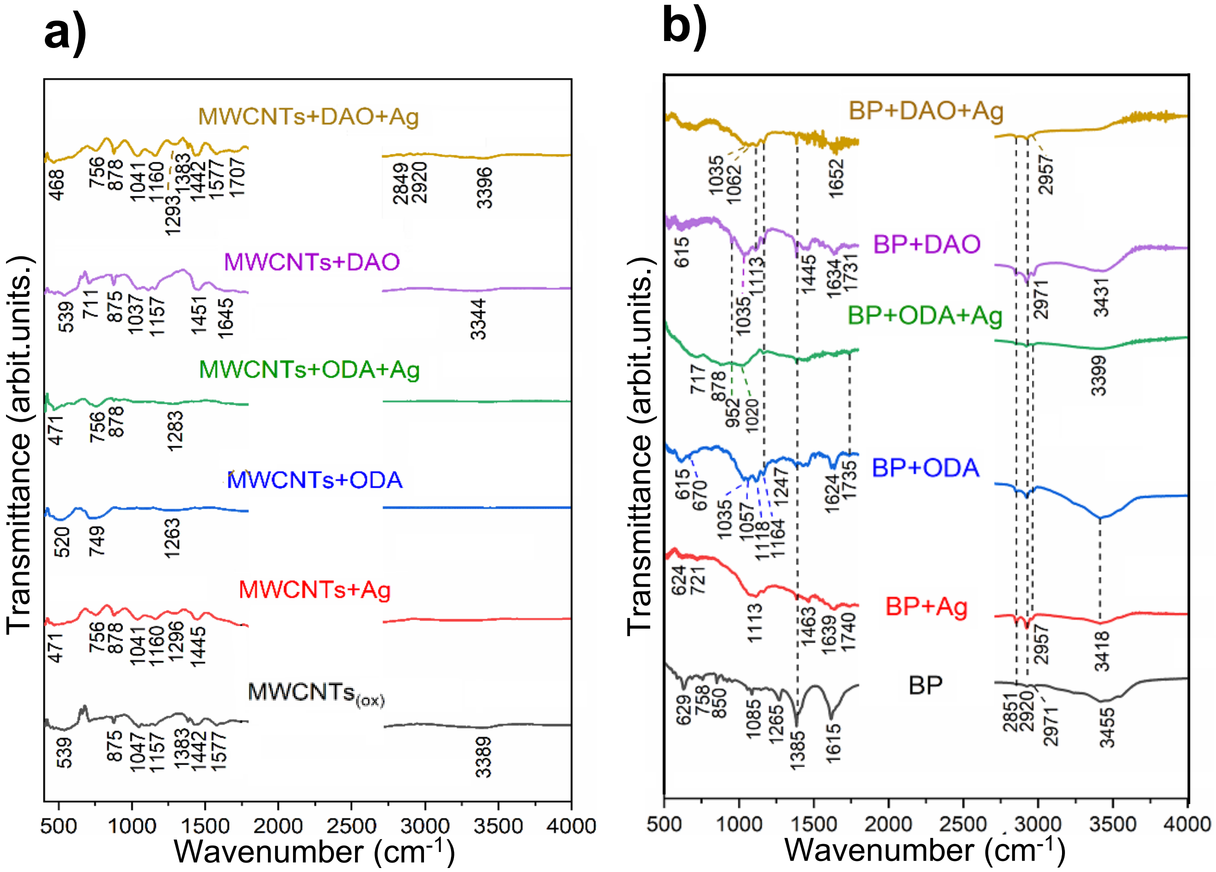

Fig. 5.3. FTIR spectra of oxidized and amine-functionalized: a) MWCNTs$_{\text{(ox)}}$, and b) BP samples before and after decoration with AgNPs.

The buckypaper-based series also exhibited distinct features between 2920 and 2849 cm^{-1}, consistent with C–H stretching vibrations of chemisorbed hydrogen,[44,45] more prominent in the powder-based series, especially in MWCNTs+DAO+Ag, pointing to a larger amount of aliphatic chains of the amines attached after the vaporous functionalization. The characteristic band at 1731-1740 cm^{-1} stems from carboxylic groups formed during acid treatment to induce oxidation;[46] this band vanished post-amine functionalization, indicating successful amidation. The appearance of bands at 1624 – 1645 cm^{-1} due to the $\nu_{\text{C=O}}$ absorption of 'amide I' and the absorption band of the C-N bond in amide/amine moieties between 1113-1118 cm^{-1}, further confirmed amine derivatization.

The bands appearing at 1442-1615 cm^{-1} are associated with C-C stretching (in-ring), whereas the one at 1383-1385 cm^{-1} arises from $\delta_{O\text{-}H}$ (in-plane). The bands in the range of 1020 – 1296 cm^{-1} demonstrate the presence of C-O bonds in various chemical surroundings.[42] Below 900 cm^{-1} bands associated with different types of deformation and bending of C-H bonds can be distinguished.[47,48]

Thermal analysis was carried out to monitor the thermal decomposition behaviour of the materials before and after amine functionalization and decoration with silver nanoparticles (for the experimental details see Chapter 2). The thermogram of MWCNTs$_{(ox)}$ (Fig 5.4a) shows two main weight losses: 98 % due to graphitic matrix combustion proceeding up to 705 °C and 2.1 % due to the combustion of the newly formed oxygenated functionalities up to 273 °C. The differential thermal analysis (DTA) curve confirms the maximum degradation rate of the graphitic lattice at 658 °C.

The weight loss pattern of MWCNTs+Ag (Fig. 5.4b) is similar to the previous sample with slight differences. The loss due to oxygen-containing groups is 1.4 % higher and their combustion is completed at 222 °C, while the combustion of the graphene backbone accounts for a loss of 94.9% of the total weight of this sample, with a maximum at 495 °C, according to the DTA curve. From the residual mass at temperatures above 589 °C, a silver content of 2.0 % is deduced.

The amine-containing samples (Figs. 5.4c,d) displayed notable differences. The ODA-functionalized sample (Fig. 5.4c) exhibited a 12.8 % mass loss up to 231 °C due to oxygenated groups and amino/amide derivatives, while the DAO-containing sample (Fig. 5.4d) showed a reduced mass loss of 5.3 % up to 225 °C, likely due to the differences in molecular weight of 1,8-diaminooctane (144.26 g/mol,[50]) compared to 1-octadecylamine (269.51 g/mol,[49]). As expected, graphitic carbon dominated in the composition of these samples, as proven by the weight loss of 77.1 % up to 546 °C for MWCNTs+ODA+Ag, and the weight loss of 94.8 % up to 856 °C for MWCNTs+DAO+Ag, while the silver content was estimated at 10.0 %, and 0.2 %, respectively. The difference in the decomposition temperature of the graphene backbone can therefore be directly associated with the metal content in all the silver-containing samples, with MWCNTs+Ag degrading at ~600 °C and MWCNTs+ODA+Ag at a lower temperature due to a five times higher metallic content. Conversely, MWCNTs+DAO+Ag decomposed at a much higher temperature because its silver content was only 1/10 that of MWCNTs+Ag. These results point to a catalytic effect of Ag as discussed in earlier studies.[38,51] The DTA curves indicate degradation maxima at 453 °C for MWCNTs+ODA+Ag and 510 °C for MWCNTs+DAO+Ag (42 °C less and 15 °C more in comparison to the non-aminated sample). These temperatures shift with the combustion completion temperatures.

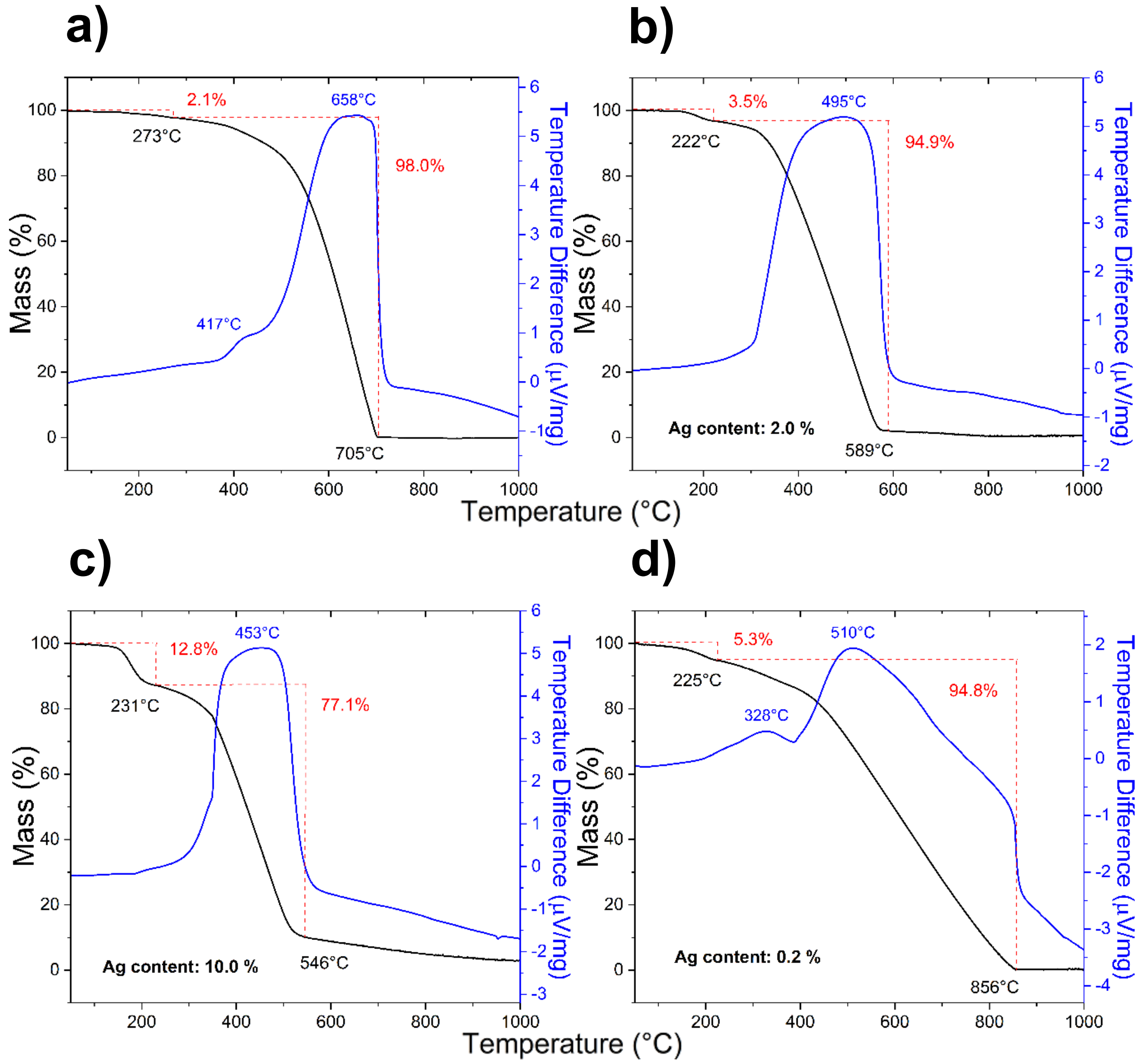

Fig. 5.4. Thermal gravimetric analysis (TGA) (black) and DTA (blue) curves for carbon nanotube-samples: a) MWCNTs$_{(ox)}$, b) MWCNTs+Ag, c) MWCNTs+ODA+Ag, and d) MWCNTs+DAO+Ag.

For the MWCNT papers, the thermal behaviour mirrored that of the powder samples. BP (Fig. 5.5a), showed 12.9 % weight loss up to 362 °C, higher than for MWCNT powder, due to pyrolysis of various species. The presence of Triton™ X-100 surfactant, which evaporates above 310 °C, contributes to this loss, with decomposition completed at 333 °C as shown in the DTA curve. Oxygen-containing groups and water molecules are lost in the first stage, with a degradation maximum at 418 °C, like MWCNTs$_{(ox)}$ (417 °C).

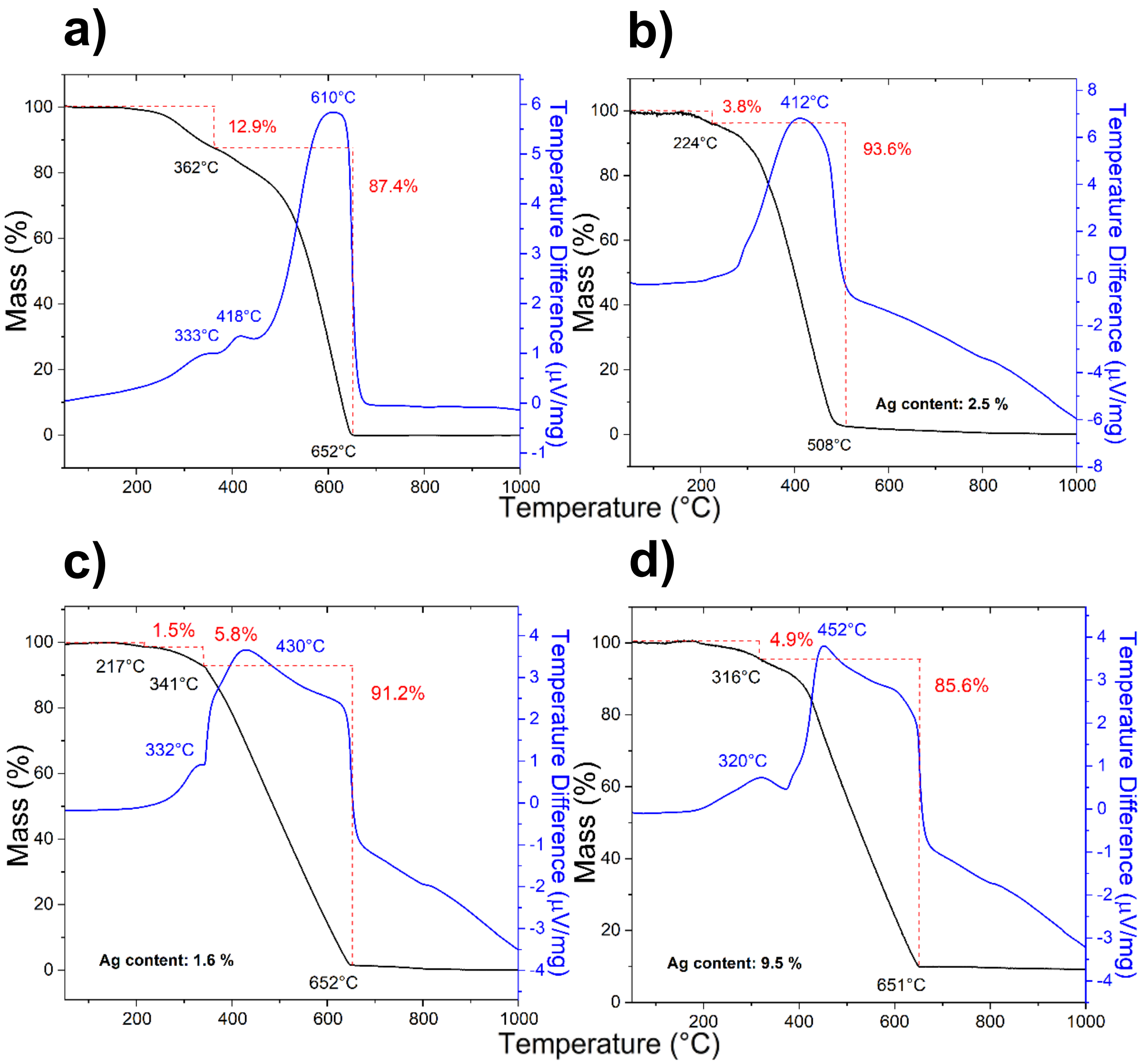

Fig. 5.5. TGA (black) and DTA (blue) curves for BP samples: a) BP, b) BP+Ag, c) BP+ODA+Ag, and d) BP+DAO+Ag.

The second weight loss corresponds to the combustion of the graphitic carbon up to 652 °C and amounts to 87.4 %. For this paper, the corresponding maximum in the DTA curve occurs at 610 °C, *i.e.* 48°C earlier than that of the pyrolysis of MWCNTs$_{(ox)}$ powder.

For the BP+Ag sample the thermos gravimetric analysis (TGA) curve (Fig. 5.5b) closely follows that of the powder homologue. While in MWCNTs+Ag the oxygenated groups contribute 3.5 % to the total weight, in the paper-like form it is 3.8 % and their removal is completed at 224 °C. The graphitic lattice comprises 93.6 % of the silver-decorated buckypaper and its combustion ends at 508 °C, compared 94.9 % for the powder sample, which also degraded at higher temperature. These differences could be attributed to the silver content, which was 2.5 wt% in BP+Ag and 2,0 wt% in MWCNTs+Ag. This 0.5 % higher Ag content can justify the earlier combustion of the paper. Its combustion is also catalyzed, with the maximum being reached at 412 °C (83 °C earlier), as clearly seen in the DTA curves.

The effect of the presence of amide and/or amine moieties on the degradation pattern of the aminated papers follows the same trend we observed for the graphene oxide–silver and -palladium nanohybrids (see Chapters 3 and 4 or refs 38,51). On one hand, the presence of oxygenated and aminated groups can be distinguished in BP+ODA+Ag (Fig. 5.5c), which first accounted for 1.5 wt% and were removed up to 217 °C, while the nitrogen-containing groups made up 5.8 wt% and pyrolyzed up to 341 °C. In BP+DAO+Ag (Fig. 5.5d) this distinction is not clearly seen and only one loss of 4.9 % up to 316 °C is observed. As for the powder samples, these mass differences could be associated with the molecular weight of each amine. The combustion of the nanotubes themselves has practically the same ending point in both cases (652 °C for BP+ODA+Ag and 651 °C for BP+DAO+Ag) with weight losses of 91.2 % and 85.6 %, respectively. However, the silver content is considerably different between them; 1.6 wt% for BP+ODA+Ag, and 9.5 wt% for BP+DAO+Ag. This difference could be explained by the two functional groups in DAO, providing twice as many coordination centres for AgNPs.[38,52-54] The DTA curves show decomposition maxima at 332 and 320 °C corresponding to the removal of oxygenated and aminated groups, and at 430 and 452 °C for the pyrolysis of the graphitic network in BP+ODA+Ag and BP+DAO+Ag, respectively.

The morphology of the powder and paper samples was studied by secondary electron scanning electron microscopy (SEM) imaging (SEI mode) as explained in Chapter 2; the micrographs of the powder samples are presented in Fig. 5.6. For MWCNTs+Ag (left column of Fig. 5.6) the powder grains appear ‘spongy’ and zooming in (central column in Fig. 5.6) µm-sized bright spots can be seen, which correspond to spherical silver nanoparticles, all of similar size (highlighted in yellow). In the highest magnification image (right column in Fig. 5.6) it is possible to distinguish the network of crisscrossed nanotubes (highlighted in green), decorated with some Ag particles (marked in yellow and red). The morphological features of MWCNTs+ODA+Ag (Fig. 5.6d-f) are similar but the ‘spongy’ nature is more pronounced (Fig. 5.6d), presumably because of the penetration of the hydrocarbonated chains into the matrix of the entangled nanotubes, and the Ag nanoparticles are more abundant and distributed more evenly (Fig. 5.6e,f). While the overall morphology of MWCNTs+DAO+Ag (Fig. 5.6g) is similar to the ODA-containing sample, the AgNPs look instead quite different (Fig. 5.6g-i). Their size and distribution are more heterogeneous and they also have various shapes. In Fig 5.6h particles as big as 2 µm are distinguished (see arrows), while the highest magnification image (Fig. 5.6i) shows a surface uniformly decorated with AgNPs of different shapes and a narrow size distribution ranging from 0.1 to 0.7 µm.

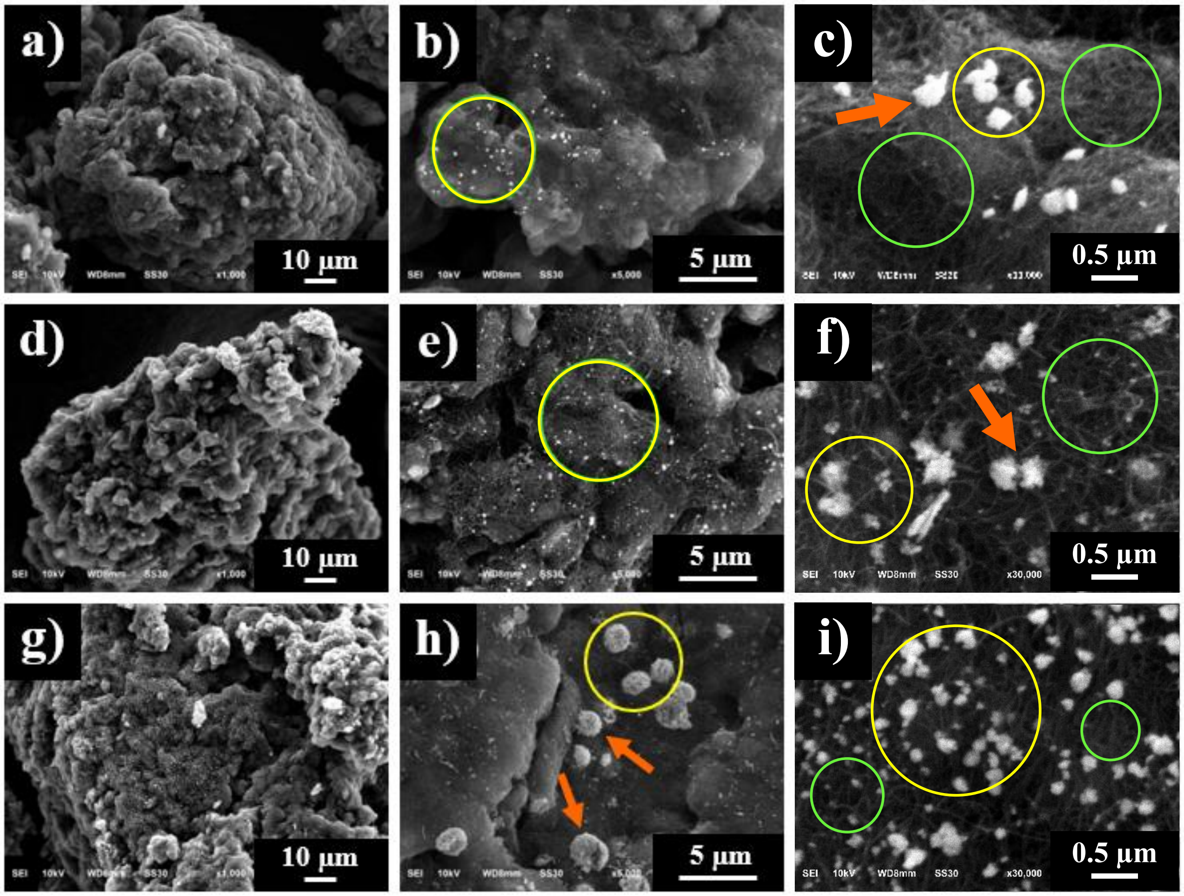

Fig. 5.6. Secondary electron SEM images of MWCNTs+Ag (a–c), MWCNTs+ODA+Ag (d–f), and MWCNTs+DAO+Ag (g–i) at different magnifications. Ag particles are highlighted in yellow and pointed out in red, whereas the nanotube network is circled in green. Scale bars: 10 μm (left column); 5 μm (middle column), and 1 μm (right column).

To highlight the differences in AgNP shape and distribution, we also collected backscattered electron SEM images (BEC mode), which enhance the contrast between light and heavy atoms (Fig. 5.7). Due to the small size of the Ag particles, the images at lowest magnification only show the dark surface of the carbon-based lattice with some degree of roughness (Figs. 5.7a,d,g). At higher magnification, for the MWCNTs+Ag an uneven particle distribution is evident in Figs 5.7b and c, with AgNP sizes ranging from less than 0.1 up to 0.5 μm. For the MWCNTs+ODA+Ag sample (Fig. 5.7e,f) the coverage of AgNPs was higher with a similar size distribution from less than 0.1 up to 0.5 μm and different shapes. In the micrographs of the MWCNTs+DAO+Ag (Fig. 5.7h,i) one sees that the AgNP coverage was much higher, the particles were predominantly spherical, with an estimated size from 0.1 to 0.7 μm. The differences in silver content were quantified with EDS and the results shown in Table 1 confirm that a higher silver content was achieved in the amine-containing samples.

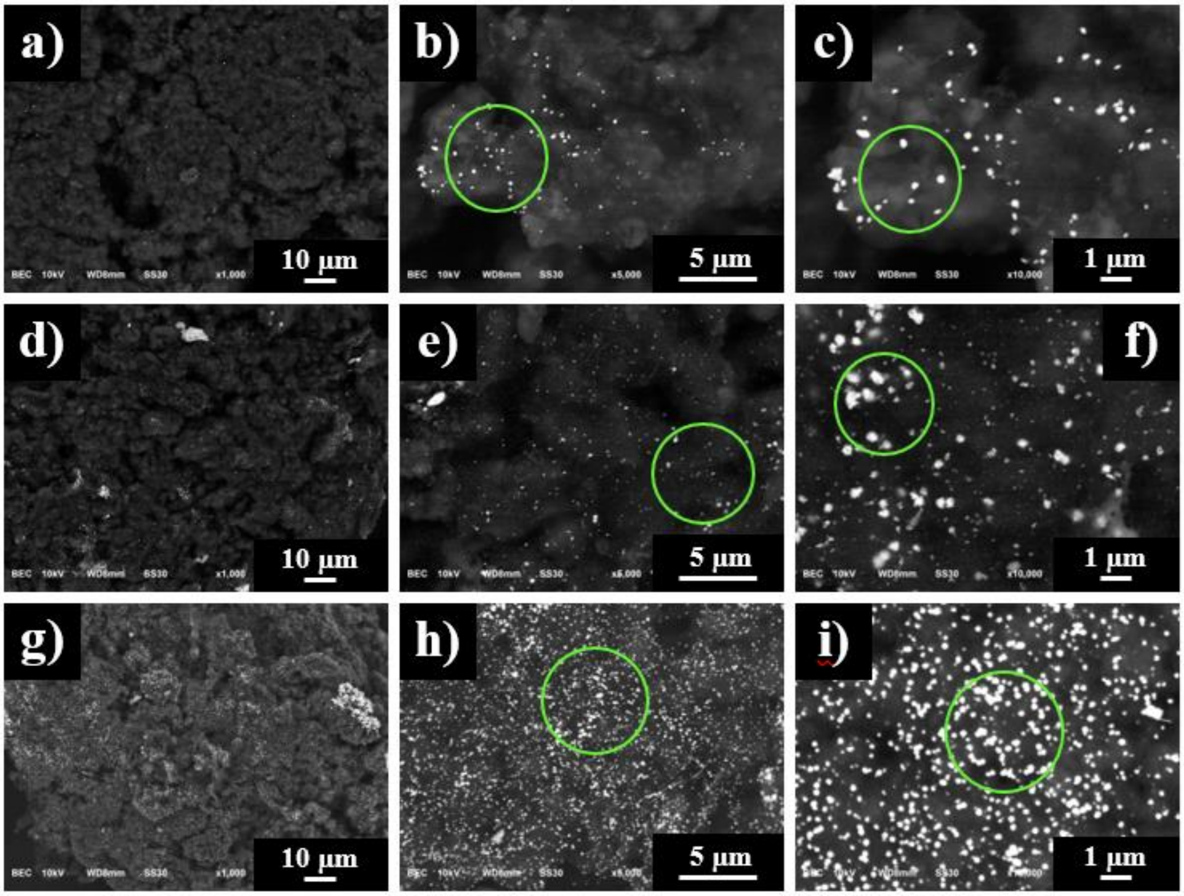

Fig. 5.7. Backscattered electron SEM images of MWCNTs+Ag (a–c), MWCNTs+ODA+Ag (d–f), and MWCNTs+DAO+Ag (g–i) at different magnification. Scale bars: 10 µm (left column); 5 µm (middle column), and 1 µm (right column).

Table 1. EDS results for the MWCNTs/AgNP series

Sample	**Weight (%)**	**Atomic (%)**
MWCNTs+Ag	C (K): 92.0 ± 0.7 O (K): 5.8 ± 0.7 Ag (L): 1.9 ± 0.5	C (K): 95.2 ± 0.4 O (K): 4.5 ± 0.5 Ag (L): 0.2 ± 0.06
MWCNTs+ODA+Ag	C (K): 86.6 ± 1.6 O (K): 9.9 ± 1.5 Ag (L): 3.6 ± 1.1	C (K): 91.7 ± 1.2 O (K): 7.9 ± 1.2 Ag (L): 0.4 ± 0.1
MWCNTs+DAO+Ag	C (K): 89.6 ± 1.6 O (K): 7.5 ± 1.2 Ag (L): 3.0 ± 0.5	C (K): 93.8 ± 1.0 O (K): 5.9 ± 1.0 Ag (L): 0.3 ± 0.06

Similarly, SEI and BEC SEM imaging was carried out to study the morphology of the buckypaper samples (Figs 5.8 to 5.10). Fig 5.8 shows structural differences in three areas of interest in the paper-like material: the cross-section, the side in contact with the filtration membrane during the buckypaper fabrication and the upper side of the paper. Fig. 5.8a,d,g show the cross-sectional images of the three samples from which the paper thickness can be determined: BP+Ag: 58 µm; BP+ODA+Ag: 59 µm, and BP+DAO+Ag: 31 µm. Comparing these thicknesses to that determined for BP (47 µm, image not shown), suggests that silver has penetrated the MWCNT network of BP+Ag and BP+ODA+Ag, leading to swelling. The opposite effect is observed in the DAO-containing sample, probably due to the cross-linking by bifunctional molecules, which leads to a more compact MWCNT network. Figs. 5.8b,e,h show the surfaces of the lower paper sides, which were in contact with the filtration membrane during buckypaper fabrication and Figs. 5.8c,f,i refer to the upper side of the papers. As expected, the lower sides exhibit a more uniform structure, whereas the upper surfaces are more disordered. A likely reason for this is that during the filtration process, well-shaped larger nanotube assemblies first sedimented on the filter surface, while the smaller and therefore lighter aggregates deposited later in a more random fashion.

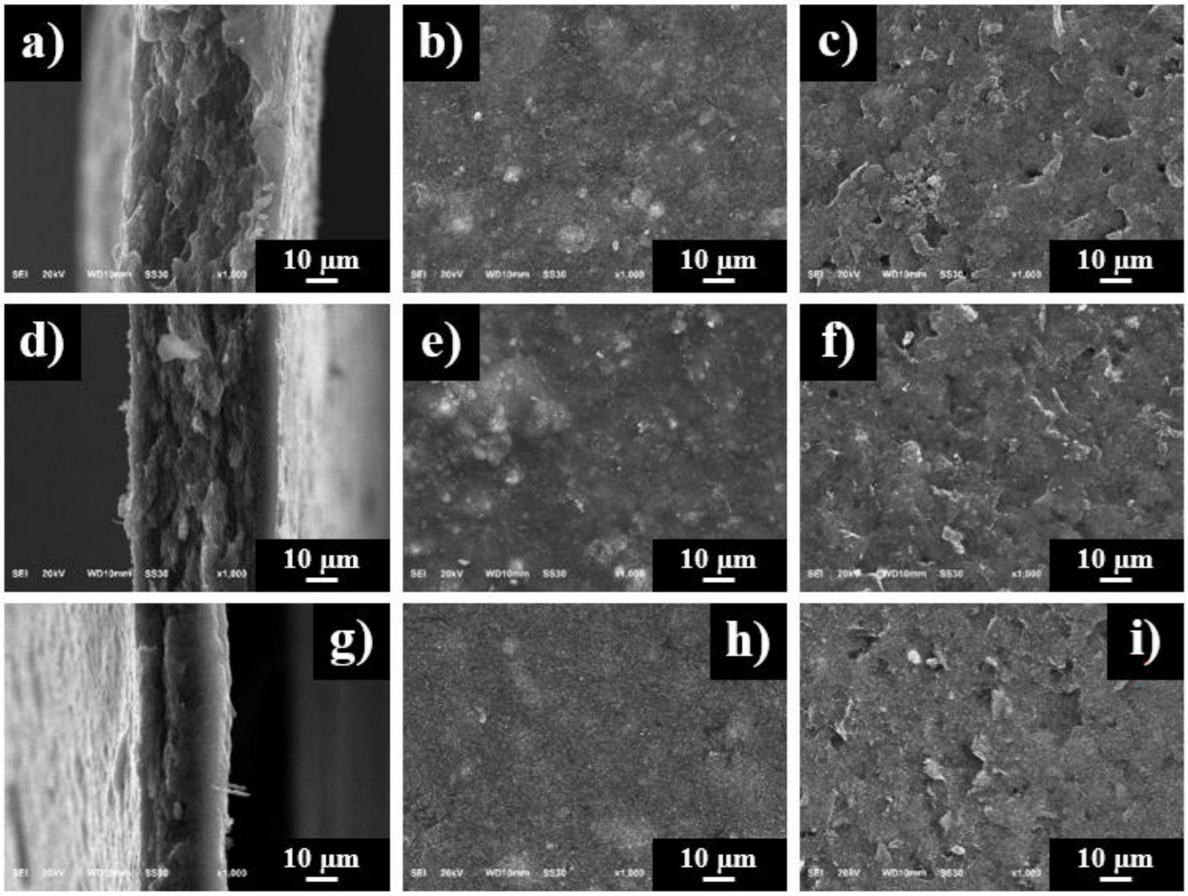

Fig. 5.8. Secondary electron SEM images of BP+Ag (a–c), BP+ODA+Ag (d–f), and BP+DAO+Ag (g–i) series. The left column (a,d,g) shows the cross-section images of the different samples; the middle column (b,e,h) refers the side of the paper that was in contact with the filter membrane during BP fabrication, and the right column (c,f,i) shows the opposite side. Scale bar: 10 µm.

To visualize the characteristics of the particles decorating both sides of the papers, SEI SEM images at higher magnification were collected (Fig. 5.9), from which the histograms of the particle sizes were obtained (Fig. 5.10). The first column in Fig. 5.9 shows the side being in contact with the filtration membrane during the BP formation, whereas the second column exhibit morphological features of the external side of the buckypapers. For the BP+Ag sample, a certain degree of agglomeration mainly on the external side of the BP can be seen. Although the lower side exhibits a slightly denser coverage, the agglomerates formed are rather dispersed. Irregularly shaped particles were formed on both sides. the average particle size on the lower side was 0.06 ± 0.03 µm, whereas on the upper side it was 0.14 ± 0.05 µm (first column in Fig. 5.10).

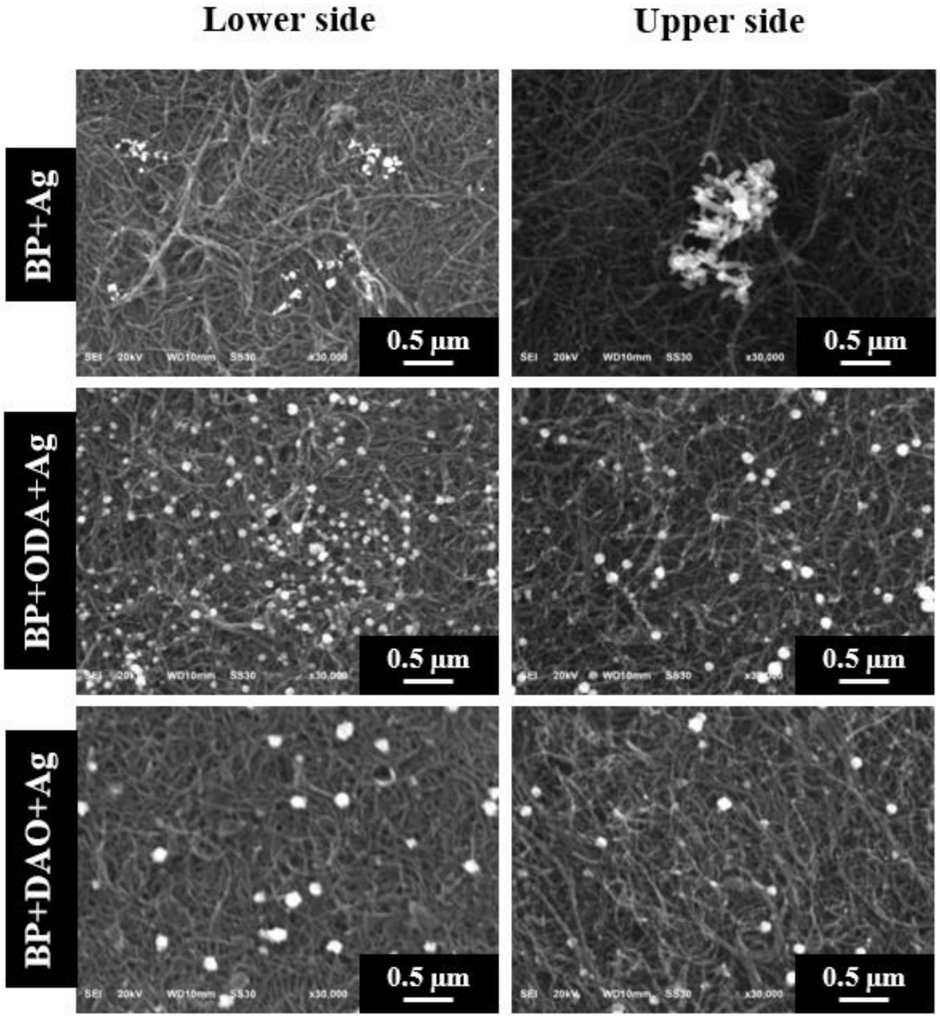

Fig. 5.9. Secondary electron SEM images for the set of the BP/AgNP series. The columns highlight the size and distribution of the particles attached on the side of the paper that was in contact with the filter membrane during paper fabrication (lower side) and on the upper side of the buckypaper. Scale bar: 0.5 µm.

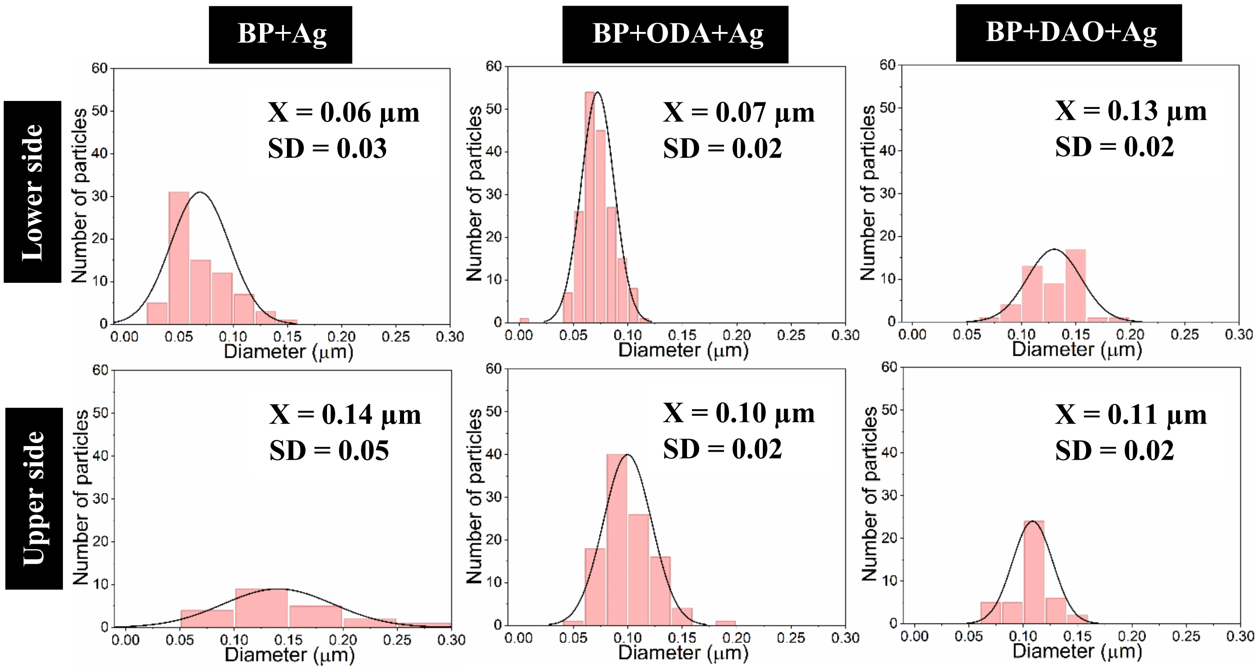

Fig. 5.10 Particle size distribution histograms obtained by SEM imaging for the set of the BP/AgNP series. The first row shows the distribution of particles on the lower paper side being in contact with the filter membrane during BP fabrication, and the second row shows the particle size distribution on the upper side.

The decoration pattern was quite different for the aminated samples. In BP+ODA+Ag, the particles were more densely and evenly distributed with a narrow size distribution as presented in the central column of Fig. 5.10, where the size on the side originally in contact with the filter was 0.07 ± 0.02 µm whereas on the opposite side it was 0.10 ± 0.02 µm. For the BP+DAO+Ag, the coverage of AgNPs was lower on both sides of the paper than for BP+ODA+Ag. On both sides, the size of the particles was larger than for BP+ODA+Ag, which is quantified in the third column of Fig. 5.10, where size distributions of 0.13 ± 0.02 µm for the lower side, and 0.11 ± 0.02 µm for the upper side are reported. Comparing both sides, one sees that the coverage was more efficient on the low side of the paper in all the cases.

To highlight the contrast between the nanotube network and the Ag particles embedded in it, BEC SEM images were acquired at different magnifications and are shown in Fig. 5.11. The first column shows the cross-sectional image for each buckypaper, whereas the images in the second and third columns were collected on the two sides of each sheet. Here two trends can be confirmed: 1) the effect of the amine modification on the decoration pattern mitigating agglomeration, and 2) the more efficient decoration with AgNPs on the lower side of the papers with the presence of ODA promoting the most homogeneous coverage. In Fig. 5.11a,d,g the penetration of some particles between the nanotubes can be observed, which is also promoted by the grafted amine moieties.

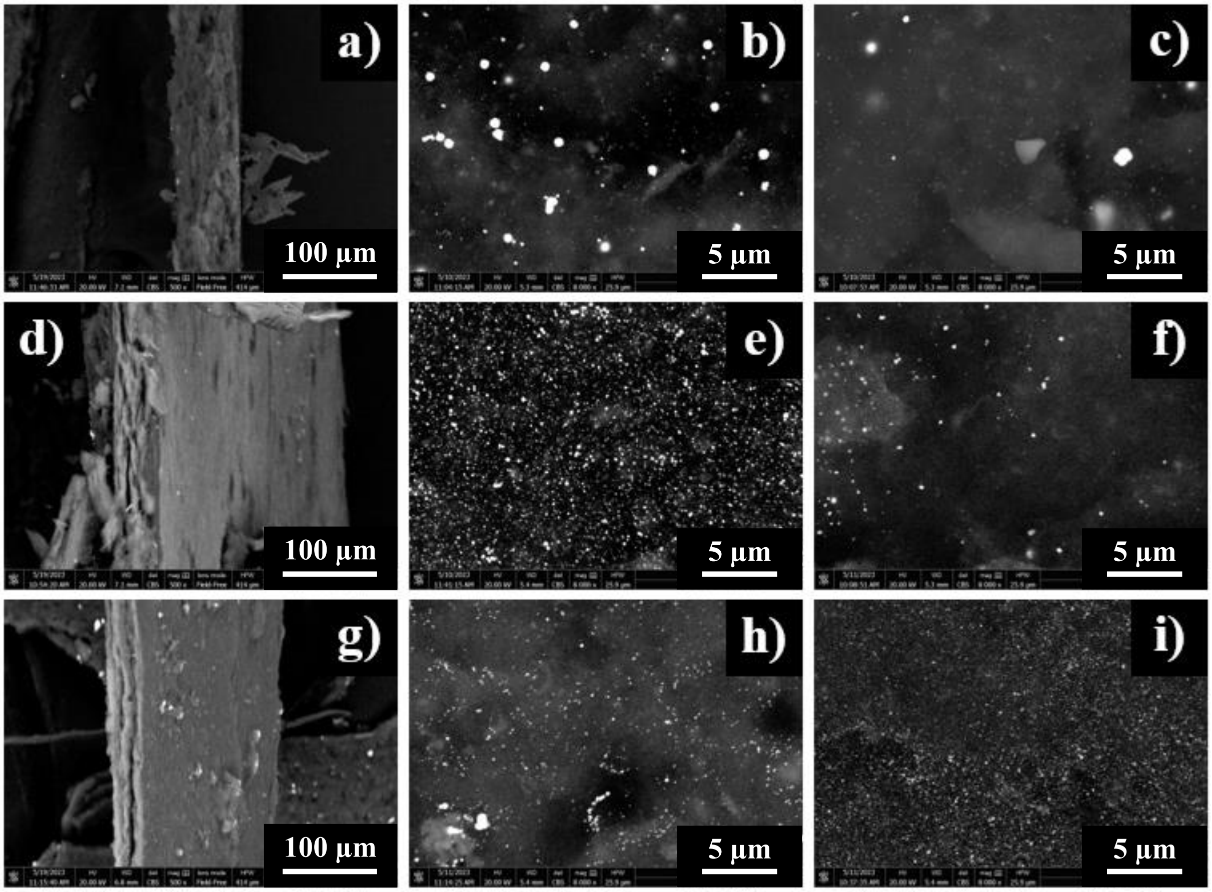

Fig. 5.11. Backscattered electron SEM images of BP+Ag (a–c), BP+ODA+Ag (d–f), and BP+DAO+Ag (g–i). The left column (a,d,g) shows the cross-section images of the different buckypapers; the middle column (b,e,h) exhibits the particle distribution within the lower side that was in contact with the filter membrane during BP fabrication, and the right column (c,f,i) shows the tendency in the upper side of the buckypaper. Scale bars: 100 µm (cross-section) and 5 µm (both sides).

All the features observed by SEM imaging were confirmed through Energy Dispersive Spectroscopy (EDS) studies (Table 2), where quantification of the Ag content demonstrates that the decoration with AgNPs is promoted by the presence of amines, being slightly more favoured by the 1-octadecylamine chains.

Table 2. EDS results for the BP/AgNPs series

	Region			
	Lower side		Upper side	
Sample	Weight %	Atomic %	Weight %	Atomic %
BP+Ag	C (K): 96.3 ± 0.2 O (K): 3.5 ± 0.1 Ag (L): 0.4 ± 0.1	C (K): 97.3 ± 0.02 O (K): 2.6 ± 0.1 Ag (L): 0.04 ± 0.01	C (K): 96.8 ± 0.8 O (K): 2.7 ± 0.9 Ag (L): 0.3 ± 0.04	C (K): 97.8 ± 0.7 O (K): 2.0 ± 0.7 Ag (L): 0.04 ± 0
BP+ODA+Ag	C (K): 95.4 ± 2.0 O (K): 3.1 ± 1.7 Ag (L): 1.5 ± 0.3	C (K): 97.5 ± 1.4 O (K): 2.4 ± 1.4 Ag (L): 0.2 ± 0.04	C (K): 96.6 ± 0.4 O (K): 2.3 ± 0.2 Ag (L): 1.1 ± 0.3	C (K): 98.2 ± 0.2 O (K): 1.7 ± 0.2 Ag (L): 0.1 ± 0.03
BP+DAO+Ag	C (K): 94.8 ± 0.4 O (K): 3.3 ± 0.7 Ag (L): 1.0 ± 0.4	C (K): 96.8 ± 0.2 O (K): 2.6 ± 0.6 Ag (L): 0.1 ± 0.04	C (K): 94.2 ± 0.5 O (K): 3.4 ± 0.5 Ag (L): 0.8 ± 0.1	C (K): 96.4 ± 0.4 O (K): 2.6 ± 0.4 Ag (L): 0.1 ± 0.02

Since some particles were too small to estimate their size by SEM, TEM imaging was performed at different magnifications as detailed in Chapter 2 (Figs. 5.12 and 5.13). The images look rather similar: the coaxial nanotube sidewalls can be discerned, as well as the inner cavity, and comparing MWCNTs+Ag (Fig. 5.12c) with MWCNTs+ODA+Ag (Fig. 5.12f), one also notices that the surface of the nanotubes is smoother in the former, probably because in the amine moieties grafted to the nanotubes in MWCNTs+ODA+Ag were decomposed by the high-energy electron beam of TEM.[55] However, where one can clearly see differences are the shape and the size of the AgNPs. In MWCNTs+Ag they have diameters from 15 to 40 nm, while in MWCNTs+ODA+Ag they measure from 10 to 60 nm and in MWCNTs+DAO+Ag their size varies between 30 to 150 nm.

Similarly, TEM studies were carried out for the buckypapers (Fig. 5.13). As for the powder samples, well-defined single nanotubes can be distinguished and in the aminated samples, the outer tube surface is covered by amorphous carbon originating from the amine decomposition, as seen for the powder samples. Remarkably, in the BP+ODA+Ag sample, the nanotubes exhibit a wider diameter, likely due to the ‘swelling’ effect caused by ODA moieties, which intercalate between the concentric cylinders of the MWCNTs increasing the space between them. The intercalation is facilitated by the fact that many nanotubes don’t seem to be capped – see for example the one below the big AgNPs in the high magnification image of BP+ODA+Ag in Fig. 5.13. This observation agrees with the trend observed in SEM where the BP+ODA+Ag sample is the thickest. The Ag nanoparticle sizes deduced from TEM imaging are smaller than for the powder samples, namely 5-10 nm for BP+Ag, 5-50 nm for BP+ODA+Ag and 10-100 nm for BP+DAO+Ag. Notably, for the latter the micrographs clearly evidence the presence of nanoclusters formed primally by spherical nanoparticles.

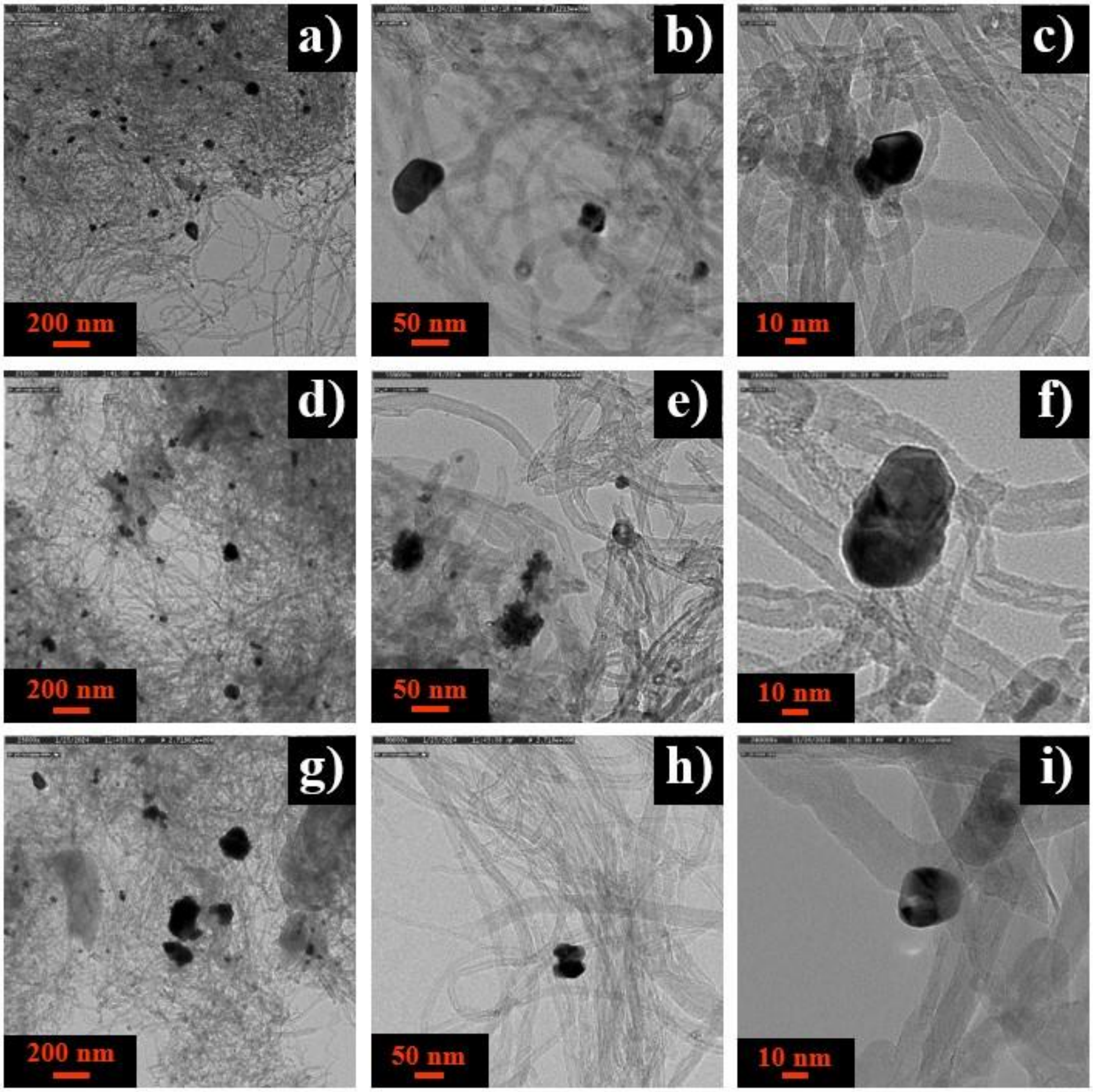

Fig. 5.12. Bright-field TEM images of MWCNTs+Ag (a-c), MWCNTs+ODA+Ag (d-f) and MWCNTs+DAO+Ag (g-i) at different magnifications. Scale bars: 200 nm (left column); 50 nm (middle column), and 10 nm (right column).

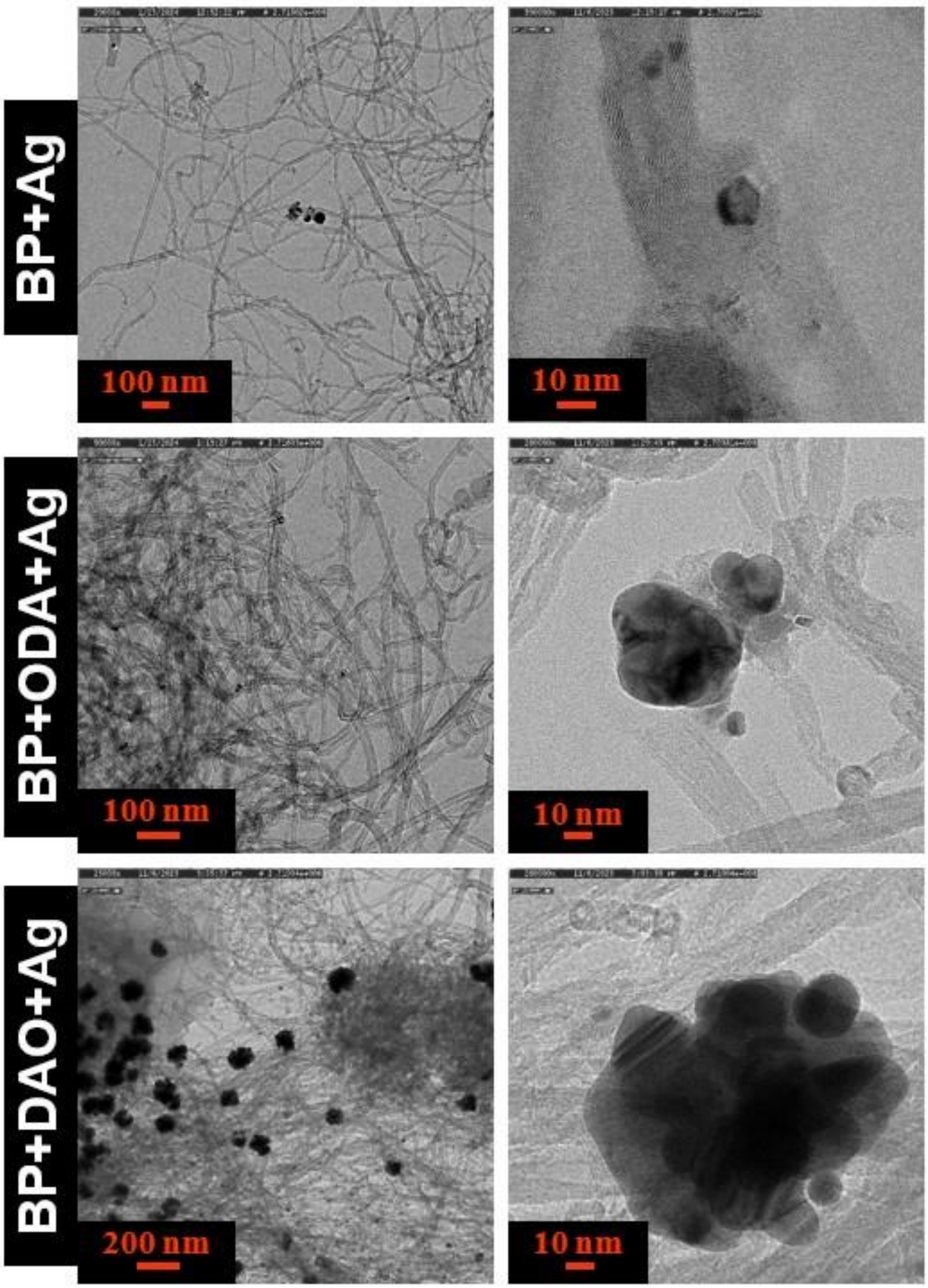

Fig. 5.13. Bright-field TEM images of the silver-containing buckypapers at different magnification. The scale bars are different for the different samples. In the left column: the scale bar is 100 nm for the BP+Ag and BP+ODA+Ag and 200 nm for BP+DAO+Ag. In the right column at the scale bar corresponds to 10 nm for all samples.

To investigate the composition of the MWCNTs$_{(ox)}$ and of the hybrids as well as gain insight into the chemical state of all the elements detected, X-ray photoelectron spectroscopy (XPS) analysis was carried out as detailed in Chapter 2. The survey spectra of the starting material and the silver-containing MWCNTs are displayed in Fig. 5.14 and show the characteristic peaks of all the elements expected: carbon and oxygen for MWCNTs$_{(ox)}$ and all hybrids, silver in all samples decorated with the metal nanoparticles and nitrogen in the amine-functionalized samples.

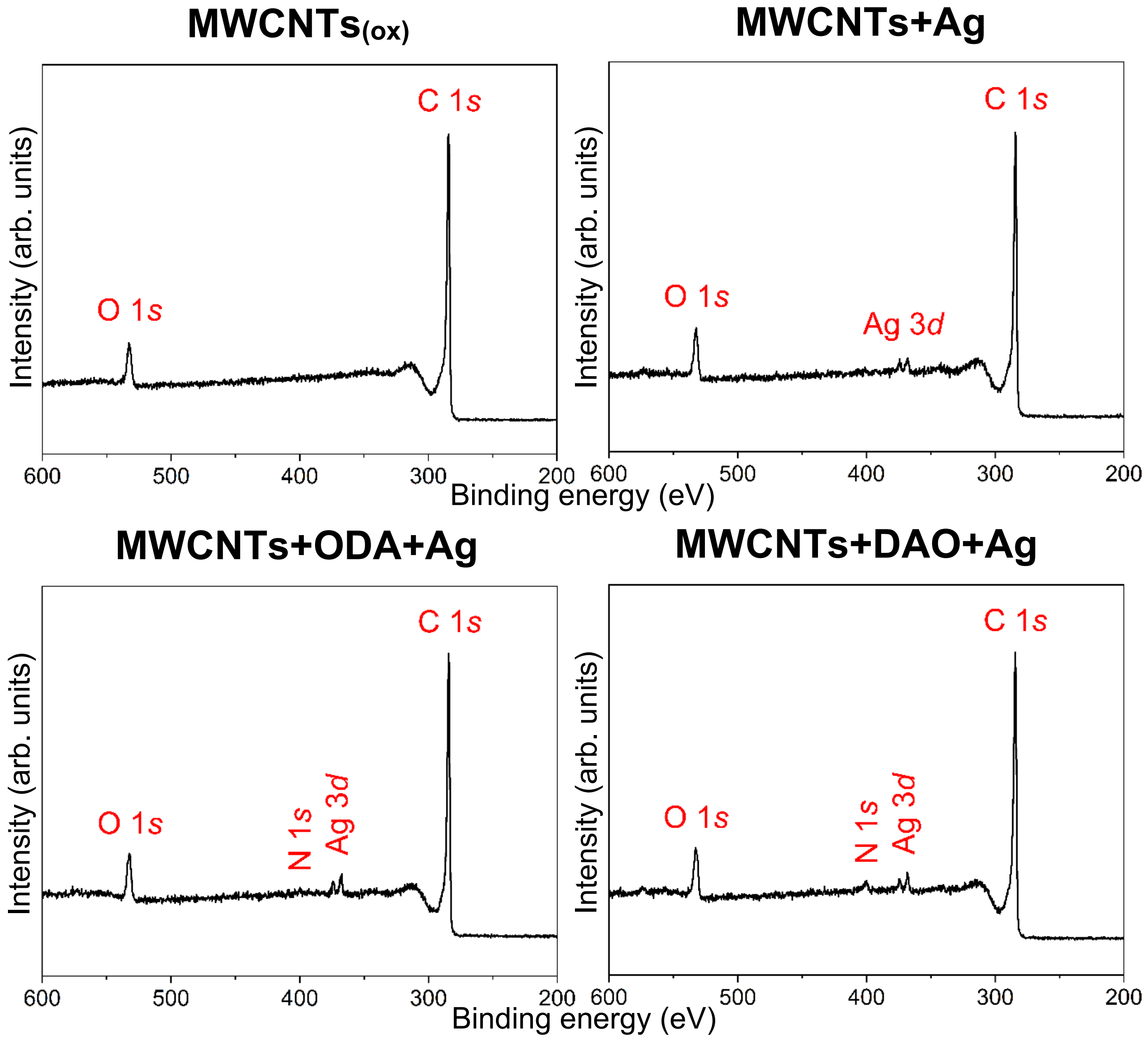

Fig. 5.14. XPS survey spectra for MWCNTs$_{(ox)}$, and for the MWCNTs+Ag, MWCNTs+ODA+Ag, and MWCNTs+DAO+Ag hybrids.

The detailed XPS spectra of the various core level regions are presented in Fig. 5.15, together with the corresponding fits. For all samples, the C 1*s* line (Fig. 5.15, left panel) can be fitted with six components but their relative intensities vary, as summarized in Table 3.

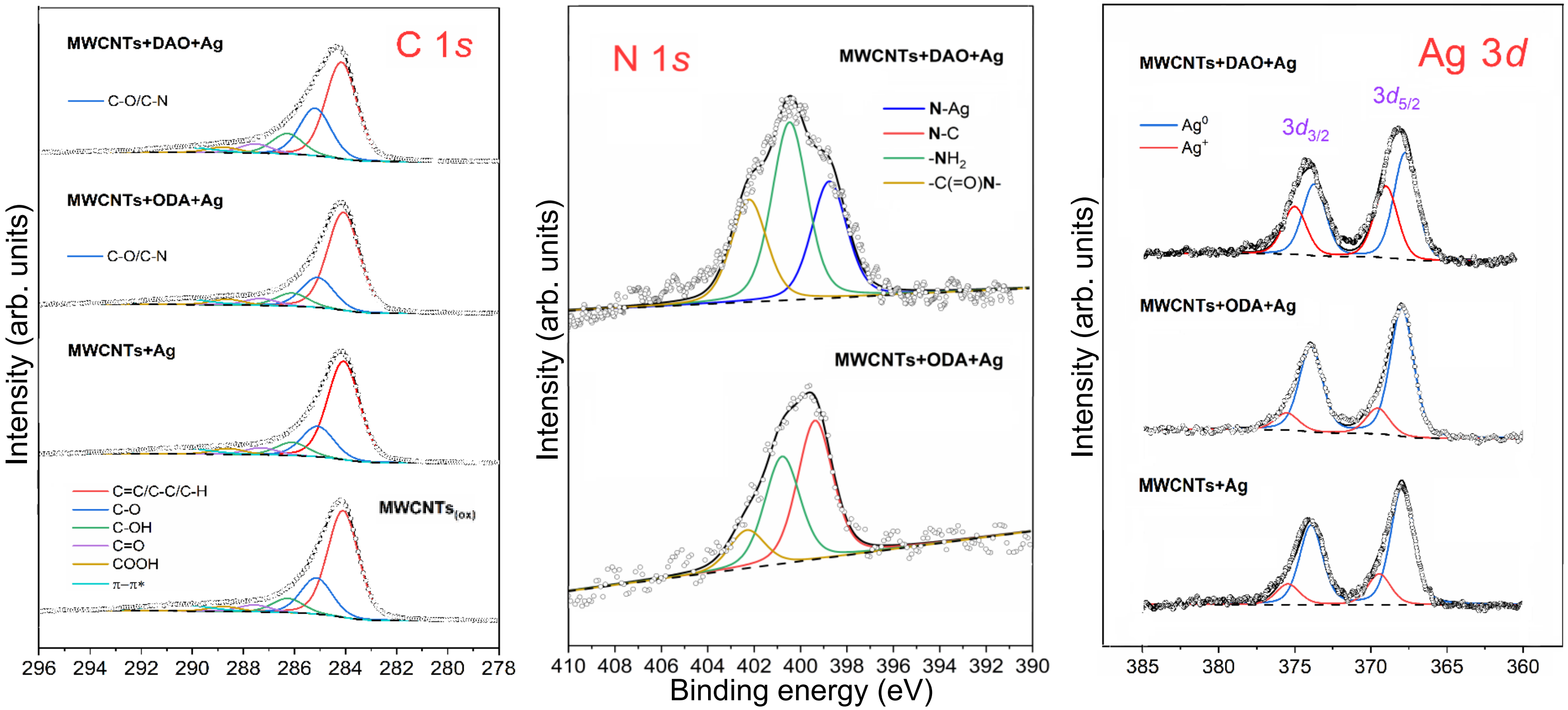

Fig. 5.15. XPS spectra of the C 1*s*, N 1*s* and Ag 3*d* core level regions for MWCNTs$_{(ox)}$, MWCNTs+Ag, MWCNTs+ODA+Ag, and MWCNTs+DAO+Ag samples. Raw spectra are shown as dots; the components derived from the fit are also shown, and sum, in black.

Table 3. MWCNTs/AgNPs series: XPS binding energies and relative contribution (in %) of the different chemical species to the total spectral intensity of the C1*s* photoemission line

Sample	Components (eV)					
	C=C/C-C/C-H (%)	**C-O (%)**	**C-OH (%)**	**C=O (%)**	**O=C-O (%)**	**π-π* shake-up (%)**
MWCNT$_{(ox)}$	**284.1** (58.8)	285.2 (20.0)	286.3 (7.8)	287.6 (3.8)	288.8 (2.8)	**290.5** (6.8)
MWCNTs+Ag	(59.3)	285.1 (18.3)	286.1 (7.9)	287.3 (4.2)	288.6 (3.5)	(6.7)
		C-O/C-N (%)				
MWCNTs+ODA+Ag	**284.2** (60.6)	**285.2** (22.3)	**286.3** (7.5)	**287.5** (3.2)	288.7 (2.8)	**290.4** (3.7)
MWCNTs+DAO+Ag	(51.2)	(25.2)	(10.8)	(4.9)	288.8 (2.9)	(5.0)

The main component at a binding energy (BE) of 284.1 eV corresponds to the C=C/C-C bonds of the MWCNTs$_{(ox)}$, but also contains contributions from C-H bonds at the open ends of the nanotubes and in the alkyl groups of the amines. Going up in binding energy, the next component at 285.1-285.2 eV stems from C-O bonds and is followed by the contributions from C-OH bonds at 286.1-286.3 eV, carbonyl groups (C=O) at 287.3-287.6 eV and carboxyl groups (O=C-O) at 288.6-288.8 eV. Finally, the small feature at a BE of 290.4-290.5 eV corresponds to the ***π-π**** shake-up satellite typical of aromatic carbon structures.[56,57] For the aminated samples the contribution at a BE of 285.2 eV not only derives from C-O but also from C-N bonds.

The relative intensities of the various components, also reported in Table 3 confirm the conclusions from the FTIR, thermal analysis and EDS: the component due to C-O bonds in the spectrum of the starting material confirms the success of the oxidation procedure. The favourable outcome of the amine-functionalization is corroborated by the main contribution due to carbon-carbon and carbon-hydrogen bonds being the most intense in the samples containing ODA, due to the long aliphatic chains as well as by the DAO-containing samples showing the highest spectral contributions due to C-O/C-N groups due to the molecule's bifunctionality.

Table 4. Aminated MWCNTs+Ag samples: XPS binding energies and relative contribution (in %) of the different chemical species to the total spectral intensity of the N1*s* photoemission line

	Components (eV)			
Sample	**N-Ag (%)**	**N-C (%)**	**$-NH_2$ (%)**	**–C(=O)N– (%)**
MWCNTs+ODA+Ag	---	399.4 (48.8)	400.8 (37.7)	402.3 (13.4)
MWCNTs+DAO+Ag	398.8 (29.4)	---	400.5 (44.8)	402.2 (25.8)

For the amine-containing samples, the detailed spectra of the N 1*s* line (bottom left panel of Fig. 5.15) along with their deconvolution are presented. Three main components can be identified. In the ODA-containing sample, the main component due to C-N bonds (48.8 %), expected for the long aliphatic amine, appears at a BE of 399.4 eV, whereas in the DAO-containing one, it refers to the dangling amino groups appearing at 400.5 eV (44.8 %). This peak is relevant as well in the ODA-containing sample appearing at 400.8 eV in a minor percentage (37.7 %) since fewer free functionalities are accounted. A common peak appears at BE 402.2-402.3 eV referring to the newly formed amide moieties, in agreement with FTIR and TGA/DTA results. The peak appearing at 398.8 eV in the DAO-containing sample suggests the successful coordination binding between nitrogen and silver. Further information regarding these peaks can be found in Table 4.

Important insight into the chemical composition of the AgNPs can be gained from the detailed spectra of the Ag 3*d* core level region (Fig. 5.15, bottom right panel). The two asymmetrical peaks correspond to the spin-orbit split Ag $3d_{5/2}$ and Ag $3d_{3/2}$ lines; for the assignment of the different components, we shall focus on the Ag $3d_{5/2}$ line.

The deconvolution of these peaks generates two components pointing to the coexistence of two chemical species. The first in a BE range of 367.7 – 368.0 eV and a contribution of 60.0 to 83.4 % to the total Ag 3*d* spectral line intensity reflects the predominance of metallic silver in the three samples. The minor component appearing at 369.0 – 369.5 eV, can be assigned to a silver (I) complex with carboxylate ions from the deprotonation of the carboxylic acids of the reducing citric acid during the AgNPs formation, as observed with palladium in Chapter 4. The spectral intensity of these species lay at 20.6, 16.6, and 40.0 % in MWCNTs+Ag, MWCNTs+ODA+Ag, and MWCNTs+DAO+Ag, respectively. The data are summarized in Table 5.

Table 5. MWCNTs/AgNPs series: XPS binding energies relative contribution (in %) of the different chemical species to the total spectral intensity of the Ag 3*d* photoemission line

	Components (eV)			
Species	**Ag (0)**		**Ag (I)**	
Line / **Sample**	**3*d*$_{5/2}$ (%)**	**3*d*$_{3/2}$ (%)**	**3*d*$_{5/2}$ (%)**	**3*d*$_{3/2}$ (%)**
MWCNTs+Ag	367.9 (79.4)	373.9	**369.5** (20.6)	**375.5**
MWCNTs+ODA+Ag	368.0 (84.7)	374.0	(15.3)	
MWCNTs+DAO+Ag	367.7 (60.0)	373.7	369.0 (40.0)	375.0

Since the XPS intensities are directly proportional to the elemental composition of the probed volume, the atomic percentage of the components of each sample is presented in Table 6. From these data concerning the stoichiometry of the surface of the powders, it can be highlighted that the ODA-containing sample exhibits the highest Ag loading (1.8 at%), followed by the DAO-containing sample (0.9 at%), and the non-aminated sample (0.7 at%). Although XPS and EDS don't probe the same depth and the probed area is different, the EDS data (Table 1) agree with the trend for the Ag-loading deduced from XPS.

Table 6. Elemental composition of the hybrids of MWCNTs and Ag nanoparticles in powder form, as deduced from the XPS spectra

Sample	Atomic %
MWCNTs+Ag	C: 91.9
	O: 7.5
	Ag: 0.7
MWCNTs+ODA+Ag	C: 86.4
	O: 9.0
	N: 3.1
	Ag: 1.6
MWCNTs+DAO+Ag	C: 90.9
	O: 5.0
	N: 3.2
	Ag: 0.9

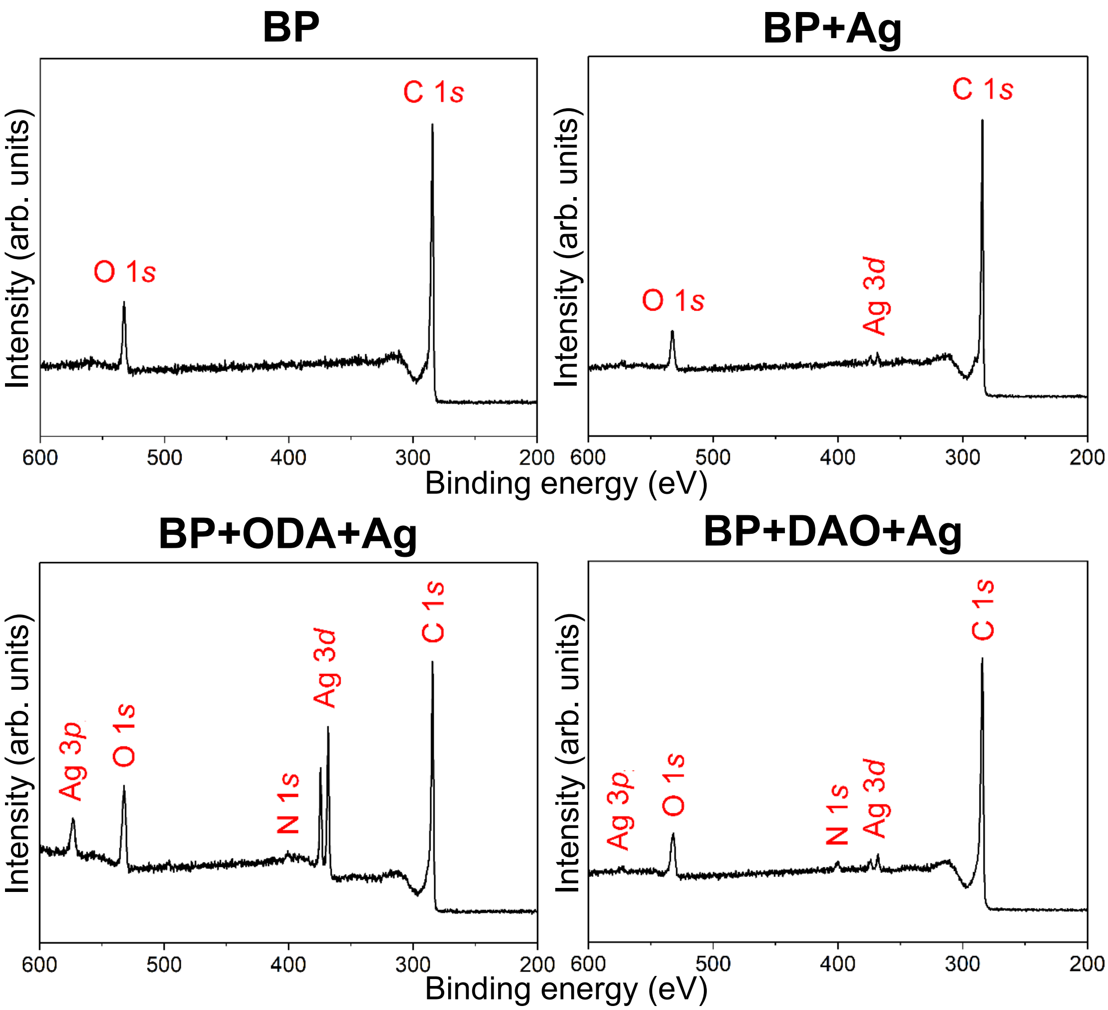

Fig. 5.16. XPS survey spectra of buckypaper prepared from MWCNTs$_{(ox)}$ before (BP) and after decoration with silver nanoparticles (BP+Ag), as well as of the paper hybrids where amine-functionalisation preceded the decoration with silver nanoparticles (BP+ODA+Ag and BP+DAO+Ag).

Turning to the buckypapers, since EDS identified the side that was in contact with the filtration membrane during paper fabrication as the one with the higher Ag loading, we decided to examine that side for all silver-containing paper samples with XPS. Fig. 5.16 presents the survey spectra of the buckypaper prepared from MWCNTs$_{(ox)}$ before and after amine-functionalization and decoration with AgNPs. As for the MWCNT powder samples, the spectral signatures of carbon, oxygen, nitrogen and silver observed here confirmed the oxidation of the MWCNTs and the subsequent chemical modification with amines and silver.

The detailed XPS spectra of the various core level regions and the corresponding fits are presented in Fig. 5.17. The C 1*s* spectral line of the buckypaper (left side in Fig. 5.17) contains the same six components as the corresponding powder samples, albeit with slightly different relative intensities as can be seen comparing Table 3 and Table 7.

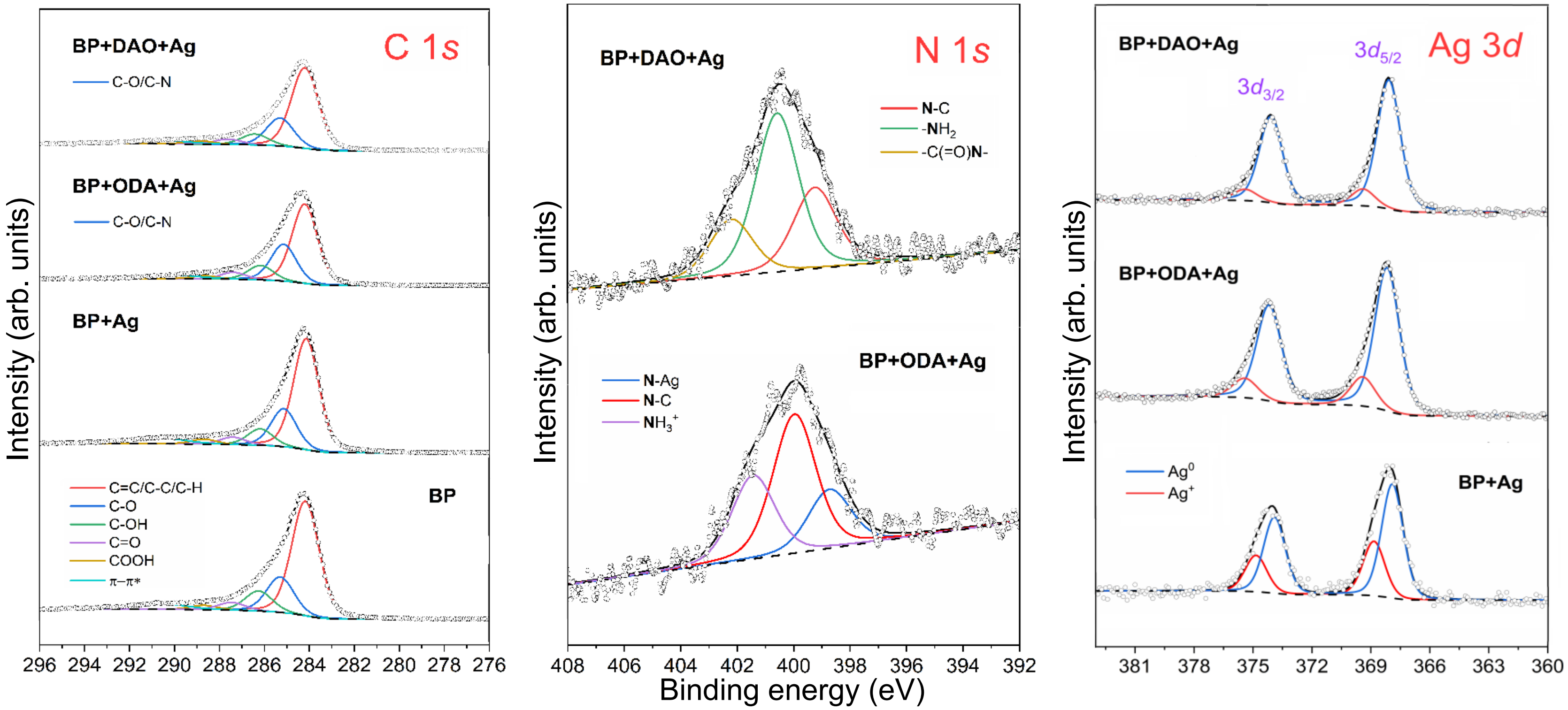

Fig. 5.17. XPS spectra of the C 1*s*, O 1*s*, N 1*s* and Ag 3*d* core level regions of buckypaper prepared from MWCNTs$_{(ox)}$ before (BP) and after decoration with silver nanoparticles (BP+Ag), as well as of the paper hybrids where amine-functionalisation preceded the decoration with silver nanoparticles (BP+ODA+Ag and BP+DAO+Ag). Raw data are shown as dots, the components identified from the deconvolution are colour-coded and the sum of the fitted components is shown in black.

Table 7. XPS binding energies and relative intensities of the components corresponding to different chemical species contributing to the intensity of the C 1*s* line of BP/AgNPs samples

	Components (eV)					
Sample	**C=C/C-C/C-H (%)**	**C-O (%)**	**C-OH (%)**	**C=O (%)**	**O=C-O (%)**	**π-π* shake-up (%)**
BP	284.2 (59.5)	285.3 (18.4)	286.3 (10.4)	287.5 (4.0)	288.7 (2.3)	290.6 (5.5)
BP+Ag	284.1 (57.5)	285.1 (20.2)	286.1 (9.0)	287.3 (4.0)	288.5 (2.7)	290.5 (6.7)
		C-O/C-N (%)				
BP+ODA+Ag	**284.2** (53.9)	285.1 (25.0)	286.2 (9.8)	287.4 (4.7)	288.6 (2.1)	289.8 (4.5)
BP+DAO+Ag	(59.8)	285.3 (20.8)	286.4 (8.1)	287.6 (3.9)	288.9 (2.4)	290.6 (5.0)

The detailed information on the N 1*s* core level region of the aminated samples can be found in the middle column of Fig. 5.17 and in Table 8. The suggested deconvolution permits to identify five nitrogenated components: 1) silver coordinated to nitrogen, 2) C-N bonds, 3) amino groups, 4) protonated -NH species, and 5) amides. In both samples, C-N bonding is distinguished as a common component appearing at 399.2 - 399.9 eV. In the case of the MWCNTs+ODA+Ag sample, contributions of N-Ag bonds and NH_3^+ appear at 398.5 eV and 401.4 eV and contribute to the N 1*s* spectral intensity with 18.3 % and 31.0 %, respectively. The appearance of this protonated species is due to the acidic treatment during the formation and deposition of silver particles (pH between 0 and 3). This trend completely agrees with the previous results for the N 1*s* peak of aminated GO-based silver (Chapter 3) and palladium (Chapter 4) hybrid materials.[38,51] In the DAO-containing sample contributions of free amino groups and newly formed amide moieties appear at a BE of 400.6 and 402.2 eV, respectively, and contribute with 53.5 % and 19.1 % of the spectral line intensity. The fact that the N-Ag bond appears in the ODA-containing hybrid indicates that coordination bonding is favoured *via* nitrogen with monodentate ligands. The abundance of silver as deduced from the intensity of the photoemission peaks matches with the histograms shown in Fig. 5.10, where the highest number of silver particles were found for BP+ODA+Ag. $-NH_2$ is observed in BP+DAO+Ag due to the dangling amino group, at the side of the aliphatic chain that does not participate in the formation of new chemical species.

Table 8. XPS binding energies and relative intensities of the components corresponding to different chemical species contributing to the N 1*s* line of the aminated BP+Ag samples

	Components (eV)				
Sample	**N-Ag (%)**	**N-C (%)**	**-NH$_2$ (%)**	**NH$_3^+$ (%)**	**–C(=O)N– (%)**
BP+ODA+Ag	398.5 (18.3)	399.9 (50.7)	---	401.4 (31.0)	---
BP+DAO+Ag	---	399.2 (27.4)	400.6 (53.5)	---	402.2 (19.1)

To determine the chemical species present during the formation/deposition of AgNPs, we examined the deconvoluted Ag 3*d* core level spectra for silver-containing samples, as shown in the right column of Fig. 5.17, with detailed fitting information presented in Table 9. Similarly to the MWCNTs/AgNPs series, the two asymmetrical well-resolved peaks correspond to the Ag 3$d_{5/2}$ and Ag 3$d_{3/2}$ lines, fitted with parameters: full width at half maximum (FWHM) = 1.3-1.5 eV, mixing ratio (M.R.) = 0.7-0.8, spin-orbit splitting Ag3*d* Δ = 6.0 eV, and intensity ratio (I.R.) = 0.6666.[58,59] As in the powder series, two contributions were identified in the fit: the main component, stemming from metallic silver, is peaked at BEs of 367.9 – 368.2 eV, making up 67.7, 83.1, and 88.4 % of the spectral line intensity in MWCNTs+Ag, MWCNTs+ODA+Ag, and MWCNTs+DAO+Ag, respectively. The secondary component, at BEs of 368.8 – 369.4 eV can be assigned to Ag(I) in a complexed form, like that observed in the powder series.

Table 9. XPS binding energies and relative intensities of the components corresponding to different oxidation states of silver contributing to the Ag3*d* line of the silver-decorated buckypapers

	Components (eV)			
Species	**Ag (0)**		**Ag (I)**	
Line / **Sample**	**3$d_{5/2}$ (%)**	**3$d_{3/2}$ (%)**	**3$d_{5/2}$ (%)**	**3$d_{3/2}$ (%)**
BP+Ag	367.9 (67.7)	373.9	368.8 (32.3)	374.9
BP+ODA+Ag	368.2 (83.1)	374.2	**369.4** (16.9)	**375.4**
BP+DAO+Ag	368.1 (88.4)	374.1	(11.6)	

Apparently, the Ag(I) species is more favoured in the non-aminated sample (32.3%) than in the aminated ones (16.9% in MWCNTs+ODA+Ag and 11.6% in MWCNTs+DAO+Ag), so that in the latter, the coordination of Ag^0 to nitrogen atoms dominates. In these hybrids, nitrogen bonding appears to assist the integration of metallic Ag by favouring electron-donating interactions that stabilize Ag in its reduced state, which is consistent with the observed stoichiometry. This phenomenon explains why aminated samples have a lower Ag(I) content: nitrogen-doping depletes the matrix electrons, causing a shift in the binding energy of Ag(I), while also decreasing its abundance by promoting the incorporation of metallic Ag.

From the XPS intensities, we also determined the surface stoichiometry of the buckypaper samples. The results are listed in Table 10. As expected, the nitrogen content in BP+DAO+Ag is more than twice higher than in BP+ODA+Ag (3.1 at % *vs* 1.3 at %). Similarly, the silver content was higher in the aminated samples with respect to the BP+Ag sample; this trend was also observed in the results derived from SEM/EDS studies (Table 2 and Fig. 5.10) and data for the powder series (Table 6), where the highest Ag loading was reached employing the monofunctional amine (1.4 at % in MWCNTs+ODA+Ag > 0.9 at % in MWCNTs+DAO+Ag > 0.3 at % in MWCNTs +Ag).

Table 10. Elemental composition (atomic percentage) of the buckypaper surface that was in contact with the filter membrane during paper fabrication after Ag NP decoration (as derived from the XPS spectra)

Sample	Atomic %
BP+Ag	C: 91.7
	O: 8.1
	Ag: 0.3
BP+ODA+Ag	C: 87.4
	O: 9.9
	N: 1.3
	Ag: 1.4
BP+DAO+Ag	C: 85.5
	O: 10.6
	N: 3.1
	Ag: 0.9

The crystallinity of the Ag-containing MWCNT hybrids was further studied by powder X-ray diffraction; the experimental details of these measurements are explained in Chapter 2. The diffractograms of oxidized nanotubes and of aminated-CNTs with and without AgNPs are shown in Fig. 5.18. For all the samples characteristic peaks are observed, appearing at 2θ: 13.5 - 13.7°, 26°, 42.5°, 43.6°, and 49.4°, and corresponding to the (001), (002), (100), and (004) planes of the hexagonal lattice, respectively[60,61]. The first peaks are very broad as expected because there are only a few layers in the MWCNTs, so the coherently diffracting domains are small. In MWCNTs+ODA+Ag the (001) peak is shifted to 14.5°, which translates to d_{001} = 0.61 nm in comparison to the d_{001} ~ 0.65 nm in the other samples. This decrease in the distance between concentric tubes could originate from the hydrophobic nature of ODA, which causes water molecules to be driven out from the intertube space when ODA intercalates, in a similar fashion as the *d*-spacing is modulated in GO,[62] as stated in Chapter 4. It is important to mention that a slight increase in the intensity of the MWCNTs peaks in the ODA-functionalized nanotubes is observed (blue line in Fig. 5.18). This is due to the more extended ordering in crystalline arrangements due to the complexation effect by the nitrogen atoms in the ODA moieties.[51]

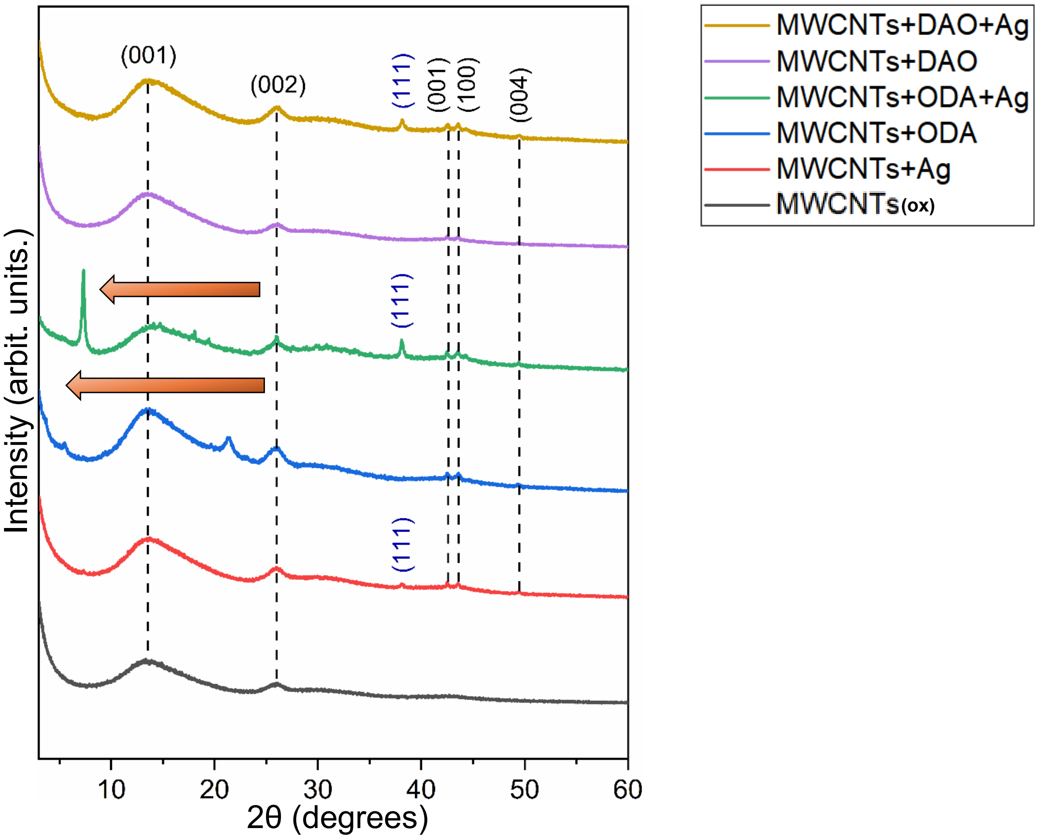

Fig. 5.18. Comparison of the XRD diffractograms for MWCNTs$_{(ox)}$ and amine-functionalized MWCNTs before and after decoration with Ag nanoparticles. (Black numbers correspond to MWCNT peaks, whereas the blue numbers refer to silver features).

All silver-decorated samples also show a Bragg reflection appearing at 2θ = 38.1° which corresponds to the diffraction from the Ag(111) planes in a face-centred cubic (fcc) crystalline structure.[63-65] This confirms the metallic nature of the AgNPs large enough to be seen in XRD. It is important to remark that this peak is more intense in the aminated samples due to the higher Ag loading in comparison to the non-aminated analogous, in agreement with the trends observed in elemental composition studies discussed above (Tables 1 and 6).

5.4 Conclusions

The research presented in this chapter successfully demonstrates an environmentally friendly approach for the preparation of nanohybrids using amine-modified multiwalled carbon nanotubes and silver nanoparticles, adhering to several principles of '***green chemistry'.*** Key aspects of this green approach include the solvent-free functionalization with benign reagents like amines, and the use of citric acid as a mild reducing and stabilizing agent. The procedure proved effective for synthesizing both powder and buckypaper hybrids. The inclusion of Triton X-100 as a surfactant in the fabrication of buckypapers notably improved their dispersion. in various solvents.

The successful grafting of the amines on the external surfaces of the MWCNTs and their intercalation between the concentric tubes, confirmed by all characterisation techniques, promoted the decoration with silver nanoparticles. While both amines yielded a higher silver loading than the hybrid prepared without functionalisation, 1-octadecylamine was particularly effective in promoting a homogeneous distribution of the AgNPs, leading to the highest silver content in the hybrid. TGA/DTA studies showed an inverse relationship between metal content and thermal stability of the hybrids, more pronounced in the powder series, which points to a catalytic effect of silver in the combustion of nanotubes. For the buckypapers electron microscopy revealed distinct differences between the two surfaces of the papers, with the side in contact with the filter membrane during paper fabrication exhibiting greater homogeneity and higher Ag nanoparticle coverage. EDS and XPS analyses gave consistent chemical compositions, with XPS revealing a higher amount of metallic silver in the corresponding samples. This was supported by XRD results where the bigger silver nanoparticles were found to crystallize in a face-centred cubic (fcc) structure. Based on these findings, it can be concluded that 1-octadecylamine (ODA) was the most effective modifier, yielding the best results in terms of particle size distribution and silver loading.

Moving forward, developing robust and scalable synthesis techniques for such nanohybrid materials is crucial to harness them for practical applications. Characterization of their structural, chemical, and physical properties is essential to understand the structure-property relationships and optimize their performance.

5.5 References

(1) Eatemadi, A., Daraee, H., Karimkhanloo, H., Kouhi, M., Zarghami, N., Akbarzadeh, A., Abasi, M., Hanifehpour, Y., & Joo, S. (2014). Carbon nanotubes: properties, synthesis, purification, and medical applications. Nanoscale Research Letters, 9(1), 393. https://doi.org/10.1186/1556-276x-9-393.

(2) Roy, S., Jain, V., Bajpai, R., Ghosh, P., Pente, A. S., Singh, B. P., & Misra, D. S. (2012). Formation of Carbon Nanotube Bucky Paper and Feasibility Study for Filtration at the Nano and Molecular Scale. *Journal of Physical Chemistry. C./Journal of Physical Chemistry. C*, *116*(35), 19025–19031. https://doi.org/10.1021/jp305677h.

(3) Sengab, A., & Picu, R. C. (2018). Mechanical behavior of carbon nanotube yarns with stochastic microstructure obtained by stretching buckypaper. *Composites Science and Technology*, *166*, 54–65. https://doi.org/10.1016/j.compscitech.2018.02.009.

(4) Tanaka, T. (2010). Filtration characteristics of carbon nanotubes and preparation of buckypapers. *Desalination and Water Treatment*, *17*(1-3), 193–198. https://doi.org/10.5004/dwt.2010.1717.

(5) Yadav, M. D., Dasgupta, K., Patwardhan, A. W., & Joshi, J. B. (2017). High Performance Fibers from Carbon Nanotubes: Synthesis, Characterization, and Applications in Composites—A Review. *Industrial & Engineering Chemistry Research*, *56*(44), 12407–12437. https://doi.org/10.1021/acs.iecr.7b02269.

(6) Singh, I., Rehni, A. K., Kumar, P., Kumar, M., & Aboul-Enein, H. Y. (2009). Carbon Nanotubes: Synthesis, Properties and Pharmaceutical Applications. *Fullerenes, Nanotubes and Carbon Nanostructures*, *17*(4), 361–377. https://doi.org/10.1080/15363830903008018.

(7) A, V., & M, S. (2017). Usage of Carbon nanotubes and nano fibers in cement and concrete: A review. *International Journal of Engineering and Technology*, *9*(2), 564–569. https://doi.org/10.21817/ijet/2017/v9i2/170902045.

(8) Sinha, N., & Yeow, J. T.-W. (2005). Carbon Nanotubes for Biomedical Applications. *IEEE Transactions on Nanobioscience*, *4*(2), 180–195. https://doi.org/10.1109/tnb.2005.850478.

(9) Popov, V. N. (2004). Carbon nanotubes: properties and application. *Materials Science and Engineering: R: Reports*, *43*(3), 61–102. https://doi.org/10.1016/j.mser.2003.10.001.

(10) Mansfield, E., Feldman, A., Chiaramonti, A. N., Lehman, J., & Curtin, A. E. (2015). Morphological and Electrical Characterization of MWCNT Papers and Pellets. *Journal of Research of the National Institute of Standards and Technology*, *120*, 304–304. https://doi.org/10.6028/jres.120.019.

(11) Vennerberg, D., & Kessler, M. R. (2014). Anisotropic buckypaper through shear-induced mechanical alignment of carbon nanotubes in water. *Carbon*, *80*, 433–439. https://doi.org/10.1016/j.carbon.2014.08.082.

(12) Endo, M., Muramatsu, H., Hayashi, T., Yoong Ahm Kim, Terrones, M., & Dresselhaus, M. S. (2005). "Buckypaper" from coaxial nanotubes. *Nature*, *433*(7025), 476–476. https://doi.org/10.1038/433476a.

(13) Rigueur, J. L., Hasan, S. A., Mahajan, S. V., & Dickerson, J. H. (2010). Buckypaper fabrication by liberation of electrophoretically deposited carbon nanotubes. *Carbon*, *48*(14), 4090–4099. https://doi.org/10.1016/j.carbon.2010.07.016.

(14) Sagadevan, S. (2013). Current Trends in Carbon Nanotubes and Their Applications. *American Journal of Nanoscience and Nanotechnology*, *1*(4), 79. https://doi.org/10.11648/j.nano.20130104.11.

(15) Njuguna, J., Silva, F., & Sachse, S. (2011). Nanocomposites for Vehicle Structural Applications. In T. Lin (Ed.), *Nanofibers - Production, Properties and Functional Applications* (pp. 401–434). InTech, Rijeka, Croatia.

(16) Amin, R., Ramesh Kumar , P., & Belharouak, I. (2020). Carbon Nanotubes: Applications to Energy Storage Devices. In P. Kumar Ghosh , K. Datta, & A. Dinkarrao Rushi (Eds.), *Carbon Nanotubes - Redefining the World of Electronics*. IntechOpen, Rijeka, Croatia.

(17) Raffaelle, R. P., Landi, B. J., Harris, J. D., Bailey, S. G., & Hepp, A. F. (2005). Carbon nanotubes for power applications. *Materials Science and Engineering: B*, *116*(3), 233–243. https://doi.org/10.1016/j.mseb.2004.09.034.

(18) Punetha, V. D., Rana, S., Yoo, H. J., Chaurasia, A., McLeskey, J. T., Ramasamy, M. S., Sahoo, N. G., & Cho, J. W. (2017). Functionalization of carbon nanomaterials for advanced polymer nanocomposites: A comparison study between CNT and graphene. *Progress in Polymer Science*, *67*, 1–47. https://doi.org/10.1016/j.progpolymsci.2016.12.010.

(19) Meng, L., Fu, C., & Lu, Q. (2009). Advanced technology for functionalization of carbon nanotubes. *Progress in Natural Science*, *19*(7), 801–810. https://doi.org/10.1016/j.pnsc.2008.08.011.

(20) Xia, W., Hagen, V., Kundu, S., Wang, Y., Somsen, C., G. Eggeler, Sun, G., Grundmeier, G., Stratmann, M., & Muhler, M. (2007). Controlled Etching of Carbon Nanotubes by Iron-Catalyzed Steam Gasification. *Advanced Materials*, *19*(21), 3648–3652. https://doi.org/10.1002/adma.200700763

(21) Xia, W., Jin, C., Kundu, S., & Muhler, M. (2009). A highly efficient gas-phase route for the oxygen functionalization of carbon nanotubes based on nitric acid vapor. *Carbon*, *47*(3), 919–922. https://doi.org/10.1016/j.carbon.2008.12.026

(22) Zhang, G., Qi, P., Wang, X., Lu, Y., Li, X., Tu, R., Bangsaruntip, S., Mann, D., Zhang, L., & Dai, H. (2006). Selective Etching of Metallic Carbon Nanotubes by Gas-Phase Reaction. *Science 314*(5801), 974–977. https://www.science.org/doi/10.1126/science.1133781.

(23) Pavan, M. V. R., & Khabashesku, V. N. (2015). *Environmental Consequences of Engineered Nanomaterials: An Awareness Campaign to Promote Safe Nanotechnology and Dispel Related Misconceptions*. Proceedings of Offshore Technology Conference, Houston, Texas, USA. https://doi.org/10.4043/26039-MS

(24) Volkov, V. S., Yakubovsky, D. I., Stebunov, Y. V., Kirtaev, R. V., Voronin, K. V., & Arsenin, A. V. (2018). Hybrid graphene-nanometallic structures. *Journal of Physics. Conference Series*, *1092*, 012161–012161. https://doi.org/10.1088/1742-6596/1092/1/012161.

(25) Tian, X., Zhang, L., Yang, M., Bai, L., Dai, Y., Yu, Z., & Pan, Y. (2017). Functional magnetic hybrid nanomaterials for biomedical diagnosis and treatment. *WIREs Nanomedicine and Nanobiotechnology*, *10*(1), e1476. https://doi.org/10.1002/wnan.1476.

(26) Ortega-Nieto, C., Losada-Garcia, N., Prodan, D., Furtos, G., & Palomo, J. M. (2023). Recent Advances on the Design and Applications of Antimicrobial Nanomaterials. *Nanomaterials*, *13*(17), 2406. https://doi.org/10.3390/nano13172406.

(27) Fisher, C., E. Rider, A., Jun Han, Z., Kumar, S., Levchenko, I., & Ostrikov, K. (Ken). (2012). Applications and Nanotoxicity of Carbon Nanotubes and Graphene in Biomedicine. *Journal of Nanomaterials*, *2012*, 1-19. https://doi.org/10.1155/2012/315185.

(28) Li, K., & Li, H. (2011). Fabrication and Applications of Carbon Nanotube-Based Hybrid Nanomaterials by Means of Non-Covalently Functionalized Carbon Nanotubes. In S. Bianco (Ed.), *Carbon Nanotubes - From Research to Applications*. InTechOpen, Rijeka, Croatia. https://www.intechopen.com/chapters/16830.

(29) Zhang, J., Zheng, Y., Yu, P., Xu, L., Lan, L., & Wang, R. (2010). The Synthesis of Gel-Like Hybrid Nanomaterials Based on Carbon Nanotube Decorated with Metal Nanoparticles at 45°C. *Soft Materials*, *8*(1), 39–48. https://doi.org/10.1080/15394451003598510.

(30) Carrillo, A., Swartz, J. A., Gamba, J. M., Kane, R. S., Nirupama Chakrapani, Wei, B., & Ajayan, P. M. (2003). Noncovalent Functionalization of Graphite and Carbon Nanotubes with Polymer Multilayers and Gold Nanoparticles. *Nano Letters*, *3*(10), 1437–1440. https://doi.org/10.1021/nl034376xé.

(31) Zhao, S., Gao, Y., Zhang, G., Deng, L., Li, J., Sun, R., & Wong, C.-P. (2015). Covalently bonded nitrogen-doped carbon-nanotube-supported Ag hybrid sponges: Synthesis, structure manipulation, and its application for flexible conductors and strain-gauge sensors. *Carbon*, *86*, 225–234. https://doi.org/10.1016/j.carbon.2015.01.033.

(32) Tian, X., Zhang, L., Yang, M., Bai, L., Dai, Y., Yu, Z., & Pan, Y. (2017). Functional magnetic hybrid nanomaterials for biomedical diagnosis and treatment. *WIREs Nanomedicine and Nanobiotechnology*, *10*(1). https://doi.org/10.1002/wnan.1476.

(33) Volkov, V. S., Yakubovsky, D. I., Stebunov, Y. V., Kirtaev, R. V., Voronin, K. V., & Arsenin, A. V. (2018). Hybrid graphene-nanometallic structures. *Journal of Physics. Conference Series*, *1092*, 012161–012161. https://doi.org/10.1088/1742-6596/1092/1/012161.

(34) Simović, A. R., Bogojeski, J., Petrović, B., & Jovanović-Stević, S. (2020). Bis-pyrazolylpyridine Complexes of Some Transition Metal Ions: Structure-Activity Relationships and Biological Activity. *Macroheterocycles*, *13*(3), 201–209. https://doi.org/10.6060/mhc200499s.

(35) Martín, J., Alés M.R., Asuero, A.G. (2018). An overview on ligands of therapeutically interest. *Pharmacy & Pharmacology International Journal*, *6*(3), 198-214. https://doi.org/10.15406/ppij.2018.06.00177.

(36) Caballero, A. B., Salas, J. M., & Sánchez-Moreno, M. (2014). Metal-Based Therapeutics for Leishmaniasis. In D. Claborn (Ed.), *Leishmaniasis - Trends in Epidemiology, Diagnosis and Treatment*. IntechOpen, Rijeka, Croatia. https://www.intechopen.com/chapters/46398.

(37) Meza-Laguna, V., Basiuk, E. V., Alvarez-Zauco, E., Acosta-Najarro, D., & Basiuk, V. A. (2007). Cross-Linking of C_{60} Films with 1,8-Diaminooctane and Further Decoration with Silver Nanoparticles. *Journal of Nanoscience and Nanotechnology*, *7*(10), 3563–3571. https://doi.org/10.1166/jnn.2007.681.

(38) Rodríguez-Otamendi, D. I., Meza-Laguna, V., Acosta, D., Álvarez-Zauco, E., Huerta, L., Basiuk, V. A., & Basiuk, E. V. (2021). Eco-friendly synthesis of graphene oxide–silver nanoparticles hybrids: The effect of amine derivatization. *Diamond and Related Materials*, *111*, 108208. https://doi.org/10.1016/j.diamond.2020.108208.

(39) Frontier, A. (2023). Reagents & Solvents. Www.chem.rochester.edu. https://www.chem.rochester.edu/notvoodoo/pages/reagents.php?page=solvent_polarity.

(40) 2-Propanol. (n.d.). Www.fishersci.com. https://www.fishersci.com/us/en/scientific-products/selection-guides/chemicals/2-propanol.html.

(41) Shun Chia Industrial Company Limited. (n.d.). TRITON Nonionic Surfactant X-100 (pp. 1–5).

(42) Fayazfar, H., Afshar, A., & Dolati, A. (2013). Controlled Growth of Well-Aligned Carbon Nanotubes, Electrochemical Modification and Electrodeposition of Multiple Shapes of Gold Nanostructures. *Materials Sciences and Applications*, *04*(11), 667–678. https://doi.org/10.4236/msa.2013.411083.

(43) Misra, A., Tyagi, PawanK., Rai, P., & Misra, D. S. (2007). FTIR Spectroscopy of Multiwalled Carbon Nanotubes: A Simple Approach to Study the Nitrogen Doping. *Journal of Nanoscience and Nanotechnology, 7(6),* 1820–1823. https://doi.org/10.1166/jnn.2007.723.

(44) Ristein, J., Stief, R. T., Ley, L., & Beyer, W. (1998). A comparative analysis of a-C:H by infrared spectroscopy and mass selected thermal effusion. *Journal of Applied Physics*, *84*(7), 3836–3847. https://doi.org/10.1063/1.368563.

(45) Yu, G.-Q., Lee, S.-H., & Lee, J.-J. (2002). Effects of thermal annealing on amorphous carbon nitride films by r.f. PECVD. *Diamond and Related Materials*, *11*(9), 1633–1637. https://doi.org/10.1016/s0925-9635(02)00111-5.

(46) Atieh, M.A., Yehya Bakather, O., Al-Tawbini, B., Bukhari, A.A., Abuilaiwi, F.A., & Fettouhi, M.B. (2010)*Effect of Carboxylic Group Functionalized on Carbon Nanotubes Surface on the Removal of Lead From Water*. *Bioinorganic Chemistry and Applications 2010*(11), 603978. https:/doi.org/10.1155/2010/603978

(47) Mawhinney, D. B., Naumenko, V., Kuznetsova, A., Yates, J. T., Liu, J., & Smalley, R. E. (2000). Infrared Spectral Evidence for the Etching of Carbon Nanotubes: Ozone Oxidation at 298 K. *Journal of the American Chemical Society*, *122*(10), 2383–2384. https://doi.org/10.1021/ja994094s.

(48) Goyanes, S., Rubiolo, G. R., Salazar, A., Jimeno, A., Corcuera, M. A., & Mondragon, I. (2007). Carboxylation treatment of multiwalled carbon nanotubes monitored by infrared and ultraviolet spectroscopies and scanning probe microscopy. *Diamond and Related Materials*, *16*(2), 412–417. https://doi.org/10.1016/j.diamond.2006.08.021.

(49) *Octadecylamine*; SDS No.1907/2006 [Online]; Sigma-Aldrich: Amsterdam, Oct 28, 2022. https://www.sigmaaldrich.com/NL/en/sds/aldrich/305391?userType=anonymous (accessed May. 11, 2024).

(50) *1,8-Diaminooctane*; SDS No. 1907/2006 [Online]; Sigma-Aldrich: Amsterdam, Mar 08, 2024. https://www.sigmaaldrich.com/NL/en/sds/aldrich/d22401?userType=anonymous (accessed May. 11, 2024).

(51) Rodríguez-Otamendi, D. I., Bizarro, M., Meza-Laguna, V., Álvarez-Zauco, E., Rudolf, P., Basiuk, V. A., & Basiuk, E. V. (2023). Eco-friendly synthesis of graphene oxide–palladium nanohybrids. *Materials Today Communications*, *35*, 106007–106007. https://doi.org/10.1016/j.mtcomm.2023.106007.

(52) Cheng, Y., Li, H., Fang, C., Ai, L., Chen, J., Su, J., Zhang, Q., & Fu, Q. (2019). Facile synthesis of reduced graphene oxide/silver nanoparticles composites and their application for detecting heavy metal ions. *Journal of Alloys and Compounds*, *787*, 683–693. https://doi.org/10.1016/j.jallcom.2019.01.320.

(53) Zeng, F., Xu, D., Zhan, C., Liang, C., Zhao, W., Zhang, J., Feng, H., & Ma, X. (2018). Surfactant-Free Synthesis of Graphene Oxide Coated Silver Nanoparticles for SERS Biosensing and Intracellular Drug Delivery. *ACS Applied Nano Materials*, *1*(6), 2748–2753. https://doi.org/10.1021/acsanm.8b00444.

(54) Abdelhalim, A. O. E., Galal, A., Hussein, M. Z., & El Sayed, I. E.-T. (2016). Graphene Functionalization by 1,6-Diaminohexane and Silver Nanoparticles for Water Disinfection. *Journal of Nanomaterials*, *2016*, 1–7. https://doi.org/10.1155/2016/1485280.

(55) Basiuk, E. V., Ramírez-Calera, I. J., Meza-Laguna, V., Abarca-Morales, E., Pérez-Rey, L. A., Re, M., Prete, P., Lovergine, N., Álvarez-Zauco, E., & Basiuk, V. A. (2015). Solvent-free functionalization of carbon nanotube buckypaper with amines. *Applied Surface Science*, *357*, 1355–1368. https://doi.org/10.1016/j.apsusc.2015.09.252.

(56) Okpalugo, T. I. T., Papakonstantinou, P., Murphy, H., McLaughlin, J., & Brown, N. M. D. (2005). High resolution XPS characterization of chemical functionalised MWCNTs and SWCNTs. *Carbon*, *43*(1), 153–161. https://doi.org/10.1016/j.carbon.2004.08.033.

(57) Chen, X., Wang, X., & Fang, D. (2020). A review on C1s XPS-spectra for some kinds of carbon materials. *Fullerenes, Nanotubes and Carbon Nanostructures*, *28*(12), 1048–1058. https://doi.org/10.1080/1536383x.2020.1794851.

(58) Crist, B. V. (2019). ***PEAK-FITTING - FACTS, RULES & GUIDELINES*. The XPS Library of XPS Technology and Science for Self-Training. https://xpslibrary.com/peak-fitting-facts-rules-guides/

(59) Moulder, J. F., Stickle, W. F., Sobol, P. E., & Bomben, K. D. (1992). *Handbook of X-ray Photoelectron Spectroscopy* (J. Chastain & R. C. King Jr, Eds.). Physical Electronics, Inc., Eden Prairie, Minnesota, U.S.A.

(60) Atchudan, R., Pandurangan, A., & Joo, J. (2015). Effects of Nanofillers on the Thermo-Mechanical Properties and Chemical Resistivity of Epoxy Nanocomposites. *Journal of Nanoscience and Nanotechnology*, *15*(6), 4255–4267. https://doi.org/10.1166/jnn.2015.9706.

(61) Mohd Pauzi, A., & Zulkepli, S. A.. (2015). The functionalization and characterization of multi-walled carbon nanotubes (MWCNTs). *AIP Conference Proceedings 1678* (1), 050033. https://doi.org/10.1063/1.4931312.

(62) Dékány, I., Krüger-Grasser, R., & Weiß, A. (1998). Selective Liquid Sorption Properties of Hydrophobized Graphite Oxide Nanostructures. *Colloid and Polymer Science 276* (7), 570–576. https://doi.org/10.1007/s003960050283.

(63) Guzmán, K., Kumar, B., Vallejo, M. J., Grijalva, M., Debut, A., & Cumbal, L. (2019). Ultrasound-assisted synthesis and antibacterial activity of gallic acid-chitosan modified silver nanoparticles. Progress in Organic Coatings, 129, 229–235. https://doi.org/10.1016/j.porgcoat.2019.01.009.

(64) Mehta, B. K., Chhajlani, M., & Shrivastava, B. D. (2017). Green synthesis of silver nanoparticles and their characterization by XRD. Journal of Physics: Conference Series, *836*, 012050. https://doi.org/10.1088/1742-6596/836/1/012050.

(65) Moosa, A., Daood, A., & Radhi, M. (2022). Green synthesis of silver nanoparticles decorated with exfoliated graphite nanocomposites. Egyptian Journal of Chemistry, 65(13), 651-659. https://doi.org/10.21608/ejchem.2022.141183.6180.

CHAPTER 6

Transformative materials: Exploring the synergy of multiwalled carbon nanotubes and palladium nanoparticles

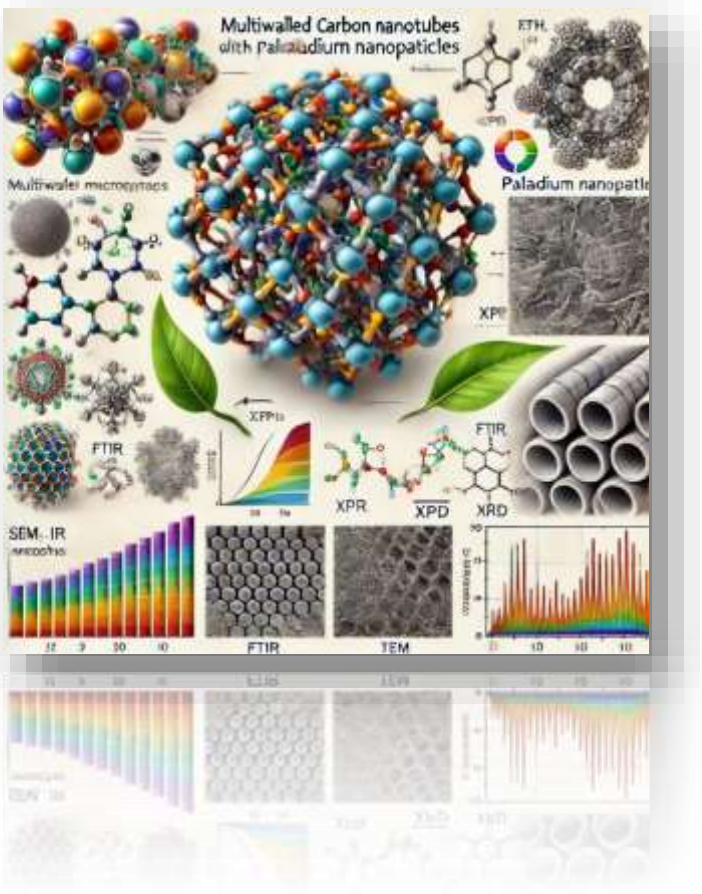

ABSTRACT

In this chapter, the synthesis and exploration of hybrids based on chemically modified multiwalled carbon nanotubes with aliphatic amines (1-octadecylamine and 1,8-diaminooctane), including crafting and ornamentation of palladium nanoparticles were monitored. For this aim, paper and powder forms were examined. Buckypaper was made under a pre-established protocol. Palladium chloride (II) and citric acid were used to produce the palladium nanoparticles.

Dispersibility tests showed that oxidized and 1-octadecylamine -containing materials preserved their hydrophobic behaviour even after palladium decoration. Fourier transform infrared and X-ray photoelectron spectroscopy confirmed covalent bonding between carbon atoms (of the graphitic matrix) and oxygen and nitrogen. Thermal analysis revealed that the functionalisation degree was higher in powdered series, particularly when 1-octadecylamine is present, and that combustion is faster for higher palladium content.

Electron microscopy showed that the microstructure of the substrate (powder or paper) is affected by both the intercalation of amine moieties and the inclusion of palladium particles. X-ray photoelectron spectroscopy results allowed us to identify six types of carbon bonds, four components in the N 1*s* core level region, and palladium in different oxidation states. X-ray diffraction confirmed the crystallinity of the graphitic matrix and revealed the presence of metallic palladium.

6.1 Introduction

Carbon allotropes such as graphene oxide (GO) and carbon nanotubes (CNTs) have gained significant attention due to their outstanding mechanical, thermal, electronic, and magnetic properties.[1-4] CNTs are particularly appealing due to their unique structural and electronic characteristics, including exceptional electrical and thermal conductivity, high surface area, and remarkable mechanical strength. These properties make CNTs an attractive choice as support materials.[5-10] However, pristine CNTs are nearly inert, limiting their versatility. Incorporating oxygenated functionalities overcomes this limitation and facilitates tuning the CNT properties for various applications.[11-16]

The solvent-free gas-phase functionalisation method explored by Basiuk *et al*. (2002),[17-22] has permitted the chemical modification of carbon nanostructured materials (CNSMs) with organic macrocycles, thiols, and amines. Among its most significant benefits is that doesn't require additional purification since surplus reagents are removed *in situ* under a dynamic vacuum and moderated reaction times, in comparison to other functionalization techniques.[23-25]

In a similar context, the enormous interest towards the synthesis and utilization of metallic nanoparticles (MNPs) in different fields results in a special effort to combine the intrinsic properties of both types of materials, leading to hybrid structures for applications in electronics, catalysis, electrochemical biosensing, drug delivery, and antimicrobial agents, among others.[26-34]

One such promising combination is the integration of multiwalled carbon nanotubes (MWCNTs) and palladium (Pd) nanoparticles, which can yield materials with improved catalytic, electronic, and mechanical characteristics making them suitable for fuel cells, sensors, etc.[35-39]

Furthermore, the production of buckypaper offers several benefits compared to MWCNTs in powder form. The flow-directed assembly of individual graphene sheets during its fabrication results in a unique interlocking tile arrangement, which confers enhanced stiffness and strength.[40-44] Another advantage is its superior electrical and thermal conductivity.[14] The interconnected network of CNTs facilitates efficient charge and heat transfer, rendering it highly suitable for electronic packaging and power applications.[9,45-47] In contrast, the powder form may face some challenges due to the inherent difficulties in achieving uniform dispersion and alignment within a device or system.[48-51]

The main purpose of this study was to demonstrate that chemically treated MWCNTs, coated with vaporous amines beforehand, make it feasible to synthesize nanohybrid materials based on MWCNTs and PdNPs in a safer and ecologically acceptable manner in comparison to other synthetic techniques.[52-56]

A detailed comparison of the properties of functionalised Pd-MWCNTs-based hybrids utilising aliphatic amines and pure nanotubes was carried out. This work expands the ecologically sustainable production of advanced materials by concentrating on the form and dispersion of PdNPs, leading to new opportunities for a variety of applications.

6.2 Experimental section

6.2.1 Materials

Multiwalled carbon nanotubes (≥ 95 wt% purity, diameter: < 8 nm and length of 10-50 μm) acquired from Nanostructured & Amorphous Materials Inc., were used. The reagents 1-octadecylamine (ODA; ≥ 99 %), 1,8-diaminooctane (DAO; ≥ 98 %), palladium chloride (≥ 99 %), and Triton™ X-100 (laboratory grade) were used to fabricate the new materials, whereas the following acids: citric (≥ 99.5 %), and hydrochloric (≥ 37 %) from Sigma-Aldrich, and nitric acid (65.7 %) from J.T. Baker were utilised as received.

6.2.2 Methodology

As explained in detail in Chapter 2, we first oxidised the raw MWCNTs to make them easier to process; the samples are hereafter called **MWCNTs$_{\mathbf{(ox)}}$** *(section 2.1.2 point 1)*. Then we fabricated buckypaper (BP) with part of the material *(section 2.1.2 point 1)* and consecutively, amine-functionalized both the MWCNT powder and the BP with either 1-octadecylamine (ODA) or 1,8-diaminooctane (DAO) *(section 2.1.3.)*. In the following, the powder samples are labelled MWCNTs+ODA and MWCNTs+DAO, whereas the paper samples are called BP+ODA and BP+DAO. The final step in our sample preparation, also described in Chapter 2, section 2.1.4.1, was to decorate both powder and paper samples with palladium nanoparticles. The amine-functionalized samples are designated hereafter as MWCNTs+ODA+Pd, BP+ODA+Pd, MWCNTs+DAO+Pd, and BP+DAO+Pd. For comparison purposes, control samples were obtained by applying the identical treatment to MWCNTs$_{(ox)}$ and BP (lacking amine functionalization) and are denoted as MWCNTs+Pd and BP+Pd.

6.3 Results and discussion

6.3.1 Characterization of MWCNTs+Pd and BP+Pd hybrids

To elucidate changes in the surface chemistry of the new hybrid materials, two sets of dispersibility tests were carried out in solvents with different polarities. Photographs were taken before and after decoration with palladium nanoparticles. The first set included MWCNTs in powder form, dispersed in water and toluene (Fig. 6.1). The second set included many types of buckypaper dispersed in water and 2-propanol (Fig. 6.2). These solvents were chosen after trials with multiple solvents, which helped to select those delivering the most remarkable differences. The images collected immediately after 10 min sonication and after resting for 24 are reported in Fig. 6.1. Here we can see that the oxidized and the ODA-containing MWCNTs preserve their hydrophobic characteristics, even after the incorporation of PdNPs. This tendency was also observed in the GO/PdNPs series, where the presence of palladium conferred hydrophobic features to the new hybrid materials. On the other hand, the DAO-containing samples exhibit a hydrophilic behaviour. This tendency completely matches the observed for GO and for palladium-decorated GO (see Fig. 4.1.). While most of the samples retained their initial features after 24 hours, the MWCNTs+DAO sample practically completely precipitated, whereas its Pd-containing analogue remained well dispersed, pointing to a stabilizing effect of PdNPs on aqueous systems, similarly to what was observed for AgNPs-decorated GO-based systems (Chapter 3).[57]

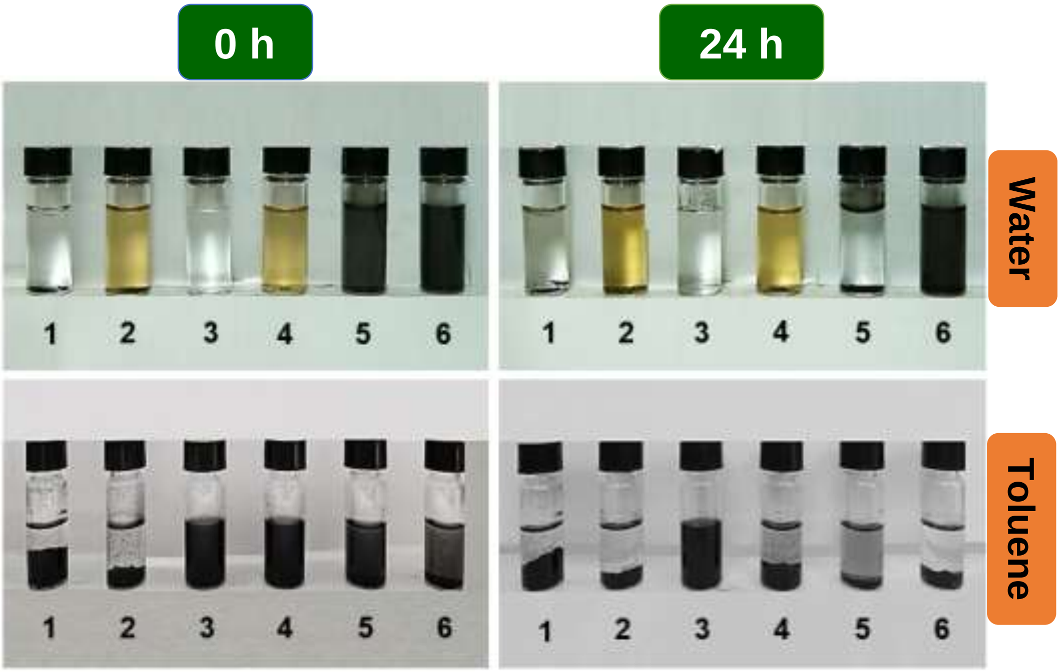

Fig. 6.1. Dispersibility tests for MWCNTs samples in water and toluene: (1) MWCNTs$_{(ox)}$, (2) MWCNTs+Pd, (3) MWCNTs+ODA, (4) MWCNTs+ODA+Pd, (5) MWCNTs+DAO, and (6) MWCNTs+DAO+Pd. The images were taken immediately after 10-min ultrasonication (0 h) and after 24 h.

On the other hand, the behaviour in toluene is completely different. Whereas MWCNTs$_{(ox)}$ and MWCNTs+Pd are only partially dispersible in this solvent, the amine-containing samples seem quite well-dispersed, independent of whether they contain PdNPs or not. After 24 hours, the non-aminated samples remained partially dispersed while the amino-functionalized ones precipitated almost completely, except for the MWCNTs+ODA sample. This tendency agrees with the apolar nature of the hydrocarbon chain of the amine.

According to these studies we can see that a partially hydrophobic character prevails in the carbon nanotubes even after the oxidation with acids and is importantly increased after the amination with the most apolar compound ODA, as observed in the second row of Fig. 6.1.

Similarly, we explored the dispersion behaviour of the newly formed papers employing water and 2-propanol as dispersing agents. At first sight, we can see that the images look quite different compared to the powder-based series. Since the surface area is lower in the paper-like materials, they don't adsorb Pd residues from the precursor, $PdCl_2$, as powdered materials do, therefore the colour of the dispersion is not yellowish.

Starting with the dispersions in water in the first row in Fig. 6.2, it can be observed that the presence of NPs has an impact on the dispersibility of the final material. For example, we can clearly distinguish that the presence of PdNPs makes the buckypaper more dispersible. This tendency was also observed in the Ag-containing series, as explained in Chapter 5, even over time. The opposite happened with graphene oxide paper, where we observed that the grafting of PdNPs rendered the material more hydrophobic (see Chapter 4). As expected, the ODA-containing samples exhibited rather a hydrophilic character, as observed for the ODA-functionalized graphene oxide; however, unlike silver (see Chapter 5), palladium confers hydrophilic characteristics to the hybrid material. The DAO-containing buckypaper dispersed in water but the dispersion was unstable over time, whereas the BP+DAO+Pd sample was quite dispersible and remained so over time. The same trend was also observed in the homologous GO-based samples (Chapter 5). In contrast, a high dispersibility was observed for BP-DAO-Pd, where the amine and the metal synergistically conferred a hydrophilic character to the hybrid.

When employing 2-propanol as a solvent, all dispersions except those of BP+ODA+Pd and BP+DAO, were unstable, and after 24 hours also these two dispersions precipitated almost completely. This behaviour follows that observed with GO paper; the main difference was seen for the GOP+DAO+Pd sample, which was quite dispersible, even over time. That trend is very different from that observed with silver, where, apart from the DAO-containing materials, practically all samples were dispersible.

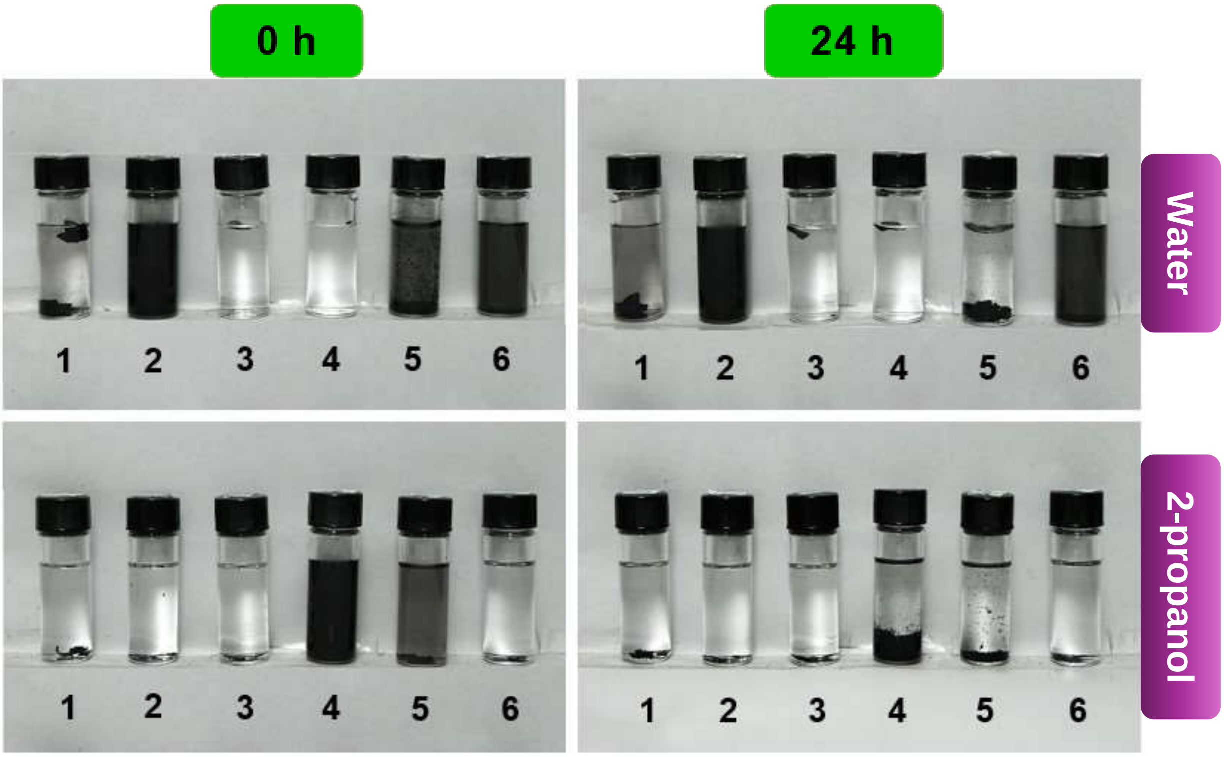

Fig. 6.2. Dispersibility tests for BP samples in water and 2-propanol: (1) BP, (2) BP+Pd, (3) BP+ODA, (4) BP+ODA+Pd, (5) BP+DAO, and (6) BP+DAO+Pd. The images were taken immediately after 10-min ultrasonication (0 h) and after 24 h.

To elucidate differences before and after modification with amines, FTIR spectroscopy studies were conducted on $MWCNTs_{(ox)}$ in paper and powder form, before and after decoration with palladium nanoparticles (Fig. 6.3; for experimental details see Chapter 2). The broadband appearing at 3382 – 3387 cm^{-1} in $MWCNTs_{(ox)}$ is attributed to -OH stretching in carboxyl and hydroxyl groups ($\nu_{O\text{-}H}$).[58] In the aminated samples, the upshifting of the band from 3409 to 3470 cm^{-1} marks the $\nu_{N\text{-}H}$ bonds in secondary amines after the covalent grafting of the amines to the MWCNTs.[59] Parallelly, in these samples the contribution of $\nu_{CH(asym)}$ of the aliphatic chains of the amines is clearly distinguished at 2920 cm^{-1} for MWCNTs and at 2918 cm^{-1} for BPs, whereas the corresponding band related to $\nu_{CH(sym)}$ is observed at 2848 cm^{-1} for the powder series and at 2850 cm^{-1} for the paper form.

The band appearing at 1725 – 1735 cm^{-1} is evidence that a small amount of carbon atoms was oxidized to carboxylic acids.[60] As observed in the amine-containing samples, this signal is downshifted to 1616-1644 cm^{-1} towards the formation of amides ($\nu_{C=O}$ absorption of 'amide I').[61,62] In the case of non-aminated samples, the bands appearing at 1442-1636 cm^{-1} refer to C-C stretching (in-ring), and the ones at 1381-1382 cm^{-1} refer to $\delta_{O\text{-}H}$ (in-plane). The bands in the range of 1025 – 1275 cm^{-1} exhibit the presence of C-O bonds in various chemical surroundings.[58] In the aminated samples characteristic absorption bands related to C-N bonds in amides and/or amines are observed between 1104-1162 cm^{-1}. Finally, below 900 cm^{-1} the signature of different types of deformation and bending modes of C-H bonds appears.[63,64]

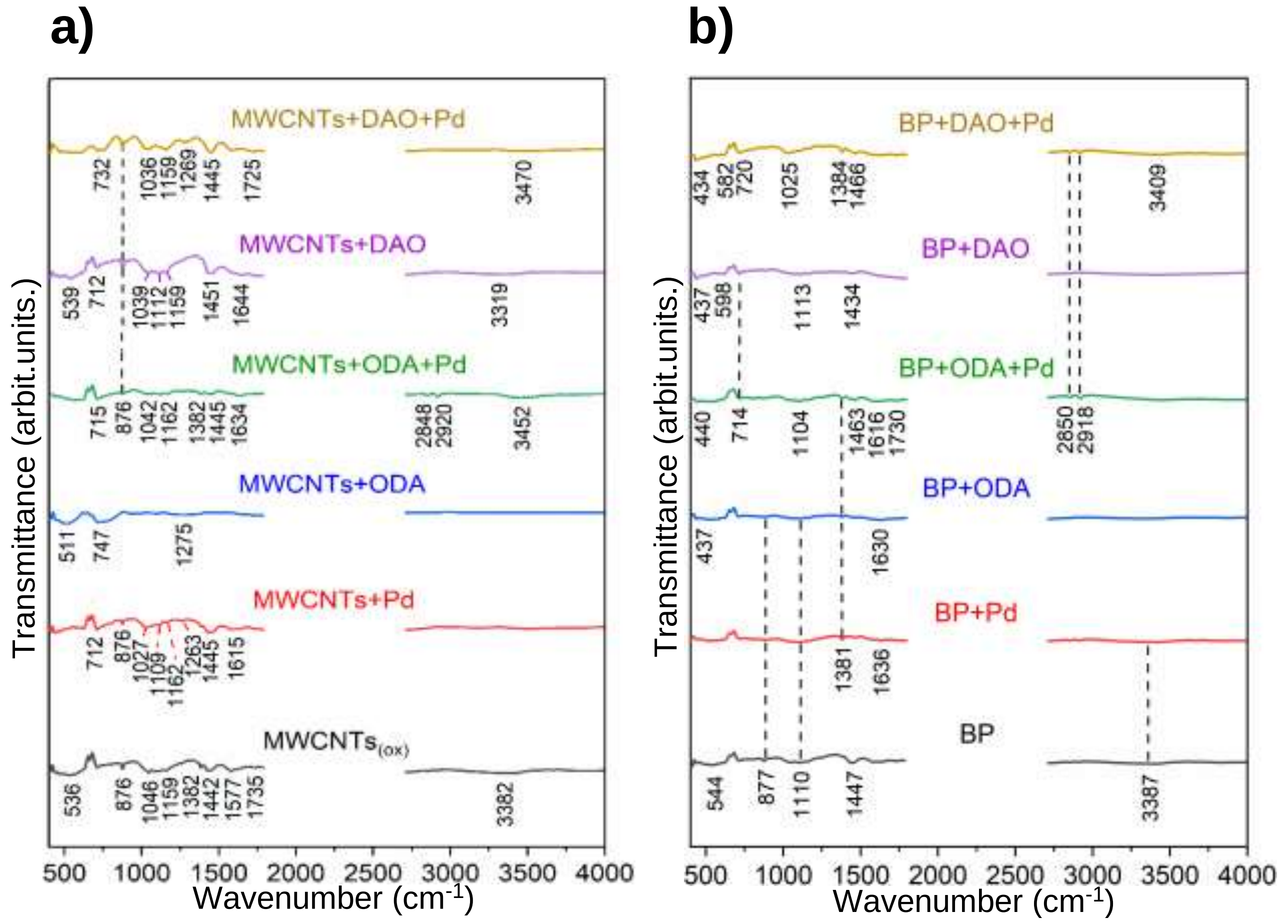

Fig. 6.3. FTIR spectra of oxidized and amine-functionalized a) MWCNTs, and b) BP samples before and after decoration with PdNPs.

The thermal stability of the samples was monitored by thermal gravimetric analysis (TGA), and differential thermal analysis (DTA), as detailed in Chapter 2. Fig. 6.4 illustrates the thermal degradation of the powder series and Fig. 6.5 that of the buckypapers. The thermogram of MWCNTs$_{(ox)}$ (presented as a reference), is displayed in Fig 6.4a. Here two main mass losses are observed, the first one up to 273 °C and amounting to 2.1 %, is associated with the oxygenated groups formed as a consequence of the initial acid treatment of the nanotubes, whereas the second loss up to 705°C makes up 98.0 % of the sample and corresponds to the combustion of the graphitic matrix. The DTA curve shows two maxima: one at 417 °C referring to the degradation of oxygenated moieties, and a main peak at 628 °C that corresponds to the maximum degradation of the C *sp*^{2} matrix.

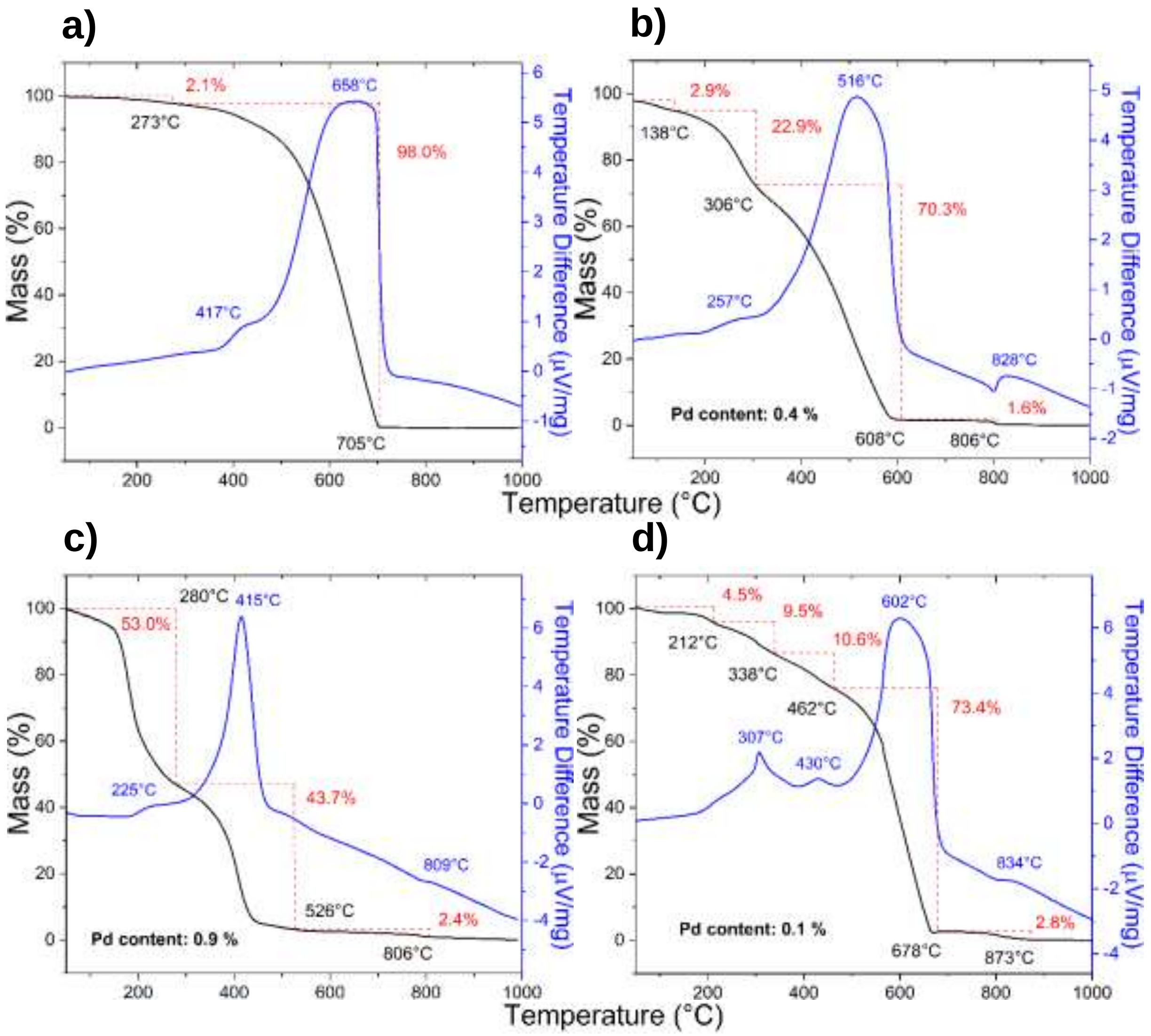

Fig. 6.4. TGA (black) and DTA (blue) of carbon nanotube powder samples: a) MWCNTs$_{(ox)}$, b) MWCNTs+Pd, c) MWCNTs+ODA+Pd, and d) MWCNTs+DAO+Pd.

The loss pattern for MWCNTs+Pd (Fig. 6.4b) has two more loss peaks than MWCNTs$_{(ox)}$. The first one 2.9 %, refers to the evaporation of physiosorbed water up to 138 °C; the second one amounting to 22.9% of the sample and finishing at 306 °C comprises the pyrolysis of oxygenated functionalities and the combustion of simple hydrocarbons whose presence was confirmed by FT-IR before (Fig. 6.3); the third loss of 70.3 %, occurring upon heating until 608 °C, represents the combustion of the MWCNTs, and the forth minor loss up to 806 °C refers to the palladium-containing species. Pd first oxidizes to PdO_2 through a reversible reaction, and above 780 °C the oxide (1.6% of the total weight) recovers to metallic Pd.[65] Until 1000 °C the total content of palladium-related species sums to around 2.0%. The DTA curve indicates three points of maximum decomposition of the sample: the first refers to single bonded carbons at 257 °C; the second to the graphitic lattice with maximum at 516 °C, and the third to the Pd conversion at 828 °C. As it can be observed, the decomposition of the lattice is downshifted 97 °C in the presence of palladium, which suggests a catalytic effect of the metal NPs on the combustion, as observed also for AgNPs on GO and on MWCNTs (described in Chapters 3 to 5, respectively).

In MWCNTs+ODA+Pd (Fig. 6.4c) three mass losses are observed instead, in analogy to the Ag-containing samples discussed in Chapter 5. The first mass loss comprises both covalently and non-covalently attached oxygen- and nitrogen-containing groups, which make up 53.0 % of the sample and degrade up to 280 °C. The second loss refers to the graphitic cylinders, which pyrolyze up to 526 °C and correspond to 43.7 % of the total weight. The loss corresponds to the oxidized palladium, which converts to metallic Pd at 806 °C. Since PdO_2 is counted in 2.4 % and Pd^0 does in 0.9 %, total palladium is accounted for 3.3 %. The DTA curve shows three crucial degradation events, that of the oxygen- and nitrogen-containing groups at 225 °C, the one of the graphitic lattice at 415 °C, and the Pd transition at 809 °C.

For the MWCNTs+DAO+Pd sample (Fig. 6.4d) the loss pattern was found to be quite complex and five mass losses could be identified: the first loss, finishing at 212 °C, involved water molecules, and some oxygenated and nitrogenated groups attached non-covalently, which together made up 4.5 % of the total weight; the second and the third losses up to 462 °C could correspond to oxygenated/nitrogenated moieties attached non-covalently and/or covalently to the graphitic lattice, amounted to 9.5 % and 10.6 %, respectively; the fourth loss, corresponds to the combustion of the largest part of the sample (73.4 %), namely the C sp^2 matrix and was completed at 678 °C. Palladium-containing species are involved in the last loss up to 873 °C**.** Firstly, Pd oxidizes to PdO_2, and above 780 °C, 2.8 % of the oxide's total weight returns to metallic Pd.$^{65.9\ \%}$ The residue, counted for 2.9% alludes to all the palladium-related species. The DTA curve shows four important degradation processes: the first and the second maxima point to the degradation of the newly incorporated functionalities attached non-covalently and/or covalently at 307 °C and 430 °C, respectively. The third and more pronounced peak indicates the combustion of the graphitic network, reaching its maximum degradation rate at 602 °C, and finally the reduction of PdO_2 to Pd at 834 °C.

When comparing these results with those obtained for the Ag-containing MWCNT powder and paper (Chapter 5), it is obvious that the catalytic effect of the metal nanoparticles influences the thermal stability of the carbon matrix, and the higher the metal content, the lower the temperature at which the combustion was completed. This trend was observed as well in the graphene oxide/silver and palladium series (Chapters 3 and 4). A remarkable difference between the samples is the amount of metal deposited. Whereas Pd does not even reach 1 wt%, an Ag loading of up to 10 wt% could be achieved. An analogous trend was observed with the GO-based series, where the metal content also reached weight percentages of 10 wt% or even more (see Chapter 3).

The thermal behaviour of the buckypapers seems quite different from that of the powder samples (Fig. 6.5). Unlike for oxidized nanotube in powder form, non-functionalized BP (Fig. 6.5a) exhibited a first mass loss up to 362 °C that was much more important - 12.9 % - than the 2.1 % for MWCNTs. This is due, among other things, to the presence of the surfactant Triton™ X-100 employed for the fabrication of the buckypaper, which evaporates above 310 °C,[66] and reaches its maximum decomposition rate at 333 °C according to the DTA curve in blue in Fig. 6.5a. The second DTA peak at 418 °C stems from the degradation of light carbon moieties and possibly some ubiquitous oxygen. The main mass loss corresponding to the combustion of the intertwined carbon nanotubes continued to 652 °C and accounted for 87.4 % of the total weight, with a DTA peak at 610 °C.

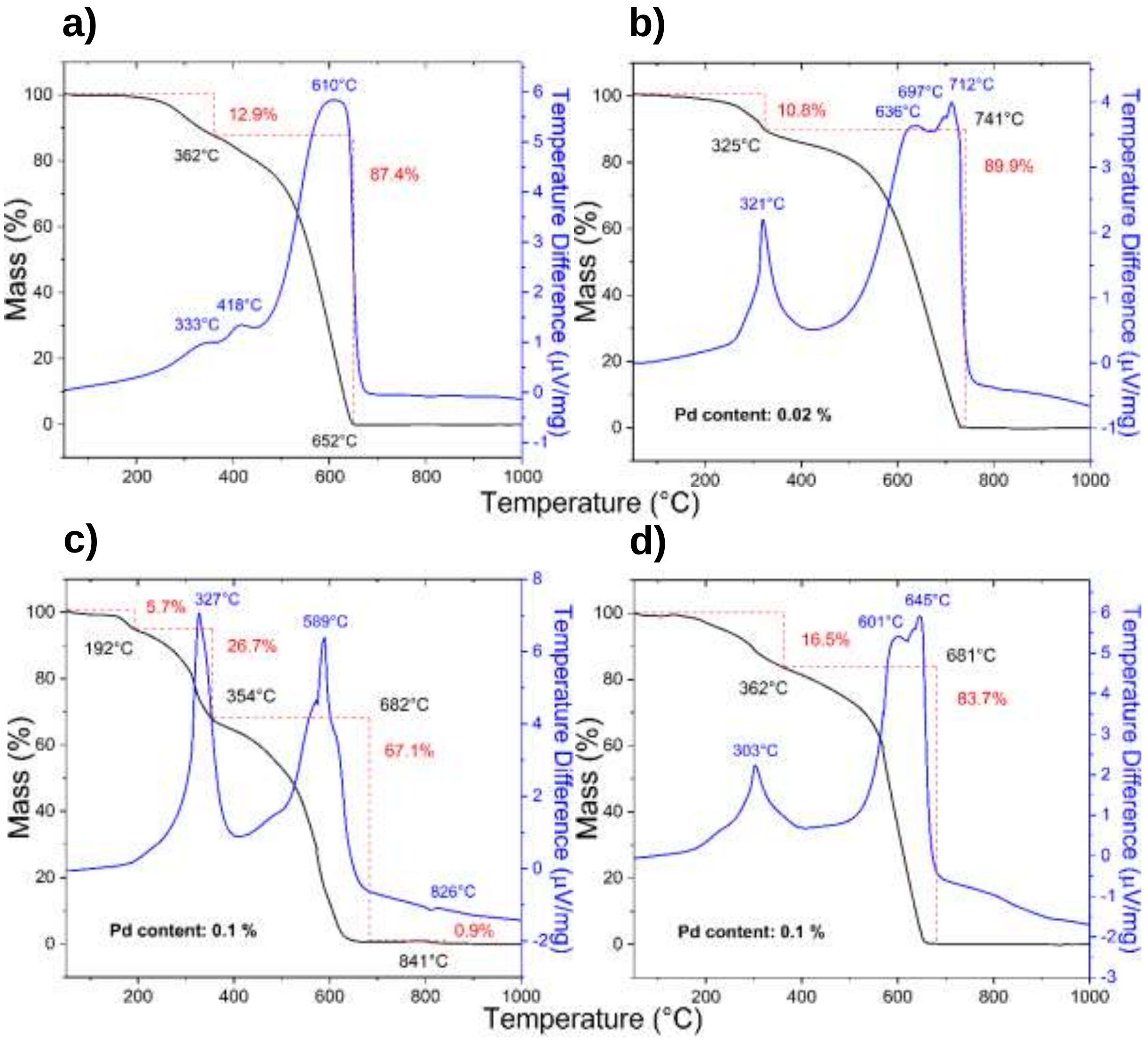

Fig. 6.5. TGA (black) and DTA (blue) of BP samples: a) BP prepared from MWCNTs$_{(ox)}$ **without further functionalization or metal decoration, b) BP+Pd, c) BP+ODA+Pd, and d) BP+DAO+Pd.**

The thermogram for the BP+Pd sample (Fig. 6.5b) resembles that of the undecorated BP, but the terminal temperatures of the weight losses differ. The initial loss, which accounted for 10.8% of the overall weight, resulted in a 37 °C drop, which could be attributed to the presence of palladium. The second loss reached 741 °C (89 °C higher than BP) and accounted for 89.9%. The residue accounts for 0.02% of Pd and falls under the error bar (less than 0.1%). The DTA curve looks somewhat different from that of the buckypaper without Pd. The first peak appeared at 321 °C, which is 12 °C lower than for non-decorated BP. Other peaks and shoulders are detected within the graphitic region, which, according to Leonte *et al.* (1986)[67], suggests changes in crystallite size due to these thermal processes which may be relevant to phase transitions in palladium-containing carbon matrices.

The thermogram of the BP+ODA+Pd sample (Fig. 6.5c) follows a different pattern than that of the MWCNTs+ODA+Pd powder sample. Here four mass losses were observed. The first one amounting to 5.7 % may include both physiosorbed ODA moieties and non-covalently bonded oxygenated functionalities and reach up to 192 °C. The second one, which accounted for 26.7 % and continued up to until 354 °C, is attributed to the pyrolysis of covalently bonded ODA functionalities to oxygen-containing groups. The third and largest loss (comprising 67.1 %) relative to the combustion of the carbonaceous matrix extended up to 682 °C, and finally, one distinguishes again the oxidation of palladium continuing up to 841 °C when the oxidized species recovers to metallic Pd.[65] From here and until 1000 °C, all the palladium-related species sum 1.0 %. The DTA curve shows three maxima corresponding to the pyrolysis of ODA and oxygenated functionalities (327 °C), the combustion of sp^2 hybridized carbon (589 °C), and the phase transition from Pd oxide to metallic Pd (826 °C).

The thermogram for BP+DAO+Pd (Fig. 6.5d) shows two main weight loss steps, the first one relative to the loss of physisorbed water and of oxygen- and nitrogen-containing functionalities up to 362 °C and accounting for 16.5 % of the initial weight, and a second one corresponding to the combustion the graphitic lattice of the nanotubes, which extends up to 681 °C and during which 83.7 % of the initial weight is lost. This thermogram shows no sign of the formation of PdO_x, and we conclude that the Pd deposited on this sample scarcely reached 0.1 wt% within the error bar (less than 0.1 %). The DTA curve exhibits three degradation maxima, of which the first corresponds to the new functionalities (303 °C), whereas the other two belong to the pyrolysis of the matrix.

If we compare the palladium content in GO and MWCNTs powder and paper hybrids (see also Chapter 4) we see that in all cases, Pd never makes up more than 0.9 wt.% of the hybrid. This is quite different from the Ag-containing hybrids (see Chapters 3 and 5) where more than 10 times higher metal loadings were found. Comparing the catalytic effect of palladium to the combustion temperature of the graphitic lattice, we conclude that below 0.4 wt% of Pd, the graphitic matrix is more thermoresistant and only above 0.6 wt% it pyrolyzes faster.

The effects of the functionalization and decoration with PdNPs were further analysed by means of electron microscopy, performed as detailed in Chapter 2. Fig. 6.6 shows the SEM images of $MWCNTs_{(ox)}$ at three different magnifications. As observed in Chapter 5, the amine-free sample exhibits a ‘’spongy’’ structure but seems denser after the surface is modified with amines. This is clearly seen in Fig. 6.6a,d,g. As the magnification increases, one distinguishes differences in the shape and distribution of the deposited particles. The images in the central column (Fig. 6.6b,e,h) show that there are abundant particles with a variety of sizes, ranging from less than 0.1 µm up to 0.8 µm and different shapes in all cases. In the micrographs taken with the highest magnification (Fig. 6.6c,f,i) multi-prismatically shaped particles can be distinguished. In MWCNTs+Pd pentagonal particles are predominant, whereas irregular prisms prevail in the amine-containing nanotube samples.

These shapes are clearly distinct from those observed for decoration with AgNPs (see Chapter 5), where the particles formed were mainly round and considerably smaller. It should be noted that the Pd decoration of GO (see Chapter 4), also gave rise to prism-shaped particles but there the particle sizes were smaller and the surface density lower.

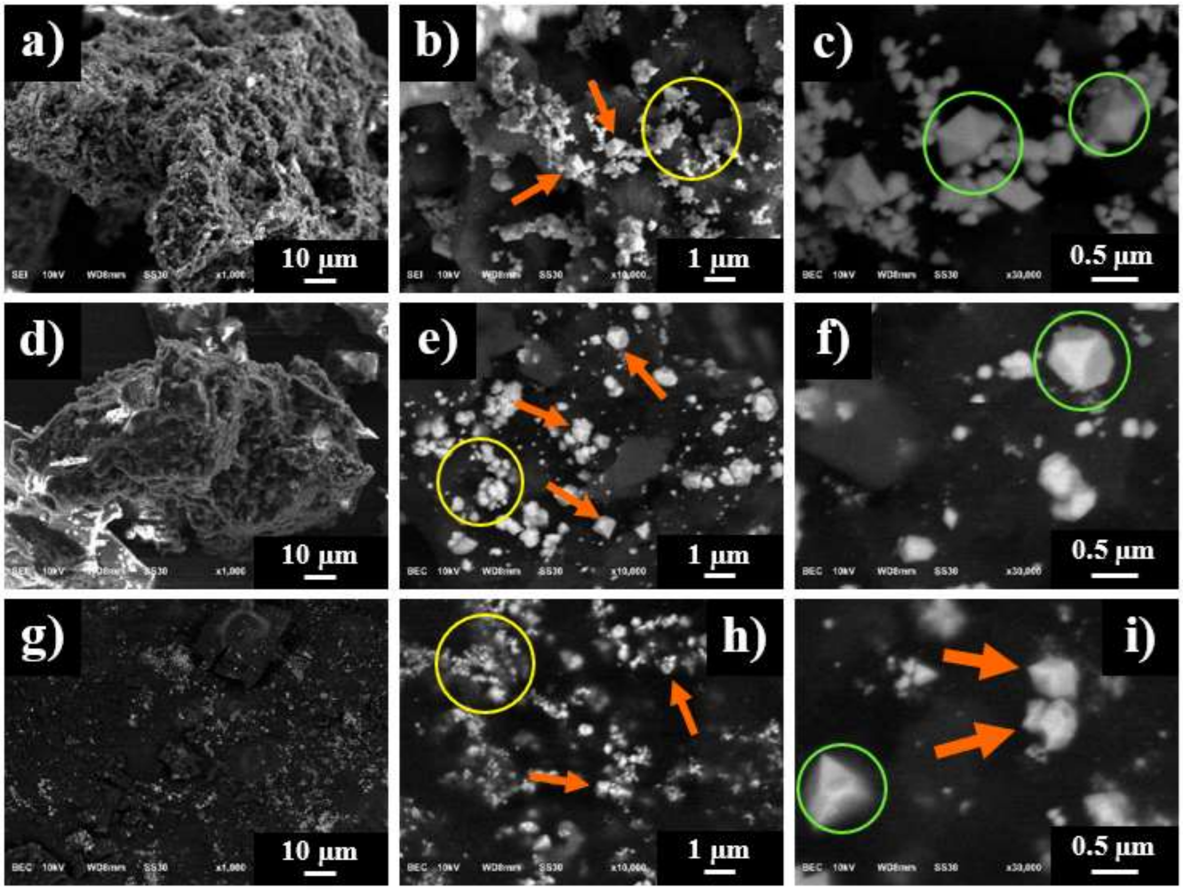

Fig. 6.6. Representative SEM images for MWCNTs+Pd (a-c), MWCNTs+ODA+Pd (d–f), and MWCNTs+DAO+Pd (g–i) at different magnifications. Scale bars: 10 µm (left column); 1 µm (middle column), and 0.5 µm (right column).

The EDS results (summarised in Table 1) confirm successful amine grafting since the carbon content is higher in the functionalized samples due to the contribution of the aliphatic chains of the amines. On the other hand, one can see that the weight percentage of Pd in MWCNTs+Pd and MWCNTs+DAO+Pd samples is similar. This trend was also observed in TGA results where the residue is equal for these two hybrids, however, the values for the Pd content differ between EDS and TGA because EDS probes only a tiny volume and the Pd distribution is not uniform.

Table 1. EDS results for the MWCNTs/PdNPs series (SEM imaging)

Sample	Weight (%)	Atomic (%)
MWCNTs+Pd	C (K): 44.5 ± 3.1 O (K): 32.4 ± 2.6 Pd (L): 5.2 ± 1.3	C (K): 58.3 ± 2.4 O (K): 33.5 ± 2.2 Pd (L): 3.5 ± 1.0
MWCNTs+ODA+Pd	C (K): 62.9 ± 0.4 O (K): 34.0 ± 0.7 Pd (L): 2.5 ± 0.4	C (K): 70.7 ± 0.5 O (K): 28.7 ± 0.5 Pd (L): 0.3 ± 0.04
MWCNTs+DAO+Pd	C (K): 61.3 ± 6.1 O (K): 33.1 ± 4.2 Pd (L): 4.8 ± 3.0	C (K): 70.4 ± 4.8 O (K): 28.6 ± 4.6 Pd (L): 0.6 ± 0.4

Similarly to the Ag-containing BP series, secondary electron images (SEI) and backscattered electron composition (BEC) micrographs were collected to study the morphological features of the cross-section and of both faces of the paper, especially with better contrast between light and heavy elements in their composition (Figs 6.7 and 6.8). Fig. 6.7a, d, g shows the images of the cross-section of each sample, which allow us to determine thickness differences: while the thickness of BP+Pd is 33 µm, BP+ODA+Pd is more than twice thicker, with a cross-section of 79 µm. In contrast, functionalisation with the diamine only marginally increased the thickness, which for BP+DAO+Pd amounts to 36 µm. According to the literature, the thickness of MWCNTs-based bucky paper is about 30 µm,[68] which agrees with the results obtained here. The slight increase of thickness in BP+Pd and BP+DAO+Pd points to the deposition of some particles inside the paper structure and not only on the outer surfaces.[57,69]. For BP+ODA+Pd the strongly increased thickness is similar to what was observed for the homologous GO-based hybrid in paper form (see Chapter 4) and due to the 'swelling' effect produced by the long ODA-alkyl chain.

The second and third columns in Fig. 6.7 show the superficial characteristics of both sides of the buckypapers. Fig. 6.7b,e,h, which refer to the sides that were in contact with the filtration membrane during the preparation of the papers, all show a compact, slightly rugous surface, whereas the opposite surfaces of the buckypapers presented in Fig. 6.7c,f,i appear rather uneven, with some randomly distributed spongy zones. As described also for the GO papers (Chapter 4), the reason for this difference in appearance is that the nanotubes in contact with the filtration membrane are more influenced by the pumping and therefore form a denser structure than those on the opposite side, which therefore arrange more randomly.

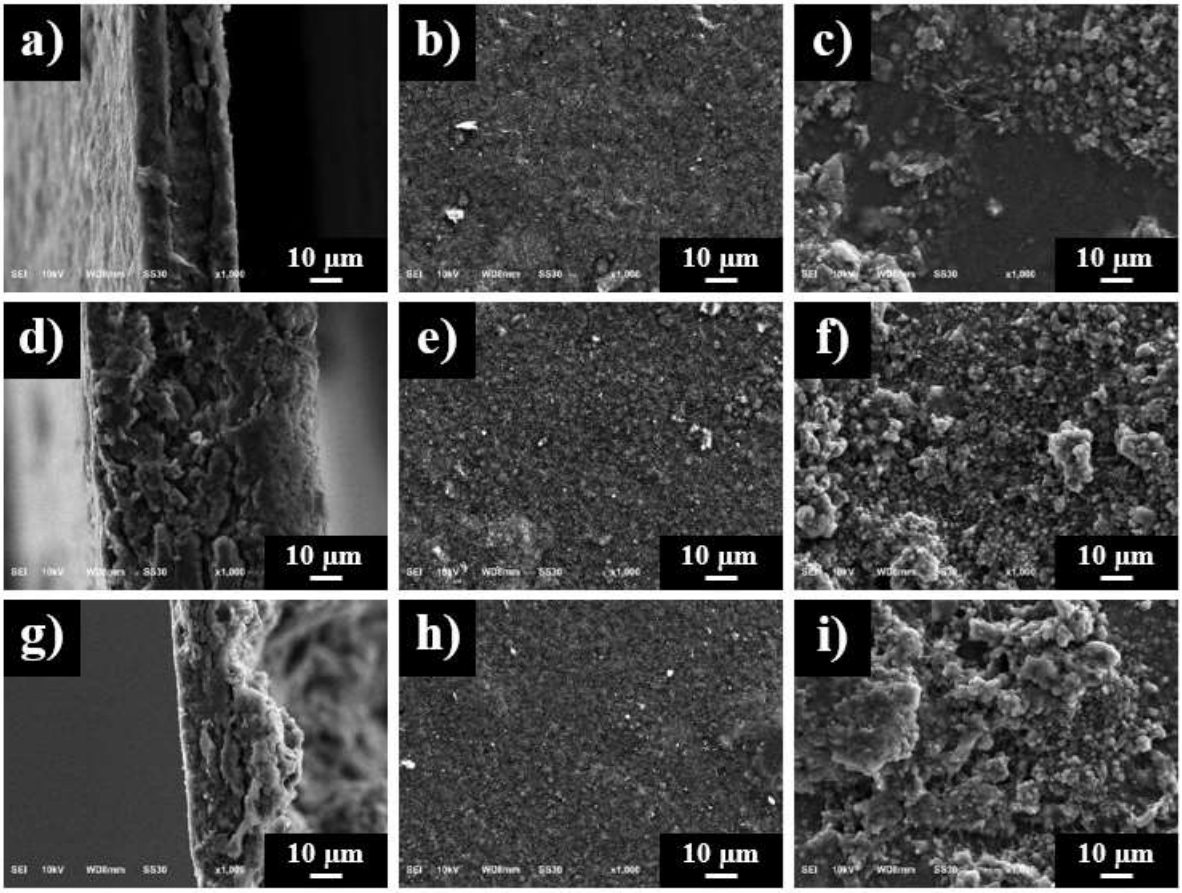

Fig. 6.7. Secondary electron SEM images of BP+Pd (a–c), BP+ODA+Pd (d–f), and BP+DAO+Pd (g–i) series. The left column (a,d,g) shows the cross-section images of the different samples; the middle column (b,e,h) presents images of the lower side of the buckypaper which was in contact with the filter membrane during BP fabrication, and the right column (c,f,i) shows the upper side of the buckypaper. Scale bar: 10 µm.

Since the presence of PdNPs cannot be clearly distinguished in these images, BEC imaging was performed as well (Fig. 6.8). The first column shows the characteristics of the paper side that was in contact with the filtration membrane during paper preparation, whereas in the second column, one sees the images of the opposite side. Notably, the PdNPs distribution is quite homogeneous in all cases, but the more compact side of the buckypaper presents a lower particle density than the opposite side with its more open structure. However, compared with graphene oxide paper, the PdNP coverage on GOP was lower, even when anchoring amines before PdNP decoration. This correlates with the surface area reported for these structures, which for BP amounted to 380 m^2/g,[70] whereas for GOP it was 3 to 10 m^2/g,[71] implying that the buckypaper is more penetrable for the metal precursor solution.

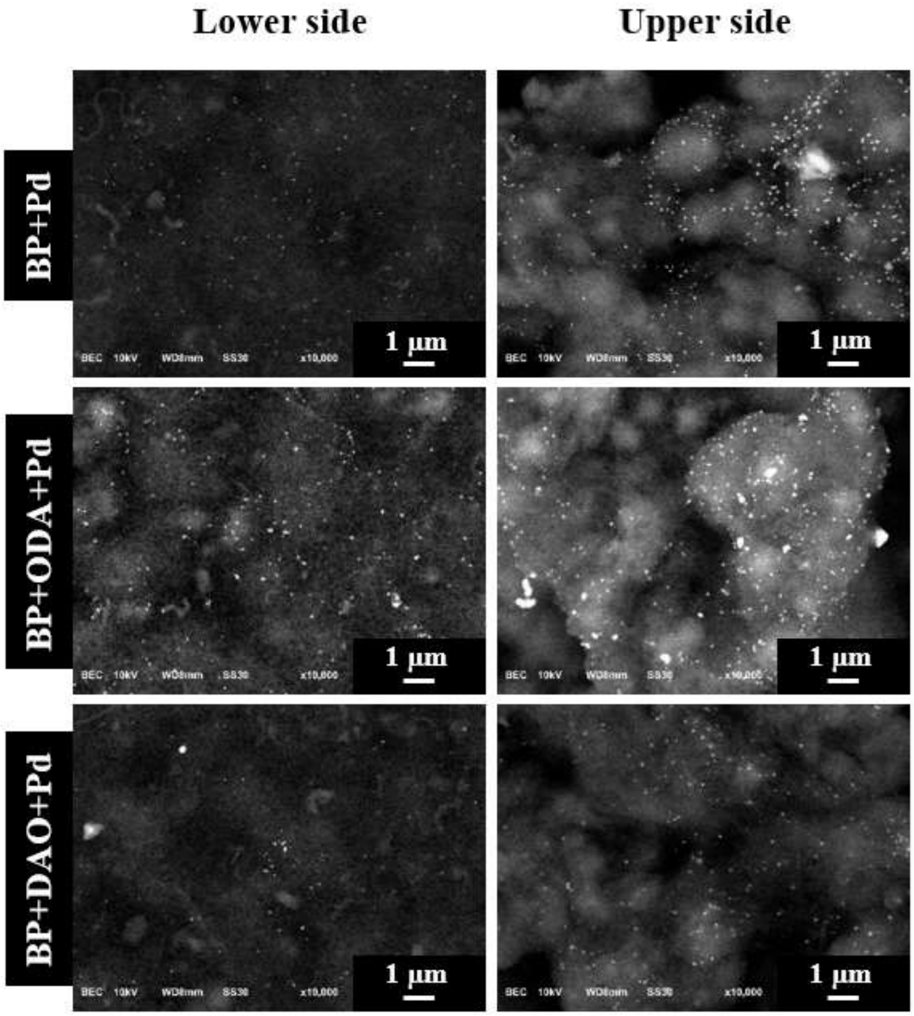

Fig. 6.8. Backscattered electrons SEM images for the set of the BP/PdNP series. The columns highlight the size and distribution of the particles attached on both faces of the buckypaper. Scale bar: 1 µm.

It is important to mention that particle agglomeration is almost absent on the denser side, whereas, on the opposite side, we observe the formation of some clusters, mainly in the ODA-containing sample. For BP+ODA+Pd most of the particles are round with a narrow size distribution, ranging from less than 0.1 µm up to 0.5 µm. Compared to decoration with silver, PdNPs are smaller, but for both metals, the paper supports favoured the formation of round particles, while on both GO and MWCNT powders different shapes occurred.

The metal content was quantified by EDS and the results are reported in Table 2. Here we can observe that the highest Pd content was found in BP+DAO+Pd, attributed to the capacity of the two coordinating nitrogen atoms to bond more palladium atoms. Since no large differences in PdNP density were seen in the SEM images of the different samples, we have to assume that also smaller particles were formed which, due to the instrumentation limitations cannot be visualized. Comparing the results in Tables 1 and 2, one notes that the oxygen and palladium content is much higher in the powder samples. This again has to do with the surface area differences: MWCNTs can reach a surface area of up to 1670 m^2/g,[72] *i.e.* more than four times that of BP (380 m^2/g).[70]

Table 2. EDS results for the BP/PdNPs series (SEM imaging)

	Region			
	Lower side		**Upper side**	
Sample	Weight %	Atomic %	Weight %	Atomic %
BP+Pd	C (K): 95.4 ± 0.5 O (K): 3.7 ± 0.5 Pd (L): 0.8 ± 0.3	C (K): 97.1 ± 0.4 O (K): 2.9 ± 0.4 Pd (L): 0.1 ± 0.03	C (K): 94.6 ± 0.8 O (K): 4.6 ± 0.9 Pd (L): 0.7 ± 0.2	C (K): 96.4 ± 0.7 O (K): 3.5 ± 0.7 Pd (L): 0.1 ± 0.02
BP+ODA+Pd	C (K): 96.2 ± 0.4 O (K): 2.8 ± 0.3 Pd (L): 1.0 ± 0.3	C (K): 97.7 ± 0.2 O (K): 2.2 ± 0.3 Pd (L): 0.1 ± 0.03	C (K): 96.0 ± 0.3 O (K): 3.3 ± 0.4 Pd (L): 0.7 ± 0.1	C (K): 97.4 ± 0.3 O (K): 2.5 ± 0.3 Pd (L): 0.1 ± 0.01
BP+DAO+Pd	C (K): 91.0 ± 0.5 O (K): 5.1 ± 0.6 Pd (L): 3.1 ± 0.3	C (K): 95.3 ± 0.4 O (K): 4.0 ± 0.4 Pd (L): 0.4 ± 0.04	C (K): 90.7 ± 0.9 O (K): 5.4 ± 0.9 Pd (L): 3.2 ± 0.1	C (K): 95.1 ± 0.7 O (K): 4.2 ± 0.7 Pd (L): 0.4 ± 0.02

If we compare the results obtained here for oxidized carbon nanotubes with those of the amine-functionalized and Pd-decorated graphene oxide, described in Chapter 4, we note that while for GOP there were important differences in the elemental composition between the two sides, in the corresponding buckypaper data are quite similar. For the powders, Pd decoration was more efficient on GO than on the nanotubes, which matches the conclusions from the micrographs, and is supported by the differences in surface area - up to 2391 m^2/g for GO[51] *vs* 1670 m^2/g for MWCNTs.[51]

Since EDS suggested the presence of Pd nanoparticles that were too small to be detected at the micrometre scale, TEM imaging was performed. Fig. 6.9 presents bright field images of the powder series. The first row shows the micrographs of the MWCNTs+Pd sample at different magnifications, where one can clearly distinguish nanometre-sized particles. The same is true for the second and third rows that show images of MWCNTs+ODA+Pd and MWCNTs+DAO+Pd. The nanoparticles differ in shape and size, the latter varying from diameters up to 50 nm for MWCNTs+Pd, from less than 5 to 30 nm for MWCNTs+ODA+Pd, and from 20 to 80 nm for MWCNTs+DAO+Pd. Compared with the Ag-containing series, we can observe that the particles formed on the non-aminated MWCNTs were smaller, but those on the aminated samples were bigger. Compared with the GO-based homologues, we can see that the particles there were significantly smaller.

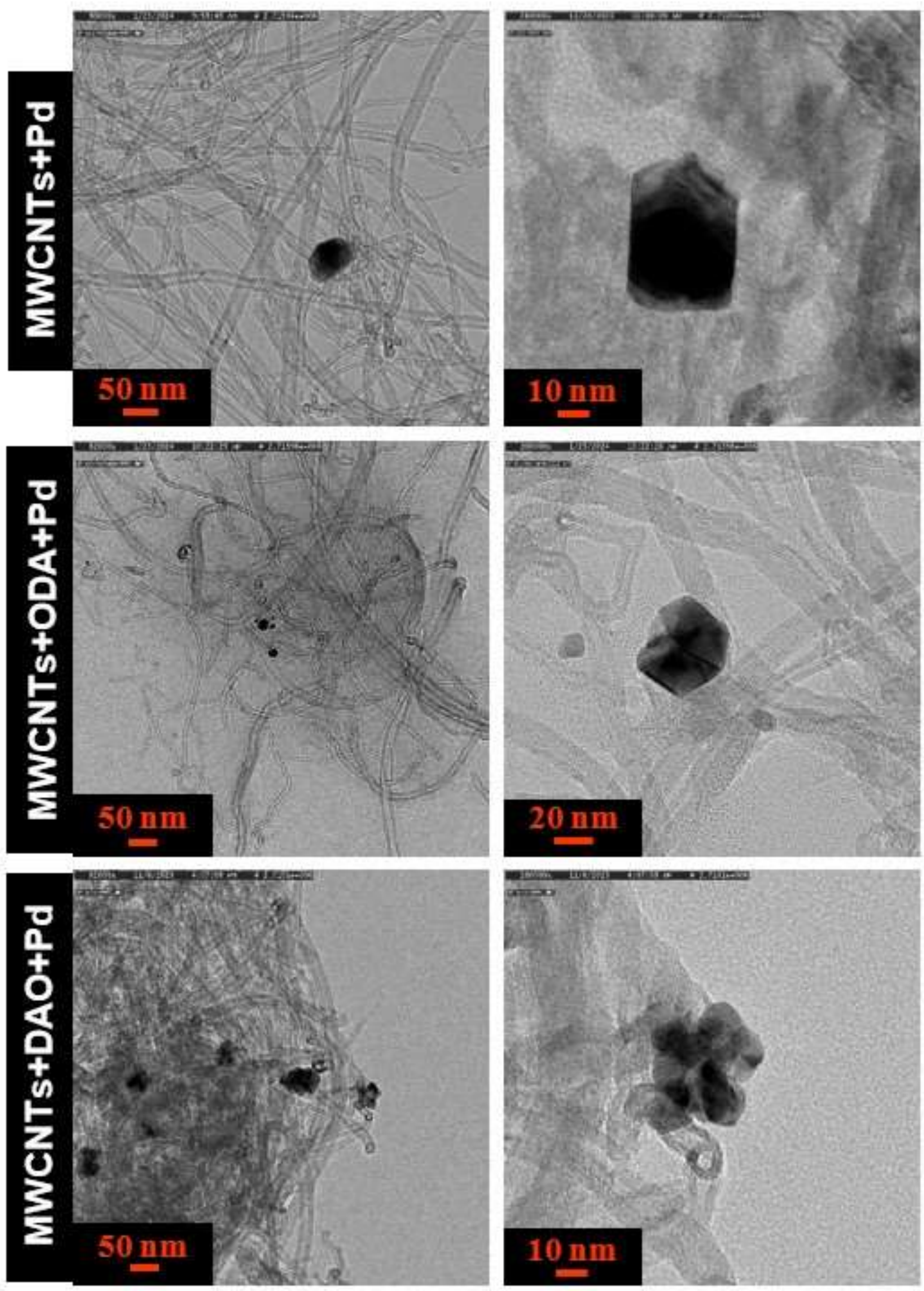

Fig. 6.9. Bright-field TEM images of the palladium containing multiwalled carbon nanotubes series at different magnification. In the left column, the scale bar corresponds to 50 nm for all the samples, while in the right column, the scale bar corresponds to 10 nm for MWCNTs+Pd and MWCNTs+DAO+Pd and to 20 nm for MWCNTs+ODA+Pd.

Focussing on the MWCNTs instead, one notes that the individual nanotubes look wider in the aminated samples, particularly at higher magnification (second column in Fig. 6.9). As discussed before, bifunctional molecules promote cross-linked structures,[17,22,73] as can be observed in the first micrograph of the DAO-containing sample.

Similarly, bright field TEM imaging was performed on the buckypaper hybrids at different magnifications, as shown in Fig. 6.10. The first row presents the micrographs for BP+Pd, where the particles reached sizes ranging from 15 to 200 nm. The second row shows particles measuring between 10 to 200 nm on BP+ODA+Pd and in the third row, one distinguishes particles with sizes varying from 5 to 20 nm on BP+DAO+Pd. As also seen in SEM, palladium particle agglomeration prevails in the first two samples, facilitating their visualization, whereas for the DAO-containing hybrid, the tiny particles seem well dispersed. Interestingly, this trend is the opposite of what was observed for the corresponding Ag series (Chapter 5), where the tiniest particles were found in BP+Ag. BP+ODA+Ag also differs from the results for graphene oxide paper, where the smallest particles were formed on GOP+Pd.

These differences depend on the coordination number and geometry in coordination complexes of silver and palladium, on the chemical and structural characteristics of the different nanocarbons applied in this study, the morphological differences between powder and paper-like forms in the same nanocarbon (graphene oxide, carbon nanotubes), on the different chemical nature between monoamine and diamine molecules, and their attachment mechanism to nanocarbon surfaces.

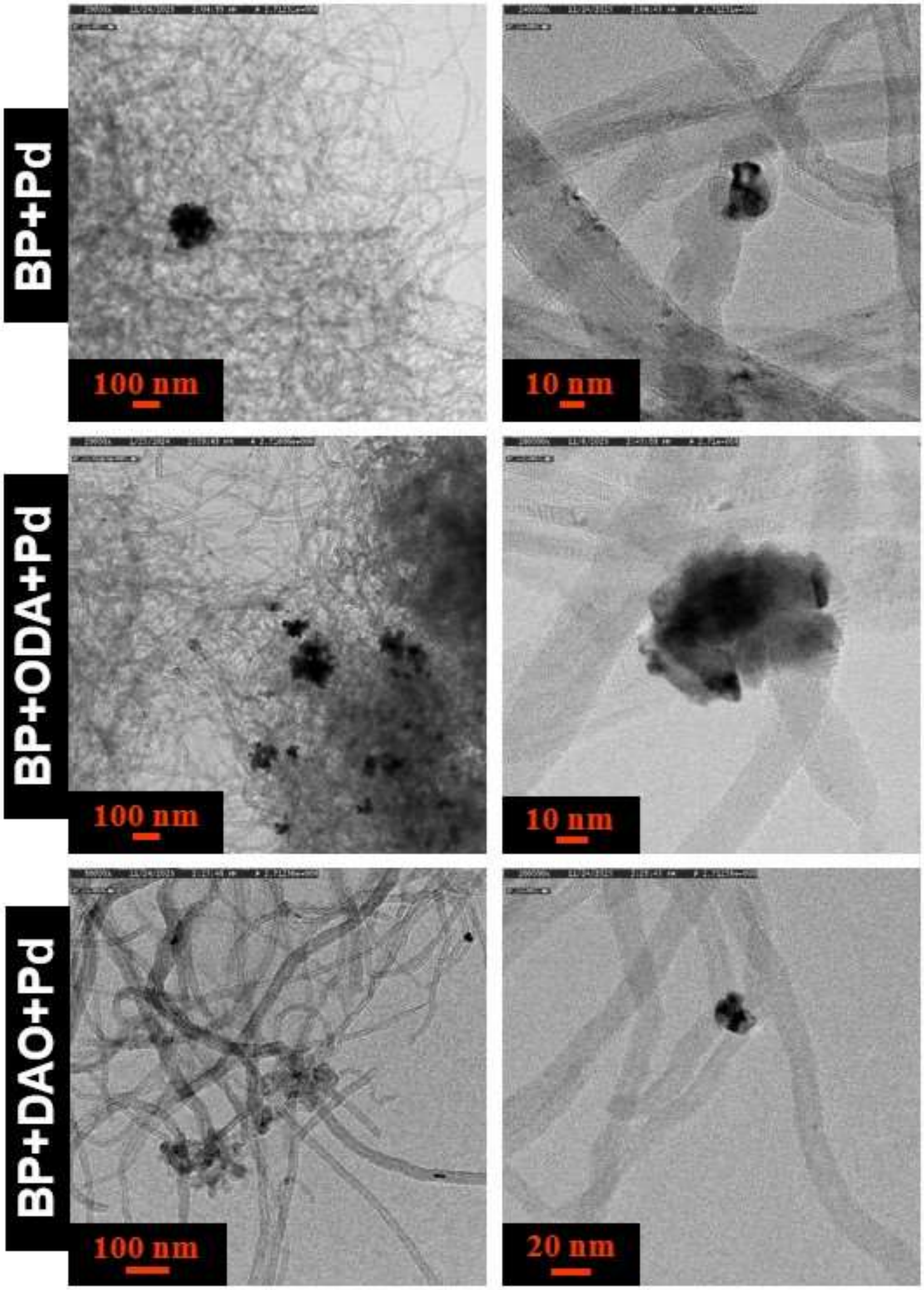

Fig. 6.10. Bright-field TEM imaging for the palladium containing buckypapers at different magnification. In the left column at the scale bar corresponds to 100 nm for all the samples, whereas in the right column it corresponds to 10 nm forBP+Pd and BP+ODA+Pd samples and to 20 nm for BP+DAO+Pd.

XPS analysis was used to explore the surface composition and bonding environment of each element that makes up the starting materials and the newly created hybrids. Fig. 6.11 shows the survey spectra of the oxidized and the palladium-containing MWCNTs, which all show the spectral signature of carbon and oxygen. The Pd-decorated hybrids all present Pd 3*d* peaks of different intensity and for the amine-functionalized MWCNTs, a N 1*s* photoemission peak can be seen, once more confirming the success of the ODA or DAO grafting and of the metal decoration protocols.

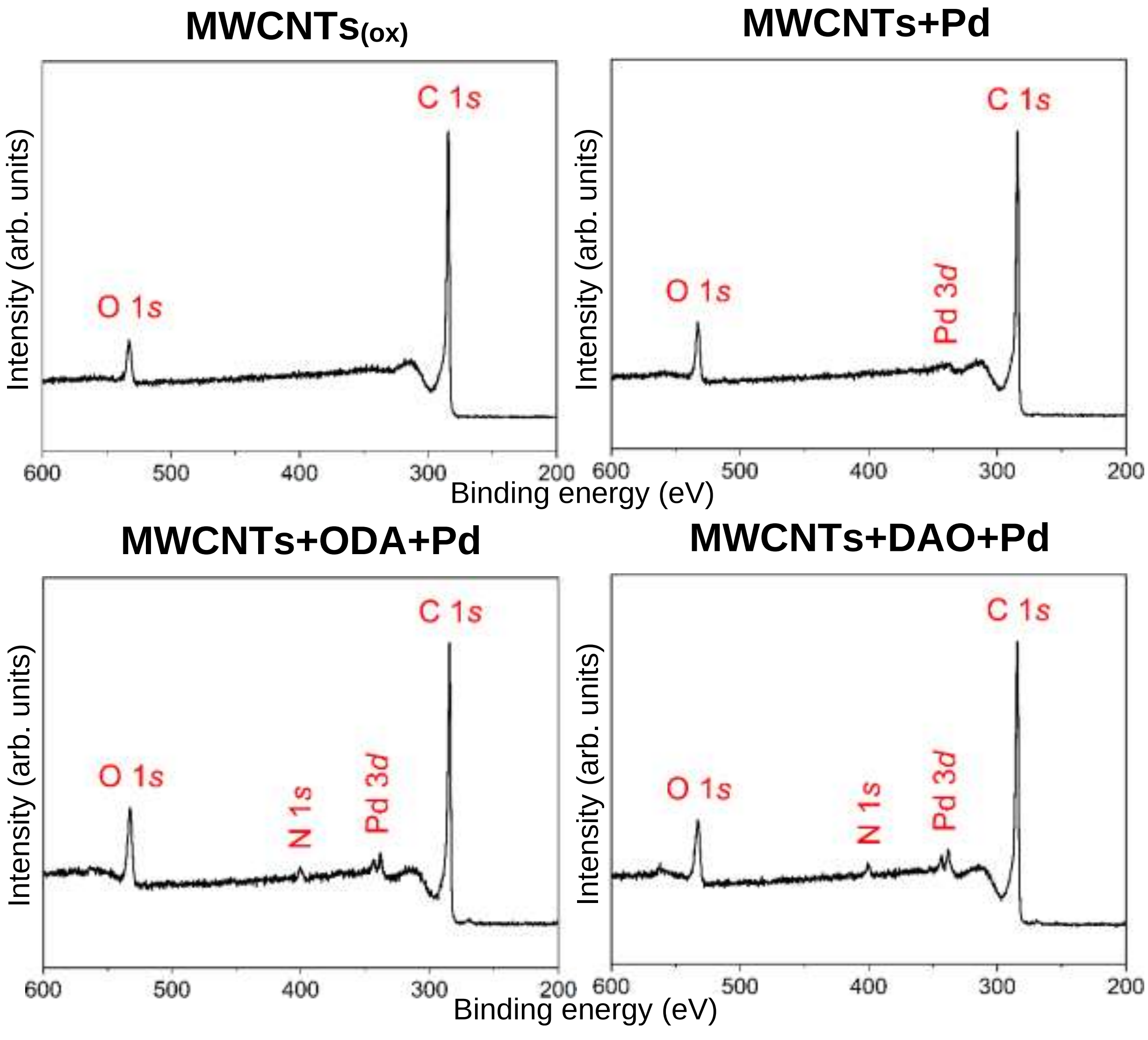

Fig. 6.11. Survey XPS spectra for MWCNTs$_{(ox)}$, MWCNTs+Pd, MWCNTs+ODA+Pd, and MWCNTs+DAO+Pd samples.

The deconvoluted detailed spectra of the different core level regions are displayed in Fig. 6.12, and the corresponding binding energy values are listed in Tables 3-5. In all the samples six peaks were derived from the deconvolution of the C 1*s* spectral line (left graphic of Fig. 6.12); their binding energy values and relative spectral intensity for each sample are reported in Table 3. The main peak, derived from sp^2/sp^3 domains of the MWCNTs, appears at a binding energy (BE) of 284.1 eV in all the samples and for MWCNTs+ODA+Pd, and MWCNTs+DAO+Pd it also contains the spectral intensity due to $-CH_2$ groups. Moving towards higher BEs, the next four contributions stem from oxygen-containing moieties: the first one at 285.1 – 285.2 eV derives from oxidized carbon in MWCNTs before and after Pd decoration, whereas in aminated samples at this binding energy, the contributions of oxidized carbon and C-N bonds overlap.[59] The second contribution appearing in the BE range of 286.1-286.4 eV, refers to hydroxyl groups from alcohol moieties, while the third contribution at BEs of 287.4-287.8 eV derives from carbonyl groups. Carboxyl groups are responsible for the contribution at BE = 288.7-289.0 eV, and at 290.5 eV the π-π* satellite[74,75] is found. Since XPS is a quantitative technique and the relative spectral intensity is directly proportional to the amount of each type of functional group in the probed volume, from the spectral intensities reported in Table 3 one can see that in general, the amount of oxygenated groups is higher in the Pd-containing samples. This is probably due to the additional acid treatment during the PdNPs nucleation process.

The middle panel of Fig. 6.12 shows the detailed spectra of the N 1*s* spectral line, which can be deconvoluted with four contributions (BE values and relative spectral intensities reported in Table 4). The first refers to the C-N bond of the aliphatic chain of the amines, appearing at a BE of 399.0 eV in MWCNTs+ODA+Pd, and at 398.7 eV in MWCNTs+DAO+Pd. The second contribution situated at 400.1 eV in ODA- and at 400.0 eV in the DAO-containing hybrid stems from the amino groups. The third contribution at a BE of 401.3 eV is associated with protonated NH_3^+ species, formed as a result of the acidic treatment during the nucleation process of palladium particles (pH around 0 and 1). The fourth component, appearing at a binding energy of 403.0 eV, points out the newly formed amide moieties, also observed in FTIR results. In these data, we can note a higher content of amino groups in the DAO-containing sample (as expected).

The Pd 3*d* core level spectra, shown in the right panel of Fig. 6.12, give insight into the different chemical states of palladium when deposited onto the graphitic matrix. The binding energies of the various components and their relative spectral intensities are listed in Table 5. Here, the spectra consist of two peaks corresponding to the spin-orbit split Pd $3d_{5/2}$ and Pd $3d_{3/2}$ lines. The peaks assignment was carried out considering that, according to the literature, three chemical states coexist in the samples: Pd(0), Pd(IV) and Pd(II). Focussing on the $3d_{5/2}$ peak, the metallic form gives rise to a component in the BE range 335.5 - 335.8 eV[76,77], while the contribution of tetravalent palladium is situated at BE=337.5 – 337.9 eV.[78,79] Bivalent palladium can be complexed with carboxylate ions derived from the deprotonation of the carboxylic acid of citric acid used as a reducing agent in the PdNPs formation.[80] The reported BE for the complex formed varies between 338.6 – 338.8 eV.[81,82]

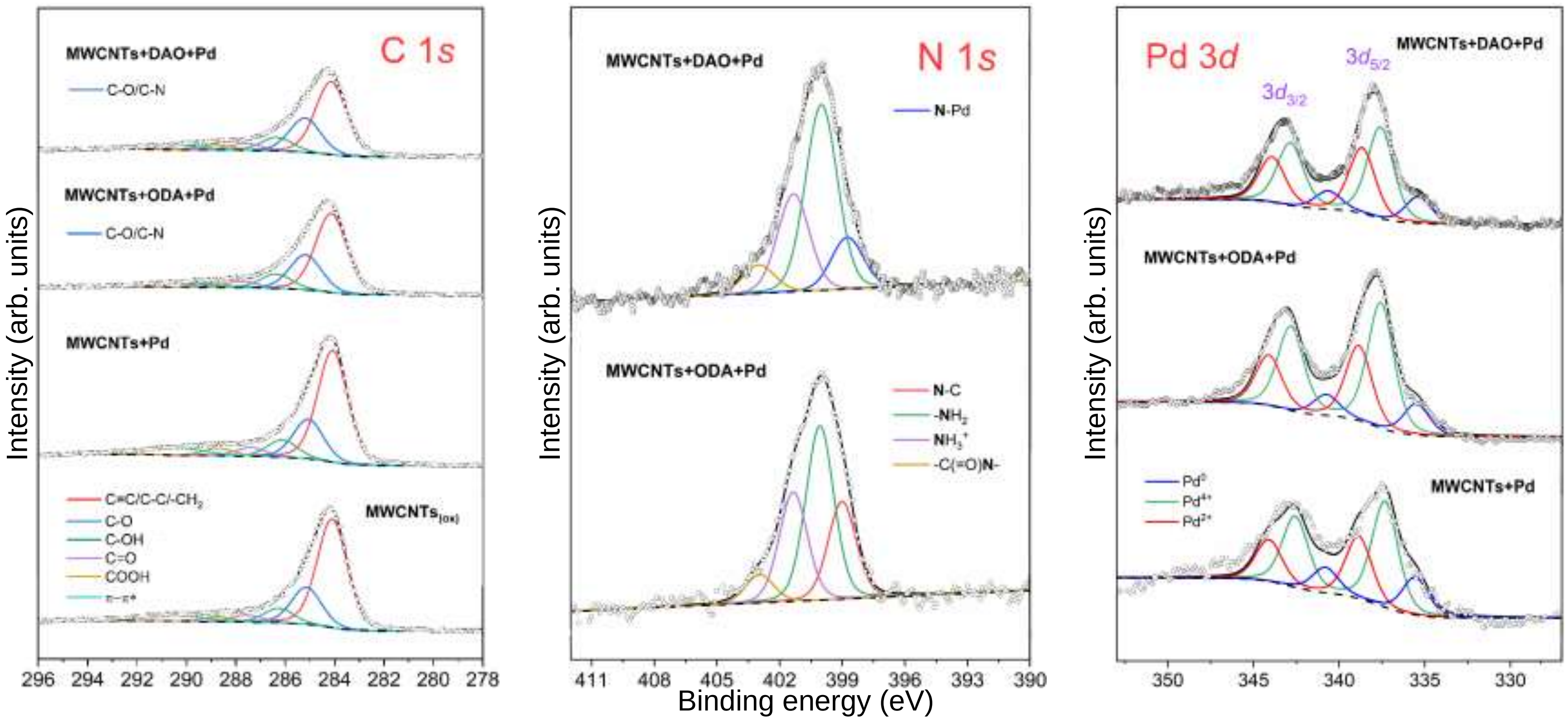

Fig. 6.12. XPS spectra of the C 1*s*, N 1*s* and Pd 3*d* core level regions for MWCNTs$_{(ox)}$, MWCNTs+Pd, MWCNTs+ODA+Pd, and MWCNTs+DAO+Pd samples. Raw spectra are shown in dots, and sum, in black.

Table 3. XPS binding energies and relative spectral intensities of the contributions from different chemical species to the C 1*s* core level spectra of the MWCNTs+Pd based series

	Component binding energy (eV)					
Sample	**C=C/C-C/-CH$_2$ (%)**	**C-O (%)**	**C-OH (%)**	**C=O (%)**	**O=C-O (%)**	**π-π* shake-up (%)**
MWCNTs$_{(ox)}$	**284.1** (58.8)	285.2 (20.0)	286.3 (7.8)	287.6 (3.8)	288.8 (2.8)	**290.5** (6.8)
MWCNTs+Pd	(56.0)	285.1 (19.9)	286.1 (8.6)	287.4 (4.4)	288.7 (3.8)	(7.3)
		C-O/C-N (%)				
MWCNTs+ODA+Pd	(54.1)	**285.2** (24.1)	286.4 (9.9)	287.8 (4.4)	289.0 (2.5)	(5.1)
MWCNTs+DAO+Pd	(51.7)	(24.3)	286.3 (9.6)	287.6 (4.8)	288.8 (3.8)	(5.7)

Table 4. XPS binding energies and relative spectral intensities of the contributions from different chemical species to the N1*s* core level spectra of the aminated MWCNTs+Pd samples

	Component binding energy (eV)			
Sample	**N-C (%)**	**-NH$_2$ (%)**	**NH$_3^+$ (%)**	**–C(=O)N– (%)**
MWCNTs+ODA+Pd	399.0 (23.8)	400.1 (42.6)	**401.3** (26.7)	**403.0** (6.9)
MWCNTs+DAO+Pd	398.7 (14.2)	400.0 (51.1)	(26.8)	(7.8)

The experimental binding energy values in the Pd 3$d_{5/2}$ photoemission line in our spectra were 335.4 – 335.5 eV for Pd(0), 337.3 – 337.7 eV for Pd(IV), and 338.7 – 338.9 eV for Pd(II) (Table 5). The corresponding components in the Pd 3$d_{3/2}$ photoemission line appear in a range of 340.7 – 340.8 eV (Pd0), 342.6 – 342.9 eV (PdIV), and 344.0 – 344.1 eV (PdII).

Table 5. XPS binding energies and relative spectral intensities of the contributions from different Pd3*d* core level components in the spectra of the palladium-containing samples

	Component binding energy (eV)					
Species	**Pd (0)**		**Pd (IV)**		**Pd (II)**	
Line **Sample**	**3*d*$_{5/2}$ (%)**	**3*d*$_{3/2}$**	**3*d*$_{5/2}$ (%)**	**3*d*$_{3/2}$**	**3*d*$_{5/2}$ (%)**	**3*d*$_{3/2}$**
MWCNTs+Pd	**335.5** (18.3)	**340.8**	337.3 (51.4)	342.6	338.8 (30.2)	**344.1**
MWCNTs+ODA+Pd	(13.4)		337.6 (54.2)	**342.9**	338.9 (32.4)	
MWCNTs+DAO+Pd	335.4 (14.5)	340.7	337.7 (49.7)		338.7 (35.8)	344.0

Derived from the information above, we can infer that tetravalent palladium, in the form of palladium dioxide prevails in all the samples. This result agrees with the TGA results, which indicated that oxidized Pd was present in a much higher proportion than the metallic species. The non-aminated sample contains the highest amount of metallic species, followed by the DAO-containing sample. As expected, Pd complexation is promoted by functional groups containing both oxygen and nitrogen atoms coexisting in the aminated systems. According to the intensities of these peaks (Fig. 6.12), we can observe that complexation is favoured *via* nitrogen coordination. Comparing the data from the Tables above, we can see that complexation *via* oxygen is promoted when ODA is present.

Starting from the spectral intensities, the atomic elemental composition of the hybrids was determined (Table 6). As expected, the nitrogen content was higher in MWCNTs+DAO+Pd (4.3 %) than in MWCNTs+ODA+Pd (0.8 %) due to its bifunctionality. Therefore, the amount of Pd deposited was higher as well (more than double) (0.9 at% *vs* 0.4 at%). These results do not agree with the values obtained from SEM/EDS (Table 1) but one can understand these variations because of the differences in probing depth and lateral size probes of the two techniques and conclude that PdNP deposition is favoured in amine-containing samples. The same result was observed also for hybrids with graphene oxide (see Chapter 4).

Table 6. Elemental composition (atomic percentage) for the MWCNTs+Pd series as determined from the XPS spectra

Sample	Atomic %
MWCNTs+Pd	C: 88.1
	O: 11.7
	Pd: 0.2
MWCNTs+ODA+Pd	C: 91.5
	O: 7.4
	N: 0.8
	Pd: 0.4
MWCNTs+DAO+Pd	C: 87.2
	O: 7.6
	N: 4.3
	Pd: 0.9

For the XPS analysis of the buckypapers, considering the EDS results reported in Table 2, we decided to concentrate only on the paper side that was ***in contact with the filtration membrane during the BP formation***. Fig. 6.13 shows the survey spectra of the buckypapers before and after amine-functionalization and/or PdNP decoration. As for the powder samples, the spectrum of starting material, the buckypaper prepared from MWCNTs$_{(ox)}$, shows only the spectral signature of carbon and oxygen, while the spectra of all samples subjected to PdNP decoration show some Pd 3*d* intensity and in the spectra of the aminated samples one can always distinguish the N 1*s* line. These spectra therefore verify that the oxidation of MWCNTs leads to a starting matrix reactive enough to allow for further chemical modification with amines and/or palladium.

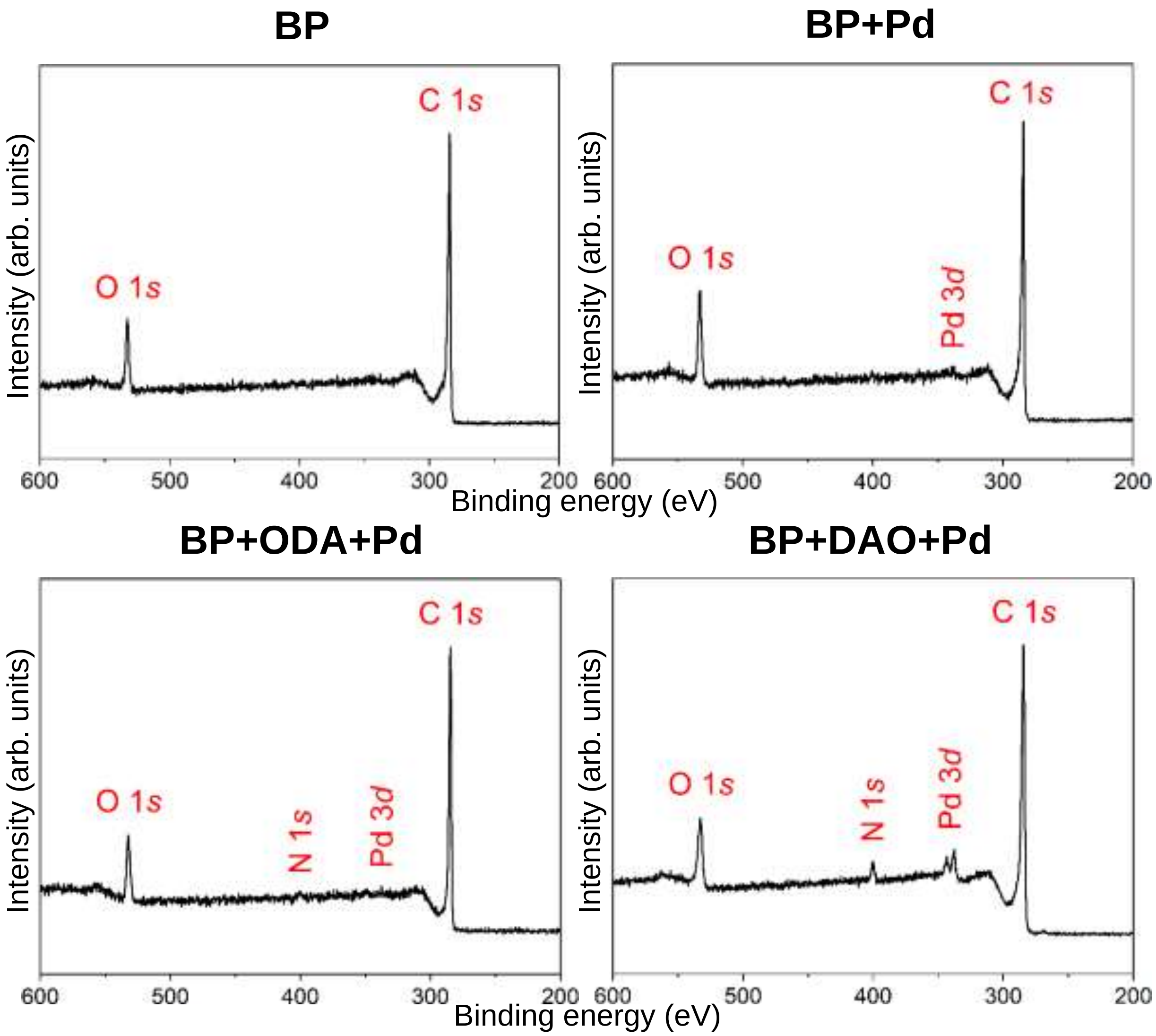

Fig. 6.13. Survey XPS spectra of BP, BP+Pd, BP+ODA+Pd, and BP+DAO+Pd.

The detailed spectra for the C 1*s*, N 1*s* and Pd 3*d* core level regions are shown in Fig. 6.14, whereas the binding energies of the different components contributing to each spectral line and their relative spectral intensities are presented in Tables 7-9.

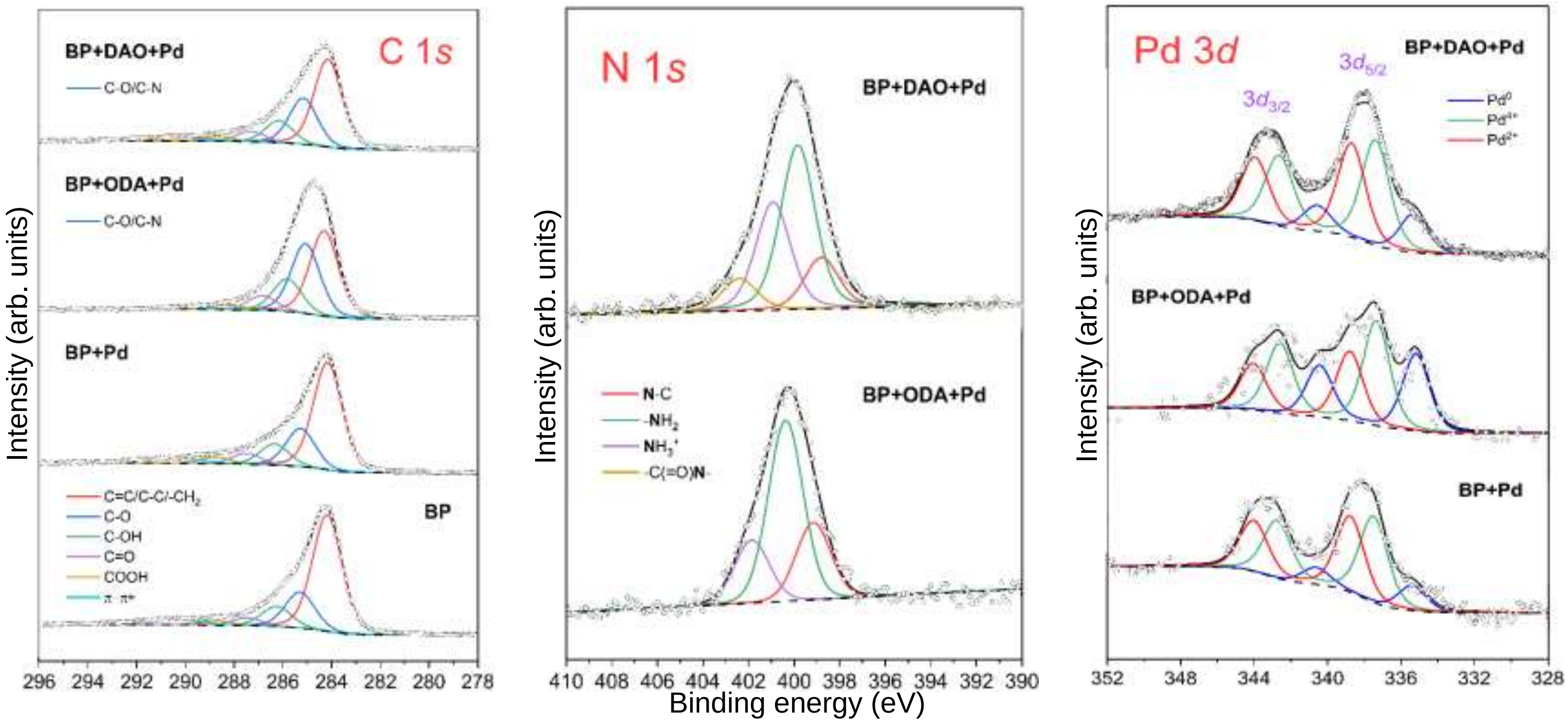

Fig. 6.14. XPS spectra of the C 1*s*, N 1*s* and Pd 3*d* core level regions of BP, BP+Pd, BP+ODA+Pd, and BP+DAO+Pd samples. Raw spectra are shown in dots, and sum, in black.

As for the powder samples, the C 1*s* spectral line of the buckypapers contains six contributions (Table 7). The main one at a binding energy of 284.1 – 284.3 eV, derives from sp^2/sp^3 domains of the graphitic matrix; for the aminated samples the contribution of -CH_2 groups also contributes to this main peak. The second contribution, situated in the BE range 285.1 – 285.3 eV, stems from oxidized carbon in the non-aminated samples, whereas the aminated ones involve contributions from both oxidized carbons and C-N bonds[59]. The third component appearing at BEs of 285.8 – 286.3 eV, can be attributed to hydroxyl groups from alcohol moieties, The fourth peak at a BE = 286.8-287.5 eV is associated with C=O groups and the fifth one at BEs ranging from 288.3 – 288.8 eV originates from O=C-O groups. The last contribution refers to the almost imperceptible π-π* satellite,[75,76] appearing in a range of 289.9 – 290.6 eV. From the relative spectral intensities of the various components (Table 8), we can highlight some trends, for example, the increased amount of oxidized carbon in the Pd-containing samples, possibly due to the reaction for preparing and depositing Pd particles, where the carbonaceous substrate is subjected to additional acid treatment, forming extra oxygenated functionalities. Apart from this, regarding the aminated samples, the peak at a BE around 285 eV also involves carbon covalently attached to nitrogen, the characteristic bonding of aliphatic amines. The fact that the BE values in the BP+ODA+Pd spectrum appear downshifted in comparison to the rest of the set can be due to different screening of the core hole when long aliphatic chains make up an important part of the sample.

Table 7. XPS binding energies and relative spectral intensities of the contributions from different chemical species to the C 1*s* core level spectra of the BP+Pd based series

	Component binding energy (eV)					
Sample	**C=C/C-C/-CH_2 (%)**	**C-O (%)**	**C-OH (%)**	**C=O (%)**	**O=C-O (%)**	**π-π* shake-up (%)**
BP	**284.2** (59.5)	**285.3** (18.4)	**286.3** (10.4)	**287.5** (4.0)	288.7 (2.3)	290.6 (5.5)
BP+Pd	(55.1)	(19.6)	(11.0)	(5.6)	288.8 (3.4)	290.5 (5. eV3)
		C-O/C-N (%)				
BP+ODA+Pd	284.3 (40.9)	285.1 (33.4)	285.8 (15.5)	286.8 (6.9)	288.3 (2.3)	289.9 (1.0)
BP+DAO+Pd	284.1 (49.0)	285.2 (25.7)	286.2 (12.2)	287.3 (5.8)	288.6 (2.8)	290.3 (4.5)

The detailed spectra of the N 1*s* core level region of the aminated samples are shown in the middle panel of Fig. 6.14 and contain four components. The corresponding binding energies and relative spectral intensities are presented in Table 10. The first component refers to C-N bonds of the aliphatic chain of the amines and appears at a BE of 399.2 eV in the spectrum of BP+ODA+Pd, and at 398.8 eV in that of BP+DAO+Pd. The second peak at 400.4 eV for BP+ODA+Pd and at 399.9 eV for BP+DAO+Pd corresponds to amino groups. The third contribution originates from protonated NH_3^+ species formed during the nucleation process of palladium particles and is situated at a BE of 401.9 eV in the spectrum of BP+ODA+Pd, and at 400.9 eV in that of BP+DAO+Pd. The fourth contribution at a BE of 402.4 eV is only found in the DAO-containing sample and refers to the amide functionalities, as was also discussed for the powder samples. The spectral fingerprint of amide functionalities is also observed in the FTIR spectra in Fig. 6.3 and their presence is inferred in the corresponding degradation pattern in Fig 6.5d. Having a look at the relative spectral intensities of these components (Table 10), from the contribution of the C-N bonds we could infer that the degree of functionalization was higher when employing ODA as a modifier. This conclusion is supported by the TGA/DTA results where the functional groups from ODA were found to give rise to a higher mass loss than the corresponding one recorded for BP+DAO+Pd (15.9 wt% more). This fact could also explain why the amino contribution was more important for BP+ODA+Pd.

Table 8. XPS binding energies and relative spectral intensities of the contributions from different chemical species to the N 1*s* core level spectra of the aminated BP+Pd samples

	Component binding energy (eV)			
Sample	**N-C (%)**	**$-NH_2$ (%)**	**NH_3^+ (%)**	**–C(=O)N– (%)**
BP+ODA+Pd	399.2 (24.1)	400.4 (56.3)	401.9 (19.6)	---
BP+DAO+Pd	398.8 (14.4)	399.9 (46.1)	400.9 (30.3)	402.4 (9.1)

As observed in the spectra presented in the right panel of Fig. 6.14, palladium is present in different oxidation states: Pd(0), Pd(IV) and Pd(II).[78,79,81-84]As observed for other series described in this dissertation, the XPS spectra of the Pd 3*d* core level region present two asymmetrical peaks corresponding to the spin-orbit split Pd $3d_{5/2}$ and Pd $3d_{3/2}$ components. The peak assignment was carried out taking into consideration the same parameters as for the powder MWCNTs/PdNPs series. We can observe that the ionic species prevail in all the samples, whereas the zerovalent species accounts for 13.4 % of the spectral intensity (Table 9) of BP+Pd, for 6.5 % of that of BP+ODA+Pd, and for 25.4 % of BP+DAO+Pd, where they give rise to contributions peaked at BEs of 335.4, 335.2, and 335.3 eV, respectively. Pd(IV) gives rise to a component at BE of 337.4 – 337.5 eV. Finally, the contribution of Pd(II) appears at BE = 338.7 – 338.8 eV. The corresponding components of the Pd $3d_{3/2}$ peak are situated in the binding energy ranges of 340.5 – 340.7 eV (Pd0), 342.6 – 342.8 eV (PdIV), and 344.0 – 344.1 eV (PdIV). Contrary to what was observed for the powder series, the highest metallic Pd content was found for the DAO-containing buckypaper, whereas the ODA-containing one showed the least metallic Pd. Like in MWCNTs+Pd series, tetravalent palladium prevails as PdO_2, which is also supported by the TGA results (Fig. 6.5). This species is predominant in BP+Pd and BP+DAO+Pd. Regarding Pd(II), as observed in powder, the upshifting of BE is due to the complexation of Pd with carboxylate ions from deprotonated carboxylic acids of citric acid during PdNP formation.[80] As seen in Table 11, this species is present in BP+Pd and BP+ODA+Pd. Summarising, we can conclude that the reaction kinetics favours palladium oxidation in the non-aminated sample and the DAO-functionalized one, whereas ODA functionalisation promotes the formation of palladium carboxylates.

Table 9. XPS binding energies and relative spectral intensities of the contributions from different Pd 3*d* core level components in the spectra of the palladium-containing samples

	Components (eV)					
Species	**Pd (0)**		**Pd (IV)**		**Pd (II)**	
Line / Sample	**$3d_{5/2}$ (%)**	**$3d_{3/2}$ (%)**	**$3d_{5/2}$ (%)**	**$3d_{3/2}$ (%)**	**$3d_{5/2}$ (%)**	**$3d_{3/2}$ (%)**
BP+Pd	335.4 (13.4)	340.7	337.5 (46.0)	342.8	**338.8** (40.6)	**344.1**
BP+ODA+Pd	335.2 (6.5)	340.5	**337.4** (28.4)	**342.6**	(42.4)	
BP+DAO+Pd	335.3 (25.4)	340.6	(46.9)		338.7 (27.7)	344.0

Based on the XPS data above, the elemental composition for the BP/PdNPs set was estimated (Table 10). As expected, the nitrogen content was higher in BP+DAO+Pd (1.4 at%) than in BP+ODA+Pd (1.0 at%) because of DAO's bifunctionality. This agrees with the results on GO-based hybrids discussed in Chapter 4. Consequently, the amount of Pd deposited is the highest (1.6 at%) in BP+DAO+Pd, followed by BP+Pd (0.4 at%), and BP+ODA+Pd (0.04 at%). This trend was also observed in the SEM/EDS results.

Table 10. Elemental composition (atomic percentages) as derived from the XPS spectra of the side of the buckypapers that was in contact with the filtration membrane during paper preparation

Sample	Atomic %
BP+Pd	C: 88.1
	O: 11.5
	Pd: 0.4
BP+ODA+Pd	C: 94.7
	O: 4.3
	N: 1.0
	Pd: 0.04
BP+DAO+Pd	C: 92.2
	O: 4.8
	N: 1.4
	Pd: 1.6

Powder XRD was used to investigate the MWCNTs/Pd hybrids' crystallinity in further detail. Fig. 6.15 compares the diffractograms of the starting material with those of the aminated-CNTs with and without PdNPs. As for the MWCNTs/AgNPs series, discussed in Chapter 5, a broad peak at 2θ =13.5 - 13.7° arises due to a few layers stacking in the MWCNTs (001) direction[85,86]; consequently, the coherently diffracting domains are small. Also, the (002) higher-order diffraction peak of the MWCNTs[70] is seen at 2θ = 25.9 - 26.1° (d_{002} ~ 0.34 nm). Additionally, peaks appearing at 42.5°, 43.6°, and 49.4°, and corresponding to the planes (001), (100), and (004) of the hexagonal plane of graphite, are distinguished in the amine-containing samples[87,88] ($d_{\{100\}}$ = 0.21 nm, and d_{004} = 0.18 nm, respectively).

As observed before, we can notice some differences in the diffractograms of the ODA-containing samples compared to those of the other samples. Firstly, slightly increased peak intensities (blue and green lines in Fig. 6.15) due to the complexation action of the nitrogen atoms in the ODA moieties that increase the size of the coherently diffracting domains,[69] as observed previously in the silver-containing series. Secondly, a small peak appearing at 5.3 – 5.5° (*d*-spacing around 1.64 nm), points to an increased interlayer spacing because of the ODA intercalation between the concentric nanotubes.[89,90] Finally, the peak appearing at 21.2 – 21.4° (*d*-spacing approx. 0.42 nm), confirms that the crystalline ODA fragments either swell or open the nanotube arrangements, as observed before in many carbon nanostructures.[90,91]

Finally, the (111) Bragg reflection for metallic palladium appears at 2θ = 40.0 – 40.1° in the MWCNTs+Pd and MWCNTs+ODA+Pd samples, where the nanoparticles formed and deposited were large enough to be detected in XRD, exhibiting a face centred cubic (fcc) crystalline structure.[92]

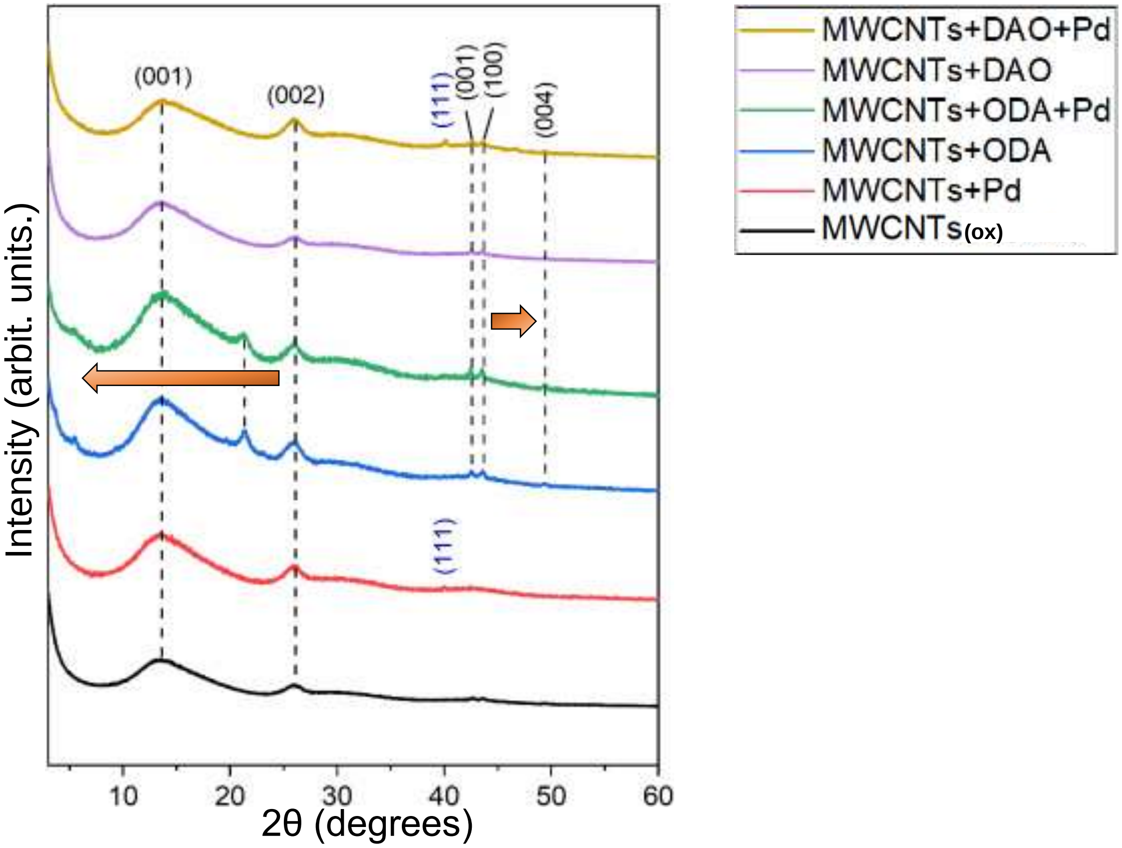

Fig. 6.15. Comparison of the XRD diffractograms for MWCNTs$_{(ox)}$ and amine-functionalized MWCNTs before and after decoration with Pd nanoparticles. (Black numbers correspond to the graphite lattice peaks, whereas the blue number refer to metallic palladium nanoparticle planes).

6.4 Conclusions

The present study represents an acceptable ecological route to prepare hybrid nanomaterials based on multiwalled carbon nanotubes, aliphatic amines and palladium nanoparticles in an efficient manner, expanding the panorama in the production and utilization of advanced materials. Starting from some principles of '***green chemistry'***, we can highlight the use of harmless reagents like 1-octadecylamine, 1,8-diaminooctane, and citric acid to achieve this aim.

Dispersibility tests evidenced that the length of the amine chain, the number of reactive units, the incorporation of noble metals, and the polarity of the solvent have an impact on the processibility of the final product and on the stability of its dispersions.

FTIR and XPS analysis confirmed the presence of oxygenated and nitrogenated functionalities in the hybrids. XPS analysis showed multiple carbon and nitrogen bonding types, several palladium oxidation states and coordination binding between Pd and oxygen and nitrogen.

At the surface, ionic Pd is more abundant than metallic Pd species, presumably because the exposure to ambient air causes surface oxidation of the PdNPs. Microscopy studies revealed changes in the substrate structure due to amine intercalation and Pd particle inclusion, impacting morphology, size, and distribution. SEM imaging showed micrometric Pd aggregates varying in size and shape. TEM imaging highlighted shape and size differences also in the smallest Pd nanoparticles.

TGA and XPS studies gave insight into the degree of (surface) oxidation and functionalization of each hybrid, as well as the metal loading. We could determine that chemical modification was more efficient in powder samples, especially with ODA as a modifier. In buckypaper the changes were less dramatic and very little Pd was deposited. The Pd content influenced the thermal stability, with higher Pd concentrations leading to faster combustion. The highest Pd loading was achieved in aminated samples. XRD results confirmed the presence of integers, highly crystalline MWCNTs, and metallic palladium. Overall, results from TGA, SEM/EDS, XPS, and XRD techniques emphasized the highest palladium content in DAO-containing samples.

This comprehensive study provides insights into the synthesis, characteristics, and properties of MWCNTs/PdNPs and BP/PdNPs nanohybrids, demonstrating the influence of amine modifications and Pd content on their behaviour and structure.

The presence of oxidized Pd at the surface of nanoparticles emphasizes the need to store the hybrids in a non-reactive atmosphere to protect the metallic species formed if the hybrids are to be used in applications where a metallic surface is needed.

Taking advantage of Pd at the nanoscale, the performance of the newly formed hybrids could be expanded to various fields, including electronics, catalysis, electrochemical biosensing, drug delivery, and antimicrobial agents. Further research needs to be done to explore the scalability of the production method and the toxicity of the final products.

6.5 References

(1) Georgakilas, V., Perman, J. A., Tucek, J., & Zboril, R. (2015). Broad Family of Carbon Nanoallotropes: Classification, Chemistry, and Applications of Fullerenes, Carbon Dots, Nanotubes, Graphene, Nanodiamonds, and Combined Superstructures. *Chemical Reviews*, *115*(11), 4744–4822. https://doi.org/10.1021/cr500304f.

(2) Hirsch, A. (2010). The era of carbon allotropes. *Nature Materials*, *9*(11), 868–871. https://doi.org/10.1038/nmat2885.

(3) Iijima, S. (2002). Carbon nanotubes: past, present, and future. *Physica B: Condensed Matter*, *323*(1-4), 1–5. https://doi.org/10.1016/s0921-4526(02)00869-4.

(4) Zhu, Y., Murali, S., Cai, W., Li, X., Suk, J. W., Potts, J. R., & Ruoff, R. S. (2010). Graphene and Graphene Oxide: Synthesis, Properties, and Applications. *Advanced Materials*, *22*(35), 3906–3924. https://doi.org/10.1002/adma.201001068.

(5) Dresselhaus, M. S., Dresselhaus, G., Charlier, J. C., & Hernández, E. (2004). Electronic, thermal and mechanical properties of carbon nanotubes. *Philosophical Transactions of the Royal Society of London. Series A: Mathematical, Physical and Engineering Sciences*, *362*(1823), 2065–2098. https://doi.org/10.1098/rsta.2004.1430.

(6) Sengupta, J. (2018). Chapter 9 - Carbon Nanotube Fabrication at Industrial Scale: Opportunities and Challenges. In C. M. Hussain (Ed.), *Handbook of Nanomaterials for Industrial Applications. Micro and Nano Technologies* (pp. 172–194). Elsevier. https://doi.org/10.1016/C2016-0-04427-3.

(7) Sengupta, J. (2020). Chapter 17 - Application of carbon nanomaterials in the electronic industry. In C. M. Hussain (Ed.), *Handbook of Nanomaterials for Manufacturing Applications. A volume in Micro and Nano Technologies* (pp. 421–450). Elsevier. https://doi.org/10.1016/C2018-0-05040-9.

(8) Soni, S. K., Thomas, B., & Kar, V. R. (2020). A Comprehensive Review on CNTs and CNT-Reinforced Composites: Syntheses, Characteristics and Applications. *Materials Today Communications*, 25, 101546. https://doi.org/10.1016/j.mtcomm.2020.101546.

(9) De Volder, M. F. L., Tawfick, S. H., Baughman, R. H., & Hart, A. J. (2013). Carbon Nanotubes: Present and Future Commercial Applications. *Science*, 339(6119), 535–539. https://doi.org/10.1126/science.1222453.

(10) Foster, J., Singamaneni, S., Kattumenu, R., & Bliznyuk, V. (2005). Dispersion and phase separation of carbon nanotubes in ultrathin polymer films. *Journal of Colloid and Interface Science*, 287(1), 167–172. https://doi.org/10.1016/j.jcis.2005.01.101.

(11) Chen, J., Li, C., Lian, Y., Chen, Y., Chen, T., & Hu, X. (2021). Understanding the oxygen-containing functional groups on multiwall carbon nanotubes toward supercapacitors. *Materials Today Chemistry*, *19*, 100414. https://doi.org/10.1016/j.mtchem.2020.100414.

(12) Dyke, C. K., & Tour, J. M. (2004). Covalent Functionalization of Single-Walled Carbon Nanotubes for Materials Applications. *Journal of Physical Chemistry A*, *108*(51), 11151–11159. https://doi.org/10.1021/jp046274g.

(13) Lavagna, L., Musso, S., & Pavese, M. (2021). A facile method to oxidize carbon nanotubes in controlled flow of oxygen at 350 °C. *Materials Letters*, *283*, 128816. https://doi.org/10.1016/j.matlet.2020.128816.

(14) Raffaelle, R. P., Landi, B. J., Harris, J. D., Bailey, S. G., & Hepp, A. F. (2005). Carbon nanotubes for power applications. *Materials Science and Engineering: B*, *116*(3), 233–243. https://doi.org/10.1016/j.mseb.2004.09.034.

(15) Wang, S. (2009). Optimum degree of functionalization for carbon nanotubes. *Current Applied Physics*, *9*(5), 1146–1150. https://doi.org/10.1016/j.cap.2009.01.004.

(16) Wepasnick, K. A., Smith, B. A., Schrote, K. E., Wilson, H. K., Diegelmann, S. R., & Fairbrother, D. H. (2011). Surface and structural characterization of multi-walled carbon nanotubes following different oxidative treatments. *Carbon*, *49*(1), 24–36. https://doi.org/10.1016/j.carbon.2010.08.034.

(17) Basiuk (Golovataya-Dzhymbeeva), Elena V., Ochoa-Olmos, O., Contreras-Torres, F. F., Meza-Laguna, V., Alvarez-Zauco, E., Puente-Lee, I., & Basiuk, V. A. (2011). “Green” Functionalization of Pristine Multi-Walled Carbon Nanotubes with Long-Chain Aliphatic Amines. *Journal of Nanoscience and Nanotechnology*, 11(6), 5546–5554. https://doi.org/10.1166/jnn.2011.3431.

(18) Basiuk, E. V., & Basiuk, V. A. (2014). Green Chemistry of Carbon Nanomaterials. *Journal of Nanoscience and Nanotechnology*, 14(1), 644–672. https://doi.org/10.1166/jnn.2014.9011.

(19) Basiuk, E. V., & Basiuk, V. A. (2015). Review of Solvent-Free Functionalization of Carbon Nanomaterials. In V. A. Basiuk & E. V. Basiuk (Eds.), Green Processes for Nanotechnology-From Inorganic to Bioinspired Nanomaterials (pp. 163–205). Springer International Publishing.

(20) Basiuk, E. V., Basiuk, V. A., Bañuelos, J.-G., Saniger-Blesa, J.-M., Pokrovskiy, V. A., Gromovoy, Taras. Yu., Mischanchuk, A. V., & Mischanchuk, B. G. (2002). Interaction of Oxidized Single-Walled Carbon Nanotubes with Vaporous Aliphatic Amines. *The Journal of Physical Chemistry B*, 106(7), 1588–1597. https://doi.org/10.1021/jp0120110.

(21) Basiuk, E. V., Monroy-Peláez, M., Puente-Lee, I., & Basiuk, V. A. (2004). Direct Solvent-Free Amination of Closed-Cap Carbon Nanotubes: A Link to Fullerene Chemistry. *Nano Letters*, 4(5), 863–866. https://doi.org/10.1021/nl049746b.

(22) Ramírez-Calera, I. J., Meza-Laguna, V., Gromovoy, T. Yu., Chávez-Uribe, Ma. I., Basiuk, V. A., & Basiuk, E. V. (2015). Solvent-free functionalization of fullerene C_{60} and pristine multi-walled carbon nanotubes with aromatic amines. *Applied Surface Science*, 328, 45–62. https://doi.org/10.1016/j.apsusc.2014.11.188.

(23) Koskin, A. P., Larichev, Y. V., Mishakov, I. V., Mel'gunov, M. S., & Vedyagin, A. A. (2020). Synthesis and characterization of carbon nanomaterials functionalized by direct treatment with sulfonating agents. *Microporous and Mesoporous Materials,* 299, 110130–110130. https://doi.org/10.1016/j.micromeso.2020.110130.

(24) Luong, N. D., Sinh, L. H., Johansson, L.-S., Campell, J., & Seppälä, J. (2015). Functional Graphene by Thiol-ene Click Chemistry. Chemistry - *a European Journal*, 21(8), 3183–3186. https://doi.org/10.1002/chem.201405734.

(25) McGlynn, R. J., Brunet, P., Chakrabarti, S., Boies, A., Maguire, P., & Mariotti, D. (2022). High degree of N-functionalization in macroscopically assembled carbon nanotubes. *Journal of Materials Science*, 57(28), 13314–13325. https://doi.org/10.1007/s10853-022-07463-7.

(26) Arora, S., Kumar, V., Yadav, S., Singh, S., Bhatnagar, D., & Kaur, I. (2014). Carbon Nanotubes as Drug Delivery Vehicles. *Solid State Phenomena*, 222, 145–158. https://doi.org/10.4028/www.scientific.net/ssp.222.145.

(27) Chu, H., Wei, L., Cui, R., Wang, J., & Li, Y. (2010). Carbon nanotubes combined with inorganic nanomaterials: Preparations and applications. *Coordination Chemistry Reviews*, 254(9-10), 1117–1134. https://doi.org/10.1016/j.ccr.2010.02.009.

(28) Eudes Lorençon, Ferlauto, A. S., Sergio de Oliveira, Miquita, D. R., Resende, R. R., Lacerda, R. G., & Ladeira, L. O. (2009). Direct Production of Carbon Nanotubes/Metal Nanoparticles Hybrids from a Redox Reaction between Metal Ions and Reduced Carbon Nanotubes. *ACS Applied Materials & Interfaces*, 1(10), 2104–2106. https://doi.org/10.1021/am900424m.

(29) Hu, Y., & Guo, C. (2011). Carbon Nanotubes and Carbon Nanotubes/Metal Oxide Heterostructures: Synthesis, Characterization and Electrochemical Property. In M. Naraghi (Ed.), Carbon Nanotubes - Growth and Applications. IntechOpen. 978-953-51-4462-5.

(30) Li, K., & Li, H. (2011). Fabrication and Applications of Carbon Nanotube-Based Hybrid Nanomaterials by Means of Non-Covalently Functionalized Carbon Nanotubes. In S. Bianco (Ed.), Carbon Nanotubes - From Research to Applications. IntechOpen. 978-953-51-5567-6.

(31) Navrotskaya, A. G., Darya Aleksandrova, Krivoshapkina, E. F., Sillanpää, M., & Krivoshapkin, P. V.(2020). Hybrid Materials Based on Carbon Nanotubes and Nanofibers for Environmental Applications. *Frontiers in Chemistry*, 8. https://doi.org/10.3389/fchem.2020.00546.

(32) Rodríguez-Manzo, J. A., Banhart, F., Terrones, M., Terrones, H., Grobert, N., Ajayan, P. M., Sumpter, B. G., Meunier, V., Wang, M., Bando, Y., & Golberg, D. (2009). Heterojunctions between metals and carbon nanotubes as ultimate nanocontacts. *Proceedings of the National Academy of Sciences of the United States of America*, 106(12), 4591–4595. https://doi.org/10.1073/pnas.0900960106.

(33) Segura, R. (2012). Non-covalent assembly of hybrid nanostructures of gold and palladium nanoparticles with carbon nanotubes. *International Journal of Materials Research*, 103(7), 901–905. https://doi.org/10.3139/146.110693.

(34) Zagal, J. H., Griveau, S., Santander-Nelli, M., Silvia Gutierrez Granados, & Fethi Bedioui. (2012). Carbon nanotubes and metalloporphyrins and metallophthalocyanines-based materials for electroanalysis. *Journal of Porphyrins and Phthalocyanines*, 16(07n08), 713–740. https://doi.org/10.1142/s1088424612300054.

(35) Dobrzanski, L. A., Blazej Tomiczek, & Macek, M. (2017). Fabrication, Composition, Properties and Application of the AlMg1SiCu Aluminium Alloy Matrix Composite Materials Reinforced with Halloysite or Carbon Nanotubes. InTech EBooks. https://doi.org/10.5772/65399.

(36) Mugadza, K., Stark, A., Ndungu, P. G., & Nyamori, V. O. (2020). Synthesis of Carbon Nanomaterials from Biomass Utilizing Ionic Liquids for Potential Application in Solar Energy Conversion and Storage. *Materials*, 13(18), 3945. https://doi.org/10.3390/ma13183945.

(37) Selvaganesh, S. V., Dhanasekaran, P., & Bhat, S. D. (2017). TiO2-nanowire/MWCNT composite with enhanced performance and durability for polymer electrolyte fuel cells. *Electrochemical Energy Technology*, 3(1). https://doi.org/10.1515/eetech-2017-0002.

(38) Morgan, R. D., Salehi-khojin, A., & Masel, R. I. (2011). Superior Formic Acid Oxidation Using Carbon Nanotube-Supported Palladium Catalysts. *The Journal of Physical Chemistry C*, 115(39), 19413–19418. https://doi.org/10.1021/jp205113s.

(39) Ye, X.-R., Lin, Y., Wai, C. M., Talbot, J. B., & Jin, S. (2005). Supercritical Fluid Attachment of Palladium Nanoparticles on Aligned Carbon Nanotubes. *Journal of Nanoscience and Nanotechnology*, 5(6), 964–969. https://doi.org/10.1166/jnn.2005.133.

(40) Arif, M. F., Kumar, S., & Shah, T. (2016). Tunable morphology and its influence on electrical, thermal and mechanical properties of carbon nanostructure-buckypaper. *Materials & Design*, 101, 236–244. https://doi.org/10.1016/j.matdes.2016.03.122.

(41) Kausar, A., Ilyas, H., & Siddiq, M. (2017). Current Research Status and Application of Polymer/Carbon Nanofiller Buckypaper: A Review. *Polymer-Plastics Technology and Engineering*, 56(16), 1780–1800. https://doi.org/10.1080/03602559.2017.1289407.

(42) Kausar, A., & Siddiq, M. (2015). Structure and properties of buckypapers based on poly(methyl methacrylate-co-methacrylic acid)/ polyamide 6,6 and carbon nanotube intercalated montmorillonite. *Journal of Composite Materials*, 50(8), 1021–1030. https://doi.org/10.1177/0021998315586079.

(43) Luo, W., Liu, Y., & Saha, M. (2017). CNT Bucky Paper Enhanced Sandwich Composites for In-Situ Load Sensing. Volume 14: Emerging Technologies; Materials: Genetics to Structures; Safety Engineering and Risk Analysis. https://doi.org/10.1115/imece2017-71550.

(44) Rigueur, J. L., Hasan, S. A., Mahajan, S. V., & Dickerson, J. H. (2010). Buckypaper fabrication by liberation of electrophoretically deposited carbon nanotubes. *Carbon,* 48(14), 4090–4099. https://doi.org/10.1016/j.carbon.2010.07.016.

(45) Boschetto, G., Carapezzi, S., & Todri-Sanial, A. (2021). Graphene and Carbon Nanotubes for Electronics Nanopackaging. *IEEE Open Journal of Nanotechnology*, 2, 120–128. https://doi.org/10.1109/ojnano.2021.3127652.

(46) Cher Ming Tan, Baudot, C., Han, Y., & Jing, H. (2012). Applications of multi-walled carbon nanotube in electronic packaging. *Nanoscale Research Letters*, 7(1). https://doi.org/10.1186/1556-276x-7-183.

(47) Zhang, L., Zhang, G., Liu, C., & Fan, S. (2012). High-Density Carbon Nanotube Buckypapers with Superior Transport and Mechanical Properties. *Nano Letters*, 12(9), 4848–4852. https://doi.org/10.1021/nl3023274.

(48) Khan, N. H., & Hassoun, S. (2012). The feasibility of Carbon Nanotubes for power delivery in 3-D Integrated Circuits. CiteSeer X (the Pennsylvania State University). https://doi.org/10.1109/aspdac.2012.6165010.

(49) Liu, J., Jiang, D., Fu, Y., & Wang, T. (2013). Carbon nanotubes for electronics manufacturing and packaging: from growth to integration. *Advances in Manufacturing*, 1(1), 13–27. https://doi.org/10.1007/s40436-013-0007-4.

(50) Maffucci, A. (2009). Carbon nanotubes in nanopackaging applications. *IEEE Nanotechnology Magazine*, 3(3), 22–25. https://doi.org/10.1109/mnano.2009.934214.

(51) Zhang, S., Wang, H., Liu, J., & Bao, C. (2020). Measuring the specific surface area of monolayer graphene oxide in water. *Materials Letters, 261*, 127098. https://doi.org/10.1016/j.matlet.2019.127098.

(52) Pełech, I., Pełech, R., Kaczmarek, A., Jędrzejewska, A., & Moszyński, D. (2016). Effect of treating method on the physicochemical properties of amine-functionalized carbon nanotubes. *International Journal of Materials Research*, *107*(1), 35–43. https://doi.org/10.3139/146.111313.

(53) Ramin Ghorbani-Vaghei, Hemmati, S., Hashemi, M., & Hojat Veisi. (2015). Diethylenetriamine-functionalized single-walled carbon nanotubes (SWCNTs) to immobilization palladium as a novel recyclable heterogeneous nanocatalyst for the Suzuki–Miyaura coupling reaction in aqueous media. *Comptes Rendus. Chimie*, *18*(6), 636–643. https://doi.org/10.1016/j.crci.2014.10.010.

(54) Lin, Y., Rao, A. M., Bindu Sadanadan, Kenik, E. A., & Sun, Y. (2002). Functionalizing Multiple-Walled Carbon Nanotubes with Aminopolymers. *Journal of Physical Chemistry B*, *106*(6), 1294–1298. https://doi.org/10.1021/jp013501v.

(55) Zhao, N., He, C., Jiang, Z., Li, J., & Li, Y. (2007). Physical activation and characterization of multi-walled carbon nanotubes catalytically synthesized from methane. *Materials Letters*, *61*(3), 681–685. https://doi.org/10.1016/j.matlet.2006.05.041.

(56) Elham Zamani Alavijeh, Saeed Kokhaei, & Dehghani, K. (2018). Fabrication and mechanical properties of aluminum composite reinforced with functionalized carbon nanotubes. *AIP Conference Proceedings*. https://doi.org/10.1063/1.5018973.

(57) Rodríguez-Otamendi, D. I., Meza-Laguna, V., Acosta, D., Álvarez-Zauco, E., Huerta, L., Basiuk, V. A., & Basiuk, E. V. (2021). Eco-friendly synthesis of graphene oxide–silver nanoparticles hybrids: The effect of amine derivatization. *Diamond and Related Materials*, *111*, 108208. https://doi.org/10.1016/j.diamond.2020.108208.

(58) Fayazfar, H., Afshar, A., & Dolati, A. (2013). Controlled Growth of Well-Aligned Carbon Nanotubes, Electrochemical Modification and Electrodeposition of Multiple Shapes of Gold Nanostructures. *Materials Sciences and Applications*, *04*(11), 667–678. https://doi.org/10.4236/msa.2013.411083.

(59) Misra, A., Tyagi, PawanK., Rai, P., & Misra, D. S. (2007). FTIR Spectroscopy of Multiwalled Carbon Nanotubes: A Simple Approachto Study the Nitrogen Doping. *Journal of Nanoscience and Nanotechnology*, *7*(6), 1820–1823. https://doi.org/10.1166/jnn.2007.723.

(60) (PDF) Effect of Carboxylic Group Functionalized on Carbon Nanotubes Surface on the Removal of Lead From Water. Available from: https://www.researchgate.net/publication/50196569_Effect_of_Carboxylic_Group_Functionalized_on_Carbon_Nanotubes_Surface_on_the_Removal_of_Lead_From_Water#fullTextFileContent [accessed May 08 2024].

(61) Barth, A. (2007). Infrared spectroscopy of proteins. *Biochimica et Biophysica Acta (BBA) - Bioenergetics*, *1767*(9), 1073–1101. https://doi.org/10.1016/j.bbabio.2007.06.004.

(62) Kong, J., & Yu, S. (2007). Fourier Transform Infrared Spectroscopic Analysis of Protein Secondary Structures. *Acta Biochimica et Biophysica Sinica*, *39*(8), 549–559. https://doi.org/10.1111/j.1745-7270.2007.00320.x.

(63) Mawhinney, D. B., Naumenko, V., Kuznetsova, A., Yates, J. T., Liu, J., & Smalley, R. E. (2000). Infrared Spectral Evidence for the Etching of Carbon Nanotubes: Ozone Oxidation at 298 K. *Journal of the American Chemical Society, 122*(10), 2383–2384. https://doi.org/10.1021/ja994094s.

(64) Goyanes, S., Rubiolo, G. R., Salazar, A., Jimeno, A., Corcuera, M. A., & Mondragon, I. (2007). Carboxylation treatment of multiwalled carbon nanotubes monitored by infrared and ultraviolet spectroscopies and scanning probe microscopy. *Diamond and Related Materials*, *16*(2), 412–417. https://doi.org/10.1016/j.diamond.2006.08.021.

(65) Yen, P.-W.; Chou, T. Temperature Programmed Oxidation of Palladium Catalyst: Effect of Support on the Oxygen Adsorption Behavior. *Applied Catalysis A-General* 2000, *198* (1-2), 23–31. https://doi.org/10.1016/s0926-860x(99)00507-4.

(66) Mitsuda, K., Kimura, H., & Murahashi, T. (1989). Evaporation and decomposition of Triton X-100 under various gases and temperatures. *Journal of Materials Science*, *24*(2), 413–419. https://doi.org/10.1007/bf01107420.

(67) O. Leonte, M. Bîrjega, D. Macovei, P. Pausescu, N. Popescu-Pogrion, & Georgescu, M. (1986). Study of supported palladium catalysis variously heat treated in hydrogen using microactivity testing, transmission electron microscopy, X-ray analysis and the extended X-ray absorption fine structure technique. *Surface and Coatings Technology*, *28*(3-4), 347–357. https://doi.org/10.1016/0257-8972(86)90091-5.

(68) Li, Z., Xu, J., O'Byrne, J. P., Chen, L., Wang, K., Morris, M. A., & Holmes, J. D. (2012). Freestanding bucky paper with high strength from multi-wall carbon nanotubes. *Materials Chemistry and Physics, 135* (2-3), 921–927. https://doi.org/10.1016/j.matchemphys.2012.05.080.

(69) Rodríguez-Otamendi, D. I., Bizarro, M., Meza-Laguna, V., Álvarez-Zauco, E., Rudolf, P., Basiuk, V. A., & Basiuk, E. V. (2023). Eco-friendly synthesis of graphene oxide–palladium nanohybrids. *Materials Today Communications*, *35*, 106007–106007. https://doi.org/10.1016/j.mtcomm.2023.106007.

(70) Rashid, Md. H.-O., Pham, S. Q. T., Sweetman, L. J., Alcock, L. J., Wise, A., Nghiem, L. D., Triani, G., Panhuis, M. in het, & Ralph, S. F. (2014). Synthesis, properties, water and solute permeability of MWNT buckypapers. *Journal of Membrane Science*, *456*, 175–184. https://doi.org/10.1016/j.memsci.2014.01.026.

(71) Srinivas, G., Burress, J. W., Ford, J., & Yildirim, T. (2011). Porous graphene oxide frameworks: Synthesis and gas sorption properties. *Journal of Materials Chemistry*, *21*(30), 11323. https://doi.org/10.1039/c1jm11699a.

(72) Raymundo-Piñero, E., Azaïs, P., Cacciaguerra, T., Cazorla-Amorós, D., Linares-Solano, A., & Béguin, F. (2005). KOH and NaOH activation mechanisms of multiwalled carbon nanotubes with different structural organisation. *Carbon*, *43*(4), 786–795. https://doi.org/10.1016/j.carbon.2004.11.005.

(73) Basiuk, E. V., Basiuk, V. A., Meza-Laguna, V., Contreras-Torres, F. F., Martínez, M., Rojas-Aguilar, A., Salerno, M., Zavala, G., Falqui, A., & Brescia, R. (2012). Solvent-free covalent functionalization of multi-walled carbon nanotubes and nanodiamond with diamines: Looking for cross-linking effects. *Applied Surface Science, 259*, 465–476. https://doi.org/10.1016/j.apsusc.2012.07.068.

(74) Okpalugo, T. I. T., Papakonstantinou, P., Murphy, H., McLaughlin, J., & Brown, N. M. D. (2005). High resolution XPS characterization of chemical functionalised MWCNTs and SWCNTs. *Carbon*, *43*(1), 153–161. https://doi.org/10.1016/j.carbon.2004.08.033.

(75) Chen, X., Wang, X., & Fang, D. (2020). A review on C1s XPS-spectra for some kinds of carbon materials. *Fullerenes, Nanotubes and Carbon Nanostructures*, *28*(12), 1048–1058. https://doi.org/10.1080/1536383x.2020.1794851.

(76) Venezia, A. M., Rossi, A., Duca, D., Martorana, A., & Deganello, G. (1995). Particle size and metal-support interaction effects in pumice supported palladium catalysts. *Applied Catalysis A: General, 125*(1), 113–128. https://doi.org/10.1016/0926-860x(94)00286-x.

(77) Tressaud, A., Khairoun, S., Touhara, H., & Watanabe, N. (1986). X-Ray Photoelectron Spectroscopy of Palladium Fluorides. *Z. Anorg. Allg. Chem, 540*, 291–299.

(78) Shafeev, G. A., J.-M. Themlin, Bellard, L., Marine, W., & A. Cros. (1996). Enhanced adherence of area-selective electroless metal plating on insulators. *Journal of Vacuum Science & Technology. A. Vacuum, Surfaces, and Films, 14*(2), 319–326. https://doi.org/10.1116/1.579895.

(79) Ki Wook Kim, Alexej Gossmann, & Winograd, N. (1974). X-ray photoelectron spectroscopic studies of palladium oxides and the palladium-oxygen electrode. *Analytical Chemistry, 46*(2), 197–200. https://doi.org/10.1021/ac60338a037.

(80) Farmer, S., Kennepohl, D., & Morsch, L. (2024). Reactions of Carboxylic Acids - An Overview. In Organic Chemistry. LibreTexts . https://chem.libretexts.org/Bookshelves/Organic_Chemistry/Organic_Chemistry_(Morsch_et_al.).

(81) Nefedov, V. I., Zakharova, I. A., Moiseev, I. I., Porai-Koshitz, M. A., Vargaftik, M. N., & Belov, A. P. (1973). Study of palladium complex compounds by X-ray photoelectron spectroscopy. *Russian Journal of Inorganic Chemistry*, *18*(12), 3264-3268.

(82) Nefedov, V. I., Salyn, Y. V., Moiseev, I. I., Sadovskii, A. P., Berenbljum, A. S., Knizhnik, A. G., & Mund, S. L. (1979). ESCA and X-ray spectral study of Pd(0), Pd(I) and Pd(II) compounds with triphenylphosphine ligands. *Inorganica Chimica Acta, 35, L343–L344*. doi:10.1016/s0020-1693(00)93391-7.

(83) Fischer, A., Krozer, A., & Schlapbach, L. (1992). Mg/Pd and Ba/Pd interfaces with and without hydrogen. *Surface Science*, *269-270*, 737–742. https://doi.org/10.1016/0039-6028(92)91342-9.

(84) Bertolini, J. C., Delichere, P., Khanra, B. C., Massardier, J., Noupa, C., & Tardy, B. (1990). Electronic properties of supported Pd aggregates in relation with their reactivity for 1,3-butadiene hydrogenation. *Catalysis Letters*, *6*(2), 215–223. https://doi.org/10.1007/bf00774723.

(85) Chen, J.; Li, Y.; Huang, L.; Li, C.; Shi, G. (2015). High-Yield Preparation of Graphene Oxide from Small Graphite Flakes via an Improved Hummers Method with a Simple Purification Process. *Carbon*, *81*, 826–834. https://doi.org/10.1016/j.carbon.2014.10.033.

(86) Imre Dékány; R. Krüger-Grasser; André Weiß. (1998). Selective Liquid Sorption Properties of Hydrophobized Graphite Oxide Nanostructures. *Colloid and Polymer Science*, *276*(7), 570–576. https://doi.org/10.1007/s003960050283.

(87) Atchudan, R., Pandurangan, A., & Joo, J. (2015). Effects of Nanofillers on the Thermo-Mechanical Properties and Chemical Resistivity of Epoxy Nanocomposites. *Journal of Nanoscience and Nanotechnology*, *15*(6), 4255–4267. https://doi.org/10.1166/jnn.2015.9706.

(88) Mohd Pauzi Abdullah, & Siti Aminah Zulkepli. (2015). The functionalization and characterization of multi-walled carbon nanotubes (MWCNTs). *AIP Conference Proceedings*. https://doi.org/10.1063/1.4931312.

(89) Wang, C.; Liu, Z.; Wang, S.; Zhang, Y. (2015). Preparation and Properties of Octadecylamine Modified Graphene Oxide/Styrene-Butadiene Rubber Composites through an Improved Melt Compounding Method. *Journal of Applied Polymer Science*, *133* (4), n/a-n/a. https://doi.org/10.1002/app.42907.

(90) Pedrosa, M. C. G., Dutra Filho, J. C., Menezes, L. R. de, & Silva, E. O. da. (2020). Chemical Surface Modification and Characterization of Carbon Nanostructures Without Shape Damage. *Materials Research*, *23*(2). https://doi.org/10.1590/1980-5373-mr-2019-0493.

(91) Xu, M., Huang, Q., Chen, Q., Guo, P., & Sun, Z. (2003). Synthesis and characterization of octadecylamine grafted multi-walled carbon nanotubes. *Chemical Physics Letters*, *375*(5-6), 598–604. https://doi.org/10.1016/s0009-2614(03)00923-0.

(92) Rahim Molaei, Farhadi, K., Mehrdad Forough, & Salahaddin Hajizadeh. (2018). Green Biological Fabrication and Characterization of Highly Monodisperse Palladium Nanoparticles Using Pistacia Atlantica Fruit Broth. *Journal of Nanostructures*, *8*(1), 47–54. https://doi.org/10.22052/jns.2018.01.006.

SUMMARY AND OUTLOOK

This PhD dissertation explores the sustainable synthesis and characterisation of novel nanostructured hybrid materials utilising graphene oxide or multi-walled carbon nanotubes as substrates. These substrates were functionalised with amine molecules and subsequently decorated with silver or palladium nanoparticles, employing environmentally friendly methodologies.

Rooted in the principles of Green Chemistry, the research aimed to develop advanced nanomaterials through a solventless gas-phase amine functionalisation technique, utilising the aliphatic amines 1-octadecylamine (ODA) and 1,8-diaminooctane (DAO) to precisely modify the surface properties of carbon nanostructures while minimizing the generation of harmful by-products. This approach was complemented by the wet impregnation of metallic nanoparticles, employing silver nitrate and palladium chloride as precursors and citric acid as the reducing/stabilizing agent. Through this path, it was achieved a predominantly uniform particle distribution and optimized the interaction between nanoparticles and the carbonaceous substrates. These eco-conscious strategies minimized waste and eliminated the need for hazardous reagents, thereby aligning with sustainability goals.

To achieve the research objectives, an array of advanced characterization techniques, including spectroscopy, electronic microscopy, and thermal analysis, were employed to confirm the successful synthesis of new materials. The findings highlighted the role of substrate morphology and functionalization in influencing particle size, distribution, and the overall properties of the nanohybrids. Computational modelling further supported these experimental results, elucidating molecular-level interactions and guiding the design of optimized nanomaterials. The study also suggested the synergistic performance of these materials in applications such as catalysis and antimicrobial technologies, addressing critical environmental and biomedical challenges while paving the way for innovations in green nanotechnology.

- **Chapter 1** provides an introduction to the principles of Green Chemistry, the environmental challenges of nanotechnology, and the materials studied in this dissertation, namely graphene oxide (GO), carbon nanotubes (CNTs), and metallic nanoparticles (silver and palladium). It emphasises the environmental benefits of sustainable synthesis methods and outlines the properties of all of these materials. Additionally, the chapter discusses functionalization techniques, the potential applicability of hybrid nanomaterials in fields like catalysis, medicine, and electronics, and the research goals of synthesizing and evaluating the structural, chemical, and functional properties of nanostructured hybrids.

- **Chapter 2** delves into the methodologies for fabricating and modifying carbon-based nanomaterials, particularly GO and multiwalled carbon nanotubes (MWCNTs) in both powder and paper forms. It describes synthesis protocols, including gaseous-amine functionalization and *in-situ* silver and palladium nanoparticle formation/deposition, aimed to boost the chemical and physical properties of the final hybrids. Characterization techniques, such as Fourier Transform Infrared Spectroscopy (FTIR), X-ray Photoelectron Spectroscopy (XPS), X-ray diffraction (XRD), and electron microscopy methods were systematically employed to investigate the structural, surface, and thermal properties of the synthesized materials. Computational modelling using Density Functional Theory (DFT) further validated the experimental findings by providing insights into the molecular interactions within the hybrids.

- **Chapter 3** discusses the green synthesis and characterisation of graphene oxide–silver nanoparticle (GO-Ag) hybrid materials in both powder and paper forms. The amine functionalization enhanced nanoparticle deposition on the GO matrix. The findings demonstrated that DAO-functionalized GO anchored the smallest and most uniform Ag particle distribution. DFT calculations corroborated these findings by elucidating the binding interactions between Ag nanoparticles and functionalized GO.

- **Chapter 4** outlines an eco-friendly pathway for developing graphene oxide–palladium (GO-Pd) nanohybrids in powder and paper forms. Through exhaustive characterization, this project revealed unique nanoparticle size, shape, and distribution profiles, particularly in the structurally enhanced amine-functionalized paper forms, which exhibited superior stability. DFT modelling provided insights into Pd-GO interactions, highlighting potential applications in catalysis, electronics, and structural performance.

- **Chapter 5** reports on the fabrication and characterization of MWCNT-based hybrids embedded with Ag nanoparticles in powder and buckypaper forms. The study highlighted the influence of ODA functionalization on improving nanoparticle dispersion and adherence, resulting in superior thermal stability and uniformity compared to DAO and non-functionalized counterparts. These characteristics significantly reinforced the structural and functional properties of the ODA-containing hybrids.

- **Chapter 6** describes the green synthesis and physical-chemical characterization of MWCNT hybrids containing Pd nanoparticles in powder and buckypaper forms. The study investigated the impact of functionalization on Pd nanoparticle distribution, morphology, and stability, with dispersibility tests revealing distinct hydrophobic/hydrophilic behaviours, depending on the amine used. Characterization demonstrated that amine-functionalized samples exhibited improved PdNP dispersion, enhanced thermal stability, and superior catalytic properties, underscoring their potential for applications in electronics, catalysis, and environmental remediation.

Comparing the palladium and silver content across GO and MWCNTs in both powder and paper form, the reported studies show that Ag loading exceeds that of Pd by approximately an order of magnitude. This difference can be attributed to several factors, primarily the coordination number and geometry in their respective coordination complexes. Silver(I) typically adopts linear or tetrahedral geometries in coordination complexes, with silver ions predominantly displaying two-, three-, or four-fold coordination. In contrast, Pd(II) complexes commonly exhibit four-coordinated square planar configurations, although a significant proportion of five-coordinated compounds also exist.

The observed variations in aggregation patterns, nucleation processes, and the shape and size distribution of the metallic nanoparticles are closely influenced by the chemical and structural properties of the carbonaceous substrates utilized throughout this study. Furthermore, these outcomes are shaped by the substrates' morphological characteristics—whether in powder or paper form—and the specific functionality of amine modifiers, which engage through distinct interaction mechanisms with the nanocarbon surfaces.

Based on the results of this PhD project, new opportunities for further research emerge. One should consider:

- performing dispersibility tests in solvents in a wider range of polarity to explore the stability of both powder and paper forms of the hybrids to evaluate their suitability for further processing.

- examining alternative routes for the production and deposition of nanoparticles to maximize the nucleation of metallic species and enhance metal loading, especially on paper-based and palladium-containing materials.

- testing if the mechanical strength of paper-like nanohybrids is sufficient for their use in water purification, selective filtration, and as conductive materials in flexible electronics.

- exploring specific applications of the nanohybrids taking into account the achieved metal loading, the predominant oxidation state of the noble metal, the shape of the nanoparticles and the pattern of decoration observed. In detail, the following hypotheses could be investigated.

1. ***GO/Ag-based series.*** Considering that GO enhances the material's surface area and dispersibility and Ag nanoparticles are well-known for their antimicrobial properties, the new hybrid materials could potentially increase the bactericidal efficiency of silver. The nanohybrids containing amines could improve the interaction between the material and bacterial membranes, enhancing antimicrobial action. The broad range of particle sizes (from nanoscale to micrometric) could generate diverse interaction mechanisms, potentially leading to better results than standard AgNP-loaded materials.

2. ***GO/Pd-based series.*** Having Pd nanoparticles in a variety of shapes embedded in a graphene oxide matrix, they provide different types of active sites used in catalytic reactions, such as hydrogenation, and cross-coupling like Suzuki or Heck reactions for organic synthesis, potentially leading a better overall efficiency and selectivity of the catalyst. The carbonaceous lattice could improve electron transfer, and thereby further enhance the reaction rate.

3. ***MWCNTs/Ag-based series.*** Thanks to the synergy of MWCNTs that offer excellent conductivity and high surface area, and Ag nanoparticles that interact with various gases, such as hydrogen, ammonia, and carbon monoxide, the new nanohybrids are promising for gas sensing. The fact that metallic Ag predominates on the surface could result in selective sensing capabilities. The nanohybrids containing amines are particularly likely to detect hazardous gases like CO, NOx, or methane, or volatile organic compounds for air quality monitoring.

4. ***MWCNTs/Pd-based series.*** Materials based on MWCNTs containing palladium in its oxidized form seem promising for electrocatalysis, particularly in fuel cells or batteries, due to their ability to facilitate redox reactions. Specifically, the role of PdO_2 nanoparticles in reactions like hydrogen oxidation can be enhanced by the nanotube support; therefore the new hybrid materials could improve both the performance and stability of future devices, offering a more cost-effective alternative to pure palladium in electrocatalysis.

SAMENVATTING EN VOORUITBLIK

Deze promotiedissertatie onderzoekt de duurzame synthese en karakterisatie van nieuwe nanogestructureerde hybride materialen met gebruik van grafeenoxide of meerwandige koolstofnanobuizen als substraten. Deze substraten werden functioneel gemaakt met aminemoleculen en vervolgens versierd met zilver- of palladiumnanodeeltjes, waarbij milieuvriendelijke methodologieën werden toegepast.

Gebaseerd op de principes van groene chemie had het onderzoek tot doel geavanceerde nanomaterialen te ontwikkelen via een oplosmiddelvrije gasfase-aminefunctionalisatietechniek, waarbij de alifatische aminen 1-octadecylamine (ODA) en 1,8-diamino-octaan (DAO) werden gebruikt om de oppervlakte-eigenschappen van koolstofnanostructuren nauwkeurig te wijzigen en tegelijkertijd de productie van schadelijke bijproducten te minimaliseren. Deze benadering werd aangevuld met natte impregnatie van metalen nanodeeltjes, waarbij zilvernitraat en palladiumchloride als precursoren en citroenzuur als reducerend/stabiliserend middel werden gebruikt. Op deze manier werd een overwegend uniforme deeltjesverdeling bereikt en de interactie tussen nanodeeltjes en de koolstofsubstraten geoptimaliseerd. Deze milieubewuste strategieën minimaliseerden afval en elimineerden de noodzaak voor gevaarlijke reagentia, wat in lijn ligt met duurzaamheidsdoelstellingen.

Voor het behalen van de onderzoeksdoelstellingen werd een reeks geavanceerde karakterisatietechnieken gebruikt, waaronder spectroscopie, elektronische microscopie en thermische analyse, om de succesvolle synthese van de nieuwe materialen te bevestigen. De resultaten benadrukten de rol van substraatmorfologie en functionalisatie in het beïnvloeden van de deeltjesgrootte, verdeling en de algehele eigenschappen van de nanohybrides. Computationele modellering ondersteunde deze experimentele bevindingen verder door moleculaire interacties te verduidelijken en het ontwerp van geoptimaliseerde nanomaterialen te begeleiden. Het onderzoek suggereerde ook de synergistische prestaties van deze materialen in toepassingen zoals katalyse en antimicrobiële technologieën, waarmee het kritieke milieuproblemen en biomedische uitdagingen aanpakt en de weg vrijmaakt voor innovaties in groene nanotechnologie.

- **Hoofdstuk 1.** In dit hoofdstuk wordt een introductie gegeven van de principes van groene chemie, de milieuproblemen van nanotechnologie en de in deze dissertatie bestudeerde materialen, namelijk grafeenoxide (GO), koolstofnanobuizen (CNT's) en metalen nanodeeltjes (zilver en palladium). Het benadrukt de milieuvoordelen van duurzame synthesemethoden en schetst de eigenschappen van al deze materialen. Daarnaast worden functionalisatietechnieken besproken, evenals de potentiële toepasbaarheid van hybride nanomaterialen in gebieden zoals katalyse, geneeskunde en elektronica. Ook worden de onderzoeksdoelen uiteengezet: het synthetiseren en evalueren van de structurele, chemische en functionele eigenschappen van nanogestructureerde hybriden.

- **Hoofdstuk 2.** Dit hoofdstuk verdiept zich in de methodologieën voor het vervaardigen en modificeren van op koolstof gebaseerde nanomaterialen, met name GO en meerwandige koolstofnanobuizen (MWCNT's) in zowel poeder- als papierformaat. Het beschrijft synthesemethoden, waaronder gasvormige aminefunctionalisatie en in-situ vorming/afzetting van zilver- en palladiumnanodeeltjes, gericht op het verbeteren van de chemische en fysische eigenschappen van de uiteindelijke hybriden. Karakterisatietechnieken zoals Fourier Transformatie Infrarood Spectroscopie (FTIR), Röntgenfoto-elektronenspectroscopie (XPS), röntgendiffractie (XRD) en methoden voor elektronische microscopie werden systematisch toegepast om de structurele, oppervlakkige en thermische eigenschappen van de gesynthetiseerde materialen te onderzoeken. Computationele modellering met behulp van Density Functional Theory (DFT) valideerde de experimentele bevindingen verder door inzicht te geven in de moleculaire interacties binnen de hybriden.

- **Hoofdstuk 3.** Hier wordt de groene synthese en karakterisatie van grafeenoxide–zilvernanodeeltje (GO-Ag) hybride materialen in zowel poeder- als papierformaten besproken. De aminefunctionalisatie verbeterde de deeltjesafzetting op de GO-matrix. De bevindingen toonden aan dat DAO-gefunctionaliseerde GO de kleinste en meest uniforme Ag-deeltjesverdeling verankerde. DFT-berekeningen bevestigden deze resultaten door de bindingsinteracties tussen Ag-nanodeeltjes en functionele GO te verduidelijken.

- **Hoofdstuk 4.** Dit hoofdstuk beschrijft een milieuvriendelijke methode voor de ontwikkeling van grafeenoxide–palladium (GO-Pd) nanohybriden in poeder- en papierformaten. Uit uitgebreide karakterisatie bleek dat vooral de structureel verbeterde amine-gefunctionaliseerde papieren vormen unieke stabiliteit en eigenschappen vertoonden. DFT-modellering verduidelijkte Pd-GO interacties en benadrukte potentiële toepassingen in katalyse, elektronica en structurele prestaties.

- **Hoofdstuk 5.** Hier wordt de fabricage en karakterisatie van MWCNT-gebaseerde hybriden met Ag-nanodeeltjes in poeder- en buckypapervormen beschreven. Het onderzoek benadrukte de invloed van ODA-functionalisatie op het verbeteren van de deeltjesverspreiding en hechting, wat resulteerde in superieure thermische stabiliteit en uniformiteit in vergelijking met DAO en niet-gefunctionaliseerde tegenhangers. Deze eigenschappen versterkten de structurele en functionele eigenschappen van de hybriden met ODA aanzienlijk.

- **Hoofdstuk 6.** Dit hoofdstuk beschrijft de groene synthese en fysisch-chemische karakterisatie van MWCNT-hybriden met Pd-nanodeeltjes in poeder- en buckypapervormen. Het onderzoek onderzocht de impact van functionalisatie op de Pd-deeltjesverdeling, morfologie en stabiliteit. Verspreidingstests onthulden onderscheidende hydrofobe/hydrofiele eigenschappen, afhankelijk van het gebruikte amine. Karakterisatie toonde aan dat amine-gefunctionaliseerde monsters verbeterde PdNP-verspreiding, verbeterde thermische stabiliteit en superieure katalytische eigenschappen vertoonden, wat hun potentieel onderstreepte voor toepassingen in elektronica, katalyse en milieusanering.

Bij vergelijking van het palladium- en zilvergehalte in zowel poeder- als papierformaten van GO en MWCNT's tonen de gerapporteerde studies aan dat de Ag-belading ongeveer een orde van grootte hoger is dan die van Pd. Dit verschil kan worden toegeschreven aan verschillende factoren, voornamelijk het coördinatiegetal en de geometrie in hun respectieve coördinatiecomplexen. Zilver(I) neemt doorgaans lineaire of tetraëdrische geometrieën aan in coördinatiecomplexen, waarbij zilverionen voornamelijk een twee-, drie- of viervoudige coördinatie vertonen. Daarentegen vertonen Pd(II)-complexen meestal vier-gecoördineerde vierkante vlakke configuraties, hoewel een aanzienlijk deel ook vijf-gecoördineerde verbindingen omvat.

De waargenomen variaties in aggregatiepatronen, nucleatieprocessen en de vorm- en grootteverdeling van de metalen nanodeeltjes worden sterk beïnvloed door de chemische en structurele eigenschappen van de koolstofhoudende substraten die in deze studie zijn gebruikt. Bovendien worden deze resultaten bepaald door de morfologische eigenschappen van de substraten—of ze nu in poeder- of papierformaat zijn—en de specifieke functionaliteit van aminemodificatoren, die via verschillende interactiemechanismen met de nanokoolstofoppervlakken samenwerken.

Nieuwe onderzoeksmogelijkheden

Op basis van de resultaten van dit promotieonderzoek doen zich nieuwe mogelijkheden voor verder onderzoek voor. Het volgende kan overwogen worden:

- **Uitvoeren van verspreidingstests** in oplosmiddelen met een breder bereik van polariteit om de stabiliteit van zowel poeder- als papierformaten van de hybriden te onderzoeken en hun geschiktheid voor verdere verwerking te evalueren.
- **Onderzoeken van alternatieve routes** voor de productie en a fzetting van nanodeeltjes om de nucleatie van metalen soorten te maximaliseren en de metaalbelading te verhogen, vooral op papiergebaseerde en palladiumhoudende materialen.
- **Testen van de mechanische sterkte** van papierachtige nanohybriden om te bepalen of deze geschikt zijn voor gebruik in waterzuivering, selectieve filtratie en als geleidende materialen in flexibele elektronica.
- **Verkennen van specifieke toepassingen** van de nanohybriden, rekening houdend met de behaalde metaalbelading, de overheersende oxidatietoestand van het edelmetaal, de vorm van de nanodeeltjes en het waargenomen decoratiepatroon. De volgende hypotheses kunnen in detail worden onderzocht:

1. ***GO/Ag-gebaseerde reeks*****.** Gezien het feit dat GO het oppervlak en de verspreidbaarheid van het materiaal vergroot en Ag-nanodeeltjes bekend staan om hun antimicrobiële eigenschappen, zouden de nieuwe hybride materialen de bacteriedodende efficiëntie van zilver mogelijk kunnen vergroten. De nanohybriden met amines zouden de interactie tussen het materiaal en bacteriële membranen kunnen verbeteren, wat de antimicrobiële werking versterkt. Het brede bereik van deeltjesgroottes (van nanometerschaal tot micrometerschaal) kan diverse interactiemechanismen genereren, wat mogelijk betere resultaten oplevert dan standaard met AgNP beladen materialen.

2. ***GO/Pd-gebaseerde reeks***. Met Pd-nanodeeltjes in verschillende vormen ingebed in een grafeenoxidematrix bieden deze materialen verschillende soorten actieve sites die worden gebruikt in katalytische reacties, zoals hydrogenering en cross-couplingreacties zoals Suzuki- of Heck-reacties voor organische synthese. Dit zou mogelijk kunnen leiden tot een betere algehele efficiëntie en selectiviteit van de katalysator. Het koolstofhoudende rooster kan de elektronoverdracht verbeteren, en daarmee de reactiesnelheid verder verhogen.

3. ***MWCNTs/Ag-gebaseerde reeks***. Dankzij de synergie van MWCNTs, die uitstekende geleidbaarheid en een hoog oppervlak bieden, en Ag-nanodeeltjes, die met verschillende gassen zoals waterstof, ammoniak en koolmonoxide interageren, zijn de nieuwe nanohybriden veelbelovend voor gassensoren. Het feit dat metallisch Ag overheerst op het oppervlak, kan resulteren in selectieve sensorcapaciteiten. De nanohybriden met amines zijn bijzonder geschikt om gevaarlijke gassen zoals CO, NOx of methaan, of vluchtige organische verbindingen te detecteren voor luchtkwaliteitsmonitoring.

4. ***MWCNTs/Pd-gebaseerde reeks***. Materialen op basis van MWCNTs die palladium in zijn geoxideerde vorm bevatten, lijken veelbelovend voor elektrokatalyse, met name in brandstofcellen of batterijen, vanwege hun vermogen om redoxreacties te vergemakkelijken. Specifiek kan de rol van PdO2-nanodeeltjes in reacties zoals waterstofoxidatie worden versterkt door de ondersteuning van nanobuizen. Daarom zouden de nieuwe hybride materialen zowel de prestaties als de stabiliteit van toekomstige apparaten kunnen verbeteren, wat een kosteneffectief alternatief biedt voor puur palladium in elektrokatalyse.

RESUMEN Y PERSPECTIVAS

Este trabajo doctoral explora una síntesis sostenible y la caracterización de materiales híbridos nanostructurados novedosos que utilizan óxido de grafeno o nanotubos de carbono de pared múltiple como sustratos. Dichos sustratos fueron funcionalizados con moléculas de aminas y posteriormente decorados con nanopartículas de plata o paladio, empleando metodologías amigables con el medio ambiente.

Basada en los principios de la Química Verde, esta investigación tuvo como objetivo desarrollar nanomateriales avanzados a través de una técnica de funcionalización con aminas en fase gaseosa y sin disolventes, utilizando las aminas alifáticas: 1-octadecilamina (ODA) y 1,8-diaminooctano (DAO) para modificar con precisión las propiedades superficiales de las nanostructuras de carbono, minimizando la generación de subproductos nocivos. Este enfoque se complementó con la impregnación húmeda de nanopartículas metálicas, empleando nitrato de plata y cloruro de paladio como precursores y ácido cítrico como agente reductor/estabilizante. A través de este método, se logró una distribución predominantemente uniforme de partículas y se optimizó la interacción entre las nanopartículas y los sustratos carbonáceos. Estas estrategias ecológicas redujeron la generación de residuos y omitieron el uso de reactivos peligrosos, alineándose con los objetivos de sostenibilidad.

Para alcanzar los objetivos de la investigación, se empleó una variedad de técnicas avanzadas de caracterización, tales como espectroscopia, microscopía electrónica y análisis térmico, que confirmaron la síntesis exitosa de nuevos materiales. Los hallazgos destacaron el papel de la morfología del sustrato y la funcionalización en la influencia sobre el tamaño, la distribución y las propiedades generales de los nanohíbridos. El modelado computacional apoyó estos resultados experimentales, elucidando las interacciones a nivel molecular y guiando el diseño de nanomateriales optimizados. El estudio también sugirió el desempeño sinérgico de estos materiales en aplicaciones como catálisis y tecnologías antimicrobianas, abordando desafíos críticos en el ámbito ambiental y biomédico, a la vez que abre camino a innovaciones en nanotecnología sostenible.

- El **Capítulo 1** da una introducción a los principios de la Química Verde, los desafíos ambientales de la nanotecnología y los materiales estudiados en esta disertación, que son: óxido de grafeno (GO), nanotubos de carbono (CNTs) y nanopartículas metálicas de plata y paladio. Este capítulo enfatiza también los beneficios ambientales de los métodos de síntesis sostenibles y describe las propiedades de dichos materiales. Además, el capítulo discute las técnicas de funcionalización empleadas, la posible aplicabilidad de los nanomateriales híbridos en campos como la catálisis, la medicina y la electrónica, y los objetivos de investigación centrados en la síntesis y evaluación de las propiedades estructurales, químicas y funcionales de los híbridos nanostructurados.

- El **Capítulo 2** profundiza en las metodologías para fabricar y modificar nanomateriales a base de carbono, particularmente GO y nanotubos de carbono de pared múltiple (MWCNTs) en formas de polvo y papel. Describe protocolos de síntesis que incluyen la funcionalización con aminas en fase gaseosa y la formación/deposición *in situ* de nanopartículas de plata y paladio, diseñados para mejorar las propiedades químicas y físicas de los híbridos finales. Aquí se emplearon técnicas de caracterización, como espectroscopía infrarroja mediante transformada de Fourier (FTIR), espectroscopía de fotoelectrones emitidos por rayos X (XPS), difracción de rayos X (XRD) y microscopía electrónica, para investigar las propiedades estructurales, superficiales y térmicas de los materiales sintetizados. El modelado computacional utilizando la Teoría del Funcional de la Densidad (DFT) validó los hallazgos experimentales al proporcionar información sobre las interacciones moleculares dentro de los híbridos.

- El **Capítulo 3** discute la síntesis verde y la caracterización de materiales híbridos a base de óxido de grafeno y nanopartículas de plata (GO-Ag) en formas de polvo y papel. La funcionalización con aminas mejoró la deposición de nanopartículas sobre la matriz de GO. Los resultados demostraron que el GO funcionalizado con DAO exhibió una distribución más pequeña y uniforme de tamaño de partículas de Ag. Los cálculos por DFT corroboraron estos hallazgos al elucidar las interacciones de unión entre las nanopartículas de Ag y el GO funcionalizado.

- El **Capítulo 4** describe una ruta ecológica para el desarrollo de nanohíbridos de óxido de grafeno y paladio (GO-Pd) en formas de polvo y papel. A través de una caracterización exhaustiva, este proyecto reveló perfiles únicos de tamaño, forma y distribución de nanopartículas, particularmente en las formas de papel estructuralmente mejoradas funcionalizadas con aminas, que exhibieron una mayor estabilidad. El modelado por DFT proporcionó información sobre las interacciones Pd-GO, destacando aplicaciones potenciales en catálisis, electrónica y desempeño estructural.

- El **Capítulo 5** informa sobre la fabricación y caracterización de híbridos basados en MWCNTs con nanopartículas de Ag en formas de polvo y papel (buckypaper). El estudio destacó la influencia de la funcionalización con ODA en la mejora de la dispersión y adherencia de las nanopartículas, lo que resultó en una mayor estabilidad térmica y uniformidad en comparación con los híbridos funcionalizados con DAO y los no funcionalizados. Estas características reforzaron significativamente las propiedades estructurales y funcionales de los híbridos que contenían ODA.

- El **Capítulo 6** describe la síntesis verde y la caracterización físico-química de híbridos de MWCNT que contienen nanopartículas de Pd en formas de polvo y buckypaper. El estudio investigó el impacto de la funcionalización en la distribución, morfología y estabilidad de las nanopartículas de Pd, con pruebas de dispersabilidad que revelaron comportamientos hidrofóbicos/hidrofílicos distintos, dependiendo de la amina utilizada. La caracterización demostró que las muestras funcionalizadas con aminas exhibieron una mejor dispersión de PdNP y mayor estabilidad térmica, destacando su potencial para aplicaciones en electrónica, catálisis y remediación ambiental.

Comparando el contenido de paladio y plata en GO y MWCNTs tanto en forma de polvo como de papel, los estudios reportados muestran que la carga de Ag supera a la de Pd aproximadamente en un orden de magnitud. Esta diferencia puede atribuirse a varios factores, principalmente al número de coordinación y la geometría en sus respectivos complejos de coordinación. La plata (I) adopta típicamente geometrías lineales o tetraédricas en los complejos de coordinación, con iones de plata que predominantemente presentan números de coordinación dos, tres o cuatro. En contraste, los complejos de Pd(II) exhiben comúnmente configuraciones planas cuadradas con número de coordinación cuatro, aunque también existe una proporción significativa de compuestos con número de coordinación cinco.

Las variaciones observadas en los patrones de agregación, los procesos de nucleación y la distribución de tamaño y forma de las nanopartículas metálicas están estrechamente influenciadas por las propiedades químicas y estructurales de los sustratos de carbono utilizados en este estudio. Además, estos resultados están condicionados por las características morfológicas de los sustratos, ya sea en forma de polvo o de papel, y la funcionalidad específica de las aminas modificantes, que interactúan mediante mecanismos distintos con las superficies de nanocarbono.

Con base en los resultados obtenidos en el desarrollo de este proyecto de doctorado, surgen nuevas oportunidades para futuras investigaciones, donde se debería considerar:

- **Realizar pruebas de dispersabilidad en disolventes con un intervalo más amplio de polaridad** para explorar la estabilidad de las formas de polvo y papel de los nuevos híbridos, evaluando su idoneidad para un procesamiento futuro.
- **Examinar rutas alternativas para la producción y deposición de nanopartículas** con el fin de maximizar la nucleación de especies metálicas y aumentar la carga de metal, especialmente en materiales en forma de papel y que contienen paladio.
- **Probar si la resistencia mecánica de los nanohíbridos tipo papel es suficiente** para su utilización en purificación de agua, filtración selectiva y como materiales conductores en electrónica flexible.
- **Explorar aplicaciones específicas de los nanohíbridos**, considerando la carga metálica lograda, el estado de oxidación predominante del metal noble, la forma de las nanopartículas y el patrón de decoración observado. En detalle, podrían investigarse las siguientes hipótesis:

1. ***Serie a base de GO y Ag.*** Teniendo en cuenta que el GO mejora el área superficial y la dispersabilidad del nuevo material híbrido, y que las nanopartículas de Ag son bien conocidas por sus propiedades antimicrobianas, los nuevos materiales podrían aumentar la eficiencia bactericida de la plata. Los nanohíbridos que contienen aminas podrían mejorar la interacción entre el material y las membranas bacterianas, potenciando la acción antimicrobiana. El amplio rango de tamaños de partículas obtenidas (desde escala nanométrica hasta micrométrica), podría generar diversos mecanismos de interacción, lo que potencialmente conduciría a mejores resultados que los materiales cargados con AgNP estándar.

2. ***Serie a base de GO y Pd.*** Las nanopartículas de Pd, en una variedad de formas, embebidas en una matriz de GO, proporcionan distintos tipos de sitios activos para reacciones catalíticas, como la hidrogenación y el acoplamiento cruzado, incluyendo reacciones de Suzuki o Heck para síntesis orgánica. Esto podría resultar en una mayor eficiencia y selectividad general del catalizador. La estructura carbonosa podría mejorar la transferencia de electrones y, por ende, acelerar aún más la tasa de reacción.

3. ***Serie a base de MWCNTs y Ag.*** Gracias a la sinergia de los MWCNTs, que ofrecen excelente conductividad y gran área superficial, y las nanopartículas de Ag, que interactúan con diversos gases como hidrógeno, amoníaco y monóxido de carbono, los nuevos nanohíbridos son prometedores para la detección de gases. El hecho de que la plata metálica predomine en la superficie podría resultar en capacidades de detección selectiva. Los nanohíbridos que contienen aminas podrían ser particularmente aptos para detectar gases peligrosos como CO, NOx o metano, o compuestos orgánicos volátiles, útiles para la monitorización de la calidad del aire.

4. ***Serie a base de MWCNTs y Pd.*** Los materiales fabricados a partir de MWCNTs que contienen paladio en su forma oxidada parecen prometedores en electrocatálisis, particularmente en pilas de combustible o baterías, debido a su capacidad para facilitar reacciones redox. Específicamente, el papel de las nanopartículas de PdO_2 en reacciones como la oxidación de hidrógeno, puede ser mejorado por el soporte de nanotubos; por lo tanto, los nuevos materiales híbridos podrían mejorar tanto el desempeño como la estabilidad de futuros dispositivos, ofreciendo una alternativa más económica al paladio puro en electrocatálisis.

LIST OF PUBLICATIONS

- **Rodríguez-Otamendi, D. I.;** Bizarro, Rudolf, P.; Basiuk, V. A.; Basiuk, E. V. Deposition of palladium nanoparticles onto graphene oxide paper: an eco-friendly approach. Draft manuscript.

- **Rodríguez-Otamendi, D. I.;** Bizarro, M.; Meza-Laguna, V.; Álvarez-Zauco, E.; Rudolf, P.; Basiuk, V. A.; Basiuk, E. V. Eco-Friendly Synthesis of Graphene Oxide–Palladium Nanohybrids. *Materials Today Communications* 2023, *35*, 106007. https://doi.org/10.1016/j.mtcomm.2023.106007.

- **Rodríguez-Otamendi, D. I.;** Meza-Laguna, V.; Acosta, D.; Álvarez-Zauco, E.; Huerta, L.; Basiuk, V. A.; Basiuk, E. V. Eco-Friendly Synthesis of Graphene Oxide–Silver Nanoparticles Hybrids: The Effect of Amine Derivatization. *Diamond and Related Materials* 2021, *111*, 108208. https://doi.org/10.1016/j.diamond.2020.108208.

CONFERENCES

- **33rd International Conference on Diamond and Carbon Materials (ICDCM).** September 10-14th 2023. Palma, Mallorca, Spain, Poster: “Fabrication of hybrid multiwalled carbon nanotubes-silver and palladium nanoparticles systems: An eco-friendly approach”.

- **IUPAC-CHAINS Conference 2023.** August 20-25th**.** The Hague, The Netherlands. Poster: “Green paper-like carbon-metal nanohybrids supporting metallic nanoparticles.”

- **NWO CHAINS 2022.** September 21-22th.Veldhoven, The Netherlands. Poster: “Eco-friendly synthesis of graphene oxide–palladium nanoparticles hybrids.”

- **ZIAM PhD Colloquium Symposium 2022.** September 15th. Poster: “Eco-friendly synthesis of graphene oxide and carbon nanotubes–palladium nanoparticles hybrids.”

- **Vlieland Meeting 2022.** June 12-14th. Vlieland, Frisian Islands, The Netherlands, Poster: “Green synthesis of nanohybrids: graphene oxide-palladium nanoparticles.’’

- **E-MRS Spring Meeting 2022.** May 30th to June 3rd. Virtual conference. Poster: “Green synthesis of paper-like nanohybrids: graphene oxide and carbon nanotubes decorated with silver nanoparticles.” *Poster award.*

- **#LatinXChem Twitter Conference 2020.** September 7th. Poster: “Green approach to synthesis of graphene oxide-silver nanohybrids”.

- **14th International Nanoscience Student Conference (INASCON 2020).** August 11-13th. Online conference. Poster: “Green approach to the synthesis of graphene oxide–silver nanohybrids’’.

Diamond & Related Materials 111 (2021) 108208

Contents lists available at ScienceDirect

Diamond & Related Materials

journal homepage: www.elsevier.com/locate/diamond

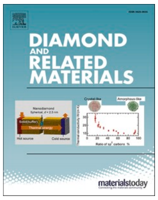

Eco-friendly synthesis of graphene oxide–silver nanoparticles hybrids: The effect of amine derivatization

Dinorah I. Rodríguez-Otamendi [a], Victor Meza-Laguna [b], Dwight Acosta [c], Edgar Álvarez-Zauco [d], Lazaro Huerta [e], Vladimir A. Basiuk [b,*], Elena V. Basiuk [a,*]

[a] *Instituto de Ciencias Aplicadas y Tecnología, Universidad Nacional Autónoma de México, Circuito Exterior, Ciudad Universitaria, 04510 Cd. México, Mexico*
[b] *Instituto de Ciencias Nucleares, Universidad Nacional Autónoma de México, Circuito Exterior, Ciudad Universitaria, 04510 Cd. México, Mexico*
[c] *Instituto de Física, Universidad Nacional Autónoma de México, Circuito de la Investigación Científica, Ciudad Universitaria, 04510 Cd. México, Mexico*
[d] *Facultad de Ciencias, Universidad Nacional Autónoma de México, Circuito Exterior C.U., 04510 Cd. México, Mexico*
[e] *Instituto de Investigaciones en Materiales, Universidad Nacional Autónoma de México, Circuito Exterior C.U., 04510 Cd. México, Mexico*

ARTICLE INFO

Keywords:
Graphene oxide
Amine derivatization
Silver nanoparticles
Characterization
DFT calculations

ABSTRACT

We addressed the deposition of silver nanoparticles (Ag NPs) onto graphene oxide (GO) in the form of powder and paper (GOP), functionalized with amines and non-functionalized, for comparison. The functionalized supports were fabricated by means of solvent-free treatment with two aliphatic amines: 1-octadecylamine (ODA) and 1,8-diaminooctane (DAO). Ag NPs were generated in situ by using silver nitrate as a precursor and citric acid as a non-toxic and eco-friendly reducing agent. Characterization of chemical composition of GO-Ag hybrids was done by Fourier-transform infrared, X-ray photoelectron and energy dispersive X-ray spectroscopy, X-ray diffraction, thermogravimetric and differential thermal analysis. The morphology was studied by scanning and transmission electron microscopy. In addition, we compared electrical conductivity of GOP before and after functionalization with amines and decoration with Ag particles. While considerable particle agglomeration was observed on pristine GOP and GO powder, the prior amine functionalization gave rise to more controlled formation of Ag NPs in terms of size and distribution, with the best results obtained on 1,8-diaminooctane-functionalized supports. According to the results of DFT calculations, Ag NP binding is the strongest on pristine GO, followed by ODA and finally DAO-functionalized material, which correlates with the size and distribution of Ag nanoparticles observed experimentally.

1. Introduction

Graphene oxide (GO) sheets incorporate a variety of oxygen-containing functionalities, including epoxy, hydroxyl, carbonyl and carboxyl groups, distributed either throughout the basal plane or at the edges. As a result, GO contains a combination of sp^2 and sp^3-hybridized carbon atoms. Subjecting the above groups to versatile chemical reactions provides opportunities for tailoring physico-chemical properties of GO (see [1–5] and references therein). In addition, it is due to polar nature of oxidized functionalities GO is able to produce stable dispersions in water, contrary to non-functionalized graphene. Furthermore, the development of paper-like material based on GO, commonly referred to as graphene oxide paper (GOP), attracted close attention due to the possibility of designing promising materials with tunable properties for such diverse application as supercapacitors, chemical and biochemical sensors, photosensors, magnetic and thermal conductive materials, nanofiltration membranes, and bactericidal agents for water disinfection, among others (see [6–10] and references therein).

Due to the great interest towards the synthesis and uses of metal nanoparticles (NPs), in particular silver nanoparticles (Ag NPs), it turned to be especially attractive to combine properties of the two types of materials, for practical applications in electronics, catalysis, electrochemical biosensing, drug delivery, and antimicrobial agents [5,11–31]. Within this area GO is considered as an excellent support for dispersing and stabilizing Ag NPs, since it combines a large specific surface area and abundant oxygenated functionalities, acting as the anchoring sites for strong attachment of nanoparticles.

The synthetic approaches to GO-supported Ag NPs (hereafter referred to as GO-Ag) rely upon the solution-phase chemical reduction of silver salts, involving a number of steps with the use of stabilizing and

---

* Corresponding authors.
E-mail addresses: basiuk@nucleares.unam.mx (V.A. Basiuk), elbg1111@gmail.com (E.V. Basiuk).

https://doi.org/10.1016/j.diamond.2020.108208
Received 8 October 2020; Received in revised form 18 November 2020; Accepted 22 November 2020
Available online 28 November 2020

dispersing agents in order to prevent Ag NP agglomeration and to control their size and morphology [5,11–31]. It is important to emphasize that both the latter parameters and Ag NP surface distribution strongly depend on the entire synthetic sequence employed. For example, the average size of Ag NPs was found to be about 18 nm when GO-Ag nanocomposite was synthesized from non-functionalized GO by the sonochemical method coupled with subsequent shock freezing [5]. A very different route suggested by Vi et al. [26,27] contemplated the attachment of Ag NPs onto GO layers through grafted thiol groups. These works [26,27] can serve as a good example of multi-step and labor-intensive approaches to GO-Ag nanohybrids, mainly due to the prior functionalization of the support material. In particular, it includes prolonged stirring and sonication-assisted reaction of GO with NaSH to produce covalently-bonded thiol groups on GO, followed by its filtering, washing and drying in vacuum. The main idea was to use NaSH as an effective cross-linker via GO–SH formation. The authors expected that the coordination to thiol groups can prevent Ag NP agglomeration and enable a precise control of particle size. Indeed, Ag content of 31–65% was afforded in this way, with 1–2 nm nanoparticle size [27]. This is an important achievement, especially in view of the well-known fact that Ag NPs, due to their high surface energy, are highly reactive and easily susceptible to agglomeration (one of the important practical consequences of this phenomenon is a loss of their antibacterial activity [28]).

The approaches using biological molecules instead of toxic chemicals, such as hydrazine and sodium borohydride, merit special mention due to their evident ecological value. They can be exemplified by the study [29], where pepsin was employed as the reducing and stabilizing agent, resulting in Ag NPs with an average size of 20 nm deposited evenly onto GO sheets. The method proposed is relatively quick, and the stabilizing action of pepsin is due to its amino groups, with hydroxyl and carboxylate groups acting as the centers of Ag NPs nucleation through the formation of coordination bonds or simple electrostatic interactions with silver ions. The results obtained [29] are in a good agreement with other reports (for example, [30]) on the preparation of GO-Ag hybrids, suggesting that the abundant oxygenated functionalities of GO sheets allow for the anchoring of metal ions and facilitate their further in situ reduction into corresponding metal NPs.

The study mentioned above [29] is not the only one which illustrates the role of amino groups in Ag NP stabilization. In the work on the graphene functionalization with 1,6-diaminohexane and further deposition of Ag NPs for water disinfection [31], the authors mentioned that among the forces stabilizing the hybrid obtained might be electrostatic attraction of amino groups and silver species to electron-rich graphene surface. The functionalization with triethylene tetramine followed by reduction under hydrothermal conditions was reported in [12] to obtain Ag NPs with sizes in the range of 10–20 nm, uniformly distributed over the surface of reduced GO due to strong adsorption interactions between the two components.

Some thermal and chemical treatments employed for GO functionalization turn to be rather harsh, giving rise to undesirable alterations in the structure of GO-based materials. In particular, this can happen in a liquid reaction medium, especially when the object of chemical modification is GOP. A promising approach which can help to avoid negative effects associated with the use of a liquid reaction medium proved to be the solvent-free functionalization. It was successfully applied by our research group for both covalent and noncovalent attachment of variable chemical species, including amines, to different carbon nanomaterials, including GO powder and GOP [2,3,32]. Provided that amine reagent (which can be aliphatic or aromatic, monofunctional or bifunctional) has sufficient thermal stability and volatility, the solvent-free approach is a fast, efficient, eco-friendly and nondestructive way to systematically tune GO properties. The general functionalization protocol contemplates moderate heating at 150–180 °C under reduced pressure, and the covalent amine attachment proceeds through both amidation of COOH groups and epoxy ring opening reactions.

It is well known that the size of metal nanoparticles is a crucial factor influencing their antibacterial and/or catalytic activity. In particular, Ag NPs with sizes of <10 nm proved to have higher bactericidal activity because of the increase in surface area and ease of cell penetration [33,34]. This factor, the fact that the smallest Ag NPs deposited onto GO were afforded due to its prior covalent functionalization, and that simple amines are suitable reagents for the latter purpose, motivated us to undertake the present study. We sought to obtain GO and GOP-based hybrid materials decorated with small-sized silver NPs without their considerable agglomeration. Stable centers for the coordination of Ag species were created by means of the-gas phase functionalization of GO and GOP with 1-octadecylamine (ODA) and 1,8-diaminooctane (DAO) as representative monofunctional and bifunctional amine, respectively. Ag NPs were generated in situ by using silver nitrate as a precursor and citric acid as a non-toxic and eco-friendly reducing agent. In control experiments, the same silver deposition procedure was carried out with non-functionalized GO and GOP. Since chemical modification of GOP without compromising its integrity is an especially challenging task (see Alzate-Carvajal et al. [3] and references therein), the main emphasis in our report is done on this material, with the results obtained on GO powder serving in some cases merely for comparison.

2. Materials and methods

2.1. Materials

GO powder (≥99 wt% purity, platelet diameter of 0.5–3 μm and thickness of 0.55–1.2 nm) from Nanostructured & Amorphous Materials, Inc., was used. 1-Octadecylamine (≥99%), 1,8-diaminooctane (≥98%), citric acid (≥99.5%), silver nitrate (≥99%), and 2-propanol (≥99.8%) from Sigma-Aldrich were used as received.

2.2. GOP fabrication

Aqueous dispersions of GO (ca. 6.66 mg/mL) were obtained with the aid of ultrasonic treatment. The dispersions were filtered through cellulose acetate membrane filters (0.45 μm pore size, 47 mm diameter, Healtcare Life Sciences, Whatman), using a vacuum Millipore filtration system. The disk-shaped mats obtained were dried in a vacuum desiccator and detached from the cellulose filter. The material obtained in this way is hereafter referred to as pristine GOP.

2.3. Functionalization of GO and GOP with amines

We followed the general functionalization protocol described previously [2,3]. Pristine GO or GOP samples were placed together with amines in a Pyrex glass reactor, at GOP/amine w/w ratio of 1:5, and GO/amine w/w ratio of 1:1. Prior to functionalization, the reactor content was degassed for 1 h at about 100 °C under constant evacuation at about 10^{-2} Torr. The functionalization reaction was carried out using static vacuum (reactor valve closed) for 2 h at a temperature maintained in the range of 160–180 °C. After finishing this procedure, the reaction zone was heated again at about 100 °C under constant evacuation for 1 h to remove the excess of amines. The functionalized samples obtained are denoted hereafter as GO + ODA, GO + DAO, GOP + ODA y GOP + DAO.

2.4. Deposition of Ag NPs

We employed the method of Ag NP deposition reported previously for the case of C_{60} films functionalized with DAO [35]. The procedure was based on the reduction of Ag^+ ions with citric acid. First, amine-functionalized GO was dispersed (with ultrasonication) and GOP was immersed (both at 0.4 mg/mL) in 2-propanol. Then, 0.01 M solution of citric acid and 0.005 M solution of $AgNO_3$, both in 2-propanol, were simultaneously added dropwise to the reaction vessel upon continuous stirring at room temperature for 30 min. After that, the samples were filtered, washed twice with 2-propanol, dried and stored under vacuum

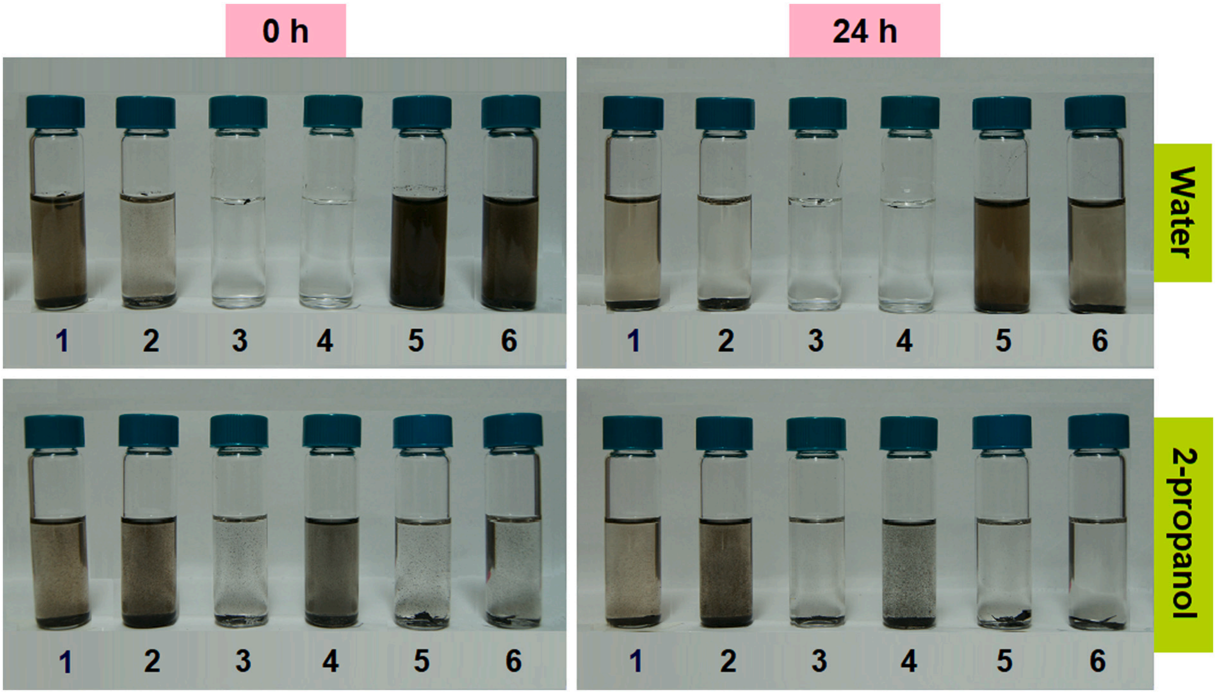

Fig. 1. Dispersibility tests for GOP samples in water and in 2-propanol: (1) pristine GOP, (2) GOP+Ag, (3) GOP+ODA, (4) GOP+ODA+Ag, (5) GOP+DAO, and (6) GOP+DAO+Ag. Images taken immediately after 10-min ultrasonication (0 h) and after further 24 h.

at room temperature. The amine-functionalized samples decorated with Ag NPs are denoted as GO + ODA + Ag, GO+DAO + Ag, GOP + ODA + Ag and GOP + DAO + Ag. The same process with pristine (non-functionalized) GO and GOP was repeated as a control experiment, and the samples obtained are denoted as GO + Ag and GOP + Ag, respectively.

2.5. Characterization

Fourier-transform infrared (FTIR) spectra were acquired by using a Nicolet iS50R Thermo-Scientific spectrometer, under room temperature and atmospheric pressure, in attenuated total reflectance (ATR) mode. For spectra acquisition, 32 scans were used, in a spectral range of 500–4000 cm^{-1}. Raman spectra were recorded on a Nicolet Almega XR Dispersive Raman Thermo-Scientific spectrometer ($\lambda = 532$ nm) in a Raman shift range of 500–4000 cm^{-1}. X-ray photoelectron spectroscopic (XPS) analysis was performed by using an ultra-high vacuum system Scanning XPS microprobe PHI5000 VersaProbe II, with a monochromatic Al K_α X-ray source ($h\nu = 1486.6$ eV). The deconvolution analysis of XPS spectra was fitted with the programs PHI Multipack© version 9.6.0.15 and SDP© v 4.1.

Thermogravimetric and differential thermal analysis (TGA–DTA) thermograms were recorded by using a STA 449C Jupiter analyzer from Netzsch-Gerätebau GmbH, under air atmosphere with air flow of 50 mL/min, and with a heating ramp of 10 °C/min up to 1000 °C.

For scanning electron microscopy (SEM) characterization of GO powder and GOP mats, we employed a JEOL JSM-6510LV instrument operated at a voltage of 20 kV, coupled to an INCA Energy 250 Energy Dispersive X-ray (EDS) Microanalysis System from Oxford Instruments. For transmission electron microscopy (TEM) bright-field studies, a JEOL JEM-2010F FEG was used, operated at 1.9 Å resolution and 200 kV voltage. For high-resolution TEM (HRTEM) studies, standard grids with collodion support films were employed, where Ag-decorated GO and GOP samples were deposited. Before HRTEM observations, all the samples were cleaned by plasma treatment. For acquiring dark-field TEM images, a JEOL JEM-ARM200F STEM Schottky FEG was used, operated at 1.0 Å resolution and 200-kV voltage.

X-ray diffraction (XRD) data were obtained using a D8 Advance Bruker diffractometer with Bragg-Brentano geometry and CuK_α radiation ($\lambda = 1.5406$ Å). For XRD studies, the sample was pulverized and afterwards sieved using different mesh. Finally, the resulting powder was deposited in a tube for XRD analysis. For crystallographic cards, The Cambridge Crystallographic Data Centre database was employed.

For conductivity measurements on GOP samples, a Keithley 2601B Source Meter Unit (SMU) was employed, operated under ambient conditions in a DC mode and controlled by a PC. For measurements, the 4-wire technique was used. The samples were cut into strips of 10–20 mm length and 3–5 mm width, and immediately rubbed on foil to eliminate static charge. The specimens were placed perpendicularly with respect to parallel copper electrodes. The dimensions of the electrodes, printed on a circuit board, were of 0.25 mm in width, separated by 2.8 mm. Electric contact was established by lightly pressing a piece of glass slide above the sample by using a clip. Before each measurement, specimens were stored in a vacuum desiccator for 24 h. The conditions optimized for the present studies were as follows: an initial and final current of 1000 nA, stabilization time of 0.5 s, and 20 measurement steps. Further technical details of the conductivity measurements can be found in Alzate-Carvajal et al. [3].

2.6. Theoretical calculations

The procedure selected for all density functional theory (DFT) calculations was Perdew-Burke-Ernzerhof (PBE) [36] correlation functional within general gradient approximation. To account for dispersion interactions, which are crucial when treating noncovalently bonded systems, PBE functional was complemented with the empirical correction introduced by Grimme [37]. This combination, usually referred to as PBE-D (or also PBE-D2), proved to be helpful and extensively used for DFT analysis of noncovalent, covalent and coordination bonding of a broad variety of chemical species to graphene and GO models [38–45].

The software package employed for calculations was the Accelrys Materials Studio, which includes the DMol^3 numerical-based module [46–49]. To be used in conjunction with PBE-D functional, the double numerical basis set DNP [49] was selected, which has a polarization *d*-function added on all non-hydrogen atoms, as well as a polarization *p*-

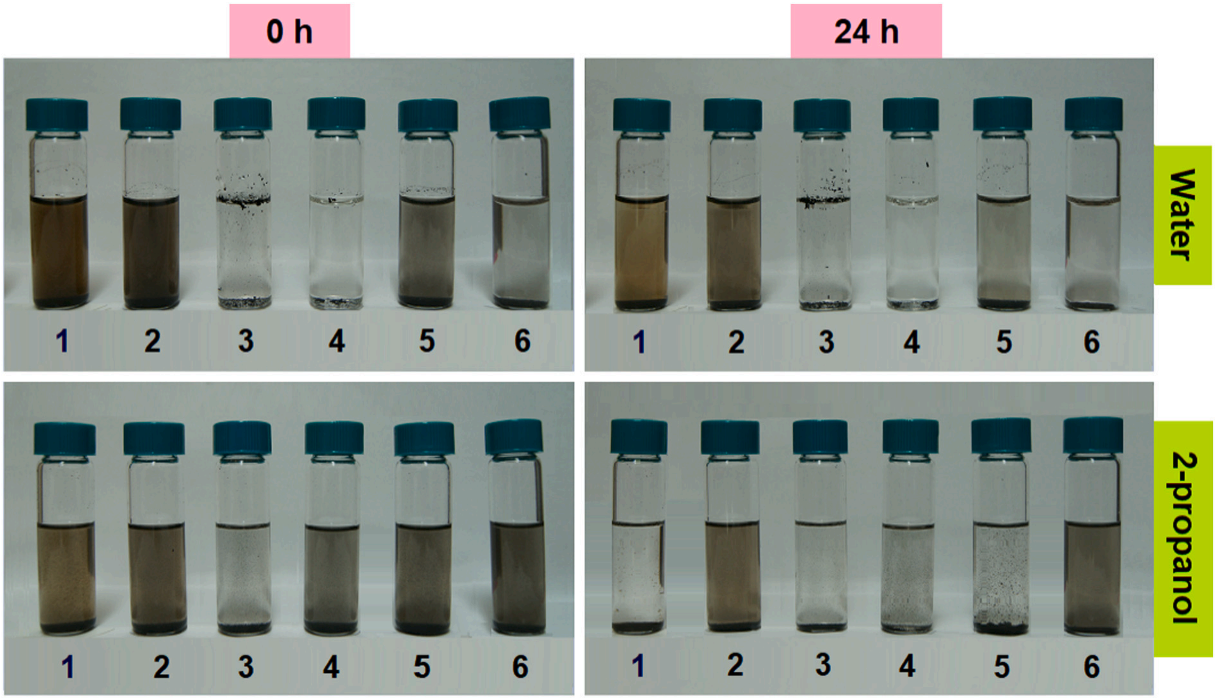

Fig. 2. Dispersibility tests for GO powder samples in water and in 2-propanol: (1) pristine GO, (2) GO+Ag, (3) GO+ODA, (4) GO+ODA+Ag, (5) GO+DAO, and (6) GO+DAO+Ag. Images taken immediately after 10-min ultrasonication (0 h) and after further 24 h.

function added on all H atoms. All the models under the study were treated as open-shell systems. 'Fine' computation quality and convergence criteria (10^{-5} Ha energy change, 0.002 Ha/Å maximum force, 0.005 Å maximum displacement, and 10^{-6} SCF tolerance), along with all-electron core treatment were the settings used for full geometry optimization and calculation of electronic parameters. Since setting orbital occupancy to Fermi-type not always allowed for the successful SCF convergence, the latter was aided by using thermal smearing, whose value was reduced stepwise from 0.005 to 10^{-4} Ha, and the final calculation was refined with Fermi orbital occupancy [50]. The value of 4.5 Å was used for global orbital cutoff: this is the minimal value which may be used for the systems incorporating Ag atoms. Correspondingly, for the sake of consistency all other isolated nanoclusters and complexes had to be calculated with the same settings.

The formation energies $\Delta E_{\mathrm{GOmodel+AgNC}}$ for the complexes (or ΔE for simplicity) of different GO models (GOmodel) with a silver nanocluster (AgNC) were calculated using the following general equation:

$$\Delta E_{\mathrm{GOmodel+AgNC}} = E_{\mathrm{GOmodel+AgNC}} - \left(E_{\mathrm{GOmodel}} + E_{\mathrm{AgNC}}\right)$$

where E_{i} is the corresponding absolute energy.

3. Results and discussion

3.1. Experimental results

In order to visualize the changes in chemical nature of GO powder and GOP samples upon functionalization with amines and further decoration with Ag NPs, we performed a simple but very illustrative dispersibility test. For this purpose, 0.5 mg/mL dispersions in water and in 2-propanol were prepared with ultrasonication for both GO powder and GOP samples (pristine, amine-functionalized, and decorated with Ag NPs; all treated using ultrasonic bath for 10 min at room temperature). The results are shown in Figs. 1 and 2 for GOP and GO powder, respectively. For the test in water (top images in Fig. 1), one can see that pristine GOP mat was dispersed completely after ultrasonic treatment, forming brown dispersion, which is consistent with generally hydrophilic nature due to the presence of a large amount of oxidized functionalities. Introduction of ODA moieties incorporating long hydrocarbon chains changed the character of GOP-ODA sample to hydrophobic, thus resulting in its immediate precipitation. At the same time, GOP-DAO formed stable (even after 24 h) brown dispersion, due to the presence of two terminal amino groups (one covalently bonded to GO surface and one dangling) in DAO moieties, enhancing hydrophilic character of this sample. The series of tests carried out in 2-propanol (bottom images in Fig. 1) gave similar results (to those obtained in water) for pristine GOP and GOP+ODA, whereas GOP-DAO mat only partially disintegrated after ultrasonication, and then remained essentially unchanged after 24 h. Such a distinctive behavior can be attributed to the effect of cross-linking adjacent GO sheets with bifunctional DAO molecules, as it was observed in our previous study on GOP amino functionalization [3]. The effect of Ag NP deposition observed in 2-propanol is generally opposite to the one found in water. That is, GOP+Ag, GOP+ODA+Ag and GOP+DAO+Ag are better dispersed than pristine GOP, GOP+ODA and GOP+DAO in 2-propanol, and vice versa, in water. In addition, one should point to evidently faster precipitation (after 24 h) of GOP+DAO+Ag than GOP+DAO in water, and higher stability of GOP+Ag and GOP+ODA+Ag dispersions in 2-propanol as compared to the corresponding mats before silver deposition.

The results obtained for GO powder samples (Fig. 2) in many regards match those presented above for GOP mats. On the other hand, very bright differences can be found for DAO-functionalized materials: in the case of aqueous medium, GO+DAO and GO+DAO+Ag are less dispersible than GOP+DAO and GOP+DAO+Ag, whereas an opposite effect is seen in 2-propanol. The increase in hydrophobicity upon decoration with Ag NPs can be observed more clearly, producing not only the decrease in dispersibility of GO+DAO+Ag in water, but also an increase in dispersibility of the same powder sample in 2-propanol, compared to GO+DAO. Of all dispersions tested, the most stable ones are those formed by GO+DAO+Ag and GO+Ag in 2-propanol, remaining almost unchanged after 24 h.

FTIR measurements were carried out to monitor changes in the chemical groups present in GO and GOP samples due to amino functionalization and decoration with Ag NPs (Figs. 3 and 4).

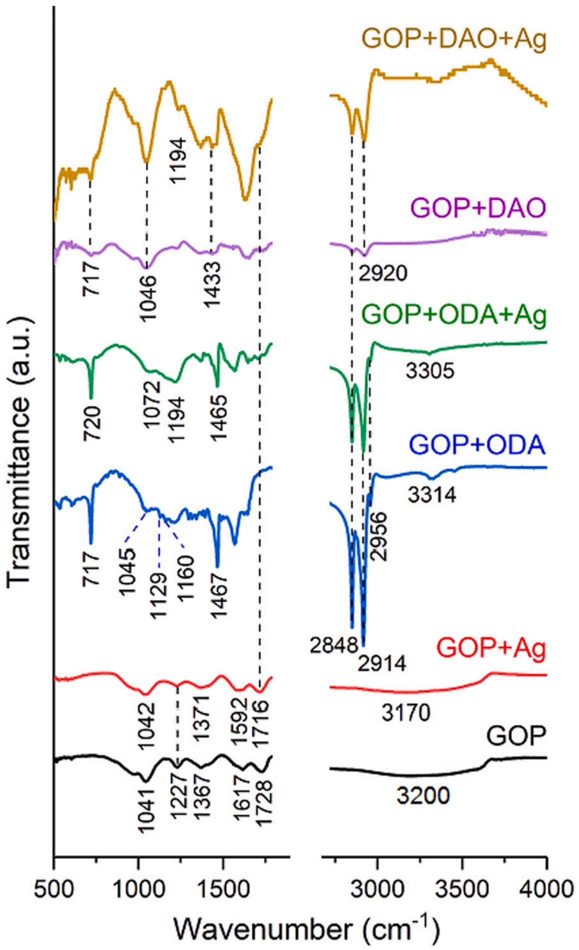

Fig. 3. FTIR spectra of pristine and amine-functionalized GOP samples before and after decoration with AgNPs.

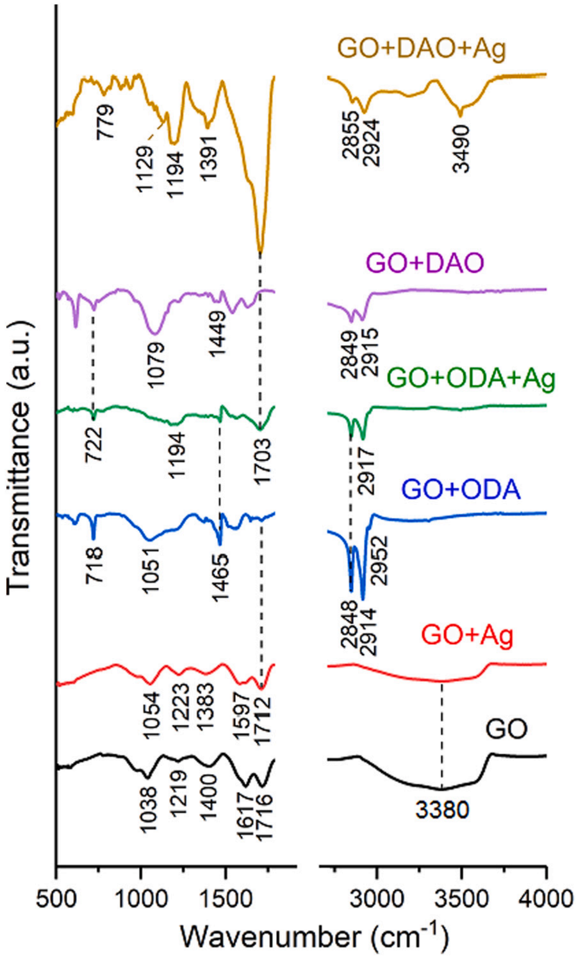

Fig. 4. FTIR spectra of pristine and amine-functionalized GO powder samples before and after decoration with AgNPs.

The spectrum of pristine GOP (Fig. 3) contains characteristic peaks due to abundant oxygen-containing functional groups. Among them are the hydroxyl ν_{OH} band at 3200 cm^{-1} with the corresponding δ_{OH} band at 1617 cm^{-1}, $\nu_{C=O}$ vibrations in COOH groups centered at 1728 cm^{-1}, asymmetric $\nu_{C\text{-}O}$ vibrations at 1367 cm^{-1} due to epoxy C–O–C groups, a peak at 1227 cm^{-1} due to bending O—H mode of C–O–H groups, and C—O single-bond stretching vibrations at 1041 cm^{-1}.

The most obvious changes caused by amine functionalization are a decrease in intensity of the $\nu_{C=O}$ band (down to its total disappearance for GOP + ODA), and of the C—O signal at 1041 cm^{-1}, along with the appearance of characteristic normal modes due to amide groups in the range of 1200–1700 cm^{-1}, serving as an evidence of COOH group derivatization. These features include an 'amide I' $\nu_{C=O}$ absorption between 1600 and 1700 cm^{-1}, with a less pronounced (mostly as a shoulder) 'amide II' δ_{NH} absorption at 1500–1575 cm^{-1}. The fact that they are not well resolved can be explained by the presence of large amounts of non-amide NH groups, whose δ_{NH} mode masks the one of 'amide I'. The plausible explanation suggested previously is that amines react not only with carboxylic groups, but also add onto epoxy functionalities, abundant in GO, via ring-opening reaction [2,3]. An 'amide III' feature might contribute into a set of bands at 1200–1400 cm^{-1}. The modes manifested themselves at lower wavenumbers can also be due to C(=O)–NH bond formation, in particular, at 625–800 cm^{-1} due to 'amide IV' and 'amide V' vibrations, as well as at 530–620 cm^{-1} due to 'amide VI' absorption [51,52]. At the same time, the band at 717–720 cm^{-1} is typical for aliphatic chains longer than $(CH_2)_4$ [53], being especially sharp in the case of GOP + ODA, which can be associated with a bigger size of hydrocarbon chains, and possibly with a higher content of ODA moieties. Correspondingly, asymmetric and symmetric ν_{CH} signals of alkyl groups in ODA and DAO at 2914–2956 and 2848 cm^{-1}, respectively, are among the most intense bands observed. Additionally, the spectrum of GOP+ODA presents amine bands ν_{NH} around 3310 cm^{-1} and $\nu_{C\text{–}N}$ at 1129–1160 cm^{-1}. Finally, the absorption features at 1433 and 1465–1467 cm^{-1} for GOP + DAO and GOP + ODA, respectively, are due to δ_{CH} vibrations.

Very similar features can be observed in the FTIR spectra of GO powder samples, both before and after amino functionalization (Fig. 4). They include a decrease down to total disappearance of carboxylic $\nu_{C=O}$ band at 1712–1716 cm $^{-1}$ and of the C—O signal at 1038 cm^{-1}, as well as the appearance of new bands in the range of 1200–1700 cm^{-1}, which are commonly associated with vibrations found in amide groups [51,52]. That is, all the above changes are consistent with the ones reported previously for amine functionalization of GO powder and GOP [2,3], where amine molecules are attached to GO sheets not only through amidation, but also through ring-opening reaction of epoxy groups. Similarly to the spectra of GOP samples [3], less specific features for amine-functionalized GO powder include sharp bands at 2848–2855 and 2914–2952 cm^{-1} corresponding to symmetric and asymmetric ν_{CH} vibrations in long aliphatic hydrocarbon chains of ODA and DAO.

The decoration of GO powder and GOP with Ag NPs does not cause dramatic changes in the general appearance of FTIR spectra discussed above. In principle, one could expect that Ag atoms/ions at NP surface might convert neutral COOH functionalities into COO^{-} ions, which would manifest themselves as a stretching COO^{-} mode at around 1600 cm^{-1}. Nevertheless, one should remember that citric acid solution used

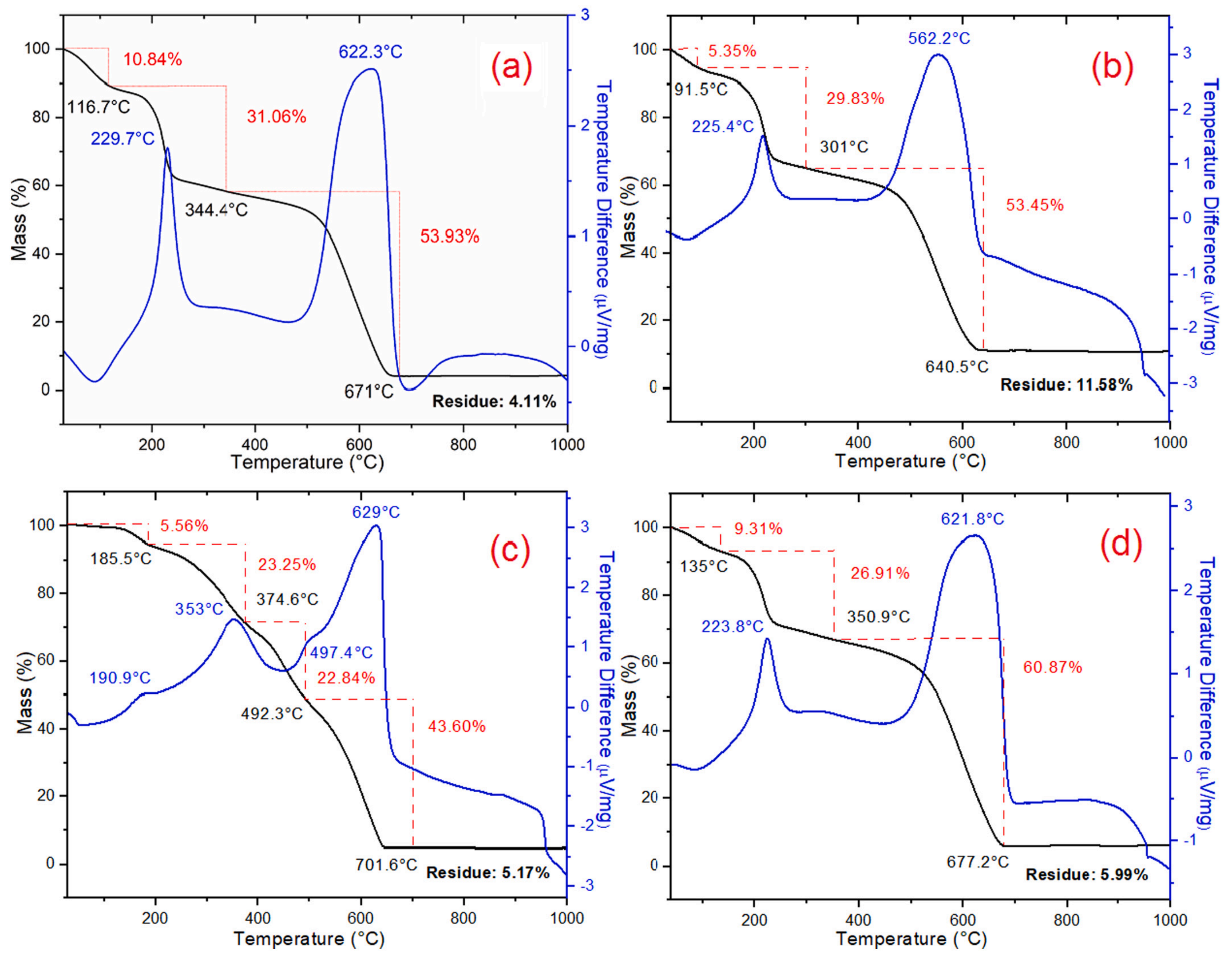

Fig. 5. TGA (black) and DTA (blue) curves for GOP samples: (a) pristine GOP, (b) GOP+Ag, (c) GOP+ODA+Ag, (d) GOP+DAO+Ag. (For interpretation of the references to colour in this figure legend, the reader is referred to the web version of this article.)

for Ag NP generation has pH ≈ 3, so that carboxylic groups remain to be protonated in GOP+Ag and GO+Ag; the same applies to unreacted COOH groups (if any) in all ODA and DAO-functionalized samples. On the other hand, in the case of GO+ODA+Ag and GO+DAO+Ag some signs of Ag deposition appear as an increase in absorption at 1194 and 1703 cm^{-1}, being much less evident for GOP+ODA+Ag and GOP+DAO+Ag samples. In addition, the appearance of a diffuse band at 3490 cm^{-1} in the spectrum of GO+DAO+Ag (Fig. 4), less clearly pronounced for GOP+DAO+Ag (Fig. 3), can be explained by coordination of Ag NPs to the nitrogen atoms in dangling NH_2 groups of 1,8-diaminooctane.

TGA–DTA measurements were used to characterize the changes in thermal behavior of GOP and GO powder due to the modification with amines and posterior decoration with Ag NPs. The TGA curve for pristine GOP (Fig. 5a) exhibits three weight loss steps, typical for graphene oxide [3]. The first weight loss (of 10.84%, until 116.7 °C) is attributed to evaporation of physisorbed water. The second one (of 31.06%, until 344.4 °C) is caused by the pyrolysis of intrinsic oxygenated, first of all COOH, groups of GO. The third step (of 53.93%, until 671.0 °C) corresponds to the graphene backbone decomposition. (The presence of 4.11% residue results from difficulties with the equipment calibration.) The DTA curve has two exothermic peaks at 229.7 and 622.3 °C matching the second and third weight loss steps in TGA. For the Ag-decorated sample, GOP+Ag (Fig. 5b), qualitatively the same weight loss pattern is observed, namely: physisorbed water evaporation (5.35%, until 91.5 °C), pyrolysis of oxygenated groups (29.83%, until 301.0 °C), and graphene network decomposition (53.45%, until 640.5 °C). The Ag content of 7.47% is obtained by subtraction of 4.11% (GOP; Fig. 5a) from the residual weight of 11.58%. The two exothermic peaks at 225.4 and 562.2 °C in DTA curve are likewise similar to those found for non-functionalized GOP, except for the second one is strongly (by 60 °C) shifted to lower temperatures. This can be explained by a catalytic effect of silver on the combustion of graphene backbone.

The thermograms obtained for amine-functionalized plus decorated with Ag NPs paper mats (Fig. 5c,d) exhibit significant differences in comparison to GOP+Ag, due to the presence of new chemical moieties. In particular, for ODA-functionalized sample the most important weight losses in TGA curve are the ones of 5.56% until 185.5 °C, of 23.25% until 374.6 °C, of 22.84% until 492.3 °C, and 43.6% until 701.6 °C. The corresponding exothermic peaks in DTA curve for GOP+ODA+Ag are found at 190.9, 353, 497.4 and 629 °C, which can be associated with the pyrolysis of initial (present in pristine GOP) oxygenated groups, of amide derivatives, of amines added onto epoxy groups, and of graphene lattice, respectively. The estimated Ag NP content is of 1.06% (a difference between 5.17% and 4.11% residue in TGA of pristine GOP). The three main weight losses recorded by TGA for GOP+DAO+Ag sample

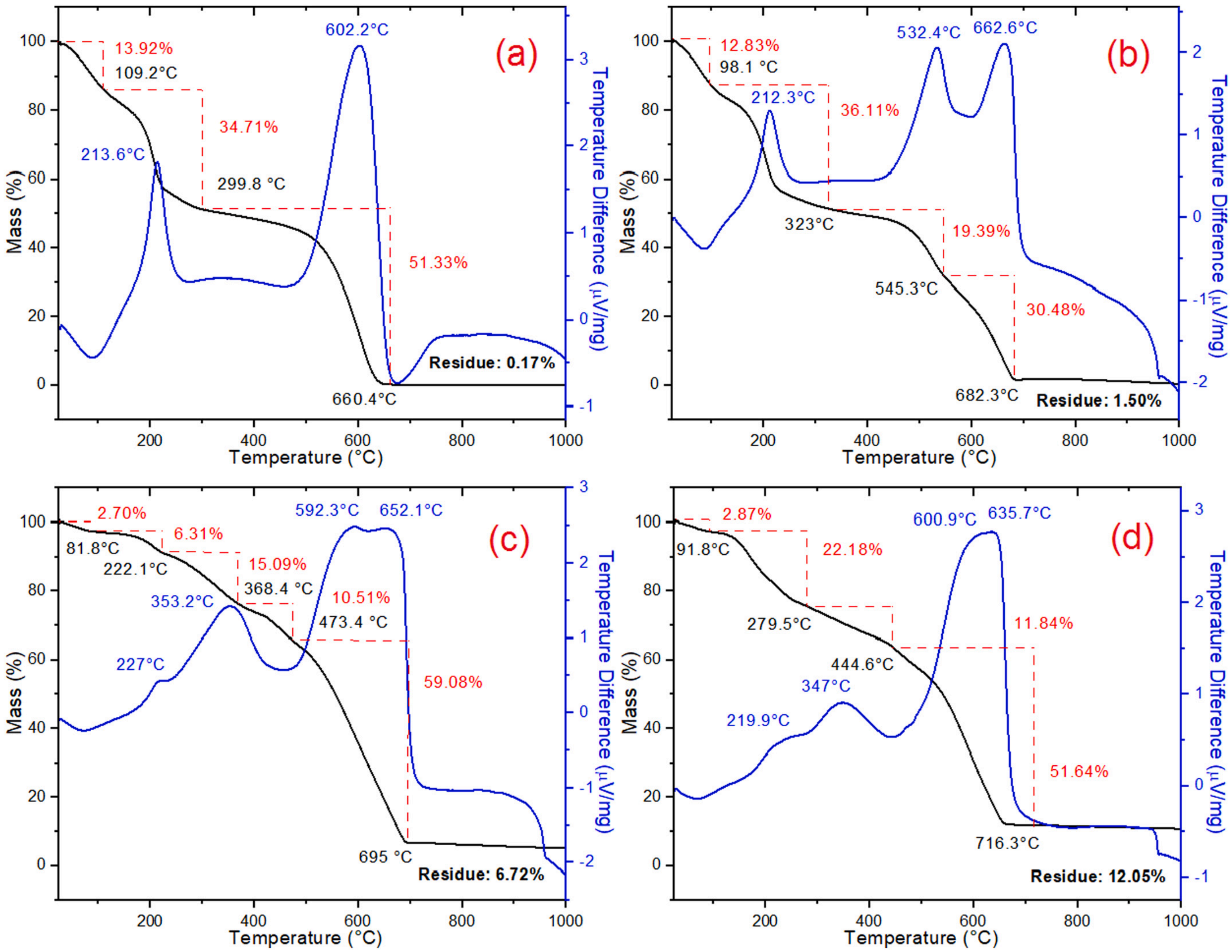

Fig. 6. TGA (black) and DTA (blue) curves for GO powder samples: (a) pristine GO, (b) GO+Ag, (c) GO+ODA+Ag, (d) GO+DAO+Ag. (For interpretation of the references to colour in this figure legend, the reader is referred to the web version of this article.)

are of 9.31% until 135 °C due to physisorbed water (DAO is hydrophilic, contrary to ODA), of 26.91% until 350.9 °C due to pyrolysis of residual (from pristine GOP) oxygenated groups along with their amino/amide derivatives, and of 60.87% until 677.2 °C, corresponding to the combustion of graphene lattice. The estimated (in the same way as for GOP+Ag and GOP+ODA+Ag) silver content is 1.88%. The peaks found in DTA are those at 223.8, at around 350.9 (low and broad) and at 621.8 °C. One should note that the final major peak due to the decomposition of graphene backbone in GOP+ODA+Ag and GOP+DAO+Ag shifted back to higher temperatures: apparently, the low Ag content of about 1–2% is insufficient to produce as pronounced catalytic effect as the one observed in the case of GOP+Ag (silver content of 7.47%).

The TGA–DTA characteristics of pristine GO powder (Fig. 6a) are generally similar to the ones obtained for pristine GOP (Fig. 5a), including three weight losses due to physisorbed water (13.92%, until 109.2 °C), pyrolysis of oxygenated functionalities (34.71%, until 299.8 °C), and graphene lattice combustion (51.30%, until 660.4 °C). The DTA curve contains two major exothermic peaks at 213.6 and 602.2 °C, matching the main weight loss steps in TGA curve. As regards GO+Ag (Fig. 6b), its characteristics turned to be notably different from those discussed above for GOP+Ag sample (Fig. 5b). The first and second steps remain essentially the same (with some variations in temperature and percentage), being related to evaporation of physisorbed water (12.83%, until 98.1 °C) and pyrolysis of oxygen-containing groups (36.11%, until 326.0 °C). However, instead of the single final weight loss due to the graphene network decomposition, two of them are clearly seen in the present case, of 19.39% until 545.3 °C and of 30.48% until 682.3 °C. This might be associated with considerably lower Ag content in GO+Ag (1.50%–0.17% = 1.33%) than in GOP+Ag (7.47%), and thus with occurrence of Ag-catalyzed and non-catalyzed combustion of graphene backbone. The three major peaks in DTA curve for GO+Ag powder are found at 212.3, 532.4 and 662.6 °C.

A less pronounced splitting of the final weight loss step can be seen in the case of GO+ODA+Ag (Fig. 6c), with two DTA maxima at 592.3 and 652.1 °C. In other regards, both TGA and DTA curves follow closely the pattern and underlying interpretation presented above for GOP+ODA+Ag (Fig. 5c). At the same time, the silver content is estimated to be much higher in the present case (6.72%–0.17% = 6.55%). A similar observation can be done for GO+DAO+Ag powder sample (Fig. 6d), where Ag fraction (12.05%–0.17% = 11.88%) is almost one order of magnitude higher than in GOP+DAO+Ag (1.88%).

When comparing the present TGA–DTA results for ODA and DAO-functionalized samples (both powders and GOP mats) decorated with Ag NPs with those reported previously for aliphatic amine-functionalized GOP [3], one can see that silver deposition lowers the final combustion temperature of graphene backbone very significantly. For example, while for GOP+ODA it was 745 °C [3], for GOP+ODA+Ag and GO+ODA+Ag it drops to 701.6 and 695 °C, respectively. For GOP

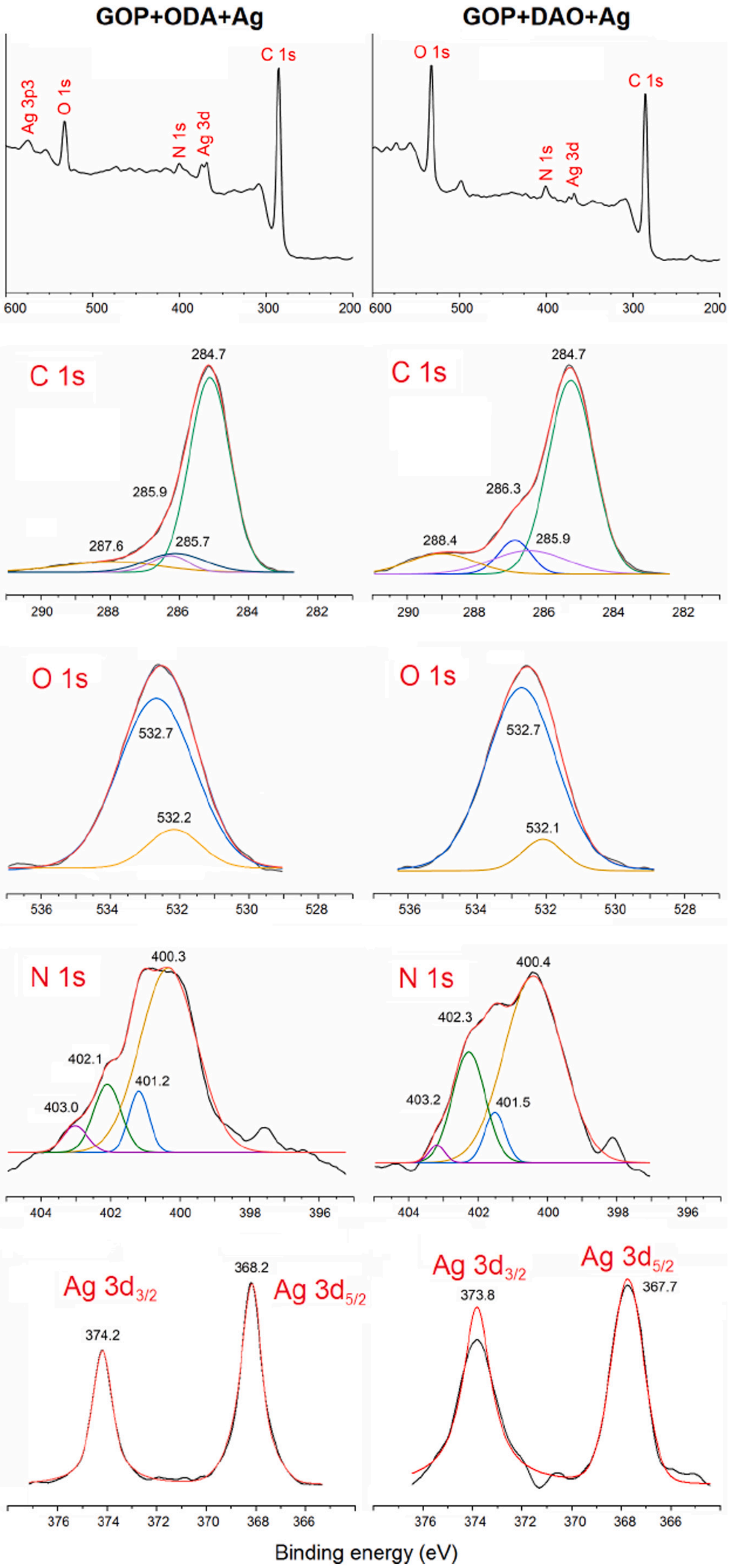

(caption on next page)

Fig. 7. XPS spectra of GOP samples amine-functionalized and decorated with AgNPs: survey spectra (top row) and deconvolution of the corresponding spectral lines (C 1s, N 1s, O 1s and Ag 3d). Raw spectra are shown in black, and sum, in red. (For interpretation of the references to colour in this figure legend, the reader is referred to the web version of this article.)

functionalized with 1,12-diaminododecane (a homologue of DAO) it was 750 °C [3], whereas for GOP+DAO+Ag and GO+DAO+Ag it is 677.2 and 716.3 °C, respectively. The second important trend has to do with whether Ag NPs were deposited onto a powder sample or onto a compact mat: the estimated silver content for GO+ODA+Ag and GO+DAO+Ag is 6.55% and 11.88%, whereas for GOP+ODA+Ag and GOP+DAO+Ag it dramatically decreases to 1.06% and 1.88%, respectively. Apparently, compacting GO powder into paper hinders the accessibility of Ag NPs to functionalizing groups within the mat. The third observation to mention is that silver content in DAO-functionalized samples is almost twice as high compared to that in ODA-derived materials. The most logical explanation is that the use of bifunctional reagents such as DAO and 1,12-diaminododecane [3] provides additional amino groups serving as coordination centers for anchoring and stabilization of Ag NPs [12,29,31].

XPS measurements provided more detailed information on the chemical state of GOP and GO powder samples functionalized with amines and decorated with Ag NPs. XPS characterization of pristine and amine-functionalized GO and GOP was presented in detail in our previous reports [2,3,42]. Therefore, we limit the discussion to Ag NP-deposited materials only. The survey spectra obtained for GOP+ODA+Ag and GOP+DAO+Ag (Fig. 7; top row) show the presence of C 1s and O 1s components typical for GOP, as well as N 1s and Ag 3d peaks. Deconvolution of C 1s peak shows the presence of several components, the one at 284.7 eV due to C—C sp^2/sp^3 bonds being predominant in all the spectra. For pristine GO and GOP, signals at 286.8 and 288.5 eV correspond to epoxy groups (C—O, C–O–C) and to carboxylic (C═O, O–C=O) moieties, respectively [2,3,54–56]. The COOH signal almost disappeared for GOP+ODA+Ag, but is still clearly visible for GOP+DAO+Ag (288.4 eV), whereas the epoxy component disappeared completely for both samples. Instead, a new signal at 285.7–285.9 eV is detected due to C—N bonds formed as a result of NH_2 addition onto epoxy groups. Both spectra exhibit a new signal at 285.9–286.3 eV due to C–O–H groups formed in the same epoxy ring-opening reaction. The component at 287.6 eV for GOP+ODA+Ag can be assigned to amide –N–C=O moieties [3,7,57–59].

As regards the analysis of O 1s spectra, we adhere to the point of view [60] that many reported assignments of the "carbon–oxygen" signatures are conflicting, for several reasons. To begin with, the O 1s photoelectron kinetic energies are lower than the ones for C 1s, the O 1s sampling depth is correspondingly smaller, and thus the O 1s signals are more surface-specific. Another reason is that a large variety of O-containing species can contribute to the O 1s peak. The last but not least is the possibility of contamination with ubiquitous atmospheric oxygen. This is why we did not attempt to carry out a fine deconvolution of the components. We can only suggest that the ones found in the spectra of GOP+ODA+Ag and GOP+DAO+Ag at 532.7 eV comprise the contribution of different groups with single C—O and O—H bonds [60,61], and at 532.1–532.2 eV, of the groups containing C=O bonds (carboxylic, amide, quinone moieties, etc.) [2,3,62].

In the case of N 1s signals, in both samples the dominating component is the one at 400.3–400.4 eV due to imine species formed as a result of NH_2 addition onto epoxy rings. The presence of the component at 403.0–403.2 eV suggests that a considerable fraction of NH species exist in protonated form: unlike the case of GO and GOP functionalized with amines in the gas phase [2,3], GOP+ODA+Ag and GOP+DAO+Ag samples passed through silver deposition step in an acidic medium. The nitrogen atoms in amide functionalities manifest themselves as a spectral signature at 401.2–401.5 eV. The origin of the fourth component found at 402.1–402.3 eV is especially interesting, and can be related to amine/imine N atom coordination to metal species [63,64].

Silver manifests itself as well-defined and symmetric Ag $3d_{3/2}$ and Ag $3d_{5/2}$ peaks at 373.8–374.2 and 367.7–368.2 eV, respectively, typical for metallic form of silver [11,63–65]. The absence of evident contributions at about 376 (Ag $3d_{3/2}$) and 370 eV (Ag $3d_{5/2}$) [66] suggests that the residual content of Ag^+ is very low (if any).

As expected, XPS spectra of the GO powder-based materials (Fig. 8), recorded for comparison, share many important features found for GOP-derived samples. In particular, deconvoluted C 1s peak includes the dominating component at 284.7 eV due to C—C sp^2/sp^3 bonds. The COOH feature was not detected for GOP+ODA+Ag, but remains clearly visible at 288.7 eV for GOP+DAO+Ag. The epoxy component, commonly observed at about 287 eV, disappeared completely for both samples, replaced by signals at 285.7–286.3 eV is detected due to new bonds formed as a result of NH_2 addition onto epoxy groups.

The O 1s spectra for GO+ODA+Ag and GO+DAO+Ag (Fig. 8) look less alike the spectra of their GOP counterparts (Fig. 7), which can be attributed to a much stronger interference of atmospheric oxygen (as well as adsorbed water) in the case of powder samples. Here, the component at 532.6–532.7 eV resulting from the existence of different groups with single C—O and O—H bonds [60,61] remains to be dominant. The lower-energy component can be due to a combination of the groups containing C=O bonds in carboxylic, amide and quinone moieties [2,3,62]. The higher-energy peak at 533.8 eV can be attributed to adsorbed water: its contribution is much higher in the case of GO+DAO+Ag, due to a higher hydrophylicity of diamine residues compared to octadecyl radicals in GO+ODA+Ag.

In the case of N 1s signals, the principal component is again the one at 400.0–400.2 eV due to imine species formed as a result of NH_2 addition onto epoxy rings. The presence of the component at 402.9 eV, which suggests that a considerable fraction of NH species exist in protonated form, is obvious for GO+ODA+Ag only. The feature at 400.8 eV in the spectrum of GO+DAO+Ag corresponds to the amide N atoms. And, finally, the component appearing at 401.9 eV in both spectra can be attributed to amine/imine N atom coordination to metal species [63,64].

The Ag 3d spectra for powder samples are very similar to each other. As in the case of GOP-derived materials, they are composed of two well-defined and symmetric Ag $3d_{3/2}$ and Ag $3d_{5/2}$ peaks at 374.2 and 368.2 eV, respectively, characteristic for metallic form of silver [11,63–65]. No evident contributions at about 376 (Ag $3d_{3/2}$) and 370 eV (Ag $3d_{5/2}$) [66], which would point to the existence of Ag^+, were detected.

General morphological changes due to the decoration of GO powder and GOP-derived materials with Ag NPs were studied by using SEM (Figs. 9 and 10). The first point of interest is the differences in mat thickness for GOP samples, determined from cross-section SEM images (Fig. 9a,d,g,j). The fact that it is about 22 μm for pristine GOP and 23 μm for GOP+Ag implies that in this particular case the amount of silver which penetrated inside the mats (between individual GO sheets) is insignificant. For their amine-functionalized counterparts, the mat thickness estimates gave 119 μm for GOP+ODA+Ag and 34 μm for GOP+DAO+Ag. In other words, while GOP+Ag and GOP+DAO+Ag samples exhibit a minor increase in the thickness, it is about five-fold for GOP+ODA+Ag compared to pristine GOP. An important contribution into this effect is due to amine functionalization: we already observed in our earlier work [3] that the pristine mat thickness of 16 μm increases to 28 μm for GOP+ODA, and also to 20 μm for GOP functionalized with 1,12-diaminododecane (a GOP+DAO analogue). Still, this 'swelling' is much weaker than the one observed for GOP+DAO+Ag (Fig. 9j) and especially for GOP+ODA+Ag (Fig. 9g), which thus can be attributed mainly to more efficient intercalation of silver into amine-functionalized GOP, even though the Ag content within the mats turned to be below

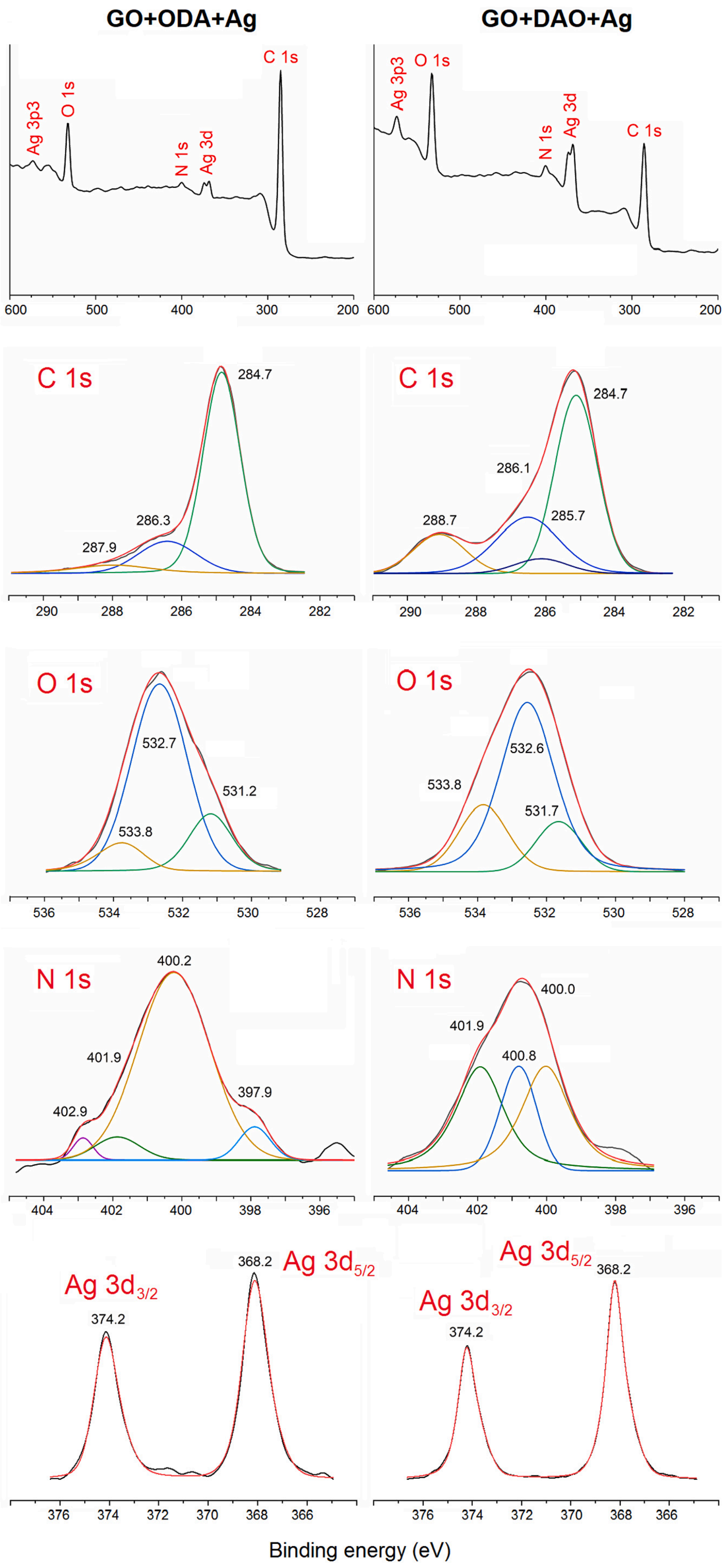

(caption on next page)

Fig. 8. XPS spectra of GO powder samples amine-functionalized and decorated with AgNPs: survey spectra (top row) and deconvolution of the corresponding spectral lines (C 1s, N 1s, O 1s and Ag 3d). Raw spectra are shown in black, and sum, in red. (For interpretation of the references to colour in this figure legend, the reader is referred to the web version of this article.)

EDS detection limit.

The SEM images grouped in the middle and right columns of Fig. 9 show the differences in surface morphologies observed at the lower and the upper (with respect to the membrane filter employed in GOP fabrication) mat sides, respectively. The lower side seems to have more compact and uniform morphology; a likely reason is that during the filtration process, well-shaped platelets first sedimented at the filter surface. Additionally, for GOP+ODA+Ag one can observe micrometer-sized (roughly 1–3 μm) white agglomerates of silver particles, which cover some surface sites rather densely (especially at the upper surface; Fig. 9i). This contrasts with GOP+DAO+Ag, where only a few such particles can be seen. Taking into account a comparable (of the order of 1%) content of elemental Ag in the two amine-functionalized samples according to TGA and XPS, as well as the limited resolution of SEM at the nanoscale, one can suggest that the size of Ag particles is typically much smaller in GOP+DAO+Ag.

Larger-sized silver particles with interesting morphology were detected in GO+DAO+Ag when imaging by SEM the powder samples

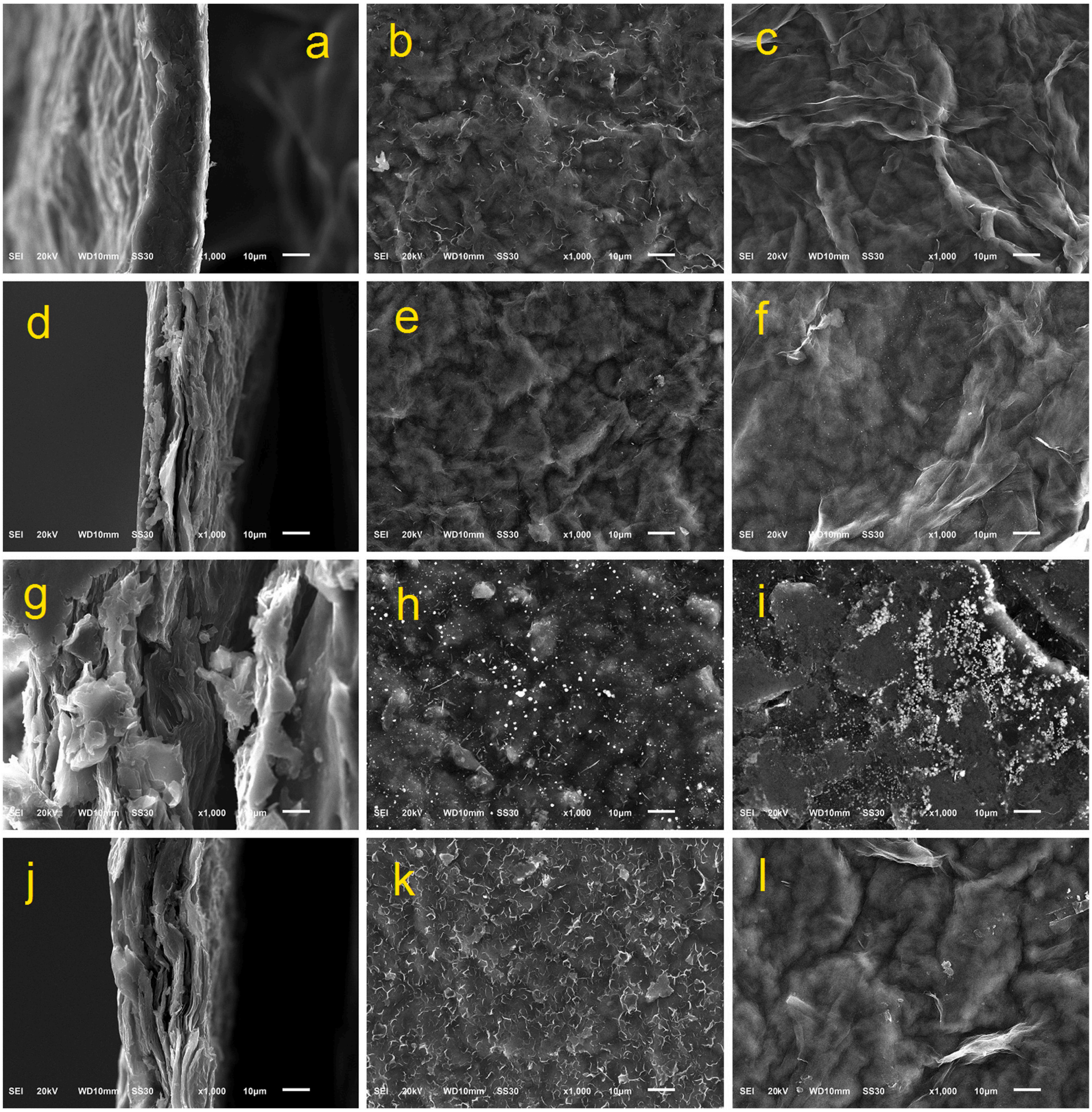

Fig. 9. Representative SEM images of pristine GOP (a–c), GOP+Ag (d–f), GOP+ODA+Ag (g–i), and GOP+DAO+Ag (j–l). Left column (a,d,g,j) shows cross-section images; middle column (b,e,h,k) corresponds to the lower mat side which was in contact with the filter membrane during GOP fabrication; right column (c,f,i,l) corresponds to the upper mat side. Scale bar, 10 μm in all images.

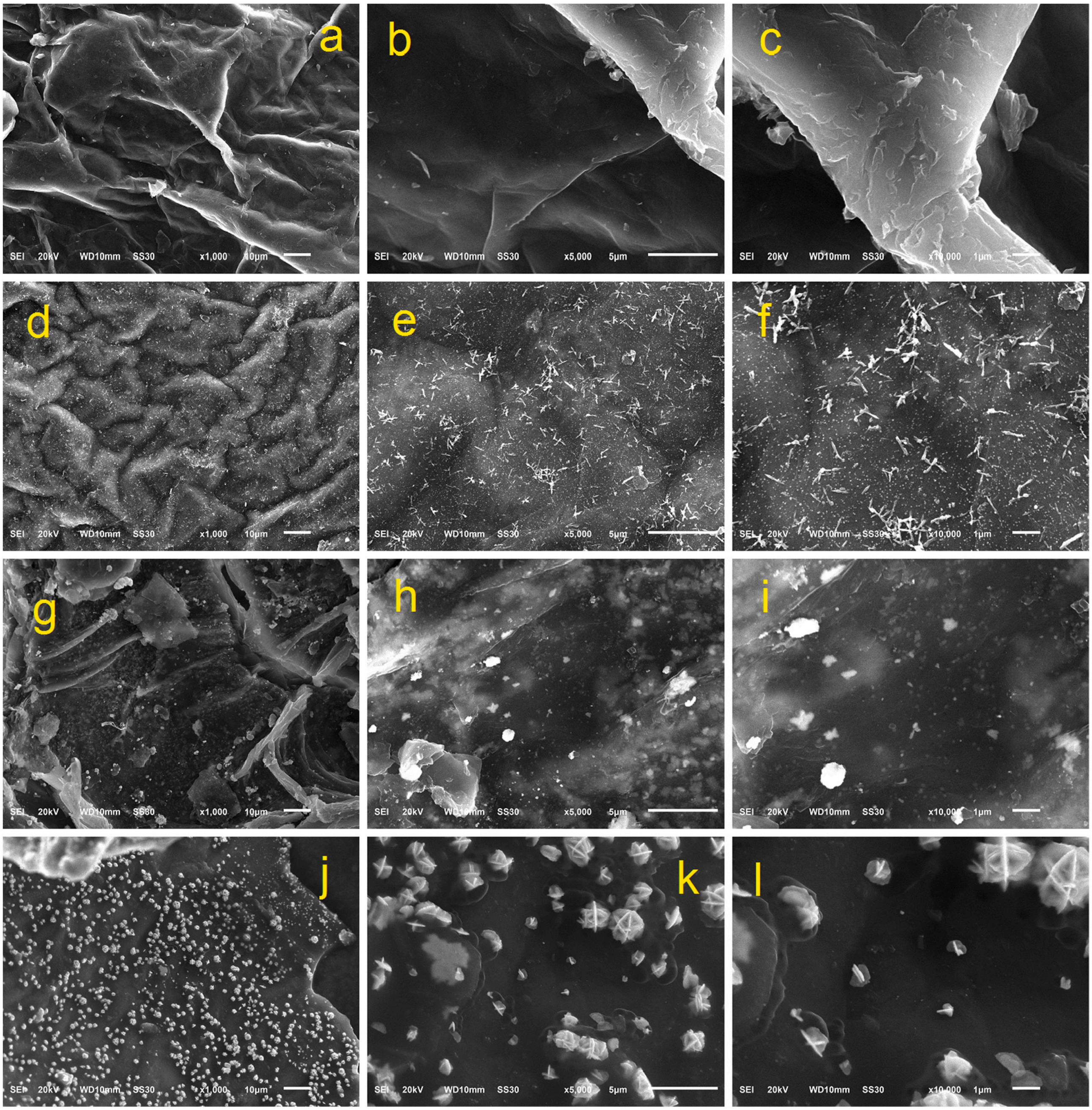

Fig. 10. Representative SEM images of pristine GO (a–c), GO+Ag (d–f), GO+ODA+Ag (g–i), GO+DAO+Ag (j–l). Scale bar: left column, 10 μm; middle column, 5 μm; right column, 1 μm.

(Fig. 10). All three Ag-decorated GO varieties look very different with respect to pristine GO powder (Fig. 10a–c), but in their own way. On GO+ODA+Ag surface (Fig. 10g–i), silver particles are irregularly shaped, notably agglomerated and broadly variable in size. In GO+DAO+Ag powder sample (Fig. 10j–l), we found remarkable flower-like particles (reminding commonly known 'desert rose' selenite in morphology), many of which being of 1–3 μm in size, covering rather uniformly some surface sites. Similar microstructures, consisting of single-crystalline plates of metallic silver, were synthesized in other studies [67,68] targeting the design of non-enzymatic H_2O_2 sensors and other bioanalytical applications, where Ag particles with high active surface area would be of special importance. The synthetic approach proposed [68] contemplates an enzyme-induced particle growth on solid substrates, and the complex morphology obtained contrasts with the auto-catalytically grown spherical particles, which maintain their overall geometrical appearance while increasing their diameter. Crystallinity of silver particles in GO+DAO+Ag can be illustrated by the results of XRD shown in Fig. 11. The pattern recorded contains several peaks which can be indexed to the (111), (200), (220), (311) and (222) crystal planes, well-known for Ag particles [67,69,70]. Possible building blocks to form desert rose-like morphologies are single-crystalline silver plates, which are intertwined to form the nanoflowers up to a size of several micrometers, with this process strongly dependent on the synthesis conditions [69,70]. An enhanced number of amine/imine centers for Ag coordination, existing in GO+DAO+Ag due to bifunctional nature of 1,8-diaminooctane used for functionalization, might be one of the factors favoring the peculiar nucleation process leading to the flower-like particles.

The formations covering GO+Ag surface (Fig. 10d–f) do not look as metal particles, be they either regularly or irregularly shaped. Instead, they remind rolled individual graphene sheets, roughly of 1 μm in length and up to 100 nm in diameter. The origin of this effect is not totally clear, but we cannot exclude the possibility that silver deposition causes strong distortion of smaller GO sheets and/or thin stacks up to their rolling. EDS measurements of Ag content at these sites yielded rampant (as for all samples) values of around 10 wt%. Taking into account that EDS analysis is very superficial and does not reflect the elemental composition inside multilayer platelets of GO, the above estimates do not contradict the averaging value of 1.33% from TGA.

Detailed information on the size and morphology of Ag NPs deposited onto GOP and GO powder was obtained by employing bright-field (Figs. 12 and 13) and dark-field (Fig. 14) TEM techniques. Both GOP+Ag and GO+Ag samples contain twin particles of round/rectangular form with different grain boundaries; this type of morphology is associated with a lack of control during the particle nucleation and growth [71,72]. Their sizes fluctuate in a range of 15–35 nm for GOP+Ag (Fig. 12c,d) and 10–30 nm for GO+Ag (Fig. 13c,d), that is, essentially in the same range. The formation of Ag NPs at non-functionalized GO surfaces is governed by the coordination of silver species to the O donor atoms of oxygenated groups, which serve as numerous and efficient sites for nanoparticle nucleation and growth, however with a clear tendency to agglomeration and/or coalescence.

In line with the results of SEM imaging (Figs. 9h,i and 10g–i), Ag NPs in GOP+ODA+Ag (Fig. 12e,f) and GO+ODA+Ag (Fig. 13e,f) were found to be generally irregularly shaped and randomly distributed. Most of them have a size of 3–15 nm, but the formation of larger agglomerates of up to ca. 200 nm can be observed as well (Fig. 13e). While similar relatively large agglomerates were found also in GOP+DAO+Ag (Fig. 12g), much more typical for the 1,8-diaminooctane-functionalized materials is the presence of small Ag NPs of around 5 nm (Figs. 12h and 13h). Here it is appropriate to mention the study by Mohan et al. [73] on morphological transformation of silver nanoparticles influenced by different factors. They showed that Ag NP agglomeration can be provoked by an oxidative environment, whereas exposure to nitrogen-rich solutions did not lead to aggregation. In the present context, one can suggest that for amine-functionalized samples, the formation of Ag NPs occurs via reduction of metal ions coordinated to N donor atoms of the covalently attached amine molecules. This results in a more homogeneous size distribution and prevents the agglomeration observed in pristine GOP and GO powder, where the interaction of Ag with oxidized functionalities provokes the formation of particles with different sizes and their coalescence.

The latter conclusions are strongly supported by the results of Z-contrast dark-field TEM imaging presented in Fig. 14, which allow for a more explicit comparison of the sizes and morphology of Ag NPs found in GO+Ag, GO+ODA+Ag and GO+DAO+Ag, nearly at the nucleation level. The image in Fig. 14c clearly shows that GO-DAO+Ag sample surface has a very homogeneous coverage with small-size Ag NPs of about 3–5 nm, contrary to GO+ODA+Ag and especially GO+Ag.

The fact that direct functionalization of prefabricated GOP is the only approach allowing for systematic tuning of its physical (including electronic) characteristics [3], motivated us to monitor the changes in conductivity/resistivity due to amine functionalization followed by Ag deposition. The results are summarized in Table 1. When analyzing the effect of amine functionalization, one can see that, compared to pristine GOP, is increases by one order of magnitude for GOP+ODA, and by two orders of magnitude for GOP + DAO: thus, the general increase in conductivity (and, correspondingly, decrease in resistivity) is consistent with our earlier results [3]. The effect of silver decoration turned to be insignificant, compared to the above. In particular, for GOP+Ag vs. pristine GOP and GOP+DAO+Ag vs. GOP+DAO, the conductivity/resistivity remains of the same order of magnitude. Only for GOP+ODA+Ag compared to GOP+ODA the conductivity increases by one order of magnitude, and correspondingly resistivity decreases to a similar degree. These results can be explained in terms of content and distribution of Ag particles in the following way. Despite of the highest silver content in GOP+Ag (7.47% according to TGA), Ag NPs deposited onto pristine GO surfaces (TEM morphology in Figs. 12c,d and 13c,d) are relative large without appreciable electric contact between them. An additional factor might be that groups of silver particles are found confined within the rolls observed by SEM (Fig. 10d–f), which contributes to their mutual isolation and consequent loss of electric contact. The differences in elemental Ag content for GOP+ODA+Ag and GOP+DAO+Ag are relatively insignificant, of 1.06% and 1.88%, respectively. However, the former contains extended surface sites densely covered with Ag particles and their agglomerates (SEM in Fig. 9i), which enhance electric contact, whereas in the latter AgNPs are small and more uniformly dispersed throughout GOP+DAO+Ag surface (as also in GO+DAO+Ag; see Figs. 13g,h and 14c).

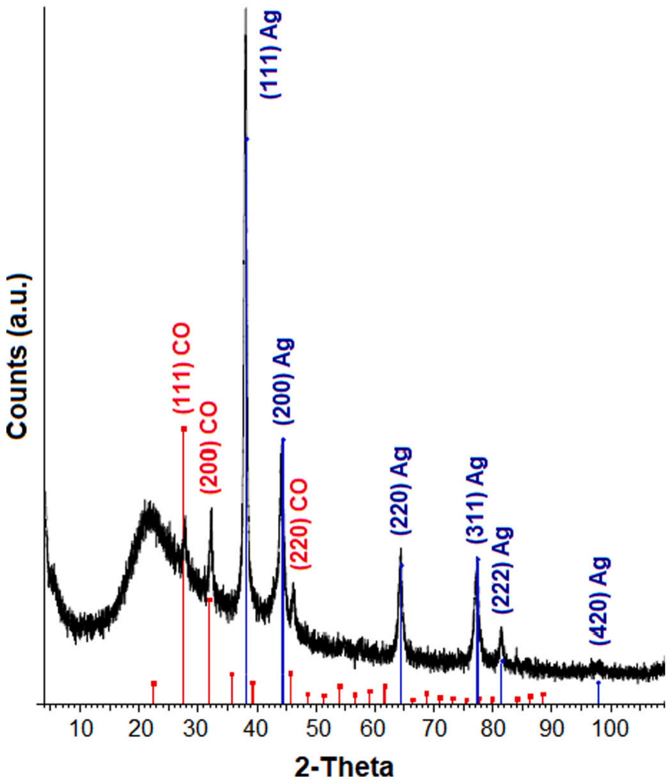

Fig. 11. XRD diffractogram for GO+DAO+Ag sample.

3.2. *Theoretical modeling*

Some explanation of the experimental results obtained was attempted by employing theoretical DFT calculations. Extended dimensions of both realistic individual GO sheets and Ag NPs are computationally prohibitive, so that the models to be handled had to be considerably smaller. One of the most appropriate choices to simulate an Ag NP proposed by Ma's group [74–76] (and also used by Lim et al. [77]) is a cluster composed of thirteen Ag atoms shown in Fig. 15. In all the above works [74–77] the computational methodology of choice was the same PBE general gradient approximation functional as the one widely employed for DFT studies of noncovalent, covalent and coordination bonding of a broad variety of chemical species to graphene and GO models [38–45]. According to Mulliken analysis for the optimized Ag_{13} geometry, the cluster contains different external atoms in terms of the sign and magnitude of charge: from negative of −0.075 to positive of 0.031 *e*. This implies the possibility of electrostatic attraction of Ag_{13} to both positively and negatively-charged atoms or functional groups of pristine and functionalized GO.

On the other hand, the models to be selected for pristine and amine-functionalized GO had to match the size of Ag_{13} cluster: the ones based

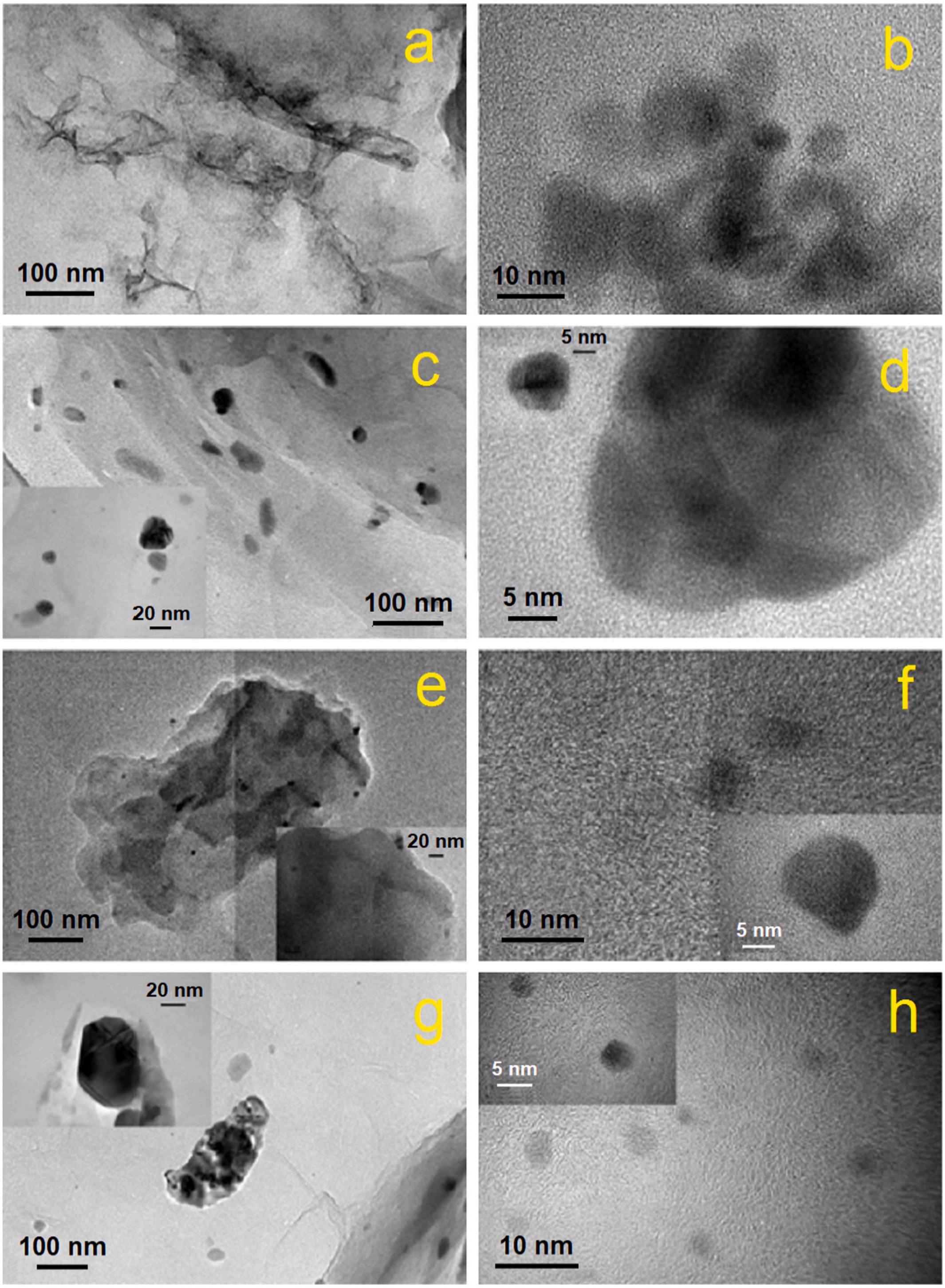

Fig. 12. TEM and HRTEM images of pristine GOP (a,b), GOP+Ag (c,d), GOP+ODA+Ag (e,f) and GOP+DAO+Ag (g,h).

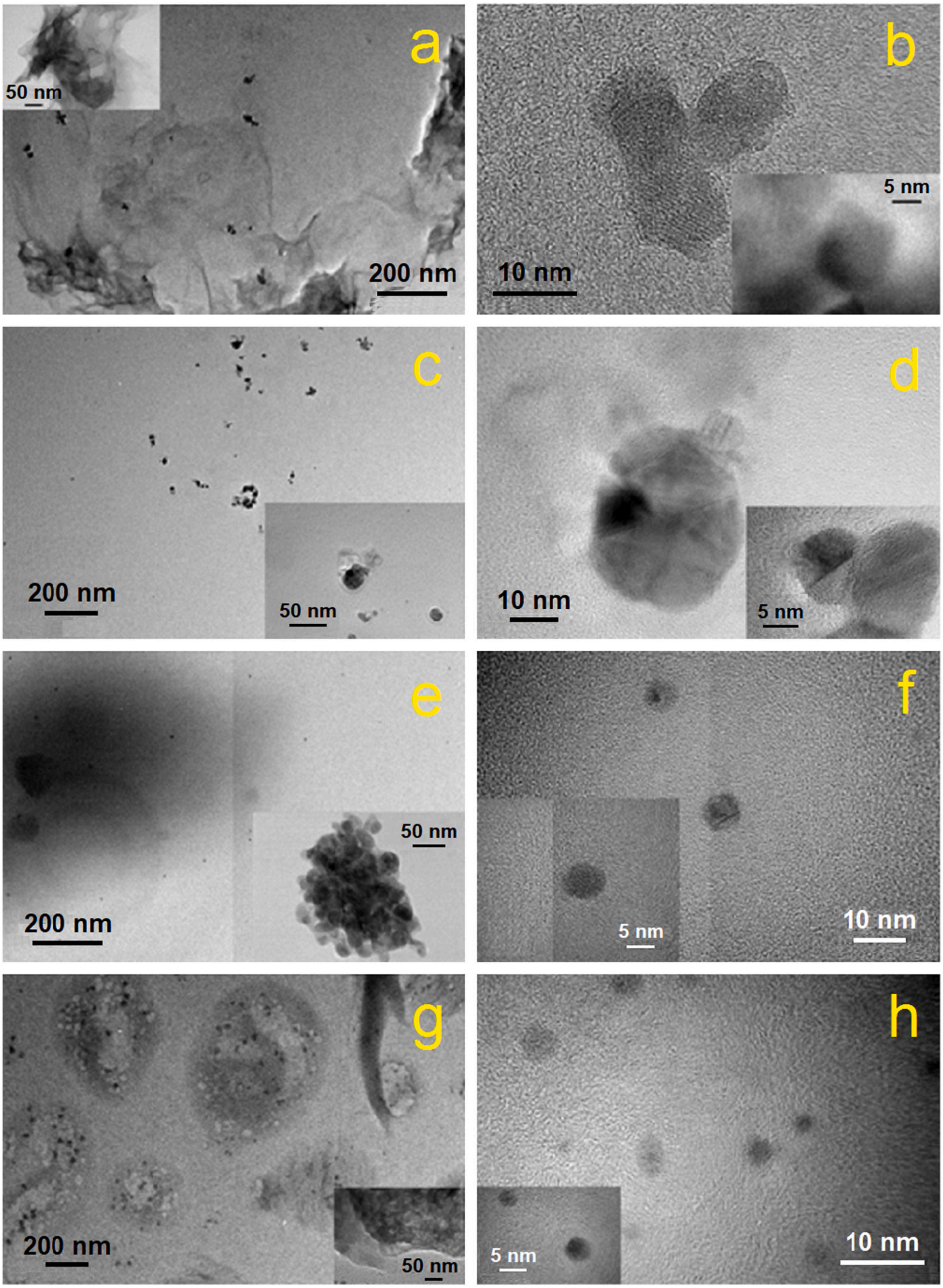

Fig. 13. TEM and HRTEM images of pristine GO (a,b), GO+Ag (c,d), GO+ODA+Ag (e,f) and GO+DAO+Ag (g,h).

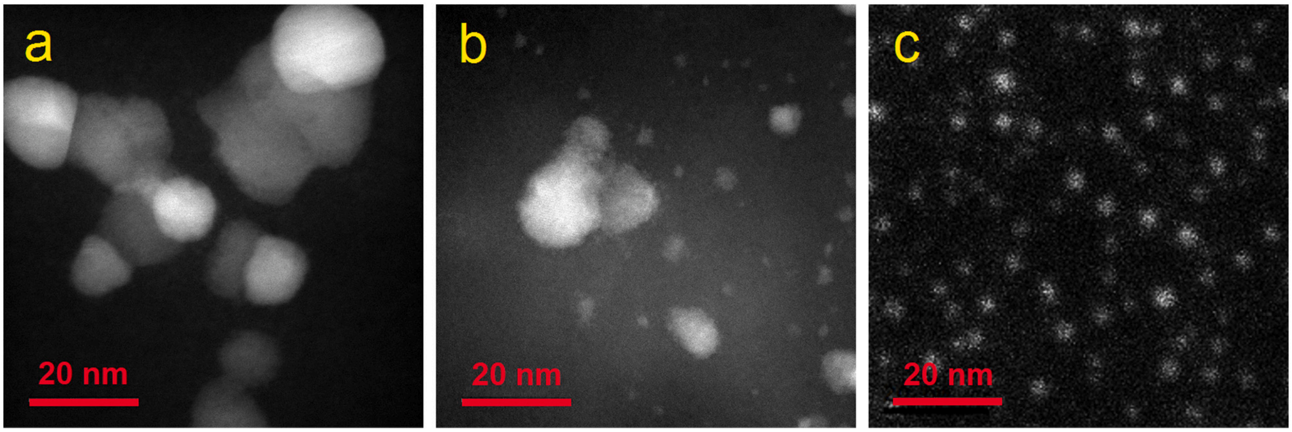

Fig. 14. Z-Contrast dark-field TEM images for: (a) GO+Ag, (b) GO+ODA+Ag and (c) GO+DAO+Ag.

Table 1
Conductivity and resistivity results for pristine and amine-functionalized GOP samples with and without Ag NPs.

Sample	Conductivity (S/cm)	Resistivity (Ω·cm)
GOP	$(1.05 \pm 0.06) \times 10^{-5}$	$(0.96 \pm 0.05) \times 10^{5}$
GOP+Ag	$(0.73 \pm 0.07) \times 10^{-5}$	$(1.38 \pm 0.13) \times 10^{5}$
GOP+ODA	$(2.04 \pm 0.12) \times 10^{-4}$	$(4.93 \pm 0.28) \times 10^{3}$
GOP+ODA+Ag	$(0.79 \pm 0.04) \times 10^{-3}$	$(1.27 \pm 0.07) \times 10^{3}$
GOP+DAO	$(2.21 \pm 0.09) \times 10^{-3}$	$(4.54 \pm 0.18) \times 10^{2}$
GOP+DAO+Ag	$(1.54 \pm 0.19) \times 10^{-3}$	$(6.58 \pm 0.89) \times 10^{2}$

on ten fused aromatic-ring system described previously [42,43] satisfy this criterion. Since due to the size limitation it is unfeasible to contemplate the whole variety of possible oxygenated functionalities existing in realistic GO, we limited them to six carboxylic and eight aromatic ketone groups, as previously described in Ref. 42 and illustrated in Fig. 16 for GO model. To simulate GO+ODA and GO+DAO species covalently functionalized with amines, all four COOH groups of GO model were converted into the corresponding amide derivatives (Fig. 16). Furthermore, in the case of GO+DAO we had to take into account that the Ag deposition takes place under acidic conditions: accordingly, all four terminal NH_2 groups, which are not involved into covalent bonding through the formation of amide derivatives, were protonated (GO+DAO-4H$^+$ model).

The numerical results of DFT calculations are summarized in Table 2. Fig. 16 schematically represents the complexation of pristine GO, GO+ODA and GO+DAO-4H$^+$ models with Ag_{13} nanocluster. One can make several important observations in terms of formation energies and geometries of the complexes. First, the strongest bonding of silver was found on pristine GO model, with the formation energy of −176.2 kcal/mol. Here, Ag_{13} is strongly attracted not only to one carboxylic groups (whose proton becomes substituted), but also to two carbonyl O atoms and one C atom of the graphene backbone; the short bonds formed can be qualified as covalent ones. The above interactions result in strong bending distortion of GO model, along with some flattening of Ag_{13} nanocluster. It is appropriate to recall the SEM images (Fig. 10d–f) revealing the effect of rolling GO sheets and/or stacks in GO+Ag sample: the above simulation results could serve as a plausible explanation of its origin.

In terms of bonding strength, GO+Ag is followed by GO+ODA+Ag_{13} (−111.3 kcal/mol) and GO+DAO-4H$^+$+Ag_{13} (−71.6 kcal/mol) complexes. Correspondingly, the pattern of interaction appears to be different for ODA and DAO moieties. In Fig. 16 one can see that Ag_{13} cluster forms as many as eight contacts (pink dashed lines) shorter than 2.8 Å with terminal alkyl groups of three octadecyl radicals of GO+ODA+Ag_{13}, whereas only one such close approach forms and with only one protonated 8-amino group of GO+DAO-4H$^+$+Ag_{13}, which explains the weaker bonding (that is, less negative formation energy).

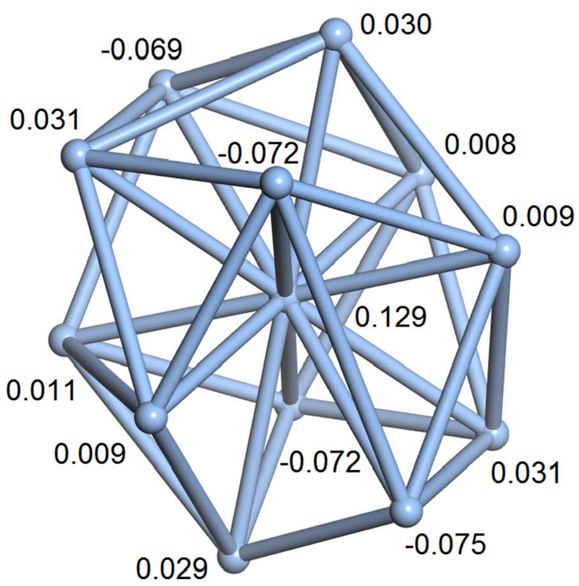

Fig. 15. Optimized geometry of the Ag_{13} cluster used to simulate Ag NPs, showing atomic charges obtained by Mulliken analysis.

The differences in electronic structure of the three complexes with Ag_{13} cluster were analyzed in terms of energy (Table 2) and distribution (Fig. 17) of frontier orbitals HOMO and LUMO. The HOMO-LUMO gap energies calculated for individual components Ag_{13}, GO, GO+ODA and GO+DAO-4H$^+$ are 0.063, 1.107, 0.860 and 0.866 eV, respectively (Table 2). Since silver nanocluster has the lowest gap energy of all, it is logical to expect that the gap values of GO, GO+ODA and GO+DAO-4H$^+$ will decrease upon complexation with Ag_{13}. Indeed, they drop by roughly one order of magnitude in all cases: to 0.103, 0.057 and 0.095 eV for GO+Ag_{13}, GO+ODA+Ag_{13} and GO+DAO-4H$^+$+Ag_{13}, respectively. While these changes are relatively uniform for all the complexes, the same cannot be said about frontier orbital localization (Fig. 17). The very strong (in terms of binding energy and formation of new bonds) interaction in the case of GO+Ag_{13} results in the localization of both HOMO and LUMO on carbon nanocluster, with only an insignificant fraction of LUMO found on Ag_{13}. Here one should remind that the most common HOMO-LUMO distribution for the complexes of carbon nanoclusters with organic and metal-containing coordination compounds is when LUMO is localized on carbon nanocluster and HOMO, on the second interacting component (see, for example [35,41,79,80] and

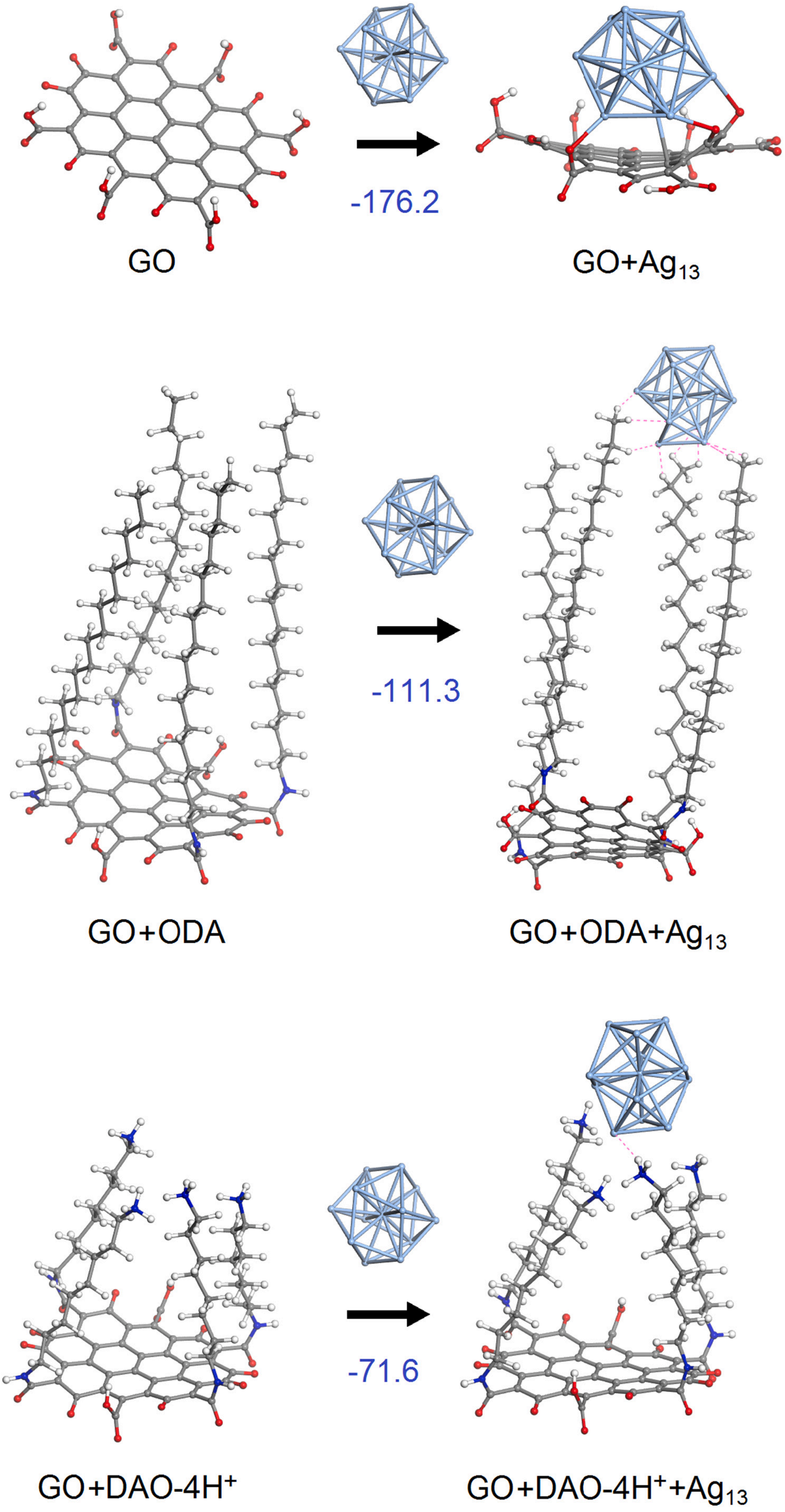

(caption on next page)

Fig. 16. Optimized geometries of GO, GO+ODA and GO+DAO-4H$^+$ models (left) and of the corresponding complexes with Ag_{13} nanocluster (right). The values shown in blue are the formation energies (in kcal/mol) for GO+Ag_{13}, GO+ODA+Ag_{13} and GO+DAO-4H$^+$+Ag_{13} complexes. The pink dashed lines show close contacts shorter than 2.8 Å. (For interpretation of the references to colour in this figure legend, the reader is referred to the web version of this article.)

Table 2

Total energies (*E*, in Ha), HOMO, LUMO and HOMO-LUMO gap energies (in eV) for separated Ag_{13} cluster, pristine and amine-functionalized GO models and their corresponding complexes with Ag_{13}, as well as formation energies (ΔE, in kcal/mol) for the complexes with Ag_{13}, as calculated by using PBE GGA functional with Grimme's dispersion correction in conjunction with DNP basis set.

Structure	*E* (Ha)	ΔE (kcal/mol)	E_{HOMO} (eV)	E_{LUMO} (eV)	HOMO-LUMO gap (eV)
Ag_{13}	−67,595.2584005		−3.415	−3.352	0.063
GO	−2954.3392083		−6.925	−5.818	1.107
GO+Ag_{13}	−70,549.8783335	−176.2	−4.868	−4.765	0.103
GO+ODA	−5702.6813267		−6.482	−5.622	0.860
GO+ODA + Ag_{13}	−73,298.1170641	−111.3	−4.220	−4.163	0.057
GO+DAO-4H$^+$	−4354.7740818		−6.599	−5.733	0.866
GO+DAO-4H$^+$+Ag_{13}[a]	−71,950.1465917	−71.6	−4.939	−4.844	0.095

[a] This is the only set of calculations which were impossible to complete with Fermi occupancy, but instead at thermal smearing of 0.0001 Ha. Nevertheless, we showed for very different model systems that cluster DFT calculations using the latter value yield the same results (geometries, total energies, spin and frontier orbital distribution, etc.) as those performed with Fermi occupancy [50,78].

references therein). In the present study, this type of HOMO-LUMO distribution can be observed only for GO+DAO-4H$^+$+Ag_{13}, whereas for GO+ODA+Ag_{13} the orbital localization is inverted. The fact that the two of them in GO+Ag_{13} are found on carbon nanocluster can be interpreted as the loss of reactivity of silver component in both electrophilic and nucleophilic processes, which in practice might have important undesirable consequences for catalytic, electrocatalytic and biomedical applications of Ag NPs deposited onto GO-based materials.

4. Conclusions

Both GOP and GO powder can be successfully functionalized with aliphatic amines and serve as supports for the decoration with Ag particles. At the same time, differences were found for the paper and powder-based materials. An important trend can be seen in the silver content estimated from TGA curves, which is 6.55% and 11.88% for GO+ODA+Ag and GO+DAO+Ag, whereas for GOP+ODA+Ag and GOP+DAO+Ag it dramatically decreases to 1.06% and 1.88%, respectively. Apparently, compacting GO powder into paper hinders the accessibility of Ag species to functionalizing groups within the mat. From the above values it follows also that silver content in DAO-functionalized samples is almost twice as high compared to that in ODA-derived materials. A logical explanation is that the use of bifunctional reagents such as DAO provides additional amino groups serving as coordination centers for anchoring and stabilization of Ag NPs.

The most relevant information on the size and morphology of Ag NPs was obtained from bright-field and dark-field TEM imaging. Both GOP+Ag and GO+Ag samples contain twin particles of round/rectangular form with different grain boundaries; this type of morphology is associated with a lack of control during the particle nucleation and growth. Their sizes vary in a range of 15–35 nm for GOP+Ag and 10–30 nm for GO+Ag. Ag NPs in GOP+ODA+Ag and GO+ODA+Ag are generally irregularly shaped and randomly distributed. Most of them have a size of 3–15 nm, but the formation of larger agglomerates of up to ca. 200 nm were observed as well. While similar relatively large agglomerates were found also in GOP+DAO+Ag, much more typical for the 1,8-diaminooctane-functionalized materials is the presence of small Ag NPs of around 5 nm. One can suggest that for amine-functionalized samples, the formation of Ag NPs occurs via reduction of metal ions coordinated to N donor atoms of the covalently attached amine molecules. This results in a more homogeneous size distribution and prevents the agglomeration observed in pristine GOP and GO powder, where the interaction of Ag with oxidized functionalities provokes the formation of particles with different sizes and their coalescence.

According to the results of DFT calculations, the binding of Ag NPs (represented by Ag_{13} cluster model) is the strongest on pristine GO, followed by ODA and finally DAO-functionalized material. This correlates with the size and distribution of Ag nanoparticles observed experimentally by TEM. In addition, the strong interaction of Ag_{13} cluster with pristine GO model causing distortion of the graphene backbone might serve as an explanation of the rolling effect detected by SEM for GO+Ag hybrid.

The results obtained expand the spectrum of possible uses of eco-friendly solvent-free functionalization techniques to the fabrication of silver-decorated carbon nanomaterials, where the size and uniform distribution of Ag NPs is an important prerequisite for successful electrochemical, catalytic and biomedical applications.

CRediT authorship contribution statement

Dinorah I. Rodríguez-Otamendi: Conceptualization, Methodology, Validation, Investigation, Visualization, Writing - original draft. **Victor Meza-Laguna:** Investigation, Validation, Visualization. **Dwight Acosta:** Investigation, Validation, Visualization. **Edgar Álvarez-Zauco:** Investigation, Validation, Visualization. **Lazaro Huerta:** Investigation, Validation, Visualization. **Vladimir A. Basiuk:** Investigation, Methodology, Validation, Visualization, Writing - review & editing. **Elena V. Basiuk:** Conceptualization, Methodology, Validation, Supervision, Project administration, Funding acquisition, Writing - review & editing.

Declaration of competing interest

The authors declare that they have no known competing financial interests or personal relationships that could have appeared to influence the work reported in this paper.

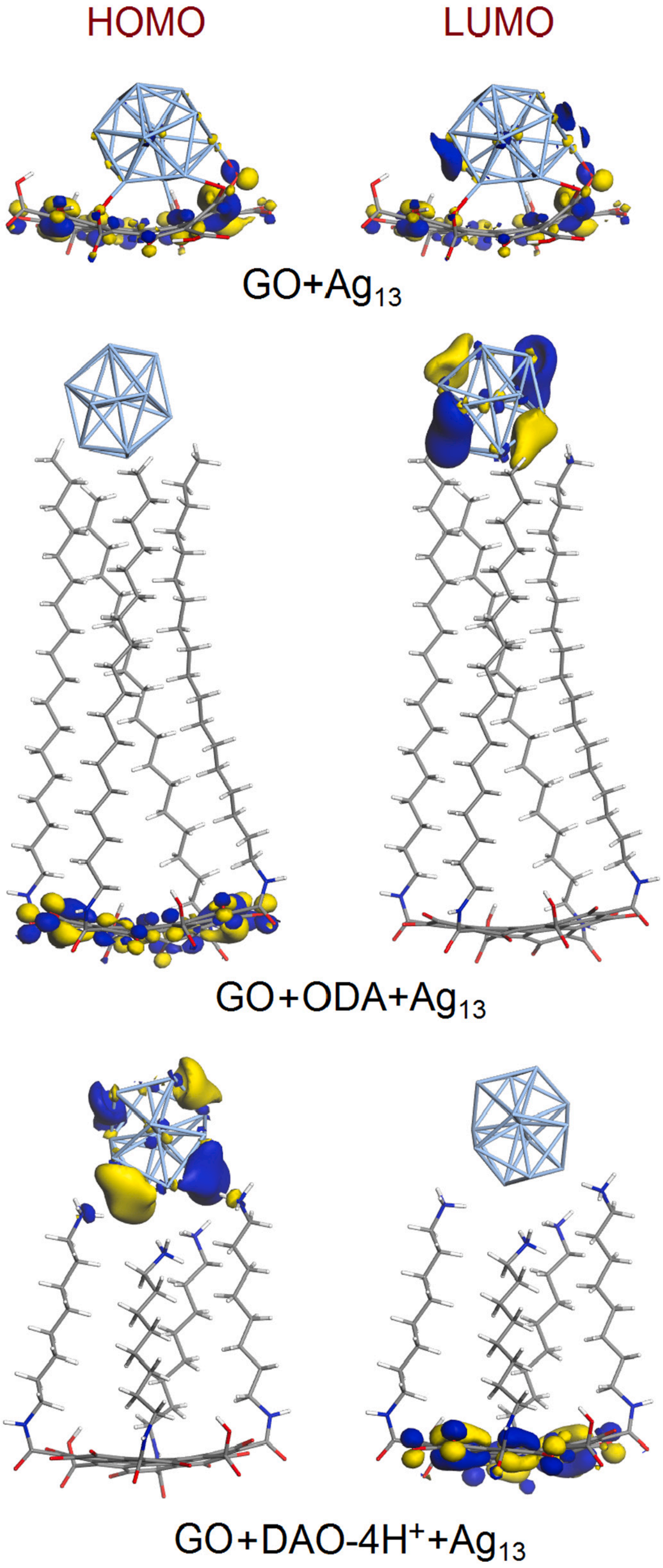

Fig. 17. HOMO and LUMO plots (isosurfaces at 0.03 a.u.) for GO+Ag_{13}, GO+ODA+Ag_{13} and GO+DAO-$4H^+$+Ag_{13} complexes.

Acknowledgements

Financial support from the National Autonomous University of Mexico (UNAM; grant DGAPA-IN101118) is greatly appreciated. D. I. R.-O. is indebted to the Postgraduate Program in Chemical Sciences of UNAM and the National Council of Science and Technology of Mexico (CONACYT) for a PhD scholarship. We are thankful to Dr. José Reyes-Gasga, as well as Drs. Samuel Tehuacanero-Núñez, Samuel Tehuacanero-Cuapa and Josué Esau Romero-Ibarra for their assistance in TEM studies. We are also grateful to Ing. Antonio Morales-Espino for assistance in XRD characterization.

References

[1] A.M. Dimiev, S. Eigler (Eds.), Graphene Oxide: Fundamentals and Applications, Wiley, Chichester, 2017.
[2] N. Alzate-Carvajal, E.V. Basiuk, V. Meza-Laguna, I. Puente-Lee, M.H. Farias, N. Bogdanchikova, V.A. Basiuk, Solvent-free one-step covalent functionalization of graphene oxide and nanodiamond with amines, RSC Adv. 6 (2016) 113596–113610.
[3] N. Alzate-Carvajal, D.A. Acevedo-Guzmán, V. Meza-Laguna, M.H. Farías, L. A. Pérez-Rey, E. Abarca-Morales, V.A. García-Ramírez, V.A. Basiuk, E.V. Basiuk, One-step nondestructive functionalization of graphene oxide paper with amines, RSC Adv. 8 (2018) 15253–15265.
[4] K.P. Loh, Q. Bao, G. Eda, M. Chhowalla, Graphene oxide as a chemically tunable platform for optical applications, Nat. Chem. 2 (2010) 1015–1024.
[5] S. Kumari, P. Sharma, S. Yadav, J. Kumar, A. Vij, P. Rawat, S. Kumar, C. Sinha, J. Bhattacharya, C. Mohan Srivastava, S. Majumder, A novel synthesis of the graphene oxide-silver (GO-Ag) nanocomposite for unique physiochemical applications, ACS Omega 5 (2020) 5041–5047.
[6] C. Vallés, J.D. Nuñez, A.M. Benito, W.K. Maser, Flexible conductive graphene paper obtained by direct and gentle annealing of graphene oxide paper, Carbon 50 (2012) 835–844.
[7] Y. Zhang, T.-S. Chung, Graphene oxide membranes for nanofiltration, Curr. Opin. Chem. Eng. 16 (2017) 9–15.
[8] D.A. Dikin, S. Stankovich, E.J. Zimney, R.D. Piner, G.H.B. Dommett, G. Evmenenko, S.T. Nguyen, R.S. Ruoff, Preparation and characterization of graphene oxide paper, Nature 448 (2007) 457–460.
[9] H. Chen, M.B. Müller, K.J. Gilmore, G.G. Wallace, D. Li, Mechanically strong, electrically conductive, and biocompatible graphene paper, Adv. Mater. 20 (2008) 3557–3561.
[10] W. Huang, Graphene oxide papers, in Nanopapers: From Nanochemistry and Nanomanufacturing to Advanced Applications, ed. W. Huang, Elsevier, Amsterdam, 1st ed., 2017, Ch. 1, pp. 1–26.
[11] M. Cobos, I. De-La-Pinta, G. Quindós, M. J. Fernández and M. D. Fernández, Graphene oxide–silver nanoparticle nanohybrids: Synthesis, characterization, and antimicrobial properties, Nanomaterials 10 (2020) 376(1−22).
[12] Y. Cheng, H. Li, C. Fang, L. Ai, J. Chen, J. Su, Q. Zhang, Q. Fu, Facile synthesis of reduced graphene oxide/silver nanoparticles composites and their application for detecting heavy metal ions, J. Alloys Compd. 787 (2019) 683–693.
[13] M. Ayán-Varela, M.J. Fernández-Merino, J.I. Paredes, S. Villar-Rodil, C. Fernández-Sánchez, L. Guardia, A. Martínez-Alonso, J.M.D. Tascón, Highly efficient silver-assisted reduction of graphene oxide dispersions at room temperature: mechanism, and catalytic and electrochemical performance of the resulting hybrids, J. Mater. Chem. A 2 (2014) 7295–7305.
[14] J. Mohammadnejad, F. Yazdian, M. Omidi, A.D. Rostami, B. Rasekh, A. Fathinia, Graphene oxide/silver nanohybrid: optimization, antibacterial activity and its impregnation on bacterial cellulose as a potential wound dressing based on GO-Ag nanocomposite-coated BC, Eng. Life Sci. 18 (2018) 298–307.
[15] S. Navalon, A. Dhakshinamoorthy, M. Alvaro, H. Garcia, Metal nanoparticles supported on two-dimensional graphenes as heterogeneous catalysts, Coordin. Chem. Rev. 312 (2016) 99–148.
[16] H. Golzar, F. Yazdian, M. Hashemi, M. Omidi, D. Mohammadrezaei, H. Rashedi, M. Farahani, N. Ghasemi, J.S. Shayeh, L. Tayebi, Optimizing the hybrid nanostructure of functionalized reduced graphene oxide/silver for highly efficient cancer nanotherapy, New J. Chem. 42 (2018) 13157–13168.
[17] N. Cai, J. Fu, H. Zeng, X.G. Luo, C. Han, F.Q. Yu, Reduced graphene oxide-silver nanoparticles/nitrogen-doped carbon nanofiber composites with mesomicroporous structure for high-performance symmetric supercapacitor application, J. Alloys Compd. 742 (2018) 769–779.
[18] J. Li, D. Kuang, Y. Feng, F. Zhang, Z. Xu, M. Liu, D. Wang, Green synthesis of silver nanoparticles–graphene oxide nanocomposite and its application in electrochemical sensing of tryptophan, Biosens. Bioelectron. 42 (2013) 198–206.

[19] F. Zeng, D. Xu, C. Zhan, C. Liang, W. Zhao, J. Zhang, H. Feng, X. Ma, Surfactant-free synthesis of graphene oxide coated silver nanoparticles for SERS biosensing and intracellular drug delivery, ACS Appl. Nano Mater. 1 (2018) 2748–2753.

[20] J. Chen, P. Xiao, J.C. Gu, Y.J. Huang, J.W. Zhang, W.Q. Wang, T. Chen, Au nanoparticle-loaded PDMAEMA brush grafted graphene oxide hybrid systems for thermally smart catalysis, RSC Adv. 4 (2014) 44480–44485.

[21] C.J. Shuai, W. Guo, P. Wu, W.J. Yang, S. Hu, Y. Xia, P. Feng, A graphene oxide-Ag co-dispersing nanosystem: dual synergistic effects on antibacterial activities and mechanical properties of polymer scaffolds, Chem. Eng. J. 347 (2018) 322–333.

[22] C. Liu, J. Shen, C.Z. Liao, K.W.K. Yeung, S.C. Tjong, Novel electrospun polyvinylidene fluoride-graphene oxide-silver nanocomposite membranes with protein and bacterial antifouling characteristics, Express Polym Lett 12 (2018) 365–382.

[23] Z. Zhu, M. Su, L. Ma, L. Ma, D. Liu, Z. Wang, Preparation of graphene oxide–silver nanoparticle nanohybrids with highly antibacterial capability, Talanta 117 (2013) 449–455.

[24] Y. Jiang, D. Carboni, L. Malfatti, P. Innocenzi, Graphene oxide-silver nanoparticles in molecularly-imprinted hybrid films enabling SERS selective sensing, Materials 11 (2018) 1674(1–17).

[25] J. Li, Y. Sun, J.L. Wang, J.H. Tian, X.Q. Zhang, H. Yang, B.P. Lin, Synthesis, structure and electrochemical properties of novel ternary composite reduced graphene oxide/Ag nanoparticles/poly(p-phenylenediamine), J. Alloys Compd. 749 (2018) 783–793.

[26] T. T. T. Vi and S. J. Lue, Preparation of silver nanoparticles loaded graphene oxide nanosheets for antibacterial activity, IOP Conf. Ser.: Mater. Sci. Eng. 162 (2016) 012033(1–5).

[27] T. T. T. Vi, S. R. Kumar, B. Rout, C.-H. Liu, C.-B. Wong, C.-W. Chang, C.-H. Chen, D. W. Chen and S. J. Lue, The preparation of graphene oxide-silver nanocomposites: The effect of silver loads on gram-positive and gram-negative antibacterial activities, Nanomaterials 8 (2018) 163(1–15).

[28] H. Yun, J.D. Kim, H.C. Choi, C.W. Lee, Antibacterial activity of CNT-Ag and GO-Ag nanocomposites against gram-negative and gram-positive bacteria, Bull. Kor. Chem. Soc. 34 (2013) 3261–3264.

[29] S. Gurunathan, J.H. Park, Y.-J. Choi, J.W. Han, J.-H. Kim, Synthesis of graphene oxide-silver nanoparticle nanocomposites: an efficient novel antibacterial agent, Curr. Nanosci. 12 (2016) 762–773.

[30] Q. Bao, D. Zhang, P. Qi, Synthesis and characterization of silver nanoparticle and graphene oxide nanosheet composites as a bactericidal agent for water disinfection, J. Colloid Interface Sci. 360 (2011) 463–470.

[31] A. O. E. Abdelhalim, A. Galal, M. Z. Hussein, and I. E.-T. El Sayed, Graphene functionalization by 1,6-diaminohexane and silver nanoparticles for water disinfection, J. Nanomater. 2016 (2016) 1485280(1–7).

[32] E. V. Basiuk, B. Monroy-Torres, J. C. Carrero, and V. A. Basiuk, Effects of solvent-free amine functionalization of graphene oxide and nanodiamond on bacterial growth, Fuller. Nanotubes Carbon Nanostruct., 2020, accepted; doi: https://doi.org/10.1080/1536383X.2020.1811235.

[33] J.R. Morones, J.L. Elechiguerra, A. Camacho, K. Holt, J.B. Kouri, J. Tapia-Ramírez, M.J. Yacaman, The bactericidal effect of silver nanoparticles, Nanotechnology 16 (2005) 2346–2353.

[34] C. Marambio-Jones, E.M.V. Hoek, A review of the antibacterial effects of silver nanomaterials and potential implications for human health and the environment, J. Nanopart. Res. 12 (2010) 1531–1551.

[35] V. Meza-Laguna, E.V. Basiuk (Golovataya-Dzhymbeeva), E. Alvarez-Zauco, D. Acosta-Najarro, and V. A. Basiuk, Cross-linking of C_{60} films with 1,8-diaminooctane and further decoration with silver nanoparticles, J. Nanosci. Nanotechnol. 7 (2007) 3563–3571.

[36] J. P. Perdew, K. Burke and M. Ernzerhof, Generalized gradient approximation made simple, Phys. Rev. Lett. 77 (1996) 3865-3568.

[37] S. Grimme, Semiempirical GGA-type density functional constructed with a long-range dispersion correction, J. Comput. Chem. 27 (2006) 1787–1799.

[38] Y. Wang, Z. Xu, Y.N. Moe, On the performance of local density approximation in describing the adsorption of electron donating/accepting molecules on graphene, Chem. Phys. 406 (2012) 78–85.

[39] P. L. Silvestrelli and A. Ambrosetti, Including screening in van der Waals corrected density functional theory calculations: The case of atoms and small molecules physisorbed on graphene, J. Chem. Phys. 140 (2014) 124107(1–8).

[40] Q. Zhou, W. Ju, X. Su, Y. Yong, X. Li, Adsorption behavior of SO_2 on vacancy-defected graphene: a DFT study, J. Phys. Chem. Solids 109 (2017) 40–45.

[41] E.V. Basiuk, M. Martínez-Herrera, E. Álvarez-Zauco, L.V. Henao-Holguín, I. Puente-Lee, V.A. Basiuk, Noncovalent functionalization of graphene with a Ni(II) tetraaza[14]annulene complex, Dalton Trans. 43 (2014) 7413–7428.

[42] V.A. Basiuk, N. Alzate-Carvajal, L.V. Henao-Holguín, E.V. Rybak-Akimova, E. V. Basiuk, Coordination functionalization of graphene oxide with tetraazamacrocyclic complexes of nickel(II): generation of paramagnetic centers, Appl. Surf. Sci. 371 (2016) 16–27.

[43] V.A. Basiuk, E.V. Rybak-Akimova, E.V. Basiuk, Graphene oxide and nanodiamond: same carboxylic groups, different complexation properties, RSC Adv. 7 (2017) 17442–17450.

[44] V.A. Basiuk, L.M. Bolivar-Pineda, V. Meza-Laguna, E.V. Rybak-Akimova, E. V. Basiuk, Carbon nanotubes and graphene promote pyrolysis of free-base phthalocyanine, J. Phys. Chem. Lett. 9 (2018) 4420–4427.

[45] V. A. Basiuk, M. Kakazey, M. Vlasova, E. V. Basiuk, Effect of structural defects on the strength of adsorption of La and Lu species on graphene, Diamond Relat. Mater. 100 (2019) 107597(1–7).

[46] B. Delley, An all-electron numerical method for solving the local density functional for polyatomic molecules, J. Chem. Phys. 92 (1990) 508–517.

[47] B. Delley, Fast calculations of electrostatics in crystals and large molecules, J. Phys. Chem. 100 (1996) 6107–6110.

[48] B. Delley, From molecules to solids with the $DMol^3$ approach, J. Chem. Phys. 113 (2000) 7756–7764.

[49] B. Delley, D.E. Ellis, A.J. Freeman, E.J. Baerends, D. Post, Binding energy and electronic structure of small copper particles, Phys. Rev. B 27 (1983) 2132–2144.

[50] V.A. Basiuk, Electron smearing in DFT calculations: a case study of doxorubicin interaction with single-walled carbon nanotubes, Int. J. Quantum Chem. 111 (2011) 4197–4205.

[51] A. Barth, Infrared spectroscopy of proteins, Biochim. Biophys. Acta 1767 (2007) 1073–1101.

[52] J. Kong, S. Yu, Fourier transform infrared spectroscopic analysis of protein secondary structures, Acta Biochim. Biophys. Sinica 39 (2007) 549–559.

[53] J. Coates, Interpretation of infrared spectra, a practical approach, in Encyclopedia of Analytical Chemistry, R. A. Meyers (Ed.), 2000, John Wiley & Sons Ltd., Chichester, pp. 10815–10837.

[54] W. Gao (Ed.), Graphene Oxide: Reduction Recipies, Spectroscopy and Applications, Springer International Publishing, Switzerland, 2015.

[55] D. Chen, H. Feng, J. Li, Graphene oxide: preparation, functionalization and electrochemical applications, Chem. Rev. 112 (2012) 6027–6053.

[56] D.R. Dreyer, S. Park, C.W. Bielawski, R.S. Ruoff, The chemistry of graphene oxide, Chem. Soc. Rev. 39 (2009) 228–240.

[57] S. Park, K.-S. Lee, G. Bozoklu, W. Cai, S.T. Nguyen, R.S. Ruoff, Graphene oxide papers modified by divalent ions—enhancing mechanical properties via chemical cross-linking, ACS Nano 2 (2008) 572–578.

[58] G. Wang, X. Shen, B. Wang, J. Yao, J. Park, Synthesis and characterisation of hydrophilic and organophilic graphene nanosheets, Carbon 47 (2009) 1359–1364.

[59] F.A. Chowdhury, T. Morisaki, J. Otsuki, M.S. Alam, Optoelectronic properties of graphene oxide thin film processed by cost-effective route, Appl. Surf. Sci. 259 (2012) 460–464.

[60] D. Yang, A. Velamakanni, G. Bozoklu, S. Park, M. Stoller, R.D. Piner, S. Stankovich, I. Jung, D.A. Field, C.A. Ventrice, R.S. Ruoff, Chemical analysis of graphene oxide films after heat and chemical treatments by X-ray photoelectron and micro-Raman spectroscopy, Carbon 47 (2009) 145–152.

[61] B. Wang, B. Luo, M. Liang, A. Wang, J. Wang, Y. Fang, Y. Chang, L. Zhi, Chemical amination of graphene oxides and their extraordinary properties in the detection of lead ions, Nanoscale 3 (2011) 5059–5066.

[62] B. Grzyb, S. Gryglewicz, A. Śliwak, N. Díez, J. Machnikowski, G. Gryglewicz, Guanidine, amitrole and imidazole as nitrogen dopants for the synthesis of N-graphenes, RSC Adv. 6 (2016) 15782–15787.

[63] I.A. Safo, C. Dosche, M. Özaslan, Effects of capping agents on the oxygen reduction reaction activity and shape stability of Pt nanocubes, ChemPhysChem 20 (2019) 3010–3023.

[64] P. Uznanski, J. Zakrzewska, F. Favier, S. Kazmierski and E. Bryszewska, Synthesis and characterization of silver nanoparticles from (bis)alkylamine silver carboxylate precursors, J. Nanoparticle Res. 19 (2017) 121(1−20).

[65] J. Xiong, X.-D. Wua, Q.-J. Xue, One-step synthesis of highly monodisperse silver nanoparticles usingpoly-amino compounds, Colloids Surf. A Physicochem. Eng. Asp. 441 (2014) 109–115.

[66] Vinita, M. Tiwari, N. Agnihotri, M. Singh, A. K. Singh and R. Prakash, Nanonetwork of coordination polymer AHMT-Ag for the effective and broad spectrum detection of 6-mercaptopurine in urine and blood serum, ACS Omega 4 (2019) 16733–16742.

[67] G.A. El-Nagar, R.M. Sarhan, A. Abouserie, N. Maticiuc, M. Bargheer, I. Lauermann, C. Roth, Efficient 3D-silver flowerlike microstructures for non-enzymatic hydrogen peroxide (H_2O_2) amperometric detection, Sci. Rep. 7 (2017) 12181–12189.

[68] H. Schneidewind, T. Schüler, K.K. Strelau, K. Weber, D. Cialla, M. Diegel, R. Mattheis, A. Berger, R. Möller, J. Popp, The morphology of silver nanoparticles prepared by enzyme-induced reduction, Beilstein J. Nanotechnol. 3 (2012) 404–414.

[69] F. Heidarpour, W. A. W. A. K. Ghani, F. R. B. Ahmadun, S. Sobri, M. Zargar and M. R. Mozafari, Nano silver-coated polypropylene water filter: I. Manufacture by electron beam gun using a modified Balzers 760 machine, Digest J. Nanomater. Biostruct. 5 (2010) 787–796.

[70] K. Anandalakshmi, J. Venugobal, V. Ramasamy, Characterization of silver nanoparticles by green synthesis method using *Pedalium murex* leaf extract and their antibacterial activity, Appl. Nanosci. 6 (2016) 399–408.

[71] J. Mo, B. Stefanov, T. Hiu-Ming Lau, S. Wu, Superior performance of Ag over Pt for hydrogen evolution reaction in water electrolysis under high over-potentials, ACS Appl. Energy Mater. 2 (2019) 1221–1228.

[72] I. Barwal, P. Ranjan, S. Kateriya and S. C. Yadav, Cellular oxido-reductive proteins of *Chlamydomonas reinhardtii* control the biosynthesis of silver nanoparticles, J. Nanobiotechnol. 9 (2011) 56(1−12).

[73] S. Mohan, J. Princz, B. Ormeci and M. C. De-Rosa, Morphological transformation of silver nanoparticles from commercial products: Modeling from product incorporation, weathering through use scenarios, and leaching into wastewater, Nanomaterials 9 (2019) 1258(1–15).

[74] W. Ma, F. Chen, Optical and electronic properties of Cu doped Ag clusters, J. Alloys Compd. 541 (2012) 79–83.

[75] W. Ma, F. Chen, Experimental and theoretical studies on the interaction between isonicotinic acid molecules and silver nanoclusters, Spectrosc. Lett. 47 (2014) 754–760.

[76] S. Zhang, W. Ma, F. Zhang, C. Jing, R. Wu, Theoretical and experimental study on adsorption of benzoic acid molecules on silver clusters, Ferroelectrics 528 (2018) 99–107.

[77] J. Lim, S. Kang, J. Kim, W. Y. Kim, and S. Ryu, Non-empirical atomistic dipole-interaction-model for quantum plasmon simulation of nanoparticles, Sci. Rep. 7 (2017) 15775(1–6).

[78] V. A. Basiuk, O. V. Prezhdo and E. V. Basiuk, Thermal smearing in DFT calculations: How small is really small? A case of La and Lu atoms adsorbed on graphene, Mater. Today Commun. 25 (2020) 101595(1–9).

[79] E. Chávez-Colorado, V.A. Basiuk, Noncovalent interactions of free-base phthalocyanine with elongated fullerenes as carbon nanotube models, Struct. Chem. 28 (2017) 1765–1773.

[80] E.V. Basiuk, L. Huerta, V.A. Basiuk, Noncovalent bonding of 3d metal(II) phthalocyanines with single-walled carbon nanotubes: a combined DFT and XPS study, Appl. Surf. Sci. 470 (2019) 622–630.

Materials Today Communications 35 (2023) 106007

Contents lists available at ScienceDirect

Materials Today Communications

journal homepage: www.elsevier.com/locate/mtcomm

Eco-friendly synthesis of graphene oxide–palladium nanohybrids

Dinorah I. Rodríguez-Otamendi[a,b,*,1], Monserrat Bizarro[c,2], Víctor Meza-Laguna[d,3], Edgar Álvarez-Zauco[e,4], Petra Rudolf[b,5], Vladimir A. Basiuk[d,6], Elena V. Basiuk[a,**,7]

[a] *Instituto de Ciencias Aplicadas y Tecnología, Universidad Nacional Autónoma de México, Circuito Exterior C.U., 04510 Cd. México, Mexico*
[b] *Zernike Institute for Advanced Materials, University of Groningen, Nijenborgh 4, 9747 AG Groningen, the Netherlands*
[c] *Instituto de Investigaciones en Materiales, Universidad Nacional Autónoma de México, Circuito Exterior C.U., 04510 Cd. México, Mexico*
[d] *Instituto de Ciencias Nucleares, Universidad Nacional Autónoma de México, Circuito Exterior C.U., 04510 Cd. México, Mexico*
[e] *Facultad de Ciencias, Universidad Nacional Autónoma de México, Circuito Exterior C.U., 04510 Cd. México, Mexico*

ARTICLE INFO

Keywords:
Graphene oxide
Palladium nanoparticles
Nanohybrids
Solvent-free functionalization
Eco-friendly approach
Characterization

ABSTRACT

Nanostructured hybrids of graphene oxide and palladium were fabricated by means of one-step solvent-free gas phase treatment of graphene oxide with the aliphatic amines 1-octadecylamine and 1,8-diaminooctane, followed by *in situ* decoration with palladium in the liquid medium using palladium chloride as the precursor and citric acid as a mild and environmentally friendly stabilizing and reducing agent. The proposed synthesis method represents an eco-friendly alternative for obtaining nanohybrids of graphene oxide and palladium nanoparticles under mild conditions. Spectroscopic studies evidenced -COOH group derivatization of graphene due to the amidation reaction; transmission electron microscopy demonstrated the formation of nanometer-sized crystalline palladium particles and evidenced that the diamine-functionalization results in a larger particle sizes than observed for monoamine- or non-functionalized substrates. The hybrids obtained have a slightly lower thermal stability than pristine graphene oxide.

1. Introduction

In recent years graphene oxide (GO) has emerged as a highly promising material for applications in energy storage (batteries and supercapacitors), catalysis [1–4], sensors, as well as building block of conducting and thermal materials, filtration membranes and bactericidal agents [5–9]. Combining the properties of metal nanoparticles with those of GO through covalent assembly results hybrid architectures offer additional technological possibilities [10–18] due to their large surface area, plasmon resonance, highly stable nature, and in general easy processing [19–21]. It has been demonstrated that amino groups, along with the oxygen-containing groups already present in GO [22], act as nucleation points for metal nanoparticles that form through coordination bonds or electrostatic interactions with metal ions [23–26]. One of the simplest methods for metal nanoparticle deposition is liquid phase chemical reduction of the respective salts with the help of stabilizing and dispersing agents, which help to avoid agglomeration and therefore control size and morphology [11–19], favouring the uniform distribution of nanoparticles on the GO surface [27].

In our previous work [28], we demonstrated that the formation of nanostructured hybrid materials employing amine-functionalized GO to support silver nanoparticles (AgNPs) can be achieved *via* a simple and eco-friendly gas-phase treatment. We have shown that this method of synthesis does not require additional purification processes because the

---

* Corresponding author at: Instituto de Ciencias Aplicadas y Tecnología, Universidad Nacional Autónoma de México, Circuito Exterior C.U., 04510 Cd. México, Mexico.
** Corresponding author.
E-mail addresses: d.i.rodriguez.otamendi@rug.nl (D.I. Rodríguez-Otamendi), elena.golovataya@icat.unam.mx (E.V. Basiuk).
[1] 0000-0001-5495-6081
[2] 0000-0002-4716-9730
[3] 0000-0002-7812-6231
[4] 0000-0003-2560-5906
[5] 0000-0002-4418-1769
[6] 0000-0001-7864-9203
[7] 0000-0003-0877-242X

https://doi.org/10.1016/j.mtcomm.2023.106007
Received 10 April 2023; Accepted 13 April 2023

surplus reagents can be eliminated *in situ* through moderate dynamic vacuum and heating conditions. With respect to conventional techniques where toxic solvents are employed and several reaction steps are involved [29,30], the one-step gas-phase amine functionalization method has the advantage of yielding AgNPs with a controlled size distribution and a higher surface density, which are important requirements for applications of GO hybrid materials in several fields [31–34]. This motivates a further study on other noble metals like palladium in view of exploiting not only the peculiar electronic, mechanical, and catalytic properties of these nanoparticles, [35–37] but also their application for therapeutic purposes based on their antibacterial and cytotoxic activity [38–40].

The main purpose of the present work was to demonstrate that it is possible under eco-friendly and mild conditions to obtain nanohybrids of GO and palladium nanoparticles (PdNPs) by applying a gas-phase pretreatment of GO with amine molecules, which thanks to their chemical affinity toward biological molecules [41], confer an additional ecological value to this study. Similar studies with pristine, non-functionalized materials will be performed as well for comparison purposes.

2. Experimental

2.1. Materials

Single-layer graphene oxide powder (≥99 wt% purity, platelet diameter of 300–800 nm and thickness of 0.7–1.2 nm) from Cheap Tube, Inc., was used. 1-Octadecylamine (ODA; ≥99%), 1,8-diaminooctane (DAO; ≥98%), citric acid (≥99.5%), palladium chloride (≥99%), 2-propanol (≥99.8%) and hydrochloric acid (≥37%) from Sigma-Aldrich were used as received.

2.2. Gas phase functionalization with amines

We followed the general procedure described in our previous works [42–44] and optimized it for the present purposes. The yield was improved employing GO/amine w/w ratios of 1:1. The functionalization process comprised three steps: (1) degassing for 15 min at temperature of 100 °C under constant evacuation pressure of 10^{-2} Torr; (2) functionalization reaction under static vacuum for 1 h in a temperature range of 160–180 °C; (3) degassing at 100 °C under constant evacuation for 30 min to remove unreacted amines.

The amine-functionalized samples are labelled GO+ODA and GO+DAO in the following.

2.3. Deposition of palladium nanoparticles

We adapted the methods of PdNP deposition based on the reduction of Pd^{2+} ions with citric acid, reported by Roy et al. [45], Dar et al. [46], and Li et al. [47]. Compared to Dar et al. [46], we reduced the reaction time from 7 h to 10 min by adopting the acidic solution of $PdCl_2$ employed by Li et al. [47] and, in order to assure the complete reduction reaction of the precursor, the citric acid concentration was 10 times higher. For achieving homogeneous dispersions, it was necessary to dissolve the metallic precursor in a 0.2 N solution of HCl assisted by heating at about 70 °C, which was then diluted with distilled water to obtain $PdCl_2$ 0.005 M.

For preparing the hybrids, amine-functionalized and pristine GO were immersed in 0.005 M $PdCl_2$ in a proportion of 5 mg/10 mL. Then, 20 mL of a 0.05 M solution of citric acid was added to the reaction vessel upon continuous stirring at room temperature for 10 min. After this, the materials were washed twice with deionized water, dried, and stored under vacuum at room temperature. The amine-functionalized samples decorated with PdNPs are labelled GO+ODA+Pd and GO+DAO+Pd in the following. An analogous sample was obtained with non-functionalized pristine GO for comparison. This hybrid is labelled GO+Pd in the following.

2.4. Characterization

Fourier-transform infrared (FTIR) spectra in attenuated total reflectance (ATR) mode were measured employing a Nicolet iS50R Thermo-Scientific spectrometer. Each spectrum was the sum of 32 scans, collected in the range of 500–4000 cm^{-1} with a resolution of 4 cm^{-1}. Measurements were performed in triplicate to verify reproducibility.

The X-ray powder diffraction (XRD) data were obtained on a D8 Advance Bruker diffractometer with a monochromatic Cu Kα X-ray source ($\lambda = 1.5418$ Å) and a secondary beam graphite monochromator; a LYNXEYE detector (1D mode) was used. The samples were finely pulverized and the patterns were recorded in a 2θ range from 3° to 60°, in steps of 0.02° and with a counting time of 1.0 s per step; duplicate spectra were acquired.

Thermogravimetric and differential thermal analysis (TGA–DTA) were carried out using a STA 449 C Jupiter analyzer from Netzsch-Geratebau GmbH. For the tests, samples of approximately 10 mg were exposed to an air flow of 100 mL/min, and a heating ramp of 10 °C/min up to 1000 °C; duplicate analysis was performed.

Scanning electron microscopy (SEM) was performed with a JEOL JSM-6510LV instrument, operated at an acceleration voltage of 20 kV, and coupled to an INCA Energy 250 Energy Dispersive X-ray (EDS) Microanalysis System from Oxford Instruments. All the samples were fixed on double-sided carbon tape and measured without coating. Two imaging modes were used: secondary electrons images (SEI) and backscattered electron composition (BEC), collecting micrographs at 10, 5 and 0.5 µm. SEM-EDS spectra were acquired for every sample in 5 different spots with a diameter of 30 µm.

Transmission electron microscopy (TEM) bright-field (BF) and dark-field (DF) studies were carried out with a JEOL JEM-ARM200F STEM Schottky FEG, operated at a 1.0 Å resolution and a 200 kV acceleration voltage. The samples were dispersed in 2-propanol, drop casted onto lacey carbon films on 200 mesh copper TEM grids manufactured by Agar Scientific, dried at room temperature and cleaned by plasma treatment before measurements. Micrographs at 200, 100 and 20 nm were performed in BF mode, whereas DF imaging at 0.5 µm, 100 and 20 nm were collected from different spots on every sample. TEM-EDS mapping was performed for every sample on 3 different spots with a diameter of 1 µm.

2.5. Theoretical calculations

To gain theoretical insight into the mechanisms of interaction of PdNPs with pristine and amine-functionalized GO as well as into the geometry and formation energies of the resulting Pd-GO hybrids, we employed density functional theory (DFT) calculations. The numerical-based DFT module $DMol^3$ [48–51] of Materials Studio was the software package of choice. We used the Perdew-Burke-Ernzerhof (PBE) functional [52] within the generalized gradient approximation, along with a long-range dispersion correction by Grimme [53] (commonly referred to as PBE-D2), which is crucial when noncovalent interactions are involved. The double numerical basis set DNP, which has a polarization *d*-function added on all non-hydrogen atoms, as well as a polarization *p*-function added on all H atoms, was combined with the DSPP pseudopotentials. The settings for full geometry optimization and calculation of electronic parameters included 'fine' computation quality and convergence criteria (namely, 10^5 Ha energy change, 0.002 Ha/Å maximum force, 0.005 Å maximum displacement, and 10^{-6} SCF tolerance). All the calculations were spin-unrestricted. The global orbital cutoff [54] was set to 4.5 Å, as defined by the presence of palladium atoms. Since setting orbital occupancy to Fermi-type not always allowed for the reasonably fast and successful SCF convergence, for the most complex systems the latter was aided by using thermal smearing [54–56], the value of which was reduced stepwise from 0.005 to 10^{-4} Ha, and the final calculation was refined with Fermi orbital occupancy (with a few exceptions).

All the calculations considered the presence of an aqueous medium, whose implicit inclusion was performed *via* the conductor-like screening model (COSMO) [57,58] with the value of 78.54 for dielectric constant of water.

The formation energies $\Delta E_{\text{GOmodel+PdNC}}$ for the complexes (or ΔE for simplicity) of different GO models (GOmodel) with a palladium nanocluster (PdNC) were calculated using the following general equation:

$$\Delta \mathrm{E}_{\text{GOmodel+PdNC}} = E_{\text{GOmodel+PdNC}} - (E_{\text{GOmodel}} + E_{\text{PdNC}})$$

where E_{i} is the corresponding absolute energy.

3. Results and discussion

3.1. Experimental results

To visualize general changes in the chemical nature of GO before and after functionalization with amines and further decoration with PdNPs, dispersibility tests were conducted in water and 2-propanol. For this purpose, 0.5 mg/mL dispersions of GO in solvent were prepared with ultrasonication for 10 min at room temperature (Fig. 1). For pristine GO, brownish dispersions were formed in both water and 2-propanol, which precipitated after 24 h. Amine-functionalized GO formed instable dispersions in water, whereas in 2-propanol the stability of the dispersions deceased with time and almost total precipitation was observed after 24 h. These results confirm that the surfaces modified with long chains of ODA and DAO acquire a more hydrophobic character. Once decorated with PdNPs, the amine-functionalized GO solids precipitated to the bottom of the beakers in both solvents practically immediately after sonication.

The effectiveness of amine derivatization *via* GO surface chemistry was checked with the help of FTIR spectroscopy (Fig. 2). The spectrum of pristine GO shows the fingerprint bands of the oxygen-containing moieties: the hydroxyl band (ν_{OH}) at 3592 cm^{-1}; the δ_{OH} signal at 1607 cm^{-1}; $\nu_{\mathrm{C=O}}$ vibrations in COOH groups at 1719 cm^{-1}; $\nu_{\mathrm{C\text{-}O(asym)}}$ in epoxy bonds [59] at 1373 cm^{-1}; the δ_{OH} signal at 1241 cm^{-1} and the $\nu_{\mathrm{C\text{-}O}}$ vibrations at 1051 cm^{-1} from C–O–H groups [60]. Unsaturated ketone groups could be responsible for the band at 964 cm^{-1} [43]. For aminated GO the $\nu_{\mathrm{C=O}}$ signal decreased in intensity and shifted, from 1704 to 1719 cm^{-1} to 1694–1699 cm^{-1}, due to the characteristic 'amide I′ band between 1600 and 1700 cm^{-1}, accompanied by the 'amide II' band at 1558–1563 cm^{-1} [22,61,62]. The set of bands located at 1200–1400 cm^{-1} can be assigned to the 'amide III' mode [61,62]. Additionally, the bands of alkyl groups are observed: the $\nu_{\mathrm{CH(asym)}}$ band at 2916–2921 cm^{-1} and the $\nu_{\mathrm{CH(sym)}}$ band at 2843–2848 cm^{-1}. These observations corroborate a successful amine derivatization.

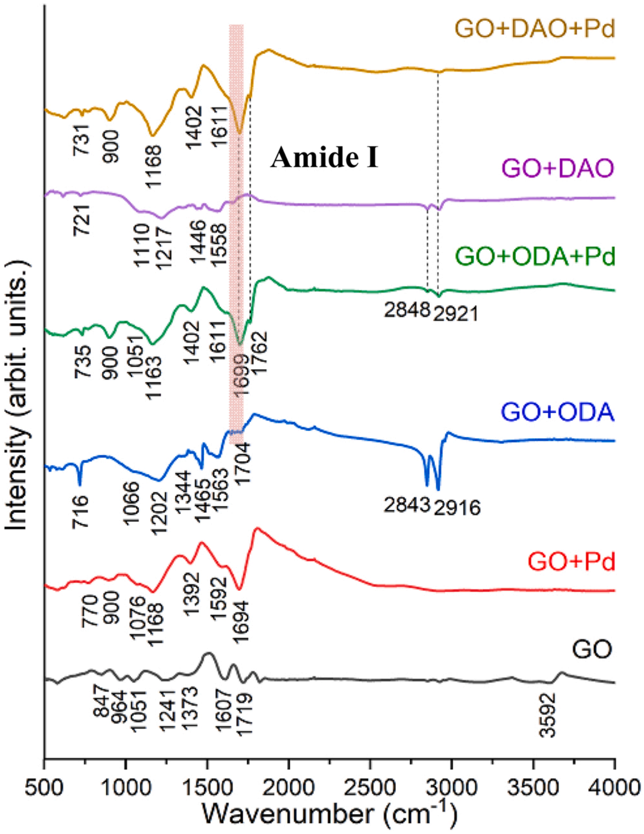

Fig. 2. FTIR spectra of pristine and amine-functionalized GO samples before and after decoration with Pd nanoparticles.

For GO-Pd samples, clear changes can be observed in the bands corresponding to the vibrations of the oxygenated groups; in particular, the increased intensity, broadening and shifting of $\nu_{\mathrm{C=O}}$ absorption band

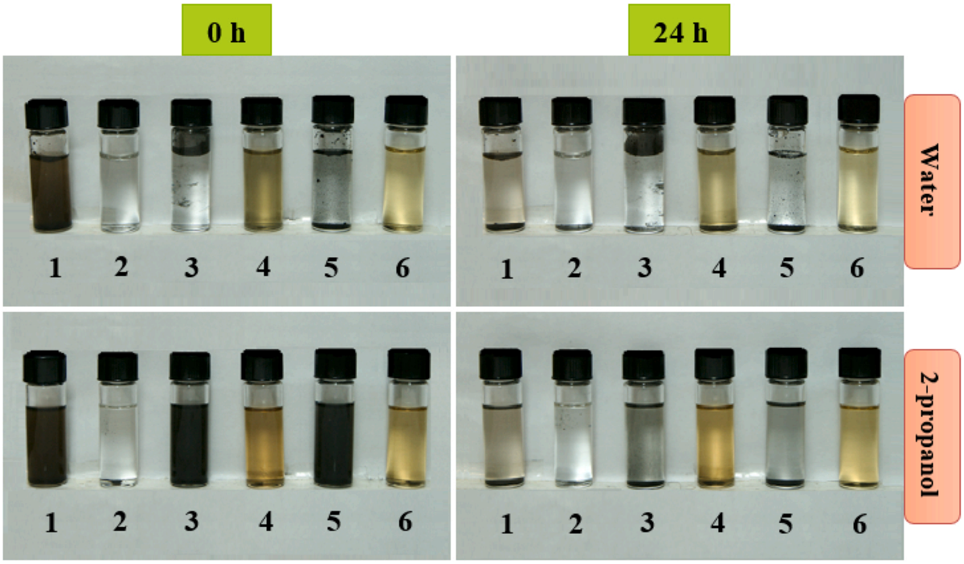

Fig. 1. Dispersibility tests for GO samples in water and 2-propanol: (1) pristine GO, (2) GO+Pd, (3) GO+ODA, (4) GO+ODA+Pd, (5) GO+DAO, and (6) GO+DAO+Pd. The images were taken immediately after 10-min ultrasonication (0 h) and after 24 h.

from COOH functionalities might indicate that the palladium nanoparticles form a coordination bond with the oxygen in these groups. GO+ODA+Pd and GO+DAO+Pd samples show the same trend. Other important changes for these samples include an almost total disappearance of ‘amide II’ δ_{NH} absorption at 1558–1563 cm^{-1}, a decrease of the $\nu_{C\text{-}O}$ band at 1051–1076 cm^{-1} and an increase in intensity of $\nu_{C\text{-}N}$ signals at 1163–1168 cm^{-1}. All these changes indicate the coordination of palladium to nitrogen and oxygen atoms present on GO+ODA and GO+DAO surfaces.

TGA and DTA were used to identify changes in the thermal behaviour of GO caused by the modification with amines and the decoration with PdNPs. The TGA curve for pristine GO (Fig. 3a) exhibits three principal weight losses that correspond to the evaporation of physisorbed water (10.3%, until 136 °C), the pyrolysis of oxygenated functionalities (28.4%, until 245 °C), and the graphene lattice combustion (60.6%, until 690 °C) [63]. The DTA curve consists of two principal peaks in 211 and 668 °C, matching the main weight loss steps in the TGA curve.

For GO+Pd (Fig. 3b), the pattern of weight loss includes four steps. The first is related to the evaporation of physisorbed water (5.6%, until 134 °C), the second refers to the pyrolysis of oxygenated groups (37.8%, until 247 °C), the third one is related to the combustion of the main graphene backbone (45.1%, until 446 °C), and the fourth weight loss (6.4%, until 797 °C) can be attributed to a portion of the palladium present in the sample. In fact, at temperatures over 420 °C, Pd slowly oxidizes to PdO_2 [64] and PdO_2 decomposes to Pd at temperatures above 780 °C. The last ramp (1.2%, until 1000 °C) mirrors the metallic Pd content. So, the total palladium content in the sample is around 11.5%. The DTA peaks refer to the combustion of the main components in the system, namely the oxygen-containing groups (239 °C), the graphene lattice (419 °C and 478 °C), and the palladium oxide (shoulder at 830 °C). The second and the third peak are strongly shifted to lower temperatures in comparison to the pristine GO sample; this can be explained by the catalytic effect of palladium on the combustion of the graphene backbone, similarly to what we saw previously for GO hybrids with silver nanoparticles [28].

For both amine-functionalized samples (Fig. 3c,d), the same percentage of 3.9% for the loss of physisorbed water was observed when heating up GO+ODA+Pd to 141 °C and GO+DAO+Pd to 138 °C. However, the loss steps for the oxygenated groups present noticeable differences; while for GO+ODA+Pd the corresponding percentage is 15.9% and the weight loss extends up to 247 °C, for GO+DAO+Pd the percentage is almost double, 29.5%, and the weight loss extends up to 293 °C. In the case of GO+ODA+Pd the main weight loss corresponds to the combustion of graphene lattice, 73.6% of the sample were lost when heating up to 500 °C, while for GO+DAO+Pd the weight loss is somewhat smaller, 63.9% and the temperature range slightly wider (heating up to 506 °C). Similarly to GO+Pd, these weight losses occur at lower temperatures compared to pristine GO, due to an apparent catalytic effect of the metal. Both thermograms show a shoulder at 828 °C, related to the decomposition of palladium oxide, which can be estimated to

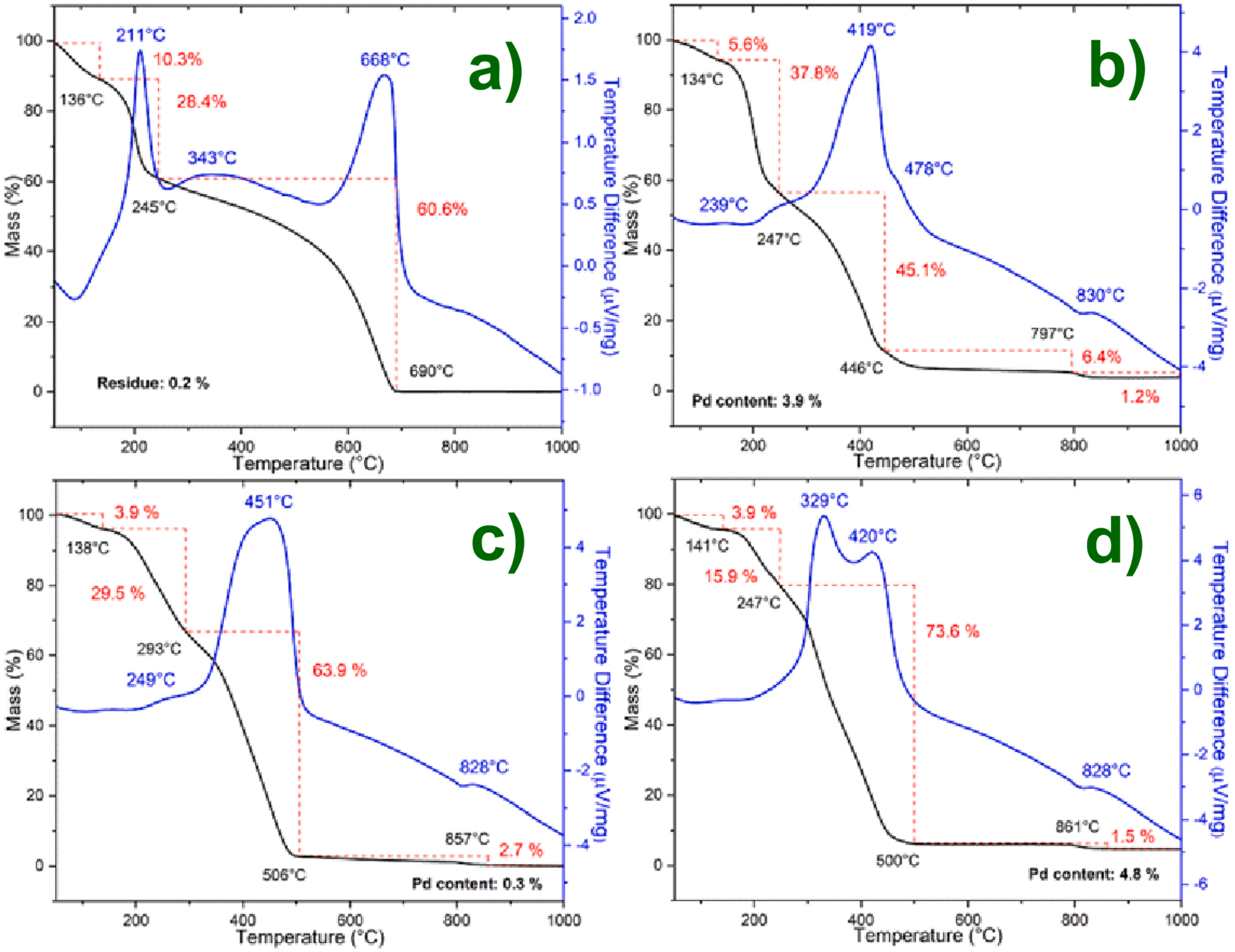

Fig. 3. TGA (black) and DTA (blue) curves for GO and GO hybrids: a) pristine GO, b) GO+Pd, c) GO+ODA+Pd, and d) GO+DAO+Pd.

make up 2.7% of GO+ODA+Pd, and 1.5% of GO+DAO+Pd. The metallic Pd content in every case is 0.3% for GO+ODA+Pd, and 4.8% for GO+DAO+Pd.

When comparing the TGA-DTA results for the GO+Pd series with those previously reported for the GO+Ag homologues [28], one notices that palladium importantly impacts the combustion temperature of the graphitic backbone; whereas for GO+Ag the pyrolysis starts at 682 °C, for GO+Pd it commences already at 446 °C. In the case of aminated samples, GO+ODA+Ag pyrolysis starts at 695 °C, but for GO+ODA+Pd it begins already at 506 °C, likewise for GO+DAO+Ag the combustion temperature is 716 °C, while for GO+DAO+Pd it is 500 °C. This testifies to a stronger catalytic effect of palladium nanoparticles. Another important difference concerns the final weight loss in the temperature range from 797° to 861°C in all the palladium-containing samples and corresponding to thermal decomposition of palladium oxide; this trend is not observed in the silver-containing hybrids because silver does not oxidize. Another difference is related to the final residue. While in the non-aminated GO hybrids the metal content is higher for palladium (GO+Pd: 11.5%; GO+Ag: 1.5%), in aminated samples one sees an opposite trend, namely a metal content of 3.0% for GO+ODA+Pd and of 6.3% for GO+DAO+Pd, while for GO+ODA+Ag the silver content amounts to 6.7% and for GO+DAO+Ag even to 12.1%.

To characterize the difference in chemical composition of the samples due to the functionalization with amines and further decoration with palladium particles, BEC SEM images were acquired (Fig. 4). The respective particle size distributions are presented in Fig. 5, where an asymmetrical distribution of size is clearly observed in all GO+Pd, GO+ODA+Pd and GO+DAO+Pd samples and small particle sizes dominate. The brightest spots highlight the presence of palladium particle agglomerates. For GO+Pd (Fig. 4a-c) triangular and octahedral shapes [65,66] with a narrow size distribution ranging from 0.04 to 0.34 µm and an average of 0.13 µm (Fig. 5a) are observed. The micrographs for GO+ODA+Pd (Fig. 4d–f), show mostly spherical palladium clusters in a broader range (0.03–1.2 µm) with an average particle size of about 0.26 µm (Fig. 5b). Similarly to the case of GO+Pd, also for GO+DAO+Pd (Fig. 4g–i) different geometric shapes are seen, from 0.02 to 0.85 µm, and the average particle size amounts to 0.14 µm (Fig. 5c). Comparing the particle size distributions, one notices that those for GO+Pd and GO+DAO+Pd are narrower than that of the ODA-functionalized sample. These observations agree with E. Ramirez et al. [67], who have demonstrated the predominant role of chemical equilibria between all potential coordinating agents in stabilizing the nanoparticles; here this concerns the ligands resulting from the precursor, the amine and the reducing agent. Since the mEq of ODA are lower than for DAO, for lower amine content we found aggregated particles but with a more regular shape. The size and shape of particles are governed by the nature of the stabilizing ligands and, in the case of weak ligands such as amines, by the quantity of ligand added.

The EDS results presented in Table 1 demonstrate that the metal content is highest for GO+Pd (10.0 ± 5.2 wt%; 1.4 ± 0.8 at%), followed

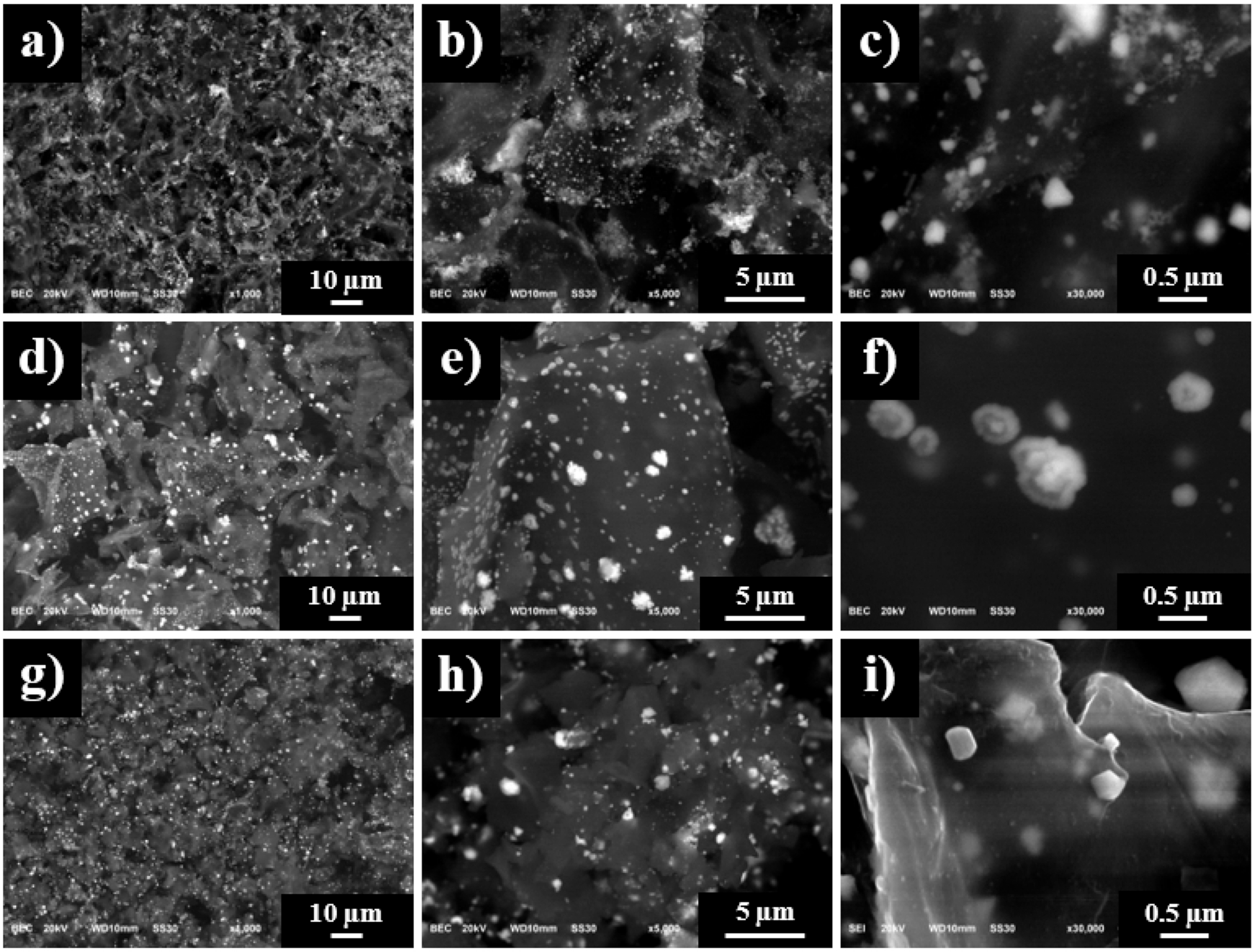

Fig. 4. Representative SEM images for GO+Pd (a-c), GO+ODA+Pd (d–f), and GO+DAO+Pd (g–i) at different magnification. Scale bars: 10 µm (left column); 5 µm (middle column), and 0.5 µm (right column).

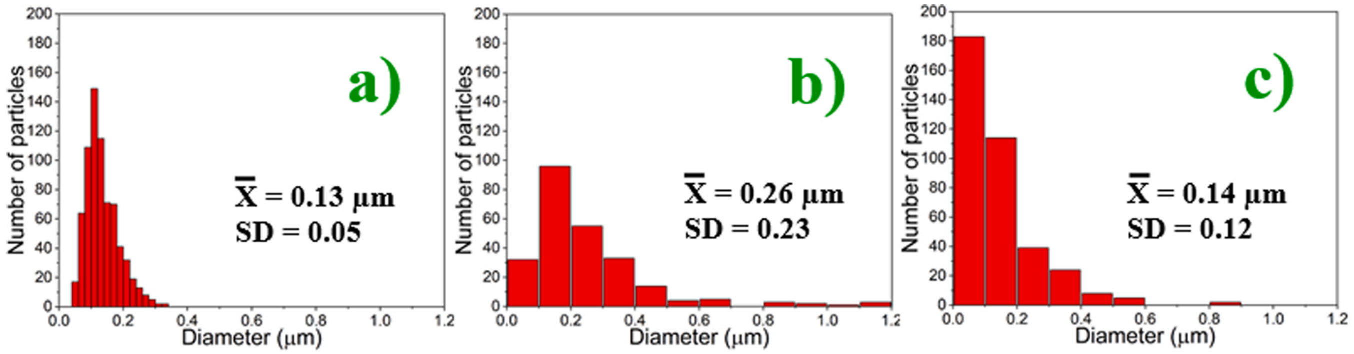

Fig. 5. Particle size distribution histograms obtained from SEM imaging of (a) GO+Pd, (b) GO+ODA+Pd and (c) GO+DAO+Pd.

Table 1
EDS results for the GO/PdNP series (SEM imaging).

Sample	Weight %	Atomic %
GO+Pd	C (K): 56.4 ± 8.8 O (K): 33.6 ± 4.3 Pd (L): 10.0 ± 5.2	C (K): 67.8 ± 6.3 O (K): 30.8 ± 5.6 Pd (L): 1.4 ± 0.8
GO+ODA+Pd	C (K): 62.9 ± 0.4 O (K): 34.0 ± 0.7 Pd (L): 2.5 ± 0.4	C (K): 70.7 ± 0.5 O (K): 28.7 ± 0.5 Pd (L): 0.3 ± 0.04
GO+DAO+Pd	C (K): 58.7 ± 6.3 O (K): 33.6 ± 3.4 Pd (L): 6.9 ± 4.1	C (K): 68.9 ± 4.4 O (K): 29.8 ± 4.0 Pd (L): 0.9 ± 0.6

by GO+DAO+Pd (6.9 ± 4.1 wt%; 0.9 ± 0.6 at%), and GO+ODA+Pd (2.5 ± 0.4 wt%; 0.3 ± 0.04 at%). Despite the differences in particle size, the tendencies observed in Fig. 5 match those of the thermal studies.

To also study the morphology, size, and distribution of smaller GO-supported palladium particles we collected bright-field (Fig. 6) and dark-field (Fig. 7) TEM micrographs. The corresponding particle size histograms are presented in Fig. 8. For GO+Pd (Figs. 6 and 7a-c) strong agglomeration of differently shaped metallic particles can be observed, leading to a broad size distribution ranging from 2 to 15 nm, and an average particle size of 5.7 ± 2.3 nm (Fig. 8a). On ODA-functionalized GO, spherical particles ranging from 1 to 13 nm are observed, with an average size of 4.2 ± 1.4 nm (Fig. 8b), whereas on DAO-functionalized GO, the particles are much larger, ranging from 6 to 450 nm, and the average size is 52.5 ± 83.5 nm (Fig. 8c).

TEM EDS mapping (Fig. 9) was carried out to supplement the micrographs with results on the chemical composition. The highest Pd content was found for the hybrid with pristine GO, followed by that for DAO-functionalized GO, and finally by that for ODA-functionalized GO. According to the elemental maps, the most homogeneous distribution with minimal agglomeration can be observed for GO+ODA+Pd, while GO+Pd and GO+DAO+Pd show a strong coalescence of particles. These results are not as informative on the average composition of the hybrids as the SEM EDS results because they represent a snapshot on the local composition of a much smaller area (TEM spot diameter 1 µm *vs.* SEM spot diameter 30 µm) but they match the trend in Pd content previously discussed in SEM EDS, and agree with the thermal behaviour of the hybrids.

The agglomeration observed in the non-aminated sample can be associated with the strong interaction of sterically unprotected Pd species with the GO surface. The smallest particle size achieved in GO+ODA+Pd can be justified by the presence of the ODA moieties, which avoid a strong attraction to the graphitic backbone. In GO+DAO+Pd, the two coordinating sites of DAO favour a higher content of metallic nanoparticles, which is mirrored by the histograms in Figs. 5 and 8, and the percentage of Pd observed in EDS studies (Tables 1 and 2).

Compared with Ag-containing samples, larger particles with a broader size distribution were observed in the GO+Pd series, despite a slightly lower palladium content. It is important to highlight a strong tendency of agglomeration of either silver or palladium nanoparticles on pristine graphene oxide, which underlines the importance of nitrogen-containing ligands for nucleation and growth regulation [67].

The crystallinity of the Pd-containing hybrids was investigated by XRD and the diffractograms acquired are shown in Fig. 10. GO presents the characteristic (001) diffraction peak at $2\theta = 11.2^\circ$ (d-spacing of 0.79 ± 0.007 nm) [68–71]. In fact, according to Dékány, Krüger-Grasser, and Weiss [72], pristine GO presents d-spacings between 0.61 up to 1.1 nm, depending on the amount of water adsorbed. The modification with amines resulted in a broadening of the main GO peak and a shifting from 11.2° to 11.7° ($d_{001} = 0.76 \pm 0.007$ nm) for GO+ODA, and to 12.5° ($d_{001} = 0.71 \pm 0.009$ nm) for GO+DAO. This slight shrinking of the interlamellar space could be associated with the hydrophobic aliphatic chain of the amine moieties. For GO+Pd, GO+ODA+Pd and GO+DAO+Pd hybrids a noticeable broadening of the graphitic peak at $2\theta = 13.4^\circ$ (d-spacing of 0.66 nm) is seen; this points to small coherently diffracting domains and hence to (partial) exfoliation [73]. According to Kaniyoor et al., this phenomenon might be provoked by the acid treatment preparing for the decoration with PdNPs; in fact a partial removal of oxygenated functionalities (a certain degree of reduction) and water molecules, decreases the interlayer spacing in comparison to pristine GO [74–77]. FT-IR and TGA/DTA results support this interpretation. It is reasonable to assume that the acidic treatment of aminated-GO also has an impact on the flake thickness *via* exfoliation-reduction [73], which causes the broad (001) Bragg reflection peak. The exfoliatiation seems to continue during Pd decoration since for both GO+ODA+Pd and GO+DAO+Pd hybrids the 001 peak has almost totally disappeared, indicating that the coherently diffracting domains are very small. The slightly narrower d-spacing for GO+DAO is probably due to cross-linking by bifunctional molecules like 1,8 diamino octane onto the GO network, resulting in a more compact hybrid [44,78].

The appearance of new peaks assigned to (111) and (200) Bragg reflections at $2\theta = 40.2^\circ$ and 46.7° respectively, in the Pd-containing hybrids confirmed that the palladium nanoparticles that are large enough to be detected in XRD, have a face centred cubic (fcc) crystalline structure [79]. The fact that the intensity of the peaks in aminated samples is higher than in the non-aminated GO+Pd indicates more periodicity in crystalline arrangements due to the complexation effect by the nitrogen in amines. The lack of these stabilizing agents on the chemical environment of GO+Pd promotes chaotic/random arrangements; as a consequence, the height of the peak is reduced. These phenomena match the discussion of the SEM and TEM images (*vide supra*) where we saw that ligand moieties have an impact on the nucleation patterns of metallic particles.

3.2. *Theoretical modeling*

We attempted to provide an explanation for the experimental results

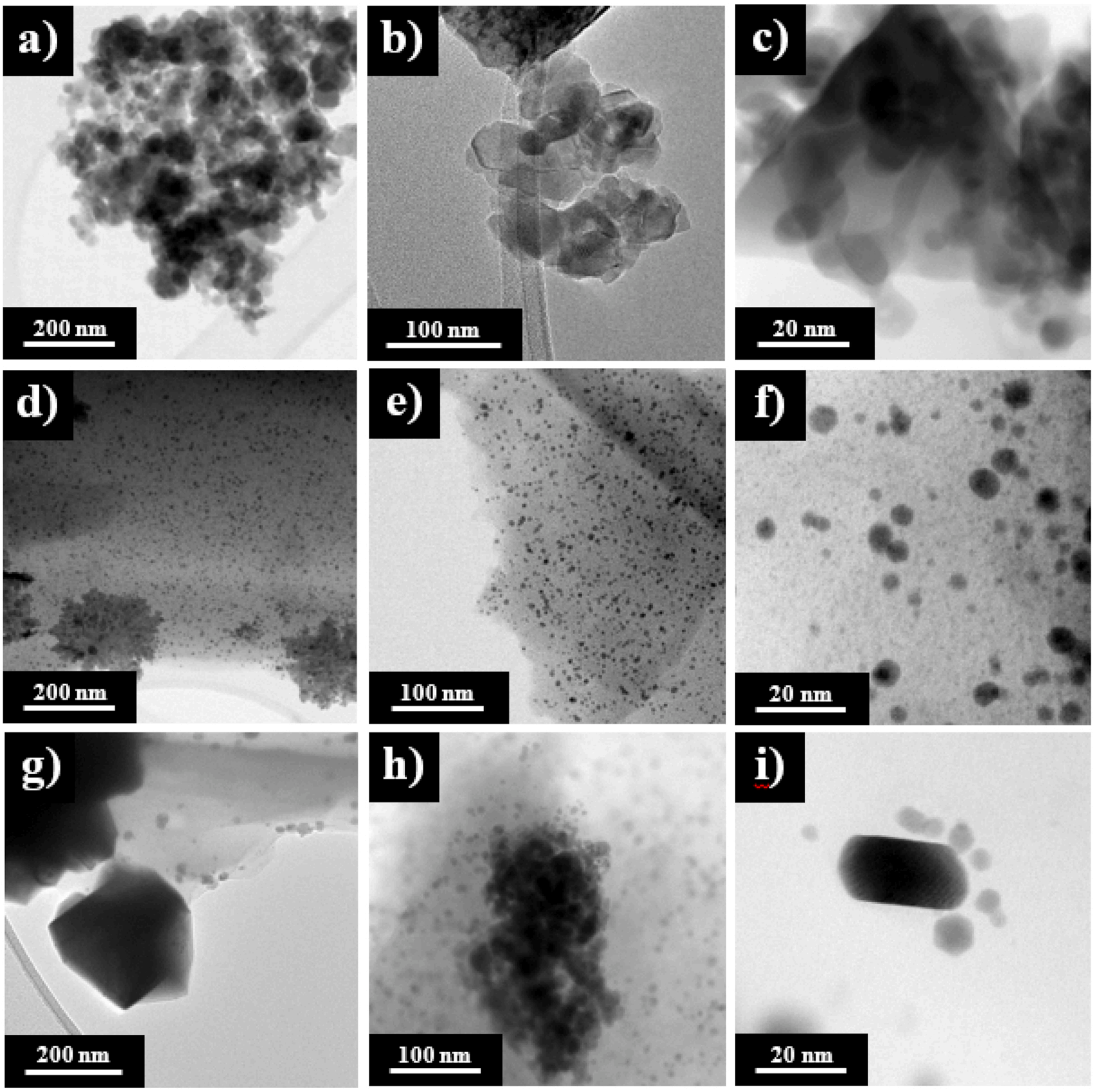

Fig. 6. Bright-field TEM imaging for GO+Pd (a-c), GO+ODA+Pd (d-f) and GO+DAO+Pd (g-i) at different magnification. Scale bars: 200 nm (left column); 100 nm (middle column), and 20 nm (right column).

by modeling the properties of the hybrids with DFT calculations. The use of realistic-size GO and PdNP models is obviously computationally prohibitive, but relatively small models can already highlight some trends. An appropriate and computationally accessible choice to simulate a Pd nanoparticle is the Pd_{16} cluster (Fig. 11), which was proposed by Nava et al. [80]. This cluster has a maximal lateral extension of 7.1 Å and can also be synthesized experimentally in a ligand-stabilized form [81]. In the case of GO, we employed the models of pristine GO, GO+ODA and GO-DAO successfully tested in our previous study on AgNP decoration of the same substrates [28].

The optimized Pd_{16} geometry (Fig. 11a) is rather symmetric. As shown by the Mulliken analysis, the atoms of the cluster differ in terms of the sign and magnitude of charge: from − 0.041 *e* to 0.013 *e*. In other words, both positively and negatively charged chemical species (either atoms or functional groups) can interact electrostatically with Pd_{16} and this will be important for how the metal nanoparticles can bind to pristine and functionalized GO.

As described previously [28], a computationally feasible choice of GO models is based on a ten fused aromatic-ring system [82,83]. To represent the oxygen-containing functionalities of GO, we introduced six carboxylic and eight aromatic ketone groups. The models for GO+ODA and GO+DAO were derived from the GO model by converting four of its six COOH groups into the corresponding amides [28]. In the case of GO+DAO we additionally accounted for the fact that the Pd deposition is carried out under acidic experimental conditions, by protonating the four NH_2 termini, which did not form amide derivatives; the resulting model is referred to as GO+DAO-4 H^+.

The DFT results related to complex formation and the frontier orbital energies are presented in Table 3. Fig. 12. schematically describes the mechanism and energy of complexation of a Pd_{16} cluster with the models for pristine GO, GO+ODA and GO+DAO-4 H^+. One can see that the weakest bonding (−62.2 kcal/mol) was found on GO+ODA. In this case, Pd_{16} remains on the top of the model, forming close contacts mainly with the terminal CH_3 groups of octadecyl moieties. The other two cases are very different, with very low negative values of formation energies (*i.e.* very strong bonding) for both GO (−135.2 kcal/mol) and especially GO+DAO-4 H^+ (−179.5 kcal/mol). The most interesting distinctive feature is that the Pd cluster directly chemisorbs on the graphene backbone by forming short Pd-C bonds, which can be qualified as covalent. This happens even on GO+DAO-4 H^+, despite the presence

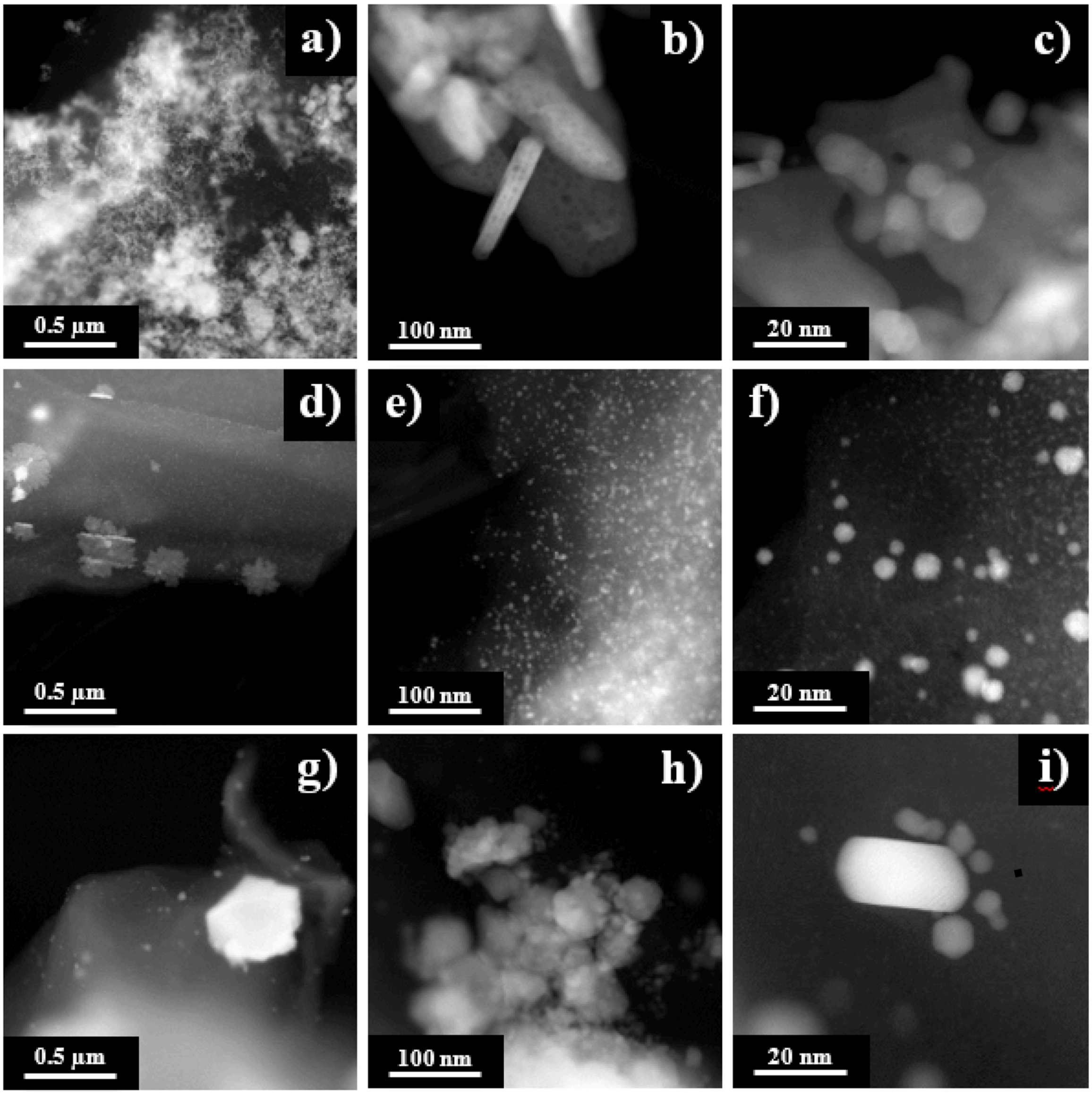

Fig. 7. Z-Contrast dark-field TEM images for GO+Pd (a-c), GO+ODA+Pd (d-f) and GO+DAO+Pd (g-i) at different magnification. Scale bars: 0.5 µm (left column); 100 nm (middle column), and 20 nm (right column).

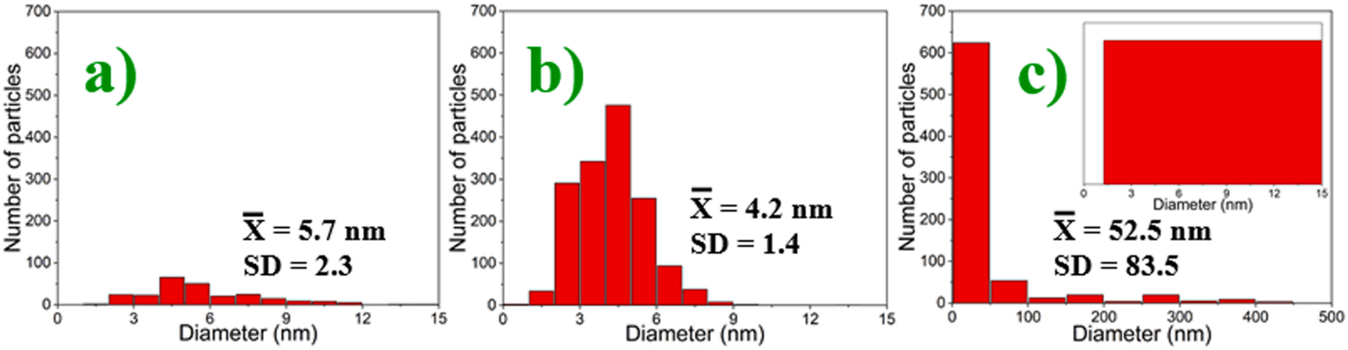

Fig. 8. Particle size distribution histograms obtained from TEM imaging of (a) GO+Pd, (b) GO+ODA+Pd and (c) GO+DAO+Pd. The inset in (c) shows the main population of particles ranging from 1 to 15 nm onwards represented by the maximum on the histogram.

of rather long DAO moieties. This direct contact between the Pd_{16} cluster and the graphene backbone 'smears' palladium atoms over the GO surface, contrary to the case of GO+ODA+Pd_{16}, where Pd_{16} generally conserves its symmetric shape. A possible explanation is that ODA substituents are sufficiently long, and thus 'shield' and protect palladium from the strong attraction to the GO surface. The 'smearing'

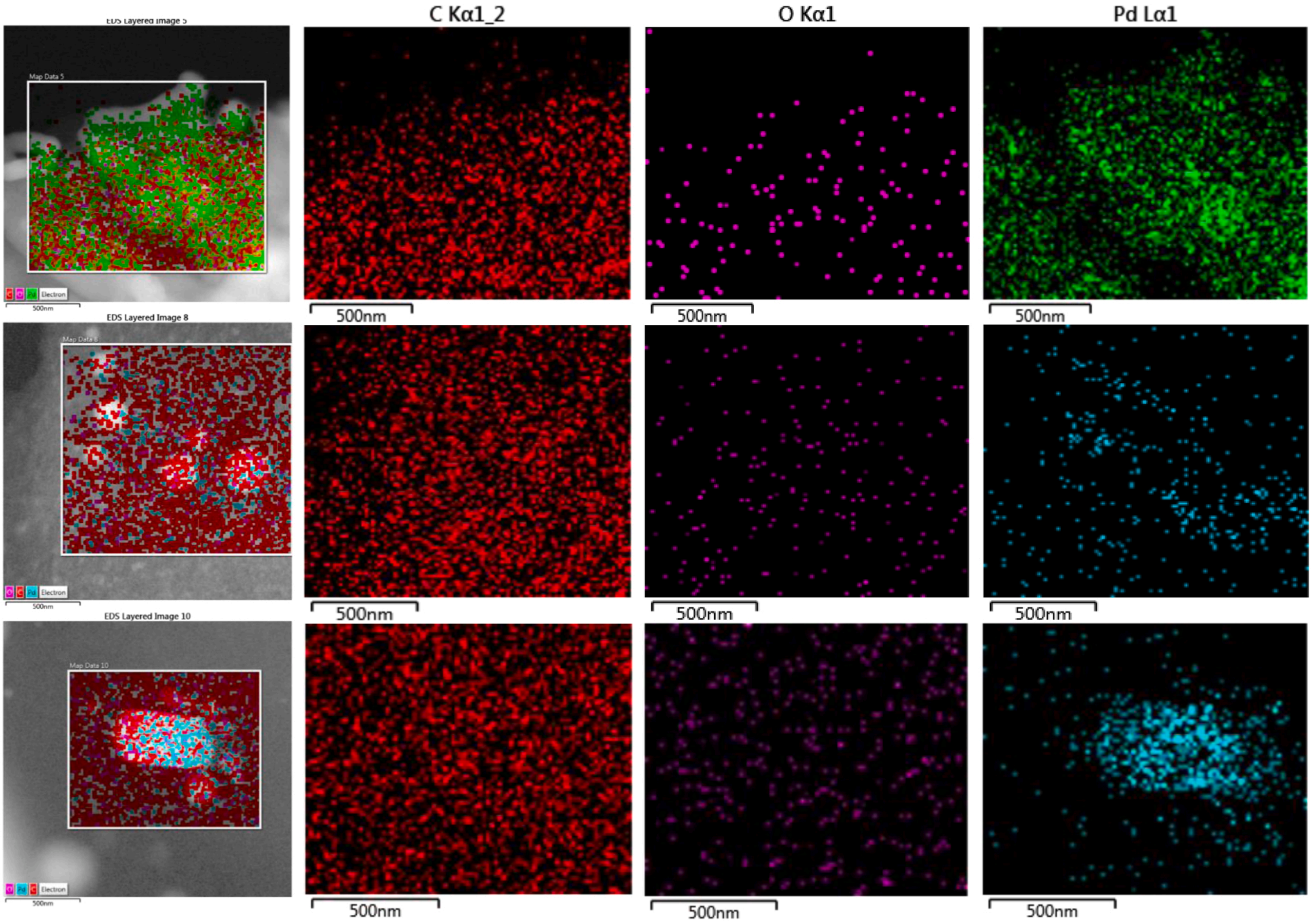

Fig. 9. C, O and Pd elemental mapping and all maps overlaid on the TEM micrograph (left. column) for GO+Pd (top row), GO+ODA+Pd (middle row) and GO+DAO+Pd (bottom row).

Table 2
EDS results for the GO/PdNPs series (TEM imaging).

Sample	Weight %	Atomic %
GO+Pd	C (K): 24.6 ± 7.6 O (K): 2.7 ± 1.4 Pd (L): 72.7 ± 6.2	C (K): 69.9 ± 10.1 O (K): 6.1 ± 4.0 Pd (L): 24.1 ± 6.1
GO+ODA+Pd	C (K): 60.0 ± 20.2 O (K): 6.9 ± 1.8 Pd (L): 33.1 ± 18.5	C (K): 86.0 ± 8.4 O (K): 8.0 ± 3.9 Pd (L): 6.0 ± 4.5
GO+DAO+Pd	C (K): 46.8 ± 16.8 O (K): 6.0 ± 4.8 Pd (L): 47.2 ± 21.6	C (K): 82.1 ± 3.6 O (K): 7.3 ± 4.1 Pd (L): 10.6 ± 7.7

of Pd atoms observed theoretically can explain PdNP coalescence and agglomeration observed experimentally on GO and GO+DAO, whereas PdNPs deposited onto GO+ODA do not tend to coalesce and remain small, though the Pd elemental content is relatively small as well.

As it could be expected, the differences in geometries and mechanisms of nanohybrid formation give rise to notable differences in the electronic structure; we analyzed specifically the energy and distribution of frontier orbitals HOMO and LUMO (Table 3 and Fig. 13). The HOMO-LUMO gap energies calculated for individual components are 0.313 eV for Pd_{16}, 1.105 eV GO, 0.854 eV for GO+ODA and 0.863 eV for GO+DAO-4 H^+ are (Table 3). It is logical to expect that, since Pd_{16} has the lowest gap energy of all these components, its complexation with GO, GO+ODA and GO+DAO-4 H^+ will result in lower HOMO-LUMO gap energies for the corresponding hybrids. As one can see, the HOMO-LUMO gap dramatically decreases to 0.163 eV for GO+Pd_{16}, 0.008 eV for GO+ODA+Pd_{16} and 0.144 eV for GO+DAO-4 H^++Pd_{16}. An especially interesting observation is that Pd functionalization decreases the gap energy by two orders of magnitude, namely from 0.854 eV for GO+ODA to 0.008 eV for GO+ODA+Pd_{16}. The frontier orbital localization (Fig. 13) matches the differences in HOMO-LUMO gap energies. The very strong interaction in the cases of GO+Pd_{16} and GO+DAO-4 H^++Pd_{16} results in the localization of both the HOMO and the LUMO on the same Pd atoms and an insignificant charge density on GO. On the contrary, in GO+ODA+Pd_{16} the HOMO and the LUMO are very well separated, with the HOMO localized exclusively on GO, and the LUMO exclusively on Pd_{16}. The fact that the LUMO in all three cases is centered on Pd might imply that the latter remains active in electrophilic processes; in addition the presence of the HOMO on the same atoms in GO+Pd_{16} and GO+DAO-4 H^++Pd_{16} can be linked to Pd cluster activity in nucleophilic processes. In turn, this might have important positive consequences for catalytic, electrocatalytic and biomedical applications of PdNPs deposited onto GO and GO-based materials. Table 4.

4. Conclusions

Dispersibility tests, FTIR, XRD, TGA/DTA, as well as SEM and TEM imaging accompanied with EDS mapping, gave indications that applying an eco-friendly gas-phase functionalization of GO with amines is useful to create supports for the decoration with Pd nanoparticles. However the palladium content in non-aminated GO+Pd samples is higher than in amine-functionalized GO. XRD results showed Pd (111) and (200) peaks, indicating that the larger palladium nanoparticles, which are

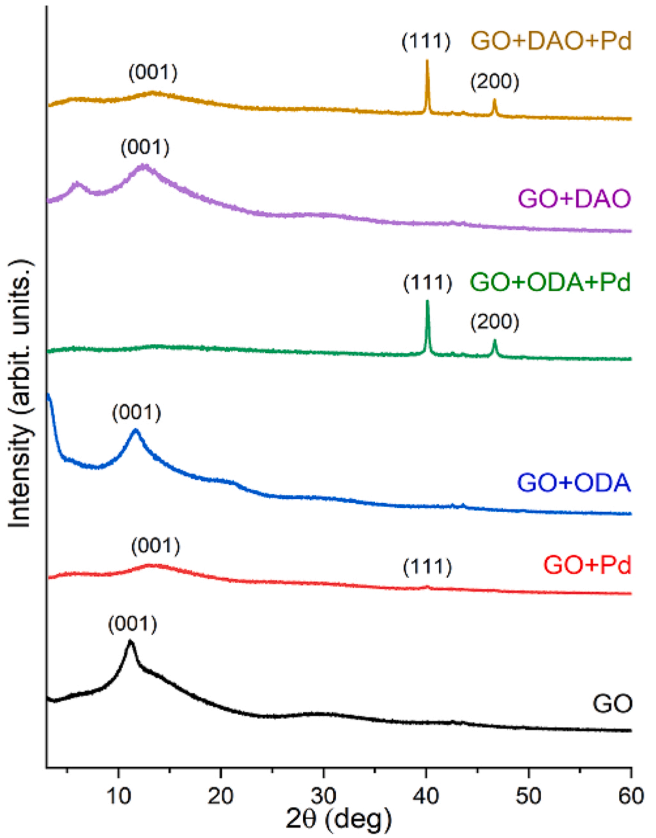

Fig. 10. XRD diffractograms of pristine and amine-functionalized GO before and after decoration with Pd nanoparticles.

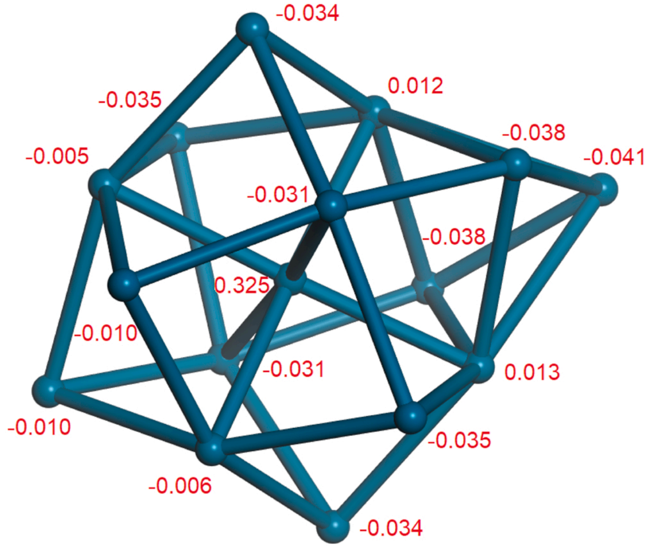

Fig. 11. Optimized geometry of the Pd16 cluster used to simulate PdNPs, showing atomic charges obtained by Mulliken analysis.

Table 3
Particle size distribution for the GO/PdNP series by SEM and TEM imaging.

Sample	Average SEM (μm)	Average TEM (nm)
GO+Pd	0.13 ± 0.05	5.69 ± 2.28
GO+ODA+Pd	0.26 ± 0.23	4.23 ± 1.37
GO+DAO+Pd	0.14 ± 0.12	52.46 ± 83.47

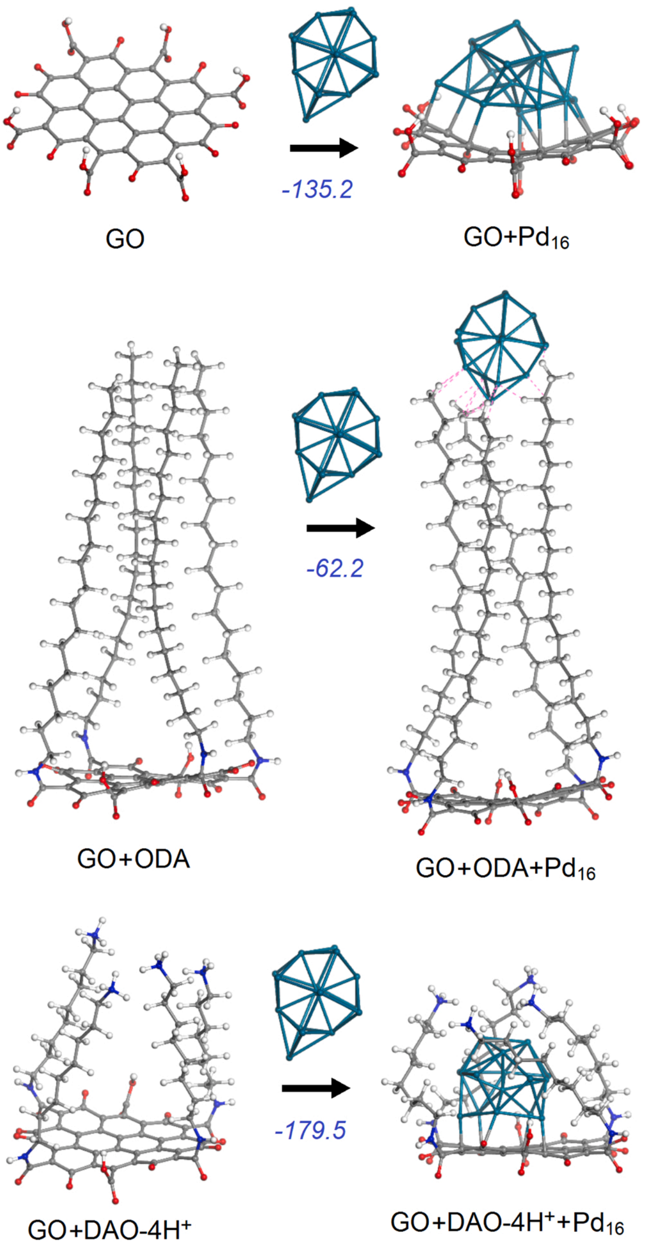

Fig. 12. Optimized geometries of the GO, GO+ODA and GO+DAO-4 H$^+$ models (left) and of their hybrids formed with a Pd$_{16}$ nanocluster (right) in aqueous medium. The values shown in blue are the formation energies (in kcal/mol) for GO+Pd$_{16}$, GO+ODA+Pd$_{16}$ and GO+DAO-4 H$^+$+Pd$_{16}$ hybrids. The pink dashed lines indicate closest approaches shorter than 2.8 Å.

visible to this technique, crystallize with a face centered cubic (fcc) structure. Electronic imaging evidence differences in PdNPs nucleation and shape with the amount of stabilizing agents (citric acid, and amine moieties).

The most relevant explanation could be obtained from bright-field and dark-field TEM imaging. GO+Pd samples we found to contain particles that generally are irregularly shaped and randomly distributed, whereas a more homogeneous size distribution preventing agglomeration was observed for ODA-functionalized GO. DAO-functionalized samples presented the formation of particles with different sizes, shapes, and coalescence. The average Pd particle sizes were found to be ten times larger on GO functionalized with diamines than on pristine GO, and on GO with monoamines.

Referring to theoretical data, the fact that the LUMO in all three cases is centred on Pd, might imply that the latter remains active in

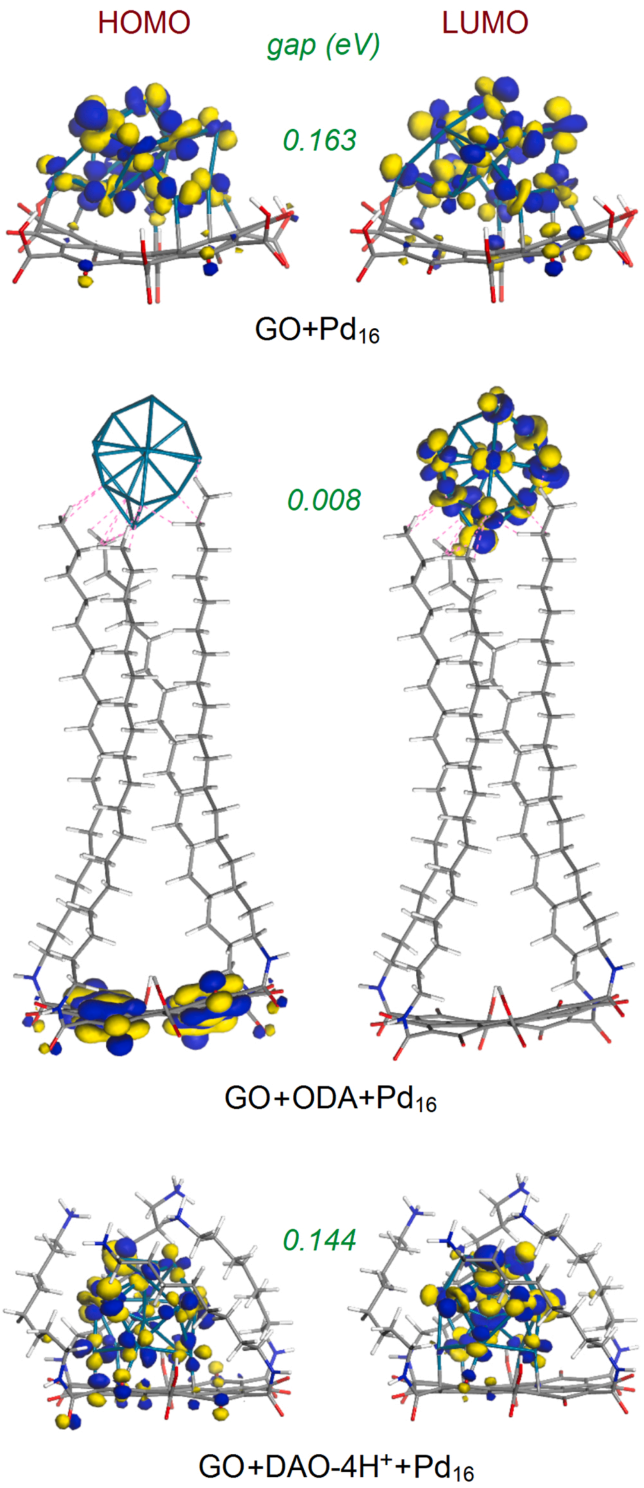

Fig. 13. HOMO and LUMO plots (isosurfaces at 0.03 a.u.) of the GO+Pd_{16}, GO+ODA+Pd_{16} and GO+DAO-4 H^++Pd_{16} hybrids, with the HOMO-LUMO gap values shown in green.

electrophilic processes; in addition the presence of the HOMO on the same atoms in GO+Pd_{16} and GO+DAO-4 H^++Pd_{16} can be linked to Pd cluster activity in nucleophilic processes. In turn, this might have important positive consequences for catalytic, electrocatalytic and biomedical applications of PdNPs deposited onto GO-based materials.

Table 4
Total energies (E, in Ha), HOMO, LUMO and HOMO-LUMO gap energies (in eV) for an isolated Pd_{16} cluster, pristine and amine-functionalized GO models and their corresponding complexes with Pd_{16}, as well as formation energies (ΔE, in kcal/mol) for the complexes with Pd_{16}, as calculated by using PBE GGA functional with Grimme's dispersion correction in conjunction with DNP basis set and DSPP pseudopotentials.

Structure	E (Ha)	ΔE (kcal/mol)	E_{HOMO} (eV)	E_{LUMO} (eV)	HOMO-LUMO gap (eV)
Pd_{16}	-2613.7569726		-4.533	-4.220	0.313
GO	-2954.3392137		-6.923	-5.818	1.105
GO+Pd_{16}	-5568.3115699	**-135.2**	-5.635	-5.472	0.163
GO+ODA	-5702.6968554		-6.476	-5.622	0.854
GO+ODA+Pd_{16}	-8316.5529615	**-62.2**	-5.037	-5.029	0.008
GO+DAO-4 H^+	-4354.7741375		-6.596	-5.733	0.863
GO+DAO-4 H^++Pd_{16}	-6968.8172249	**-179.5**	-5.763	-5.619	0.144

CRediT authorship contribution statement

Dinorah I. Rodríguez-Otamendi: Conceptualization, Methodology, Validation, Investigation, Visualization, Writing – original draft. **Monserrat Bizarro Sordo**: Investigation, Validation, Visualization. **Victor Meza-Laguna**: Investigation, Validation, Visualization. **Edgar Alvarez-Zauco**: Investigation, Validation, Visualization. **Petra Rudolf**: Validation, Visualization, Supervision, Writing – review & editing. **Vladimir A. Basiuk**: Investigation, Methodology, Validation, Visualization, Writing – review & editing. **Elena V. Basiuk**: Conceptualization, Methodology, Validation, Supervision, Project administration, Funding acquisition, Writing – review & editing.

Declaration of Competing Interest

The authors declare that they have no known competing financial interests or personal relationships that could have appeared to influence the work reported in this paper.

Data Availability

No data was used for the research described in the article.

Acknowledgements

Financial support from the National Autonomous University of Mexico (UNAM; grant DGAPA-IN100821) is greatly appreciated. This work was also supported by the Advanced Materials research program of the Zernike National Research Centre under the Bonus Incentive Scheme (BIS) of the Dutch Ministry for Education, Culture and Science. D. I. R. O., is indebted to the Postgraduate Program in Chemical Sciences at UNAM and the National Council of Science and Technology of Mexico (CONACyT), as well as the Double Degree Program between the UNAM and the University of Goningen for a PhD scholarship. We thank the technical support from the University Spectroscopic Characterization Laboratory (LUCE_ICAT_UNAM) and the technician, Dr. Selene Rubí Islas Sánchez for her assistance in the acquisition of FT-IR spectra. We are also grateful to Dr. Josué Esaú Romero-Ibarra for assistance in the TEM studies.

References

[1] K.S. Kumar, N. Choudhary, Y. Jung, Y. Thomas, Recent advances in two-dimensional nanomaterials for supercapacitor electrode applications, ACS Energy Lett. 3 (2) (2018) 482–495.
[2] G.I. Zhuang, Y.F. Gao, X. Zhou, X.Y. Tao, J.M. Luo, Y.J. Gao, Y.I. Yan, P.Y. Gao, X. Zhong, J.G. Wang, ZIF-67/COF-derived highly dispersed Co_3O_4/N-doped porous carbon with excellent performance for oxygen evolution reaction and Li-ion batteries, Chem. Eng. J. 330 (2017) 1255–1564.

[3] A. Díez-Pascual, J. Luceño Sánchez, R. Peña Capilla, P. García Díaz, Recent developments in graphene/polymer nanocomposites for application in polymer solar cells, Polymers 10 (2) (2018) 1–22.

[4] M. Hu, Z. Yao, X. Wang, Graphene-based nanomaterials for catalysis, Ind. Eng. Chem. Res. 56 (13) (2017) 3477–3502.

[5] D.A. Dikin, S. Stankovich, E.J. Zimney, R.D. Piner, G.H.B. Dommett, G. Evmenenko, S.T. Nguyen, R.S. Ruoff, Preparation and characterization of graphene oxide paper, Nature 448 (2007) 457–460.

[6] C. Vallés, J.D. Núñez, A.M. Benito, W.K. Maser, Flexible conductive graphene paper obtained by direct and gentle annealing of graphene oxide paper, Carbon 50 (2012) 835–844.

[7] Y. Zhang, C. Tai-Shung, Graphene oxide membranes for nanofiltration, Curr. Opin. Chem. Eng. 16 (2017) 9–15.

[8] H. Chen, M.B. Müller, K.J. Gilmore, G.G. Wallace, D. Li, Mechanically strong, electrically conductive, and biocompatible graphene paper, Adv. Mater. 20 (18) (2008) 3557–3561.

[9] W. Huang, Graphene oxide papers, in: W. Huang (Ed.), Nanopapers: From Nanochemistry and Nanomanufacturing to Advanced Applications, 1st ed.,, Elsevier, Amsterdam, 2017, pp. 1–26. Ch. 1.

[10] M. Cobos, I. De-La-Pinta, G. Quindós, M.J. Fernández, M.D. Fernández, Graphene oxide–silver nanoparticle nanohybrids: synthesis, characterization, and antimicrobial properties, Nanomaterials 10 (376) (2020) 1–22.

[11] Y. Cheng, H. Li, C. Fang, L. Ai, J. Chen, J. Su, Q. Zhang, Q. Fu, Facile synthesis of reduced graphene oxide/silver nanoparticles composites and their application for detecting heavy metal ions, J. Alloy. Compd. 787 (2019) 683–693.

[12] M. Ayán-Varela, M.J. Fernández-Merino, J.I. Paredes, S. Villar-Rodil, C. Fernández-Sánchez, L. Guardia, A. Martínez-Alonso, J.M.D. Tascón, Highly efficient silver-assisted reduction of graphene oxide dispersions at room temperature: mechanism, and catalytic and electrochemical performance of the resulting hybrids, J. Mater. Chem. A 2 (20) (2014) 7295–7305.

[13] S. Navalon, A. Dhakshinamoorthy, M. Álvaro, H. Garcia, Metal nanoparticles supported on two-dimensional graphenes as heterogeneous catalysts, Coord. Chem. Rev. 312 (2016) 99–148.

[14] H. Golzar, F. Yazdian, M. Hashemi, M. Omidi, D. Mohammadrezaei, H. Rashedi, M. Farahani, N. Ghasemi, J.S. Shayeh, L. Tayebi, Optimizing the hybrid nanostructure of functionalized reduced graphene oxide/silver for highly efficient cancer nanotherapy, N. J. Chem. 42 (15) (2018) 13157–13168.

[15] N. Cai, J. Fu, H. Zeng, X. Luo, C. Han, F. Yu, Reduced graphene oxide-silver nanoparticles/nitrogen-doped carbon nanofiber composites with mesomicroporous structure for high-performance symmetric supercapacitor application, J. Alloy. Compd. 742 (2018) 769–779.

[16] F. Zeng, D. Xu, C. Zhan, C. Liang, W. Zhao, J. Zhang, H. Feng, X. Ma, Surfactant-free synthesis of graphene oxide coated silver nanoparticles for SERS biosensing and intracellular drug delivery, ACS Appl. Nano Mater. 1 (6) (2018) 2748–2753.

[17] C. Shuai, W. Guo, P. Wu, W. Yang, S. Hu, Y. Xia, P. Feng, A graphene oxide-Ag co-dispersing nanosystem: dual synergistic effects on antibacterial activities and mechanical properties of polymer scaffolds, Chem. Eng. J. 347 (2018) 322–333.

[18] Y. Jiang, D. Carboni, L. Malfatti, P. Innocenzi, Graphene oxide-silver nanoparticles in molecularly-imprinted hybrid films enabling SERS selective sensing, Materials 11 (9) (2018) 1–17, 1674.

[19] A. Kumar, B. Mazinder Boruah, X.-J. Liang, Gold nanoparticles: promising nanomaterials for the diagnosis of cancer and HIV/AIDS, J. Nanomater. (2011) 1–17.

[20] V.K. Sharma, C.M. Sayes, B. Guo, S. Pillai, J.G. Parsons, C. Wang, B. Yan, X. Ma, Interactions between silver nanoparticles and other metal nanoparticles under environmentally relevant conditions: a review, Sci. Total Environ. 653 (2019) 1042–1051.

[21] P.K. Singh, P. Kumar, A. Kumar, Unconventional physical methods for synthesis of metal and non-metal nanoparticles: a review, Proc. Natl. Acad. Sci. India A - Phys. Sci. 89 (2) (2018) 199–221.

[22] D.R. Dreyer, S. Park, C.W. Bielawski, R.S. Ruoff, The chemistry of graphene oxide, Chem. Soc. Rev. 39 (2009) 228–240.

[23] S. Gurunathan, J.H. Park, Y.-J. Choi, J.W. Han, J.-H. Kim, Synthesis of graphene oxide-silver nanoparticle nanocomposites: an efficient novel antibacterial agent, Curr. Nanosci. 12 (6) (2016) 762–773.

[24] Q. Bao, D. Zhang, P. Qi, Synthesis and characterization of silver nanoparticle and graphene oxide nanosheet composites as a bactericidal agent for water disinfection, J. Colloid Interface Sci. 360 (2) (2011) 463–470.

[25] Z. Li, J. Gao, X. Xing, S. Wu, S. Shuang, C. Dong, M.C. Paau, M.M.F. Choi, Synthesis and characterization of n-alkylamine-stabilized palladium nanoparticles for electrochemical oxidation of methane, J. Phys. Chem. C 114 (2) (2010) 723–733.

[26] A.M. Dimiev, S. Eigler (Eds.), Graphene Oxide: Fundamentals and Applications, Wiley, Chichester, 2017.

[27] J. Li, D. Kuang, Y. Feng, F. Zhang, Z. Xu, M. Liu, D. Wang, Green synthesis of silver nanoparticles–graphene oxide nanocomposite and its application in electrochemical sensing of tryptophan, Biosens. Bioelectron. 42 (2013) 198–206.

[28] D.I. Rodríguez-Otamendi, V. Meza-Laguna, D. Acosta, E. Alvarez-Zauco, L. Huerta, V.A. Basiuk, E.V. Basiuk, Eco-friendly synthesis of graphene oxide–silver nanoparticles hybrids: The effect of amine derivatization, Diam. Relat. Mater. 111 (2021) 1–21.

[29] S. Kumari, P. Sharma, S. Yadav, J. Kumar, A. Vij, P. Rawat, S. Kumar, C. Sinha, J. Bhattacharya, C. Mohan Srivastava, S. Majumder, A novel synthesis of the graphene oxide-silver (GO-Ag) nanocomposite for unique physiochemical applications, ACS Omega 5 (10) (2020) 5041–5047.

[30] T.T.T. Vi and S.J. Lue, Preparation of silver nanoparticles loaded graphene oxide nanosheets for antibacterial activity, IOP Conf. Ser.: Mater. Sci. Eng. 162 (2016) 012033 (1–5).

[31] H.-S. Kim, H. Lee, K.-S. Han, J.-H. Kim, M.-S. Song, M.-S. Park, J.-Y. Lee, J.-K. Kang, Hydrogen storage in Ni nanoparticle-dispersed multiwalled carbon nanotubes, J. Phys. Chem. B 109 (18) (2005) 8983–8986.

[32] L.-M. Ang, T.S. Andy Hor, G.-Q. Xu, C. Tung, S. Zhao, J.L. Wang, Electroless plating of metals onto carbon nanotubes activated by a single-step activation method, Chem. Mater. 11 (8) (1999) 2115–2118.

[33] P.S. Karthik, A.L. Himaja, S.P. Singh, Carbon-allotropes: synthesis methods, applications and future perspectives, Carbon Lett. 15 (4) (2014) 219–237.

[34] D. Zhang, T. Liu, J. Cheng, S. Liang, J. Chai, X. Yang, H. Wang, G. Zheng, M. Cao, Controllable synthesis and characterization of tungsten disulfide nanosheets as promising nanomaterials for electronic devices, Ceram. Int. 45 (9) (2019) 12443–12448.

[35] V.R. Bakuru, B. Velaga, N.R. Peela, S.B. Kalidindi, Hybridization of Pd nanoparticles with UiO-66(Hf) metal-organic framework and the effect of nanostructure on the catalytic properties, Chem. A Eur. J. 24 (60) (2018) 15978–15982.

[36] D.K. Pattadar, J.N. Sharma, B.P. Mainali, F.P. Zamborini, Anodic stripping electrochemical analysis of metal nanoparticles, Curr. Opin. Electrochem 13 (2019) 147–156.

[37] S.B. Yaqoob, R. Adnan, R.M. Rameez Khan, M. Rashid, Gold, silver, and palladium nanoparticles: a chemical tool for biomedical applications, Front. Chem. 8 (376) (2020) 1–15.

[38] C.P. Adams, K.A. Walker, S.O. Obare, K.M. Docherty, Size-dependent antimicrobial effects of novel palladium nanoparticles, PLoS ONE 9 (2014) 85–98.

[39] K. Chaloupka, Y. Malam, A.M. Seifalian, Nanosilver as a new generation of nanoproduct in biomedical applications, Trend Biotechnol. 28 (11) (2010) 580–588.

[40] V. Leso, I. Iavicoli, Palladium nanoparticles: toxicological effects and potential implications for occupational risk assessment, Int. J. Mol. Sci. 19 (2018) 503.

[41] J. Bandekar, Amide modes and protein conformation, Biochim Biophys. Acta 1120 (2) (1992) 123–143.

[42] N. Alzate-Carvajal, E.V. Basiuk, V. Meza-Laguna, I. Puente-Lee, M.H. Farias, N. Bogdanchikova, V.A. Basiuk, Solvent-free one-step covalent functionalization of graphene oxide and nanodiamond with amines, RSC Adv. 6 (2016) 113596–113610.

[43] N. Alzate-Carvajal, D.A. Acevedo-Guzmán, V. Meza-Laguna, M.H. Farías, L. A. Pérez-Rey, E. Abarca-Morales, V.A. García-Ramírez, V.A. Basiuk, E.V. Basiuk, One-step nondestructive functionalization of graphene oxide paper with amines, RSC Adv. 8 (2018) 15253–15265.

[44] E.V. Basiuk, V.A. Basiuk, V. Meza-Laguna, F.F. Contreras-Torres, M. Martínez, A. Rojas-Aguilar, M. Salerno, G. Zavala, A. Falqui, R. Brescia, Solvent-free covalent functionalization of multi-walled carbon nanotubes and nanodiamond with diamines: looking for cross-linking effects, Appl. Surf. Sci. 259 (2012) 465–476.

[45] P.S. Roy, J. Bagchi, S.K. Bhattacharya, Size-controlled synthesis and characterization of polyvinyl alcohol coated palladium nanoparticles, Transit. Met. Chem. 34 (4) (2009) 447–453.

[46] R.A. Dar, L. Giri, S.P. Karna, A.K. Srivastava, Performance of palladium nanoparticle–graphene composite as an efficient electrode material for electrochemical double layer capacitors, Electrochim. Acta 196 (2016) 547–557.

[47] J. Li, W. Chen, H. Zhao, X. Zheng, L. Wu, H. Pan, J. Zhu, Y. Chen, J. Lu, Size-dependent catalytic activity over carbon-supported palladium nanoparticles in dehydrogenation of formic acid, J. Catal. 352 (2017) 371–381.

[48] B. Delley, An all-electron numerical method for solving the local density functional for polyatomic molecules, J. Chem. Phys. 92 (1990) 508–517.

[49] B. Delley, Fast calculations of electrostatics in crystals and large molecules, J. Phys. Chem. 100 (1996) 6107–6110.

[50] B. Delley, From molecules to solids with the DMol3 approach, J. Chem. Phys. 113 (2000) 7756–7764.

[51] B. Delley, D.E. Ellis, A.J. Freeman, E.J. Baerends, D. Post, Binding energy and electronic structure of small copper particles, Phys. Rev. B 27 (1983) 2132–2144.

[52] J.P. Perdew, K. Burke, M. Ernzerhof, Generalized gradient approximation made simple, Phys. Rev. Lett. 77 (1996) 3865–3868.

[53] S. Grimme, Semiempirical GGA-type density functional constructed with a long-range dispersion correction, J. Comput. Chem. 27 (2006) 1787–1799.

[54] E.V. Basiuk, L. Huerta, V.A. Basiuk, Noncovalent bonding of *3d* metal(II) phthalocyanines with single-walled carbon nanotubes: a combined DFT and XPS study, Appl. Surf. Sci. 470 (2019) 622–630.

[55] V.A. Basiuk, Electron smearing DFT Calc.: A case Study doxorubicin Interact. Single-walled Carbon Nanotub. 111 (2011) 4197–4205.

[56] V.A. Basiuk, O.V. Prezhdo, E.V. Basiuk, Thermal smearing in DFT calculations: how small is really small? A case of La and Lu atoms adsorbed on graphene, Mater. Today Commun. 25 (2020), 101595.

[57] A. Klamt, G. Schüürmann, COSMO: a new approach to dielectric screening in solvents with explicit expressions for the screening energy and its gradient, Soc. Perkin Trans. 2 (1993) 799–805.

[58] B. Delley, The conductor-like screening model for polymers and surfaces, Mol. Simul. 32 (2006) 117–123.

[59] B.T. McGrail, B.J. Rodier, E. Pentzer, Rapid functionalization of graphene oxide in water, Chem. Mater. 26 (2014) 5806–5811.

[60] R. Yuan, J. Yuan, Y. Wu, L. Chen, H. Zhou, J. Chen, Efficient synthesis of graphene oxide and the mechanisms of oxidation and exfoliation, Appl. Surf. Sci. 416 (2017) 868–877.

[61] A. Barth, Infrared spectroscopy of proteins, Biochim. Biophys. Acta 2007 (1767) 1073–1101.

[62] J. Kong, S. Yu, Fourier transform infrared spectroscopic analysis of protein secondary structures, Acta Biochim. Biophys. Sin. 39 (2007) 549–559.

[63] K. Spyrou, P. Rudolf, An Introduction to Graphene, in Functionalization of Graphene, ed. V. Georgakilas, Wiley-VCH Verlag GmbH & Co. KGaA, Weinheim, 1st ed, 2014, Ch. 1, pp. 1–20.

[64] P.-W. Yen, T.-C. Chou, Temperature programmed oxidation of palladium catalyst: effect of support on the oxygen adsorption behavior, Appl. Catal. A-Gen. 198 (2000) 23–31.

[65] X. Liu, X. Zhao, M. Zhou, Y. Cao, H. Wu, J. Zhu, Highly Stable and Active Palladium Nanoparticles Supported on a Mesoporous UiO66@reduced Graphene Oxide Complex for Practical Catalytic Applications, Eur. J. Inorg. Chem. (2016) 3338–3343.

[66] T. Premkumar, K. Lee, K.E. Geckeler, Shape-tailoring and catalytic function of anisotropic gold nanostructures, Nanoscale Res Lett. 6 (547) (2011) 1–12.

[67] E. Ramirez, S. Jansat, K. Philippot, P. Lecante, M. Gomez, A.M. Masdeu-Bultó, B. Chaudret, Influence of organic ligands on the stabilization of palladium nanoparticles, J. Organomet. Chem. 689 (2004) 4601–4610.

[68] J. Chen, B. Yao, C. Li, G. Shi, An improved Hummers method for eco-friendly synthesis of graphene oxide, Carbon 64 (2013) 225–229.

[69] J. Chen, Y. Li, L. Huang, C. Li, G. Shi, High-yield preparation of graphene oxide from small graphite flakes via an improved Hummers method with a simple purification process, Carbon 81 (2015) 826–834.

[70] C. Wang, Z. Liu, S. Wang, Y. Zhang, Preparation and properties of octadecylamine modified graphene oxide/styrene-butadiene rubber composites through an improved melt compounding method, J. Appl. Polym. Sci. 133 (2016) 42907.

[71] W. Gao, The Chemistry of Graphene Oxide, in: W. Gao (Ed.), Graphene Oxide: Reduction Recipes, Spectroscopy, and Applications, Springer, Cham, Switzerland, 2015, pp. 61–95.

[72] I. Dékány, R. Krüger-Grasser, A. Weiss, Selective liquid sorption properties of hydrophobized graphite oxide nanostructures, Colloid Polym. Sci. 276 (7) (1998) 570–576.

[73] A. Kaniyoor, T.T. Baby, T. Arockiadoss, N. Rajalakshmi, S. Ramaprabhu, Wrinkled graphenes: a study on the effects of synthesis parameters on exfoliation-reduction of graphite oxide, J. Phys. Chem. C. 115 (2011) 17660–17669.

[74] N. Díez, A. Sliwak, S. Gryglewicz, B. Grzyb, G. Gryglewicz, Enhanced reduction of graphene oxide by high-pressure hydrothermal treatment, RSC Adv. 5 (2015) 81831.

[75] S. Choudhary, H.P. Mungse, O.P. Khatri, Dispersion of alkylated graphene in organic solvents and its potential for lubrication applications, J. Mater. Chem. 22 (2012) 21032–21039.

[76] H.P. Mungse, O.P. Khatri, Chemically functionalized reduced graphene oxide as a novel material for reduction of friction and wear, J. Phys. Chem. C. 118 (2014) 14394–14402.

[77] G. Wang, J. Yang, J. Park, X. Gou, B. Wang, H. Liu, J. Yao, Facile synthesis and characterization of graphene nanosheets, J. Phys. Chem. C. 112 (2008) 8192–8195.

[78] W.-S. Hung, C.-H. Tsou, M. De Guzman, Q.-F. An, Y.-L. Liu, Y.-M. Zhang, C.-C. Hu, K.-R. Lee, J.-Y. Lai, Cross-linking with diamine monomers to prepare composite graphene oxide-framework membranes with varying *d-Spacing*, Chem. Mater. 26 (9) (2014) 2983–2990.

[79] R. Molaei, K. Farhadi, M. Forough, S. Hajizadeh, Green biological fabrication and characterization of highly monodisperse palladium nanoparticles using pistacia atlantica fruit broth, J. Nanostruct. 8 (1) (2018) 47–54.

[80] P. Nava, M. Sierka, R. Ahlrichs, Density functional study of palladium clusters, Phys. Chem. Chem. Phys. 5 (2003) 3372–3381.

[81] N.T. Tran, M. Kawano, L.F. Dahl, High-nuclearity palladium carbonyl trimethylphosphine clusters containing unprecedented face-condensed icosahedral-based transition-metal core geometries: proposed growth patterns from a centered Pd_{13} icosahedron, J. Chem. Soc. Dalton Trans. 19 (2001) 2731–2748.

[82] V.A. Basiuk, N. Alzate-Carvajal, L.V. Henao-Holguín, E.V. Rybak-Akimova, E. V. Basiuk, Coordination functionalization of graphene oxide with tetraazamacrocyclic complexes of nickel(II): generation of paramagnetic centers, Appl. Surf. Sci. 371 (2016) 16–27.

[83] V.A. Basiuk, E.V. Rybak-Akimova, E.V. Basiuk, Graphene oxide and nanodiamond: Same carboxylic groups, different complexation properties, RSC Adv. 7 (2017) 17442–17450.